THE UNIVERSITY of EDINBURGH

CALCULATIONS OF ELECTRON FLUX SPECTRA IN WATER - IRRADIATED WITH MEGAVOLTAGE ELECTRON AND PHOTON BEAMS WITH APPLICATIONS TO DOSIMETRY.

ALAN E. NAHUM, B.A.

THESIS PRESENTED FOR THE DEGREE OF DOCTOR OF PHILOSOPHY OF THE UNIVERSITY OF EDINBURGH, JULY 1975.

"We have
a Grand Master of chess
made of electronic circuits.

But above all
we have
the ability ....
to seek
the right screw
under the sofa
for hours

This
gives us
wings."

From 'Wings'
by Miroslav Holub.

I hereby declare that the work
described herein was carried out,
and this thesis composed,
entirely by myself.

Alan E. Nahum

June 1975

CONTENTS

ABSTRACT

Certain experimental determinations of $G(Fe^{3+})$, the chemical yield in the ferrous-sulphate dosimeter, had indicated that there was a difference between $G(Fe^{3+})$ for high-energy electron beams and high-energy photon beams of similar effective electron energy, the value being significantly higher for photons. This 'G-value difference' was totally unexpected on the basis of elementary theoretical arguments about the behaviour of the $FeSO_4$ dosimeter. As the most convincing experimental evidence for the 'G-value difference', the work of Law and Naylor (1971, 1972), involved the use of factors to convert the reading of a calibrated ionization chamber to absorbed dose in water (C_E for electron beams, C_λ for photon beams) which were based on similar elementary theoretical arguments, it became evident that this whole area of dosimetry was in need of a detailed investigation.

Consequently, an electron-photon cascade calculation was set up to compute the total electron flux spectrum at various depths in water irradiated by high-energy electron and photon beams between 1 and 40 MeV. The three component parts of the cascade program - Monte Carlo simulations of electron and photon transport, and a depth-independent computation of the electron flux between T_c, the Monte Carlo cutoff, and 100 eV - are described in detail, including some preliminary results which demonstrated that the three separate parts of the complete program were functioning satisfactorily.

The electron flux spectra for monoenergetic electron beams of initial energies of 5, 10, 20 and 30 MeV at several z/r_0 are in close agreement with the results of Berger and Seltzer (1969) although the electron transport model is somewhat different in this work. In addition, depth-dose curves for the electron beams are presented, illustrating the 'tail' due to bremmstrahlung transport.

For the photon beams, efforts were made to use as 'realistic' initial photon spectra as were available, including spectra corresponding to both betatron (thin-target) and linac (thick-target) x-ray machines. The electron flux spectra presented illustrate the transition of the spectrum at the surface to the 'equilibrium shape' beyond the build-up region for the high-energy x-ray beams (e.g. 31 MV betatron x-rays), as well as the very gradual 'softening' of the flux spectrum with depth for the lower energy qualities such as ^{60}Co gamma and 2 MV x-radiation.

Water/air mass stopping-power ratios are derived for the electron and photon beams using the electron flux spectra in a somewhat modified version of the Spencer-Attix theory; the dissipation by the track ends is carefully considered, and the effect of photon interactions in the cavity is taken into account in an approximate manner. Results are presented for three values of the cutoff Δ - 0.001, 0.01 and 0.1 MeV, as well as for the Bragg-Gray ratio evaluated from the primary electron flux spectrum.

For the electron beams, it is shown that similarly comprehensive calculations of the stopping-power ratio by Berger et al. (1975) are not in particularly good agreement with the present results due to the failure of Berger et al. to include the track-end dissipation. For the photon beams, the results are compared to the usual very approximate evaluation of the Bragg-Gray ratio; for the higher energy beams this approximate 'effective electron energy' method gives values that are as much as 2% too low. There is also a difference of the order of 1% between stopping-power values for betatron and linac x-ray beams.

The theory of the important ionization chamber conversion factors, C_E and C_λ, is examined in some detail; the present calculation of these factors as given in the ICRU (1971, 1972) reports is shown to be inconsistent. A careful consideration of the dimensions and composition of the walls of the cavity in a Baldwin-Farmer ionization chamber, to which C_E and C_λ apply, indicates that it is appropriate to treat the B-F chamber as a water-walled air cavity for which the cavity size parameter is about 0.3 - 0.4 MeV. This is very different from the Bragg-Gray assumptions of Greene and Massey in the ICRU C_λ values. In particular, the cavity must behave predominantly as a photon detector at the calibration radiation i.e. ^{60}Co γ- or 2 MV x-rays. The values of C_λ calculated are as much as 4% higher than the ICRU (1969) figures and exhibit a rather different variation with increasing photon energy, going through a maximum at around 4 MV. The C_E values are fairly close to those calculated by Kessaris (1970a) and given in ICRU (1972) but this agreement is partly accidental.

The local energy dissipation spectra, derived from the electron flux spectra for a cutoff of 100 eV, are applied to the calculation of $G(Fe^{3+})$ for the electron and photon beams using an approach similar to that of Burch (1959). It is shown convincingly that there are no theoretical grounds for the 'G-value difference'. When the experimental results of Law and Naylor are re-calculated using the values of C_E and C_λ derived in this work, the 'G-value difference' comes well within experimental error, in line with the theoretical findings. It is finally concluded that no 'difference' exists when the inconsistencies between the derivation of C_E and C_λ are removed.

CHAPTER 1

INTRODUCTION

1.1 BACKGROUND TO THE INVESTIGATION

The increasingly widespread use in radiotherapy of electron and photon beams with maximum energies of up to 30 or 40 MeV has necessitated the development of accurate methods of dosimetry for such high-energy radiations. Ideally one would employ an absolute dosimetric system as provided by calorimetry, where the only physical quantity involved in converting the measured effect, the temperature rise, to the energy absorbed, is the specific heat of the calorimetric medium. Specific heat is, of course, independent of any characteristics of the radiation under measurement.

For routine purposes, a calorimeter is too complex and unwieldy an instrument to be practical, and secondary standards such as the Fricke chemical dosimeter or, more conveniently, the Farmer-Baldwin ionization chamber, must be relied on. Implicit in the use of these secondary instruments is a knowledge of the appropriate factors to relate the measured chemical change or ionization produced by the radiation to the energy absorbed in some standard medium, usually water. In general, these conversion factors vary with the nature and energy of the incident radiation.

The accuracy of the dosimetry depends on how well the conversion factors are known, and consequently much effort has gone into their determination. Theory has played an important part in understanding which

parameters of the radiation the dosimetric conversion factors depend on, and in what way. Calculations can then be made which may be compared with experimental determinations at particular radiation 'qualities' and extended to predict values of the factors at other qualities e.g. at higher radiation energies. The present work is most readily classified as part of this theoretical side of radiation dosimetry, though the fundamental quantity calculated, the energy spectrum of the electron flux in an irradiated medium, has much wider applications in the interpretation of the biological effect of radiation and related areas.

Recent experimental determinations of the G-value, the number of ferric ions produced per 100 eV of energy absorbed, for the Fricke ($FeSO_4$) dosimeter, have seemed difficult to reconcile with the values for $G(Fe^{3+})$ expected from elemetary theoretical considerations. For electron beams, G has been found to be constant at a value of about 15.5 for primary electron energies between 1 and 30 MeV. For photon beams, G appears to increase with increasing photon energy, rising from 15.5 at ^{60}Co quality to around 15.9 for bremsstrahlung beams with a maximum photon energy of 20 MeV or more.

If we take the average primary photon energy, for a 20 MV X ray spectrum, to be 8 MeV, then the average initial energy of the electrons produced in the irradiated medium, in this case the $FeSO_4$ solution, will be about 4 MeV. In this very approximate manner, we might expect that a 20 MV X ray beam is equivalent

Figure 1.1 THE 'G-VALUE DIFFERENCE'

(adapted from Law and Naylor, 1972)

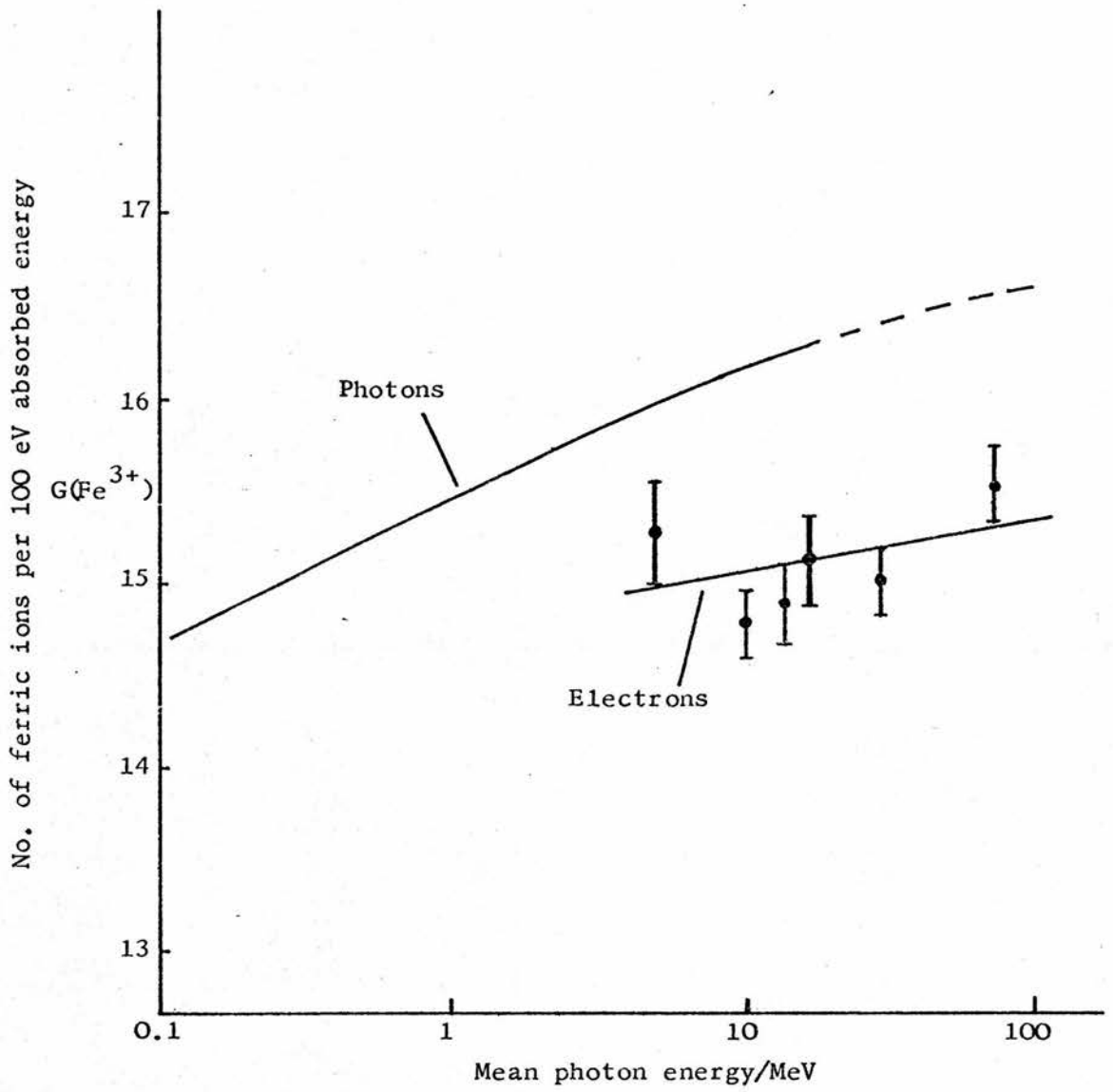

The curve for photons was drawn by Law and Naylor on the basis of their earlier photon measurements (Law and Naylor, 1971).

to a 4 MeV primary electron beam. Given that it is the electrons which produce the ionizations and excitations leading to the observed chemical changes, and that the Ferrous Sulphate solution has no way of distinguishing between an electron of a certain energy originating from a photon interaction and one from a primary electron beam, it has been argued that $G(Fe^{3+})$ should be the same for the 20 MV X ray beam as for, say, a 5 MeV electron beam. Hence there is this puzzling 'G-value difference' between electron and photon beams in the MeV energy range.

From measurements using an aluminium calorimeter, Almond (1968, 1974) reported confirmation of the G-value difference, finding a value of 15.9 ± 0.35 for 22 MV X radiation in agreement with the value recommended in a review by Shalek and Smith (1969). With the same calorimeter, Almond (1967) had previously obtained G-values in the range $15.3\text{-}15.4 \pm 0.35$ for electron beams with primary energies between 13 and 24 MeV. Law and Naylor (1972), from their G determinations using an ionisation chamber to measure the dose to the $FeSO_4$ solution, provided further evidence for the G-value difference between 'equivalent' electron and photon radiation. These authors considered that the difference lay outside reasonable estimates of experimental error. Figure 1.1, taken from their paper, shows up the discrepancy; the primary energies of the electron and photon radiations have been represented by a 'mean photon energy', the basis for

which is explained in their paper following the arguments about 'equivalent' energy outlined above.

The report of the International Commission on Radiation Units and Measurements on electron dosimetry (ICRU, 1972) recommended a G-value for the $FeSO_4$ dosimeter of 15.7 for energies between 2 and 30 MeV. This value is considerably higher than that obtained in several calorimetric determinations for electron beams, which would put G around 15.4. Greening (1971) has stated that the value of 15.7 for electron beams was chosen largely on the basis of the recommendations of ICRU (1969) which dealt with dosimetry for photon beams. In that report, a G-value of 15.7 was recommended for 11 to 30 MV X ray beams. Thus the ICRU had argued just as we have that there could be no difference between G for 'equivalent' energy electron and photon beams, in spite of experimental evidence to the contrary. This was clearly an unsatisfactory situation.

Almond's photon beam G-value is especially valuable as it is, to date, the only calorimetric determination for photons above ^{60}Co (1.25 MeV) in energy, besides Fregene's (1967) determination for a 14 MV X ray beam. All the other determinations of $G(Fe^{3+})$ for high-energy photon beams have been carried out using an ionisation chamber and therefore can be no more accurate than the accuracy to which the factor converting ion chamber reading to absorbed dose is known. However, the appropriate factor for photon radiation of a particular energy, known as C_λ, has,

Figure 1.2 IRRADIATION OF A PHANTOM BY A PHOTON BEAM (SCHEMATIC).

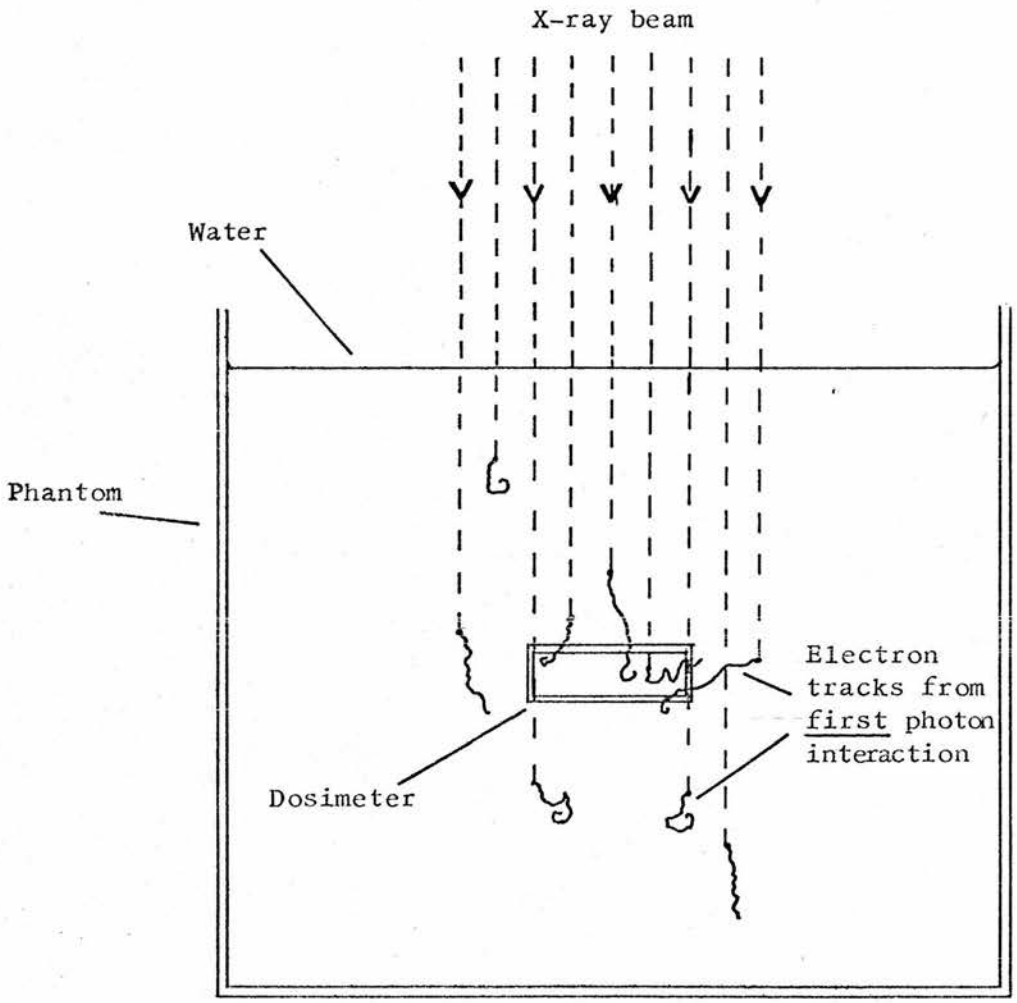

up to now, been calculated by assigning to an X-ray beam an 'equivalent electron energy' on the basis of precisely the same theoretical reasoning as has been used in connection with the G-value difference (Greene and Massey, 1968; SCRAD, 1971). It now becomes clear that elementary assumptions about the equivalence of photon and electron beams need careful investigation. The calculations reported in this work were primarily designed to carry out such an investigation.

How well, in reality, would we expect the 'equivalent electron energy' description of a photon beam to account for the variation of $G(Fe^{3+})$ or C_λ with maximum photon energy? Consider the situation depicted in figure 1.2. An X ray beam is incident on a water phantom. The dosimeter occupies a small volume at a depth of several centimetres. The beam consists of a continuous distribution of photon energies up to 20 MeV. The incident photons interact with the medium at various depths, giving rise to a broad distribution of electron (and positron) energies. Some of these electrons have sufficient kinetic energy to dissipate their energy along a track several centimetres long. Thus many of the electrons crossing the dosimeter volume will have originated from photon interactions some way 'upstream'. We would expect the spectrum of 'primary' electron energies 'seen' by the dosimeter to be very complicated, in no way resembling that produced by a monoenergetic electron beam, where all the electrons 'originated' from the

surface with the same energy.

As we shall see in later sections of this work, while calculations of both C_λ and $G(Fe^{3+})$ utilize the energy spectrum of electrons within the dosimeter, they depend on this spectrum in very different fashions. The chemical yield varies with a quantity known as the Linear Energy Transfer of the electrons and is critically dependent on the relative numbers of high-energy primary and low-energy secondary electrons. The absorbed dose to ionisation ratio is influenced primarily by the energy spectrum of the primary electrons above 1 MeV. Neither is obviously a simple function of the mean energy of the electrons. The starting-point, then, for any credible theoretical determination of the conversion factors used in the dosimetry of photon and electron beams, is a calculation of the energy spectrum or 'flux' of all the electrons dissipating their energy in the dosimeter volume.

1.2 CONCEPTS AND DEFINITIONS OF RADIATION QUANTITIES

Some of the quantities used in connection with the energy dissipation of radiation in a medium are introduced in this section.

1.2.1 Absorbed Dose

The absorbed dose, D, is the quotient of $d\bar{\epsilon}$ by dm, where $d\bar{\epsilon}$ is the mean energy imparted by ionizing radiation to the matter in a volume element of mass dm (ICRU, 1971).

$$D = \frac{d\bar{\epsilon}}{dm} \qquad .....(1.1)$$

Note that this is a non-stochastic quantity. We are not concerned with the fluctuations in the energy imparted to a small volume. It is important also to distinguish between the initial kinetic energy of the particles liberated in a volume, and the energy actually deposited in that volume by these particles. Some of the energy may escape from the volume either as bremsstrahlung or by diffusion.

1.2.2 Electron Flux

ICRU (1971) defines the fluence, Φ, of particles as the quotient of dN by da, where dN is the number of particles which enter a sphere of cross-sectional area da. The flux density or fluence rate is then the fluence per unit time. This distinction is not of concern in this work as only time-independent situations are considered. The quantity of central importance in this investigation is the distribution of electron flux density or flux in kinetic energy, $\Phi(T)$. The quantity $\Phi(T)dT$ is then the number of electrons

per unit area with kinetic energies between T and T+dT.

If the distribution $\Phi(T)$ is integrated over a volume V, one obtains the distribution of electron path length in energy in this volume, F(T)

$$F(T) = \int_V \Phi(T)\, dV \qquad .....(1.2)$$

It is this quantity, F(T), that will be referred to throughout this work as the electron flux, or, more fully, the energy spectrum of the electron flux. It is the same quantity as the so-called electron slowing-down spectrum. The symbol F(T) will also be used to refer to the number per unit area except where it is necessary to differentiate between this distribution and its average over a volume, the pathlength spectrum. The electron flux should be carefully distinguished from the volume distribution of electron energies, N(T).

1.2.3 Stopping Power

Charged particles lose energy in a slowing-down medium in a large number of predominantly very small steps. The concept of stopping power is therefore meaningful. This is not the case for photon absorption, for instance. The stopping power of a material for charged particles is the rate of loss of energy with distance. It is generally written as S or dT/dx. In this work it usually refers to electron stopping power. Division by the density of the material, ρ, yields the mass stopping power, S/ρ. The unit of distance is then of the form $cm^2.g^{-1}$.

The mass stopping power of condensed materials and gases therefore become comparable.

The total stopping power, S_{tot} or $(dT/dx)_{tot}$, is the sum of the collision stopping power, S_{col}, and the radiative stopping power, S_{rad}.

$$S_{tot} = S_{col} + S_{rad} \qquad .....(1.3)$$

For electrons in water, S_{tot} varies from about 2 $MeV.cm^{-1}$ in the MeV kinetic energy region to a maximum of around 300 $MeV.cm^{-1}$ at about 100 eV.

1.2.4 Linear Energy Transfer (LET) and LET distributions

The occasional large collisional energy losses that a charged particle experiences give rise to energetic secondary electrons (δ-rays) which may result in the energy of the δ-ray being deposited an appreciable distance from the track of the primary particle. This had led to the use of a collision stopping power that excludes energy losses above a certain energy, Δ, and is termed the Linear Energy Transfer, written as L_Δ or $(dT/dx)_\Delta$. The cutoff, Δ, is usually expressed in electron volts. The term local LET or local stopping power is frequently used in the literature. 'Local' refers to the energy losses less than the cutoff that are locally deposited i.e. close to the primary electron track.

The chemical and biological effect of radiation can often be shown to be a function of LET. This may refer to an average value, $\bar{L}_\Delta$, or to some sort of LET

Figure 1.3 DISTRIBUTION OF ABSORBED DOSE IN LET FOR WATER FOR THE ELECTRONS SET IN MOTION BY ^{60}Co GAMMA RAYS.
(adapted from ICRU, 1970)

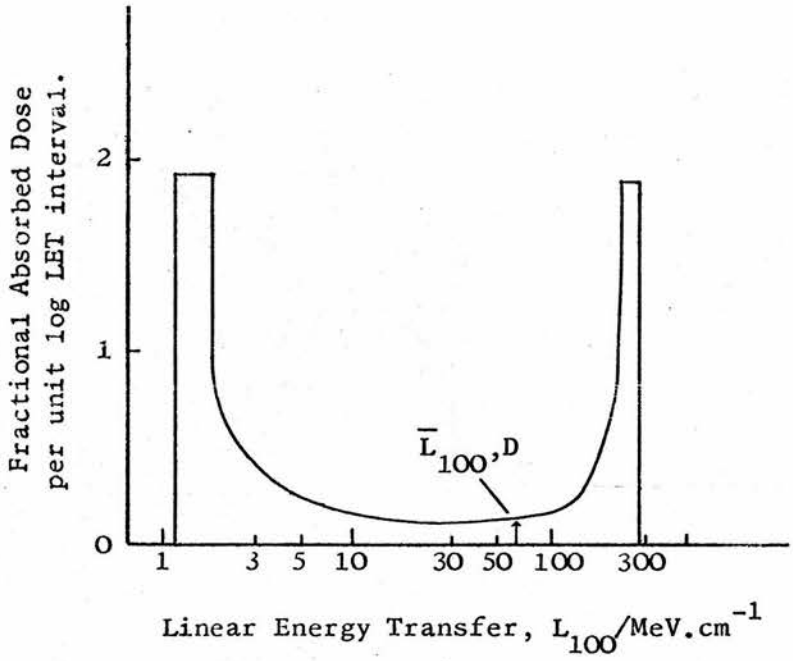

The cutoff is 100 eV. The peak at the low-LET end represents the local dose due to the high energy electrons. The peak at the high-LET end is due to the very low energy secondary electrons.

distribution. The distribution of absorbed dose in LET, $D(L_\Delta)$, is the most useful form of LET distribution for this investigation. The quantity $D(L_\Delta)dL$ represents the fraction of the absorbed dose, D, delivered in energy transfers less than Δ(the local dose), by electrons with an LET between L_Δ and $L_\Delta + dL$. An example of this type of LET distribution is shown in figure 1.3, for the dose delivered by electrons set in motion by ^{60}Co gamma rays in water. Here the cutoff is 100 eV. The value of the absorbed dose average, $\bar{L}_{100}$, is indicated on the figure. The use of an average value to characterise the typical double-peaked distribution is often unsatisfactory.

1.2.5 Local Energy Dissipation Spectrum

This distribution of the local absorbed dose, for a particular cutoff Δ, is the same as the distribution $D(L_\Delta)$ discussed above, except that the variable L_Δ is transformed into the electron kinetic energy, T. Burch (1957a etc.) made extensive use of this distribution to describe the quality of different radiations. He denoted it by Q_T and his nomenclature is followed here. The distribution Q_T is of particular use when the radiation effect under study is suspected of being a function of electron kinetic energy rather than local LET. Q_T can be related to $D(L_\Delta)$ by

$$Q_T \, dT = D(L_\Delta) \, dL \qquad .....(1.4)$$

1.2.6 Stopping-Power Ratios and Related Quantities

The absorbed dose, D_m, in an irradiated medium in the immediate vicinity of a small gas-filled cavity may be determined from the ionization in the cavity by the Bragg-Gray equation:

$$D_m = J_g \, (\bar{W}/e) \, \bar{s}_{mg} \qquad .....(1.5)$$

where

J_g is the quotient of the ionization charge by the mass of gas,

$\bar{W}$ is the average energy expended by electrons in the gas per ion pair formed,

e is the charge of the electron, and

$\bar{s}_{mg}$ is a weighted mean ratio of the mass stopping power of the medium to that of the gas for the electrons crossing the cavity.

From this relation, it can be seen that the absorbed dose to ionization ratio, D/J, is simply related to the stopping-power ratio, $\bar{s}_{mg}$. Spencer and Attix (1955) modified the Bragg-Gray theory to take explicity into account the size of the cavity, via a cutoff energy, Δ. The stopping powers used to evaluate the stopping-power ratio, $s_{air}^{water}(\Delta)$, as it is often written, are then the restricted collision stopping powers, $(dT/dx)_{\Delta}^{water}$ and $(dT/dx)_{\Delta}^{air}$. The stopping-power ratios discussed in the present work always refer to an air cavity, usually with carbon or water (or water-equivalent) walls.

Two functions of the stopping-power ratio frequently employed in what is to follow are C_E, for primary electron beams of initial energy E or T_o, and the corresponding quantity for photon beams, C_λ. These factors are used to relate the absorbed dose in water, D_W, to the reading of a calibrated, standard type of ionization chamber, such as the Baldwin-Farmer chamber:

$$D_W = R.N_c.C_E \qquad .....(1.6)$$

where R is the instrument reading corrected for temperature, pressure and humidity and N_c is the exposure calibration factor given by a standardizing laboratory for ^{60}Co gamma rays or 2 MV X rays. The evaluation of C_E and C_λ involves the calculation of water/air stopping-power ratios for the particular photon or electron beam. No distinction need be made at this stage of the work between D/J ratios, $\bar{s}_{mg}$ and C_E (for electron beams) or C_λ (photon beams) when calculations of the conversion ratios for ionization chambers are being discussed.

1.3 REVIEW OF THE LITERATURE

There now follows a review of the work done in determining the electron flux in a medium irradiated by electrons or photons. Emphasis is placed on the applications of the flux spectrum to yield LET distributions, stopping-power ratios and other quantities of use in specifying the quality of radiation beams. Finally, we look closely at the applicability or otherwise of published work to the problems outlined in section 1.1.

1.3.1 Theoretical

1.3.1.1 Depth-independent calculations

If it is assumed that an electron loses energy in infinitely small steps, then the flux, F(T), is simply given by the reciprocal of the total stopping power. This is the continuous-slowing-down approximation (c-s-d-a). It specifically disregards the production of secondary electrons. Cormack and Johns (1952) and Johns et al. (1954) used this approximation to give the primary electron flux in water irradiated with 200 kV, 1 MV and 25 MV X radiation. They tabulated the initial energy distributions of the Compton and pair electrons produced by photons of energy 10 keV up to 25 MeV. These distributions were used together with theoretical photon energy spectra for the X ray beams to give the energy distribution of all the electrons set in motion, $N(T_i)dT_i$. The electron flux, F(T), was then given by

$$F(T) = \frac{1}{S(T)_{total}} \int_{T}^{T_{max}} N(T_i) dT_i \qquad .....(1.7)$$

where a 'running total' had been performed over the distribution $N(T_i)$ above T. It should be noted that no scattered photon radiation was taken into account except for the 200 kV X rays and equilibrium conditions were assumed over a distance equal to the range of the maximum-energy electron. From their flux distributions, Cormack and Johns (1952) evaluated the mean ion density, a quantity that can be related to mean LET.

Spencer and Fano (1954) tackled the problem of calculating the total electron flux including all generations of secondary electrons. They started from the "slowing down equation"

$$\int_{0}^{T} F(T_o,T)\ k(T,q)\ dq = \int_{0}^{T_o} F(T_o,T+q)\ k(T+q,q)\ dq \qquad .....(1.8)$$

where $k(T,q)dq$ is the probability per unit path length that an electron of energy T experiences an energy loss between q and q+dq. This equation does not contain any position or angular variables as it assumes that the electrons of initial energy T_o are slowing down in a uniform, infinite medium. The Moller relativistic electron-electron cross-section was employed to give the initial energy distribution of the secondary electrons. Bremsstrahlung loss was also included.

Spencer and Fanos' solution of this equation was mathematically rather involved, making use of a recursion procedure. Their results, for $F(T_o,T)$ for

Figure 1.4 SLOWING-DOWN SPECTRUM:
O.103 MeV ELECTRONS IN WATER.

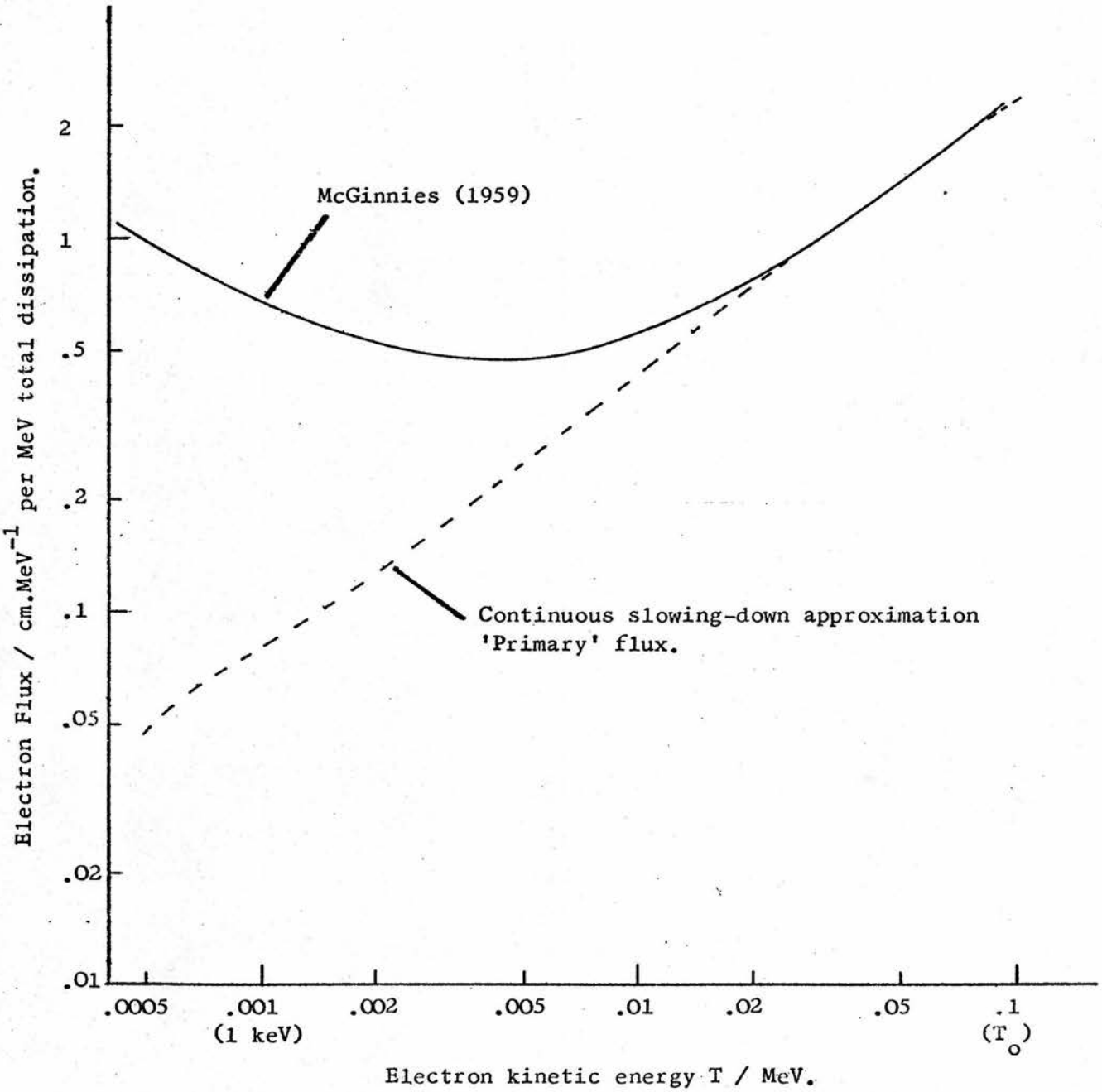

electron source energies of $4mc^2$ and $80mc^2$ in aluminium and lead, were compared to the flux given by the c-s-d-a. They found only small differences close to the source energy, due to the electrons 'missing out' some of the energy levels because of the occasional large losses. At lower energies, very large numbers of secondary electrons could be seen, giving a total flux very much greater than the flux from the continuous-slowing-down model.

McGinnies (1959) carried out extensive computer calculations of the electron flux, using the Spencer-Fano theory. She produced tabulations of the flux in units of tracklength, differential in electron kinetic energy, for nine elements and compounds, including water, for source energies ranging from 10 MeV to 6 keV. McGinnies discussed the limitations to the accuracy of the calculations, the principal one being the use of the Moller free electron cross-section at electron energies comparable with the binding energies of the atomic electrons in the slowing-down media. For the light elements, the error was expected to be small down to 400eV, the lowest energy at which values of the flux were given. The results of McGinnies for electrons of initial energy 0.103 MeV are plotted in figure 1.4. They are compared to the flux given by the c-s-d-a for the same normalization, calculated from the total stopping power (for the same mean ionization potential, I = 74 eV, as McGinnies used) by the writer.

Spencer and Attix (1955) took into account the production of energetic secondary electrons or δ-rays in a refinement of the Bragg-Gray cavity ionization theory. They required the total electron flux down to an energy cutoff, Δ. For a particular cavity size, Δ was the kinetic energy of electrons that could just cross the cavity. From an approximation to the Spencer-Fano theory, they derived the function $\bar{R}(T_o,T)$, which represented approximately the ratio of the total electron flux to the flux of primary electrons alone. They calculated the total flux, $F(T_o,T)$, from

$$F(T_o,T) = \bar{R}(T_o,T)/(dT/dx)_{total}$$

They could then evaluate a stopping-power ratio $s^{carbon}_{air}(T_o,\Delta)$ by averaging the restricted stopping-power, $L_\Delta(T)$, over the total electron spectrum down to the cutoff energy Δ. The calculations of stopping-power ratios for ionization chambers of different sizes made of different materials were in much closer agreement with experimental measurements than had hitherto been the case when δ-rays had been disregarded in the Bragg-Gray theory.

Burch (1955) also proposed a theory of cavity ionization which required the total electron flux and he evolved a method of taking into account the production of δ-rays (Burch and Bird, 1956; Burch, 1957, 1957a) which was mathematically much less involved than the Spencer-Fano theory. Collisions were divided into two categories; those below 100 eV

were considered to be 'local', the energy being dissipated on the track of the parent electron; those δ-rays above 100 eV were treated as separate tracks with their own rate of energy dissipation per unit tracklength. The choice of 100 eV was somewhat arbitrary, following Lea (1946) who assumed that 100 eV electrons produced clusters of ionizations sufficiently compact to behave as units with an associated volume no bigger than that of an isolated primary ionization.

Burch divided the electron kinetic energy range into logarithmic intervals. Appearing in a given interval were:

i) Electrons from the interval immediately above by continuous-slowing down.

ii) δ-rays produced by electrons in higher energy intervals.

iii) Electrons that 'jumped' over the interval immediately above due to large energy losses due to either δ-ray or bremsstrahlung production.

iv) Primary electrons that had their initial energy in this interval e.g. electrons produced by X-ray photons.

The energy distribution of δ-rays was given by the Moller cross-section and the bremsstrahlung losses were calculated using the theoretical expressions of Bethe and Heitler. Burch started at the highest energy interval, and worked his way down in stepwise manner through all the energy intervals down to the lowest one which was 0-100 eV. In this way the number of

electrons, N_T, appearing in each interval was calculated. Burch then derived his local energy dissipation spectrum, $Q_T \Delta T$ from the expression

$$Q_T \Delta T = \frac{N_T \ (dT/dx)_{100eV} \cdot \Delta T}{(dT/dx)_{total}} \qquad .....(1.9)$$

The distribution $Q_T \Delta T$ was calculated for 25 MV betatron X rays, 2 MeV and 1 MeV electrons, ^{60}Co γ rays, 220 kV primary X rays, 200 kV total X rays, tritium β particles, and also ^{210}Po and 1 MeV α particles. The internal consistency of the calculations was checked by verifying that $\Sigma Q_T \Delta T$ was equal to the total initial energy.

Burch and Bird (1956) calculated average $(dT/dx)_{100eV}$ values from the $Q_T \Delta T$ distributions for the different primary photon radiations. They compared these values with mean LET values derived from the 'average linear ion densities' calculated for the same radiations by Cormack and Johns (1952). The inclusion of δ-rays resulted in large differences between the two sets of calculations. Burch and Bird also found that the difference between $\bar{L}_{100}$ for the 25 MV X rays and 200 kV X rays was only about 20%, whereas the Cormack and Johns calculations, based on the c-s-d-a, had resulted in a difference by a factor of nine. Unfortunately, the situation was confused by Burch (1957), who derived different values for the mean LET from his $Q_T \Delta T$ distributions, based on a different set of figures for $(dT/dx)_{100eV}$ below 2.4 keV. These 'revised' L_{100} values, deduced from some experimental observations

of the ranges of low-energy electrons by Davis (1955), differed from those values Burch had used previously by as much as a factor of three at 100 eV. This discrepancy underlined the uncertainty in electron stopping-power values below a few keV.

Burch's work is especially important with respect to the present investigation as he went on to use the local energy dissipation spectra he had previously calculated in a theoretical treatment of the variation of the yield of chemical dosimeters with radiation quality (Burch, 1959). Employing a simplified reaction scheme for the irradiation of aereated solutions of ferrous and ceric sulphate in 0.8 N H_2SO_4 (the usual 'prescription' for the $FeSO_4$ dosimeter), and the Jaffe intratrack combination formula to give the LET dependence of the reaction yields, Burch was able to derive an approximate relation between the local LET and $G(Fe^{3+})$. This relation was calculated to be consistent with a $G(Fe^{3+})$ of 15.47 for Co^{60} radiation and 6.13 for Po^{210} α radiation taken from the literature on experimental work. From his theory, Burch obtained a value of 12.9 for the tritium β particle $G(Fe^{3+})$, in complete agreement with the 'best' experimental determinations at the time. However, the theory was not in such good agreement with experimental $G(Fe^{3+})$ values for higher energy radiations. In particular, Schuler and Allen (1956) had determined G for 2 MeV electrons as 15.45 ± 0.11, whereas Burch's theory gave 15.7. We can note here that Burch did not allow for

scattered photon radiation in his ^{60}Co γray $Q_T\Delta T$ calculations and that he used the same set of 'high' $(dT/dx)_{100eV}$ values as he had done in Burch (1957). Considerable use will be made of a modified version of Burch's $G(Fe^{3+})$ vs local LET relation later in this work.

Schneider and Cormack (1959) investigated the validity of the calculation of the primary electron flux from the continuous-slowing-down model in a Monte Carlo calculation. In an earlier electron slowing-down calculation, Till (1954) had devised a particularly simple method of taking into account all generations of secondary electrons. Till assumed that the "continuous" model gave the correct primary flux, $F_1(T)$, from the same expression (equ. 1.7) that Johns et al. (1954) had given. He used this primary flux and the collision cross section $k(T,T_i)$ to calculate the production of the first generation of secondaries, $N_2(T_i)$

$$N_2(T_i)\, dT_i = \left[\int_{2T_i}^{T_{max}} N_1(T)\, k(T, T_i)\, dT\right] dT_i \qquad .....(1.10)$$

yielding a secondary electron flux of

$$F_2(T) = \frac{1}{S(T)} \int_{T}^{T_{max}/2} N_2(T_i)\, dT_i$$

The fluxes N_3, N_4, etc., of higher order were found progressively and added together to give the total flux.

Figure 1.5 THE TWO-GROUP MODEL OF ELECTRON SLOWING-DOWN.

(adapted from Schneider and Cormack, 1959)

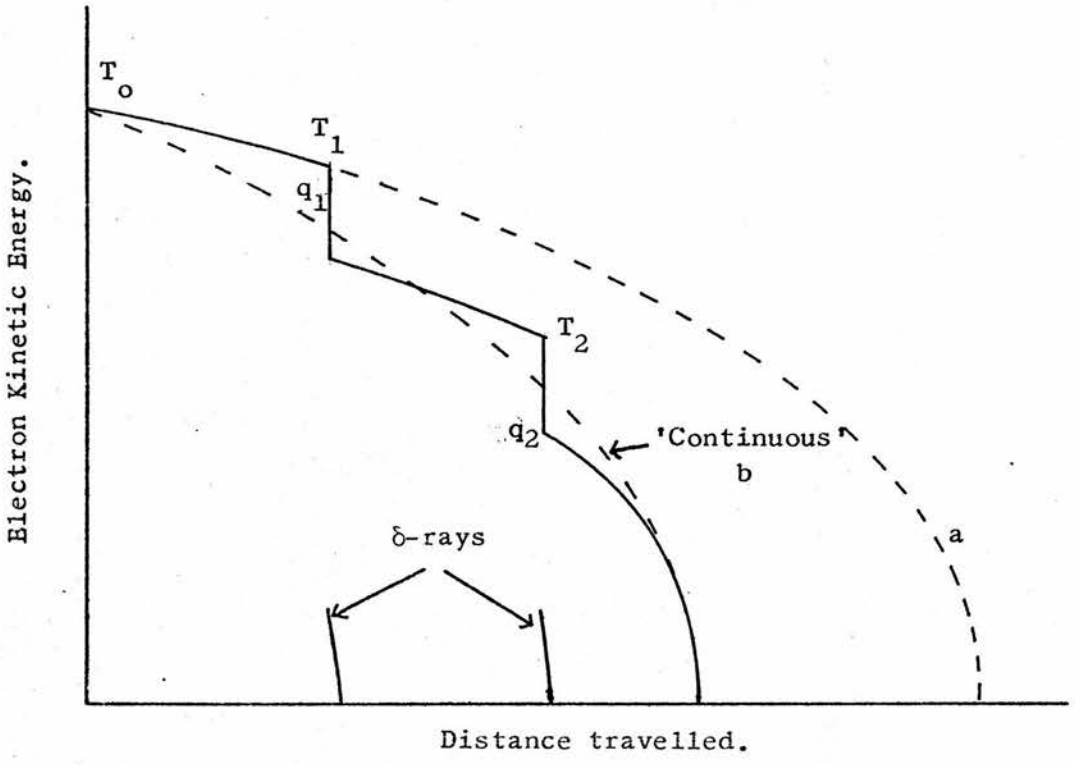

Energy-distance plot of a hypothetical electron case history. Curve 'a' depicts the 'smooth' energy loss of the two-group model of electron slowing down. Curve 'b' depicts the energy loss involved in the 'continuous' model.

In their Monte Carlo scheme, Schneider and Cormack divided the electron energy losses into 2 groups, in much the same way as Burch had done. Collisions resulting in an energy loss greater than the cutoff were assumed to give rise to δ-rays and to the consequent 'skipping' of energy regions by the primary electrons. These 'major' or 'catastrophic' collisions were randomly sampled for individually from the electron-electron inelastic collision cross-section in Monte Carlo fashion (see chapter 2). Between these major collisions, it was assumed that the electron lost energy continuously at a rate $(dT/dx)_{\Delta}$, the collision stopping-power restricted to losses less than Δ. This schematization of energy losses is depicted in figure 1.5, re-drawn from the Schneider and Cormack paper. They carried out Monte Carlo calculations for source energies of 50 keV and 30 keV and cutoffs of 0.1 and 0.3 keV. The calculations yielded the primary electron volume distributions, $N(T,\Delta)$ i.e. the numbers of electrons per unit volume existing at energy level T. The primary electron flux, $F_1(T)$, is then given by

$$F_1(T) = \frac{1}{(dT/dx)_{\Delta}} \cdot N(T,\Delta)$$

They found that the results for the primary flux were very similar for either value of the cutoff, Δ, and were in excellent agreement with the flux calculated from the continuous model. The only deviation was close to the source energy, where a peak at T_o was

evident in the more exact calculation. This peak for monoenergetic sources was also noted by Spencer and Fano (1954). Similar close agreement between the c-s-d-a flux and the Monte Carlo primary flux was obtained for a source energy of 1.5 MeV and a Δ of 3 keV. Schneider and Cormack were able to conclude that Till's method of calculating the total electron flux using the c-s-d-a was completely justified. This is an important conclusion for this work as a method essentially the same as Till's has been used to calculate the low-energy component of the electron flux. This is described in chapter 5.

Danzker, Kessaris and Laughlin (1959) calculated the total electron flux for several kilovoltage X ray beams, 1 MV X rays, ^{60}Co gamma rays and 25 MV betatron X rays. From the primary photon energy flux, they derived the primary electron source distribution. They integrated this to obtain the cumulative primary electron source distribution. They then made use of the ratio of total to primary electron flux $\bar{R}(T_o,T)$ at energy T for source electrons of initial energy T_o, as derived by Spencer and Attix (1955), to calculate the cumulative <u>total</u> electron source distribution Q(T). Finally, the total electron flux, F(T), was given by dividing this total electron source distribution, Q(T), by the total stopping power. Thus their method was parallel to that of Cormack and Johns (1952), except that Danzker et al. could calculate the <u>total</u> electron flux with the use of the function $\bar{R}(T_o,T)$.

They compared the integrated electron source density, Q(T), with the function N_T from Burch (1957a) for the ^{60}Co and 25 MV photon radiations. The good overall agreement indicated that both the Spencer-Fano theory and Burch's simpler, stepwise method for including the secondary electrons produced very similar results. From the total electron flux, two distributions of the number of electrons per unit LET were derived. In one case the LET was the collision stopping power restricted to losses less than a cutoff, Δ, of 5.1 keV. These LET distributions were not the more useful absorbed dose per unit LET distributions described in the previous section. However, Danzker et al. did give the expression for calculating the local absorbed dose, D, from the electron flux, F(T), first derived by Spencer and Attix (1955):

$$D = \int_{\Delta}^{\infty} F(T)\ S(T,\Delta)\ dT/\rho \qquad \ldots\ldots(1.11)$$

where ρ is the density and $S(T,\Delta)$ is the local stopping power. Absorbed dose to cavity ionisation ratios, D/J, were calculated for all the photon radiations using the Spencer-Attix theory, for a 5.1 keV cutoff, corresponding to a 0.6 mm air cavity. Values of D/J were evaluated for water-, lucite- and polystyrene-walled cavities.

Bruce et al. (1963) performed calculations of the LET distribution of absorbed dose resulting from 250 kV X radiations and ^{137}Cs and ^{60}Co gamma rays. Their method of deriving the total electron flux was

very similar to that of Danzker et al. (1959) except that they used the computer program of McGinnies (1959) to calculate the electron slowing-down spectrum, $F(T_o,T)$, in water for different initial electron energies, T_o. In fact, they extended her calculations down to T = 0.11 keV. Bruce et al. pointed out that as the binding energy of the K electrons of oxygen was 0.48 keV, the extension to lower energies was not entirely valid, but that no satisfactory theory existed which took into account the effect of the binding energy on electron scattering.

The photon spectra for the 250 kV radiation were obtained from scintillation spectroscopy, both at the surface and at a depth of 10 cm in water. Electron source distributions were then calculated corresponding to the primary photon radiation and also to the primary plus scattered radiation at a depth in water. The slowing-down spectra, $F(T_o,T)$ for monoenergetic electron sources, were used together with the source distributions to yield the total electron flux at the surface and at 10 cm depth. It is important to note that this calculation was only possible because the ranges of the photon-ejected electrons are very much less than the change of depth that results in an appreciable change in the photon spectrum. The dose distribution in LET was calculated from the flux spectrum for a cutoff at 100 eV, showing the relatively small change in this distribution with depth. Bruce et al. calculated LET distributions for ^{137}Cs and ^{60}Co gamma

Figure 1.6 LET DISTRIBUTIONS PRODUCED BY ^{137}Cs GAMMA RAYS IN WATER: TWO DEPTHS.

(adapted from Bruce et al., 1963)

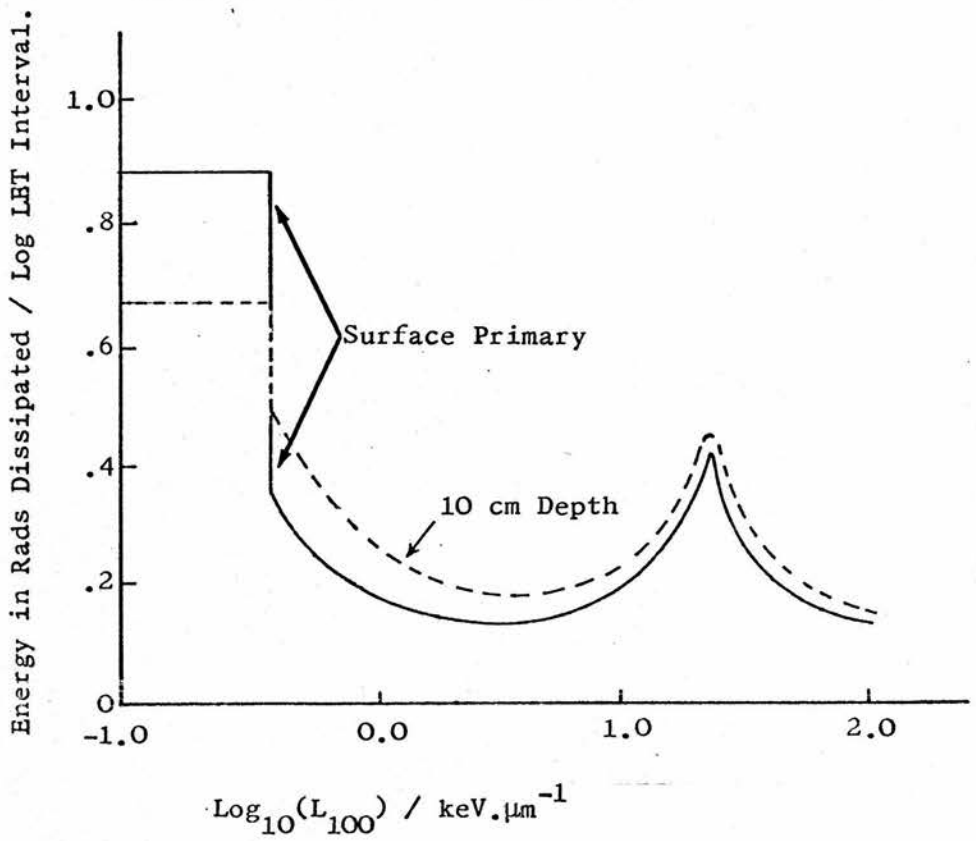

The cutoff is 100 eV. The areas under the histograms represent the energy dissipated by electrons with LET from 0.1 to 0.4 keV.μm^{-1}.

rays, at depths of 0 and 10 cm. The spectra of scattered photons at a depth for these radiations was calculated by the Monte Carlo method. For ^{60}Co gamma rays, the primary radiation has an energy of 1.25 MeV, which can give rise to electrons of maximum energy 1.1 MeV. These electrons have a range of about 0.5 cm. Thus to disregard diffusion of the electrons is still justified even for ^{60}Co gamma radiation. The LET distributions that Bruce et al. calculated for ^{137}Cs radiation are given in figure 1.6.

Abillon (1972) obtained the complete electron slowing-down spectrum in gaseous methane irradiated with monoenergetic photon sources. Her calculations assumed an infinite medium as she used the initial electron distribution produced by the complete absorption of the photons in the medium. Her results do not, therefore, correspond to any practical irradiation geometry, except for very low initial photon energies. Abillon did include Auger electrons, however, and in this respect her calculations were more rigorous than any so far discussed. Burch (1957a) considered that Auger electrons were of little importance in water. This assumption is looked at critically in the work to be described.

All the calculations of electron flux mentioned above have one feature in common. None of them takes into account the transport of the electrons. As we have seen, for photon energies of up to about 1 MeV, it is justified to assume that the electrons dissipate

their energy at their point of origin. The electron flux, $F(T_o,T)$, as obtained from McGinnies' calculations or the local energy dissipation spectrum, $Q_T\Delta T$, that Burch calculated for a 1 MeV electron source are averages over the complete electron track. They cannot yield information about the change in electron flux with depth in a medium irradiated with a beam of electrons.

1.3.1.2 Depth-dependent calculations

A lot of work has been carried out on the transport of electrons through an absorbing medium. The reason behind much of the recent effort has been the strong dependence of the stopping-power ratio for use with air ionisation chambers on electron energy above about 1 MeV. This energy dependence is due to the so-called Density Effect which at relativistic energies reduces the stopping power of electrons in condensed materials below the theoretical value calculated on the basis of interactions with the individual atoms of the medium. Consequently, it is present in water or carbon, but not in air. Thus it becomes important to know the change of the electron energy spectrum with depth in a medium irradiated with a beam of high-energy electrons in order to calculate the absorbed dose of ionisation ratio, D/J.

Spencer (1955, 1959) tackled the problem of the spatial energy dissipation of electrons in a medium by the moment-method based on the Lewis equation for electron transport. The applications were limited to an unbounded and homogeneous medium. Spencer (1955)

obtained depth-dose distributions for electron beams below 1 MeV incident on a variety of substances. He extended the calculations up to 10 MeV for a number of low atomic number elements (Spencer, 1959). Kessaris (1964) further developed the moments method, taking into account the production and absorption of bremsstrahlung and the effects of secondary electron production, but the spatial diffusion of the electrons was still calculated assuming continuous-slowing down. He calculated the depth-dose distributions for plane, monodirectional and monoenergetic electrons beams of energies 39, 30 and 20 mc^2 incident on an infinite water medium. Kessaris (1966, 1970) was able to obtain the electron flux spectra at various depths in water for these same electron beam energies. The primary electron spectrum was calculated first and subsequently served as the source of secondaries for which a further computation was carried out. Kessaris (1970a) applied his depth-dependent electron flux results to the calculation of absorbed dose to cavity ionisation ratios for water and carbon-walled ion chambers, using the Spencer-Attix theory.

The Monte Carlo method, first developed to solve the neutron transport problem, has been extensively applied to electron transport since the advent of fast digital computers with large memory capacities. This is a much more flexible technique than the analytical solution of the transport equation, and can readily be adapted to boundary problems and

inhomogeneous media. However, due to the very large number of interactions that an electron experiences as it slows down, direct simulation of all the physical processes is not feasible. The electron collisions are grouped together, and numerical computation is combined with the use of multiple-scattering theories. Among early Monte Carlo electron work, we can mention Leiss et al. (1957) who calculated range-straggling distributions for high-energy electrons in carbon. They used the simple gaussian angular multiple-scattering distribution which excludes large-angle scattering, and the Landau ionisation straggling distribution. Perkins (1962) carried out similar calculations for electrons with initial energies between 0.4 and 4 MeV normally incident on carbon, aluminium and copper absorbers. He used the more exact Moliere multiple-scattering distribution. He compared his computation of the spatial distribution of energy deposition to the results of Spencer's moments method calculation for 4 MeV electrons, in aluminium, finding qualitative, though not particularly close agreement.

Berger (1963) dealt in great detail with the application of the Monte Carlo method to the solution of electron and proton transport problems. He proposed various models for constructing condensed particle histories, based on different approximations for the energy loss, such as continuous slowing-down or the Landau straggling theory, and different multiple-scattering theories, including those of

Figure 1.7 CALCULATIONS OF SPATIAL ENERGY DISSIPATION BY 1 MeV ELECTRONS IN ALUMINIUM.

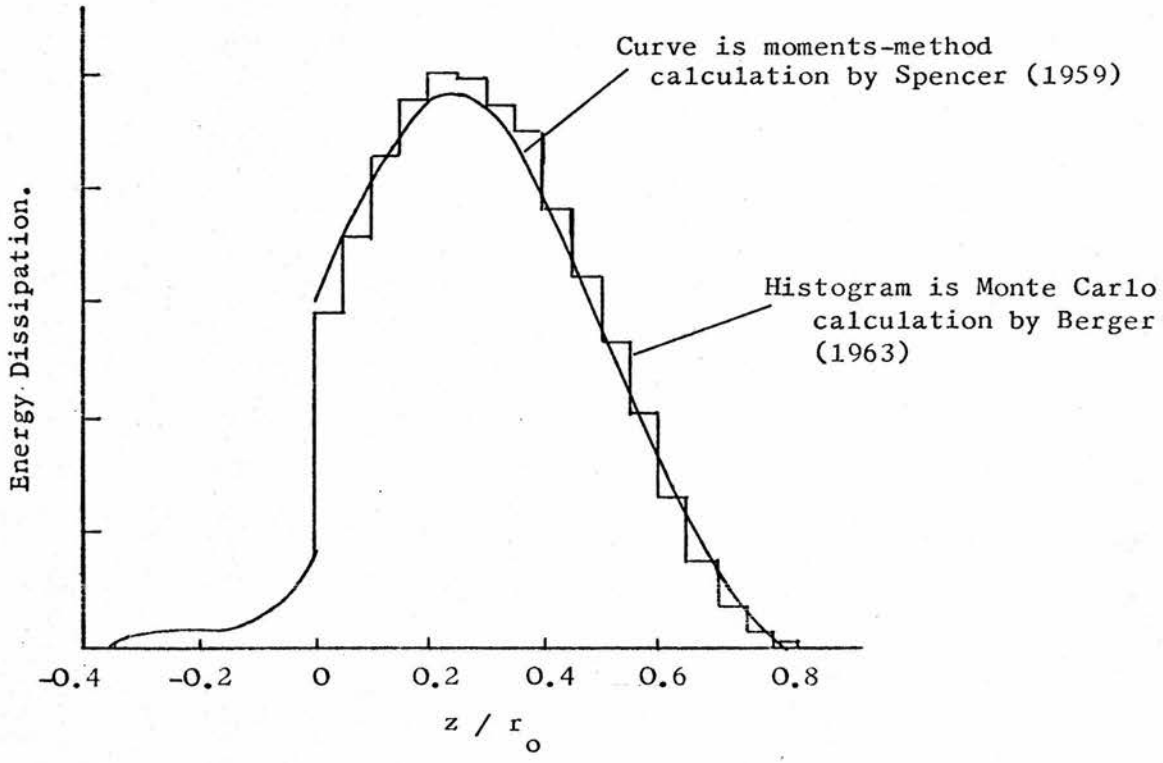

Spencer's calculation corresponds to an infinite medium and so his values extend to 'negative' depths. The Monte Carlo histogram was derived from 5000 histories.

Moliere and Goudsmit-Saunderson. Berger looked at the effect of different models on the results of quantities such as backcattering. He found good agreement between his calculations of electron transmission through gold and aluminium foils and experimental measurements. His calculations also included the spatial energy dissipation of electrons and figure 1.7 shows his results for 1 MeV electrons in aluminium compared to those of Spencer (1959).

In an extension of this work, Berger (1965) carried out Monte Carlo calculations of depth-dose curves for monoenergetic (1, 2, 5, 10 and 20 MeV) electron beams incident on a semi-infinite water medium. The computation was based on the continuous-slowing-down approximation. Secondary electrons were assumed to deposit their energy at their of origin, their diffusion not being included, and bremsstrahlung photons were assumed to escape entirely from the medium. The results also included tables of the lateral deposition of energy for a narrowly collimated beam. A comparison with the depth-dose results of Kessaris (1964) for 10 MeV electrons indicated good agreement only at large depths.

Berger and Seltzer (1969, 1969a) subsequently presented the results of a very sophisticated computer calculation of both the energy deposition and total electron flux at different depths in water irradiated by high-energy electron beams. The inclusion of energy-loss straggling and energy transport by

Figure 1.8 THE ELECTRON FLUX SPECTRUM CALCULATED BY BERGER AND SELTZER (1969) FOR 20 MeV ELECTRONS SLOWING DOWN IN WATER.

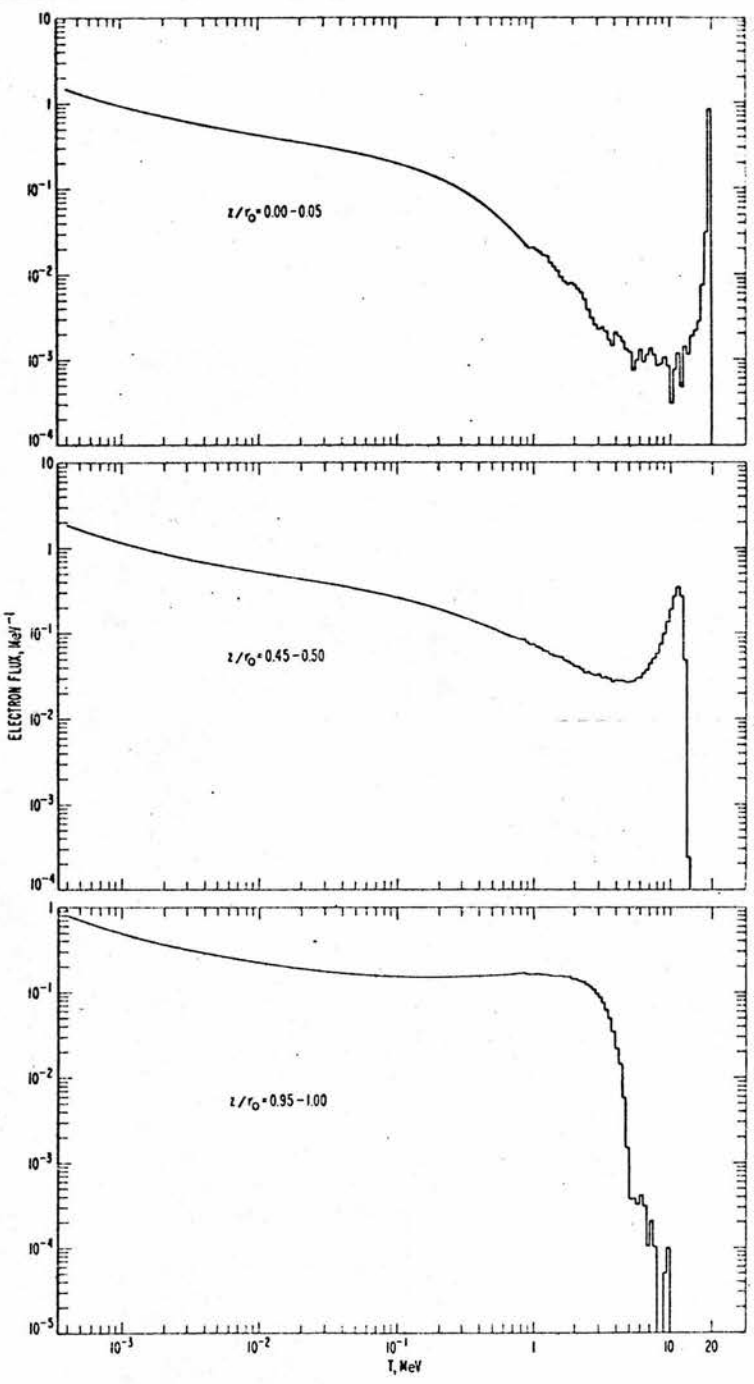

FIGURE 9. Electron flux, differential in energy, at various depths in a water phantom irradiated with a 20-mev beam. Units of flux are $mev^{-1}\,cm^{-2}\,sec^{-1}$; normalization corresponds to an incident current of one electron $cm^{-2}\,sec^{-1}$.

bremsstrahlung resulted in appreciably different depth-dose histograms from the earlier calculations (Berger, 1965). The primary and all secondary electrons were followed in the Monte Carlo scheme down to a cutoff energy, T_c. The cutoff was chosen such that the range of electrons with kinetic energy T_c was less than the size of the depth divisions of the medium. In order to compute the electron flux below T_c, a depth-independent Spencer-Fano calculation was 'tacked' onto the Monte Carlo program. Graphs of the electron flux down to 400 eV at three different depths for a 20 MeV electron beam are given in their 1969 paper and reproduced in figure 1.8. Berger and Seltzer (1969a) show clearly how the low energy flux is almost independent of initial energy and depth when the results are normalized to unit absorbed dose. The primary flux at high energies changes rapidly with depth, a result that Kessaris (1970) and Harder (1965), in a simplified Monte Carlo calculation down to 1 MeV, had also obtained.

Very recently, Berger et al. (1975) applied their comprehensive electron transport program to a systematic evaluation of carbon/air and water/air stopping-power ratios. The total electron flux for a series of depths in water and carbon was computed for electron beam energies between 1 and 60 MeV. These spectra were used in the Spencer-Attix expression for the stopping-power ratio, calculated for a cutoff of 15 keV. The calculated results compared closely

with the calorimetric determinations of the absorbed dose to ionisation ratio for a carbon-walled ion chamber reported in the same paper. Agreement with the parallel theoretical calculations of Kessaris (1970a) was not so close and Berger et al, concluded that this was a result of the more refined calculation of the electron flux.

The theoretical treatment of the transport of photons has also received considerable attention (Fano, Spencer and Berger, 1959). Here also the Monte Carlo method has been found most useful. The penetration and scattering of photons in the MeV energy region and below is a much less complex problem than for electrons and can essentially be regarded as solved.

Bruce and Johns (1960) used the Monte Carlo method to study the change of X-ray spectra with depth in water. Their calculations extended up to ^{60}Co photons (1.25 MeV) in energy. They also derived depth-dose curves for monoenergetic beams for different irradiation field sizes and found close agreement with measurements. Bruce and Johns compared their calculated intensity spectra for a plane monodirectional source incident on a semi-infinite medium with the results of a moments method calculation by Goldstein and Wilkins (1954). Agreement was reasonable considering that the moments calculation applied to an infinite medium and a source emitting photons in both directions.

Brysk (1954) considered both the transport of a primary photon beam and the diffusion of the electrons produced in the medium by the photon interactions. He started with a 40 MV bremsstrahlung spectrum incident on water and first calculated the spatial moments of the X ray distribution resulting from scattering and absorption of the incident photons. This was accomplished by the method of Spencer and Fano (1951). Then the spatial moments of the electron and positron distribution were derived and used as the source in an electron diffusion equation. The solution of this equation eventually yielded the spatial distribution of electrons at each energy. This remarkably sophisticated calculation produced a depth-dose curve, in close agreement with experimental measurements, and also the 'primary' electron flux spectra at various depths. Brysk pointed out that the elementary calculation of electron spectra by Cormack and Johns (1952), described above, pertained to zero depth. The shape of their electron spectrum for the 25 MV betatron radiation resembled Brysk's curve corresponding to the smallest depth, 0.9 cm.

Patau (1972) developed a Monte Carlo program that included the transport of both electrons and photons. Thus for a primary electron beam, the transport of bremsstrahlung photons was included and for a primary photon beam, the transport of the 'secondary' electrons was taken into account. Berger and Seltzer (1969) had effectively developed such a photon-electron cascade

Monte Carlo calculation, though they did not apply it to primary photon beams. Patau's cutoff energy (analoguous to Berger and Seltzers' T_c) was 60 keV for initial photon or electron energies up to 2 MeV but 1 MeV for initial energies above 2 MeV. Patau was not primarily interested in the electron flux and thus did not include a low-energy depth-independent flux calculation to extend his results below the Monte Carlo cutoff as Berger and Seltzer had done. Patau applied his work to the calculation of spatial energy distribution in the neighbourhood of an interface between two dissimilar media (Patau et al., 1972). It is in solving this type of problem that the Monte Carlo method is especially powerful.

Finally, the calculation by Berger and Seltzer (1970) of the bremsstrahlung photon spectrum resulting from electron bombardment of thick tungsten targets can be mentioned in this section. This is perhaps the most complex application to date of their Monte Carlo program. The excellent agreement of the results with the measurements by O'Dell et al. (1968) is an indication of the high degree of confidence that can be attached to the treatment of electron and photon transport by the Monte Carlo method.

1.3.2 Experimental

Problems of experimental technique have so far prevented measurement of the electron flux in an irradiated medium for as wide a range of energy as can be calculated by theoretical methods. Birkhoff et al.

Figure 1.9 MEASUREMENT OF ELECTRON FLUX AT VERY LOW ENERGIES. (McConnell et al., 1968)

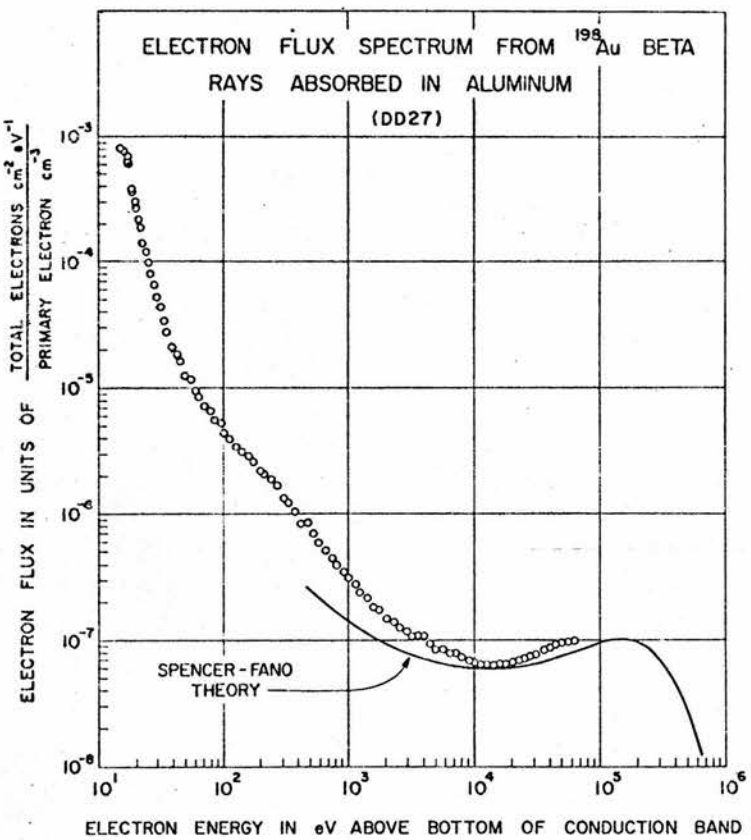

(1953) used a magnetic spectrometer to measure the energy spectrum of the electron flux arising from P^{32} beta ray sources uniformly dispersed in a large bakelite medium. Their measurements were limited to energies above 50 keV. The geometrical arrangement of the irradiation ensured equilibrium conditions and therefore the measured spectrum could be directly compared to a calculation of the electron flux using the Spencer-Fano theory. The agreement was good above 0.35 MeV and the authors did not consider the slight discrepancies in the 0.05 to 0.35 MeV region significant in view of the measurement difficulties and the approximations made to the 'exact' Spencer-Fano theory. Wilkie and Birkhoff (1963) subsequently carried out a similar type of flux measurement for an 'infinite' copper medium containing the positron emitter Cu^{64}. The spectrometer used was a NaI scintillation counter connected to a multichannel analyser. Discrimination against negative and secondary electrons permitted observation of the primary positron slowing-down flux. The results were compared with the flux calculated on the basis of the continuous-slowing-down model, using the initial positron β spectrum. The excellent agreement served as an experimental confirmation of the results of the Monte Carlo calculations by Schneider and Cormack (1959).

The development of the Keplertron, a spherical electrostatic focusing spectrometer, enabled McConnell et al. (1968) to measure electron flux in the energy region from 65 keV down to as low as 1 eV. Figure 1.9

Figure 1.10 EXPERIMENTAL MEASUREMENTS OF EPP ET AL. (1965, 1972).

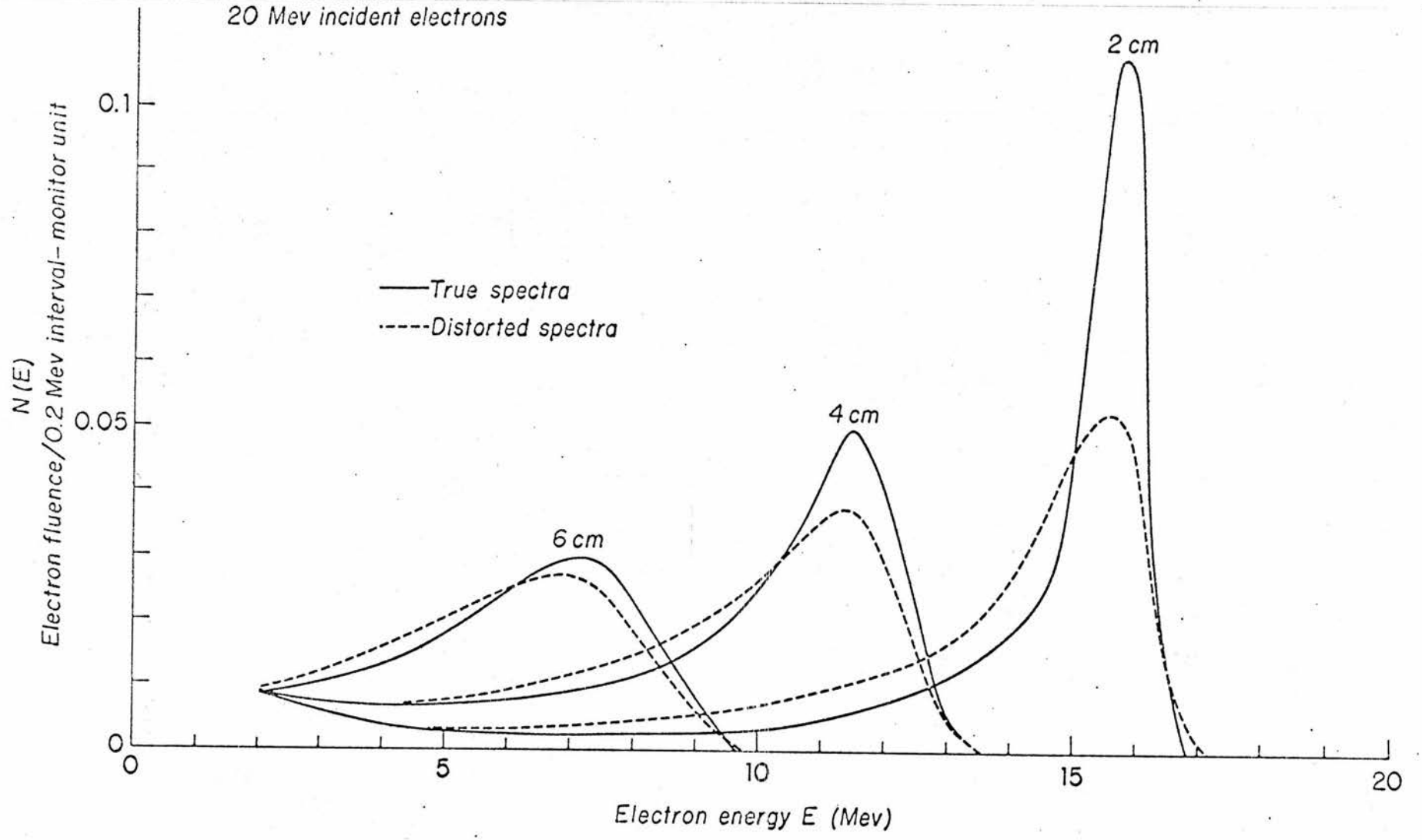

taken from their paper, shows up the considerable discrepancy between the flux calculated by the Spencer-Fano theory and their measurements below about 10 keV. This result underlines the very approximate theoretical treatment of electron slowing-down at energies close to the atomic binding energies of the medium. McConnell et al. suggested that the inclusion of Auger electrons in the calculation might reduce the discrepancy.

Harder (1966,1967) used a scintillation spectrometer to obtain the spectra of electrons behind layers of carbon, water and lead for electron beams with primary energies between 10 and 20 MeV. The measurements were limited to the energy range above 1 MeV. Harder found close agreement between these measured flux spectra and his Monte Carlo calculations, which were an extension of the work of Leiss et al. (1957).

Epp et al. (1965, 1972) measured the total flux spectra of slowed-down electrons at points in water irradiated with betatron electron beams with energies of 10, 15 and 20 MeV. A narrow evacuated leadout pipe was positioned within the water medium at an angle θ to the beam direction. The spectra at various angles θ at a given depth were graphically integrated to give results corresponding to 4π geometry. The nonzero energy resolution of the scintillation spectrometer was corrected for. An example of their results for 20 MeV incident electrons is shown in figure 1.10. The lowest energy that could be measured was 2 MeV.

Epp et al. derived the distribution of electron flux in LET, F(L), from the measured energy flux, F(T), using

$$F(L) = F(T)\ (dL_{\Delta}(T)/dT)^{-1} \qquad .....(1.12)$$

The cutoff for the LET, $L_{\Delta}(T)$, was chosen to be 100 eV. As $L_{100}(T)$ varies extremely slowly above 2 MeV, the distributions are not particularly useful. Kessaris' (1970) theoretical flux spectrum was used below 2 MeV in order to calculate the locally absorbed dose per unit energy down to 150 keV. This distribution is the same as Burch's local energy dissipation spectrum, Q_T. Epp et al. remark that their distribution for a 20 MeV electron beam appears similar to a calculation of Q_T performed for a 14 MeV beam by Haynes and Dolphin (1959) using Burch's method. Epp et al. discuss the difficulty of directly comparing the theoretical flux spectra of Kessaris with their experimental measurements. They conclude that the agreement is as good as could be expected considering the beam geometries were different and Kessaris' treatment of δ-ray and bremsstrahlung production did not allow for the possibility of large energy losses in a single interaction.

Inada et al. (1969) managed to extend the energy range down to a few hundred keV by the use of a magnetic spectrometer. Their irradiation and measurement geometry was identical to that of Epp et al. The energies of the electron beams incident on the water phantom were 27.0, 18.6 and 13.1 MeV. The build-up of the secondary electron flux

below about 2 MeV can clearly be seen from their results. The electron flux spectra were used to calculate tissue to air and water to air stopping power ratios and the results compared with evaluations based on the c-s-d-a. Unfortunately, the authors do not say exactly how they did these calculations, what cutoff energy they used etc. For this reason they cannot be meaningfully compared with stopping-power ratios based on theoretical flux spectra e.g. Berger et al. (1975).

1.3.3 Comment

It is apparent from what has been said above that a great deal more attention has been paid to the determination of electron flux in media irradiated by high-energy electron beams than is the case for high-energy photon beams. The only calculations reported in the literature for a photon beam of higher energy than ^{60}Co gamma rays have been for a 25 MV bremsstrahlung beam. Cormack and Johns (1952), Burch (1957a) and Danzker et al. (1959) all used the same initial photon energy spectrum, a theoretical distribution for a 25 MV betatron given by Johns et al. (1950). Though the calculations of Burch and Danzker et al. did take into account the production of δ-rays, none of these treatments considered the transport of the electrons, differentiated between electrons and positrons, or made any allowances for scattered photon radiation. The shape of the depth-dose distribution for such a high-energy bremsstrahlung beam, with its maximum

displaced several centimetres away from the surface, shows clearly enough the effect of the spatial diffusion of the photon-ejected electrons.

The Brysk (1954) moments method calculation is unique in the literature in giving the electron flux at different depths in a medium irradiated by a high-energy photon beam. Brysk's calculations indicated that the shape of the electron flux spectrum did change with depth, though the variation was a much more gradual one than was later found for electron beams. Brysk's calculations were not extensive enough to enable him to evaluate quantities such as LET distributions or stopping-power ratios, as the lowest energy in his spectrum was 1 MeV and δ-rays were not included.

The comprehensive calculations of stopping-power ratios for electron beams by Kessaris (1970) and Berger and Seltzer (1969a) have not been paralleled by any similarly sophisticated work for high-energy X-ray beams, despite the fact that is is just as important to know as accurately as possible the conversion factors for ionisation chambers for photon as for electron radiation. As has been pointed out earlier, the marked variation of these factors with depth for electron beams accounts for much of this imbalance.

However, the experimental work of Svensson (1971) suggests that there may well be a variation of about 2% in the stopping-power ratios at different depths in

water for high-energy photons. His findings led the Nordic Association of Clinical Physics (NACP) to recommend a slightly different set of C_λ values for X-ray beams above 10 MV than the ICRU (1969) C_λ's. The reason for this was that the NACP chose a different calibration depth to the ICRU. There are, to date, no theoretical calculations based on the total electron flux which could be used to substantiate these recommendations.

The specification of the quality of an X ray beam by the maximum energy of the photons in the spectrum, e.g. 25 MV, results in another area of imprecision as far as the use of C_λ factors is concerned. The very approximate calculation of C_λ is based on the photon spectrum from a betatron i.e. 'thin target' radiation. However, linear accelerators (linacs) are also in common use, especially at X ray energies below about 20 MV. Linacs give rise to a 'thick-target' photon energy spectrum. Johns and Rawlinson (1972) emphasised this important distinction by presenting calculated spectral distributions for a linac and a betatron of the same nominal energy, 25 MV. The differences are striking, especially when aluminium is used instead of lead as the beam-flattening filter. Approximate calculations by the author based on the mean photon energy for the linac and betatron spectra given by Johns and Rawlinson indicate that the difference in C_λ to be expected may be as much as 2%. The present

use of one energy to characterise an X-ray beam ignores this difference.

Finally we come to the question of theoretical calculations of $G(Fe^{3+})$. As has already been discussed, the 'best' experimental values of this quantity are a matter of some controversy. One must ask whether the work done to date on the determination of electron flux spectra and related quantities such as Burch's $Q_T \Delta T$ distribution permits a detailed investigation to be made into whether the experimentally suspected 'G-value difference' can be accounted for on theoretical grounds. Burch (1959) only applied his G-theory to 25 MV X rays and not to high-energy electron beams. Such an application could anyway only have given information appropriate to an average over the whole electron track. Burch's calculation of $Q_T \Delta T$ did not take into account any depth-dependence.

While the calculations of Berger and Seltzer of electron flux spectra in water irradiated by high-energy electron beams, if extended down to 100 eV, could be used in Burch's theory to predict electron G-values, no such detailed calculations exist for a range of photon beam energies. It would not be very satisfactory to use the Berger and Seltzer depth-dependent flux spectra for an electron beam and the depth-independent flux spectrum calculated by, say, Danzker et al. (1959) for the 25 MV X ray beam, in order to try and calculate a G-value difference. It would not be sufficiently clear that

'like' was being compared with 'like'.

No calculations have been carried out for both high-energy photon and electron beams by the same workers. It is precisely this type of determination, using the same method involving the same approximations, that is necessary in a theoretical investigation of the G-value difference.

1.4 AIMS OF THE PROJECT

To calculate the energy spectrum of the electron flux down to 100 eV at different depths in water irradiated by

a) Monoenergetic electron beams with initial energies between 1 and 30 MeV.

b) Cobalt-60 gamma rays and clinical X ray beams with maximum photon energies between 2 and 30 MeV.

To apply the results of the flux calculations to the evaluation of stopping-power ratios for use with air ionization chambers, more particularly for the photon beams.

To apply the results of the flux calculations in a theoretical study of the variation of $G(Fe^{3+})$ with the quality of the high-energy radiations, taking the work of Burch (1959) as the starting point. In particular, an effort is to be made to account theoretically for the suspected difference in photon and electron G-values.

1.5 THE APPROACH TO THE CALCULATION OF ELECTRON FLUX SPECTRA

The Monte Carlo method has proved its accuracy and versability in numerous applications to problems involving the spatial diffusion of radiation in an absorbing medium. The availability of extensive computing facilities at the University of Edinburgh, where this work was carried out, was also a factor in the choice of the Monte Carlo method to tackle the problem in hand. A large and necessarily complex computer program was constructed to calculate the total electron flux spectrum at different depths in water irradiated by electron and photon beams, taking into account all the physical processes considered to be important for the subsequent applications of the results.

The computation consists of three main components: a Monte Carlo simulation of electron transport down to a cutoff energy, a Monte Carlo simulation of photon transport, and a depth-independent calculation of the electron slowing-down flux for the energy range below the Monte Carlo cutoff down to 100 eV. One of the principal objectives behind the program construction was that the electron flux spectra produced by either primary photon or primary electron radiation should be calculated on the same basis, enabling direct comparisons to be made between them.

The photon Monte Carlo program is similar to many to be found in the literature. It is described in chapter 3. The electron Monte Carlo program has

features in common with the work of Berger (1963) and Patau (1972). It was intended to be almost as comprehensive as that described by Berger and Seltzer (1969), though of simpler construction. It is described in chapter 4. The low-energy electron slowing-down spectrum calculation is described in chapter 5. It makes use of the continuous-slowing-down approximation to give the primary flux. This is considered to be an adequate approximation. This part of the calculation was designed to be able to fit 'smoothly' on to the Monte Carlo electron simulation.

Many results other than electron spectra can be extracted from a Monte Carlo calculation. As a check on the faithfulness of the simulations, quantities such as backscattering coefficients, transmission factors and depth-dose distributions are compared with calculations and measurements by other workers. A great deal of effort has gone into ensuring that the complete electron-photon cascade simulation is internally consistent. Careful checks are made to see if the total energy put into the system via the energy of primary radiation beam is equal to the total energy dissipated by the electron flux in the medium.

The programming was done in the Edinburgh language IMP and the programs were run on an ICL 4/75 and an IBM 370/158 computer.

CHAPTER 2

THE MONTE CARLO METHOD

2.1 GENERAL DESCRIPTION

As its name implies, the Monte Carlo method is equivalent to playing a game of chance. Consider the problem of the scattering and absorption of neutrons in a medium. The neutron undergoes a number of interactions with the atomic nuclei of the medium. The energy a neutron loses or the angle it is scattered through at an interaction is, in effect, a selection from a probability distribution. These distributions are the interaction cross-sections, differential in energy, or angle as the case may be. This is the actual physical situation. Any measurements made on the neutrons such as the number penetrating a given thickness of the medium or the energy spectrum of these neutrons are merely averages of these quantities over large numbers of neutron paths.

If the differential interaction cross-sections are known, then we can simulate the path of a neutron by calculation. Using a sequence of random numbers we can select from these cross-sections or probability distributions the distance a neutron travels to the next interaction, the angle it is scattered through, whether it is absorbed or not etc. Carrying out such a simulation for a sufficiently large number of neutron paths or Histories, we can build up information about the transport of neutrons through the medium. This is known as a Monte Carlo calculation.

In general, the Monte Carlo method is used to solve problems which depend in some way on probability. Often an analytical treatment of the same problem is impossible or extremely complicated asisthe case for neutron penetration and for the transport of electrons and photons which are the problems tackled in the present work. Similarly, experimentation may be impracticable and can rarely yield information about as many of the variables involved as can an analysis of a set of Monte Carlo histories.

While the Monte Carlo simulation of radiation transport has the considerable merit of conceptual and mathematical simplicity, in marked contrast to analytical treatments such as the Moments method, see for example Spencer (1955), the computer program constructed to perform the simulation can be very long and complicated if it is to simulate all the physical processes as faithfully as possible. In addition, in order to produce statistically significant results, a very large number of particle histories, often of the order of ten thousand, may be necessary. This can mean a considerable amount of run-time on the computer and in practice effort must be directed towards reducing the computation time to a manageable amount.

Accounts of the particular computational techniques used in Monte Carlo simulations of radiation transport can be found in the literature. See, for example, Fano, Spencer and Berger (1959), Bruce and Johns (1960), Zerby (1963), Berger (1963). A description of only the most basic of such techniques is given here.

Figure 2.1 SELECTION OF A RANDOM VARIABLE BY C.P.D. METHOD

a. Probability Distribution

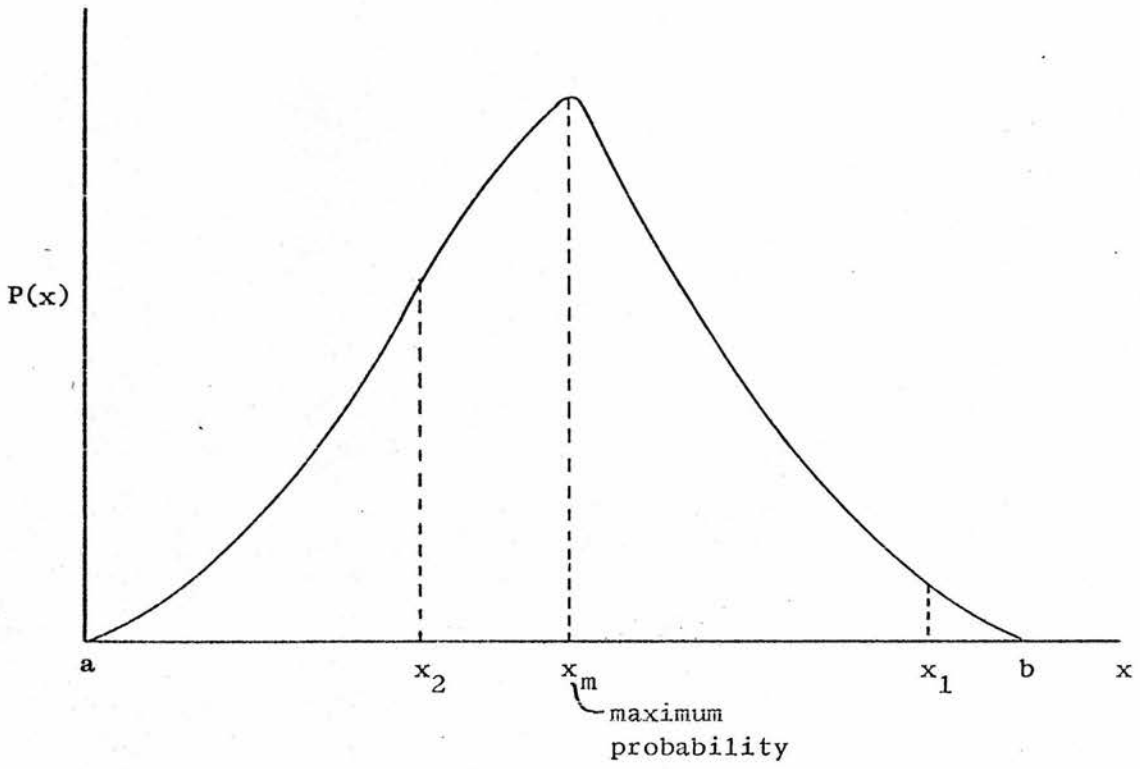

b. Cumulative Probability Distribution

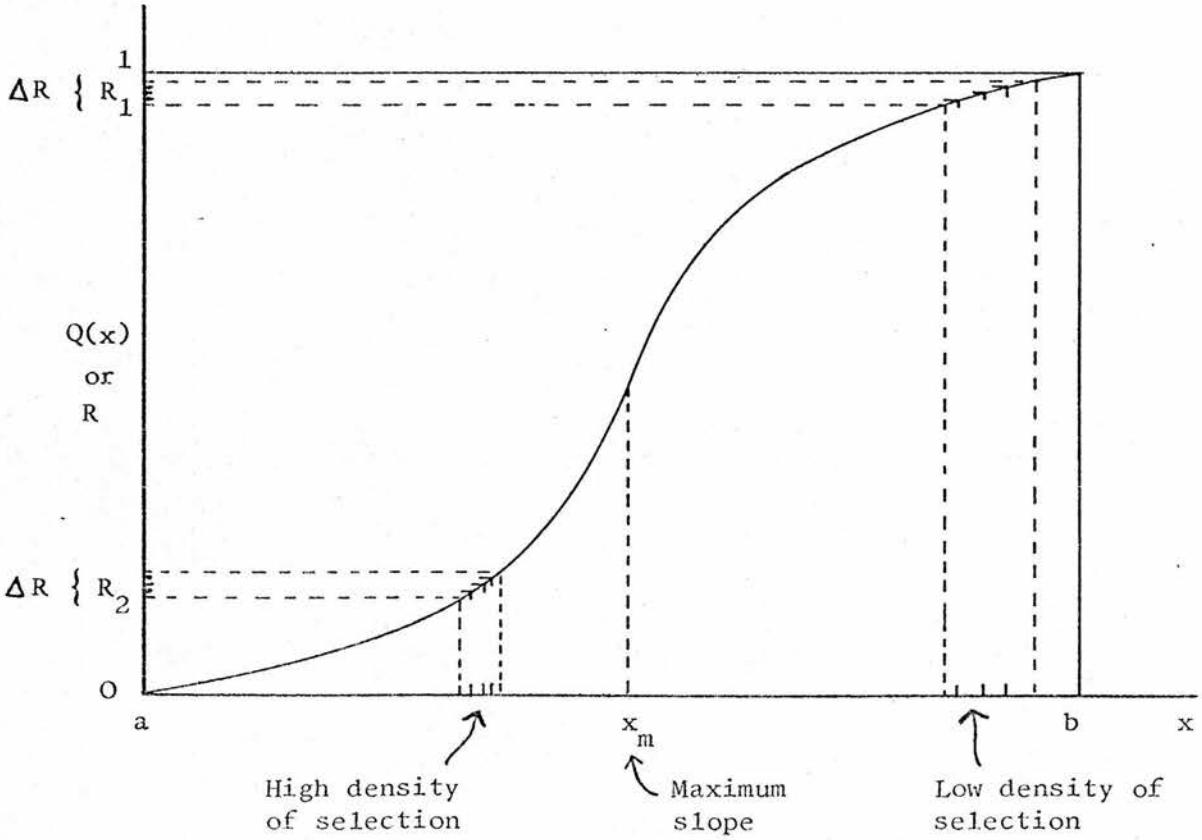

2.2 SELECTION OF A RANDOM VARIABLE FROM A DISTRIBUTION

The selection of a variable from a probability distribution is basic to the Monte Carlo method. There are two main ways of doing this: one using the Cumulative Probability Distribution and the other known as the Rejection Technique. All selection methods require a set of random numbers distributed uniformly between zero and one. Tables of random numbers are available but when using a computer in a simulation needing hundreds of thousands of random numbers, it is much more convenient to generate so-called pseudo-random numbers as they are required. The algorithm used for the generation of the random numbers is described in Appendix 1.

2.2.1 The Cumulative Probability Distribution (C.P.D.)

Consider that a variable x has a probability distribution function P(x). It is required to select values of x at random such that the number of selections of x between x and x+dx is proportional to P(x)dx. Integrating P(x) over the allowed range of values of x and normalizing the integrand to unity at $x=x_{max}=b$, we have the Cumulative Probability Distribution Q(x). - see figure 2.1

$$Q(x) = \int_a^x P(x)dx. \qquad .....(2.1)$$

Figure 2.2 THE REJECTION TECHNIQUE.

a. The Principle of the Method

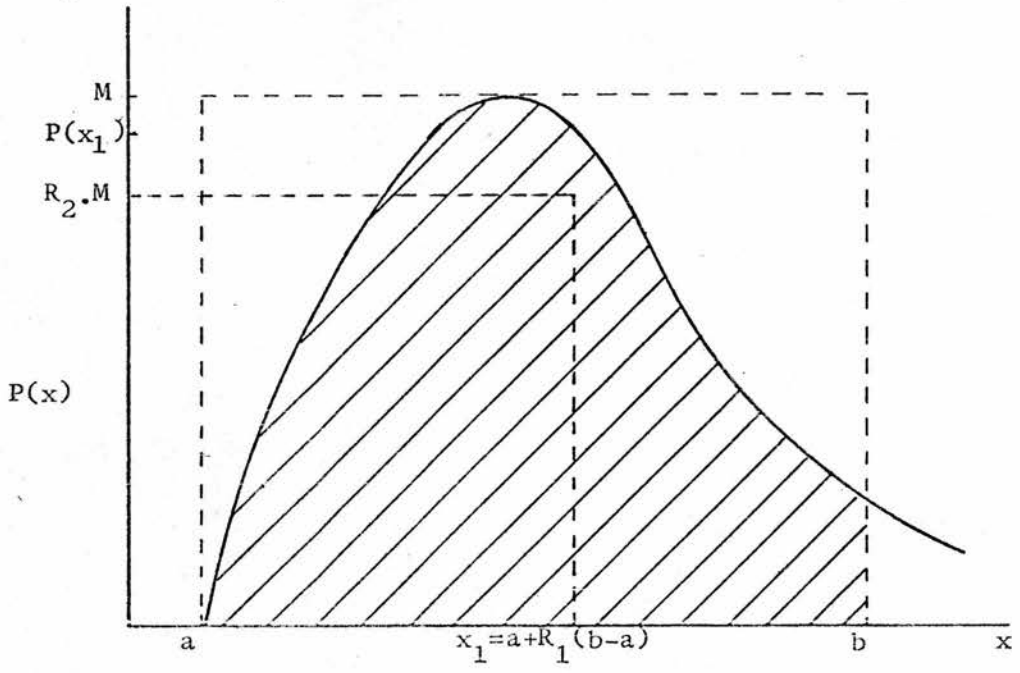

b. Low Efficiency of Selection

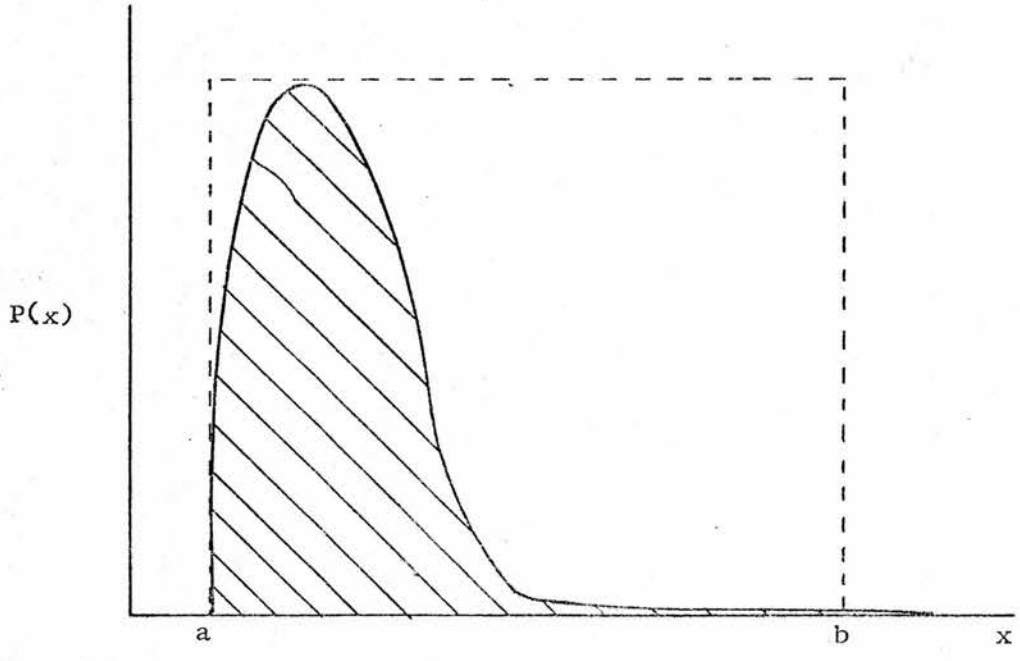

Taking now Q(x) as a random variable, it can easily be seen from fig. 2.1b that for a uniform density of selections of Q(x) between 0 and 1, the density of the corresponding x values is proportional to the slope of the curve which is simply $d(Q(x))/dx = P(x)$, the required probability distribution of x selections. Thus for our random number R we have

$$R = Q(x) \qquad .....(2.2)$$

and solving for our random variable x',

$$x' = Q^{-1}(R) \qquad .....(2.3)$$

Providing we can solve for x without too much computation, then this is the simplest method of selecting a random variable. Where this is not the case and we wish to avoid having extensive tabulations of $Q^{-1}(R)$ values, the so-called Rejection Technique often involves much less computation time.

2.2.2 The Rejection Technique

Consider again the probability distribution P(x) limited to the range x=a to x=b as depicted in fig. 2.2. The maximum of P(x) is M. We choose two random numbers R_1 and R_2 and compute $x_1=a+R_1(b-a)$. If $R_2M<=P(x_1)$, then x_1 is accepted as a random variable. If $R_2M>P(x_1)$, R_1 and R_2 are rejected and the selection process is repeated with a new pair of random numbers. As all values of x_1 between x=a and x=b are equally likely, then the probability of acceptance is simply $P(x_1)/M$ i.e. proportional to P(x) as required. The ratio of acceptances to the total number of selections,

the efficiency of the method, is equal to the ratio of the area under the curve (shaded in fig. 2.2) to the area of the enclosing rectangle, (b-a)M.

In contrast to the C.P.D. selection method, the rejection technique can only be employed when the random variable is restricted to a finite range of values. If the efficiency of selection is such as to make the average computation time per accepted selection too long, then the rejection technique is not employed; e.g. if P(x) is of a form as in fig. 2.2.b.

There are many other methods available for sampling from a distribution (e.g. Kahn, 1954) most of them being variations of the two techniques described above. The ones employed in the present work are referred to as necessary.

2.2.3 Selection from an exponential distribution

The exponential distribution

$$f(x) = Ae^{-bx}$$

will be met frequently in what follows and serves as an example of the C.P.D. method of selecting a random variable. The distance a photon travels between interactions is governed by the above expression for example. Integrating f(x) from x=0 to x=∞, the cumulative probability distribution is given by

$$Q(x) = (1-e^{-bx})$$

Choosing a random number R

$$R = Q(x) = (1-e^{-bx}) \qquad .....(2.4)$$

Figure 2.3 COORDINATE TRANSLATION.

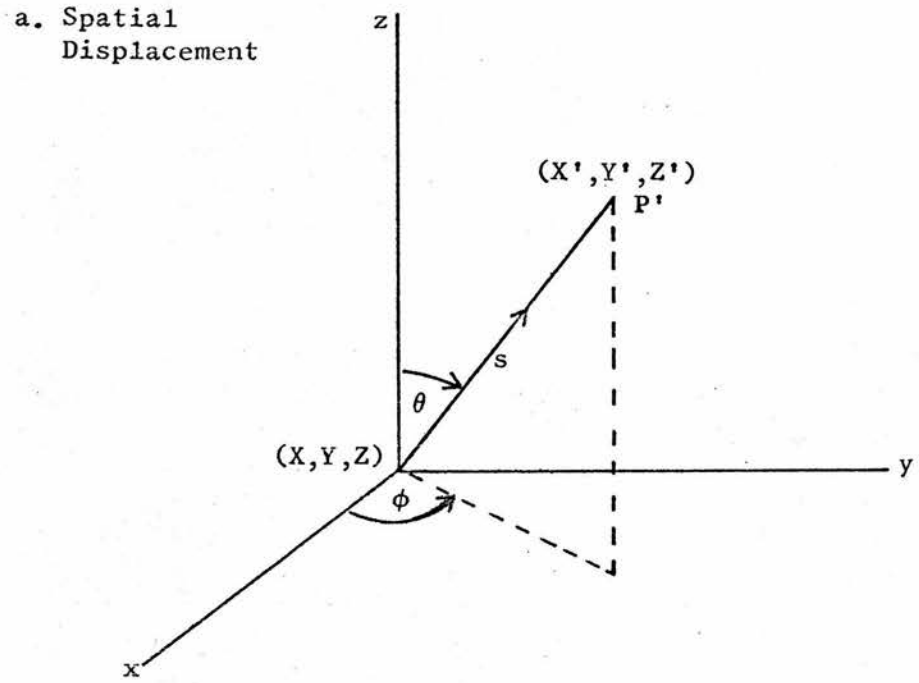

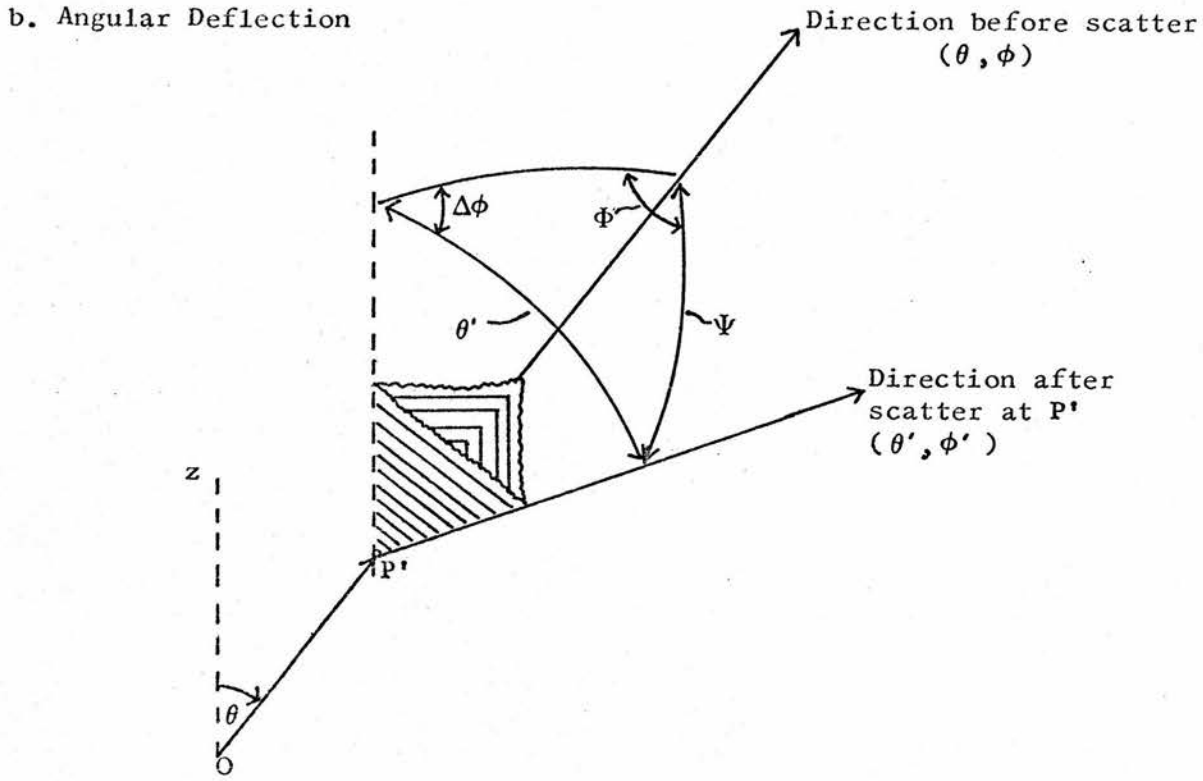

and solving for x'

$$x' = -1/b.\log_e R \qquad .....(2.5)$$

where x' is the required random variable.

2.3 COORDINATE SYSTEM

In the simulation of photon and electron paths, cartesian coordinates X,Y,Z are used with spherical polar angles θ,ϕ to define the direction. - see fig. 2.3a.

2.3.1 Spatial Displacement

To calculate new X,Y,Z after distance s travelled in θ,ϕ direction, we have

$$X' = X + s.\sin\theta.\cos\phi \qquad .....(2.6)$$

$$Y' = Y + s.\sin\theta.\sin\phi \qquad .....(2.7)$$

$$Z' = Z + s.\cos\theta \qquad .....(2.8)$$

2.3.2 Angular Deflection

If the particle at X' ,Y' ,Z' is scattered through polar angle Φ, azimuthal angle Ψ, relative to the θ,ϕ direction, as in fig. 2.3b, then we wish to calculate the new θ',ϕ' direction relative to the X,Y,Z axes. This is given by the following standard relations in spherical trigonometry

$$\cos\theta' = \cos\theta.\cos\Psi + \sin\theta\sin\Psi\cos\Phi \qquad .....(2.9)$$

$$\sin\theta' = \sqrt{1 - \cos^2\theta'} \qquad .....(2.10)$$

$$\sin\Delta\phi = \sin\Psi\frac{\sin\Phi}{\sin\theta'} \qquad .....(2.11)$$

$$\cos\Delta\phi = \frac{\cos\Psi - \cos\theta'\cos\theta}{\sin\theta'\sin} \qquad .....(2.12)$$

where $\phi' = \phi + \Delta\phi$

and therefore

$$\cos\phi' = \cos\phi \cos\Delta\phi - \sin\phi \sin\Delta\phi \qquad .....(2.13)$$

$$\sin\phi' = \sin\phi \cos\Delta\phi + \cos\phi \sin\Delta\phi \qquad .....(2.14)$$

In the actual computation of these relations during a simulation, equation (2.14) was used only to give the sign of $\sin\phi'$, the accurate value of which was calculated from

$$\sin\phi' = \pm\sqrt{1 - \cos^2\phi'} \qquad .....(2.15)$$

as it was found in practice that evaluation using equation (2.14) could lead to unwanted errors due to the finite accuracy of the computer arithmetic.

2.3.3 Selection of Azimuthal Deflection

As we are dealing with unpolarized radiation, there can be no preferred value for the azimuthal deflection in any interaction. The deflection angle, Φ, is equally distributed between 0 and 2π. The selection is therefore made according to

$$\Phi = 2\pi R \qquad .....(2.16)$$

for random number R equally distributed between zero and one.

CHAPTER 3

MONTE CARLO PROGRAM FOR PHOTON TRANSPORT

3.1 REQUIREMENTS OF THE CALCULATION

It is desired to simulate the transport of photons in water. The computation has to be able to handle accurately the spatial energy deposition for photon beams of initial energy up to 40 MeV. The program is to be coupled to an electron simulation and therefore must include the calculation of the initial parameters of the electrons produced by the photons which will be the input data for the electron program.

The limitation of a finite amount of computer time dictates that the execution time per photon history should be as fast as possible without at the same time resorting to approximations which would significantly diminish the validity of the results. As we shall see, the nature of the photon interactions with the medium make the construction of a fast Monte Carlo computer program relatively straightforward. This is in marked contrast to the program for electron transport.

3.2 THE INTERACTION OF PHOTONS WITH MATTER

A photon interacts with matter though any one of a number of competing mechanisms. The total interaction cross-section is the sum of the cross-sections for the different processes and determines the average distance the photon travels between interactions. In water, in the energy range we are dealing with, the most important processes are Compton Scattering, Photoelectric Absorption and Pair Production.

3.2.1 The Main Interactions

In Compton scattering, the photon interacts with an atomic electron as if it were free. An appreciable fraction of the energy of the photon may go into the kinetic energy of the Compton electron, with the photon being deflected in the process. Compton scattering is the dominant interaction process in water in the photon energy range 30 keV to 20 MeV.

As the photon energy decreases, Photoelectric absorption becomes increasingly important, taking over from Compton scattering below about 20 keV in water. The photon is absorbed, its energy ejecting a photoelectron, usually from one of the tightly-bound, inner shells of the atom.

Above 1.02 MeV (twice the rest mass of the electron), Pair production can occur. The energy of the photon goes into the production and kinetic energy of an electron-positron pair. Pair production begins to dominate the interaction processes as the photon energy increases, being equal in probability to Compton scattering at 24 MeV in water.

3.2.2 Auger Electrons

The photoelectric effect and Compton scattering both involve the ejection of an electron from its bound state in the atom, leaving the atom ionized or excited. The atom reverts to the ground state with the emission of either a photon or an Auger electron. For the K-shell, the fluorescence yield, which is the ratio of the number of K photons emitted to the number of K-shell vacancies, is close to zero for the light elements, being 0.003 for Oxygen (Storm and Israel, 1967).

Thus we can neglect the K-shell fluorescence photons and assume that for every K-Oxygen electron ejected there will also be a K-Auger electron produced. These Auger electrons have a kinetic energy

$$T_{aug} = E_k - 2E_l \qquad .....(3.1)$$

where E_k is the energy of the K-edge and E_l the energy of the L-edge. Auger electrons constitute a monoenergetic source of about 500 eV in addition to the Pair, Compton and photoelectrons resulting from the scattering and absorption of the photon beam in water.

3.2.3 Coherent Scattering, Nuclear Interactions

A photon can be scattered without any change in wavelength. This is Rayleigh (coherent) scattering. In water it is most important at around 25 keV where it is 12% of the total interaction cross-section. At this energy a photon has a mean free path of the order of 2 cm and can be Rayleigh-scattered through large angles. Thus coherent scattering can influence the spatial energy deposition of a photon beam and for this reason it has been included in the simulation unlike most of the Monte Carlo photon schemes in the literature.

Finally we mention Photonuclear interactions. These can occur above a threshold of about 12 MeV for Oxygen and 2 MeV for Hydrogen. The photon is absorbed and usually a neutron is emitted. The cross-section goes through a maximum which is a few MeV in width. In all cases, the maximum value of the total cross section for all photonuclear reactions is smaller than

5% of the total cross section of the same atom for Compton and pair-production interactions (Evans 1963). We will be dealing with relatively small numbers of photons above 10 MeV in energy in these calculations and in view of the small effect any neutrons or protons emitted in photonuclear reactions would have on the results, it was decided not to include these interactions in the simulation. Nevertheless, in a completely rigorous treatment of photon energy dissipation, the simulation of the transport of secondary particles would have to include these neutrons and protons at the cost of a considerable increase in complexity.

3.3 SIMULATION OF THE INTERACTIONS

A photon on average undergoes relatively few interactions with a medium before it is absorbed by ejecting a photoelectron or producing an electron-positron pair. It may, of course, be scattered out of the medium depending on the geometry of the irradiation. A 1 MeV photon in water will typically be Compton-scattered thirteen times before photoelectric absorption. It is quite feasible, therefore, to simulate each interaction separately and the Monte Carlo histories are then direct analogues of the physical events. This is what is done in the program constructed in this work. In the sections immediately following, we detail the calculations involved in generating the photon histories.

3.3.1 Distance between Interactions

The attenuation of a photon beam in a medium is given by the exponential law

$$P = \exp(-\mu(k)s) \qquad .....(3.2)$$

where P is the probability that a photon of energy k will not have interacted with the medium at a depth of penetration s. $\mu(k)$ is the total narrow beam attenuation coefficient at this photon energy. The inverse of this

$$\bar{s} = 1/\mu(k) \qquad .....(3.3)$$

is the mean free path of the photon between interactions.

The total attenuation coefficient is the sum of the attentuation coefficients for the different

Table 3.1 PHOTON MEAN FREE PATHS IN WATER

Photon Energy (MeV)	Mean free path (cm)
0.001	0.0002
0.002	0.0016
0.003	0.0052
0.005	0.0238
0.008	0.0979
0.01	0.1908
0.02	1.263
0.03	2.715
0.05	4.422
0.08	5.452
0.1	5.859
0.2	7.308
0.3	8.431
0.5	10.33
0.8	12.71
1	14.15
2	20.29
3	25.23
5	32.94
8	41.18
10	45.09
20	55.20
30	58.61
40	59.69

interactions. Thus in this case

$$\mu(k)_{tot} = \mu(k)_{pair} + \mu(k)_{Comp.} + \mu(k)_{Ray.} + \mu(k)_{photo.} \quad .....(3.3)$$

3.3.1.1 Input Data

The medium concerned is water for which the interaction coefficients can be evaluated from those for its constituent elements, Oxygen and Hydrogen. If μ is the attenuation coefficient per atom or molecule, then

$$\mu_{H_2O} = 2\mu_H + \mu_O \quad .....(3.5)$$

The 'mixture rule', which ignores changes in the atomic wave-functions due to molecular binding, is expected to be accurate to within a few per cent or less above 10 keV (Hubbell 1969).

The values of the total attenuation coefficients for Oxygen and Hydrogen have been taken from the compilation by Storm and Israel (1970). They are accurate to within 5% in the Photoelectric effect region, to within 3% in the Compton scattering region, and to within 5% above 10 MeV where Pair production begins to dominate. The units have been converted from barns/atom to cm^2/gm giving the mean free path in cm in water. Representative values are given in Table 3.1.

3.3.1.2 Selection of Distance to next Interaction

Selection from an exponential distribution is straightforward. Using the C.P.D. method, we have

$$s = \frac{-1}{\mu_{tot}} \log_e R \quad \text{from equ. 2.5}$$

where R is a random number.

Figure 3.1 SELECTION OF PHOTON INTERACTION.

a. Variation of Interaction Probability with Photon Energy (Water).

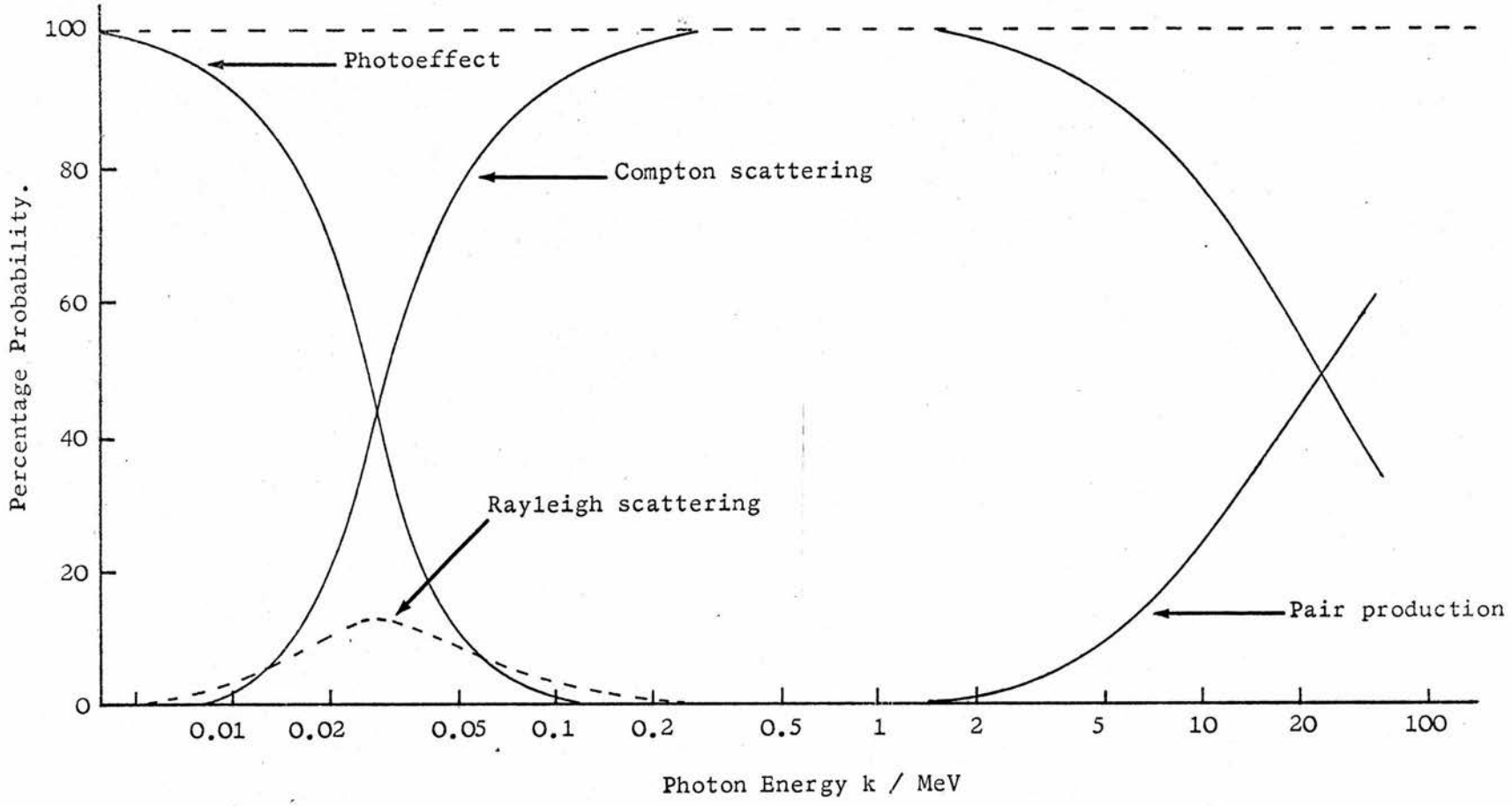

The values of μ_{tot} used in the program are calculated from a polynomial fit in $\log_e(k^6)$. The fit is in two sections, 1 keV <= k < 0.08 MeV and 0.08 <= k <= 40 MeV and is within 1% of the Storm and Israel data over this energy range.

3.3.2 Selection of the Interaction

3.3.2.1 Input Data

We require to know the relative probabilities at photon energy E that the interaction is Compton scattering, photoelectric absorption etc. This is given by the ratio of the particular interaction cross section to the total cross section at energy k. These probabilities have been tabulated for the pair, Compton, photo and Rayleigh processes from the Storm and Israel data adapted for water. They are plotted in figure 3.1a.

As used in the program, the relative probability data are divided into 2 sections. For k <= 1 MeV, pair production values are zero, the Compton values are interpolated from a tabulation and the Rayleigh probabilities are calculated from a rational fit in $\log_e(k^3)/\log_e(k^4)$. The difference of the sum of these from unity gives the photoelectric figures. Above 1 MeV, we need only consider Compton and pair interactions. The Compton values are calculated from a polynomial fit in $\log_e(k^5)$.

3.3.2.2 Selection procedure

This is trivial and is illustrated by the flow diagram in figure 3.1b. In this figure, R is a random

b. Flow Diagram for Selection.

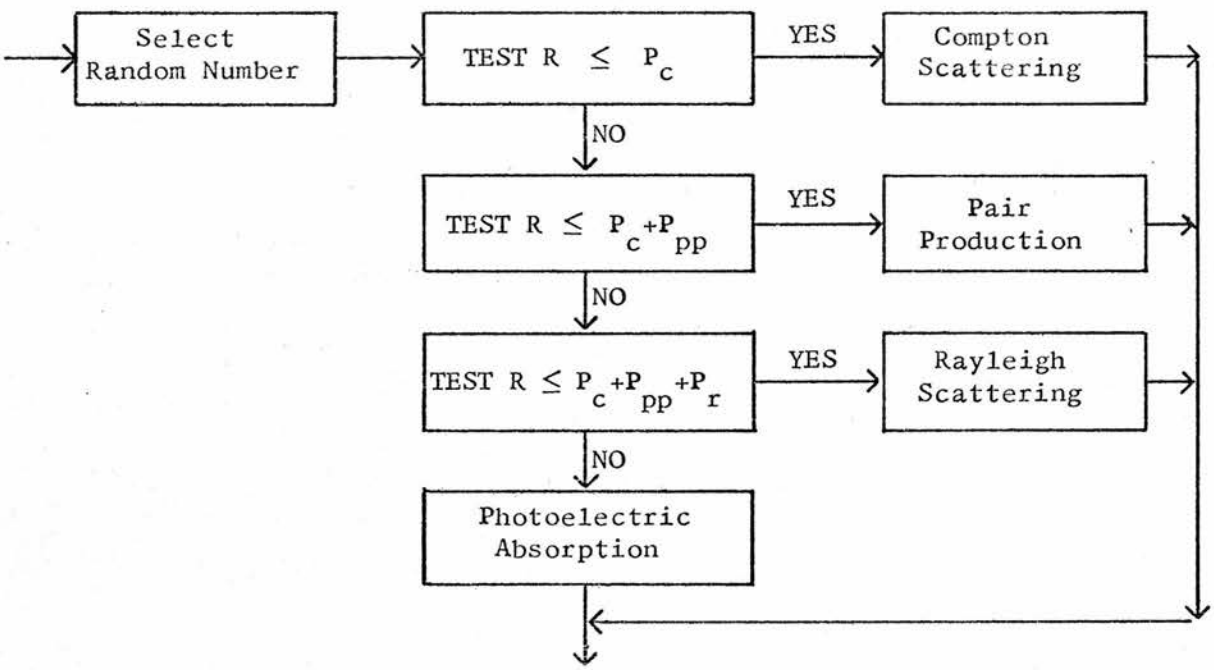

Figure 3.2 COMPTON SCATTERING.

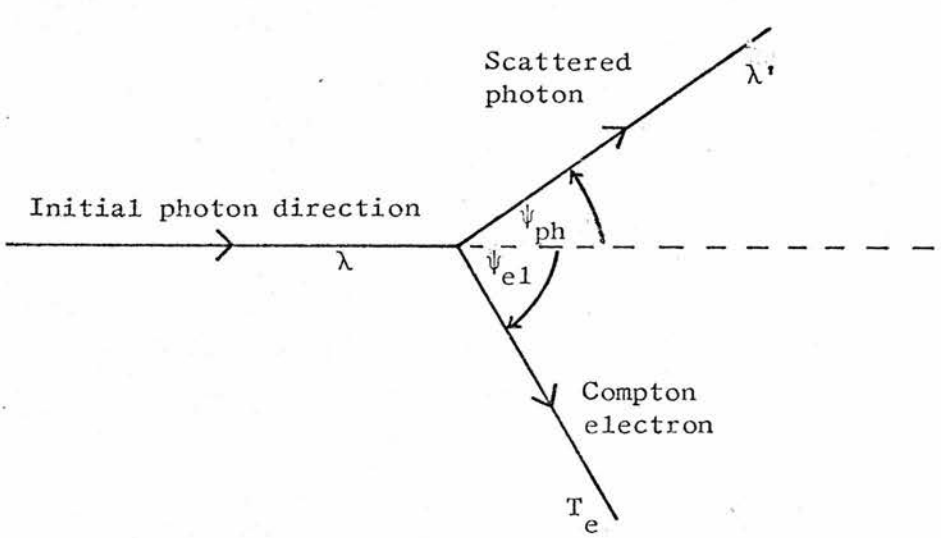

number, and P_c, P_{pp}, P_r and P_{ph} are the relative probabilities for Compton scattering, pair production, Rayleigh scattering and photoelectric absorption respectively.

3.3.3 Compton Scattering

3.3.3.1 Klein-Nishina differential cross-section

The differential cross section for the inelastic scattering of unpolarized photons by free electrons is given by the Klein-Nishina (K-N) formula

$$\frac{d\sigma}{d\lambda'} = \pi R_o^2 \frac{\lambda^2}{\lambda'^2} \left\{ 2\lambda - 2\lambda' + \lambda'^2 + \lambda^2 - 2\lambda\lambda' + \frac{\lambda}{\lambda'} + \frac{\lambda'}{\lambda} \right\} \quad .....(3.6)$$

where $\lambda = \frac{mc^2}{K}$, the Compton wavelength of the photon and the photon is scattered from wavelength λ to λ'. ($R_o = e^2/m\,c^2$, the classical electron radius.) It can easily be shown that the change in wavelength is given by

$$\Delta\lambda = \lambda' - \lambda = 1 - \cos\Psi_{ph} \quad .....(3.7)$$

where Ψ_{ph} is the angle the photon is scattered through. Thus the maximum change in wavelength is 2 Compton units. The kinetic energy of the Compton electron, neglecting the atomic binding energy is given by

$$T_e = mc^2 (1/\lambda - 1/\lambda') \quad .....(3.8)$$

At photon energies comparable with the binding energy of the electron, the K-N cross section is not strictly applicable and the appropriate correction factor, the incoherent scattering function, has been incorporated into the Storm and Israel data. Ellett et al. (1968) discussed the error introduced

into the results of photon Monte Carlo calculations due to use of the K-N formula for sampling the change in photon wavelength when binding effects are non-neglible. They concluded that any errors will be very small.

3.3.3.2 Selection Procedure

The K-N cross section can be integrated to give the Cumulative Probability Distribution, but then solving the resulting expression for λ' for a given λ and random number R is very involved (see section 2.2.1). A straightforward application of the Rejection Technique (see section 2.2.2) turns out to be rather inefficient, needing as many as 19 pairs of random numbers per accepted selection of λ' at 10 MeV.

Photon Monte Carlo programmers are indebted to Kahn (1954) for providing a feasible and relatively simple selection procedure for the wavelength change from the K-N expression (equ. 3.6). It is a modified type of Rejection technique, requiring 3 random numbers per trial. The efficiency is better than 50% for photon energies below several MeV. The flow diagram used to program the Kahn method is given in Appendix 2.

As Compton scattering is an interaction of the photon with a free electron, it follows that there is an equal probability that the electron is any one of the ten that are attached to a H_2O molecule. Thus one fifth of all Compton scatters involves a K-Oxygen electron. This in turn results in an Auger electron of about 500 eV kinetic energy. We therefore put the following extra steps into the routine for the

selection of Compton electron energy, T_e, in the photon simulation:

If $R \leq 0.2$ and $T_e > E_k$

then $T'_e = T_e - T_{aug}$

and an Auger electron is ejected with K.E. T_{aug}. The energy of the Oxygen L-shell is only about 20 eV so that we can take E_k and T_{aug} to be equal - see eq.(3.1).

3.3.3.3 Angular Deflections

The polar deflection angle Ψ_{ph} for the scattered photon is given by equ.(3.7) for wavelength change $\Delta\lambda$. The initial direction of the Compton electron is fixed by the conservation of energy and momentum in the interaction. The polar deflection Ψ_{el}, relative to the initial photon direction, is given by

$$\tan \Psi_{el} = \frac{\frac{1}{\lambda'} \sin \Psi_{ph}}{\frac{1}{\lambda} - \frac{1}{\lambda'} \cos \Psi_{ph}} \qquad .....(3.9)$$

The directions of scattered photon and the Compton electron lie in the same plane. Thus if the selected azimuthal deflection for the photon is Φ_{ph} (from equ. 2.16), then the corresponding deflection for the electron, Φ_{el}, is $\pi + \Phi_{ph}$.

3.3.4 Pair Production

3.3.4.1 Electron, positron energy distribution

Pair production takes place predominantly in the field of a nucleus. The energy of the photon minus twice the rest mass of the electron, $2mc^2$, (= 1.02 MeV) is shared between the kinetic energy of the electron

Figure 3.3 DISTRIBUTION OF ELECTRON AND POSITRON ENERGIES IN PAIR PRODUCTION.

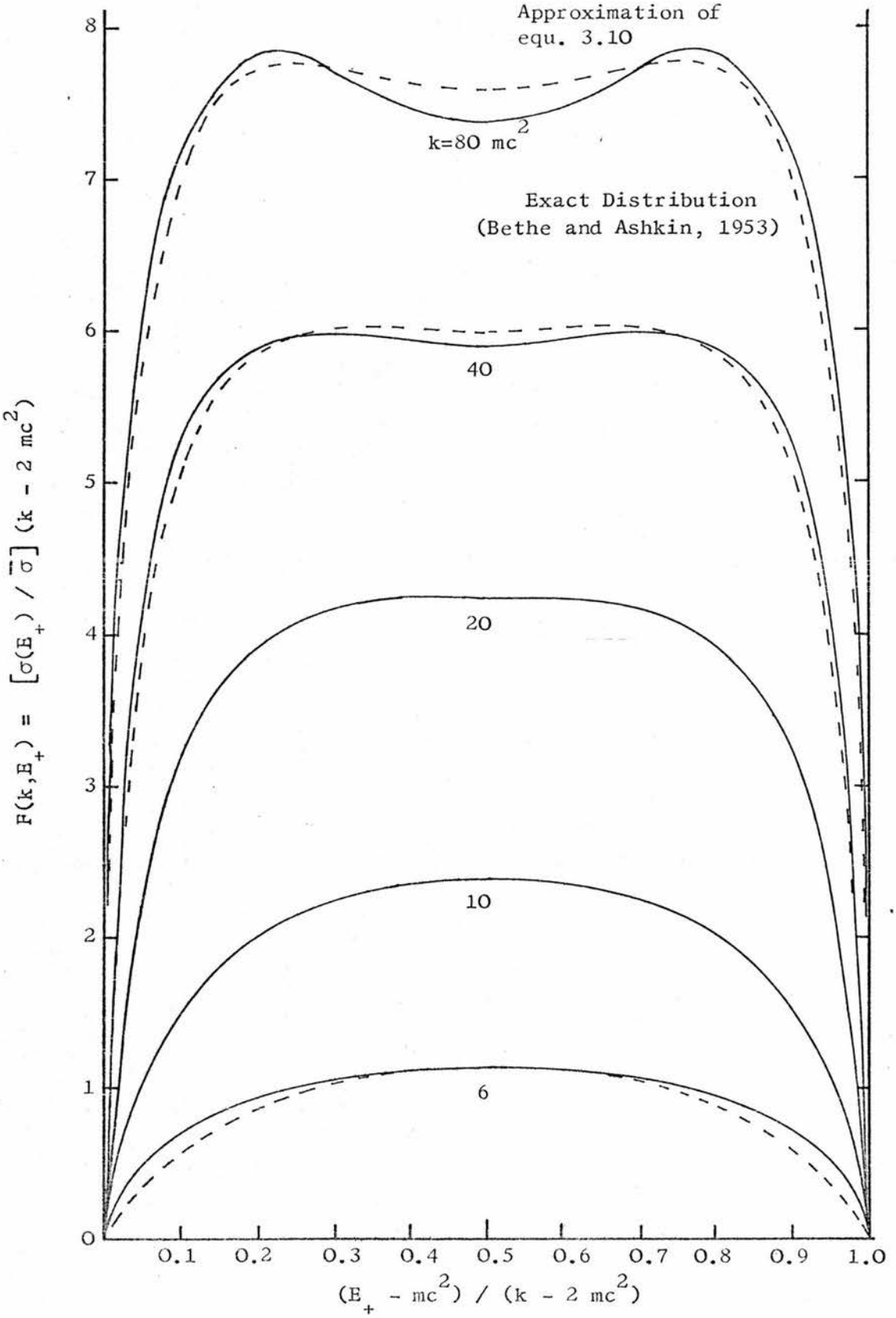

and positron. The exact differential cross-section describing this distribution of electron (or positron) energy is a complicated expression. For the case of intermediate electron and positron energies, the cross section reduces to (Bethe and Ashkin, 1953)

$$d\sigma(E_+) = 4\bar{\sigma}\, dE_+ \frac{E_+^2 + E_-^2 + \frac{2}{3} E_+ E_-}{k^3} \left(\log_e \frac{2E_+E_-}{k.mc^2} - \frac{1}{2} \right) \quad .....(3.10)$$

$\bar{\sigma} = \frac{Z^2}{137} r_o^2$, E_+, E_- are the positron and electron total energies respectively and $k = E_+ + E_-$ is the photon energy.

In Figure 3.3, this expression is compared to the exact formula for photon energies 80,40,20,10 and 6 mc^2. The quantity $(E_+ - mc^2)/(k - 2mc^2)$ is the ratio of the positron K.E. to the total energy available for positron and electron K.E. It is seen that the agreement is very good in the 5-20 MeV region. Below about 6 mc^2, eq.(3.10) goes negative for values along the abcissa close to zero and unity. Bearing in mind that for the purpose of selecting the positron energy it is only the shape of the distribution that matters, it was considered that equ.(3.10) was a sufficiently good approximation to be used in the simulation. For photon energies below 6 mc^2 (3.06 MeV), the distribution for $k = 6\ mc^2$ was employed. Anyway, pair production is only 3% of the total interaction cross section in water at 3 MeV so that any approximation in the distribution of electron and positron kinetic energies makes a negligible difference to any results from the simulation.

Figure 3.4 FLOW DIAGRAM FOR SELECTION OF PAIR ELECTRON ENERGIES
(Rejection technique)

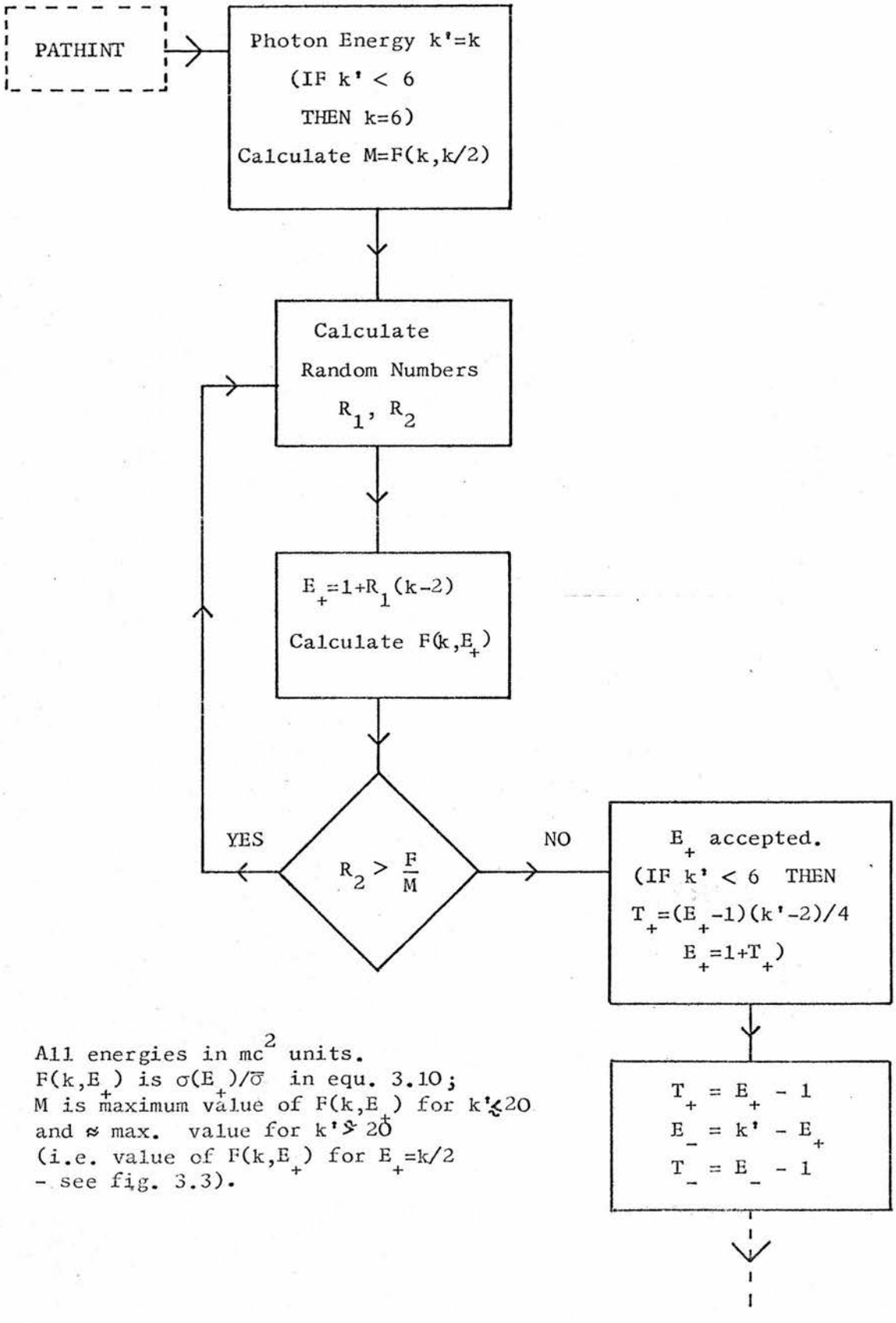

All energies in mc^2 units.
$F(k,E_+)$ is $\sigma(E_+)/\bar{\sigma}$ in equ. 3.10;
M is maximum value of $F(k,E_+)$ for $k' \lesssim 20$
and $\approx$ max. value for $k' \gtrsim 20$
(i.e. value of $F(k,E_+)$ for $E_+ = k/2$
- see fig. 3.3).

For the same reason, the slight asymmetry in the electron-positron distribution due to the Coulombic force of the positively charged nucleus, which is only important in water for very low positron and electron kinetic energies, has been neglected.

Pair production can also take place in the field of an electron. The threshold for this process is 4 mc^2 (2.04 MeV) in order to conserve energy and momentum. The ratio of 'electronic' to 'nuclear' cross-sections increases with photon energy, being 0.01 at 3 MeV and 0.12 at 40 MeV in water. The energy distribution of the electron and positron pair is the same as in the nuclear field case for photon energy k large compared to mc^2 and the recoil electron has an energy distribution heavily weighted towards the low energy end. In view of these facts, no distinction has been made in the simulation between pair production in the field of an electron and in the field of a nucleus.

In order to select the energy of the electron and positron, we make use of the rejection technique. The shape of the curves in figure 3.3 indicates that the efficiency of selection (section 2.2.2) is acceptable even at the lowest photon energy. The number of trials per selection is 1.36 for $k <= 3$ MeV, decreasing to 1.08 at $k = 40$ MeV. The flow diagram for programming this selection procedure is sketched in figure 3.4.

3.3.4.2 Angular coordinates of pair electrons

The kinetic energies of the electron and positron do not uniquely determine their directions relative to

the photon direction as the recoil momentum of the nucleus or electron (in the electronic field case) comes into the momentum balance. The angular distribution for low photon energy is not particularly well-known but fortunately this does not matter. We are only interested in the direction of the positron or electron if its range is such as to influence the spatial energy distribution produced by the photon beam, in which case the electron path must be simulated in the electron programme. An electron of kinetic energy 0.5 MeV has a range of about 0.17 cm. and its angular coordinates are therefore unlikely to be required.

At higher photon energies, where the ranges of the pair electrons can be appreciable, most of the pair electrons are emitted in the forward direction. The Schiff cross-section, differential in electron energy and angle (Schiff, 1951), has been evaluated for variable Ψ at different values of the photon energy in order to investigate the dependence of the deflection angle on electron and photon energy.* The Schiff cross section was used in order to be consistent with the treatment of bremsstrahlung photon production by electrons as described in the chapter on the electron Monte Carlo program. From the quantum theory point of view, the process of pair creation by photons can be considered as the inverse of the production of a photon from the kinetic energy of an electron. Thus the same cross section can be used for the distribution of the angle between photon and electron, positron directions.

*see section 4.4.2.3.

Figure 3.5 ANGULAR DEFLECTION IN PAIR PRODUCTION

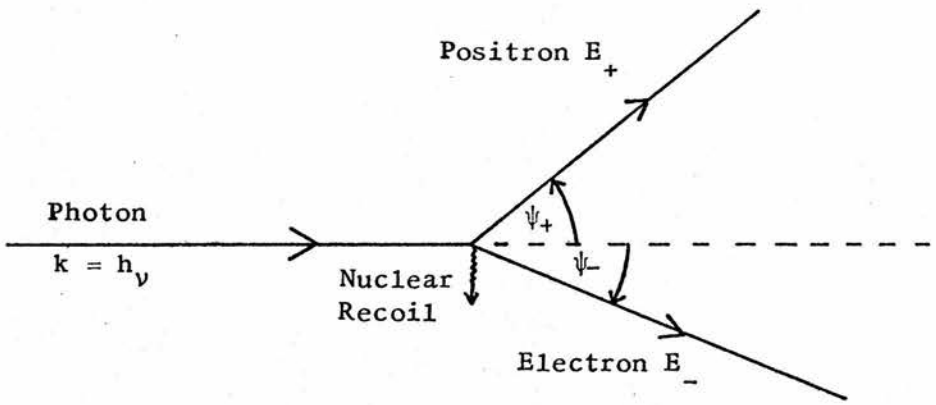

It is found that there is only a very weak dependence on photon energy, the distribution being weighted more and more heavily towards small angles as the electron energy increases. Values of the mean deflection angle have been calculated by numerical integration of the Schiff cross section for electron kinetic energies between 0.1 and 40 MeV. It is shown in Chapter 4 in the section on bremsstrahlung production that the angular distribution is adequately approximated for our purposes by an exponential with mean angle $\bar{\Psi}$

$$P(\Psi)\, d\Psi = \exp(-\Psi/\bar{\Psi})\, d\Psi \qquad .....(3.11)$$

A table of values of $\bar{\Psi}$ for different E_+, E_- is given in ch.4. It will be seen that $\bar{\Psi}$ is of the order of $2\ mc^2/E_+$ or E_-.

The deflection angle is selected from the exponential distribution using the C.P.D. method. We have

$$\Psi = -\bar{\Psi} \log_e(1 + R(\exp(-\pi/\bar{\Psi})-1)) \qquad .....(3.12)$$

for random number R and mean angle $\bar{\Psi}$. This expression differs from (2.5) as the value of Ψ extends only up to π and not to infinity as is the case for distance between photon interactions for example. A derivation of (3.12) is given in Appendix 3. The mean angle is interpolated from a tabulation of $\log_e \bar{\Psi}$. Note that no correlation is assumed between Ψ_- and Ψ_+. They are selected separately using $\bar{\Psi}_-$ and $\bar{\Psi}_+$ respectively.

The electron and positron trajectories are assumed to be in the same plane. Thus if the azimuthal deflection selected (from equ. 2.16) for

the electron is Φ_-, then the azimuthal deflection for the positron is $\Phi_- + \pi$.

3.3.5 Photoelectric Absorption

This interaction becomes important in water for photons of relatively low energy. At 0.1 MeV, photoelectric absorption accounts for only 1.6% of the total interaction cross-section. It follows that the angular distribution of the ejected photoelectrons is immaterial. There are virtually no photoelectrons of sufficiently high energy that their subsequent spatial diffusion could have an effect on any results.

There is no selection required for the kinetic energy of the photoelectron. This is simply

$$T = k - E_k$$

where E_k is the binding energy of the K-shell. If the interaction is with an electron from the L-shell, then this would be $k - E_1$ and so on. In fact, we find that for H_2O, the contribution to the total photoelectric cross-section from the two Hydrogen atoms is negligible at all photon energies of importance. For the Oxygen atom, Hubbell (1969) gives the ratio of the photoelectric cross section for the K-shell to the total for all shells as 0.94, this ratio being substantially energy independent. Accordingly, no error of any significance is incurred if it is assumed that all photoelectric interactions in water are with the K-electrons of the Oxygen atom.

In exactly the same way as with one out of five Compton interactions, every photoelectric event is assumed to give rise to an Auger electron of energy T_{aug} ~ 500 eV. The kinetic energy of the photoelectron is thus

$$T = k - T_{aug} \qquad .....(3.13)$$

There is no need to test if the photon energy is greater than T_{aug} as in practice there are no photons below about 10 keV in energy (Ellet et al., 1968). This was confirmed by the results of the present work.

3.3.6 Rayleigh Scattering

As has been explained at the beginning of this chapter, Rayleigh or coherent scattering is of minor importance in influencing the energy dissipation of photons in water. An approximate procedure is therefore adequate for determining the angular deflection due to Rayleigh scattering.

The differential cross section for Rayleigh scattering for unpolarized photons can be written as (Hubbell, 1969)

$$\frac{d\sigma_r}{d\Omega}(\Psi) = \frac{r_o^2}{2}(1 + \cos^2\Psi)(F(q,Z))^2 \ \frac{cm^2/atom}{steradian} \qquad .....(3.14)$$

where F(q,Z) is the "atomic form factor" and the square of this quantity is the probability that the Z electrons of an atom take up a recoil momentum, q, without absorbing any energy.

Hubbell gives graphs of the cumulative angular distribution of σ_r based on values of F(q,Z). We make use of the '75%' curve for Carbon. By this it is meant

Figure 3.6 MEAN RAYLEIGH SCATTERING ANGLE vs PHOTON ENERGY

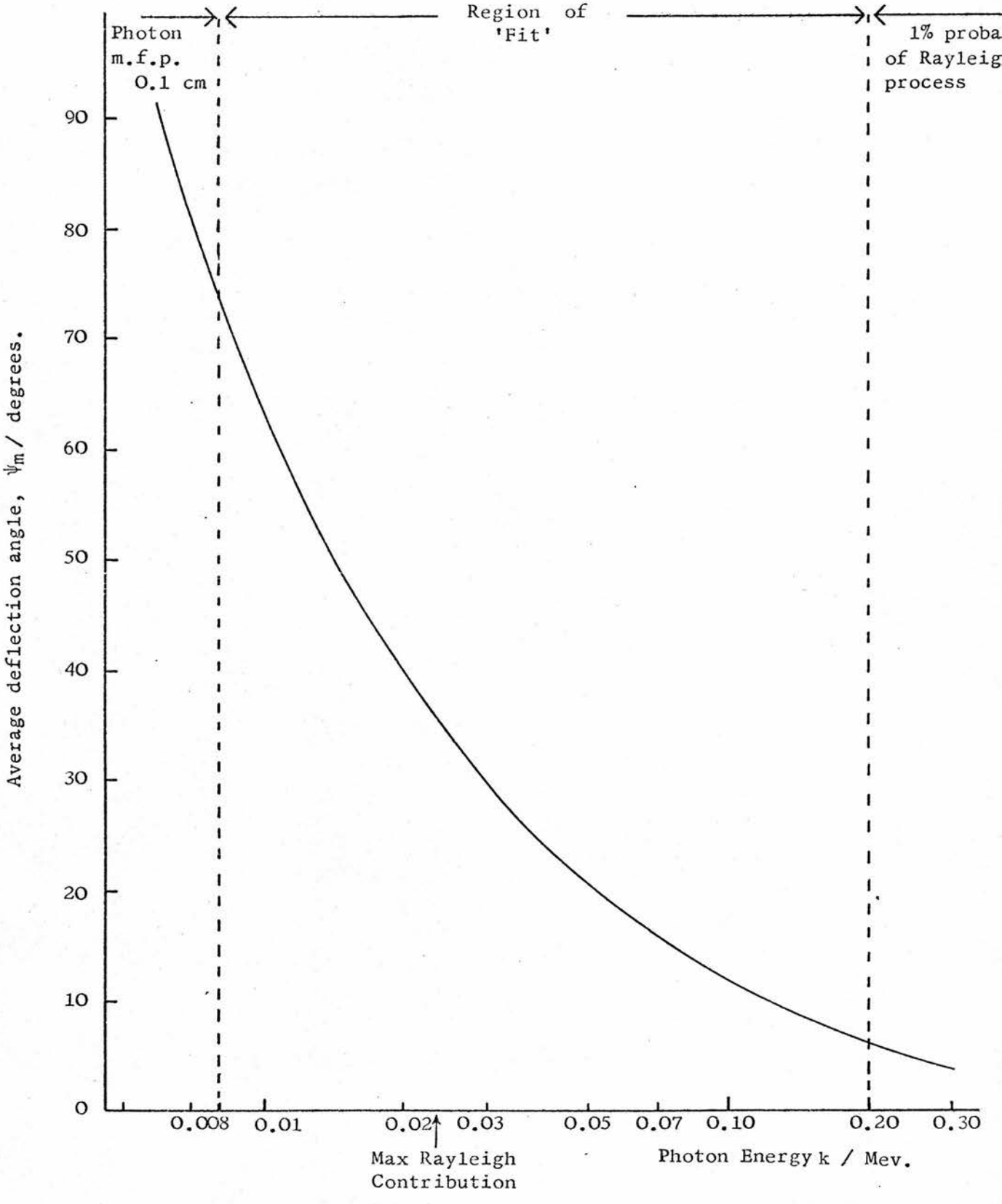

that the opening half-angle, Ψ_c, contains 75% of the Rayleigh-scattered photons. Dependence of Ψ_c on Z is slow so that we can take these Ψ_c values to apply to Oxygen. In common with the photoelectric effect, the contribution from the Hydrogen atoms to the total coherent scattering cross section is negligible.

If we approximate the differential cross section by an exponential distribution with mean angle ψ_m, then ψ_m is given by

$$\frac{\int_0^{\Psi_c} \exp(-\Psi/\psi_m)\,d}{\int_0^{\pi} \exp(-\Psi/\psi_m)\,d} = 3/4$$

and integrating

$$4\exp(-\Psi_c/\psi_m) - 3\exp(-\pi/\psi_m) = 1 \qquad .....(3.15)$$

This identity for ψ_m has been solved numerically by an interative procedure. The variation of the mean scattering angle with photon energy is illustrated in figure 3.6.

Referring to table 3.1, it can be seen that the mean free path of a photon in water has fallen below 0.1 cm at an energy of 0.008 MeV. This has been taken as the minimum energy of interest as far as the value of ψ_m is concerned. As remarked in the previous section, there are almost no photons below 10 keV anyway. The upper energy limit of interest can conveniently be 0.20 MeV where the contribution of Rayleigh scattering to the total interaction probability has fallen to 1%. Values of ψ_m used in the

photon simulation program are calculated from a polynomial fit to ψ_m in $\log_e(k^3)$ in the energy range $k = 0.008$ to 0.20 MeV.

The C.P.D. method, for Ψ restricted to the range 0 to 180^o, is employed to select the polar deflection angle, Ψ_R

$$\Psi_R = -\psi_m \log_e (1 + R(\exp(-\pi/\psi_m) - 1)$$

The azimuthal deflection is uniformly distributed between 0 and 2π.

Figure 3.7 FLOW DIAGRAM FOR THE PHOTON SIMULATION.

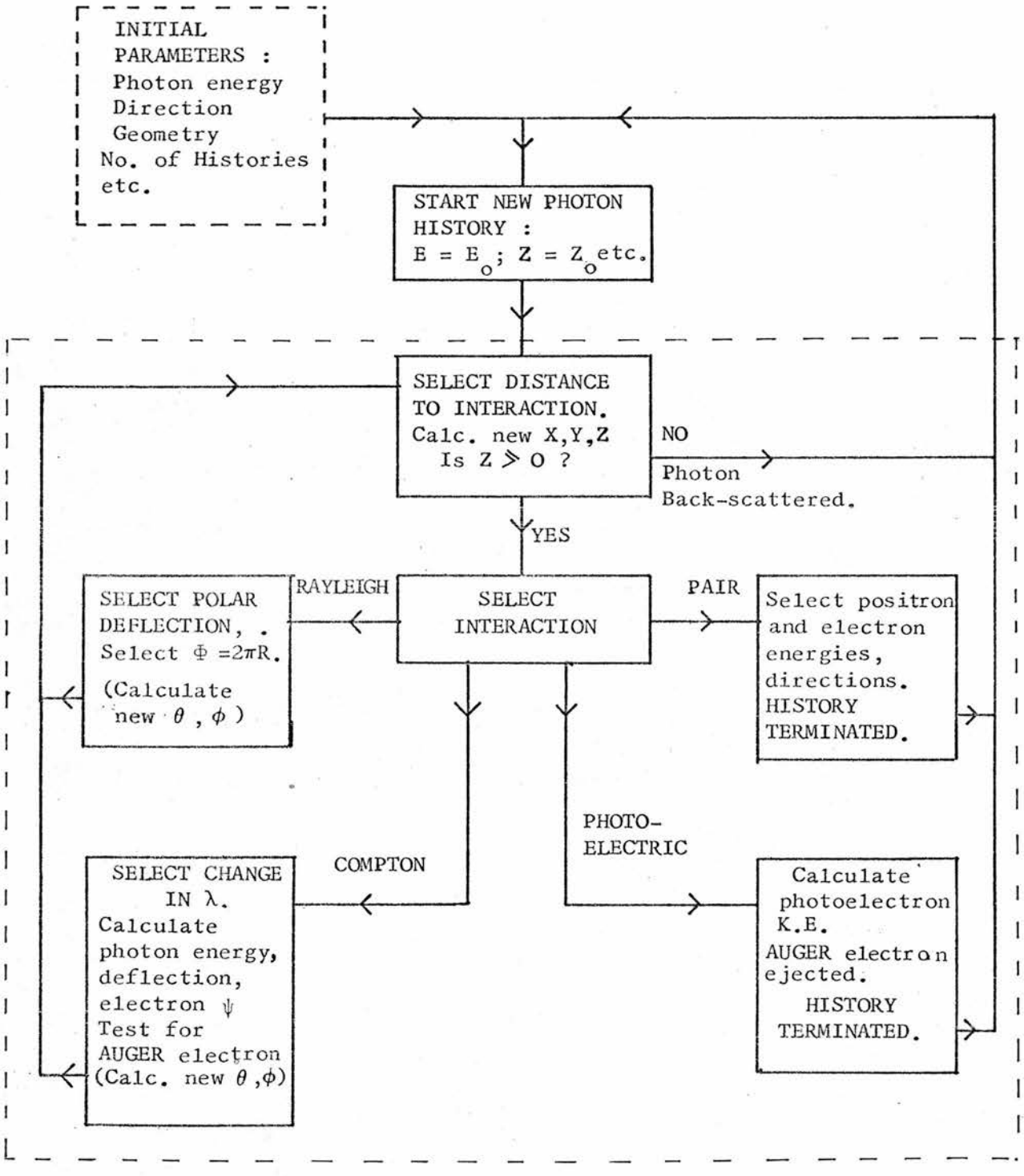

Figure 3.8 'ROUTINE' FLOW DIAGRAM.

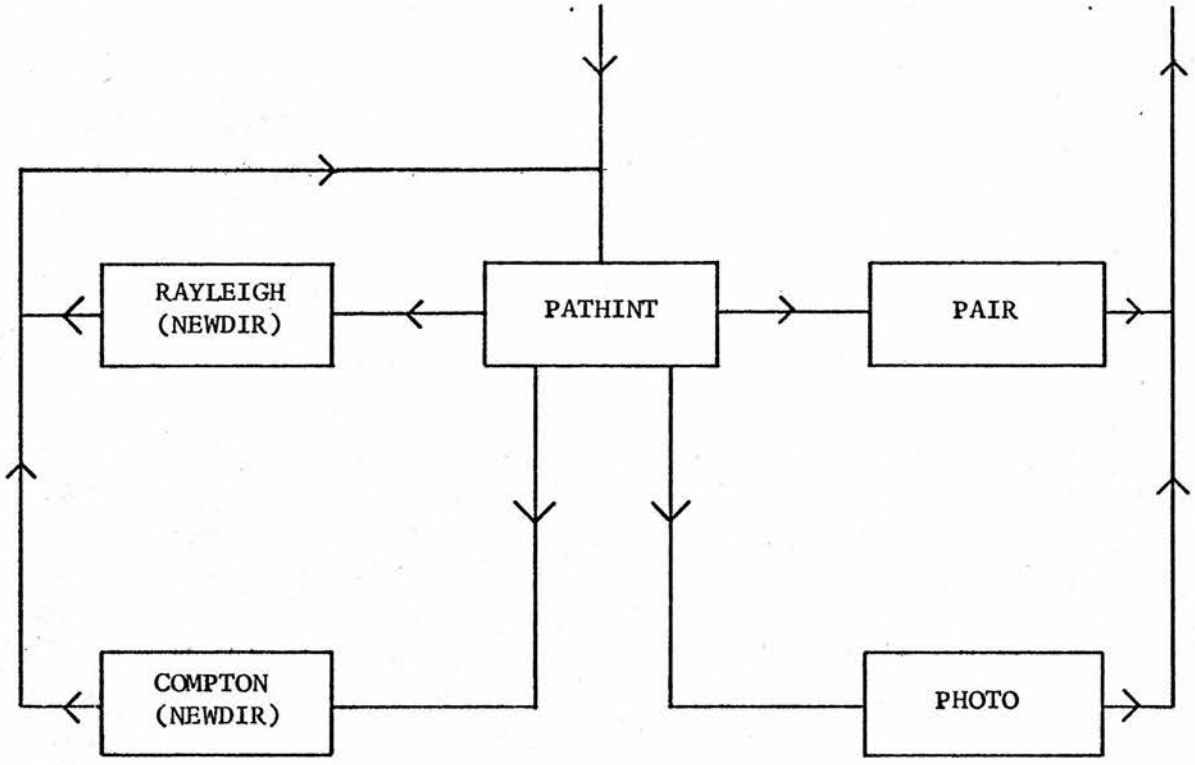

3.4 THE COMPLETE PROGRAM

3.4.1 The Flow of the Simulation

The way in which the component parts of the calculation are put together in order to simulate the physical events can be seen by reference to figure 3.7. Sufficient detail to indicate the 'flow' of the computations is given in the figure. Operations not indicated in the 'boxes' include the calculation of the directions θ, ϕ, for the pair positron and electron, and the storing of the initial coordinates of the Compton, photo-, pair and Auger electrons ejected by the photons. Also not shown is the termination of a photon history when the photon energy falls below a certain cut-off value. This would be included in the same 'box' as the test for $Z \geq 0$ (i.e. backscattering).

3.4.2 Routines

A second flow diagram is shown in figure 3.8. This corresponds to the part of figure 3.7 enclosed by the dotted line.

In practice, when writing the computer program, all the operations involved in, say, Compton scattering, are written together as a 'Routine' named COMPTON. In a similar manner, we have routines RAYLEIGH, PAIR and PHOTO which comprise all the operations indicated in the respective 'boxes' for these interactions in figure 3.7. The selection of the distance between interactions, and the selection of interaction

type are included together in the routine PATHINT.

When programming the logical flow of the simulation, we can then refer to all the operations outlined in a particular box in figure 3.7, by the name of the routine. The actual description of the routine, which may be long and complicated, can then be relegated to the end of the program. To the best of the author's knowledge, this procedure is possible in most high-level programming languages.

In figure 3.7, the operations for Rayleigh and Compton scattering include the statement "Calculate new θ, ϕ." This operation is performed by the routine NEWDIR which contains the relations described in section 2.3.2. Figure 3.8, then, is a description of the more detailed flow diagram in figure 3.7 in terms of the routines used in the photon Monte Carlo program.

3.4.3 Structure of the Complete Photon Program

The Monte Carlo computer program is made up of 4 main sections:

i) Input of Data

This includes both the 'adjustable' variables such as photon energy and number of histories, and the 'fixed' data i.e. those which do not alter from one run to another, such as the tabulation of values of $P_c(E)$, the probability of an interaction being Compton scattering.

ii) Generation of the Histories

This has been dealt with in the previous two sections. The logic of this part of the program

is essentially given in figure 3.7. The use of routines enables the coding of the simulation of the sequence of the physical events to be reduced to a few lines of program. The same logical sequence is repeated for the number of histories specified in the input data.

iii) Output of the results

iv) Description of the routines

This is invariably the longest section, consisting of several different routines. The routines are all put together after the code for the printout of the results in order to make the structure of the program clearer.

3.4.4 Calculation of Results

The photon histories generated can be analysed to yield any number of physical parameters such as percentage backscatter, energy spectrum of scattered photons, spatial energy dissipation etc. It is possible to store all the coordinates describing a set of histories in a data file and subsequently run a separate program to extract the particular information required from the histories. This requires an enormous amount of storage space for large numbers of histories and generally makes the whole calculation more difficult to handle.

The procedure adopted in this work is effectively to analyse each history as it is carried out. A simple example of this is the calculation of the number of back-scattered photons. Each time the condition Z >= 0

Figure 3.9 IRRADIATION GEOMETRY.

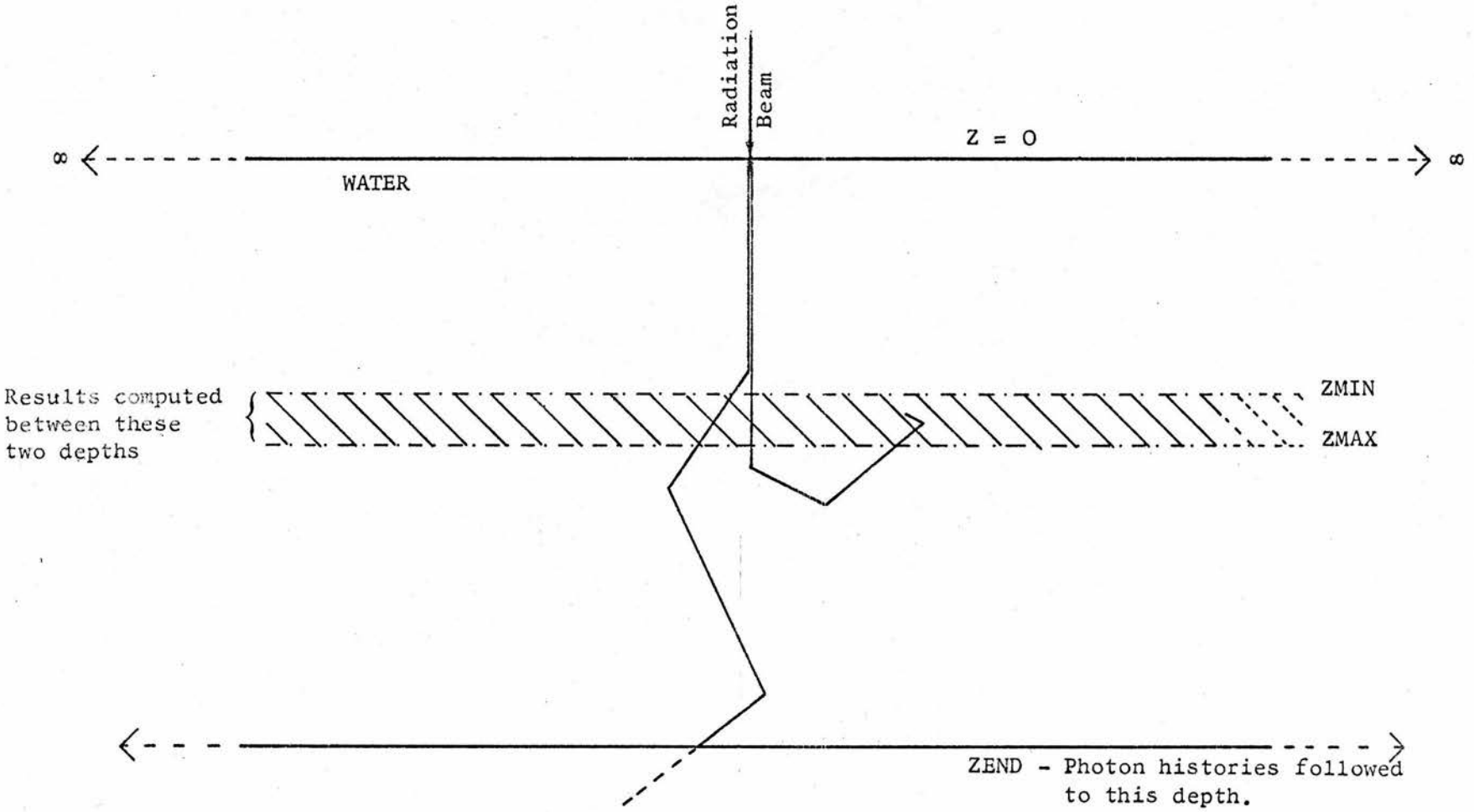

is not satisfied, the variable BAC is augmented by one. Such steps are included in the appropriate routines. The basic logical sequence of the simulation is not altered by the inclusion of extra lines of code to extract more information from a particular run, though the size and run-time of the program may be appreciably increased. The statistical accuracy of any results obtained is, of course, dependent on the number of histories.

3.4.5 Geometry

The introduction of boundaries into the medium presents no problem in Monte Carlo calculations. The geometry of the incident photon beam for the calculations described in this work, for reasons discussed elsewhere, is usually plane perpendicular incident on a semi-infinite medium. Information about the photon histories is generally required only for the first 30 cm of penetration. Consequently, the histories can be terminated if Z exceeds a certain value ZEND. This also avoids using any more computer time than is necessary for a given number of histories.

As will be illustrated by the results presented in section 3.5, information is frequently desired about the spectrum or energy dissipation between 2 depths as in figure 3.19. All that is necessary to effect this is a line:

```
IF ZMIN <=  Z <= ZMAX THEN .....
```

followed by the code to record the energy dissipation etc.

Figure 3.10 SAMPLE COMPUTER PRINTOUT FOR THE PHOTON MONTE CARLO PROGRAM.

```
COMMAND:RUN(OMK2PHO)
DATA:2              Photon Energy (MeV)
DATA:0.001          Low-energy cut-off (MeV)
DATA:0              X_o (cm.)
DATA:0              Y_o (cm.)
DATA:0              Z_o (cm.)
DATA:0                 (degrees)
DATA:0                 (degrees)
DATA:500               Number of Histories
DATA:4087721           Random Number Initializer

PHOTON TRANSPORT SIMULATION

NARROW BEAM OF MONOENERGETIC PHOTONS
SEMI-INFINITE WATER MEDIUM

PHOTON ENERGY =    2.0000 MEV
NUMBER OF HISTORIES -    500

INITIAL COORDINATES:      X =     0.00 CM
                          Y =     0.00 CM
                          Z =     0.00 CM
                      THETA =     0.00 DEGREES
                        PHI =     0.00 DEGREES

PHOTOEFFECT IMPOSED AT  0.0010 MEV

   5.5260SEC  }
              }     Execution time for the 500 histories.
  45.7870SEC  }

NO. OF HISTORIES  H =   500
NO. OF INTERACTIONS  N =    6590
NO. AUGER ELECTRONS  AUG =    1487
NO. OF RAYLEIGH SCATTERS  NR =     266
NO. OF BACKSCATTERED PHOTONS  BAC =    95
NO. OF TIMES EPH<CUT-OFF  IMP =     0
```

3.4.6 Some Practical Details

A typical printout of a run of one of the early versions of the photon simulation is reproduced in figure 3.10. The input data does not include a geometrical cut-off so the photons are 'followed' to absorption unless they are back-scattered. The low-energy cut-off is never imposed as the photons never drop to such a low energy (1 keV in this case) before being absorbed. In later versions, this cut-off was dispensed with . The 500 histories took 45 seconds to execute, giving a run-time per history of just less than one tenth of a second. This is a typical figure. For photons of a lower initial energy, there are less interactions per history and consequently the execution time is reduced. In this example, no distributions such as energy spectra were calculated from the photon histories.

Several versions of the photon program have been written, differing mainly in the amount of information extracted from the histories. The simplest version, which calculates only the information in the printout in figure 3.10, is about 350 statements of IMP and occupies 8 Kbytes in compiled form. A later version, which analyses the histories to give the electron source spectrum, is over 600 statements with a corresponding increase in the size of the object program.

Considerable efforts were made to reduce the execution time per photon history. The details need not concern us here, but let it suffice to mention that

some of the selection methods described in the previous sections were replaced by faster techniques devised by Von Neumann. Details of these can be found in Zerby (1963). Also a more efficient way of using the random number generator was employed. A total reduction in run-time by a factor 2 was achieved by such modifications. It must be noted in this connection, that the execution time of the photon program is not the critical factor when it is to be linked to an electron simulation program as in this work. As will be emphasised in the next chapter, the execution time per electron history is invariably an order of magnitude greater than that for photon histories.

3.5 INTERMEDIATE RESULTS

The photon Monte Carlo program was written in order to be linked to the electron program for the purpose of calculating the electron flux in water irradiated by primary photon beams. Nevertheless, a few of the results obtained from runs of the photon program before it was amalgamated with the electron simulation are presented here. It can be seen that the photon results are consistent with those of other workers as well as illustrating one or two important features of photon energy dissipation.

3.5.1 Depth-absorbed dose histogram

For a photon beam of initial energy less than about 1 MeV, the range of the Compton electrons is negligible compared to the mean free path of the photons producing them. Consequently, the subsequent diffusion of these secondary* electrons has little or no influence on the spatial energy dissipation resulting from the absorption of the photon beam.

It is assumed that the energy of the secondary electrons is deposited at the position where the interaction occurred. This assumption is valid as long as there are no positrons produced, which eventually result in the emission of two annihilation photons of energy 0.511 MeV, and that the secondary electrons do not give rise to appreciable numbers of high-energy bremsstrahlung photons. Both these conditions are amply fulfilled for photons of energy less than a few MeV.

---

*referred to as photon-ejected or primary electrons later in this work.

Figure 3.11 DEPTH-ABSORBED DOSE HISTOGRAM FOR 0.5 MeV PHOTON BEAM IN WATER.

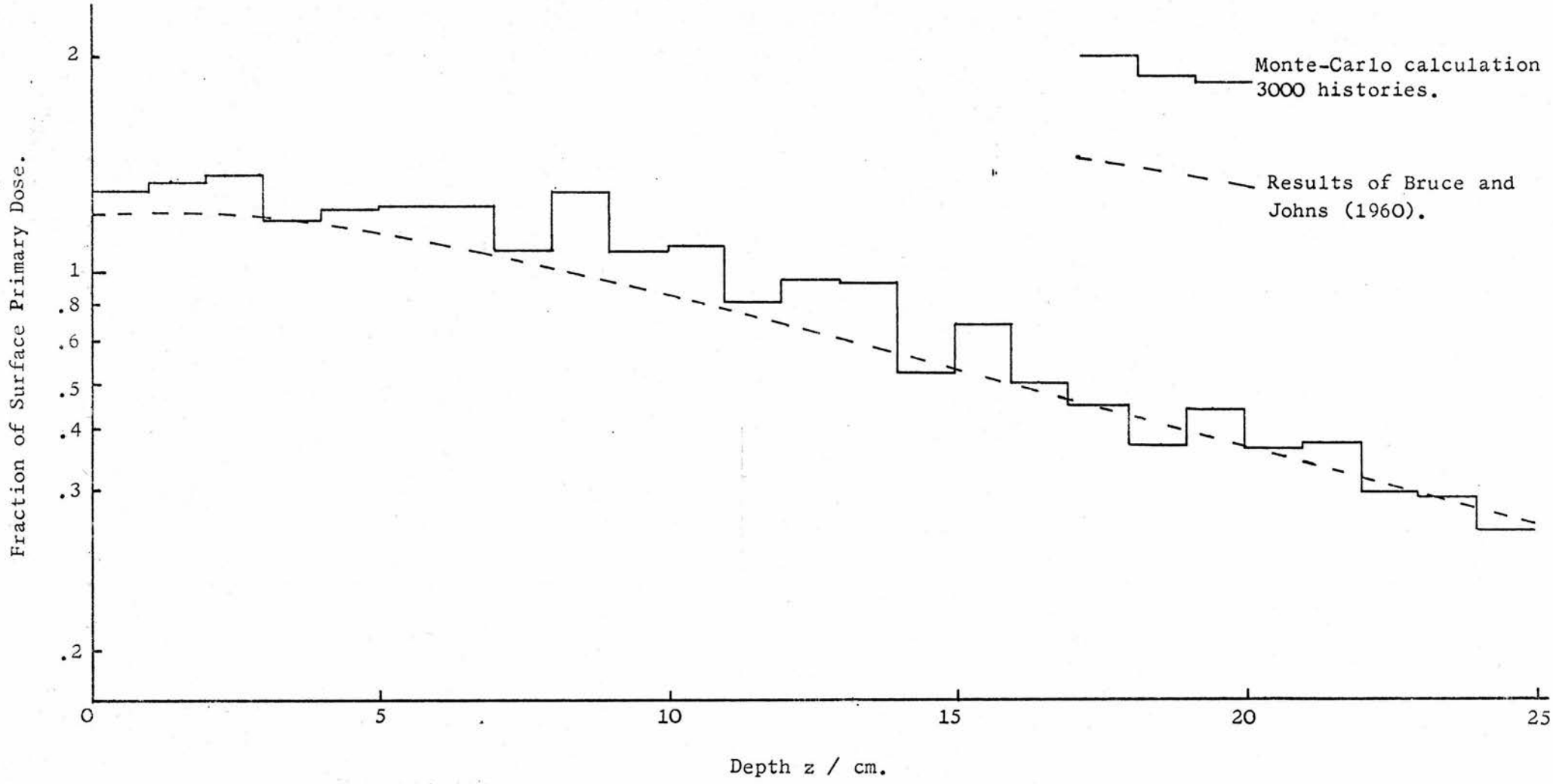

Figure 3.12 SOURCE SPECTRUM OF ELECTRONS SET IN MOTION BY A 1 MeV PHOTON (Infinite medium).

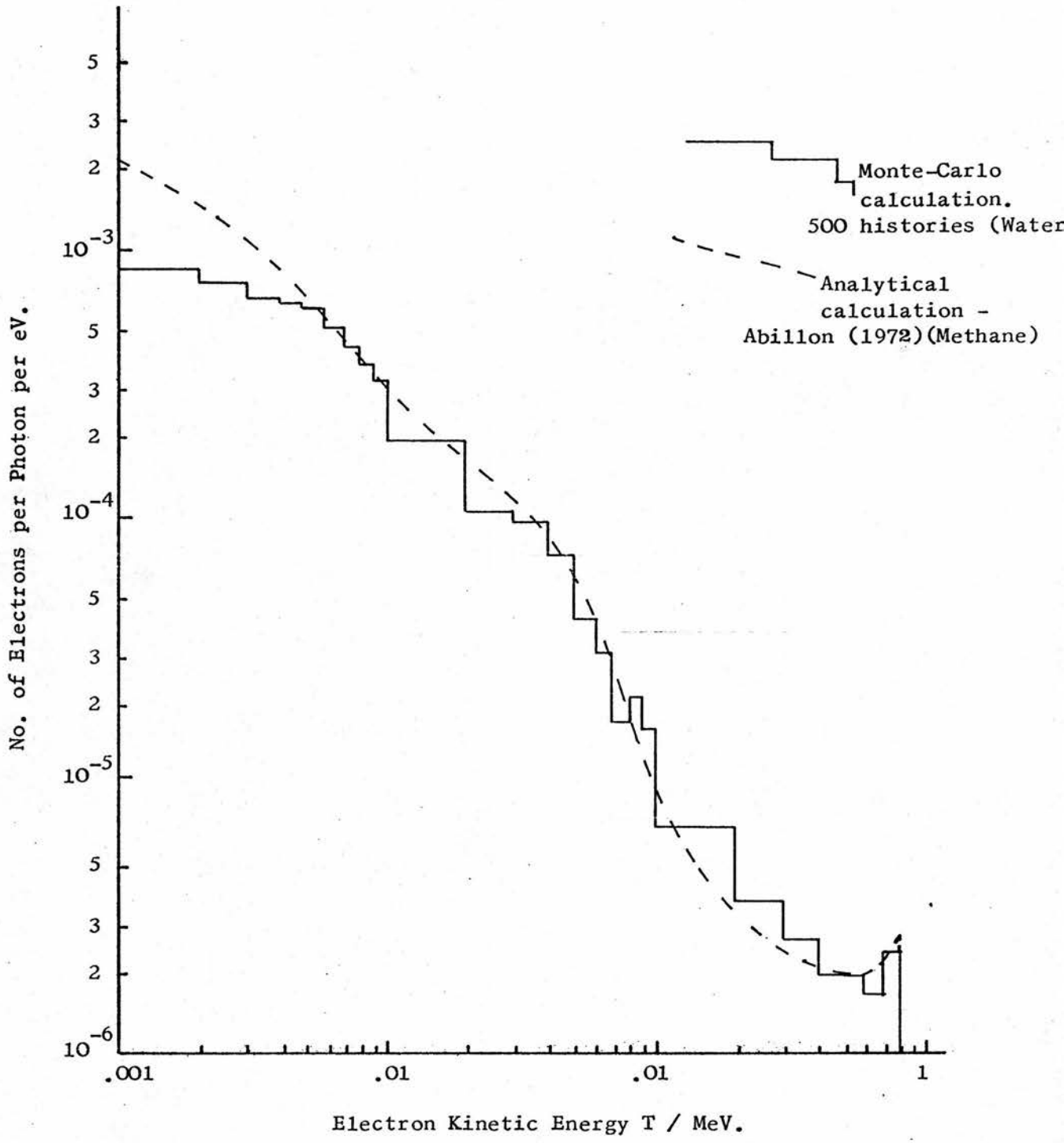

By adding up the energies of the secondary electrons deposited in 1 cm layers in the Z direction, a histogram is built up as drawn in figure 3.11. Superimposed on this histogram is the depth-absorbed dose curve calculated by Bruce and Johns (1960) for the same photon energy and geometrical conditions i.e. central axis dose; infinite field; infinite FSD, in radiotherapy parlance. The agreement is satisfactory. Bruce and Johns used a combination of analytical and Monte Carlo techniques to handle the photon transport. The Monte Carlo calculation was organized so as to produce results normalized in the same way as those of Bruce and Johns. It can be seen that 3000 histories do not give a particularly 'smooth' histogram, emphasising the effect of the small number of 'catastrophic' events in each photon history.

3.5.2. Initial energy spectrum of electrons and positrons

The photon histories can be analyzed to give the numbers of electrons (including positrons) of different energies. The first histogram shown of this 'source' spectrum of the ejected electrons is for an infinite, as opposed to semi-infinite, medium. This is achieved by simply putting Z_o equal to a sufficiently large value so as to preclude any back-scattering. In figure 3.12, we compare the histogram to the results of an analytical calculation by Abillon (1972). Her medium was Methane, not Water, but this leads only to a difference in the number of low-energy electrons

Figure 3.13 ELECTRON SOURCE SPECTRUM PRODUCED BY A 10 MeV PHOTON BEAM IN WATER : 2 DIFFERENT GEOMETRIES

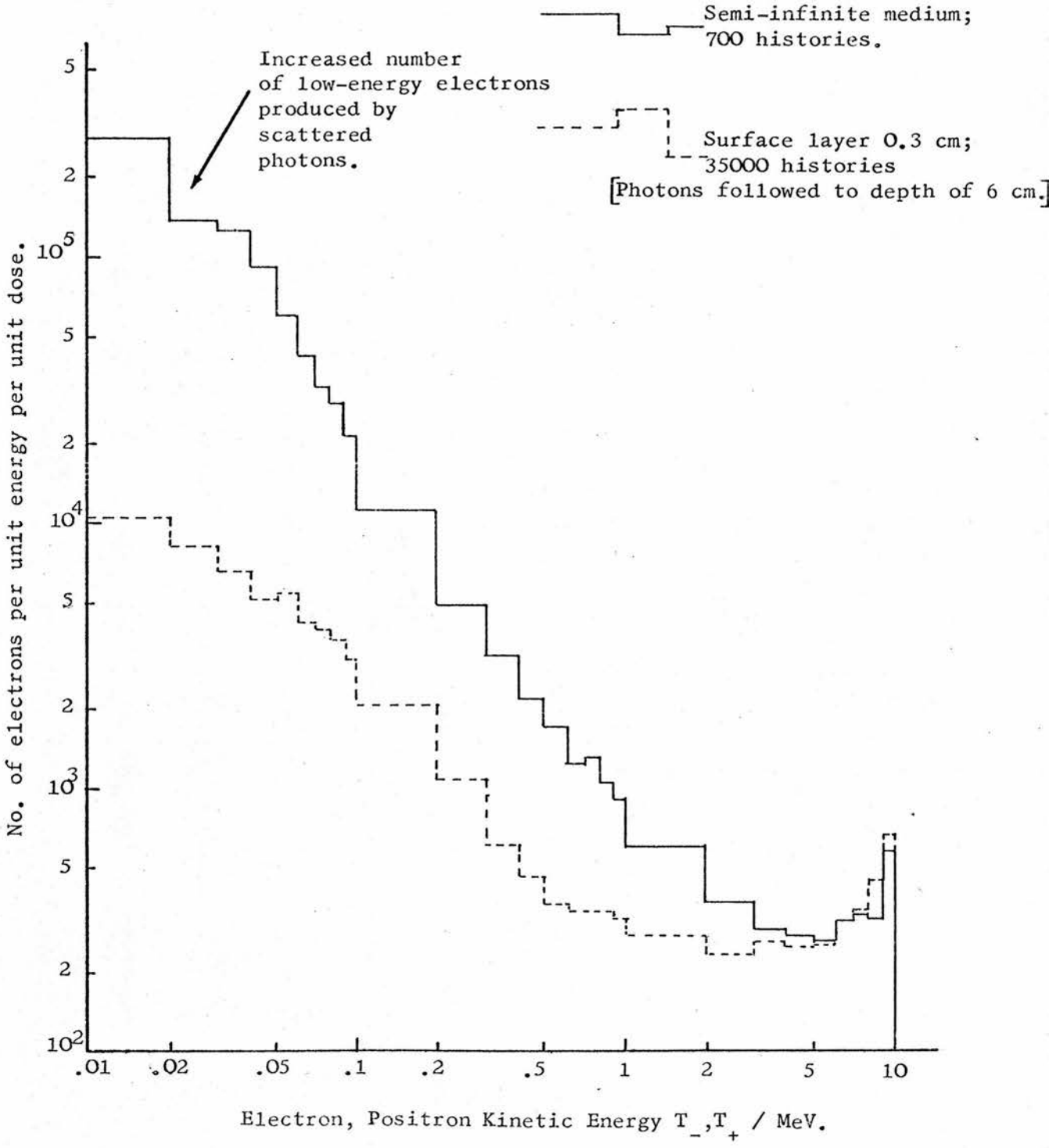

produced by the photoelectric effect. The energy distribution of Compton electrons is not affected. The so-called Compton edge is evident at the high-energy end of the spectrum. The maximum energy of a Compton electron is about 0.8 MeV. This corresponds to the maximum photon wavelength change of 2 Compton units (see equ. 3.7) for the 1 MeV primary photons. The energy range only extends to 1 keV so that the large numbers of Auger electrons at 500 eV are not shown.

Secondly, in figure 3.13,the influence of the scattered photons on the shape of the electron source spectrum is illustrated. For 10 MeV photons, 2 runs were carried out for different geometries. In the case of the semi-infinite medium, there are a large number of low-energy Compton electrons arising from multiply-scattered photons. For the surface layer geometry, most of the Compton electrons arise from the first photon scatter. This change of initial electron spectrum with depth for a photon beam will be seen to be of some significance later in this work. We can note that a much larger number of photon histories was necessary to achieve the same 'resolution' in the 0 - 3 cm geometry as in the semi-infinite case. This is to be expected since on average a 10 MeV photon has only 0.2 interactions in the 3 cm layer compared with about 11 interactions before it is absorbed.

CHAPTER 4

MONTE CARLO PROGRAM FOR ELECTRON TRANSPORT

4.4 REQUIREMENTS OF THE CALCULATION

The program is required to yield information about the spatial diffusion of electrons in water. In particular, the results must include the total electron flux spectrum at different depths produced by primary electron beams with initial energies between 5 and 40 MeV. The electron simulation is also to be coupled to the photon Monte Carlo program in order to handle the transport of photon-ejected electrons and yield electron flux spectra produced by primary photon beams at various depths of interest. The electron program, in turn, calculates the initial parameters of bremsstrahlung photons produced by electron interactions which serve as input data for the photon transport program. The electron histories are terminated when the kinetic energy of the electron falls below a cutoff, T_c, such that further spatial diffusion is unimportant.

The construction of the program has also been guided by the practical limitation of the amount of computer time available, which has influenced the simulation scheme adopted and the approximations employed. The final Monte Carlo program is, in effect, a compromise between a fast execution time to extract the desired information and an accurate simulation of the physical processes involved in electron transport and energy loss.

4.2 ELECTRON INTERACTIONS WITH MATTER

4.2.1 Ionizations and Excitations

The dominant mode of electron energy loss, in the energy range of interest in this work, is through inelastic collisions with the bound electrons of the atoms or molecules of the slowing-down medium. The atoms are either ionized, with the ejection of an electron, or left in an excited state. This is the start of the chain of events leading to chemical and biological changes in certain substances.

The size of the energy transfers is heavily weighted towards the low-energy end, following very closely a $1/q^2$ distribution, for energy transfer q, except for transfers close to the binding energies of the electrons of the medium. The average energy loss, which is largely independent of the electron kinetic energy above a few keV in the light elements, is of the order of 60 eV. This means that a 1 MeV electron will produce about 20,000 ionizations and excitations in slowing down to an energy of a few eV. Quantum theory dictates that it is not possible to say which of the two electrons emerging from a collision is the primary and which is the secondary. By convention, the electron with the lower energy is taken to be the secondary. This results in the maximum possible energy of a secondary electron, or δ-ray, being half of the energy of the primary before the interaction. This would not be the case for a primary positron, for example.

The average rate of energy loss due to ionizations and excitations is represented by the collision stopping power, $(dT/dx)_{col}$, already referred to in chapter 1. This is usually evaluated from the theoretical Bethe-Bloch expression. The theory assumes that the electrons of the slowing-down medium are free and is therefore only valid for electron energies well above the binding energies of the atomic electrons. This restriction is not important for the electron energies involved in the Monte Carlo simulation, which do not extend below the cutoff, T_c, which is never less than 0.1 MeV.

The lower limit to the size of the energy transfer enters into the theory through the parameter I, the mean ionization potential. This depends on the electron energy levels and corresponding oscillator strengths for the atoms of the medium concerned. Theoretical evaluations for I for all but the simplest atoms have so far proved to be too complicated. The accepted values for different elements have been deduced from experimental measurements of the ranges of protons in various materials (see, for example, NAS-NRC 1133 (1964); Dalton and Turner (1968)).

Electron collision stopping powers in the MeV energy region in condensed media are reduced below the values given by the Bethe-Bloch theory due to the so-called density effect. The assumption that the medium can be treated as a collection of individual, uncorrelated atoms has to be modified to take into account the screening of the

electric field experienced by electrons distant from the primary electron track. This screening is due to the polarization of the intervening atoms. Consequently, there is a reduction in the energy loss due to 'distant' collisions. The theory of the polarization or density effect has been developed to the point of numerical application for a wide range of elements and compounds by Sternheimer (1952, 1956). In water, the reduction in the total collision stopping power rises from 1% at 0.85 MeV to 18% at 40 MeV. The significance for ionization dosimetry of this reduction, which is entirely negligible in gases at these energies, has already been discussed in chapter 1. It can be noted here that evaluations of the restricted collision stopping power tacitly assume that the size of the energy transfers affected by the density effect is less than the cutoff, Δ . This assumption, for values of Δ as low as 10^0 eV, is examined critically in a later chapter.

4.2.2 Bremsstrahlung

In the field of a nucleus, or an atomic electron, an electron can lose energy through the production of photons, known as bremsstrahlung. This process is analogous to the classical radiation of energy by an accelerating or deccelerating electric charge. The process begins to dominate over collision energy losses at relativistic energies, more particularly for the heavy elements as the cross section is approximately proportional to Z^2, or $Z(Z+1)$ if radiation in the field

of the atomic electrons is also included.

Associated with bremsstrahlung energy loss is the radiation stopping power, $(dT/dx)_{rad}$, and another useful quantity, the radiation yield, Y_{rad}. This is defined as the fraction of its initial kinetic energy that an electron will radiate in the course of slowing down. In water, for an electron energy of 1 MeV, $(dT/dx)_{rad}$ is less than 1% of the total stopping power and Y_{rad} is 0.0049. At 40 MeV, these figures are 30% and 0.16 respectively. The so-called critical energy, when radiative and collision stopping powers are equal, is reached at 92 MeV in water, well above the maximum energy concerned in the present work.

The distribution of bremsstrahlung photon energy, k, roughly approximates to a 1/k law. An electron may lose up to all its kinetic energy in the production of a photon. Bremsstrahlung energy loss tends to be less 'continuous' in nature than that due to inelastic electron-electron collisions, there being a greater probability of large energy losses.

4.2.3 Scattering

In both the energy-loss mechanisms described above, the primary electron is deflected. However it is elastic coulomb interactions between the electron and the heavy nucleus of charge Z that dominate the electron scattering process. Rutherford first derived the distribution of the electron deflections assuming that the nucleus was a point charge. More refined treatments have included the effect of the finite size

of the nucleus and the screening of the nuclear field by the atomic electrons.

In the course of slowing down, the electron is scattered many thousands of times in a short section of its path mostly through very small angles. This has led to the development of theories of multiple scattering. Distributions have been calculated for the size of the deflection angle after the electron has travelled a given distance. Such multiple scattering distributions vary in their complexity depending on which single scattering cross section they are based upon etc. The simplest of these, the Gaussian distribution, which does not take into account the occasional large angular deflection, will be shown to be adequate for the present purposes.

4.2.4 Electron Range

Bubble chamber pictures show very clearly the considerable straggling of electron tracks. Nevertheless, the concept of an average range of an electron is useful. A commonly used quantity is the c-s-d-a range, r_o. This theoretically calculated range is the total pathlength assuming that an electron of initial energy, T_o, loses energy continuously at the rate given by the total stopping power. Hence

$$r_o = \int_o^{T_o} 1/(dT/dx)_{tot}.dT \qquad .....(4.1)$$

Due to the scattering of the electron, r_o is always greater than any measurable quantity such as the maximum depth of penetration. Values of r_o in water

range from 0.17 cm at 0.5 MeV to 9.2 cm at 20 MeV, increasing by roughly 1 cm for every 2 MeV above an electron K.E. of about 2 MeV.

4.3 COMPUTATIONAL SCHEME

4.3.1 The Grouping of Collisions

As has been outlined above, an electron undergoes a vast number of interactions in slowing down. This is in complete contrast to a photon, which experiences on average a dozen or so catastrophic interactions before absorption. A photon Monte Carlo simulation can be a direct analogue of the physical events. This is out of the question when dealing with electrons. It becomes necessary to group together large numbers of the electron interactions, effectively treating the electron track as a manageable number of sections.

The question then arises as to which particular scheme is to be used to group the collisions together. The steps can be regulated by the energy of the particle or the pathlength. As Berger (1963) points out, the arbitrary pre-selection of energies is reasonable for protons, which can only lose a tiny fraction of their energy in an individual collision and thus traverse a practically continuous range of energies. Electrons, on the other hand, can lose a major fraction of their energy in a single interaction, so that they may jump over certain energy intervals altogether.

In view of the fact that δ-rays with energies above the Monte Carlo cutoff, T_c, and bremsstrahlung

photons were to be included in the complete simulation, a 2-group scheme naturally suggested itself. In this type of calculation, individual events resulting in energy losses above a certain cutoff, Δ, are excluded from the grouping. The distance between these 'catastrophic' events as well as the size of the energy loss and deflection are selected individually. Over the pathlength sections between catastrophic events, the energy loss can be calculated from the continuous-slowing-down approximation, or from a theoretical straggling distribution to take into account energy-loss fluctuations. The angular deflection is selected from a suitable multiple scattering distribution.

The 2-group scheme was employed in an electron Monte Carlo calculation by Schneider and Cormack (1959) (see fig. 1.5), who experimented with different cutoff values, finding that this influenced only slightly their results for the primary electron flux in an infinite water medium. Berger (1963), who referred to such schemes as class II, discussed their advantages over class I schemes which group all the collisions together, regardless of the magnitude of the energy loss involved. In particular, he pointed out that the initial state of the δ-rays is indicated unambiguously, that the angular deflections due to inelastic scattering can be calculated more accurately, and the correlation between energy-loss fluctuations and multiple-scattering deflections is preserved more

faithfully. In the present case, these remarks can be extended to include the fairly frequent, large energy losses due to bremsstrahlung, which may be expected to have an appreciable effect on the shape of the electron spectrum at high energies.

4.3.2 Choice of catastrophic cutoff

The lowest value used for the energy at which the Monte Carlo histories were terminated, T_c, was never less than 0.1 MeV for reasons given later. Therefore, it was not strictly necessary to be able to calculate the initial parameters of δ-rays below T_c. However, the choice of such a high cutoff as 0.1 MeV for the sampling of catastrophic events would have necessitated the use of an ionization-loss straggling distribution rather than the simpler c-s-d-a for the energy loss between catastrophic events if realistic depth-dependent flux spectra were to be derived from the electron histories. A comparison of the electron spectra from calculations by Kessaris (1966, 1970), based on the c-s-d-a, and by Harder (1965), based on the Landau straggling distribution, shows this very clearly. It was desirable to avoid the complications involved in the use of a straggling distribution for the 'non-catastrophic' energy losses. Further, as the mean free path of a 0.1 MeV photon is about 6 cm, the spatial diffusion of bremsstrahlung photons with initial energies below the cutoff could not have been ignored, implying that a different, lower cutoff value would have been necessary for bremsstrahlung events in order

that the photons could have been included in the photon MC simulation. This, too, would have unnecessarily complicated the program. Consequently, it was desirable to have as low a cutoff energy, Δ, as possible.

For a 5 MeV electron, a cutoff of 100 eV results in around 860 collisions per cm. This is clearly far too many steps to be feasible in terms of computer time. If Δ is increased to 10 keV, then there is an average of only 9 catastrophic collisions per cm, or a total of about 30 steps per history, not including bremsstrahlung events. This was considered to be a manageable number. However, for a 30 MeV electron, a 10 keV cutoff would result in around 200 steps, which is not so manageable. The use of a variable cutoff was therefore indicated. A cutoff proportional to the electron energy, T, would have given an unnecessarily large number of steps at low energies close to T_c where the small residual range of the electron makes an accurate treatment of the diffusion less important. As a compromise, a cutoff $\Delta(T)$ was chosen which varied linearly with electron energy, T, from 30 keV at 40 MeV to 10 keV at 0.5 MeV:

$$\underset{[keV]}{\Delta(T)} = \underset{}{0.5063}.\underset{[MeV]}{T} + 9.747 \qquad .....(4.2)$$

The use of this variable cutoff for catastrophic events, whether electron-electron collisions or bremsstrahlung production, together with the c-s-d-a for calculating

the energy loss along the intervening pathlength steps, was considered to be a sufficiently accurate simulation of the fluctuation of the energy loss of an electron along its track. Effectively, all the energy-loss straggling is assumed to be due to losses greater than $\Delta(T)$.

It must be emphasised that the validity of the particular scheme adopted, with its associated, often arbitrary approximations, can ultimately only be demonstrated by the agreement or otherwise of results calculated from the electron histories with those from other determinations, both theoretical and experimental. The 'proof of the pudding is in the eating' as it were.

4.4 SIMULATION OF THE INTERACTIONS

In the sections immediately following, details are given of the calculations that were involved in simulating the electron tracks. The so-called catastrophic events are dealt with first, and then the pathlength sections or steps between these large energy losses. Input data were prepared for carbon and aluminium as well as for water in order to be able to compare preliminary results with those of other workers for these media. The minimum energy possible for the Monte Carlo cutoff, T_c, was taken as 0.1 MeV. At this energy, an electron has a range, r_o, of only 0.014 cm in water.

4.4.1 Catastrophic δ-ray production

There are two basic quantities involved. Firstly, an effective attenuation coefficient, μ_δ, and associated mean free path, $\bar{s}_\delta$, between collisions resulting in a δ-ray of energy greater than the cutoff, $\Delta(T)$, must be calculated. Secondly, a selection has to be made of the energy of the δ-ray, which lies between $\Delta(T)$ and $T/2$. The Møller relativistic cross section for coulumb interactions between free electrons was employed to derive these quantities. This can be written as (Berger, 1963)

$$\frac{d\sigma}{d\epsilon} = \frac{C}{T}.\left(\frac{1}{\epsilon^2} + \frac{1}{(1-\epsilon)^2} + \left(\frac{\tau}{\tau+1}\right)^2 - \frac{2\tau+1}{(\tau+1)^2} \cdot \frac{1}{\epsilon(1-\epsilon)}\right) \qquad .....(4.3)$$

Table 4.1 ATTENUATION COEFFICIENT FOR δ-RAY PRODUCTION (WATER)

T (MeV)	Δ(T) (keV)	μ_δ (cm^{-1})	$\bar{s}_\delta$ (cm)
0.5	10.0	10.58	0.0945
1	10.25	9.07	0.1102
5	12.28	6.98	0.1432
10	14.81	5.77	0.1735
40	30.0	2.84	0.3517

where

$\epsilon = q/T$, the energy transfer in units of the electron kinetic energy

$\tau = T/mc^2$

and $C = \frac{2\pi e^4}{mv^2}$, with v as the electron velocity.

The above cross section per electron must be multiplied by $\rho . N_A . \langle \frac{Z}{A} \rangle$ to give values per unit volume of material, where N_A is the Avogardo Constant and $\langle \frac{Z}{A} \rangle$ signifies the average by weight for compounds or mixtures.

4.4.1.1 Attentuation coefficient, μ_δ

The attenuation coefficient, μ_δ , which is the probability, per unit pathlength, of an inelastic scattering with energy transfer greater than $\Delta(T)$ is given by

$$\mu_\delta = \rho N_A . \langle \frac{Z}{A} \rangle \int_{\frac{\Delta(T)}{T}}^{1/2} \frac{d\sigma}{d\epsilon} . d\epsilon \qquad .....(4.4)$$

The quantity, μ_δ , has been tabulated for values of the electron energy, T, from 0.1 up to 40 MeV. Table 4.1 gives some of these figures for water together with values of the mean free path between δ-ray production, $\bar{s}_\delta$ $(=1/\mu_\delta)$ and the variable catastrophic cutoff, $\Delta(T)$. The number of events varies from over 10 per cm at 0.5 MeV to under 3 per cm at 40 MeV.

4.4.1.2 Selection of δ-ray energy

The energy transfer must be selected from the exact distribution, as given by the Møller differential

Figure 4.1 THE 1 / q^2 APPROXIMATION TO THE MØLLER DISTRIBUTION

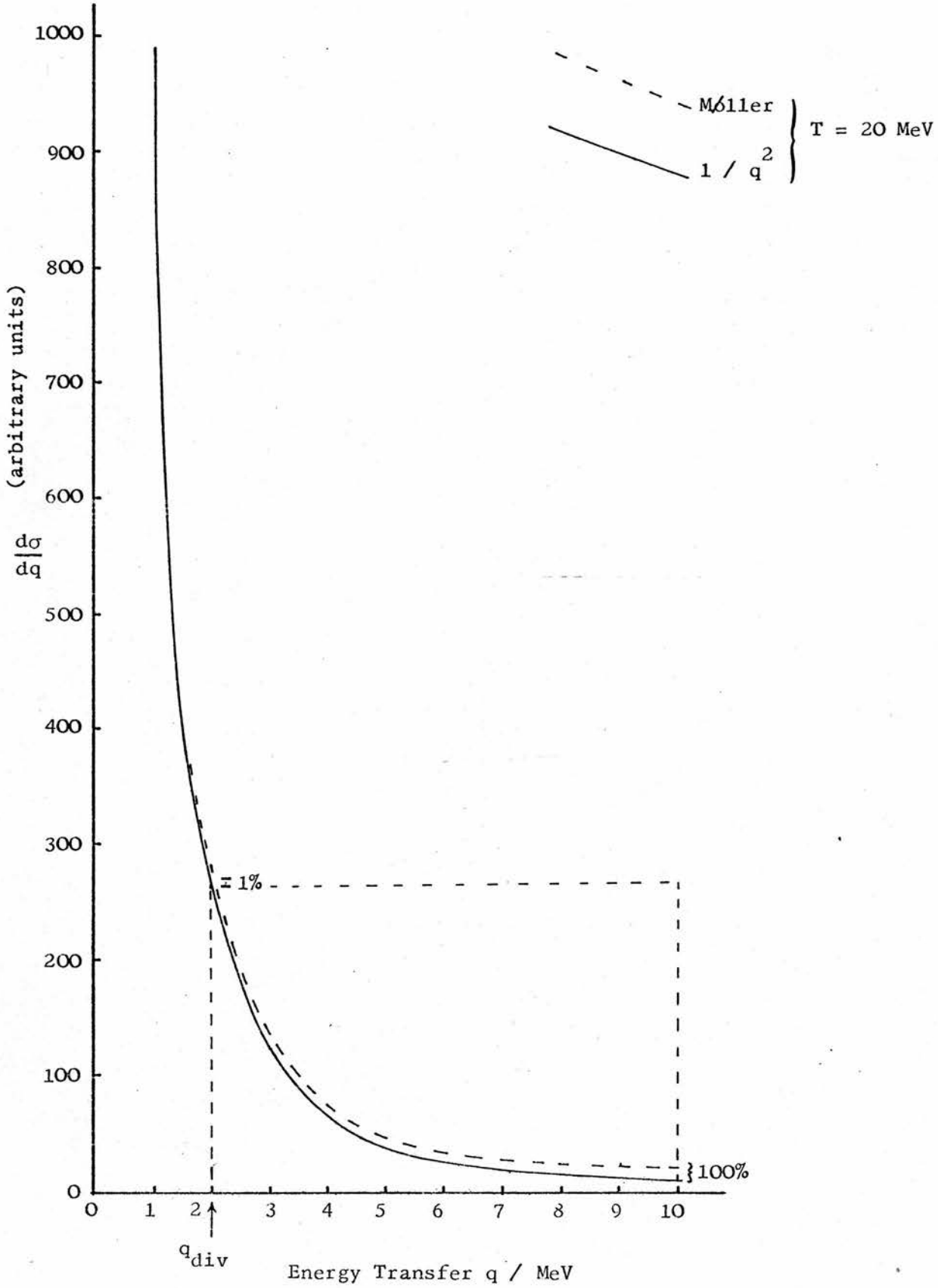

cross section, $d\sigma/d\epsilon$ or $\sigma_{moll}(T,q)$, in order that the average energy loss per unit pathlength comes out correctly. The analytical form of σ_{moll} does not lend itself to selection by the C.P.D. method, although the expression given in equ.4.3 can be integrated easily. However, except close to $\epsilon = 1/2$, all terms are small compared to $1/\epsilon^2$. Figure 4.1 shows the exact Møller distribution, for T = 20 MeV, compared with the $1/q^2$ approximation. The differences are entirely negligible for $q < 1$ MeV or so. A systematic investigation of these differences for different T demonstrated that a value of the energy transfer, q, could be chosen for any T such that $1/q^2$ was an excellent approximation to the Møller expression. Values of this dividing energy, q_{div}, were given by

$$\begin{aligned} q_{div}(\text{MeV}) &= 0.025 && \text{for } T<0.5 \text{ MeV} \\ &= 0.5\ (0.21111.T - 0.05555) \\ &\quad \text{for } 0.5 \leqslant T < 5 \text{ MeV} \\ &= 0.1\ T && \text{for } T \geq 5 \text{ MeV} \end{aligned} \qquad \ldots\ldots(4.5)$$

This set of equations gives a value for q_{div} which is constant for T below 0.5 MeV, varies linearly with T up to T = 5 MeV and is then proportional to T above this energy. These somewhat arbitrary values were chosen on the basis of ensuring that the collision stopping power, restricted to losses between T/2 and 100 eV, calculated using $\sigma \propto 1/q^2$ for losses between q_{div} and $\Delta(T)$, was within about 0.2% of the value calculated using σ_{moll} for all $q \geq 100$ eV, i.e.

$$(dT/dx)_{\Delta}^{T/2} = \rho . N_A . \left\langle \frac{Z}{A} \right\rangle . T \int_{\Delta(T)/T}^{1/2} \epsilon \, . \frac{d\sigma}{d\epsilon} \, . d\epsilon \qquad .....(4.6)$$

The probability, P_q, that a catastrophic δ-ray has an energy less than q_{div}, for which the $1/q^2$ distribution may be used, is then required. This is given by

$$P_q(T) = \frac{\int_{\Delta(T)/T}^{q_{div}/T} \frac{d\sigma}{d\epsilon} \, . d\varepsilon}{\int_{\Delta(T)/T}^{1/2} \frac{d\sigma}{d\epsilon} \, . d\varepsilon} \qquad .....(4.7)$$

On evaluation, P_q was found to vary from 0.635 at $T = 0.5$ MeV to 0.991 at 20 MeV. For values of q between $\Delta(T)$ and q_{div}, selection from the $1/q^2$ distribution is straightforward. Making use of the C.P.D. method, for a random number R we have

$$\frac{1}{q} = \frac{1 - R}{\Delta(T)} + \frac{R}{q_{div}} \qquad .....(4.8)$$

If q lies in the region $q_{div} < q \leq T/2$, then the Møller distribution must be employed. This corresponds to the part of figure 4.1 enclosed by the dotted lines. It can be seen that a straightforward application of the rejection technique to the selection of q would be very inefficient. Patau (1972) has given a modified rejection procedure to deal with such cases. The use

Table 4.2 SELECTION OF δ-RAY ENERGY

T (MeV)	%Eff. ($q > q_{div}$)	P_q ($q < q_{div}$)	time (sec) (5000 sel.)	$\bar{q}$ (kev)
0.5	28	0.635	14.1	33
1	42	0.888	7.5	41
5	48	0.978	7.0	69
10	52	0.987	7.0	92
20	47	0.991	6.7	132

of this procedure results in a greatly increased efficiency and hence computing speed when the distribution is of a form which decreases monotonically from a maximum value. The application of Patau's method to the selection of $q>q_{div}$ from the Møller distribution is described in Appendix 4. Table 4.2 includes the efficiency of selection from the Patau rejection procedure and the CPU time for 5000 selections of q (for $\Delta(T) \leqslant q \leqslant T/2$) together with P_q. A selection time of about 2 milliseconds was acceptably fast.

A very convenient check to make sure that the whole selection procedure is functioning correctly is to calculate the average value of the catastrophic δ-ray energy transfer, $\bar{q}$, from the q's selected (see table 4.2). This should be equal to the average value of q calculated from the product of the mean free path between collisions, $\bar{s}_\delta$, and the stopping power restricted to losses greater than $\Delta(T)$, as evaluated from equation 4.6 using the Møller cross section:

$$\bar{q} = \bar{s}_\delta . \left(dT/dx\right)_{\Delta(T)}^{T/2} \qquad .....(4.9)$$

It was verified that the evaluation of $\bar{q}$ from the selection procedure and from equ.4.9 were in agreement for a wide range of T values, given allowances for statistical fluctuations.

4.4.1.3 Auger electrons

The Møller cross section applies to free electrons. It is implicitly assumed that each bound

electron of the absorbing medium contributes equally to the total cross section. This is a justified assumption provided that the energy of the primary electron is large compared to the binding energies of the 'free' electrons of the medium, as is the case in the Monte Carlo program for which T_c is never less than 0.1 MeV. Therefore, when dealing with water, it can be assumed that one out of five catastrophic δ-rays comes from the K-shell of the oxygen atom. As has been discussed in chapter 3 when dealing with the ejection of electrons by the Compton and photoelectric effects, any K-shell vacancy will result in the ejection of an Auger electron from the L shell, with a kinetic energy of around 500 eV. For water, the spectrum of electrons is to be computed (down to 100 eV). Consequently, these Auger electrons must be included. Thus, the part of the program for the calculation of δ-ray energy, if the medium is water, includes the steps:

$$\text{If } R < 0.2, \text{ then } T_\delta = q - T_{aug}$$

where T_{aug} is the K.E. of the δ-ray and q is the selected value for the energy transfer. The inclusion of the Auger electrons can be considered to be an approximate way of taking into account the binding energy of the K-oxygen electrons. This is discussed at greater length in chapter 5 on the computation of the electron spectrum in water below the Monte Carlo cutoff, T_c.

Figure 4.2 FLOW DIAGRAM FOR ROUTINE NOKLOS.

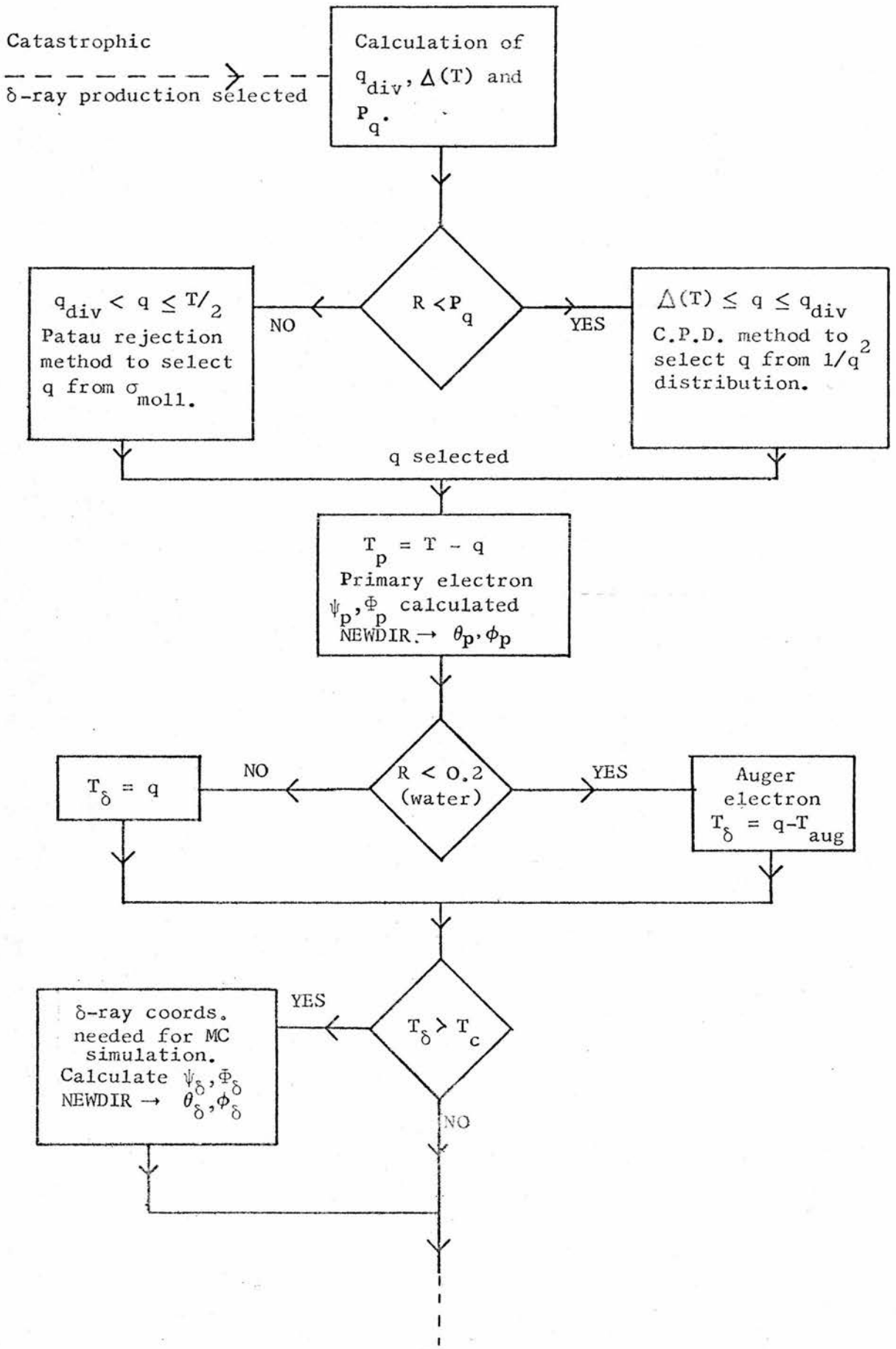

4.4.1.4 Angular Deflections

The polar deflection Ψ_p of the primary electron due to inelastic scattering resulting in an energy transfer, q, is given by the conservation laws:

$$\sin^2\Psi_p = \frac{2\varepsilon}{2+(1-\varepsilon)\tau} \qquad .....(4.10)$$

and for the δ-ray

$$\cos^2\Psi_\delta = \frac{\varepsilon(2+\tau)}{2+\varepsilon.\tau}$$

For the azimuthal deflections, $\Phi_p = 2\pi R = \pi + \Phi_\delta$. Naturally, the calculation of the deflection angles for the δ-ray is only necessary if $T_\delta > T_c$ and the δ-ray is to be included in the simulation.

4.4.1.5 Flow Diagram

Within the electron Monte Carlo program, the routine NOKLOS contains the code which computes the energy loss and deflection resulting from catastrophic δ-ray production, given that such an event has been selected in the first place. The general flow of the calculations involved in the execution of NOKLOS is indicated in figure 4.2. The dotted lines mark the entry and exit to the routine. NEWDIR is the routine that calculates the new θ, ϕ from the polar and azimuthal deflections resulting from the interaction, as discussed in chapter 3.

4.4.2 Bremsstrahlung Production

Analagous to δ-ray production, an attenuation coefficient, μ_b, representing the probability per unit pathlength of the creation of a photon with energy greater than $\Delta(T)$, is required. The Schiff (1951)

differential cross section for bremsstrahlung production has been employed to calculate μ_b and to give the distribution of photon energy, k, from which the energy loss is selected. Schiff integrated the double-differential cross section over angle to obtain the energy spectrum:

$$\frac{d\sigma}{dk}(E_o,k) = \frac{2Z^2}{137}\left(\frac{e^2}{mc^2}\right)\frac{1}{k}\left\{\left(\frac{E_o^2 + E^2}{E_o^2} - \frac{2E}{3E_o}\right) x \left(\log_e M + 1 - \frac{2}{b}\tan^{-1}b\right) + \frac{E}{E_o}\left[\frac{2}{b^2}\log_e(1+b^2) + \frac{4(2-b^2)}{3b^3}\tan^{-1}b - \frac{8}{3b^2} + \frac{2}{9}\right]\right\} \quad .....(4.11)$$

with $\frac{1}{M} = \left(\frac{mc^2 k}{2E_o E}\right)^2 + \left(\frac{Z^{1/3}}{111}\right)^2$

and $b = 2E_o E Z^{1/3}/111\, mc^2 k.$

where $E_o = T + mc^2$, the total energy of the electron before the interaction

and $E = E_o - k$, the total energy after energy loss, k.

4.4.2.1 Attenuation coefficient, μ_b

The maximum value that the photon energy, k, can take is equal to the kinetic energy of the electron, T. In the present scheme, the minimum value is fixed by the cutoff, $\Delta(T)$, for catastrophic energy losses. Consequently, μ_b is given by

$$\mu_b = \rho . N_A . \frac{1}{A}\int_{\Delta(T)}^{T} \frac{d\sigma}{dk} \cdot dk \quad .....(4.12)$$

Unlike the Møller cross section, $\sigma_{sch}(E_o,k)$ could not be integrated analytically. Therefore μ_b had to be evaluated by numerical integration, employing equal log intervals owing to the nature of the variation of σ_{sch} with k. In order to take into account bremsstrahlung in the field of the atomic electrons, the factor Z^2 in equ. 4.11 was replaced by Z(Z+1). Values of the attenuation coefficient, in units of $cm^2.g^{-1}$, were tabulated for water, carbon and aluminium for electron kinetic energies between 0.1 and 40 MeV.

Berger and Seltzer (1964) evaluated the stopping power due to bremsstrahlung losses for electrons in a wide range of substances. Their evaluation was based on the use of various differential cross sections for bremsstrahlung production combined with empirical corrections taken from the comprehensive review by Koch and Motz (1959). It was desirable that average values of the radiation loss in the electron simulation should be consistent with the tabulations of $(dT/dx)_{rad}$ given by Berger and Seltzer. This was clearly not going to be the case if the values of μ_b calculated from the unmodified Schiff cross section were used. The Schiff cross section, based on the Born approximation, is not accurate for low electron energies and for photon energies close to T. In order to derive the appropriate correction factors for different values of the electron energy, the radiation stopping power based on the unmodified Schiff differential cross section, as given by equ. 4.11, was calculated:

Table 4.3 ATTENUATION COEFFICIENT FOR BREMSSTRAHLUNG PRODUCTION (WATER)

T (MeV)	Δ(T) (keV)	f_b	$f_b \mu_b$ (cm^{-1})	$\bar{s}_b$ (cm)
0.1	9.80	2.427	0.131	7.63
0.5	10.0	1.413	0.125	8.00
1	10.25	1.247	0.138	7.25
5	12.28	1.004	0.173	5.78
10	14.81	0.990	0.194	5.16
40	30.0	0.990	0.228	4.39

$$(dT/dx)_{rad} = \rho . N_A . \frac{1}{A} \int_0^T k . \frac{d\sigma}{dk} . dk \qquad .....(4.13)$$

Values of $(dT/dx)_{rad}$ evaluated from this equation for water, carbon and aluminium were compared with the Berger and Seltzer tabulations. Table 4.3 includes some values of the factor $f_b = (dT/dx)_{B+S}/(dT/dx)_{Schiff}$ together with the 'corrected' attenuation coefficient, $f_b . \mu_b$, and the inverse of this, $\bar{s}_b$, the average distance between catastrophic bremsstrahlung events. The ratio f_b is constant at 0.990 for electron energies between 7 and 40 MeV, indicating that the Schiff cross section provides a fairly accurate description of the bremsstrahlung process at these energies. If the values for $\bar{s}_b$ are compared with $\bar{s}_\delta$ from table 4.1, it can be seen that energy losses greater than $\Delta(T)$ due to bremsstrahlung are going to be much fewer in number than those resulting in δ-rays.

It was important to ascertain whether or not radiation losses needed to be included in the restricted stopping power, corresponding to energy transfers less than the catastrophic cutoff. This restricted stopping power would be needed for the energy loss between catastrophic events. Photons of energy less than $\Delta(T)$ could not be generated individually and hence could not be included in the input to the photon simulation. It would have had to have been assumed, therefore, that they dissipated their energy at the position of origin. However, reference to table 3.1 shows that the mean free path of

a 30 keV photon is nearly 3 cm, only becoming negligible at about 10 keV (these 2 energies corresponding to the range of values of $\Delta(T)$). Equation 4.13 was evaluated with the lower limit of the integral altered to $\Delta(T)$ in order to calculate the contribution to the radiation stopping power from losses less than $\Delta(T)$. It was found that this contribution decreased from 5% at 0.5 MeV to 0.5% at 5 MeV. At 40 MeV it was only 0.1%. At all electron energies between 0.1 and 40 MeV, bremsstrahlung losses less than $\Delta(T)$ contribute less than 0.3% of the total stopping power, indicating that it was justified to ignore all 'non-catastrophic' bremsstrahlung losses. This demonstrated that the magnitude of $\Delta(T)$ chosen was appropriate to deal with bremsstrahlung as well as δ-ray events.

4.4.2.2 Selection of photon energy

The photon energy, k, is to be selected from the distribution given by equ. 4.11 for a given E_o. The Schiff distribution is expected to be accurate except for k close to T (the high-frequency limit), k close to zero (we are only concerned with $k \geq \Delta(T)$) and for small T (Berger and Seltzer, 1964). For electron energies less than about 1 MeV, bremsstrahlung is a very small fraction of the total energy loss so the use of an approximate distribution for the photon energies will not lead to any appreciable error. The closeness of the factor f_b to unity for electrons above about 5 MeV, as mentioned above, implies that the Schiff distribution

Figure 4.3 SELECTION OF THE PHOTON ENERGY, k, FROM THE SCHIFF DIFFERENTIAL CROSS-SECTION, dσ / dk.
(T = 10 MeV, Z = 8)

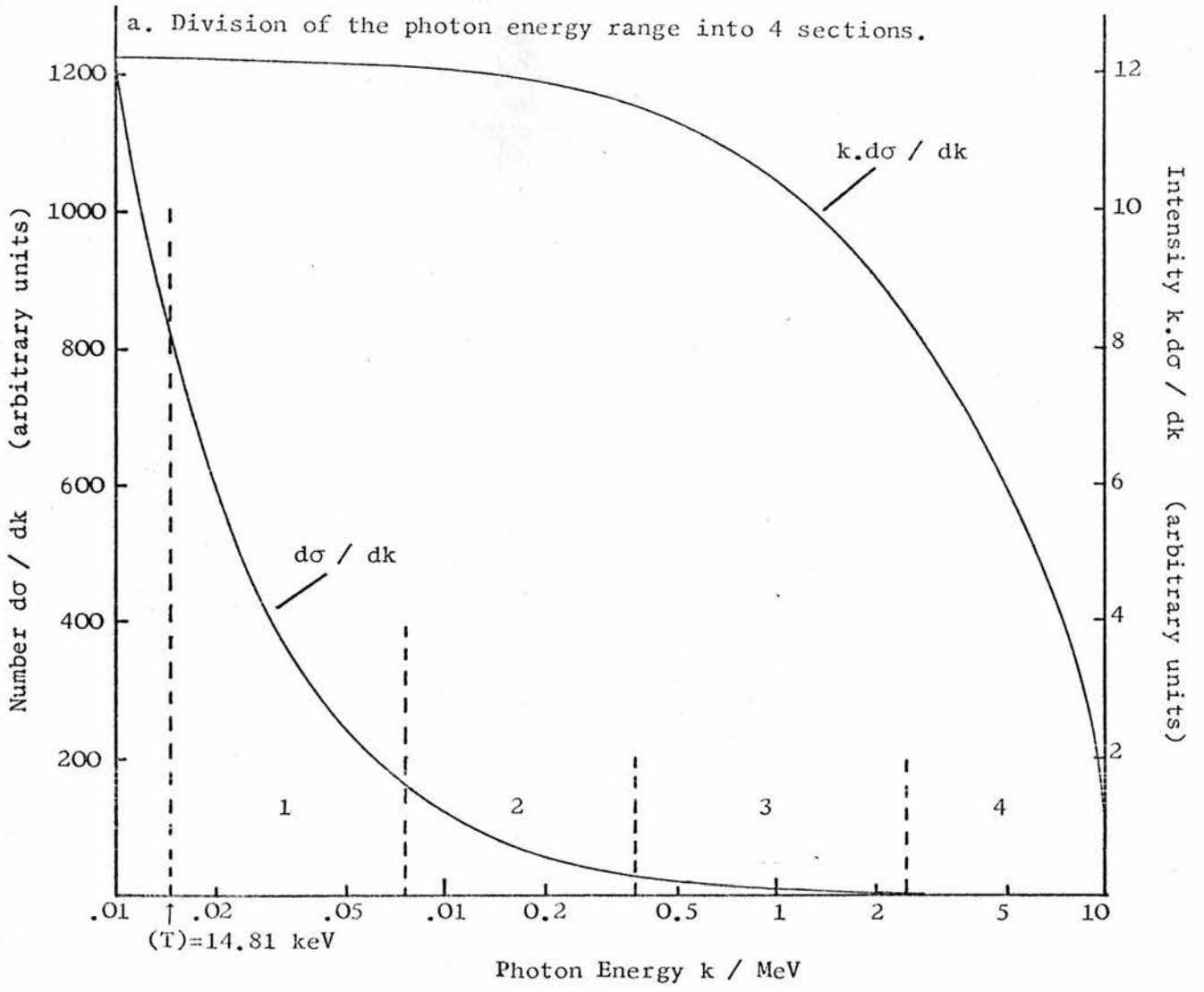

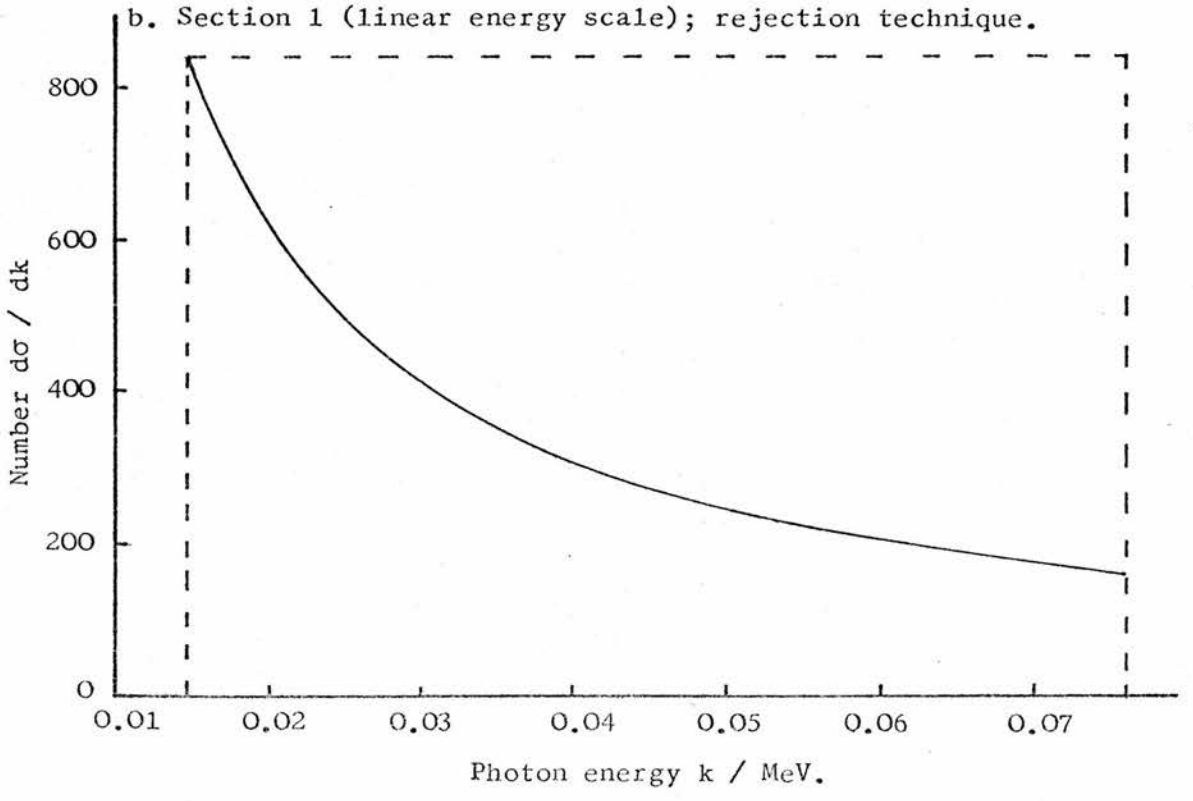

cannot be very different from theoretical differential cross sections which take into account more precisely the effect of screening etc. Anyway, bremsstrahlung production is a secondary effect for electron energies below about 20 MeV. The use of the unmodified Schiff photon energy distribution at all electron energies considered in the present calculations appeared to be amply justified.

Values of $\sigma_{sch}(E_o,k)$, the number distribution, and $k.\sigma_{sch}$, the intensity distribution, are plotted in figure 4.3 for an electron energy of 10 MeV down to a photon energy of 10 keV. The near constant value of the intensity indicates that, except for k close to T, σ_{sch} is approximately proportional to 1/k. However, the approximation is not close enough to be able to make use of it over a wide enough range of values of k, unlike the $1/q^2$ approximation in the case of σ_{moll}.

The use of an unmodified rejection procedure for selecting k would be hopelessly inefficient. The Patau modification (see Appendix 4) would not improve matters either, as it requires the range of k values to be divided into equal intervals, whereas equal log intervals seem more appropriate in this case. A simple calculation, assuming $\sigma_{sch} \propto 1/k$, indicated that if the k range was divided into 4 equal sections on a logarithmic scale, then the average efficiency of selection by the rejection technique should be about 40%, being of the same order for each section. This is illustrated graphically by figure 4.3b, in which one of

the sections in fig. 4.3a is re-drawn with a linear scale for the photon energy.

The selection procedure employed was therefore as follows:

The range of k values, $\Delta(T) \leq k \leq T$, was divided into 4 equal log intervals. For each interval, k_i to k_{i+1}, the probability, P_b^i, that k lies in this interval was evaluated from

$$P_b^i = \frac{\int_{k_i}^{k_i+1} \sigma_{sch} \cdot dk}{\int_{\Delta(T)}^{T} \sigma_{sch} \cdot dk} \qquad .....(4.14)$$

If $R \leq P_b^1$, then k lies in section 1, if not then R is compared to $(P_b^1 + P_b^2)$ and so on. In this way, one of the four sections is selected. Then the rejection technique is used in straightforward fashion to select the random variable k in the chosen section from $\sigma_{sch}(E_o,k)$. Values of P_b^i were not evaluated from 4.14 during each execution of the selection procedure, but interpolated from tabulations for different T prepared beforehand and comprising part of the input data for a particular medium. In order to further reduce the computing time, advantage was taken of simplifications in the expression for σ_{sch}. For $b \gg 1$, the square bracket term that multiplies E/E_o in equ. 4.11 reduces to 2/9, and can be neglected for $b < 3$ (Schiff, 1951). Note also that for water, for which the contribution to the total cross section due to the hydrogen atoms is

Table 4.4 SELECTION OF THE BREMSSTRAHLUNG PHOTON ENERGY (WATER)

T (MeV)	%Eff.	time (sec) (5000 sel.)	$\bar{k}$ (keV)
0.5	49	38	78
1	46	41	123
10	35	46	941
40	33	50	3890

only about 1/18 th of that due to the oxygen atom, $Z^{1/3}$ can be taken as equal to 2 (Z=8 for oxygen) with negligible error, thus avoiding a separate evaluation of σ_{sch} for hydrogen and oxygen.

The salient features of the bremsstrahlung selection procedure are summarized in table 4.4. The times given are appreciably longer than the corresponding values for δ-ray energy selection given in table 4.2. However, the frequency of bremsstrahlung events is very much lower than that for δ-rays so the relatively slow bremsstrahlung procedure will not appreciably increase the average execution time per catastrophic event. The most striking feature from comparing table 4.4 with table 4.2 is the very much larger average energy loss, $\bar{k}$, resulting from bremsstrahlung production. This was to be expected from the fact that $\sigma_{sch} \propto 1/k$ (approx.) whereas $\sigma_{moll} \propto 1/q^2$. Electrons are much more likely to lose a large fraction of their energy in creating a photon than in ejecting a δ-ray, although in total there will be far more δ-rays than photons produced in catastrophic events.

4.4.2.3 Angular Deflections

No attempt was made to select the angle of photon emission, relative to the electron direction, from an exact theoretical distribution. Such distributions are exceedingly complicated, even more so than for the photon energy. Consider a 10 MeV electron. It has a range of less than 5 cm in water. The average energy

Figure 4.4 DISTRIBUTION OF BREMSSTRAHLUNG PHOTON EMISSION ANGLE.
(Electron k.E. = 10 Mev ; Z - 8)

a. Variation of distribution with photon energy, k.

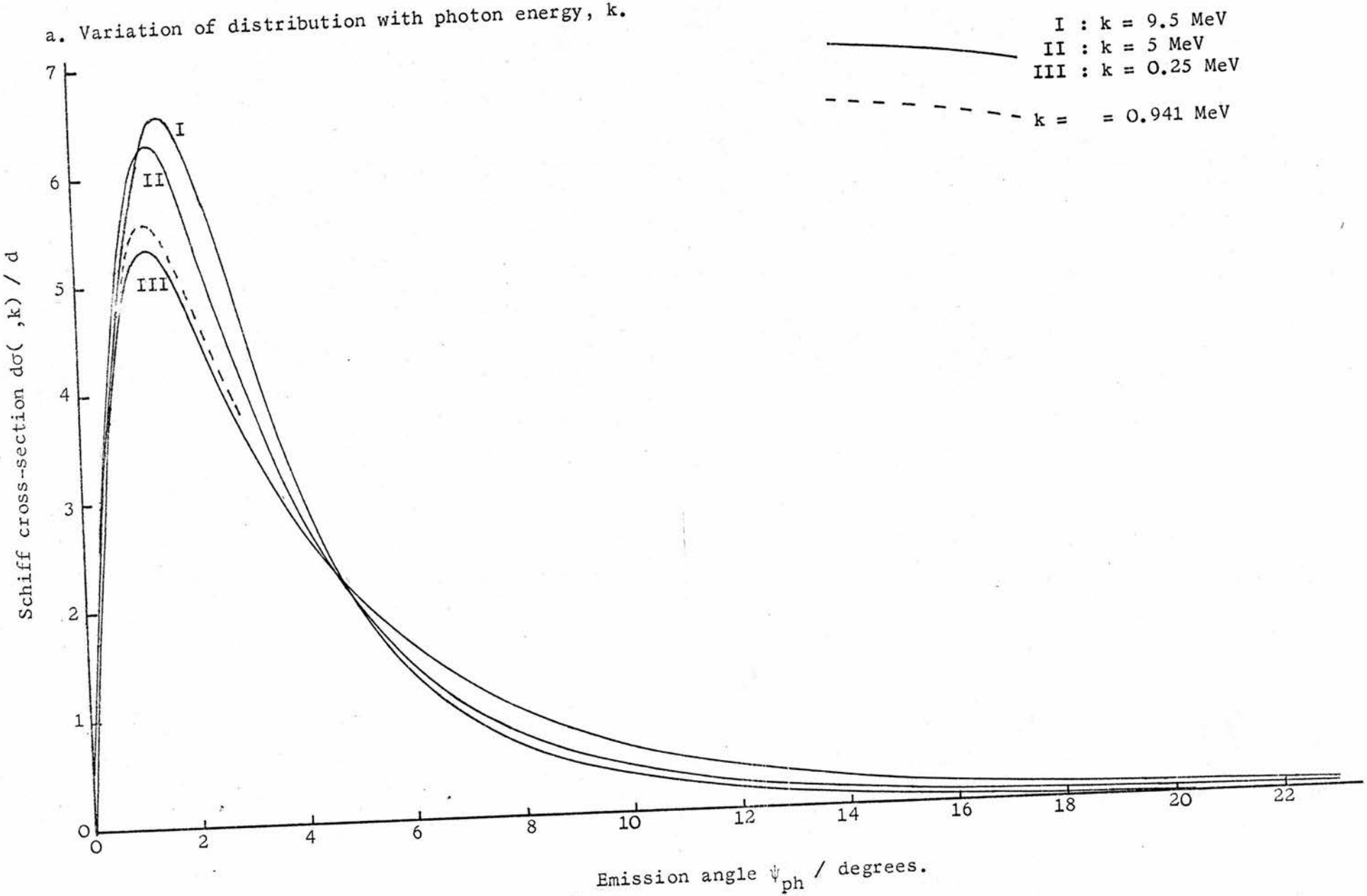

b. Exponential, Gaussian distributions with the same mean angle, $\bar{\psi}_{ph}$

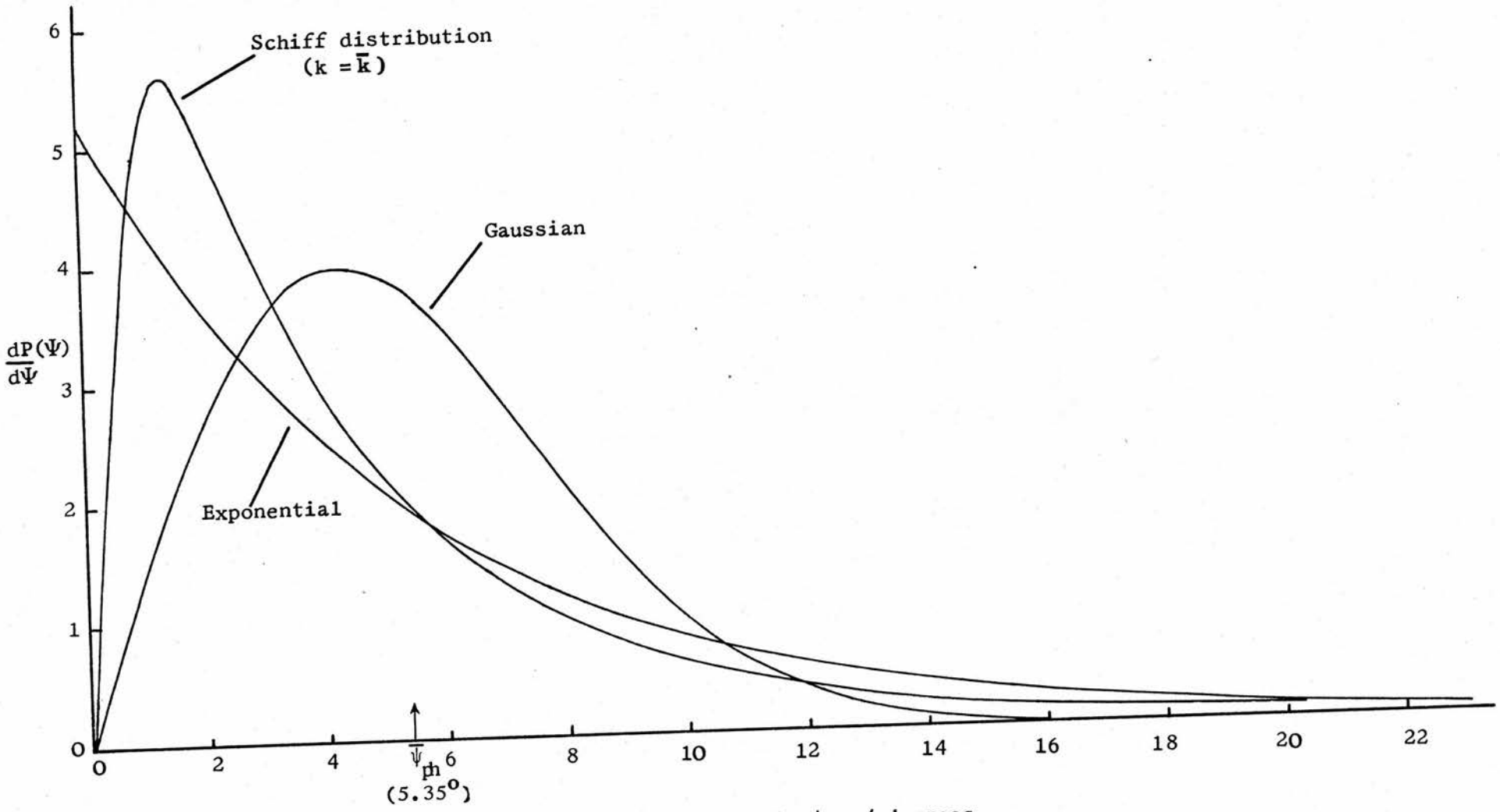

of a bremsstrahlung photon emitted by the electron is about 900 keV, and has a mean free path of nearly 14 cm. Add to this the fact that for $E_o \gg mc^2$ the photon is likely to be emitted within a cone of very small angle in the forward direction, and it can be seen that much of the energy dissipated by bremsstrahlung photons will be beyond the end of the primary electron track. This applies to all the electron with energies for which bremsstrahlung production is appreciable. For values of T of a few MeV and below, the argument about the forward emission direction no longer holds but bremsstrahlung only constitutes a very small fraction of the energy loss, so again, an accurate treatment of the deflection angle would not seem to justify the extra complications involved.

In order to find a suitable approximation for the angular distribution of the bremsstrahlung, the double-differential cross section given by Schiff (1951) was evaluated. The distribution is shown in figure 4.4a, for three different values of the photon energy, at an electron kinetic energy of 10 MeV. It is clear that the angle of emission is only weakly dependent on k for a given T. Below this, figure 4.4b illustrates the attempt to approximate $\sigma_{sch}(E_o, \Psi)$ by an exponential and by a Gaussian, both having the same mean angle, $\bar{\Psi}_{ph}$, and the same normalization as the Schiff distribution. In this figure, the Schiff curve corresponds to $k = \bar{k}$. The exponential, somewhat

Table 4.5 AVERAGE ANGLE OF BREMSSTRAHLUNG EMISSION (Z=8).

T (Mev)	$\bar{k}$ (MeV)	$\bar{\psi}_{ph}$ (deg.)	$\bar{\psi}_{ph}$ (radians)	mc^2/E_o
0.1	0.0335	55.4	0.968	0.836
0.5	0.7833	39.0	0.681	0.505
1	0.123	28.6	0.500	0.338
5	0.477	9.55	0.167	0.093
10	0.941	5.34	0.093	0.049
20	1.90	2.88	0.050	0.025
40	3.89	1.52	0.026	0.013

Figure 4.6 ELECTRON AND PHOTON DEFLECTIONS IN BREMSSTRAHLUNG EVENTS.

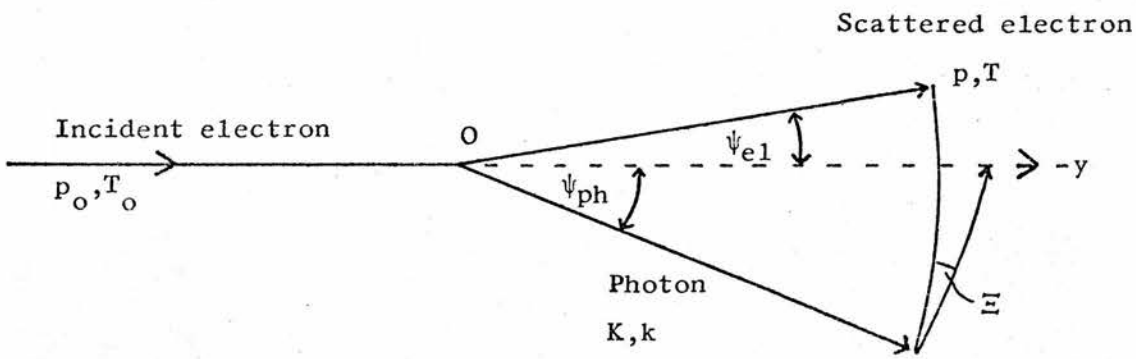

surprisingly, is a much better 'fit' and consequently, was employed in the selection of Ψ_{ph}. This is carried out according to

$$\Psi_{ph} = - \bar{\Psi}_{ph} . \log_e(1 + R.(\exp(-\pi/\bar{\Psi}_{ph} - 1)))$$

Values of $\bar{\Psi}_{ph}$ were calculated from the Schiff distribution with $k = \bar{k}$ for electron kinetic energy, T. Some of these values are listed in table 4.5. Alongside $\bar{\Psi}_{ph}$, expressed in radians, the value of mc^2/E_o is given. This is a commonly quoted approximation for the mean angle of photon emission. It can be seen that the approximation is not a particularly good one.

The deflection of the primary electron must also be considered. As with pair production by a photon, the conservation laws must take into account the momentum of the recoil nucleus or electron. The polar deflection for the electron, Ψ_{el}, is not uniquely determined by the value of Ψ_{ph}. Patau (1972) considered the problem of calculating Ψ_{el}. He supposed that the angle Ξ in figure 4.6, was zero, which is the same as assuming that the directions of incident and scattered electron and the photon all lie in the same plane. If also the momentum of the recoil nucleus is assumed to have the same direction as the scattered electron, it may be eliminated by resolving the momenta in the y direction and in a direction perpendicular to y, giving

Figure 4.7 FLOW DIAGRAM FOR ROUTINE BREMLOS.

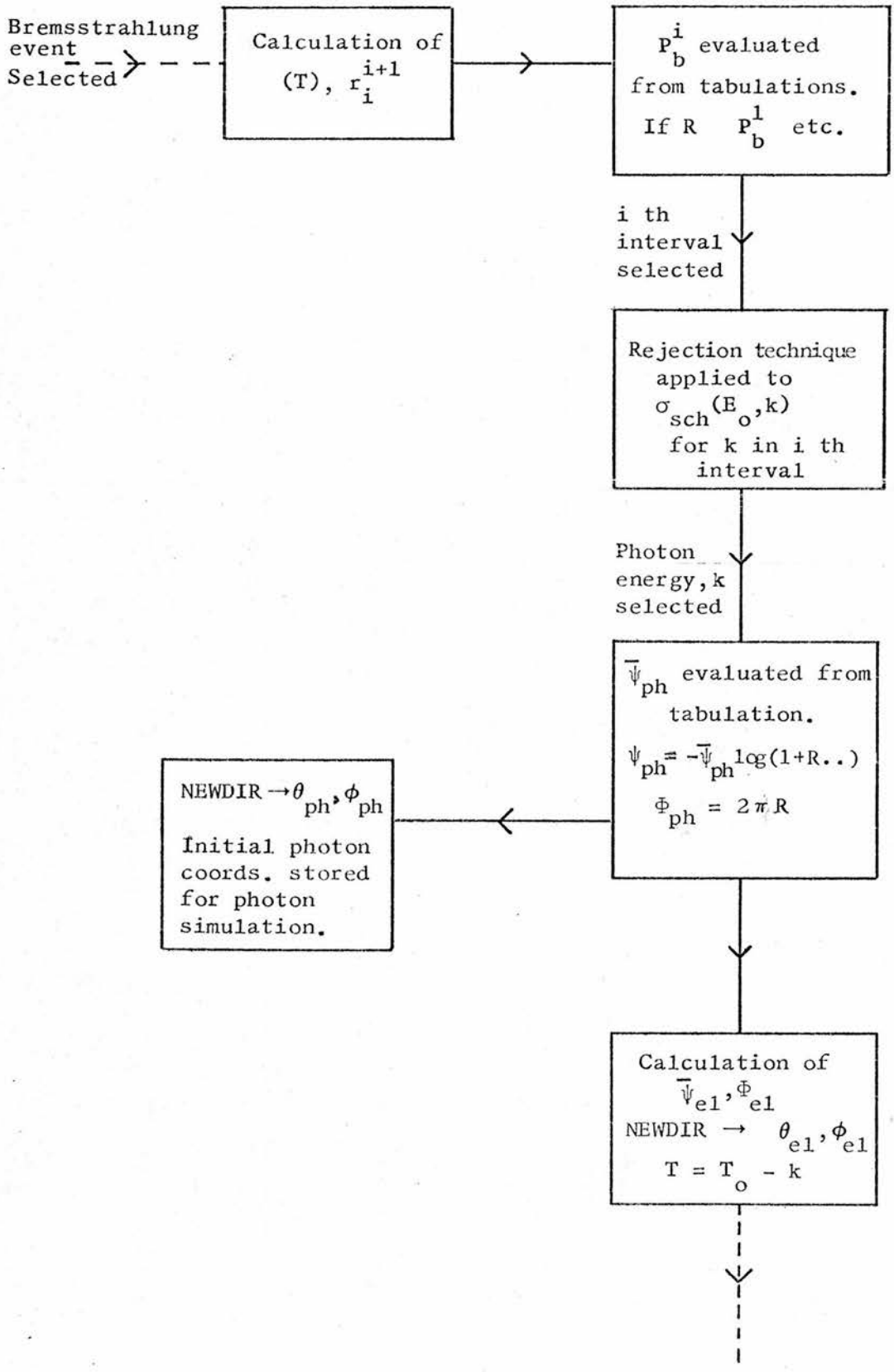

$$\sin \Psi_{el} = \frac{K \sin \Psi_{ph}}{\sqrt{p_o^2 + K^2 - 2 p_o K \cos \Psi_{ph}}}$$

$$\text{and} \quad \cos \Psi_{el} = \frac{p_o - K \cos \Psi_{ph}}{\sqrt{p_o^2 + K^2 - 2 p_o K \cos \Psi_{ph}}} \qquad .....(4.15)$$

where $\vec{p}_o$, $\vec{p}$ and $\vec{K}$ are the momenta of the incident and scattered electron, and photon respectively (Patau, 1972). The azimuthal deflections, Φ_{ph} and Φ_{el}, are

$$\Phi_{el} = \pi + \Phi_{ph} \quad \text{where } \Phi_{ph} = 2\pi R$$

to be consistent with the above assumptions.
In general, K is small compared to p_o, which results in Ψ_{el} being much smaller than Ψ_{ph}. For a 20 MeV electron giving rise to a photon of energy $\bar{k}$ = 1.9 MeV, with a deflection Ψ_{ph}, of 2.9^o, the electron deflection given by the above expressions is 0.27^o. Clearly, the electron will almost always be scattered through a very small angle. A more rigorous procedure for calculating Ψ_{el} would not make any discernible difference to any results and anyway would not be justified, given the approximate manner in which Ψ_{ph} has been derived.

4.4.2.4 Flow Diagram

The computer code for selecting the energy loss and deflections involved in bremsstrahlung events is contained in the routine BREMLOS. Figure 4.7 is a flow diagram corresponding to BREMLOS. The parameter r_i^{i+1} is the ratio of k at the beginning of the i th interval

to k at the beginning of the i+1 th interval. It is used to calculate k_{max} and k_{min} for the interval selected (see section 4.4.2.2). The initial angular coordinates θ_{ph}, ϕ_{ph} for any photon energy, are calculated from the polar and azimuthal deflections, Ψ_{ph} and Φ_{ph} using NEWDIR. The initial photon parameters are stored for subsequent use as input data for the photon Monte Carlo program. This is shown in the figure, although the electron and photon simulations were not actually coupled together until a later stage (see chapter 6).

4.4.3 Total Probability of Catastrophic Energy Loss

Having dealt with bremsstrahlung and δ-ray production separately, in the previous 2 sections, it remains to combine them together in the simulation, in a similar fashion to the different photon interactions in chapter 3.

4.4.3.1 Distance Between Events

The effective total attenuation coefficient for catastrophic losses, μ_{cat}, is the sum of the coefficients for δ-ray and bremsstrahlung events:

$$\mu_{cat} = \mu_{\delta} + \mu_{b} \qquad .....(4.16)$$

It is understood that μ_b has been adjusted by the factor f_b as described above. The distance between events, s_{cat}, is then selected from the exponential distribution, $\exp(-\mu_{cat}.s)$:

$$s_{cat} = - 1/\mu_{cat}.\log_e R \qquad .....(4.17)$$

Table 4.6 TOTAL PROBABILITY FOR CATASTROPHIC EVENTS (WATER)

T (MeV)	μ_{cat} (cm^{-1})	$\bar{s}_{cat}$ (cm)	μ_b / μ_{cat}
0.1	19.86	0.0504	0.00662
0.5	10.70	0.0934	0.0117
1	9.210	0.109	0.0150
5	7.154	0.140	0.0241
10	5.959	0.168	0.0326
20	4.506	0.222	0.0474
40	3.071	0.326	0.0741

It is implicitly assumed with this scheme that the change in electron energy, T, between events does not result in any appreciable change in μ_{cat}. The figures in table 4.6 for μ_{cat}, in this case for water, show that it varies slowly with T. At 20 MeV, for a distance s_{cat}, equal to the mean value $\bar{s}_{cat}$, and taking an approximate value of 1.50 MeV.cm^{-1} for $(dT/dx)_{\Delta}(T)$, the decrease in electron energy is approximately 1.50. 0.2 ≃ 0.30 MeV, which is small enough to justify using μ_{cat} evaluated at 20 MeV.

4.4.3.2 Event Type

Given that a catastrophic event has 'occurred', the probability that it is a bremsstrahlung event is simply the ratio of the attenuation coefficient for bremsstrahlung to the total attenuation coefficient:

$$P_{brem} = \mu_b / \mu_{cat}$$

and hence: If $R \leq P_{brem} \rightarrow$ then bremsstrahlung loss

If not $\rightarrow$ then δ-ray loss.

The ratio μ_b / μ_{cat} is included in table 4.6. At 0.5 MeV, just over 1 in a 100 events are bremsstrahlung, increasing to 1 in 13 at 40 MeV. At the same time, the average photon energy selected is much larger than the average δ-ray energy selected, as has been pointed out earlier. If the stopping powers $(dT/dx)_{rad}$ and $(dT/dx)_{col}$, restricted to losses greater than $\Delta(T)$, are compared, then it is found that above about 25 MeV in in water, the average loss due to radiation exceeds that due to δ-ray production (see figure 4.8 in the next section). The values of μ_b / μ_{cat} and μ_{cat}

for each medium have been tabulated and form part of the input data for the electron simulation.

4.4.4 C-S-D-A Pathlength Steps

4.4.4.1 Energy loss

In between catastrophic events, the electron is assumed to lose energy continuously at a rate given by the stopping power restricted to losses less than $\Delta(T)$, $(dT/dx)_{\Delta}$. It was shown in section 4.4.2.1 that negligible error is incurred if radiation losses are ignored and $(dT/dx)_{\Delta}$ is taken to be equal to the collision stopping power (which can also be written as $L_{\Delta}(T)$ or $L(T,\Delta)$). This has been evaluated from the Bethe-Bloch theory as formulated by Rohrlich and Carlson (1954):

$$L(\tau,\Delta) = \frac{2\pi \; N_A \; R_o^2 \; mc^2}{\beta^2} \left\langle \frac{Z}{A} \right\rangle \left\{ \log_e \left[\frac{2(\tau+2)}{(I/mc^2)^2} \right] + F(\tau,\Delta) - \delta \right\} \qquad .....(4.18)$$

with $F(\tau,\Delta) = -1-\beta^2 + [\log_e (\tau-\Delta)\Delta] + \tau/(\tau-\Delta)$
$+[\Delta^2/2 + (2\tau+1)\log(1-\Delta/\tau)]/(\tau+1)^2$

where

$R_o^2 = (e^2/mc^2)^2$; $\beta = v/c$; $\tau = T/mc^2$; $\Delta = \Delta'/mc^2$; δ is the density effect correction.

The value of the mean ionization potential, I, has been taken equal to 71.3 eV for water, following the results of the re-analysis of experimental data by Dalton and Turner (1968). This value is somewhat different from the figure of 65.1 eV recommended by NAS-NRC 1133 (1964) and used by Berger and Seltzer in

Figure 4.8 STOPPING POWERS IN WATER ; I = 71.3 eV.

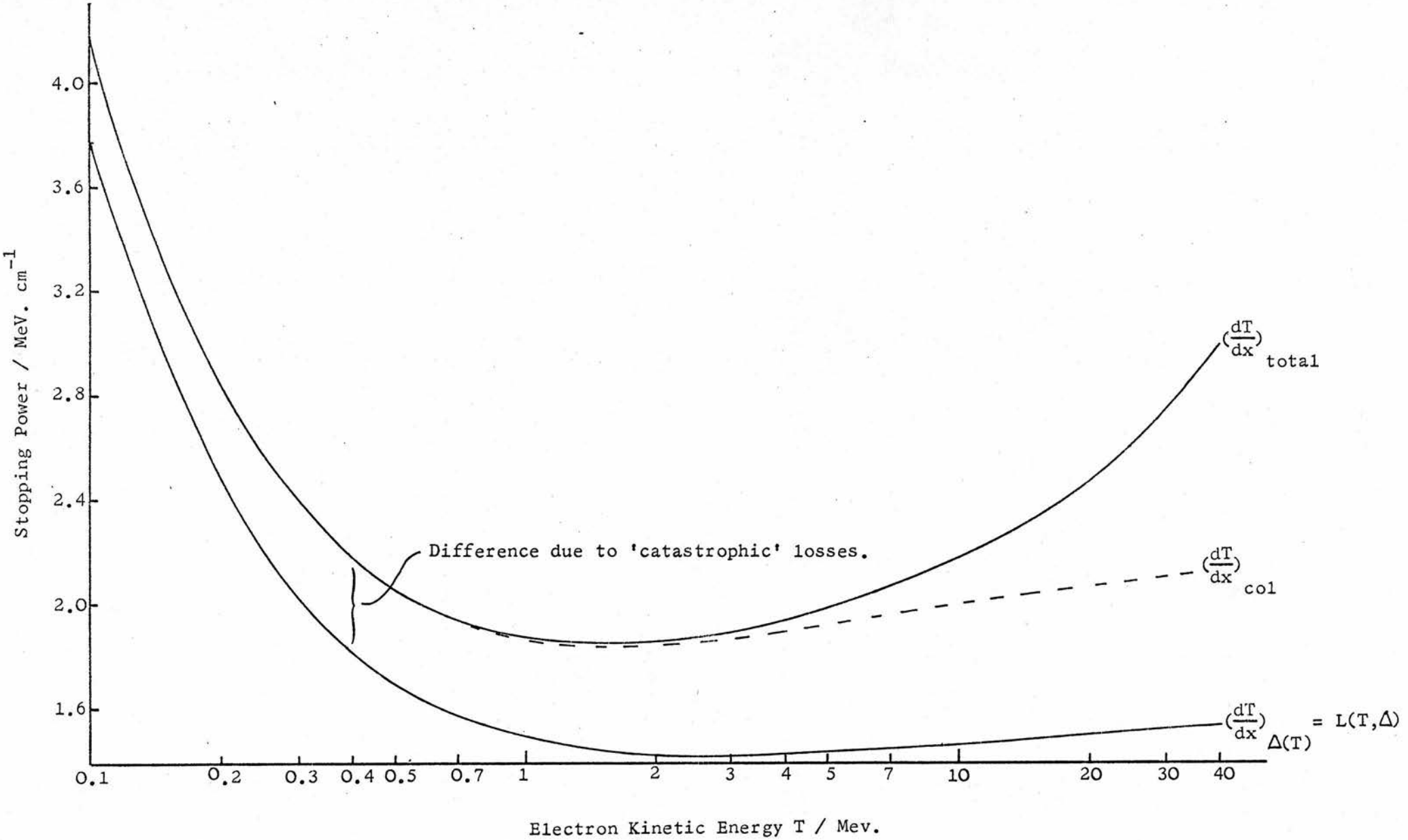

their Monte Carlo work. For carbon and aluminium, Dalton and Turner gave only slightly different values from NAS-NRC 1133 and values from the latter have been used i.e. I(carbon) = 78.1 and I(aluminium) = 163.3 eV. Sternheimer's (1952, 1956) theory has been used to evaluate δ. In these two papers, Sternheimer gave a formula for δ corresponding to 2 different sets of I-values, I_1 and I_2. The 1956 I-values are identical to the ones used here for carbon and aluminium, but for water, 71.3 lies in between I_1 and I_2. The procedure used by Berger and Seltzer (1964) has therefore been employed to calculate δ for water:

$$\delta = [\delta_1 . \log(I_2/I) + \delta_2 . \log(I/I_1)] / \log(I_2/I_1) \qquad .....(4.19)$$

Figure 4.8 is a graph of $(dT/dx)_\Delta$ for electrons in water between the energies 0.1 and 40 MeV, which is the range of energies that is covered in the Monte Carlo simulation. Also shown is the total stopping power, with the contribution to this from bremsstrahlung losses indicated by the difference between the dotted and full curves. The total collision stopping power was calculated from equ. 4.18 by putting $\Delta = \tau/2$.

For a pathlength step, s, the energy loss is then given by

$$T_a - T_b = s . L(T_a, \Delta) \qquad .....(4.20)$$

where T_a and T_b are the kinetic energies of the electron at the beginning and end of the c-s-d-a step. If T_b, as calculated from equ. 4.20, comes out to be

less than T_c, then T_b is put equal to T_c and s re-calculated as $(T_a - T_c)/L(T_a, \Delta)$. This ensures that the electron energy cannot come out to be less than T_c at the end of the final c-s-d-a step. It is sufficiently accurate to evaluate $L(T, \Delta)$ at $T = T_a$ as the variation of the restricted stopping power with energy is slow except below 0.5 MeV, where an accurate treatment of spatial diffusion is less important anyway. In the program, $L(T, \Delta)$ is interpolated from tabulations prepared beforehand.

4.4.4.2 Multiple scattering

In this work, the Gaussian distribution has been employed to give the polar deflection between the electron direction at the beginning and end of a pathlength step. The distribution, for a mean square scattering angle, $\overline{\Psi^2}$, can be written as

$$P(\Psi).d\Psi = 2.\frac{\Psi}{\overline{\Psi^2}}.\exp\left(\frac{-\Psi^2}{\overline{\Psi^2}}\right).d\Psi \qquad .....(4.21)$$

It is derived on the basis of assuming that the net angular deflection is the result of the combined effect of many small individual deflections, each of the same order of magnitude. The mean square scattering angle, $\overline{\Psi^2}$, was evaluated from the Rutherford single scattering cross section, for pathlength s, as given by ICRU (1972):

$$\overline{\Psi^2} = s.\ 16\pi\rho.N_A \left\langle\frac{Z}{A}\right\rangle^2 .R_o^2 \left(\frac{mc^2}{\beta.p.c}\right) \log_e\left(\frac{137\ p.c}{Z^{\frac{1}{3}}\ .mc^2}\right)$$

$$.....(4.22)$$

where p is the electron momentum and $\left\langle\frac{Z}{A}\right\rangle^2$ is an average by weight, equal to 66/18 in the case of water.

The above expression for $\overline{\psi^2}$ corresponds to neglecting the effect of the finite size of the nucleus. This is a good approximation if

$$\frac{280}{A^{1/3}} \cdot \frac{mc}{pc}^2 > 1$$

This condition is fulfilled for the media and range of electron energies involved in the Monte Carlo program.

The use of the Gaussian multiple scattering distribution specifically excludes the effect of occasional large individual deflections, which the more exact Moliere and Goudsmit-Saunderson (G-S) theories take into account. The G-S distribution may also be evaluated for any desired single-scattering cross-section as discussed with examples by Berger (1963). However, Leiss et al. (1957), who used the Gaussian distribution in their electron Monte Carlo calculations, reported that a pilot calculation based on a more exact theory of Snyder and Scott did not greatly influence the results for the straggling of electron penetration depths. Harder (1965) extended the Monte Carlo program of Leiss et al. to calculate the spectrum of electrons behind thick layers of carbon. The good overall agreement he obtained with experimental measurements provided further evidence that the use of the Gaussian distribution would result in very similar results for electron penetration as the use of the much more complicated Moliere or G-S expressions.

Figure 4.9 ELECTRON MULTIPLE-SCATTERING DISTRIBUTIONS
(2 MeV electrons in aluminium ; 0.057 g.cm^{-2} pathlength)

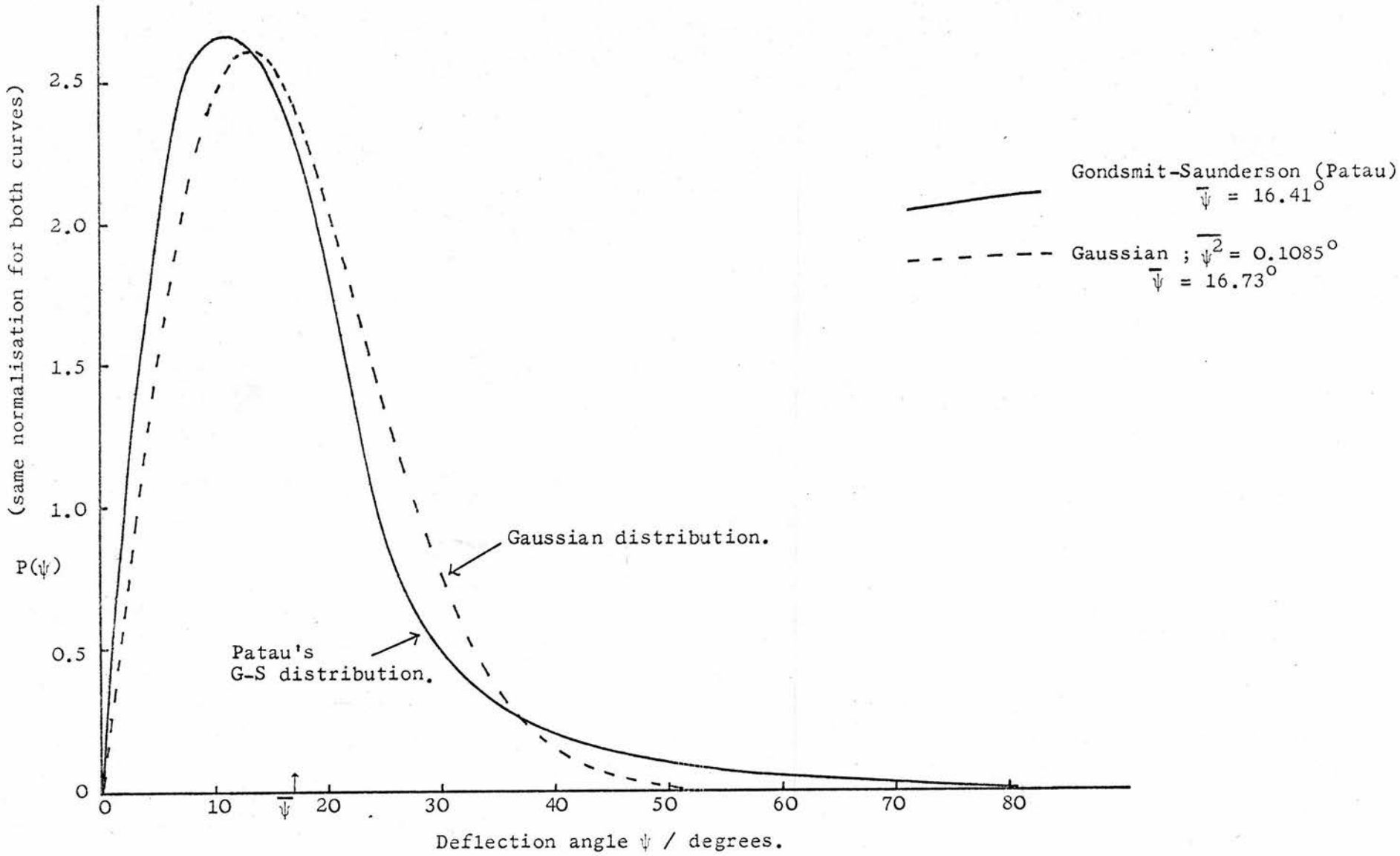

Patau (1972) evaluated the G-S distribution as part of his Monte Carlo scheme and presented graphs of the distribution for several electron energies in aluminium. In figure 4.9, Patau's curve for a 2 MeV electron is compared to the Gaussian distribution evaluated from the expression given above. The pathlength is 0.057 $g.cm^{-2}$ corresponding to a fractional energy loss $\Delta T/T \simeq 0.04$. The two distributions have almost identical mean deflections. The effect of the inclusion of large deflections in the G-S theory can be clearly seen. In general, the comparison indicates that the Gaussian is likely to be an adequate approximation for the present purposes of the electron simulation.

Selection of the deflection angle from the Gaussian distribution is straightforward. Setting a random number, R, equal to the expression for the normalised cumulative probability distribution,

$$R = \frac{\int_0^{\Psi} \Psi . \exp(-\Psi^2/\overline{\Psi^2}) . d\Psi}{\int_0^{\infty} \Psi . \exp(-\Psi^2/\overline{\Psi^2}) . d\Psi}$$

and solving for Ψ,

$$\Psi = \left[\overline{\Psi^2}\right]^{1/2} . \left[-\log_e R\right]^{1/2} \qquad .....(4.23)$$

The upper limit of the integral in the denominator above can be taken as infinity due to the very small value of the distribution for large angles - see fig. 4.9. The ease of selection from the Gaussian

Figure 4.10 POLAR DEFLECTION DUE TO MULTIPLE SCATTERING IN A C-S-D-A PATHLENGTH STEP.

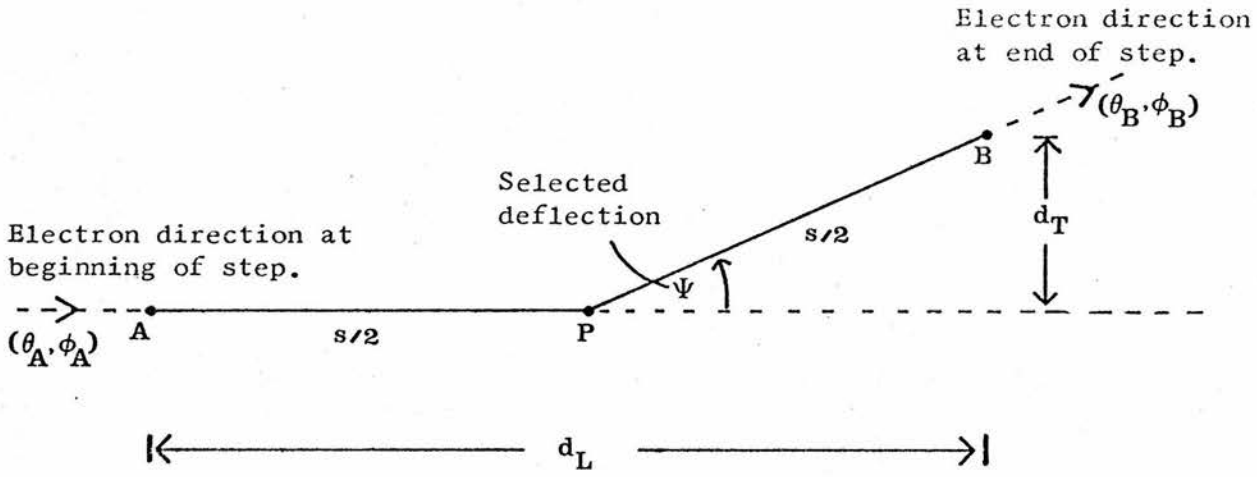

expression is a great advantage in a Monte Carlo calculation.

The use of a multiple scattering distribution to give the final deflection at the end of a section of a pathlength actually consisting of a large number of very small deflections necessarily involves some assumption as to the geometry to be employed in calculating the position of the electron at the end of the section. Clearly, the straight-line distance between the beginning and end of the step will be less than the pathlength s. The schematization depicted in figure 4.10 was adopted to take this into account in an approximate manner. Berger (1963) justified the use of this geometry by reference to Yang (1951) who derived a distribution for the longitudinal displacement, d_L based on the Gaussian small angle approximation. For small Ψ, which is the case for the majority of steps in the simulation, the expression

$$d_L = \frac{s}{2}.(1 + \cos \Psi) \qquad .....(4.24a)$$

gives the correct average value and is anyway very close to $d_L = s$. Leiss et al. (1957) took d_L as equal to the pathlength for their steps of 1/4 cm in carbon, stating that Yang had estimated that this introduced an error of less than 1% in their calculations. The lateral displacement, d_T, with this scheme, is given by

$$d_T = \frac{s}{2}. \sin \Psi \qquad .....(4.24b)$$

Figure 4.11 VARIATION OF MASS ANGULAR SCATTERING POWER WITH ELECTRON ENERGY.
(Electrons in water).

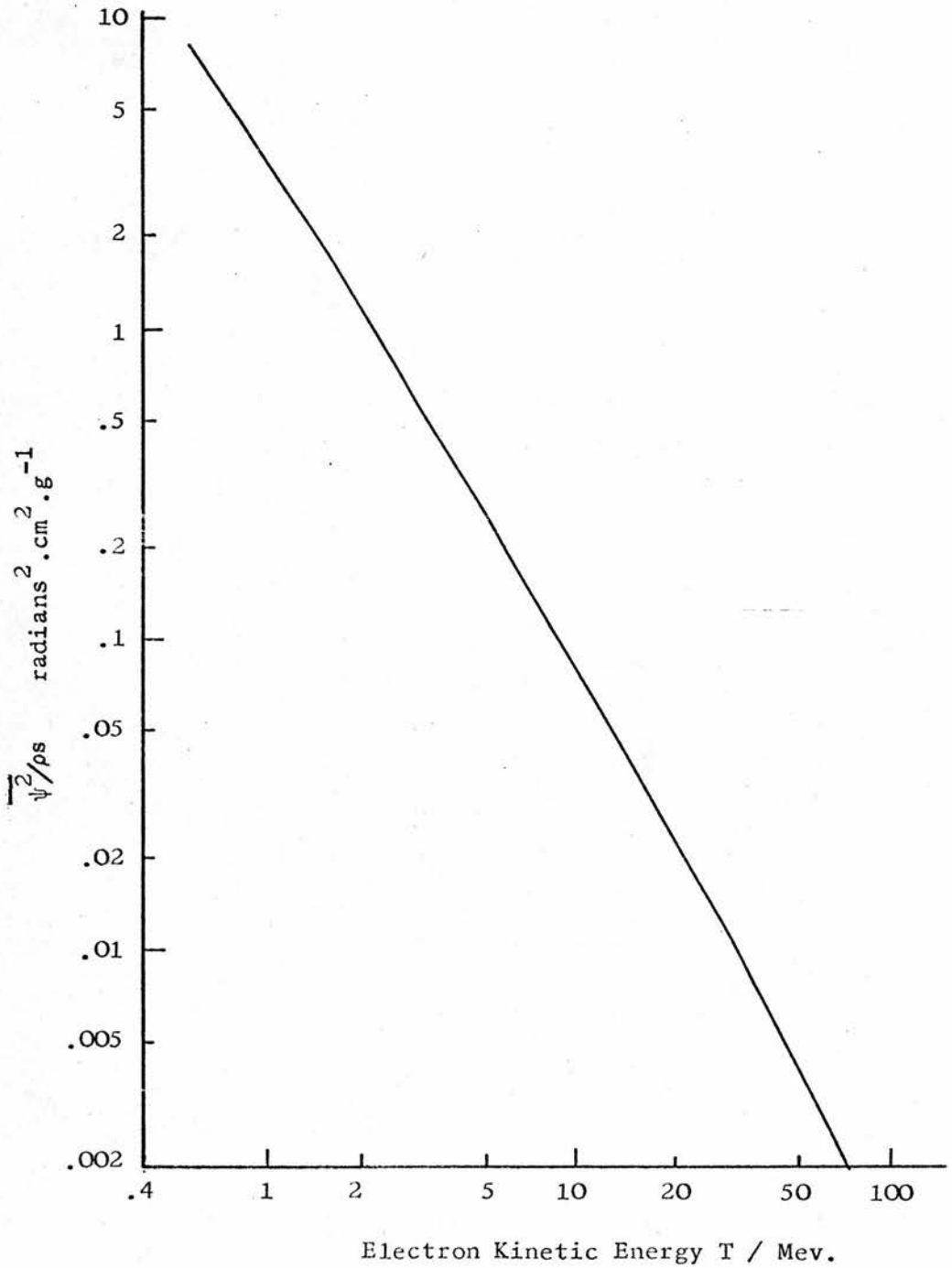

Table 4.7 STEP LENGTH FOR A GIVEN FRACTIONAL CHANGE IN T OR $\overline{\psi^2}$ (Values for water)

T (MeV)	$\bar{s}_{cat}$ (cm)	s_{max} (4% change)*	s_{max} ($2\frac{1}{2}$% change)
0.1	0.0504	0.0011	0.0007
0.5	0.0934	0.012	0.0075
1	0.109	0.027	0.017
5	0.140	0.139	0.089
10	0.168	0.272	0.170
20	0.222	0.533	0.352

*Note that changes in T of 4% and $2\frac{1}{2}$% are equivalent to changes in $\overline{\psi^2}$ of 8% and 5% respectively.

The azimuthal deflection, Ψ, is distributed uniformly between 0 and 2 π. The point P is taken as the mid-point of the step and the 'continuous' energy dissipation is assumed to take place at P.

4.4.4.3 Maximum Step Size

Unlike the restricted collision stopping power, $L(T, \Delta)$, and the attenuation coefficient, μ_{cat}, the parameter involved in the selection of the multiple scattering deflection, $\overline{\Psi^2}$, does vary quite rapidly with electron energy, T. Figure 4.11 is a graph of the variation of the mass angular scattering power, $\overline{\Psi^2}/\rho.s$, with electron kinetic energy, T. It is desirable to evaluate $\overline{\Psi^2}$ at the average energy, $(T_a+T_b)/2$, of the electron within a pathlength step. Further, one is led to inquire whether the values of the step length, as given by the distance between catastrophic events, will not result in too large a variation in $\overline{\Psi^2}$ within a step. The form of the log-log plot for $\overline{\Psi^2}$ vs T suggests that approximately

$$\frac{1}{\rho.s} \cdot \frac{d\overline{\Psi^2}}{dT} \propto \frac{\overline{\Psi^2}}{T} \qquad \ldots\ldots(4.25)$$

and hence, for a roughly equal percentage change in $\overline{\Psi^2}$ per step, $\Delta T/T$ should be constant. Table 4.7 lists values for the pathlength step s corresponding to a 4% and a 2½% change in T, compared with the average distance between catastrophic events, $\bar{s}_{cat}$, at the same energies. It is clear from these figures that $\bar{s}_{cat}$ is unnacceptably large below about 5 MeV for a valid evaluation of the deflection angle resulting from such a step.

As a result of these considerations, it was decided to limit the size of any step to a maximum value, s_{max}, calculated on the basis of a maximum percentage change in the electron energy during the step. For a given percentage change in T, δ_T, the maximum allowed pathlength is given by

$$s_{max} = \frac{0.01 . \delta_T . T}{L(T, \Delta)} \qquad .....(4.26)$$

If a value of s, as selected from equ. 4.17, is such that $s > s_{max}$, then the step is terminated at $s = s_{max}$ and a value calculated for $\overline{\Psi^2}$ for the step. Then another value of s is selected, and again, the step is only terminated by a catastrophic event if $s < s_{max}$. Note that the introduction of a maximum c-s-d-a step size does not alter the distribution of the distance between catastrophic events. This is shown in Appendix 5. The above steps are included in a flow diagram of the complete electron simulation given in the next section.

Patau (1972) chose a value for the constant fractional energy loss per step such that $\Delta/T = 1 - 2^{-1/16}$ which is equivalent to $\delta_T \simeq 4$ as in the third column in table 4.7. Berger and Seltzer (1965) also adopted this value of the ratio in their c-s-d-a scheme. Previously, Berger (1963) had investigated the effect of varying the step size on the results of electron backscattering and concluded that decreasing the ratio below the above value made very little difference. It is perhaps surprising that

the results from the electron Monte Carlo calculations of Harder (1965) who followed the scheme of Leiss et al. (1957), came out as well as they did when one notes that he employed a constant step size of 1/4 cm in carbon. This is approximately equivalent to the 4% s_{max} value in water at an energy of 5 MeV (see table 4.7).

In all the electron Monte Carlo calculations to be reported in this work, δ_T has been set equal to 4. From table 4.7, it can be seen that above about 5 MeV most of the steps will be terminated by catastrophic events, whereas as the energy decreases below this value, s_{max} becomes much smaller than $\bar{s}_{cat}$, with the result that only a few steps will end with catastrophic losses, most of them being of length s_{max}. Thus, for low initial electron energies, the slowing-down scheme approaches the complete continuous-energy-loss model, as used by Berger (1965).

For a typical value of the step size at 20 MeV, 0.23 cm, the mean deflection works out at about 3½ degrees. At 1 MeV, with a pathlength of 0.02 cm, the deflection averages 13 degrees. With values of s_{max} calculated for $\delta_T = 4$, the mean deflection per step is restricted to this sort of size at low electron energies.

Figure 4.12 FLOW DIAGRAM FOR THE ELECTRON SIMULATION.

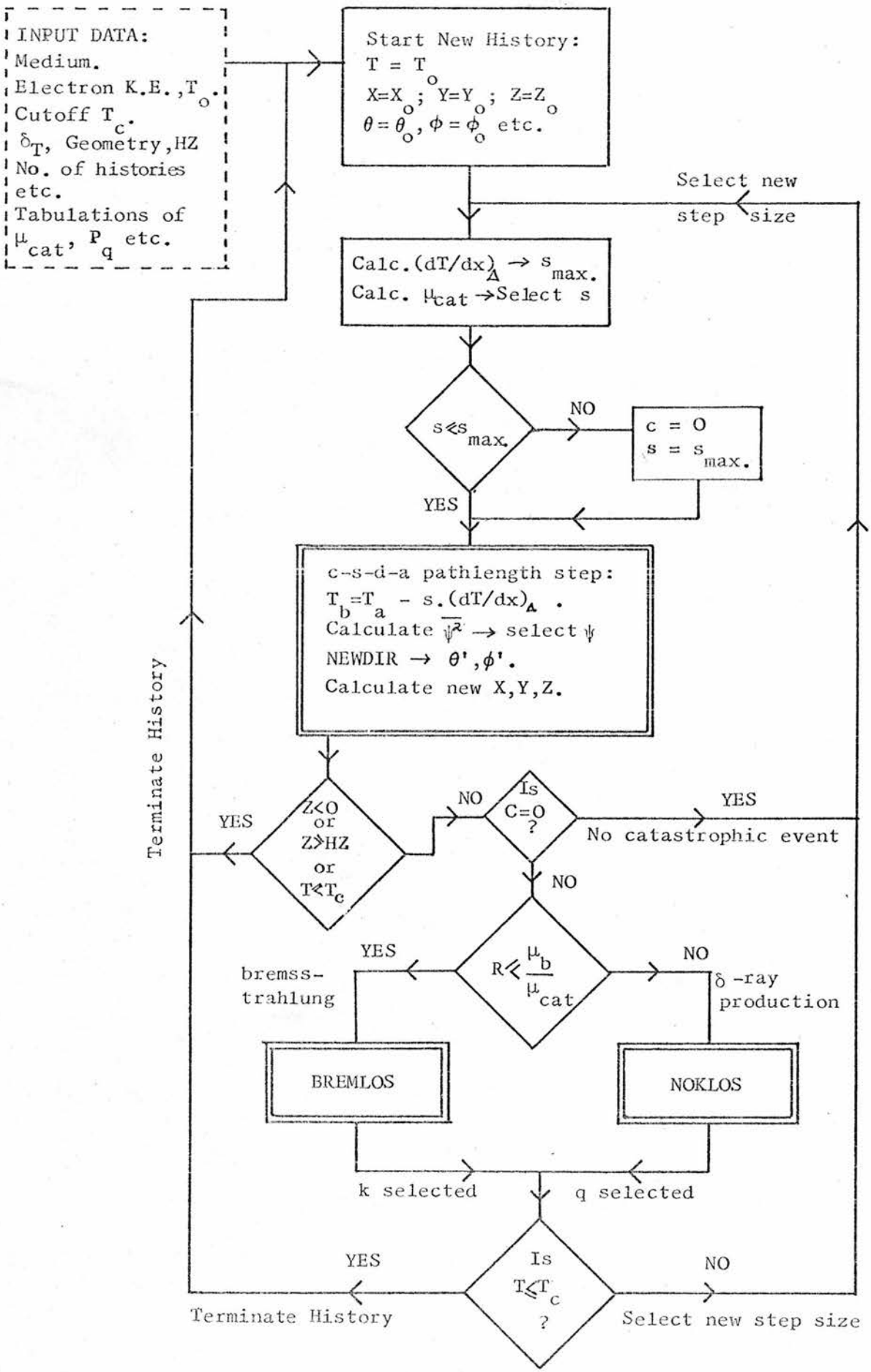

4.5 THE COMPLETE PROGRAM

The various operations involved in the electron scheme, as detailed in the previous section, are put together to form the complete simulation. Much of what has been written under this heading in the previous chapter for the photon Monte Carlo program, such as Routines (3.4.2), Structure (3.4.3) and Geometry (3.4.5), applies equally well to the electron simulation. Consequently, the material in those sections need not be repeated here. One feature of the electron simulation that does not find a parallel in the photon program is the inclusion of secondary electrons. A separate section is devoted to this below.

4.5.1 The Flow of the Simulation

A flow diagram for the basic logic of the electron simulation is given in figure 4.12. This diagram corresponds to the generation of primary electron histories which are terminated when the electron energy drops below T_c or if the electron is backscattered ($Z<0$) or the depth of penetration exceeds a specified value, HZ. The doubly-enclosed box representing the operations involved in a c-s-d-a step are carried out by the routine CSDALOS in the program. The operations involved in the routines BREMLOS and NOKLOS have been described in previous sections.

The diagram does not include any of the calculations which extract information from the electron histories, such as the energy deposited at

the mid-point of a c-s-d-a step or the number of electrons backscattered. As with the photon simulation, none of these operations alters the basic logical sequence followed in the generation of histories.

4.5.2 Inclusion of δ-ray histories

If secondary electrons, for which $T > T_c$, are to be included in the simulation, then two ways of effecting this suggest themselves. Either each primary history and the secondaries, tertiaries produced by the primary can be followed one after another before going onto the next primary history, or all the primary histories, then all the secondaries etc. can be executed. The former scheme has been adopted, mainly because it does not require the vast amount of storage of initial δ-ray parameters that the latter could entail, especially for runs involving very large numbers of primary histories.

For each δ-ray to be followed, there is a total of ten initial parameters which are generated within the routine NOKLOS: T_δ; X,Y,Z; $\cos\theta$, $\sin\theta$; $\cos\phi$, $\sin\phi$; PPOS and PR. The last two label the electron as a negatron or positron, and as primary or secondary. The need for these labels is explained in later chapters. For each primary history, the number of secondaries to be followed is added up. At the end of the primary history, if this aggregate number is non-zero, then the first secondary history, starting from the δ-ray's initial energy, position and direction is executed. Any δ-ray resulting from this history is simply added

Figure 4.13 SAMPLE COMPUTER PRINTOUT FOR THE ELECTRON MONTE CARLO PROGRAM.

```
COMMAND:RUN(EMCEL4)

ELECTRON TRANSPORT SIMULATION

NARROW BEAM OF MONOENERGETIC ELECTRONS
SEMI-INFINITE GEOMETRY
PRIMARY ELECTRONS ONLY

MEDIUM: 'WATER'
KE(MEV):10  ------  T0
RO G/CM2:4.890
TMIN:0.45  ------  Tc
MAXDMSC:8
XI G/CM2:0
YI G/CM2:0
ZI G/CM2:0
THETA(DEG):0
PHI (DEG):0
RANDOM STARTER:49975019
NO. HISTORIES:1000

 2.8400 SEC  }
468.4800SEC  }   0.466 sec per history
468.5000 SEC

RESULTS :     WATER
--------
INITIAL ELECTRON K.E. = 10.000 MEV
AVERAGE VALUES PER PRIMARY ELECTRON HISTORY:
FINAL ELECTRON K.E. =  0.4427 MEV
NO. OF STEPS =  77.53
TOTAL PATHLENGTH =  4.724 GM/CM2
PENETRATION DEPTH WHEN TO<=TMIN =  3.625 GM/CM2
NO. OF KNOCK-ON ELECTRONS PRODUCED =  33.659
NO. OF KNOCK-ON ELECTRONS WITH K.E.>  0.45 MEV =  0.7390
TOTAL ENERGY OF THESE ELECTRONS =  0.7675 MEV
NO. OF BREMSSTRAHLUNG PHOTONS PRODUCED =  0.7890
TOTAL ENERGY DISSIPATED AS BREMSSTRAHLUNG PHOTONS =  0.4124 MEV
THUS RADIATION YIELD = 0.0412

DEPTH DOSE HISTOGRAM:
ALL BREMSSTRAHLUNG PHOTONS ASSUMED TO ESCAPE
FROM REGION OF INTEREST
ALL SECONDARY ELECTRONS ASSUMED TO DEPOSIT THEIR ENERGY
AT POINT OF ORIGIN
ENERGY OF ELECTRON AT CUTOFF ASSUMED DEPOSITED
AT POINT WHERE SIMULATION STOPPED

 Z/RO            Z GM/CM2        ENERGY ABSORPTION  MEV.CM2/GM.EL

 0.00 - 0.05      0.122             2.0531
 0.05 - 0.10      0.367             1.9954
 0.10 - 0.15      0.611             2.0453
 0.15 - 0.20      0.856             2.0794
 0.20 - 0.25      1.100             2.0688
 0.25 - 0.30      1.345             2.2096
 0.30 - 0.35      1.589             2.2350
 0.35 - 0.40      1.834             2.3525
 0.40 - 0.45      2.078             2.3386
 0.45 - 0.50      2.323             2.5048
```

onto the total number of δ's. In this way, each δ-ray is followed in turn until there are no more left. Then the next primary history can be started. The total number of δ-ray histories per primary history never averaged more than fifteen, even with T_o equal to 40 MeV, and T_c equal to 0.1 MeV. Thus no more than a few hundred initial δ-ray parameters needed to be stored at any one time during the execution of the electron program.

4.5.3 Some Practical Details

The computer printout reproduced in figure 4.13 illustrates many of the features of the electron Monte Carlo computation. The input data includes the c-s-d-a range, r_o, in units of $g.cm^{-2}$. This is used as a scaling parameter. It was found to be most convenient to keep all the distances in units of $g.cm^{-2}$, as the medium was not always water (for which $\rho = 1$), but also could be carbon or aluminium. The parameter δ_T has effectively been set to 4 through putting MAX%DMSQ, the maximum allowed percentage change in $\overline{\Psi^2}$, equal to 8. This version of the program did not include the penetration depth cutoff HZ.

The parameter that largely determines the execution time per history is the number of steps. This refers to the average number of pathlength sections that each history is divided into. It has already been shown that at high electron energies most of these steps will be terminated by a catastrophic event, but at low energies this will only be the case

for a small fraction of the steps. Consequently, the execution time per step is not quite constant, but decreases gradually with decreasing electron energy. The number of steps per history depends on the value of T_o and T_c, being approximately proportional to $\log(T_o/T_c)$ when δ-rays are not included as in the case in the example shown. It will be seen later that T_c = 0.45 MeV is a typical value for T_o = 10 MeV and thus 77.53 steps is also a typical figure. The execution time per history of around 0.5 sec can be compared with 0.1 sec for a photon history comprising about 13 interactions. The inclusion of secondary electron histories in the simulation increases the execution time per primary history in proportion to the increase in the number of steps. For a run with T_o = 20 MeV and T_c = 0.5 MeV, the number of steps per primary history increased from 100 to 120 when secondaries were included.

The results for the total pathlength (when there is negligible backscattering and no Z-cutoff) and the radiation yield, both underlined in figure 4.13, provide a valuable means of checking that the simulation of the rate of energy loss with electron pathlength is functioning as intended. Such indirect checks are very important for a relatively complex computer program as is the case here. The total pathlength can be compared to the quantity $r_o(T_o) - r_o(T_c)$. This was evaluated from the tabulations of Berger and Seltzer (1964) with a small adjustment, in the case

of water, to account for the difference in I values - 71.3 eV in this work, 65.1 eV used by B+S. Values of the radiation yield were also presented by Berger and Seltzer, evaluated in the continuous-slowing-down-approximation. It should be noted that this quantity, as derived from the electron histories, is subject to large statistical fluctuations due to the relatively small number of bremsstrahlung events - 0.789 per history in this example for 10 MeV electrons and only about 3.5 for 40 MeV electrons. Values of 4.74 and 0.0416 from the B+S tabulations compare favourably with 4.724 and 0.0412 in figure 4.13 for the pathlength and radiation yield respectively. This comparison was carried out for many of the preliminary runs of the electron simulation and the agreement was satisfactory, allowing for the statistical fluctuations from a finite number of histories and considering the approximations involved in both the calculation of radiation yield by Berger and Seltzer and in equating r_o to an arithmetic average of the electron pathlength. This latter point has been discussed by Berger (1963).

The input data necessary to run the electron program includes tabulations of quantities such as μ_{cat}, μ_b/μ_{cat}, $L(T,\Delta(T))$ etc. for values of the electron energy from 0.1 MeV to 40 MeV (energies 0.1, 0.2, 0.3,.....0.9, 1.0, 2.0 and so on). Values of these parameters at a particular energy are then interpolated from the tabulations (either linearly or logarithmically as appropriate). Different sets of

data were prepared for water, carbon or aluminium as the slowing-down medium. The total of 9 quantities tabulated comprises only just over 200 numbers. This is very much less than the numerous tables of values of the probability density functions for the selection of random variables from the Goudsmit-Saunderson multiple-scattering distribution and the modified Landau energy-loss straggling distribution involved in the electron Monte Carlo schemes of Patau (1972) and Berger and Seltzer (1969, 1969a).

Finally, the size of the Monte Carlo program should be mentioned. This depended on the amount of information to be extracted from the electron histories and whether or not δ-rays were included. The simplest version of the simulation consisted of 536 statements of code. This increased to 744 statements for a version which calculated the electron flux spectrum down to $T = T_c$ for all generations of electrons. The version that produced the results shown in figure 4.13, which included a depth-dose histogram but not the transport of secondaries, was intermediate in size between the figures quoted above. It must be remembered that the electron Monte Carlo simulation was only one component of the complete program used to calculate the electron flux down to 100 eV for primary photon or electron beams.

4.6 INTERMEDIATE RESULTS

Some of the results from the Monte Carlo electron program are presented in this section. These preliminary results were calculated in order to see how good the agreement was with other determinations of these quantities. It was primarily in order to be able to carry out such comparisons that input data for carbon and aluminium had been calculated. For the same reason, the cutoff T_c was extended down to 0.1 MeV when 0.5 MeV had been considered low enough for the eventual application of the electron simulation. As these applications were to involve the computation of electron flux at various depths in an irradiated medium, it was especially important to be sure that the results for depth-dependent quantities such as energy dissipation and electron transmission were in reasonable agreement with accepted values. In this way, one could be confident that the particular combination of multiple-scattering distribution and energy-loss scheme adopted modelled the spatial characteristics of the electron tracks in a sufficiently accurate manner.

4.6.1 Backscattering

Calculations of the Albedo, the fraction of backscattered to incident particles, have been carried out for 4,2,and 1 MeV electrons incident perpendicularly on a semi-infinite aluminium medium. The assumption implicit in the derivation of the albedo is that a negligible fraction of the backscattered electrons have

Figure 4.14 ALBEDO VALUES FOR ELECTRONS INCIDENT ON A SEMI-INFINITE ALUMINIUM MEDIUM. (Initial energy T_o)

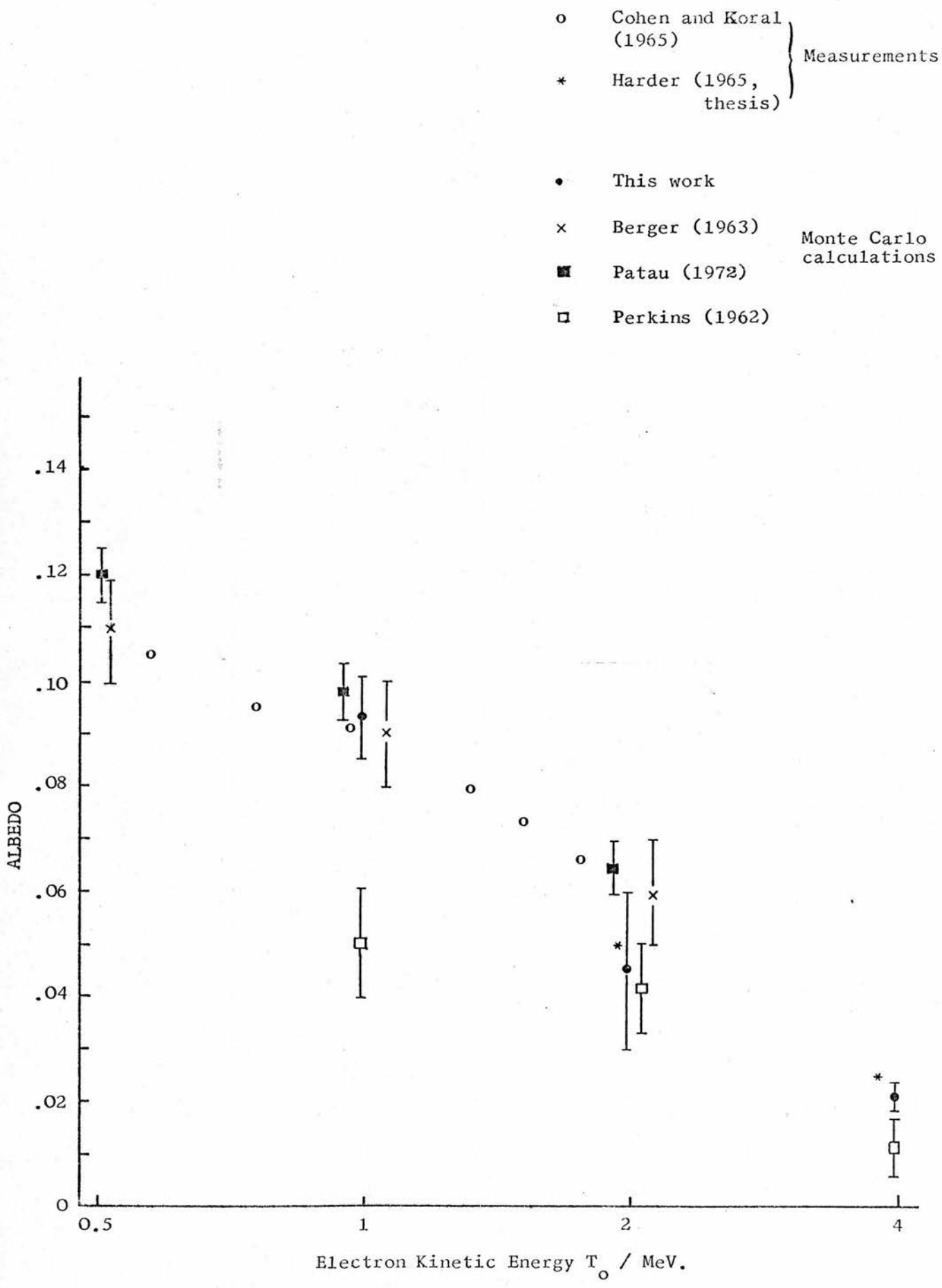

an energy below the Monte Carlo cutoff, T_c. As the minimum value of T_c had been set at 0.1 MeV, it was considered to be invalid to calculate the Albedo for T_c any lower than 1 MeV.

Figure 4.14 shows the results compared to several other determinations. The error bars have been calculated from $\sqrt{A.(1-A)/H}$ for an albedo A derived from H histories (Berger, 1963). The latter was varied between 200 for T_o = 2 MeV and 5000 for T_o = 4 MeV. The percentage of incident energy reflected was also calculated. At 2 MeV, the figure was 4.16% which can be compared with another Monte Carlo value, 4.8 $\pm$ 0.2, from Patau (1972) and 4.0% measured by Wright and Trump (1962).

The good overall agreement with other calculations and measurements is a little surprising considering the approximations involved in the use of the Gaussian multiple-scattering distribution. Berger's MC results came from a program employing the Moliere theory and Patau used the Goudsmit-Saunderson distribution. One can deduce from this that relatively few of the electrons are backscattered due to large individual deflections at these energies. However, for higher incident energies, the measurements of Harder (1965) indicate a much slower fall-off in albedo than that derived from the Monte Carlo histories. The albedo has come out consistently as 0.000 for incident electron energies of 10 MeV and above in carbon and water.

Figure 4.15 TRANSMISSION OF 1 MEV ELECTRONS IN ALUMINIUM
(Monte Carlo calculations)

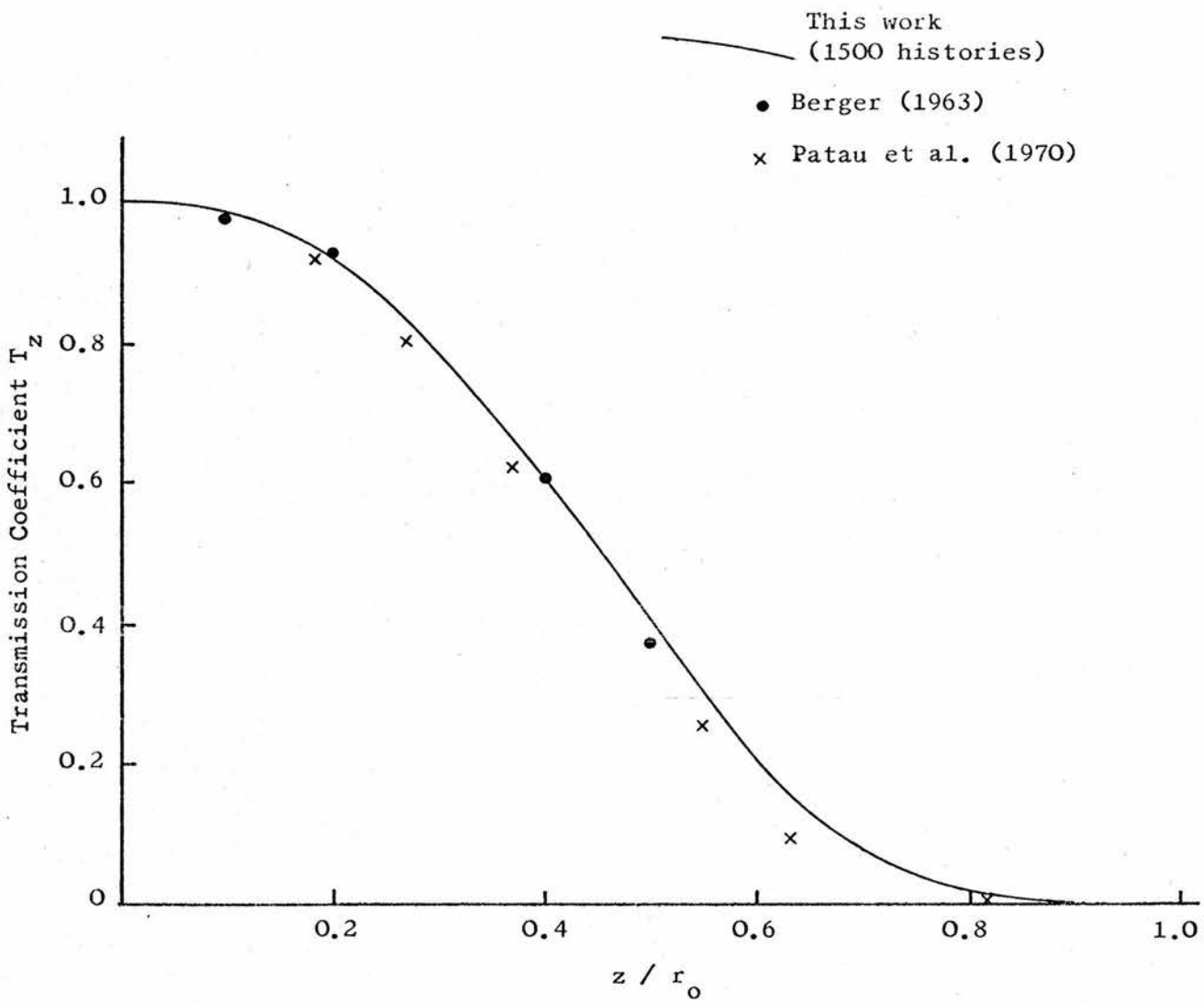

Figure 4.16 TRANSMISSION OF 20 MeV ELECTRONS IN CARBON.

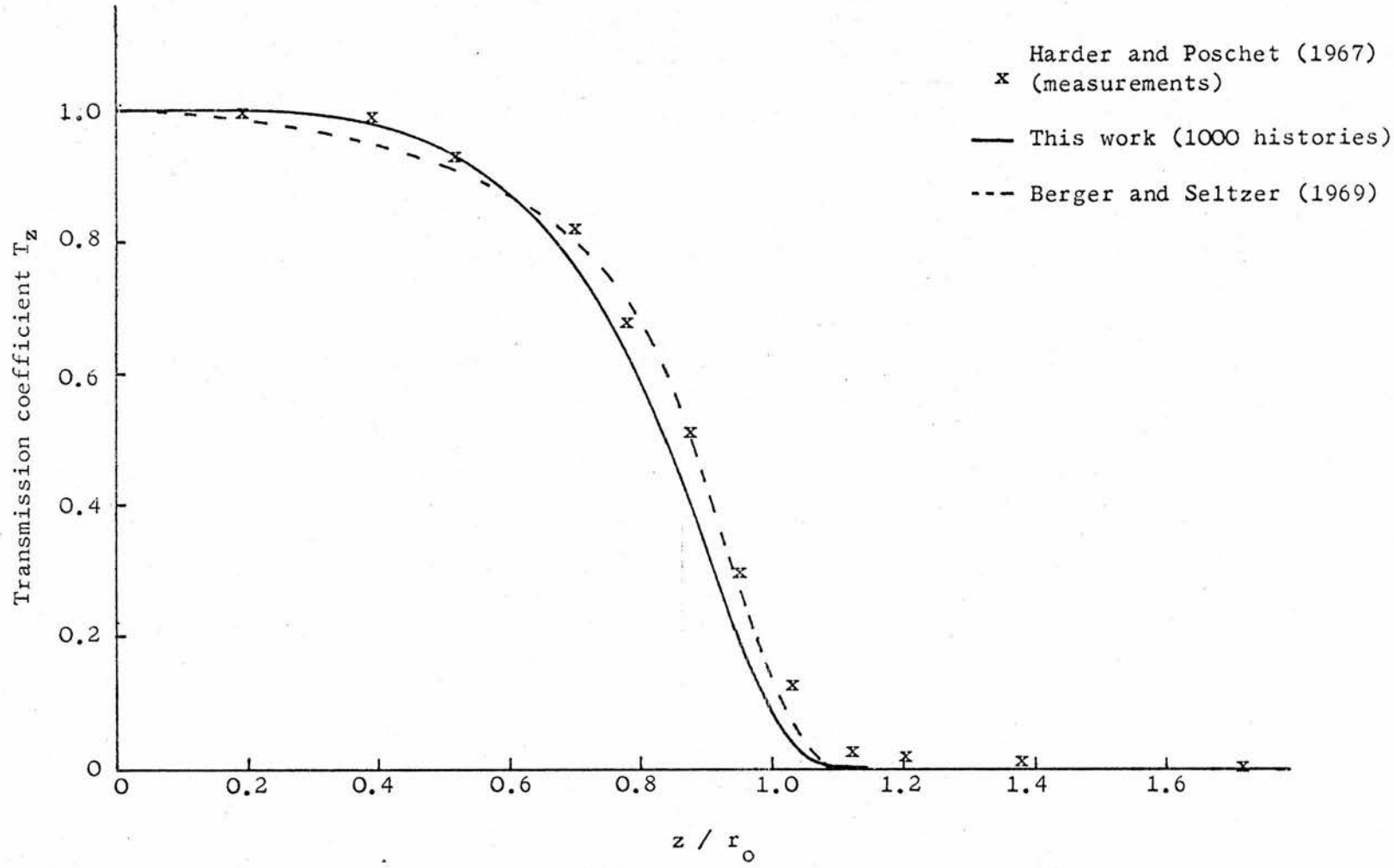

4.6.2 Transmission

The transmission coefficient at depth z, T_z, is the fraction of incident electrons that penetrate at least to depth z. Some of the calculations and measurements of this quantity reported in the literature have included secondary electrons, leading to values of T_z greater than one, but only primary electrons are considered here. When the depth of penetration is expressed in units of z/r_o, the values of the transmission coefficients are very similar for different T_o.

Results from the present Monte Carlo calculations are compared with other MC work and with measured values in figures 4.15 and 4.16. The Berger values in fig. 4.15 were based on the c-s-d-a and the Moliere multiple-scattering distribution. Berger (1963) found that the results for the transmission were only very weakly dependent on the particular multiple-scattering distribution used.

In figure 4.16, at intermediate depths the Monte Carlo calculations of Berger and Seltzer lie closer to the measured values than the results from the present work, possibly due to the more rigorous treatment of energy-loss straggling in the B+S simulation. Leiss et al. (1957) had demonstrated the considerable effect on the results due to the inclusion of ionization and radiation straggling. The complete neglect of energy-loss straggling implicit in the use of the c-s-d-a, for instance, would have produced poor

agreement with measured values in figure 4.16 due to the influence of bremsstrahlung losses.

4.6.3 Depth-Dose Histograms

The results presented correspond to a pencil beam of monoenergetic electrons incident perpendicularly on a semi-infinite medium. The energy deposited in layers of thickness 0.05 r_o, of infinite extent, is added up from the electron histories. All bremsstrahlung photons are assumed to escape from the medium. The transport of secondary electrons is not included and so it is assumed that the kinetic energy of the δ-rays is deposited at the position of origin. Note that the transport of bremsstrahlung and δ-rays, for which T is greater than T_c, is included in the calculation of depth-dose histograms presented in later chapters.

The energy loss in a c-s-d-a pathlength step is assumed to take place at the mid-point of each step, P, as defined in section 4.4.4.2. Where a step lies partly in one 0.05 r_o layer and partly in another, no attempt is made to divide up the energy deposition between the two layers. This should not lead to any systematic error, given that the average value of the step length is much less than 0.05 r_o, which it is.

The choice of 0.05 r_o for the thickness of the depth divisions, following the practice of Berger (1963) and Berger and Seltzer (1969), also determines the value of an upper limit for the Monte Carlo cutoff, T_c. Logically, this is the energy of an electron which has a residual range such that it has only a small chance

Figure 4.17 DEPTH-DOSE HISTOGRAM.
(1 MeV electrons incident on semi-infinite aluminium medium)

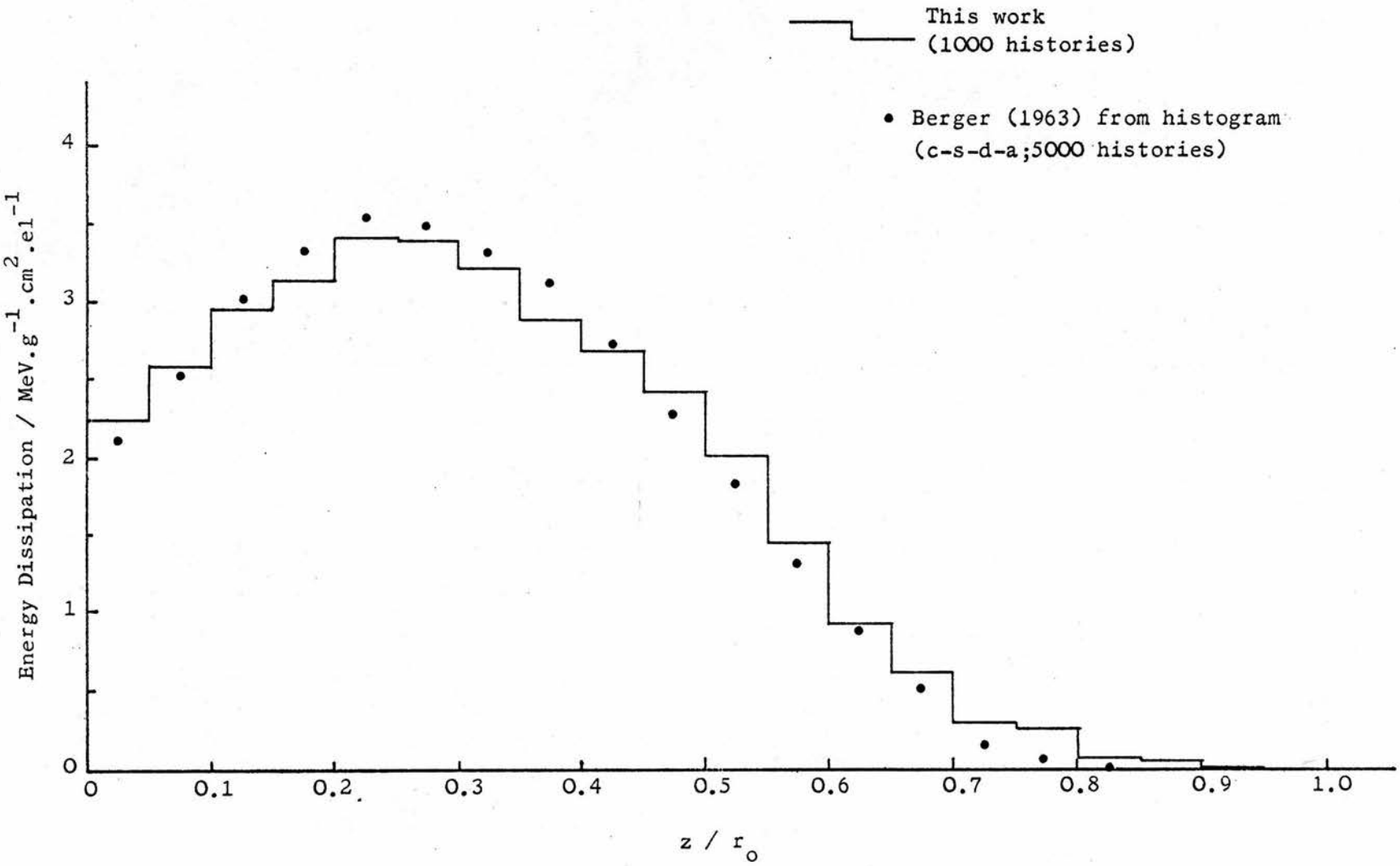

Figure 4.18 DEPTH-DOSE HISTOGRAM.
(4 MeV electrons incident on semi-infinite aluminium medium)

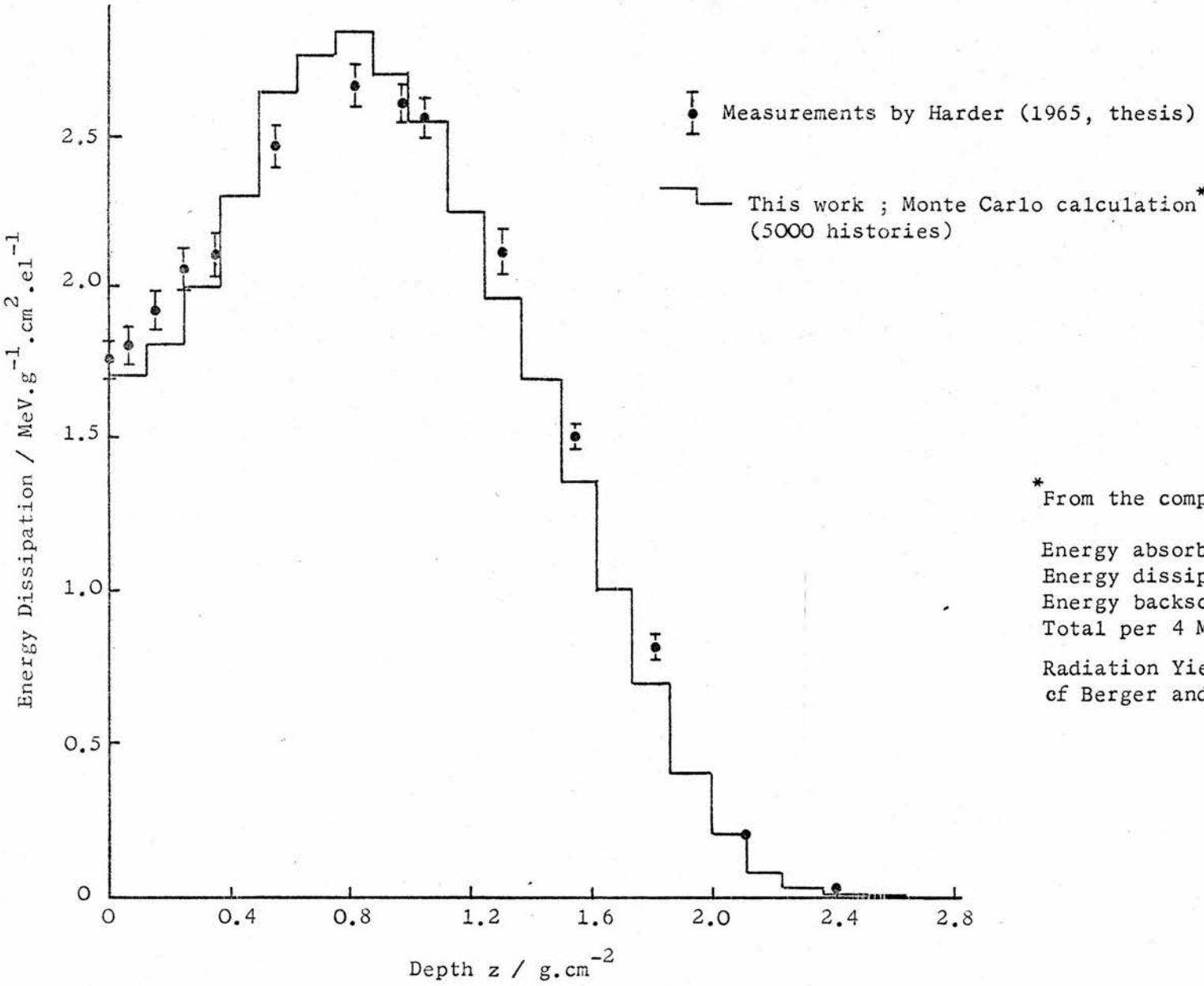

*From the computer printout:

Energy absorbed between O-2z/r$_o$	= 3.8401
Energy dissipated as bremsstrahlung	= 0.1302
Energy backscattered	= 0.0277
Total per 4 MeV incident electron	: 3.9930

Radiation Yield = .0326
cf Berger and Seltzer (1964) - .0335

of leaving the layer it is in when the history is terminated. Thus for 10 MeV electrons incident on water, for example, 0.05 r_o is 0.025 cm and T_c has been set equal to 0.45 MeV corresponding to a c-s-d-a range of 0.015 cm which is effectively shortened somewhat due to angular deflections.

Figure 4.17 is a comparison of a depth-dose histogram for a 1 MeV electron beam derived from 1000 histories in aluminium with a Monte Carlo calculation by Berger (1963) derived from 5000 histories based on the c-s-d-a. This calculation of Berger, drawn as a histogram in figure 1.7, was shown there to be in good agreement with a moments method result of Spencer (1959). Reasonably good agreement has also been obtained with measurements in aluminium by Harder (1965) for a 4 MeV electron beam as figure 4.18b illustrates. The depth is expressed in units of $g.cm^{-2}$ on this graph. The units of energy dissipation have been normalized to MeV per $g.cm^{-2}$ per incident electron by dividing the total energy deposited in each layer by the thickness of the layer, 0.05 r_o, and by the number of histories. On figure 4.18 some extra figures from the computer printout of the 5000 history run are given. The internal consistency of the energy dissipation computation is demonstrated. The radiation yield comes out to be very close to the figure given by Berger and Seltzer (1964) for 4 MeV electrons in aluminium.

Figure 4.19 DEPTH-DOSE HISTOGRAMS
(10 MeV electrons in water)

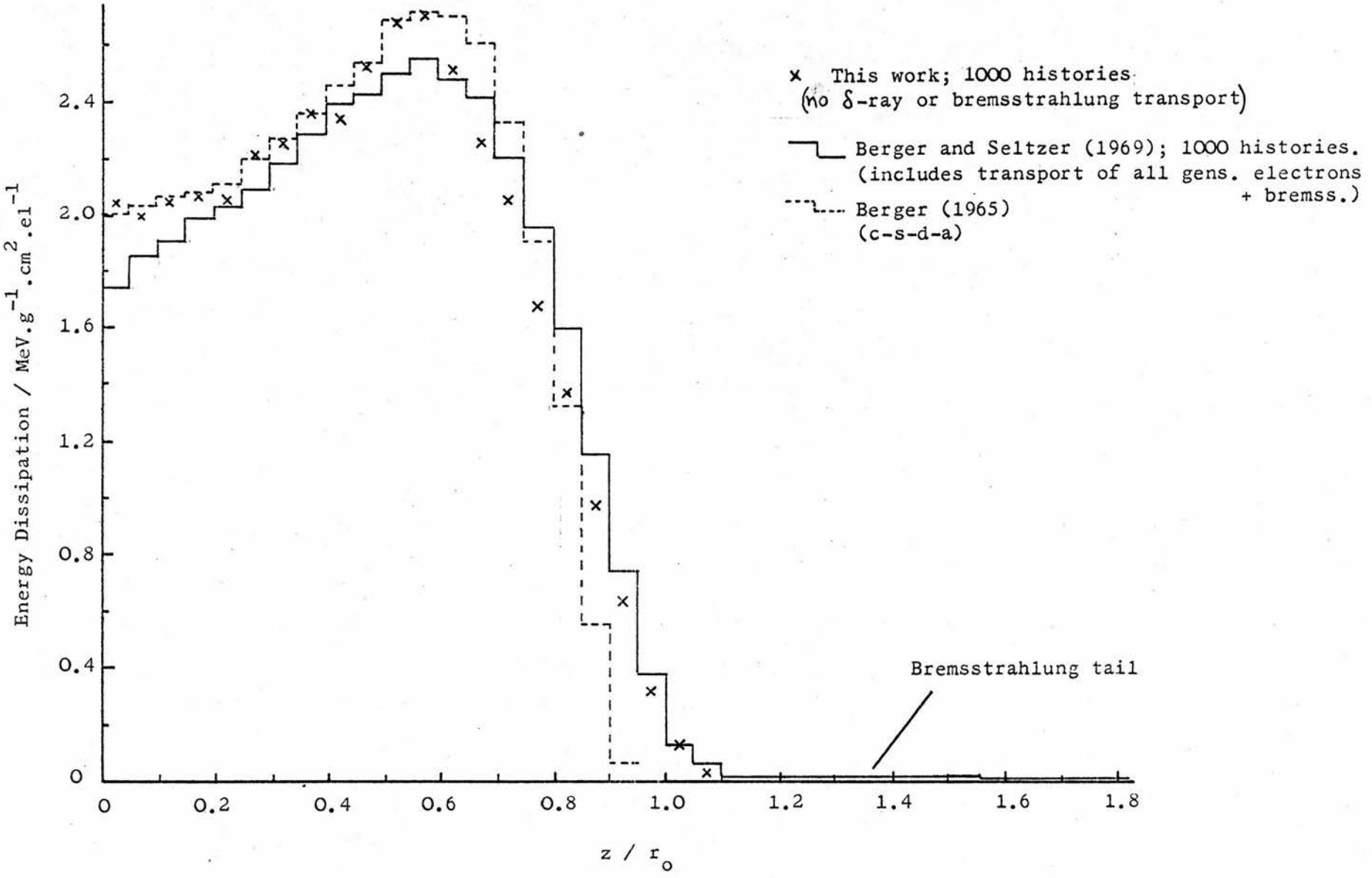

Figure 4.19 contains an interesting comparison of the present results for 10 MeV electrons in water, shown as a series of crosses, with the two histograms given in Berger and Seltzer (1969). The dotted histogram was derived from the Berger (1965) set of Monte Carlo calculations based on the c-s-d-a. It can be seen that the results from this work lie closer to their later histogram which was derived from a program taking into account energy-loss straggling. The 'tail' is due to the inclusion of energy transport by bremsstrahlung. The agreement, especially for z/r_o close to unity, demonstrates that the 2-group model with cutoff $\Delta(T)$ for catastrophic events, is more or less equivalent to the Berger and Setlzer (1969) scheme that explicitly makes use of a straggling distribution for the collision energy loss. The lack of agreement between the solid histogram and the present calculation close to the surface is partly due to the neglect of forward δ-ray diffusion. This discrepancy was much reduced in a later calculation that included δ-ray transport.

The relatively 'smooth' electron depth-dose histograms obtained from only a few thousand histories contrast interestingly with the results from the photon MC program for the spatial deposition of photon energy. A very large number of photon histories are required to produce a 'smooth' histogram, of the order of 10,000 or more. This is to be expected from the nature of the photon interactions with matter, which result in very little uniformity between different photon tracks.

Although the execution time per photon history is appreciably less than per electron history, it actually takes more total computer run-time to produce photon rather than electron depth-dose histograms with the same order of statistical uncertainty.

4.6.4 Electron Flux Spectra

The energy spectrum of the electron flux is the physical quantity that is central to this investigation. It is derived from the electron histories by adding up the total tracklength in the different energy intervals within a given volume. This pathlength spectrum is the flux spectrum averaged over the volume in question. The geometry is the same as that for the depth-dose calculation - except that the upper and lower limits of the layer or layers can be varied. At this stage of the work, the low-energy electron program (see chapter 5) had not yet been developed and therefore the spectrum could not be computed below the Monte Carlo cutoff, T_c.

4.6.4.1 Computation details

Before giving examples of some preliminary results, the steps involved in extracting the pathlength spectrum from the electron histories will be described. The first parameters that must be specified are Z_i and Z_h, the values of z that enclose the volume of interest. It will be assumed for the moment that the program computes the spectrum within only one layer, though subsequent versions could accommodate any desired number of different geometries. The number of equal log energy intervals, N_i, can be varied with the

Figure 4.20 POSSIBLE CONFIGURATIONS OF A PATHLENGTH STEP wrt. THE SPECTRUM GEOMETRY.

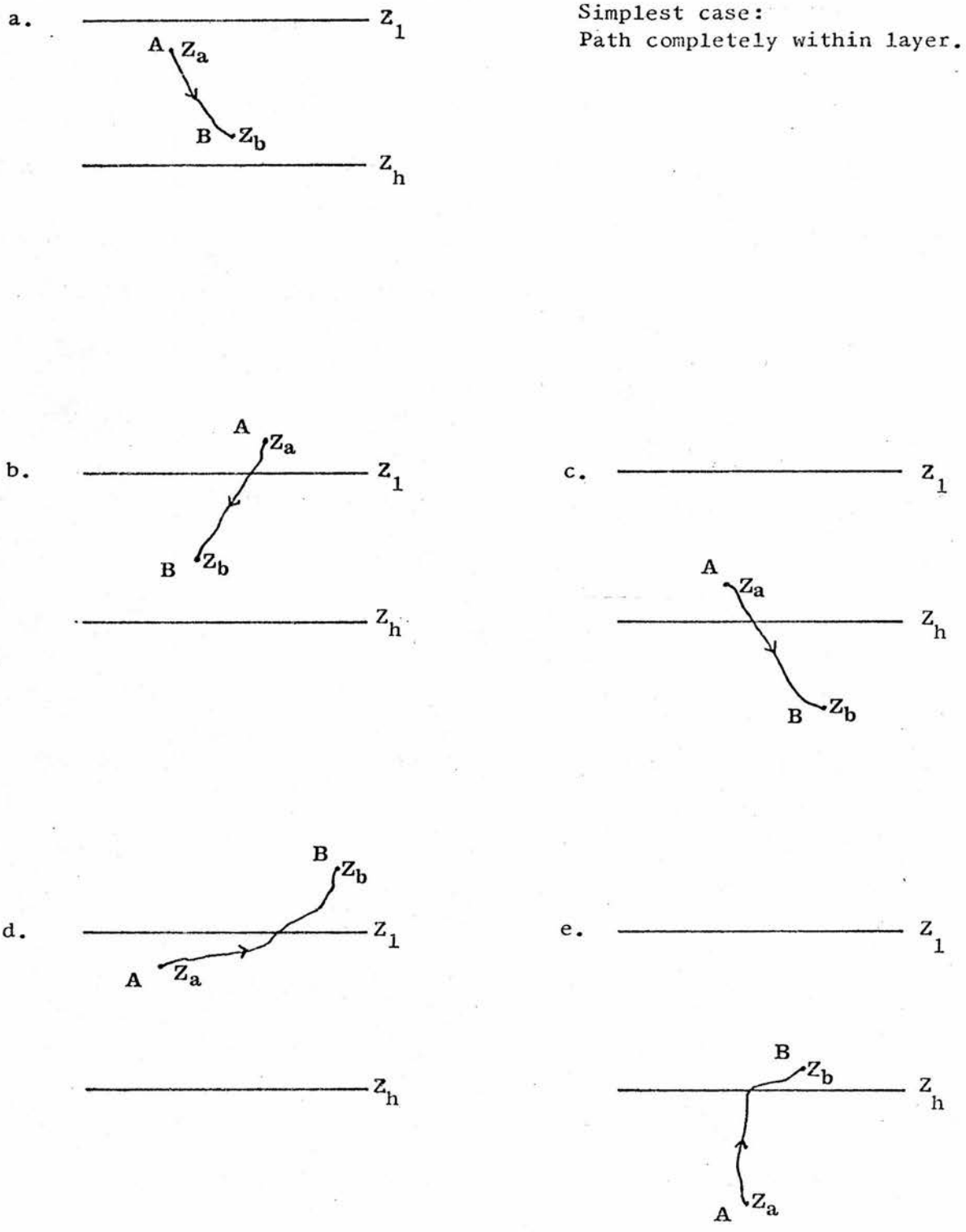

limitation that the maximum allowed energy loss by an electron during a c-s-d-a step does not result in more than two adjacent energy intervals being involved. This means that for a ratio r between intervals,

$$1 - 1/r \geq 0.01\delta_T \qquad .....(4.27)$$

where r is given by

$$r = \exp\left(\log_e(T_o/T_c)/N_i\right) \qquad .....(4.28)$$

In practice, this did not prove to be a limitation due to the small size of $\Delta T/T$ ($=0.01\delta_T$), but was retained in the computation to make sure that the value of N_i chosen could not lead to an invalid calculation of the spectrum as will be made clear below.

The spectrum calculation takes place during the execution of the routine CSDALOS in the electron program* (see section 4.5.1). Firstly, the value of z at the beginning and end of each pathlength step is compared to ascertain whether any part of the electron track section lies within the layer for which the spectrum is to be computed. Any one of five possible configurations may be involved. These are sketched in turn in figure 4.20a-e. In all the cases, the track section starts at A, where $T = T_a$, and ends at B, where $T = T_b$. For all but 4.20a, the length of track within the layer must be calculated.

Consider the configuration 4.20b, which is enlarged in figure 4.21a. The track interacts the boundary, $z = Z_1$, at I. The pathlength, s_f, between I and B is given by

---

*Later the spectrum calculation was transferred to a separate routine, SPECTOT.

Figure 4.21 DETAILS OF SPECTRUM COMPUTATION FROM A TRACK SEGMENT.

a. Pathlength Subdivision.

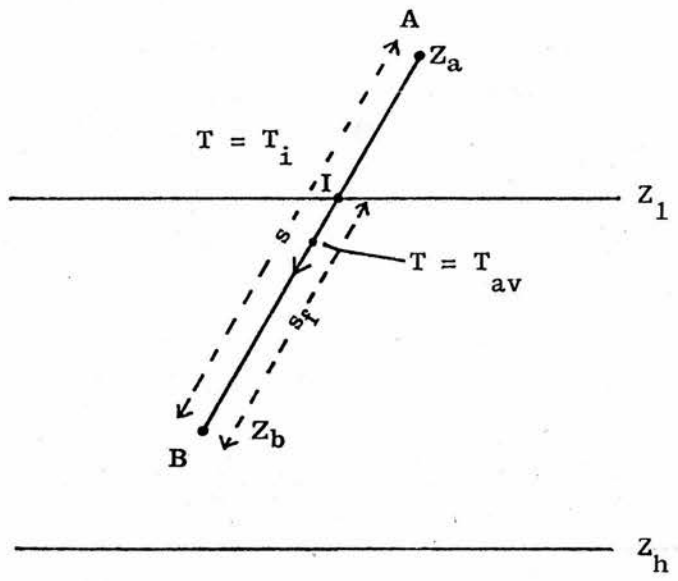

b. Energy Subdivision.

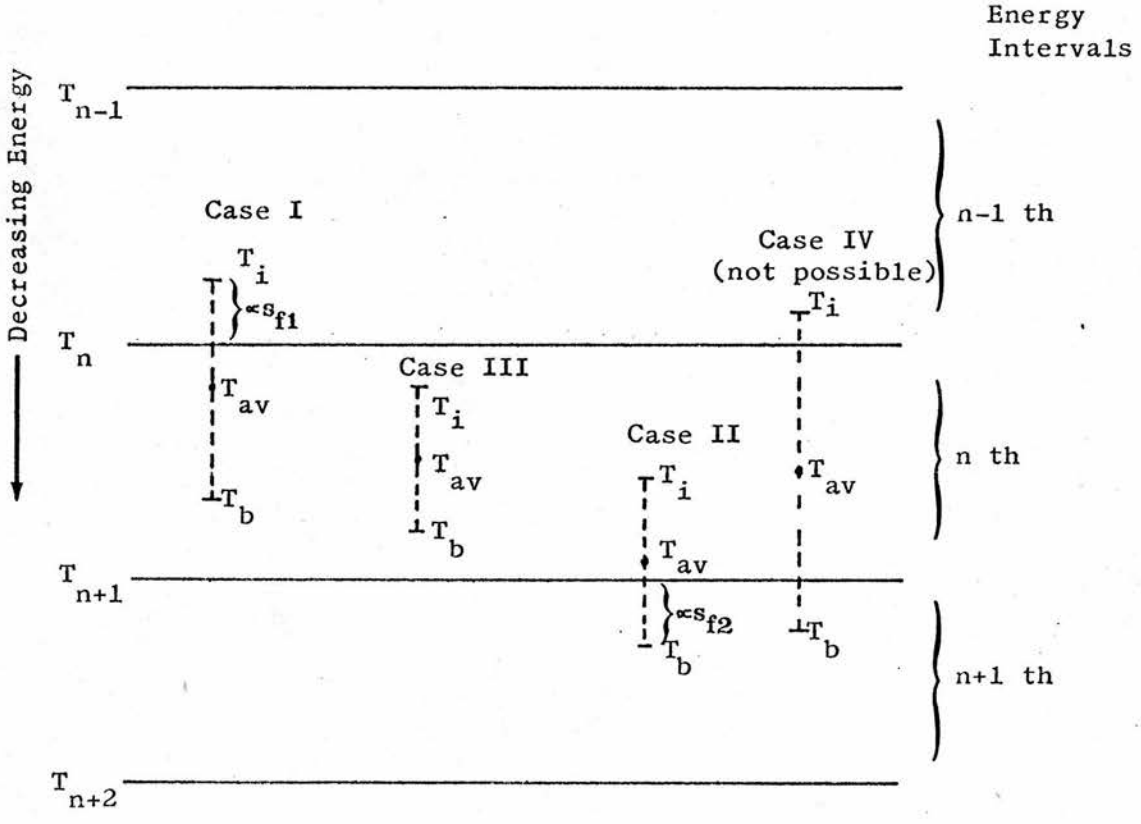

$$s_f = s \cdot \frac{Z_b - Z_1}{Z_b - Z_a}$$

and the energy, T_i, at I by

$$T_i = T_a + \frac{s}{s_f} \cdot (T_b - T_a)$$

These relations are obtained by assuming that the track is straight. No systematic error should be incurred by this assumption. Anyway, the pathlength steps have been approximated by two straight-line sections in order to incorporate the multiple-scattering deflection in a simple manner.

The second calculation concerns the subdivision of the segment IB into different energy intervals. This is illustrated schematically in figure 4.21b. The spectrum interval, n, corresponding to $T = T_{av} = (T_i + T_b)/2$, is first determined from

$$n = 1 + Ip(\log_e(T_o/T_{av})/\log_e r)$$

where Ip(...) denotes the integer part of (...) and n = 1 is the highest energy interval, T_o to T_o/r. The upper and lower limits of the n th interval are denoted by T_n and T_{n+1} respectively. T_i is compared to T_n. If T_i is greater than T_n, then part of the segment lies in the next higher energy interval, n-1 (case I). The length of this part of the segment, s_{f1}, is then:

$$s_{f1} = s_f \cdot \frac{T_i - T_n}{T_i - T_b}$$

and s_{f1} is added to the total pathlength so far recorded in the (n-1)th energy interval. The remainder of the track, $s_f - s_{f1}$, is added to the total pathlength in the n th energy interval. If T_i is not greater than T_n, then the electron energy at the end of the step, T_b, is compared to T_{n+1}. If $T_b < T_{n+1}$, part of the track lies in the next lower energy interval, n-1 (case II), and s_{f2} is calculated etc. If neither $T_i > T_n$ nor $T_b < T_{n+1}$, then both T_i and T_b lie within the n th energy interval and the pathlength s_f is added to the total tracklength in this energy interval (case III). Note that it is not possible for both T_i to be in the n-1 th interval and T_b to be in the n+1 th interval, as in case IV, due to the restrictions on the size of r expressed by equation 4.27 above. There is thus no need to allow for this possibility, which prevents the calculations from being further complicated. It is not difficult to see how the above details are modified to accommodate the other configurations depicted in figure 4.20.

Originally the whole of the track section under consideration was assumed to contribute to only one spectrum interval, determined by the energy T_{av}. All cases were effectively treated as case III in fig. 4.21b. This approximation lead to artifacts in the results for particular values of N_i, the number of spectrum intervals. For a 1 MeV electron beam and semi-infinite geometry, a maximum value of the flux was consistently produced in the 0.8 to 0.9 energy region, completely contrary to expectation on theoretical

Figure 4.22 PRIMARY ELECTRON FLUX SPECTRA IN INFINITE WATER MEDIUM.

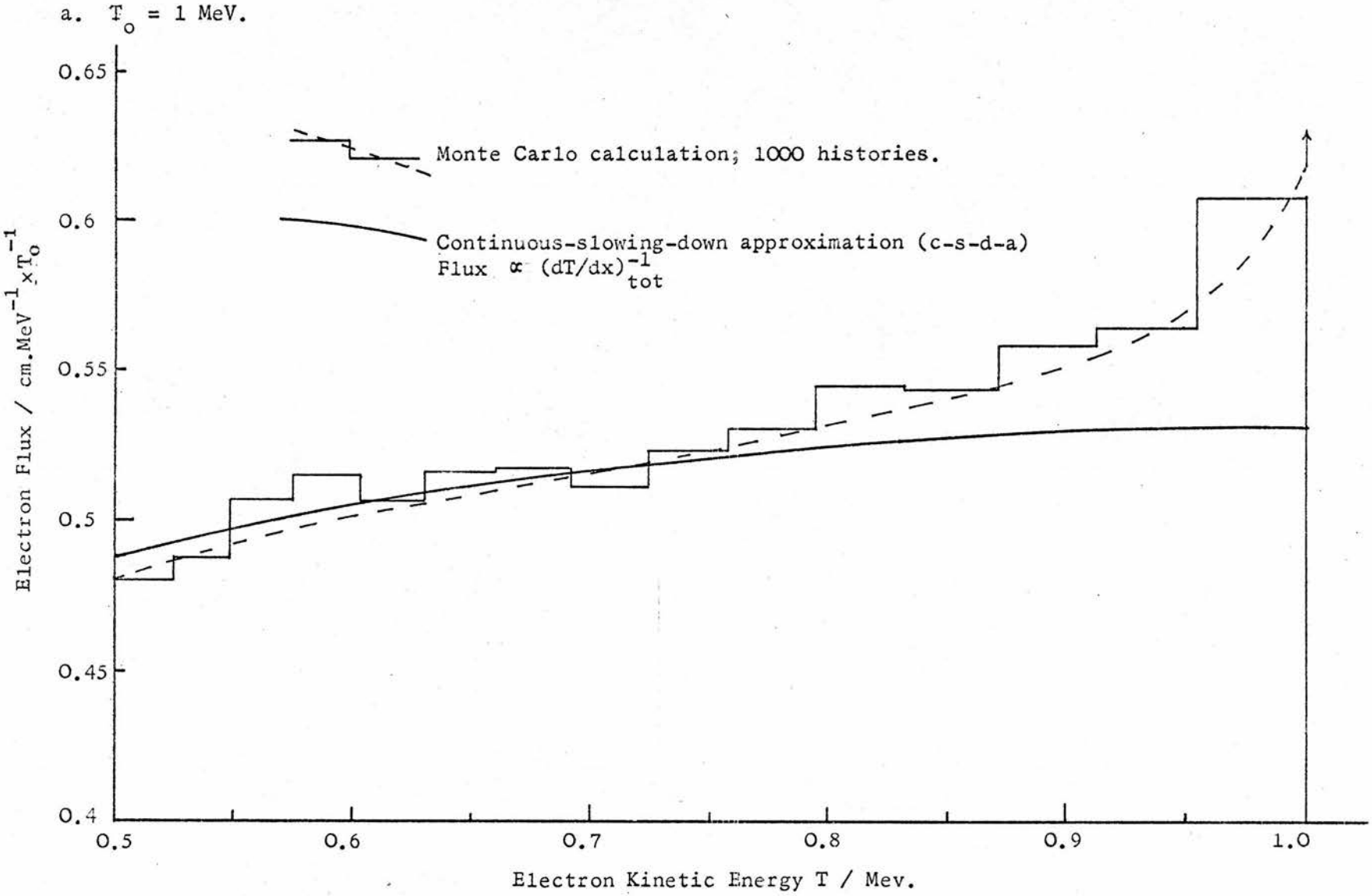

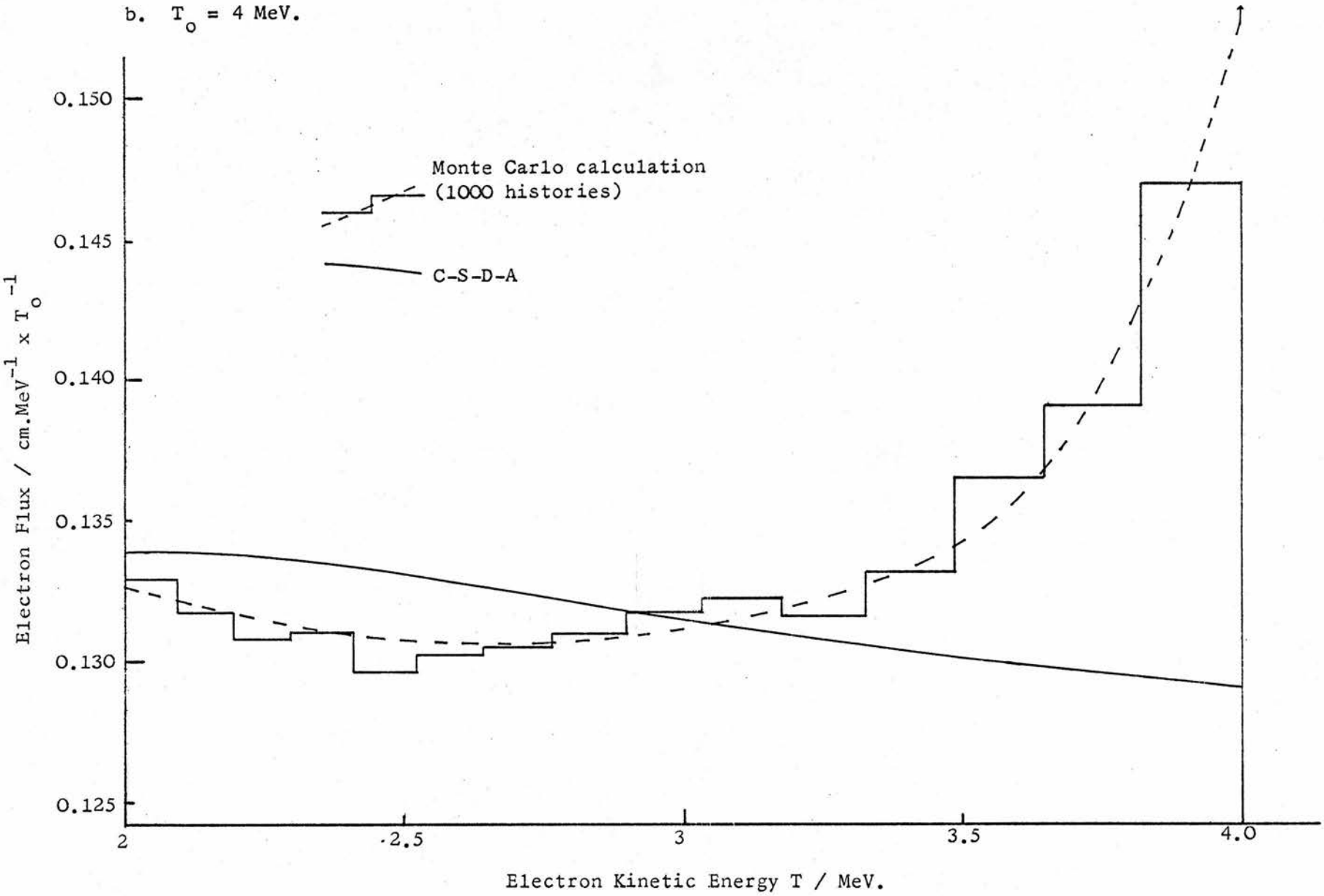
b. T_o = 4 MeV.
Monte Carlo calculation
(1000 histories)
C-S-D-A
Electron Flux / cm.MeV^{-1} x T_o^{-1}
0.150
0.145
0.140
0.135
0.130
0.125
2
2.5
3
3.5
4.0
Electron Kinetic Energy T / MeV.

grounds. The cause of this anomaly in the results was eventually traced to a particular combination of c-s-d-a steps, of size and hence energy loss determined by $s = s_{max}$, and of spectrum energy intervals. One of these intervals happened to include the mid-point energy, T_{av}, of two successive c-s-d-a steps, whereas adjacent intervals included only one such energy. This would not have happened with higher energy electrons for which the majority of pathlength steps are terminated by a catastrophic event after a randomly selected distance rather than in predetermined '$s = s_{max}$' fashion. As expected, the artifact disappeared with the introduction of the subdivision of the track into different energy intervals. This example illustrates very clearly the need to check carefully the validity of results derived from a set of artifically constructed electron tracks.

The operations involved in calculating the contribution of each c-s-d-a step to the energy spectrum were eventually coded together as the routine SPECTOT. This routine was therefore executed from within the routine CSDALOS.

4.6.4.2 Sample Results

It was considered useful to calculate first the flux spectrum for infinite geometry. The results for the primary spectrum could then be compared to the flux calculated from the reciprocal of the total stopping power (c-s-d-a). Figures 4.22a and b give such comparisons for T_o = 1 and 4 MeV in water. The units are cm per MeV per electron (i.e. per MeV input energy).

Figure 4.23 ELECTRON FLUX SPECTRA DOWN TO T = T_c AT THREE DIFFERENT DEPTHS. (T_o = 20 MeV).

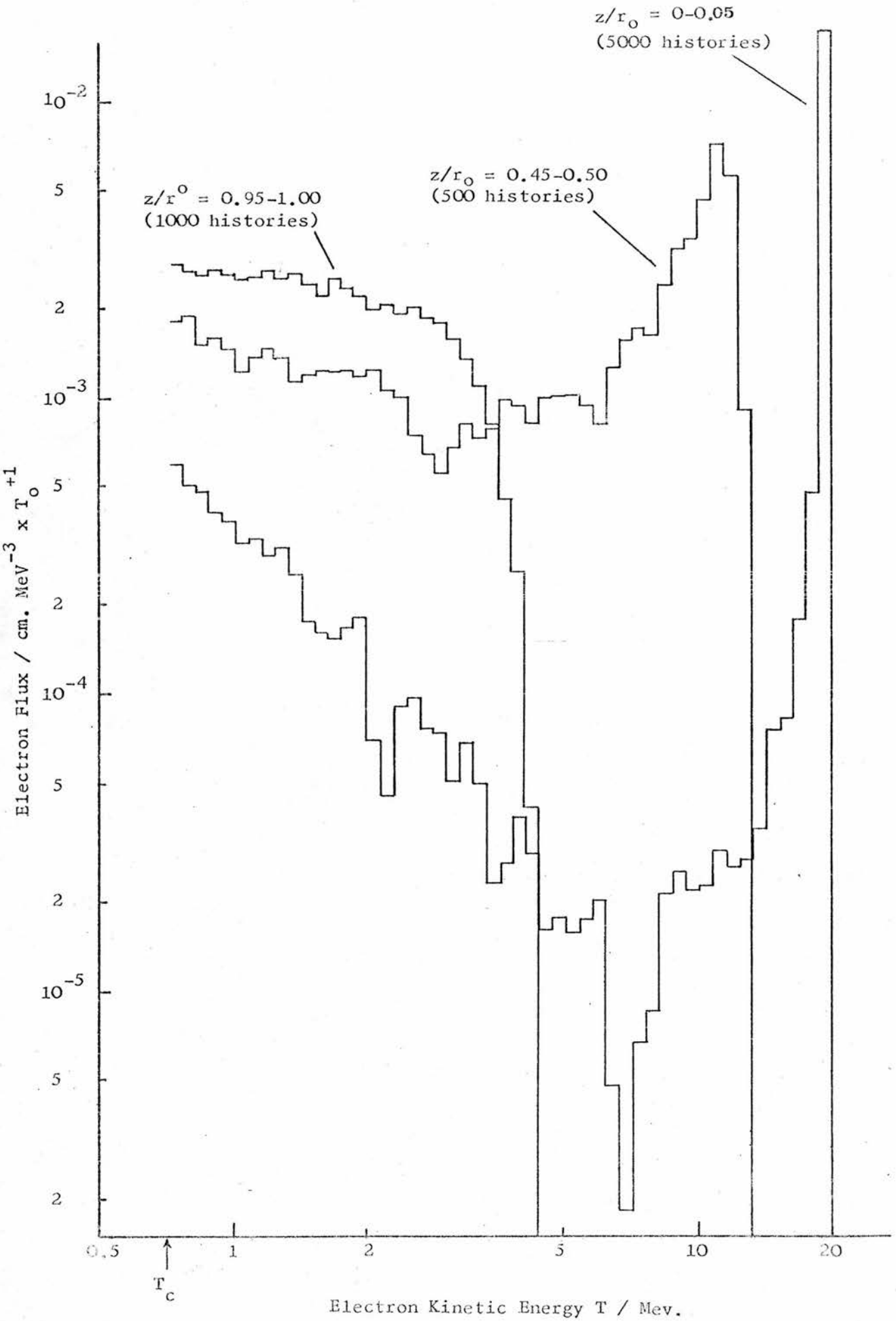

At both energies, 15 energy intervals between T_o and T_c ($=T_o/2$) were chosen. The features of such depth-independent spectra noted by Spencer and Fano (1954) are exhibited in the figure. There is a peak at the source energy, then the spectrum lies slightly below the c-s-d-a value. The difference between the c-s-d-a curve and the histogram is greater at 4 MeV than at 1 MeV as expected due to the greater influence of bremsstrahlung losses at the higher energy.

The change in the total electron flux with depth is shown in figure 4.23. The energy range extends down to 0.75 MeV which is a suitable value of T_c for the 0.05 r_o layers. There are large statistical fluctuations in the electron flux histogram between 5 and 10 MeV for the 0.0 - 0.05 r_o geometry, even though 5000 histories were analyzed compared to only 500 and 1000 at the other depths. These fluctuations are due to the effect of the large straggling in the bremsstrahlung losses which resulted in primary electrons of around 7 MeV in energy. The build-up of the flux at lower energies due to secondary electrons is evident.

The shapes of the 3 histograms correspond very closely to the results of Berger and Seltzer (1969) for electrons in water at the same three depths (see figure 1.8). In particular, the maximum flux values in the 0.45 - 0.50 r_o geometry are at the same energy - 11.4 MeV. The tail on their spectrum between 0.95 - 1.0 r_o must be due to electrons generated by the interactions of bremsstrahlung photons with the medium.

Such electrons could not be included in the simulation at this stage as the photon transport simulation program had not yet been coupled to the electron program. This 'coupling' is described in chapter 6.

4.7 SUMMARY

A detailed description has been given of a Monte Carlo program constructed to simulate the transport of high-energy electrons (up to 40 MeV) in water. The program is the most extensive component in the computation of the total electron flux spectrum at different depths in water irradiated by electron and photon beams.

The main features of the transport and energy-loss scheme can be summarised as follows:

i) The size of the energy losses are divided into two groups by a cutoff $\Delta(T)$. Above the cutoff, the energy transfer and angular deflection involved in each 'catastrophic' event are selected from the appropriate cross-sections. In between catastrophic events, the electrons are assumed to lose energy 'continuously' at a rate given by the collision stopping power restricted to losses less than $\Delta(T)$, radiation losses smaller than $\Delta(T)$ being negligible.

ii) The cutoff $\Delta(T)$, which varies from 30 keV for T = 40 MeV to 10 keV for T = 0.5 MeV, was chosen to be as low as was compatible with a feasible number of individual 'catastrophic' interactions per electron history.

iii) The energy of the δ-rays resulting from catastrophic collision losses are sampled from the Møller inelastic electron cross-section, which is adequately approximated by a $1/q^2$ distribution except for q close to T/2. One in five of the δ-rays is accompanied by an Auger electron. The deflections involved in the collision are determined from energy-momentum considerations.

iv) The energy of bremsstrahlung photons resulting from catastrophic radiation losses are sampled from the Schiff cross-section. A selection procedure was devised which is a modification of the rejection technique. An exponential distribution with a mean angle given by the Schiff cross-section is used to give the photon deflection. The photon coordinates are stored to be used as input data for the photon Monte Carlo program.

v) The Møller and Schiff cross-sections were integrated (down to an energy transfer $\Delta(T)$) and added to give an effective attenuation coefficient for catastrophic events, μ_{cat}, which was tabulated for different values of the electron energy, T. This is used to select the distance between catastrophic events. The event type, i.e. δ-ray or bremsstrahlung photon, is determined from the ratio of bremsstrahlung attenuation coefficient, μ_b, to μ_{cat}.

vi) The Schiff cross-section used in v) was multiplied by a factor, f_b, which varied with electron energy, in order that the average radiation loss, $(dT/dx)_{rad}$, should come out equal to that given in the Berger and Seltzer (1964) tabulations.

vii) The deflection resulting from the 'continuous loss' pathlength steps between the catastrophic events is selected from the simple Gaussian multiple-scattering distribution, which does not take into account the occasional large-angle deflection, but otherwise has been shown to be a reasonable approximation to the more exact Goudsmit-Saunderson distribution.

viii) The pathlength steps are restricted to a maximum size such that the energy loss in a step is not greater than 4% of the electron energy at the beginning of the step. This is so that the mean square deflection angle in the Gaussian distribution should only change by a small percentage over each step, which would not always be the case for the distance selected between catastrophic events.

ix) The primary electrons and all δ-rays are followed until their energy drops below T_c, the Monte-Carlo cutoff, generally chosen such that further spatial diffusion is unimportant. T_c cannot be less than 0.1 MeV.

x) The program requires several tabulations as 'permanent' input data, amounting to only a few hundred numbers. These sets of data were pre-calculated for carbon and aluminium as well as water in order to be able to compare the results of certain quantities calculated for these media with other theoretical and experimental determinations.

The program can be compared with similarly comprehensive electron transport simulations by Berger and Seltzer (1969, 1969a) and Patau (1972) and owes much to the poineering work of Berger (1963) on Monte Carlo schemes for fast charged-particle transport. It differs from the programs by Patau, and Berger and Seltzer, in two important aspects. Firstly, the Gaussian multiple-scattering distribution is used instead of the Goudsmit-Saunderson distribution. Though the latter distribution is more exact, it is somewhat involved to evaluate and requires a large number of tables of input data in order to make the selection process efficient. The Gaussian distribution,

by contrast, can be sampled by the straightforward C.P.D. method, requiring no pre-calculated input data at all. Secondly, the use of a two-group scheme for the energy loss, with as low a value of $\Delta(T)$ as possible, has meant that explicit use of energy-loss straggling distributions could be avoided. Effectively, it is assumed that all the energy-loss straggling is due to losses greater than $\Delta(T)$. Both Berger and Seltzer and Patau had to employ a modified version of the Landau ionization-loss straggling distribution to simulate the fluctuations in the energy loss in the pathlength steps where the continuous-slowing-down-approximation is used in this work. These straggling distributions again involved large amounts of pre-calculated data which was not necessary in the present case.

Finally, the intermediate results for backscattering transmission, spatial energy deposition (i.e. depth-doses) and flux spectra are in good agreement with other work and indicate that the Monte Carlo electron program is functioning satisfactorily and can be applied with confidence to the specific problems to be investigated. In particular, the approximate treatment of energy-loss straggling and multiple scattering seems to be fully justified.

CHAPTER 5

CALCULATION OF THE ELECTRON FLUX SPECTRUM IN WATER BETWEEN T = T_c AND 100 eV

5.1 REQUIREMENTS OF THE CALCULATION

The electron flux spectrum is to be calculated down to 100 eV. The electron Monte Carlo program extends down to the cutoff T_c chosen such that further spatial diffusion can be disregarded. Consequently, a depth-independent method* will suffice to compute the spectrum between T_c and 100 eV. The input for this calculation is provided by all the electrons from the Monte Carlo simulation that have initial energies between T_c and 100 eV viz the 'track ends' of energy just less than T_c and all δ-rays of energy less than T_c produced by these histories in the course of slowing down to T_c. For the case of a primary photon beam, there will also be the Compton, pair and photoelectrons that have initial energies less than T_c. Auger electrons must also be included in the depth-independent, slowing-down process using the same assumptions as have been employed in the Monte Carlo programs.

The maximum energy for which the depth-independent spectrum calculation will be valid is not only governed by spatial diffusion considerations but also by bremsstrahlung production. Clearly, all bremsstrahlung produced by electrons below T_c would have to be assumed

---

*The computation is also referred to as the low-energy spectrum program.

to dissipate energy outside any region of interest. The photons could not be included in the Monte Carlo photon transport simulation as their initial parameters would not have been 'selected'. Consequently, T_c has to be an energy such that bremsstrahlung production is negligible over the remainder of the electron track below this energy. This consideration dictates that the Monte Carlo cutoff is not greater than about 2 MeV, where the bremsstrahlung yield is only 0.009 and the radiation stopping power is 2% of the total.

It will be seen that the accuracy of the spectrum below about 1 keV in water is primarily limited by the uncertainty in the total stopping power at these low energies. The calculation described here is not expected to be particularly accurate in this energy region in view of the approximations used. Its main purpose was to be a self-consistent extension of the Monte Carlo spectrum down to low energies in order to be able to compare the relative magnitudes of the slowing-down spectrum produced in water by various electron and photon beams. The applications of the spectra to be described in chapters 9 and 10 do not anyway depend critically on the absolute magnitude of the flux below about 1 keV.

Finally, it can be noted that execution time is not a problem with the low-energy electron spectrum program. It is only executed once, after all the Monte Carlo electron histories have been generated. Naturally, the spectrum from the depth-independent computation must join smoothly onto the Monte Carlo histogram at $T = T_c$.

Figure 5.1 DEPTH-INDEPENDENT ELECTRON FLUX CALCULATIONS.

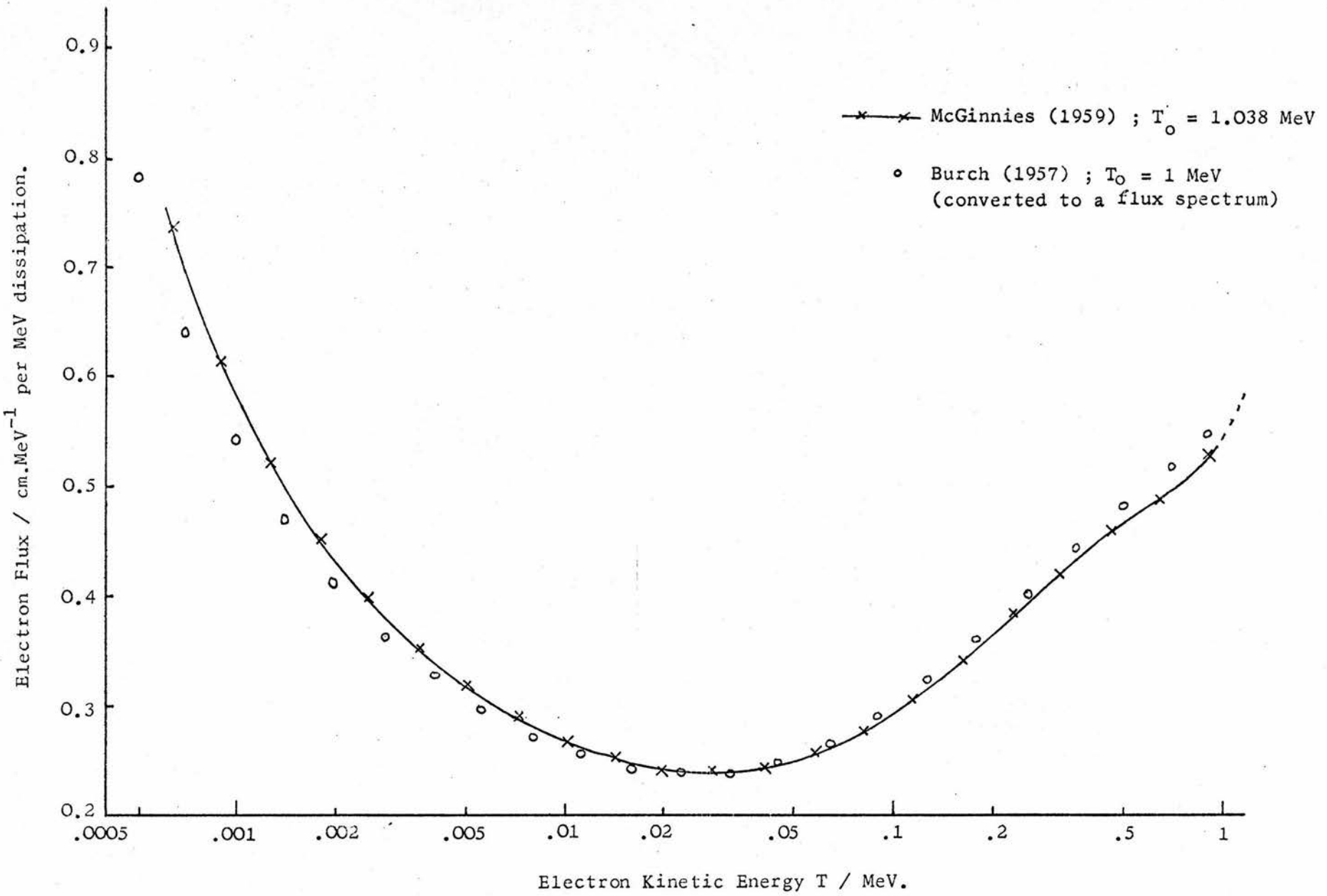

5.2 SLOWING-DOWN SCHEME

The review of the literature in chapter 1 included a discussion of the methods used to take into account all generations of electrons in the slowing-down problem. The Spencer-Fano theory was used by Berger and Seltzer (1969) to extend their Monte Carlo calculations of the electron flux down to about 400 eV. In this work, a modification of the less involved approach of Burch (1957a) has been employed.

Burch calculated the local energy dissipation in energy interval ΔT, $Q_T \Delta T$, which can be related to the electron flux spectrum, $F(T)\Delta T$, by

$$Q_T \Delta T = F(T).(dT/dx)_{100} \Delta T \qquad .....(5.1)$$

Thus $F(T) = Q_T/(dT/dx)_{100}$ or Q_T/L_{100} .....(5.2)

where Q_T is the local energy dissipation per unit energy interval. Burch's (1957) $Q_T \Delta T$ spectrum for 1 MeV electron radiation has been converted to a flux spectrum using equ. 5.2 and the $(dT/dx)_{100}$ values given by Burch and Bird (1956). Figure 5.1 is a comparison of the Burch 1 MeV spectrum with the McGinnies (1959) computation of the tracklength spectrum, $Y(T_o,T)$, for T_o = 1.038 MeV in water, both normalized to the same units. The agreement is good, demonstrating that Burch's stepwise method gives very similar results to the more sophisticated Spencer-Fano theory on which the McGinnies computation was based.

Burch chose relatively wide energy bands in his scheme. It was considered desirable to use somewhat finer energy intervals in this work in order to treat more accurately the wide range of input energies to the low-energy computation from the Monte Carlo histories as well as to increase the precision of the method itself. However, a straightforward decrease in the energy interval size with no other modifications to Burch's method would not have produced valid results. Burch allowed for the 'missing-out' of bands due to large energy losses by the primary electrons slowing down in a given band. His model was therefore a type of 2-group scheme as described by Schneider and Cormack (1959). These workers showed that if $N_{\Delta}(T)\,dT$ is the number of electrons slowing down 'continuously' through the energy interval T to T+dT, for a cutoff Δ, then the electron flux is given by $N_{\Delta}(T)/L_{\Delta}(T)$*. Burch's cutoff, Δ, was effectively the minimum energy loss that could result in the next energy interval being 'jumped over', though he did not discuss this point. Burch derived his $Q_T\,\Delta T$ distribution from

$$Q_T\,\Delta T = N(T)\,\frac{(dT/dx)_{100}}{(dT/dx)_{total}}\,\Delta T \qquad .....(5.3)$$

---

*This is effectively how the spectrum is derived from the electron histories in the Monte Carlo program.

Eliminating $Q_T \Delta T$ between 5.1 and 5.3, gives

$$F(T) = N(T) / L_{total} \qquad .....(5.4)$$

which is only valid for a scheme based entirely on the continuous-slowing-down approximation, for which the cutoff is T/2 and therefore L_Δ is identical to L_{total}. Burch should have calculated $Q_T \Delta T$ from

$$Q_T \Delta T = N(T) \frac{L_{100}}{L_\Delta} \Delta T \qquad .....(5.5)$$

However, the size of his energy intervals was such that L_Δ was always very close to L_{total}. Consequently, his calculations appeared to be internally consistent in spite of this approximation.

As the interval size is decreased, the effective value of Δ is decreased and L_Δ would have to be evaluated for each energy band in a 2-group model, increasing the complexity of the calculations especially if bremsstrahlung losses were included. Schneider and Cormack (1959) showed convincingly that a slowing-down scheme with the primary flux given by the c-s-d-a would yield the total flux in very good agreement with the 2-group model except close to the source energy. In particular, they found that the 'peak' at the source energy in the more accurate spectrum based on the 2-group model was found to contribute only 0.5 - 0.6% of the total energy distribution.

It was decided, therefore, to use the c-s-d-a in this work. This means that all the electrons in one energy band are assumed to slow down 'continuously' into

the next lowest energy band, there being no jumps over bands. The actual computational details of this modified Burch scheme are described in section 5.4. The scheme is the same as that which Till employed to calculate the total electron flux, though Schneider and Cormack did not give details of his computational method or results beyond his use of equ. 5.4 to give the electron flux (see also section 1.3.1.1).

5.3 ELECTRON STOPPING POWER AT LOW ENERGIES

As the flux calculation is to extend down to 100 eV this means that values for the total stopping power are required down to this energy. The binding energy of the K-shell oxygen electrons is about 500 eV. It is clear, therefore, that the Bethe-Bloch theory for calculating the stopping power in water will not be valid at energies of a few keV and below. This is based on the Møller free electron cross section and a mean ionization potential, I, which is an average over all the atomic electrons. A simple modification to the theoretical evaluation of dT/dx has been devised which is also consistent with the treatment of Auger electron production.

5.3.1 Modified Theoretical Evaluation

Storm and Israel (1970) give the atomic energy levels of the oxygen atom as follows; the K-shell energy is 533 eV, then the 3 L-shell energies are 24, 9 and 9 eV respectively. The hydrogen ground-state energy level is 13.6 eV. If it can be assumed that these levels are not drastically altered when the atoms combine to form a water molecule, then it is only the K-shell electrons of the oxygen atom which invalidate the use of the stopping-power formula down to 100 eV. These are only 2 out of 10 electrons per water molecule. It has been assumed, therefore, that the K-shell electrons play no part in the energy loss process below about 1 keV. Consequently, at low energies there are only 8 electrons per molecule and a new value of the

mean ionization potential, I_{eff}, must be calculated corresponding to these 8 loosely-bound electrons. Then the stopping power is calculated from the usual-theoretical expression, as given in the Rohrlich-Carlson formulation by equ. 4.18, with I replaced by I_{eff} and the electron density multiplied by the factor 0.8.

5.3.2 Calculation of I_{eff}.

The mean ionization potential, I, in stopping power theory is given by

$$\log I = \Sigma_i f_i \log h\nu_i \qquad .....(5.6)$$

where f_i is the oscillator strength corresponding to energy level $h\nu_i$. Values of I calculated from this expression do not, in general, agree with the I-values that are determined from analyses of the results of stopping power measurements. Sternheimer (1952, 1956) required values for the atomic frequencies, ν_i, which were consistent with the empirically determined I values for the evaluation of his density effect theory. He defined a correction factor, A_I, from

$$\log I = \Sigma_i f_i \log (A_I h\nu_i) \qquad .....(5.7)$$

such that the adjusted frequencies, $\nu_i = A_I \nu_i$, when used in equ. 5.6, yielded the same I-values as those used in evaluating dT/dx.

This procedure has been followed here, except that the factor A_I has not been applied to the K-oxygen electron energy level. This seems physically reasonable as it corresponds to the assumption that the energy levels of the more loosely-bound outer electrons should

Figure 5.2 ELECTRON STOPPING POWER IN WATER AT LOW ENERGIES.

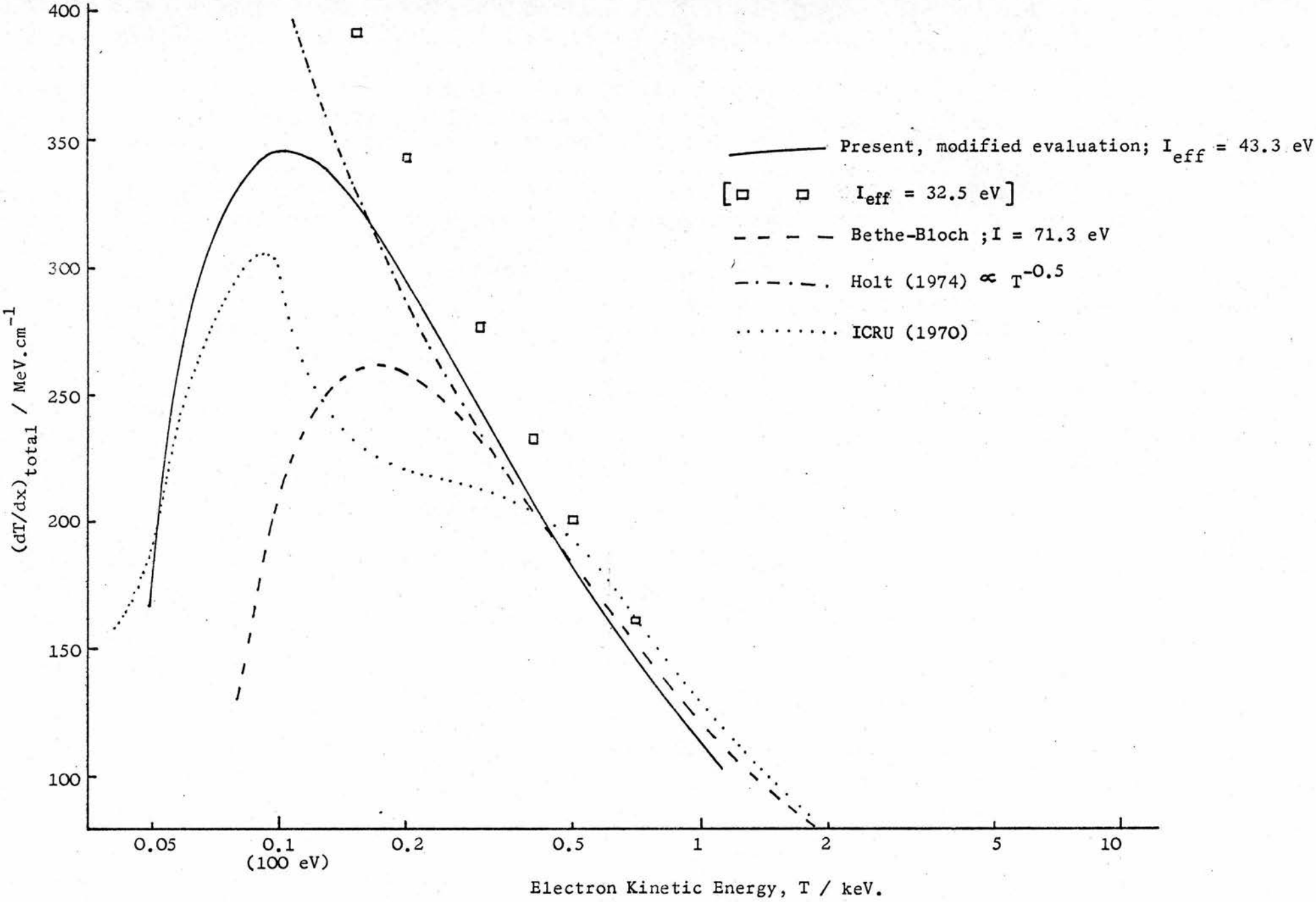

be adjusted by proportionately more than the energies of the tightly bound K-shell electrons.

The I-values for hydrogen, 18.2 eV, and oxygen, 101 eV, have been taken from Turner et al. (1970) to be consistent with the I-value used for water. For the oxygen atom, therefore,

$$\log 101 = \frac{1}{4} \log 533 + \frac{1}{4} \log(24\ A_I) + \frac{1}{2} \log(9\ A_I) \quad \text{from equ. 5.7}$$

giving $A_I = 4.65$.

Thus
$$\log I_{eff} = \frac{1}{3} \log (24\ A_I) + \frac{2}{3} \log (9\ A_I) \qquad .....(5.8)$$

yielding I_{eff} (oxygen) = 57.8 eV, with I_{eff} (hydrogen) simply equal to 18.2 eV. The f_i have been set equal to the corresponding occupation numbers divided by Z following Sternheimer. Thus in equ. 5.8 the effective value of Z becomes 6 rather than 8, giving f_i equal to 2/6.

It remains to calculate the I_{eff} for water from the values for hydrogen and oxygen. Using Bragg's additivity rule,

$$\log \langle I \rangle = \left\langle \frac{Z}{A} \right\rangle^{-1} \frac{1}{\rho} \sum_j \frac{Z_j}{A_j} \rho_j \log I_j \qquad .....(5.9)$$

giving I_{eff}(water) = 43.3 eV
(32.5 eV if A_I applied to all shells)

5.3.3 Comparison with other values

Stopping power evaluated using I_{eff} and the 0.8 factor are compared to values from other 'prescriptions' in figure 5.2. It can be seen that the dT/dx based on

TABLE 5.1 ELECTRON STOPPING POWERS IN WATER

T(eV)	dT/dx (MeV.cm^{-1}) (I_{eff}= 43.3 eV)*	dT/dx (MeV.cm^{-1}) (I = 71.3 eV)$^{+}$
1000	115	122
700	147	152
500	182	183
400	208	205
300	243	231
200	294	258
150	325	261
120	341	245
100	346	214
70	316	84
50	207	-176 (!)

*Not expected to be valid below about 100 eV.

$^{+}$Valid down to about 500 eV.

I_{eff} = 43.3 eV deviate substantially from the unmodified Bethe-Bloch dT/dx below 400 eV, following fairly closely Holt's figures down to about 150 eV. These latter values were derived from target theory as applied to measurements of the inactivation of ribonuclease by various radiations (Marshall et al., 1970). The ICRU (1970) values were derived from experimentally determined ranges in air and collodion foils. In the absence of a definitive set of values for dT/dx in the energy range 1 keV to 100 eV, it was considered that the use of the Bethe-Bloch theory with I = 71.3 eV above 500 eV and I_{eff} = 43.3 eV between 500 eV and 100 eV provided a plausible compromise. Values of dT/dx evaluated according to these prescriptions are given in table 5.1.

It should be noted that the assumption that only 8 out of the 10 electrons per molecule are effective in the slowing-down process for electrons below 500 eV implies that the Møller cross section for δ-ray production by these low-energy electrons must also be multiplied by 0.8.

5.4 COMPUTATIONAL DETAILS*

5.4.1 Energy Bands

The lowest energy of interest is 100 eV. It is convenient, therefore, to fix the lowest energy level at exactly 100 eV. Logarithmic intervals are the obvious choice in this type of calculation (Burch, 1957a; Holt, 1974). This implies the use of a constant ratio, r, to calculate the energies in successive bands. Thus if the lowest energy band begins at 100 eV, then the next band begins at 100.r eV and so on. A band width parameter, B_W, can be defined such that B_W bands cover a factor 2 in energy. The band width, B_W, and the ratio r are related by

$$r = \exp(\log_e 2/B_W) \qquad .....(5.10)$$

The present calculation was organized so that B_W could be varied. In Burch's scheme it was effectively fixed at a value of 2, though he set the first level above 100 eV at 150 eV, whereas in this scheme it would be $100.2^{1/2} = 141$ eV. It should be added that Burch did not have the flexibility afforded by a computer at his disposal. Calculations 'by hand' become prohibitively complicated for a B_W greater than 2.

The maximum energy with which the low-energy spectrum program has to deal fixes the highest energy band, which is designated as the first band, i = 1. Thus for maximum energy T_{max}, the number of the band starting at 100 eV, l_{100}, is given by

$$l_{100} = 2 + Ip(\log(T_{max}/0.0001)/\log r) \qquad .....(5.11)$$

---

*I am indebted to P.D. Holt (priv. commun.), who lent me a copy of his computer program based on Burch's scheme, for some of the basic ideas in this section.

Figure 5.3 ENERGY BANDS IN THE LOW-ENERGY PROGRAM

$B_w = 2$

$\underline{l}$	Electron K. E. (MeV)			Burch (1957a) : ΔT intervals
1	1.1585	-	0.8192	1.2288 - 0.8192
2	0.8192	-	0.5793	0.8192 - 0.6144
3	0.5793	-	0.4096	0.6144 - 0.4096
..	.....	.	.....	....
..	.....	.	.....	....
33	0.000200	-	0.000141	0.000200 - 0.000150
34	0.000141	-	0.000100	0.000150 - 0.000100
35 = 1_{100}				

$B_w = 10$

$\underline{l}$	Electron K. E. (MeV)		
1	1.00844	-	0.94091
2	0.94091	-	0.87790
3	0.87790	-	0.81911
...	.....	.	.....
...	.....	.	.....
131	0.000123	-	0.000115
132	0.000115	-	0.000107
133	0.000107	-	0.000100
134 = 1_{100}			

where T_{max} is in MeV. Note that T_{max} will usually be equal to the Monte Carlo cutoff T_c.

The band containing energy T is given by -

$$l = l_{100} - 1 - Ip(\log(T/0.0001)/\log r) \quad .....(5.12)$$

where the energy at the top of band l, T_l, is

$$T_l = 0.0001\ r^{(l_{100} - l)} \quad .....(5.13)$$

and this band extends from T_l to $T_{l+1} = T_l/r$. An example of the energy band structure is given in figure 5.3 for B_w's of 2 and 10, for the case where the maximum energy is, say, 1 MeV. Also shown alongside the $B_w = 2$ energies are the intervals that Burch employed. It can be seen that an energy of 1.01 MeV would belong in the next higher band for $B_w = 10$ but not for $B_w = 2$. Similarly, an energy of 0.94 would go in the next lower band in one case but not in the other.

The value of the electron flux calculated for each band is to be interpreted as an average over that band and the effective electron energy in each band for the purpose of calculating dT/dx etc. is taken to be the geometric mean energy in the band, $\bar{T}_l$ which is equal to $T_l/r^{1/2}$.

5.4.2 Number of Electrons in Each Band, N_l

Starting from the highest energy, the number of electrons slowing down through successive bands, N_l, must be determined. In a given band there will be three separate contributions to N_l:

i) Primary electrons with initial energies within the band, $N_l^{p'}$.

ii) δ-rays starting in this band produced by electrons in higher energy bands, ΣN_l^{δ}. (These start at the top of the band.)

iii) The electrons slowing down 'continuously' from the band above, N_{l-1}^{tot}. (This comprises the total number of electrons in band l-1 as no jumps are allowed in this scheme.)

The primary electrons in i) may have a range of energies within the band. It was not found to be a sufficiently good approximation to assume that they all enter at the top of the band. Consequently, for a primary of energy T_p between T_l and T_{l+1}, the fraction $(T_p - T_{l+1})/(T_l - T_{l+1})$ is added onto the aggregate total $N_l^{p'}$. Another variable, N_l^p, is needed simply to add up the number of these primaries in order that they can all be included in the total number that slow down into the next band, N_l^{tot}.

The Møller cross section is used to compute the number and energy distribution of secondaries produced by the electrons slowing-down in band l. Rauth and Simpson (1964) have shown that the Møller distribution is satisfactory for losses above about 100 eV from their measurements of electron energy loss through extremely thin foils. The Møller cross section, when multiplied by $N_A \rho \langle Z/A \rangle$ and integrated between appropriate limits, gives the number of secondary electrons produced per unit pathlength of the primary. This can be converted to the number per unit energy dissipation by dividing by dT/dx.

The energy dissipation, E_l^d, by the N_l electrons in band l, is given by

$$E_l^d = (N_{l-1}^{tot} + \Sigma N_l^{\delta})(T_l - T_{l+1}) + E_l^p \qquad .....(5.14)$$

where E_l^p is the contribution from the primary electrons that start in the band . This has to be evaluated as an aggregate of the energies $(T_p - T_{l+1})$ for each primary, similar to $N_l^{p'}$ above. The number of δ's starting at the top of band m as a result of dissipation by the N_l electrons in band l is then given to a good approximation by

$$N_{m,l}^{\delta} = \left[\rho N_A \langle Z/A \rangle \frac{d\sigma}{d\varepsilon}. (\varepsilon_m - \varepsilon_{m+1})/(dT/dx)\right]. E_l^d \qquad .....(5.15)$$

where $\varepsilon_m = T_m/(T_l/r^{1/2})$; T_m is the δ-ray energy and $\frac{d\sigma}{d\varepsilon}$ is the Moller cross section per electron per unit fractional energy transfer, as given by equation 4.3. For each band l, δ-rays are produced in all bands from $m = l+B_w$ to $m = l_{100}$. The band $l+B_w$ has an energy T_m equal to $T_l/2$, the maximum energy possible for a δ-ray produced by a primary of energy T_l.

Burch drew up a table of values of the quantity in the square brackets in equ. 5.15 for all bands m for each band l, which included the number of electrons in a band that jumped over the next band due to 'discontinuous' bremsstrahlung or δ-ray losses. For reasons discussed in section 5.1, bremsstrahlung has not been included in the present computation of electron flux at low energies.

The calculation begins at the highest energy band for which there are any primary electrons. For each successive band, the number of electrons slowing down in the band, N_l, is determined as described above:

$$N_l = N_l^{p'} + \Sigma N_l^{\delta} + N_{l-1}^{tot}$$

The total energy dissipation by these electrons in the l th band is calculated, enabling $N_{m,l}^{\delta}$ to be evaluated for each band. The $N_{m,l}^{\delta}$'s are added to the aggregate number $\Sigma_l N_{m,l}^{\delta}$ resulting from all the higher energy bands. The total number of electrons slowing down into the next band, N_l^{tot}, given by

$$N_l^{tot} = N_l^{p} + \Sigma N_l^{\delta} + N_{l-1}^{tot}$$

is then added to the $(N_{l+1}^{p'} + \Sigma N_{l+1}^{\delta})$ electrons starting in band l+1 and the process is repeated. The final band of interest is l_{100}-1 for which the lower energy level is 100 eV.

5.4.3 The Electron Flux

The electron flux averaged over band l, F_l, is given by

$$F_l = N_l/(dT/dx)_{total}$$

It was required to know how large a value of B_w was necessary to yield sufficiently accurate values of F_l, and to check that increasing B_w resulted in flux values that converged to a limit. This was most easily done by comparing the total 'local' energy dissipated by the spectrum, F_l, with the total energy input, in the same way as Burch had checked the internal consistency of his calculations.

The energy dissipated by the flux of all generations of electrons above 100 eV in energy in 'local' transfers of less than 100 eV, $Q_T T$ or D_{100}, is given by

$$D_{100} = \sum_{l=1}^{l=l_{100}-1} F_l . (dT/dx)_{100} . \Delta T + \left[N^{tot}_{l_{100}-1} + \Sigma N^{\delta}_{l_{100}} \right] . T_{l_{100}}$$

where

$T = T_l - T_{l+1}$; $(dT/dx)_{100}$ is evaluated at $\bar{T}_l$; $T_{l_{100}} = 100$ eV.

The second term is the energy dissipated by the 100 eV track ends. These track ends comprise the total number of electrons that enter at the top of the band starting at 100 eV, band l_{100}, i.e. the electrons slowing down from the previous band, $N^{tot}_{l_{100}-1}$, and the δ-rays, $\Sigma N^{\delta}_{l_{100}}$. Note that this track end contribution to the local energy dissipation corresponds exactly to Burch's $Q_T \Delta T$ for his lowest energy interval, 0 - 100 eV.

The program was executed for various monoenergetic electron sources and for different values of B_w. The flux was normalized by dividing by the input energy. It was found that increasing B_w beyond about 10 made very little difference to the results, as is shown by the following figures for T_o = 2 MeV:

B_w	Total Dissipation per MeV input energy	Number of Track Ends
5	0.9947	944.8
10	0.9968	927.0
20	0.9980	919.5

For B_w = 10, the computation is internally consistent to within 0.3% which was considered good enough.

Figure 5.4 DEPTH-INDEPENDENT ELECTRON FLUX CALCULATIONS.

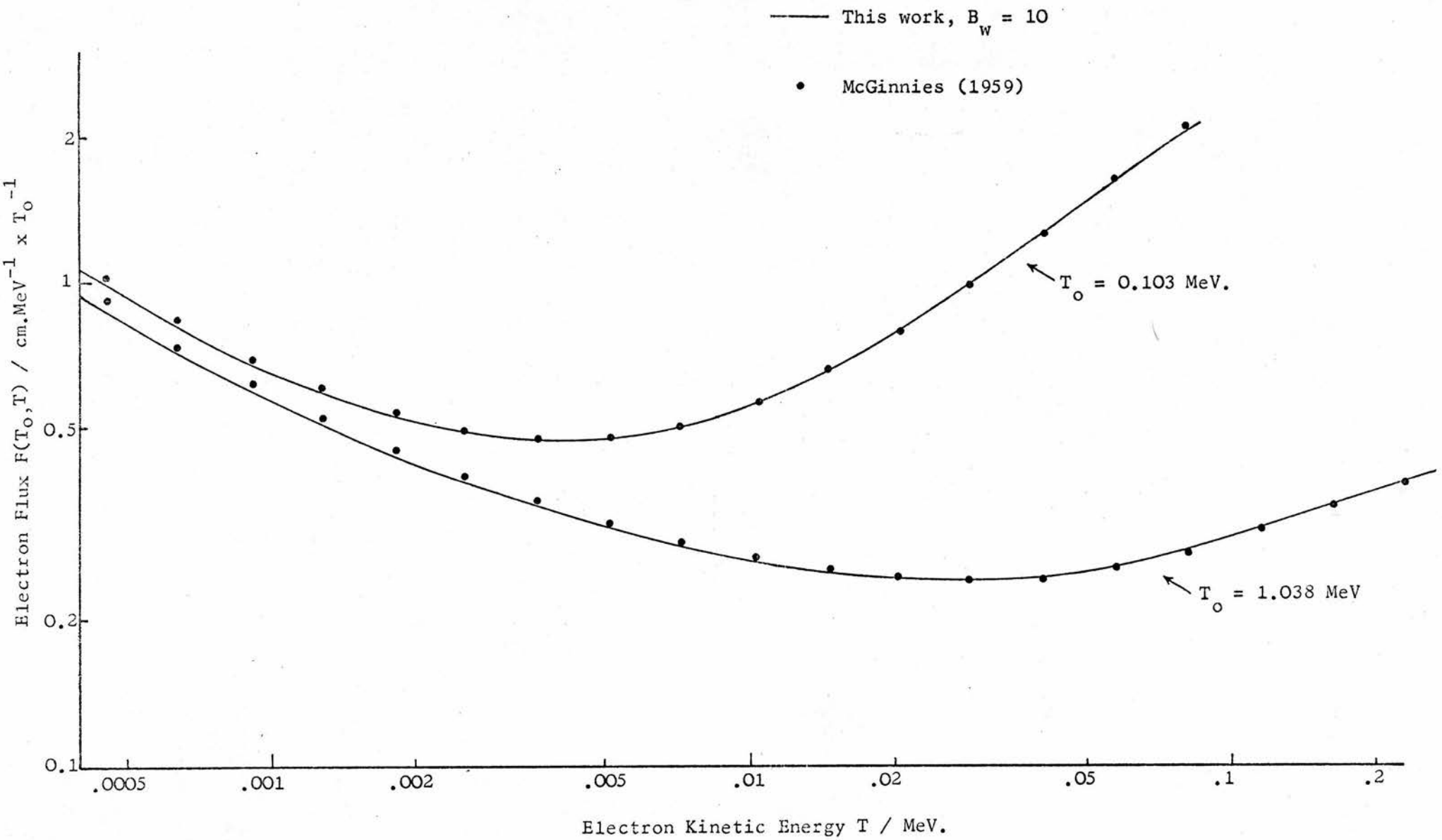

If we write the first term in equ. 5.16 in terms of the number of electrons in band l, N_l, it becomes $\sum N_l \cdot (dT/dx)_{100}/(dT/dx)_{total} \cdot \Delta T$, which is the expression that Burch used in calculating $Q_T \Delta T$. As the Møller cross section, $d\sigma/d\varepsilon$, is used to calculate the number of δ-rays produced, to be consistent the following relation must hold:

$$(dT/dx)_{total} - (dT/dx)_{100} = \int_{.0001/T}^{1/2} \frac{d\sigma}{d\varepsilon} \, d\varepsilon \quad .....(5.17)$$

This is in fact ensured by the use of the Rohrlich-Carlson expression, given by equ. 4.18, for the total and restricted stopping powers as its derivation involved the Møller cross section (Rohrlich and Carlson, 1954). It is not clear that the values Burch used for the ratio of local to total stopping were consistent with equ. 5.17.

Values of the electron flux for monoenergetic electron sources in water down to an energy of 450 eV have been tabulated by McGinnies (1959) and it was considered worthwhile worthwhile to carry out computations that could be directly compared to her results as a further check on the validity of the method described here. McGinnies' values were given in units of $g.cm^{-2}(mc^2)^{-1}$. This was converted to the units in figure 5.4 by multiplying by the factor $MeV(mc^2.T_o)$. McGinnies used I = 74.1 eV and did not include the density effect. There was no modification to the energy loss, as given by the Møller cross section, at low energies. This is equivalent to using the unmodified stopping power down to the lowest energy in the present scheme. Consequently, all these features were temporarily written into the program in order to

calculate flux values that could be directly compared to McGinnies' results. The agreement obtained, as shown in figure 5.4 was excellent.

From this comparison, it was concluded that the computation of the depth-independent electron flux, for $B_w = 10$, produced results equivalent to those that would have been calculated by the use of the more involved Spencer-Fano theory. As the latter treatment allowed for discontinuous energy losses, it can be further concluded that the use of a 2-group model for the energy loss would have made very little difference to the results, except for the 'peak' at the source energy.

5.4.4 Auger Electrons and Low-Energy dT/dx

Nothing has been said so far about the inclusion of Auger electrons in the low-energy program. It is convenient to fix the energy T_{aug} at the lowest T_i energy above 500 eV. For $B_w = 10$, this is 528 eV. This value is also taken as the energy below which the stopping power is evaluated using $I_{eff} = 43.3$ eV as discussed in section 5.3. To take into account Auger electron production, and the use of the modified stopping power at low energies, some minor changes must be made to the calculation of the number of electrons in each band detailed in section 5.4.2:

Case 1 $\bar{T}_l > T_{aug}$ and $T_m > T_{aug}$

One fifth of the energy transfers of size T_m resulting from the energy dissipation by electrons in the l th band, will produce Auger electrons. Therefore, 0.2 $N^{\delta}_{m,l}$ is added to the number of δ's starting with energy T_{aug}. One fifth of the $N^{\delta}_{m,l}$'s now have energy $T = T_m - T_{aug}$ and thus 0.2 $N^{\delta}_{m,l}$ is added to the number of electrons in category i) in section 5.4.2 in the band containing the energy T_δ (These T_δ electrons must go into this category as their energy no longer exactly corresponds to the energy at the top of a band). Finally, 0.8 $N^{\delta}_{m,l}$ is added to the number of δ's starting in band m, instead of simply $N^{\delta}_{m,l}$ when Auger electrons are not included.

Figure 5.5 THE EFFECT OF AUGER ELECTRON PRODUCTION ON THE SLOWING-DOWN SPECTRUM.

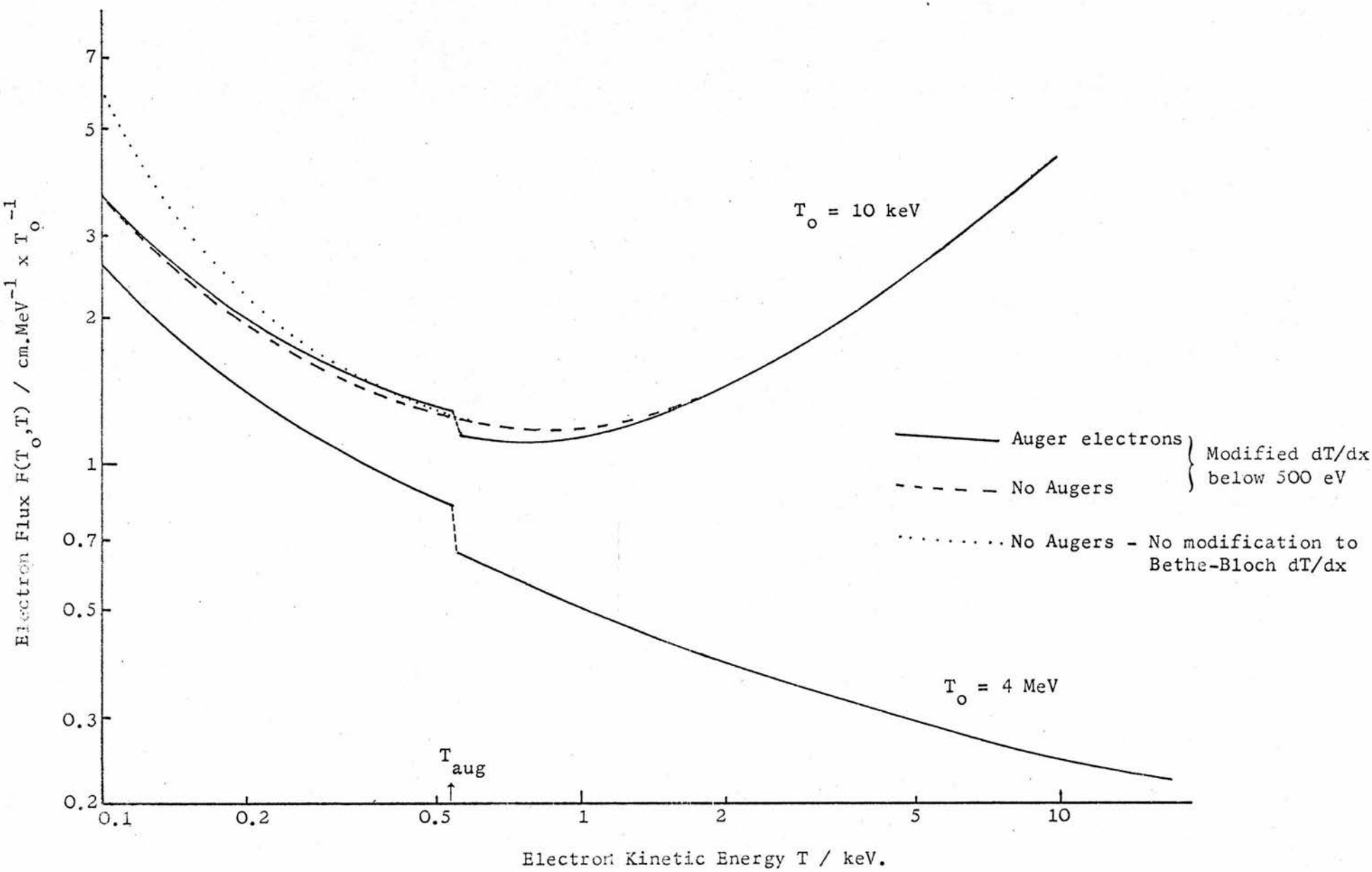

Case 2 $\bar{T}_l > T_{aug}$ and $T \ll T_{aug}$

Augers' are not possible as the energy transfer, T_m, is not large enough to eject a K-oxygen electron. No modifications are made to the procedure; $N^{\delta}_{m,l}$ added to the δ's in band m.

Case 3 $\bar{T}_l \ll T_{aug}$

K-oxygen electrons do not take part in the slowing-down process. Only 8 out of the 10 electrons per molecule are to be included in the Møller cross section for δ-ray production. Thus only 0.8 $N^{\delta}_{m,l}$ is added to the number of δ's starting in band m.

The effect of these modifications on the spectrum at low energies can be seen in figure 5.5. It seems as if the flux at 100 eV is hardly affected by the inclusion of Auger electrons, despite the 'jump' that they cause in the flux at T_{aug}. Such a sharp discontinuity cannot be expected to occur in reality, but the order of magnitude of the increase around 500 eV should be correct. Much the largest uncertainty in the flux calculation at low energies is due to inadequate knowledge of the stopping power. The difference between the curves calculated with and without the stopping power modification indicate the sort of absolute accuracy that can be estimated for the flux below about 1 keV.

The internal consistency of the flux calculation was not affected by the Auger and dT/dx modifications. Note that $(dT/dx)_{100}$ must be evaluated in the same way as $(dT/dx)_{total}$ for $T<T_{aug}$. The version of the low-energy program that is amalgamated with the Monte Carlo electron

program, as described in the following section, included Auger electron production and the evaluation of the stopping power below T_{aug} using I_{eff}. The value of B_w is set permanently equal to 10.

5.5 AMALGAMATION WITH THE ELECTRON MONTE CARLO PROGRAM

The low-energy spectrum computation described in the previous sections of this chapter was developed specifically to be combined with the electron Monte Carlo (MC) program. Thus the low-energy program will now have a distribution of source energies from T_c, the energy at which the electron histories are terminated, down to the lowest energy of interest, which is 100 eV. The calculation of the number of electrons in successive bands, giving the electron flux, is no different to that for the sample results for monoenergetic sources already given. This section deals with how the source energies are derived from the electron histories and the way in which the programs are fitted together. Some preliminary results are given which demonstrate that the complete spectrum computation for any geometry from the input energy T_o in the Monte Carlo simulation down to 100 eV is functioning satisfactorily.

5.5.1 Input of electrons from MC Histories

These fall into five categories. For the geometry of interest, for which $Z_l \leq Z \leq Z_h$, they are as follows:

(a) Primary electrons that have dropped below T_c.

(b) δ-rays which were included in the simulation and have dropped below T_c.

(c) δ-rays of energy greater than $\Delta(T)$ and therefore selected as catastrophic losses.

Electrons from these 3 sources belong in category i) described in section 5.4.2 as they do not have energies exactly equal to some T_i. The reason for distinguishing

between the electrons in (a) and (b) is that the electron flux due to the primaries only is required for one of the applications of the results, to be described in due course.

(d) Auger electrons resulting from catastrophic δ-ray production.

(e) δ-rays of energy between Δ(T) and 100 eV which have been effectively included in the energy dissipated in c-s-d-a pathlength steps.

Electrons in (d) and (e) belong in category ii) in 5.4.2. as their energies are organized to be equal to T_l for some value of l. The δ-rays in (e), none of which has been individually selected in the Monte Carlo simulation, require special consideration.

5.5.1.1 δ-rays from the c-s-d-a steps

The energy dissipated in that section of a pathlength step which lies within the 'Z-slice' for which the spectrum is required can be denoted by W^{Δ}. Recalling the notation used in section 4.6.4,

$$W^{\Delta} = (T_a - T_b)\frac{s}{s_f} = T_i - T_b \qquad .....(5.18)$$

The fraction of W^{Δ} corresponding to energy transfers between $\Delta(T_a)$ and 100 eV, W_{100}, is then given by

$$W^{\Delta}_{100} = W^{\Delta}(1 - L_{100}/L_{\Delta}) \qquad .....(5.19)$$

with the ratio of restricted stopping powers evaluated at $T = T_a$.

This energy W^{Δ}_{100} has to be partitioned according to the Møller distribution into numbers of δ-rays to go into the bands covering the energy range from $\Delta(T_a)$ to 100 eV.

It was shown in section 4.4.1.2 that the Møller distribution could be adequately approximated by $1/q^2$, for energy transfer q, except for q close to T/2. Therefore, for a given total energy W^{Δ}_{100}, the number of δ's entering at the top of band m will be proportional to $(T_m - T_{m+1})/T_m^2$. The proportionality constant, K, will be given by

$$W^{\Delta}_{100} = K\int_{0.0001}^{\Delta(T_a)} q.\frac{1}{q}2.dq \qquad .....(5.19)$$

yielding

$$K = \frac{W^{\Delta}_{100}}{\log_e[\Delta(T_a)/0.0001]} \qquad .....(5.20)$$

Consider the calculation of the number of δ's per band, N_m, for a given c-s-d-a step for which s_f and hence W^{Δ}_{100} are non-zero. The first band, m', will be that corresponding to the highest T_m less than $\Delta(T_a)$. Into this band must go $K.(T_{m'} - T_{m'+1})/T_{m'}^2$ δ-rays. Similarly for the next band, m = m'+1 and so on, up to m = l_{100}. There are between 65 and 80 bands between m' and l_{100}, depending on T_o and T_c, for B_w = 10. This would add up to an appreciable amount of computing time per execution of a c-s-d-a step. However, the cutoff $\Delta(T_a)$ cannot be less than $\Delta(T_c)$, the minimum possible value of which is 9.80 keV for T_c = 0.1 MeV. Similarly, $\Delta(T_a)$ cannot be greater than $\Delta(T_o)$, the maximum value of which is 30 keV for T_o = 40 MeV. (see, for instance, table 4.3). Consequently, all 65 bands between 9.80 keV and 100 eV are involved in receiving δ-rays whatever T_a is. There is no need to 'fill up' these bands with δ's from each separate c-s-d-a step. Provided that the K's from each c-s-d-a step are all added up to

give the aggregate value ΣK, then the total number of δ's to be added to these bands will be given by

$$\sum_{csda} N^{\delta}_{m} = \Sigma K.[T_m - T_{m+1}]/T_m^2 = \Sigma K.[1 - 1/r]/T_m^2 \quad .....(5.21)$$

The only bands for which N^{δ}_{m} need be evaluated in the c-s-d-a step spectrum calculations are those in the energy range between $\Delta(T_a)$ and $\Delta(T_c)$, at most 15 bands and in practice not more than 10 for the particular values of T_o and T_c chosen. Naturally, the values of N^{δ}_{m} and $\sum_{cdsa} N^{\delta}_{m}$ must be modified to include the production of Auger electrons but this has already been dealt with in section 5.4.4. Note that the case $\bar{T}_1 \leq T_{aug}$ does not arise as the electrons producing the δ-rays all have energies greater than T_c which is never less than 0.1 MeV.

5.5.2 Practical Details

The code for the computation of the flux below T_c, which essentially contains the operations described in section 5.4, has been written as the routine LOWENCAL. The routine DELSORT fills up the bands with c-s-d-a step δ's for which $\Delta(T_c) < T_m < \Delta(T_a)$. It is therefore executed within SPECTOT, which totals up the pathlength sections in different energy intervals from these c-s-d-a steps for a particular geometry (see section 4.6.4). The sources of electrons, (a)-(e), are added to the total number already in the appropriate categories as they are generated from the electron histories. The routine LOWENCAL is then executed after all the histories have been terminated. The first operation in LOWENCAL is the filling up of the final 65 bands with the $\sum_{csda} N^{\delta}_{m}$ electrons as explained above.

Figure 5.6 SCHEMATIC REPRESENTATION OF THE AMALGAMATION OF THE MONTE CARLO AND LOW-ENERGY ELECTRON COMPUTATIONS.

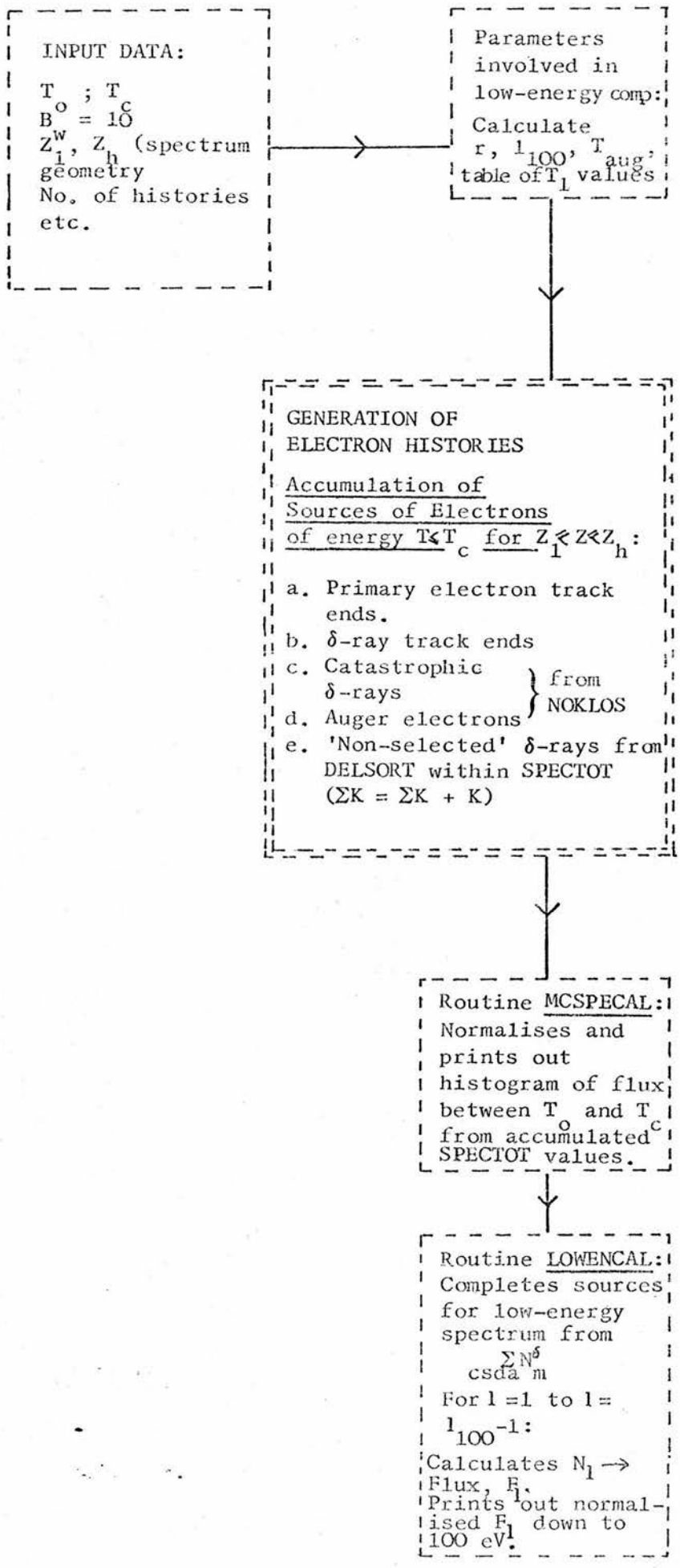

This completes the input of electron sources from the electron histories. The low-energy spectrum computation from $l=1$ to $l=l_{100}-1$ is then carried out.

Figure 5.6 illustrates how the programs are combined together. Only those operations relevant to the amalgamation are indicated. The addition of the spectrum computation below T_c increases the length of the complete program by 150 statements or so. The increase in total execution time per electron history due to the extension of the spectrum from T_c down to 100 eV is negligible.

The exact value of T_c must now be chosen with some care. The energy at the top of the first band will be such that T_c lies in this band as T_c will be the maximum energy of the electron sources. Thus, if T_c is to be about 1 MeV, then it should be set equal to a value just less than 1.00844 MeV as this is one of the T_l values for $B_w = 10$ (see fig. 5.3). In this way, it is ensured that the flux values, F_l, in the energy bands take over exactly from the energy T_c at which the Monte Carlo histogram terminates.

The spectrum F_l must be normalized to the same units as the Monte Carlo spectrum. To convert F_l to 'per MeV input energy' it is necessary to divide by $H.T_o$, where H is the number of electron histories.

5.5.3 Preliminary Results

The most direct test of the validity of the extension of the spectrum below T_c was provided by the comparisons of the results shown in figures 5.7 and 5.8. In both cases, the Monte Carlo program was run for an infinite spectrum

Figure 5.7 THE 'JOIN' AT T = T_c BETWEEN MONTE CARLO AND DEPTH-DEPENDENT FLUX SPECTRA.
(T_o = 2 MeV; Infinite Water Medium)

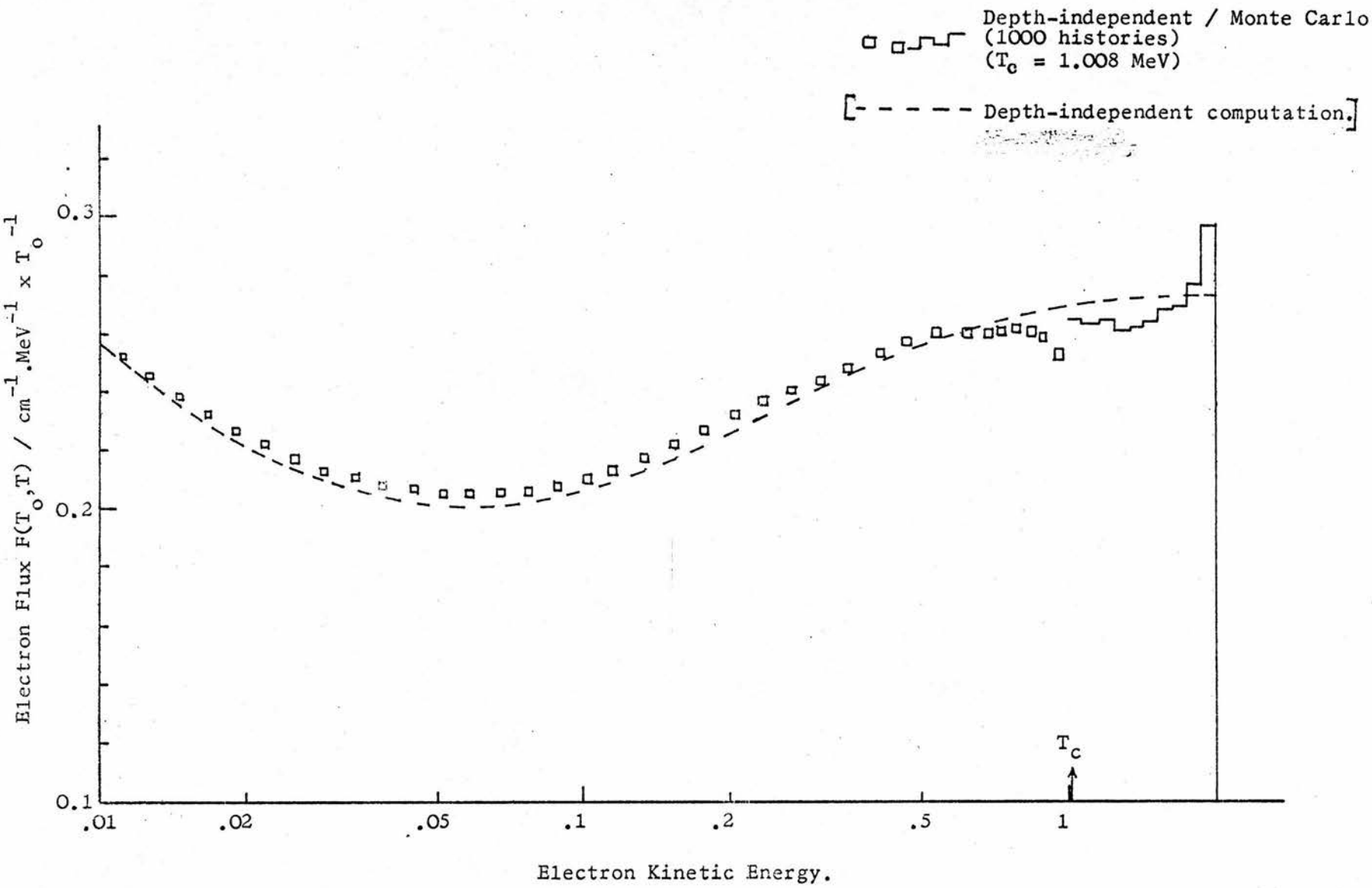

Figure 5.8 COMPARISON BETWEEN DEPTH-INDEPENDENT AND MONTE CARLO ELECTRON FLUX COMPUTATION DOWN TO 100 eV.
(Infinite Water Medium)

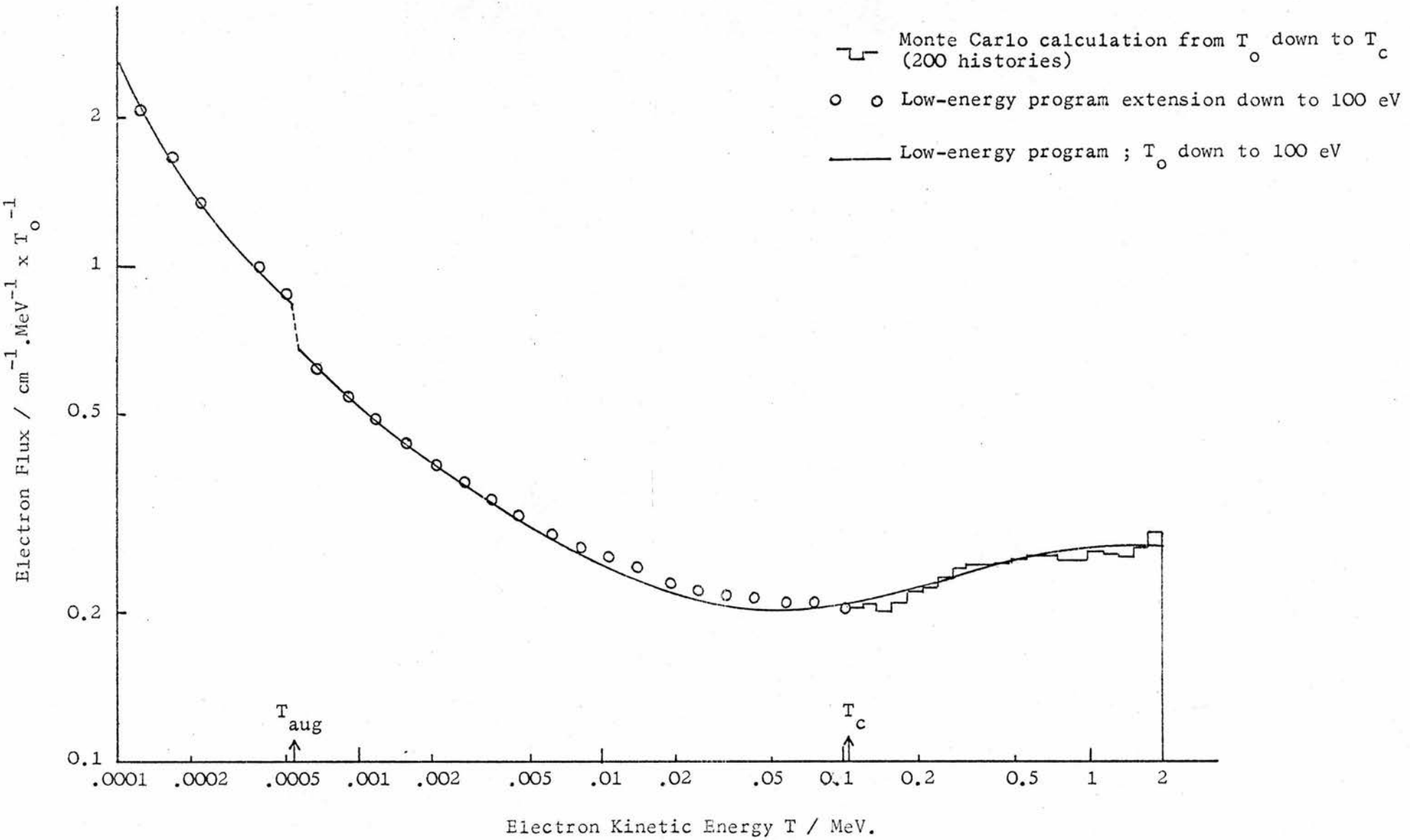

geometry, and the electron flux was compared to that calculated from the depth-independent program with the same monoenergetic source energy.

In fig. 5.7, the 'join' between the MC histogram and the F_1 values at T_c = 1.008 MeV is clearly shown. The low F_1 values close to T_c are exactly what would be expected, due to the c-s-d-a on which the calculation of F_1 is based. As T_c is here nearly equal to $T_o/2$, the number of δ's close to T_c will be very small. Consequently, there is a virtually monoenergetic input of electron sources into the first band i.e. only from categories (a) and (b) above. The discontinuity at T_c is therefore the exact counterpart of the peak at T_o in the MC histogram which is not present in the c-s-d-a spectrum at that energy. Note that the 2 spectra follow each other very closely below about 0.7 MeV.

The spectrum from the Monte Carlo histories in figure 5.8 extends down to T_c = 0.102 MeV. In this case, the source of electrons just below T_c will include some δ-rays produced by the Monte Carlo histories (category (c) above) as T_c is considerably less than $T_c/2$. Thus the input to the first few bands is no longer approximately monoenergetic, with the result that the join between the two spectra is smoother. The very good agreement with the T_c = 2 MeV depth-independent flux (the full line) right down to 100 eV was regarded as a conclusive demonstration that the combined Monte Carlo and low-energy computation of the electron flux was functioning correctly.

Figure 5.9 DEPTH-DEPENDENT ELECTRON FLUX COMPUTATION
(T_o = 20 MeV, T_c = 0.76 MeV, z/r_o = 0.40 - 0.60)

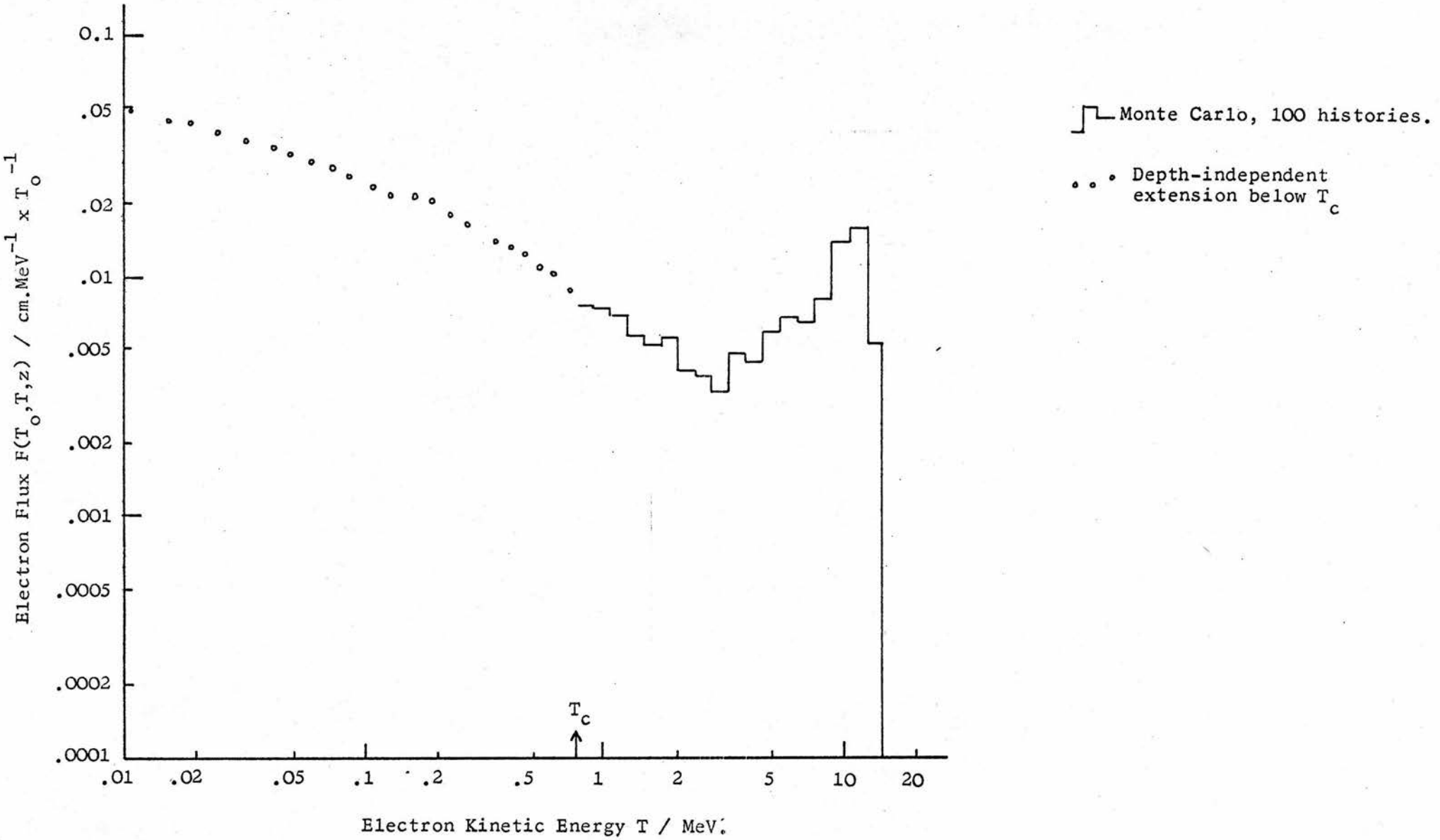

The Monte Carlo electron simulation was written in order to compute depth-dependent electron flux spectra. In fact, the comparison in figure 5.8 effectively demonstrates the redundancy of the Monte Carlo method when only the flux in an infinite medium is required. An example of the extension of the flux spectrum below T_c for the geometry 0.4 - 0.6 z/r_o is given in figure 5.9. Note that the units are the same as for the spectra in the previous figures, for which '$x T_o^{-1}$' (i.e. per MeV input energy) for an infinite medium is effectively the same as 'per MeV dissipation'. However, only a certain fraction of the total input energy, T_o = 20 MeV, will be dissipated between $z = 0.4\ r_o$ and $z = 0.6\ r_o$. Therefore the spectrum in figure 5.9 is not normalized to the same total energy dissipation as the 2 MeV spectra.

Extensive results of the electron flux computations down to 100 eV for both electron and photon beams are given in chapters 7 and 8. The chapter immediately following deals with the steps involved in combining the photon Monte Carlo simulation (see chapter 3) with the amalgamated electron program described here.

CHAPTER 6

THE COMPLETE PHOTON-ELECTRON CASCADE SIMULATION

6.1 INTRODUCTION

The final stage in the development of the computer calculations is the combination of the photon and electron transport simulations into one 'cascade' program. Thus electrons set in motion by the primary photon histories serve as the input data to the electron Monte Carlo simulation which may result in bremsstrahlung photons to be followed in the photon MC simulation, leading to more electrons and so on. The combined procedure is required primarily to deal with the transport of electrons produced by primary photon beams, and the transport of bremsstrahlung photons produced by primary electron beams. Thus the processes dealt with cannot strictly be called cascades. The initial energies are not high enough. Nevertheless, the name 'cascade simulation' is used for convenience.

The extension of the flux spectra produced by the Monte Carlo electron program from T_c down to 100 eV has been dealt with in the previous chapter. In this chapter, the way in which the photon MC simulation is combined with this electron program is described. The only extra approximations involved concern the treatment of the transport and energy loss of positrons.

The considerable length and complexity of the final program makes it essential to carry out extensive checks on the internal consistency of the calculations. These checks are described in some detail. The actual results calculated with the final version of the cascade simulation

are presented in subsequent chapters but many of the features of these computations are dealt with in this chapter. In the work reported in the literature, only Patau (1972) and Berger and Seltzer (1969) have coupled Monte Carlo photon and electron simulations together in the MeV energy range, and only the latter workers have extended the calculation of the electron flux below the Monte Carlo cutoff.

Figure 6.1 PHOTON ENERGY DISSIPATION BY POSITRONS.

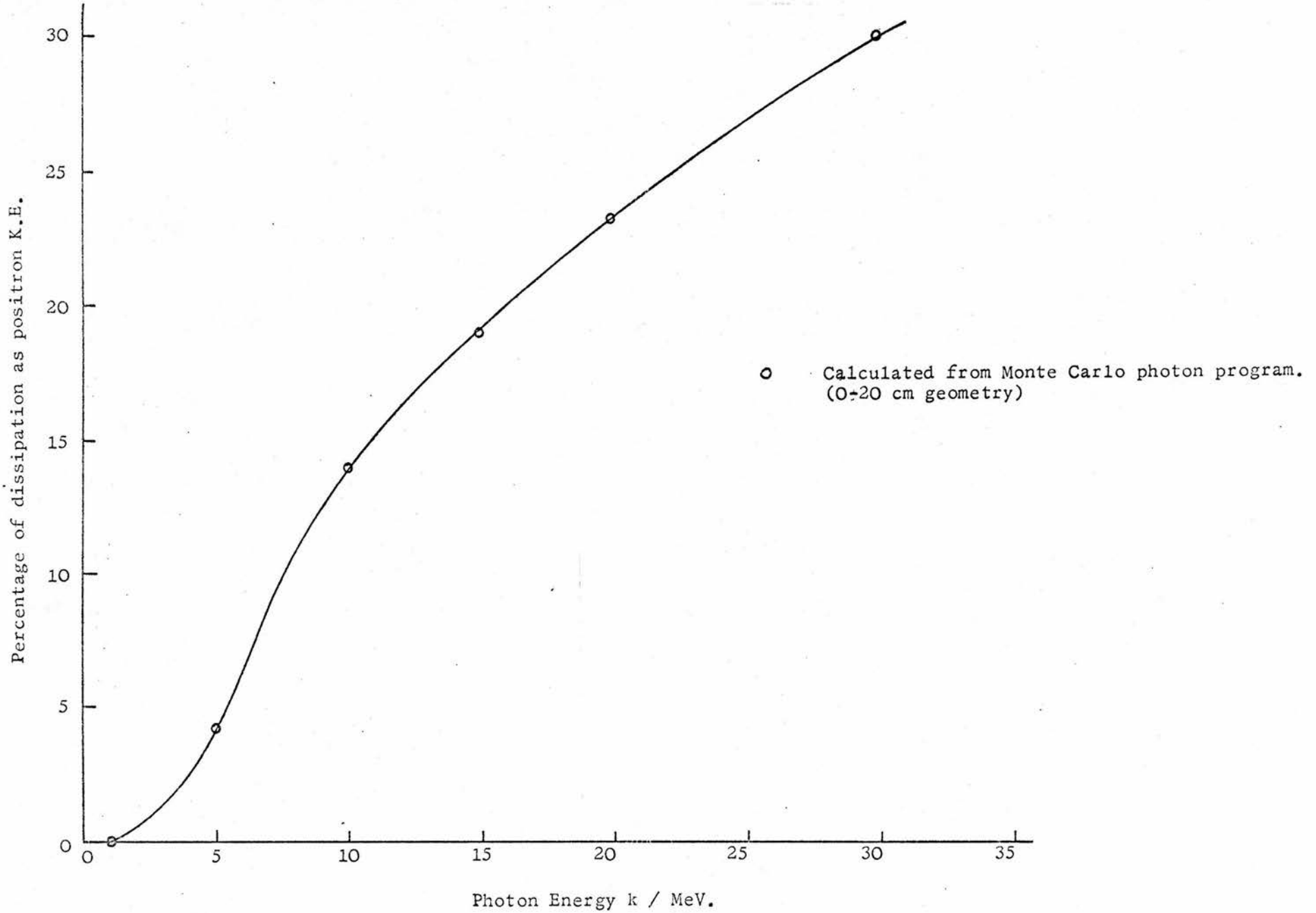

6.2 POSITRONS

6.2.1 General Considerations

The charged particles set in motion by photons through pair production consist of equal numbers of both negative and positive electrons. On average, these positrons and electrons will have the same distribution of initial direction and kinetic energy. It is necessary to consider whether the transport and slowing-down of the positrons should be treated in a different way to that for electrons. In chapters 4 and 5, it has been assumed that only electrons were involved. One obvious difference is that a positron undergoes annihilation due to electron capture, creating two photons in the process. In the case of annihilation of the positron when it has lost all its kinetic energy, the photons have energy mc^2. This effectively puts back into the medium the 2 mc^2 'removed' in creating the electron-positron pair in the first place.

The number of positrons produced as a result of pair production by bremsstrahlung photons arising from the slowing-down of primary electrons is clearly going to be a very small contribution to the total 'electron' flux. However, for high-energy primary photons this is not the case. The percentage of the total charged particle K.E. due to positrons for photon absorption in 20 cm of water (a realistic geometry for dosimetry purposes) is shown in figure 6.1. These figures were calculated using the photon Monte Carlo program. Consider a 35 MV betatron X-ray beam. If it is assumed that the average photon energy is 15 MeV, then approximately 19% of the energy dissipation will be due to positrons. For a 20 MV beam, this would be about 11%.

Table 6.1 COMPARISON OF POSITRON AND ELECTRON ENERGY LOSS AND RANGE (Berger and Seltzer, 1964)

Kinetic Energy (MeV)	Carbon		
	$\frac{(dT/dx)^+_{col}}{(dT/dx)^-_{col}}$	$\frac{(dT/dx)^+_{tot}}{(dT/dx)^-_{tot}}$	$\frac{r^+}{r^-}$
0.01	1.08		
0.02	1.07		
0.05	1.05		
0.1	1.03		
0.2	1.01		
0.5	0.992		
1.0	0.982		
2.0	0.978		
5.0	0.977		
10.0	0.978		
20.0	0.979	0.980	1.02
50.0	0.981	0.983	1.02

6.2.2 Energy loss and scattering

The mean ionization potential, I, is independent of the charge and mass of the charged particles and the value of δ, the density effect reduction, is also the same for positrons and electrons. The small difference in the collision stopping powers is mainly due to the fact that a positron can lose all its kinetic energy in an inelastic collision with an atomic electron, whereas an electron may only lose up to half its energy as a result of the indistinguishability principle. Rohrlich and Carlson (1954) showed that the appropriate cross-section for positron-electron interactions, the Bhabha formula, was very similar to the Møller cross section. Except for large energy transfers, these distributions reduce to the value given by their common leading term, $1/\varepsilon^2$, for fractional energy transfer ε. Thus both the collision stopping power and the distribution of energy losses are very similar for positrons and electrons. Berger and Seltzer (1964) stated that for energies above about 30 mc^2 the radiation loss for positrons should be given by the Schiff cross section, as for electrons, and that for lower energies the corrections to the theoretical formulae for positrons were not known. Their figures for positron-electron energy loss and range differences in carbon (similar to water in atomic number) are reproduced in table 6.1. It can be seen that these are negligible above 0.1 MeV, which is the minimum energy of the Monte Carlo cutoff, T_c.

Rohrlich and Carlson also looked at the differences to be expected in elastic scattering by the nuclei of the slowing-down media. They found that theory predicted slightly weaker multiple scattering of positrons than electrons. In particular, in the light elements positrons penetrated only a few per cent farther than electrons before losing the memory of their initial direction. Rohrlich and Carlson stated that there was no experimental evidence yet for a difference in range, possibly due to the fact that the small probability of positron annihilation in flight masked any differences due to the weaker multiple scattering. Berger (1963) evaluated the Goudsmit-Saunderson multiple scattering distribution using the Mott electron and positron single-scattering cross-sections. Over short pathlength sections of 1 MeV particles in aluminium, the calculations indicated very small differences. It can be noted that the Rutherford single-scattering cross section, used with the Gaussian multiple-scattering distribution in this work, does not predict any difference between positrons and electrons.

6.2.3 Particle flux spectrum

It was concluded that treating the scattering and slowing down of positrons in exactly the same way as for electrons would lead to entirely negligible errors in the spatial energy dissipation and in the flux spectrum derived from the MC histories for a primary photon or electron beam. Only primary positrons are involved, anyway, and the number and energy distribution of δ-rays produced by these positrons not be appreciably different from those of the primary pair electrons as discussed above.

The second consideration is whether or not it is necessary to distinguish between the positron and electron flux. As far as the evaluation of stopping-power ratios is concerned, the total and restricted collision stopping powers are very similar for positrons and electrons in water and air. In particular, the important density effect reduction is the same for both particles. Theoretically, no difference in $\bar{W}$, the mean energy to form an ion pair, is to be expected either. The flux spectra are also to be used to investigate the variation of $G(Fe^{3+})$ with radiation quality. Again, there are no problems here as G is assumed to be a function only of LET for which there are negligible differences, as has been emphasised. In fact, the neglect of photonuclear reactions, discussed in section 3.2.3, is considered to be a less justifiable approximation with respect to the above considerations.

6.2.4 Annihilation Radiation

It is clear that only the creation of annihilation photons necessitates any distinction between positrons and electrons in the computer programs. The identical treatment with respect to the computation of the total 'electron' flux implies that electron capture is assumed to occur only when the positron kinetic energy has fallen below 100 eV. The theory of positron annihilation (Heitler, 1954) shows that there is only a small probability of annihilation before the positron has come to rest. The two photons have energy mc^2 (0.511 MeV) and are oppositely directed, with no preferred direction.

In the cascade program, these annihilation photons are generated either at the end of a positron history, when T_+ has fallen below T_c, or by the photon MC simulation if the initial positron energy is not greater than T_c. In the latter case it is effectively assumed that the positron is annihilated at the position of creation. Thus a photon history leads directly to another two photons, which can be considered analogous to δ-ray production by electrons. Naturally, the transport of the two 0.511 MeV photons is simulated by the photon MC computation. Photons of this energy have a mean free path of 10.4 cm in water and so lead to energy deposition at an appreciable distance from their position of origin.

6.3 COMBINATION OF THE ELECTRON AND PHOTON PROGRAMS

6.3.1 Flow of the Monte Carlo Simulation

It was necessary to devise a suitable way of getting the cascade sequence to 'tick'. The problem is essentially analogous to the inclusion of δ-rays in the electron simulation, as discussed in section 4.5.2. It was shown that dealing with each primary history and all generations of δ-rays resulting from this history in turn was more elegant than executing all the primary histories, then all the secondaries and so on. In particular, very much less storage of initial δ-ray parameters was involved. The same arguments apply to the photon-electron cascade simulation.

It was found to be convenient to have two separate versions of the cascade program; one which handled primary photon beams and the other, primary electron beams. Consider the photon version, CASCFO. A primary photon history is executed. The initial parameters of all the electrons to be followed, i.e. those for which $T>T_c$, are stored. Then these electron histories are executed in turn, including any δ-rays generated. When there are no more electron histories left, the bremsstrahlung and annihilation photons generated by these electrons are followed by the photon MC procedure. These effectively second-generation photon histories may give rise to further electrons to be followed, in which case the Monte Carlo electron simulation is entered for the second time. Assuming that no further bremsstrahlung photons result, the next primary photon history can then be executed. The principle is the same for the primary electron version.

Figure 6.2 FLOW DIAGRAM OF THE PHOTON-ELECTRON CASCADE SIMULATION.
(Primary photons - CASCFO)

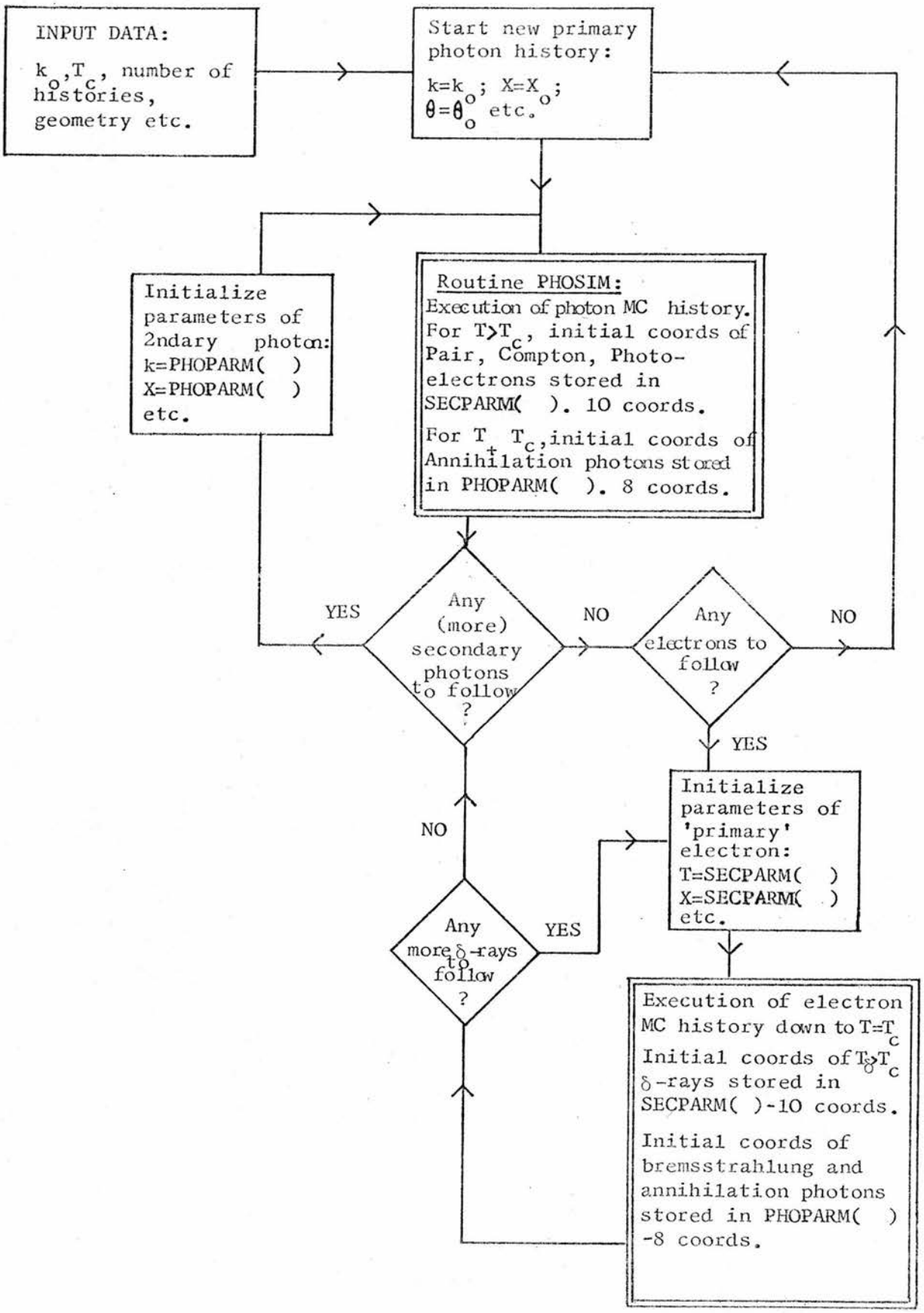

A primary electron history and any resulting δ-ray histories are executed before the bremsstrahlung photons are followed and so on.

Thus for each primary history, be it a photon or an electron, all the histories of one type are carried out, then all the histories of the other type, until there are no more left. Thus, if a photon history results in a positron with initial kinetic energy less than T_c, the histories of the two annihilation photons will be executed before any Compton, pair and photo electron histories are dealt with.

A flow diagram representing the cascade scheme for primary photons is given in figure 6.2. The routine PHOSIM consists of the instructions which govern the logical flow of the photon simulation as described in section 3.4.1. Thus within PHOSIM, calls are made on PATHINT, PAIR etc. as necessary (see section 3.3). Similarly, the second double-walled box in fig. 6.2 represents the instructions to carry out the electron simulation which includes calls on CSDALOS, NOKLOS etc. (see section 4.5).

The initial parameters of the secondary photons are stored sequentially in the array PHOPARM(..). SECPARM(..) fulfills the equivalent role for the electrons. The two extra parameters (10 instead of 8) label the electron as positron or negatron and as primary or secondary. The electrons set in motion directly by the photons are labelled 'primary'. This is in order to be able to evaluate the Bragg-Gray stopping-power ratio for reasons given in chapter 9.

It is not difficult to see how the flow of the computation depicted in fig. 6.2 is modified for the case of a primary electron beam. The positions of the two double-walled boxes are exchanged and 'photon' replaces 'electron' and vice-versa in the other boxes.

The scheme adopted in this work to handle the cascade simulation can be contrasted with the one which Patau (1972) employed. Firstly, Patau neglected bremsstrahlung production by electrons below 2 MeV in energy. Secondly, he assumed that only bremsstrahlung photons with energies below 2.94 MeV need be included in the simulation. For a primary photon beam, of initial energy T_c, first all the primary and secondary electrons were followed down to an energy of 2 MeV. The initial parameters of all the bremsstrahlung photons produced in the course of these histories were put onto magnetic tape. Then these photon histories were executed, one after another, the parameters of the resulting electrons being stored on magnetic tape. Finally, the electron simulation followed these photon-ejected electrons down to an energy of 60 keV, the primary and secondary electrons of energy 2 MeV (together with) resulting from the termination of the histories from the first electron program.

This type of scheme cannot be called a cascade simulation, as the possibility of further bremsstrahlung photons arising from the photon-ejected electrons and being followed is excluded. It should be noted that Patau was not concerned with primary photon beams above 2 MeV in energy, and thus did not need to consider secondary

bremsstrahlung or annihilation photons, unlike in the present investigation. For 3000 primary electron histories in aluminium, Patau's Monte Carlo scheme required the storage of the initial parameters of about 75000 photons. Berger and Seltzer (1969) did not give many details of their MC cascade scheme, but implied that they used one single program combining the photon and electron MC simulations as in this work.

6.3.2 Inputs to the low-energy flux computation from the photon histories

The Compton, pair and photo-electrons that have initial kinetic energies below T_c are not followed in the electron Monte Carlo simulation, but must be added to the number of electrons in the appropriate energy bands between T_c and 100 eV. In addition, there are the Auger electrons that result from photoelectric absorption and Compton K-oxygen electron ejection, as discussed in chapter 3. Of course, this only applies to electrons which are ejected at a depth z such that $Z_l \leqslant z \leqslant Z_h$ where Z_l and Z_h define one of the geometries for which the eletron flux spectrum is desired.

As the electrons liberated directly by photon interactions are to be regarded as primaries, they all belong in category (a), as defined in section 5.5.1. The Auger electrons are not included in this category, but go in (d) with the Augers accompanying δ-ray production. Thus the routines COMPTON, PAIR and PHOTO are sources of low-energy electrons in addition to NOKLOS, CSDALOS and the primary and δ-ray track ends in the Monte Carlo electron simulation. It has already been mentioned that no distinction is made between a positron and an electron in the slowing-down scheme, either above or below T_c.

6.4 PRACTICAL CONSIDERATIONS

6.4.1 Input Data

6.4.1.1 Permanent

A total of 15 sets of figures are required as permanent input data to both the primary electron and photon cascade programs, i.e. data that are not altered from run to run. Nine of these sets are utilized in the execution of the electron Monte Carlo simulation and have already been described in section 4.5.3. One of them, the tabulation of the natural logarithm of the bremsstrahlung photon deflection angle for different electron energies, is also used in the photon MC simulation as the values apply equally well to the deflection angles in pair production (see section 3.3.4.2). These nine tabulations consist of 23 numbers each.

The photon simulation also requires tabulations of 56 energy values (0.001, 0.0015, 0.002.....,0.95, 1; MeV) and the corresponding probabilities that an interaction is Compton scattering. The remaining three tabulations, of 49 values each, are connected with the evaluation of $G(Fe^{3+})$, which is described in chapter 11.

In addition, the band width parameter, B_W, is set permanently equal to 10, and the maximum step size parameter, δ_T, to 4 (see section 4.4.4.3). For water, I = 71.3 eV, I_{eff} = 43.4 eV and Z/A = 0.55556.

6.4.1.2 Variable

The variable input data to run the final version of the electron cascade program are somewhat more extensive than those illustrated in the computer printout reproduced

Figure 6.3 VARIABLE INPUT DATA TO THE CASCADE PROGRAM.

Primary Electron beam

KE(MEV): 20.000
TMIN: 1.0080
NO. HISTORIES: 2000
XI(G/CM2): 0.00
YI(G/CM2): 0.00
ZI(G/CM2): 0.00
RO(G/CM2): 9.20
ZSTOP/RO : 3.50
ZEND G/CM2 (PHOTONS): 33.00
THETA(DEG): 0.0
PHI(DEG): 0.0
NO. MC SPEC. INT: 27

NO. SPECTRA: 8

MINZ/RO: 0.000
MAXZ/RO: 0.100

MINZ/RO: 0.200
MAXZ/RO: 0.300
.....
.....
.....

RANDOM STARTER: 2650613

Primary Photon beam

NO. ENERGIES: 32

MAXIMUM (MEV): 30.50
NO. HISTORIES: 400
WEIGHT: 0.900

ENERGY: 29.50
NO. HISTORIES: 400
WEIGHT: 6.000
.....
.....
.....

ENERGY: 0.2
NO. HISTORIES: 200
WEIGHT: 200.000

XI(G/CM2): 0.00
YI(G/CM2): 0.00
ZI(G/MC2): 0.00
RO(G/CM2): 15.00
ZEND (G/CM2): 34.00
THETA(DEG): 0.0
PHI(DEG): 0.0
TMIN(ELECTRONS): 2.0168
NO. MC SPEC. INT: 30

NO. SPECTRA: 5

MINZ/RO: 0.000
MAXZ/RO: 0.133

MINZ/RO: 0.267
MAXZ/RO: 0.400
.....
.....
.....

RANDOM STARTER: 4507721

in figure 4.13, which corresponded to an intermediate version of the MC program. The only extra parameter that specifically pertains to the cascade simulation is ZEND, the value of z at which the photon histories are terminated. This is usually set to about 3.5 r_o, there being no point in simulating bremsstrahlung transport to any greater depths. Any number of spectrum geometries may be selected, with each pair of Z_l and Z_h values in units of r_o, which is a convenient scaling parameter. A list of the variable input parameters for the primary electron cascade program is given in the left half of figure 6.3. The figures correspond to the final run for a 20 MeV electron beam.

The input data to the primary photon version only differ with respect to the initial energy of the radiation. The photon beams of interest are not monoenergetic, but have a continuous spectrum of energies with the exception of primary ^{60}Co gamma radiation. For a 30 MV bremsstrahlung beam, there are appreciable numbers of photons with energies from 30 MeV down to about 0.2 MeV. A sufficiently accurate representation of such a spectrum can be achieved by dividing it into about 20 energy intervals, each of the same sort of width. However, the shape of a typical bremsstrahlung spectrum is such that there are many more photons towards the lower energy end of the distribution. It was desirable, therefore, to be able to weight differently the contribution of different photon energies to the final results, such as the electron flux spectra, in order that similar numbers of histories could be executed for each photon energy. To give an example:

for the 31 MV betatron spectrum (described in chapter 8), the highest photon energy was taken as 30.5 MeV and the 400 histories assigned a weight of 0.9. At the low-energy end, the 200 histories for photons of initial energy 1.5 MeV are weighted by a factor 1100. It would obviously not have been feasible to have executed 1100/1.8 times as many histories for k_o = 1.5 MeV than for k_o = 30.5 MeV.

The photon cascade program was modified to incorporate a distribution of primary photon energies, with two parameters for each energy; the number of histories, H_j, and the weighting factor W_j. All the quantities resulting from the set of photon histories starting with $k_o = k_{o,j}$ are then multiplied by W_j. The effective number of histories, given by $\sum_j H_j.W_j$, is used to normalize results, such as the number of electron steps,'to per primary photon history.'

The parameter r_o has been retained in the photon version, as a scaling distance, but it is set to an arbitrary value, unlike in the electron version where it is the c-s-d-a range. A list of the variable input data for a primary photon beam is given in the right half of figure 6.3. The numerical values are actually those used to generate the final results for the 31 MV betatron X-ray spectrum. Note that information was only required down to a depth of about 25 cm. Thus the photon histories were terminated at ZEND = 35. The parameter ZSTOP, the depth at which the electron histories are terminated, does not appear explicitly. It is automatically set equal to ZEND.

6.4.2 Length of the Computer Code

The first version of the cascade programs only included the calculation of depth-dose histograms; CASCEL1, CASCFO1. These programs were each about 1450 statements. The second version incorporated the computation of the electron flux down to 100 eV and this added an extra 500 or so statements. Further modifications included the accomodation of any number of spectrum geometries and, in the primary photon program, the input of a distribution of energies and weighting factors. The final versions, CASCEL6 and CASCFO6, consist of nearly 2400 statements of code. They include the calculation of water/air mass stopping-power ratios and the evaluation of $G(Fe^{3+})$ for each spectrum geometry (see chapters 9 and 11).

A breakdown, by line numbers, of CASCFO6 is given in Appendix 6. The position and relative length of the various parts of the program are indicated together with references to the sections of the work where the details of these procedures are to be found. A similar description of CASCEL6 is not given as the differences from CASCFO6 are minimal. The object program compiled from the source CASCFO6 requires a space of 54 Kbytes on the IBM 370/158 on which the final runs were executed. This is well within the capacity of this computer.

6.4.3 Run-times

The execution time per primary electron history is not appreciably increased by the inclusion of the simulation of the transport of bremsstrahlung photons. It has been shown in sections 3.4.6 and 4.5.3 that a Monte Carlo photon

Table 6.2 EXECUTION TIME OF THE PHOTON CASCADE PROGRAM

CASCF01
100 histories
0 - 50 cm geometry
T_c = 1.12 MeV

k_o (MeV)	Per Primary Photon History				
	No. secondary photons followed	No. of inter-actions	No. electrons followed	No. of steps	Execution Time(sec)
40	2.45	18.7	1.150	83.6	0.63
20	1.15	9.6	0.98	49.9	0.36
10	0.73	8.5	0.92	33.9	0.24
5	0.10	6.6	0.91	19.5	0.14
2	0.04	8.7	0.59	3.9	0.050
1	-	10.2	-	-	0.034
0.1	-	7.1	-	-	0.023

history takes much less time to execute than an electron history. Moreover, the difference is increased by the fact that the electrons are in most cases to be followed to the end of their range (i.e. down to T_c), whereas the high-energy primary photons have, on average, very much longer tracks of which only the first 30 cm or so need be simulated for the results required in this work. It is to be expected, therefore, that the inclusion of the transport of the electrons liberated by the photon interactions will drastically increase the execution time per primary photon history. The magnitude of the increase depends critically on the value of T_c. For k_o = 2 MeV, say, putting T_c = 1 MeV (i.e. neglecting the final 0.5 cm of the electron tracks) results in very little electron MC computation as the maximum energy of the electrons produced is only just above T_c in energy. For k_o = 15 MeV and T_c = 2 MeV the situation is completely different.

These points are illustrated in table 6.2. The CPU time per primary history is given for k_o ranging from 40 MeV down to 0.1 MeV, for a constant value of T_c. The figures were taken from preliminary runs of CASCF01 with the photon histories terminated at a depth of 50 cm. The number of electrons followed does not vary all that much, but the number of steps, which determines the electron MC computation time, decreases rapidly as k_o becomes closer to T_c. The figure of 0.63 seconds per history for k = 40 MeV is of the same order as the execution time for a 20 MeV electron history with the same T_c. The table also includes the number of secondary photon followed and the total number of photon interactions.

The computation of the electron flux was found to increase the run-time for the Monte Carlo histories by about 5% per extra geometry. The execution of the routines MCSPECAL and LOWENCAL and the printing out of all the results i.e. stopping-power ratios, $G(Fe^{3+})$ and the electron flux from T_o, or k_o, to 100 eV, add another five to seven seconds per geometry onto the total run-time. For large numbers of Monte Carlo histories, this printout time is negligible.

The final results for primary photon and electron beams, which are presented in chapters 7, 8, 9, 10 and 11 were derived from a sufficiently large number of histories to reduce the statistical uncertainties on the quantities required to an acceptably small level. The maximum total run-time came out to be 1500 seconds for 2000 primary electron histories of initial energy 30 MeV. The execution of 9600 photon histories making up the 31 MV betatron X-ray spectrum was about 100 seconds less than this figure.

6.4.4 Checks on the Internal Consistency

As the cascade versions of the simulation were developed, from CASCEL1, CASCF01 through to CASCEL6 and CASCF06, various tests were carried out to make sure that all the physical processes simulated were consistently accounted for. Through such checks, several errors were discovered and corrected.

The inclusion of the transport of bremsstrahlung photons made the checking of the 'energy input = energy dissipated' relation for a primary electron beam somewhat

less straightforward than had been the case in chapter 4. Totalling up the energy deposited in the depth-dose histogram, between z = 0 and z = $2r_o$, did not take into account the dissipation beyond $2r_o$ due to bremsstrahlung transport. Consequently, two extra parameters were necessary. One of them, ENFLY, added up the electron K.E. that escaped inclusion in the depth-dose histogram. The other one, PHOFLY, added up the energy of the photon that did not become converted into electron K.E. due to termination of the photon histories at z = ZEND. One such energy accountability check, for T_o = 40 MeV, is illustrated by the following figures taken from a computer printout:

PER PRIMARY ELECTRON HISTORY:	MEV
PHOTON ENERGY BACKSCATTERED	0.0972
ENERGY ESCAPING DUE TO Z>ZEND (PHOFLY)	3.1601
ELECTRON ENERGY BACKSCATTERED	0.0000
ELECTRON ENERGY NOT INCLUDED IN D-D HISTOGRAM (ENFLY)	1.7740
ENERGY DEPOSITED IN D-D HISTOGRAM Z=0-2.r_o	34.9979
For input energy per history of 40 MeV — cf	39.9992

A similar check for a 40 MeV photon beam gave a total of 39.9998. These figures were considered to be satisfactory.

The other important quantity to be looked at carefully was the local energy dissipation, D_{100}, calculated from the electron flux spectrum. The evaluation of this quantity over the low-energy spectrum, F_1, has been discussed in section 5.4.3 (see, in particular, equ. 5.16). The extension of the calculation of D_{100} to include the MC histogram spectrum from T_o, or

k_o, down to T_c as well as the F_l values is straightforward. Thus

$$D_{100} = \Sigma Q_T \Delta T$$

$$= \sum_{1}^{N_i} F_{MC}(\bar{T}_i) . \Delta T_i . \left(\frac{dT}{dx}\right)_{100} + \sum_{l}^{l_{100}-1} F_l(T) . \Delta T . \left(\frac{dT}{dx}\right)_{100}$$

$$+ N_{100} . 0.0001 \text{ (MeV)} \qquad \ldots\ldots(6.1)$$

where N_i is the number of spectrum energy intervals between T_o, or k_o, and T_c. $F_{MC}(T_i)$ is the flux averaged over the i 'th interval (i.e. the MC histogram value) and ΔT_i is the width of the interval. The restricted stopping power, $(dT/dx)_{100}$, is evaluated at $T = T_i$, the geometric mean energy in the band. The final term is the contribution from the 100 eV track ends. In the cascade programs, the first term is evaluated during the execution of the routine MCSPECAL (see fig. 5.6) and the second and third terms within LOWENCAL.

It will be recalled that for 2 MeV electrons the low-energy flux computation, with $B_w = 10$, led to the value $D_{100} = 0.9968$ MeV per MeV input energy. It was expected, therefore, that D_{100} would be within 0.5% or so of the 'exact' value for the flux spectra produced by the cascade program, assuming everything was functioning correctly. For test runs with infinite geometries, CASCEL2 yielded $D_{100} = 0.9947$ MeV per MeV energy input for $T_o = 40$ MeV and $T_c = 1.158$ MeV, and $D_{100} = 0.9949$ MeV for $T_o = 20$ MeV and $T_c = 0.764$ MeV. Then for a primary photon beam and infinite geometry, 1000 histories generated by CASCF02 for $k_o = 2$ MeV and $T_c = 1.880$ MeV resulted in $D_{100} = 0.9953$ MeV per MeV input energy. These results were satisfactory.

Another run for an infinite medium and k_o = 2 MeV was carried out. This time T_c was set equal to 0.1023 MeV, a much lower value. The join between the MC and 1-band spectra at T_c was found to be equally 'smooth' for the two different values of T_c. There were negligible differences in the values of the spectra in the two cases. The agreement between the two spectra is illustrated in figure 6.5 in section 6.6.

A further check that can be mentioned was ensuring that the weighting factor in the primary photon version did not alter any results. For a single photon energy, the value of W_j was set equal to different values for runs with no other parameters changed. The results per effective photon history, including the electron flux, were required to be unaltered from run to run as all the quantities should have been multiplied by W_j during the execution of the MC histories and LOWENCAL, and then divided by W_j before being printed out. This test unearthed a typing error in the computer code that would never have been found otherwise.

6.5 NORMALIZATION OF THE FLUX TO PER UNIT ABSORBED DOSE

The electron flux spectrum is calculated in units of $cm.MeV^{-1}$ per MeV input energy in the routines MCSPECAL and LOWENCAL. In order to normalize the flux for any geometry to per unit absorbed dose, all the values are divided by D_{100} (MeV), where D_{100} is evaluated as described in the previous section. Thus all the electron flux spectra presented in the chapters to follow are in units of $cm.MeV^{-1}$ per MeV local energy dissipation. In addition, the local energy dissipation spectrum, also normalized to 1 MeV total dissipation, is calculated for each energy interval, in units of per unit log energy i.e. $Q_T \Delta T/(\log_{10} \Delta T . D_{100})$. Thus the area under the curve represents the energy dissipated if the ordinate is in MeV units with a logarithmic energy scale.

The normalization and printing out of the electron flux and local energy dissipation spectra for each geometry is carried out by the routine SPECOUT in the final version of the cascade program. This is the last routine to be executed, after MCSPECAL and LOWENCAL (see Appendix 6).

It can be noted that the relation 6.1 from which D_{100} is calculated can also be written more generally as

$$D_\Delta = \int_\Delta F(T).L_\Delta.dT + N_\Delta.\Delta \qquad .....(6.2)$$

where local dissipation refers to losses less than Δ. If Δ is such that there will be some electrons produced directly by photon interactions with initial energies less than Δ, then the energy of these electrons must be included in the track-end term $N_\Delta.\Delta$ if the correct local energy

deposition is to be obtained. For a cutoff of 100 eV, the numbers of photon-ejected electrons concerned is entirely negligible, but for the cutoffs of 10 and 100 keV involved in the evaluation of the stopping-power ratio this is not always the case (see chapter 9). Similarly, for $\Delta > T_{aug}$, those Auger electrons resulting from energy transfers larger than Δ must also be included in the track-end term. It was found that for flux spectra that had been normalized by dividing by D_{100}, the evaluation of D_Δ for the different Δ used in the stopping-power ratio calculations was within 1½% or so of 1 MeV, as was to be expected. This was the case for all the different primary electron and photon beams.

Berger and Seltzer (1969a) also presented values of their electron flux spectra normalized to unit dose, $F(T,z)/D_\Delta(z)$, but it is not clear that they evaluated $D_\Delta(z)$ correctly as the equation they wrote down for $D_\Delta(z)$ did not explicitly include the track-end term. ICRU (1972) give the relation for calculating the absorbed dose from the restricted stopping power and the total electron flux:

$$D = \int_{\Delta}^{E_o} \Phi_E . (S/\rho)_{col,} \, . dE \qquad \text{(2.14 in ICRU (1972))}$$

which again does not include the term $N_\Delta . \Delta$ in equ. 6.2 above. This question is discussed further in chapter 9.

Figure 6.4 DEPTH-DOSE HISTOGRAMS (WATER) FROM THE PHOTON-ELECTRON CASCADE PROGRAM.

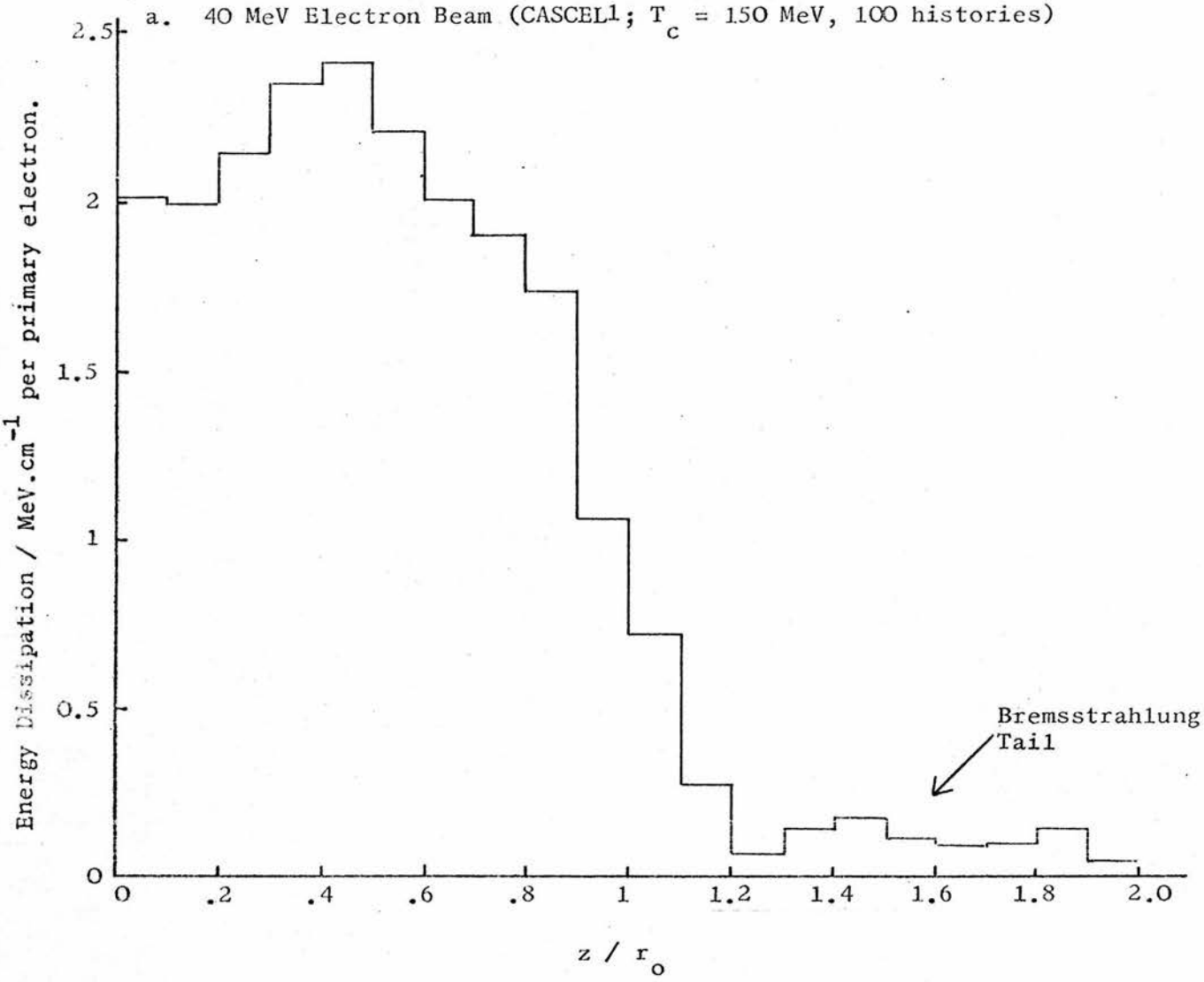

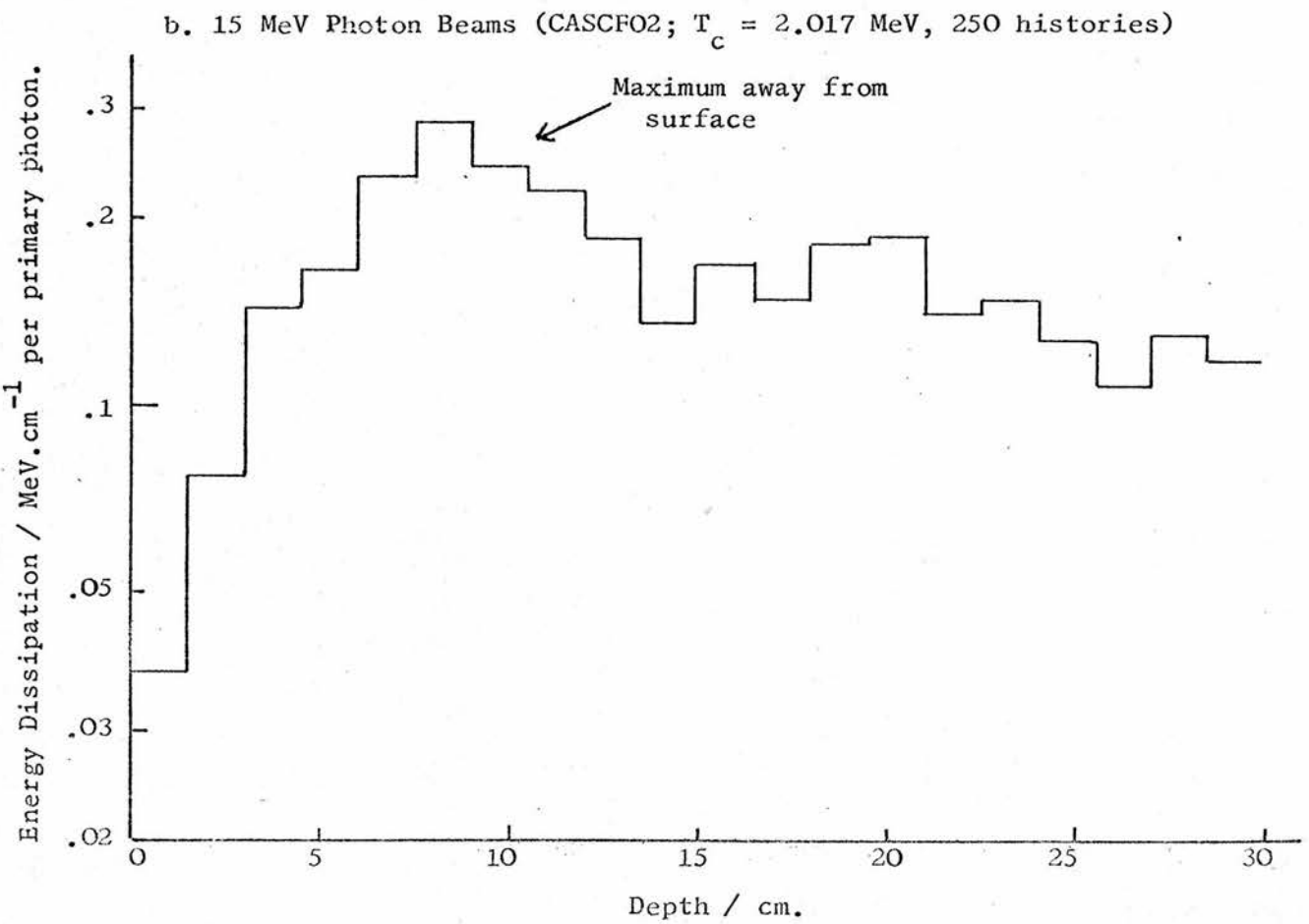

Figure 6.5 ELECTRON FLUX SPECTRUM PRODUCED BY 2 MeV PHOTONS IN AN INFINITE (Water) MEDIUM.

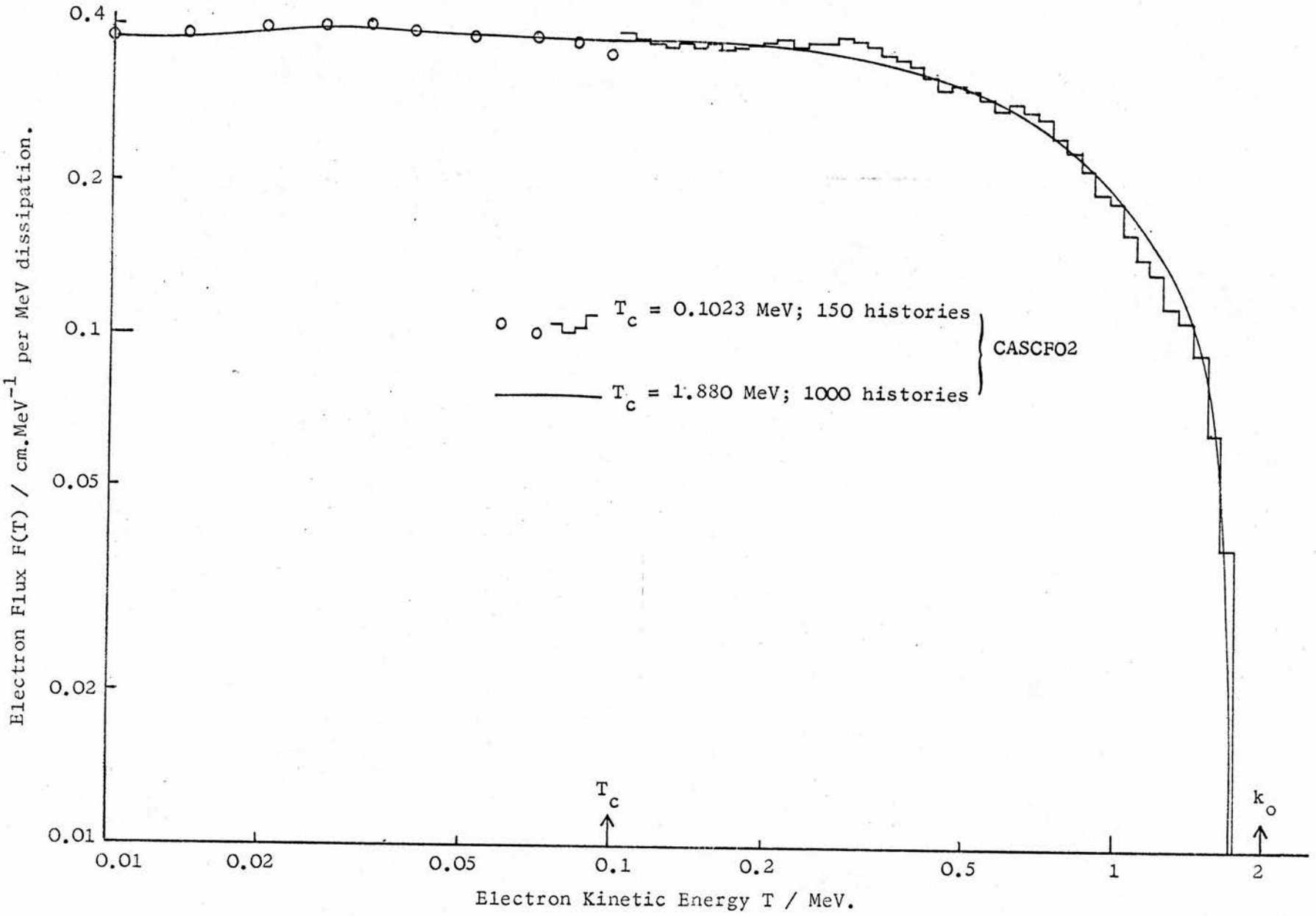

6.6 PRELIMINARY RESULTS

The two most obvious features of the results that can be derived from the Monte Carlo cascade program, but not from the photon or electron simulations alone, are to be found in the depth-dose histograms. For a primary electron beam, the transport of bremsstrahlung results in a 'tail' extending well beyond the range of the primary electrons. For a primary photon beam, the transport of the electrons results in a displacement of the maximum away from the surface. These features are illustrated in figures 6.4 a and b. The histograms are somewhat 'bumpy' as the results were derived from only a small number of histories.

In addition, the electron flux spectrum resulting from the absorption of 2 MeV photons in an infinite medium is given in figure 6.5. The energy scale only extends down to 0.01 MeV as the figure is primarily intended to illustrate the very close agreement between the one spectrum calculated with T_c = 0.1023 MeV and the other with T_c = 1.880 MeV (i.e. no electrons followed). These spectra demonstrate that the three components of the cascade program viz. the photon Monte Carlo simulation, the electron Monte Carlo simulation, and the depth-independent electron flux computation, have been combined together satisfactorily.

CHAPTER 7

ELECTRON BEAM RESULTS - FLUX SPECTRA AND RELATED QUANTITIES

7.1 DESCRIPTION OF THE CALCULATIONS

7.1.1 General

The main purpose of computing the electron flux spectrum at different depths in water was to be able to calculate water/air stopping-power ratios and,more particularly, to investigate the suspected difference in $G(Fe^{3+})$ between high-energy electron and X-ray beams. Thus the spectra presented in this chapter are not to be considered as the end-point of the electron beam calculations. Indeed, the results are very similar to that important and extensive work by Berger and Seltzer (1969, 1969a), the main differences being the inclusion of Auger electron production and the extension to a slightly lower energy, 100 eV, as compared to the 200 eV cutoff at which Berger and Seltzer terminated their computations. The incident electron energies chosen were 5, 10, 20, and 30 MeV which cover the range of clinical beam energies commonly employed and hence of dosimetric interest.

7.1.2 Irradiation Geometry

The calculations correspond to a point, monoenergetic beam incident perpendicularly on a semi-infinite water phantom. The quantities derived, such as flux spectra and energy deposition,are computed over a layer perpendicular to the incident beam direction and of infinite lateral extent. In practice, this would correspond to either an infinite plane detector or an average over all positions

Figure 7.1 IRRADIATION GEOMETRY

a. Point, monodirectional beam and infinite detector.

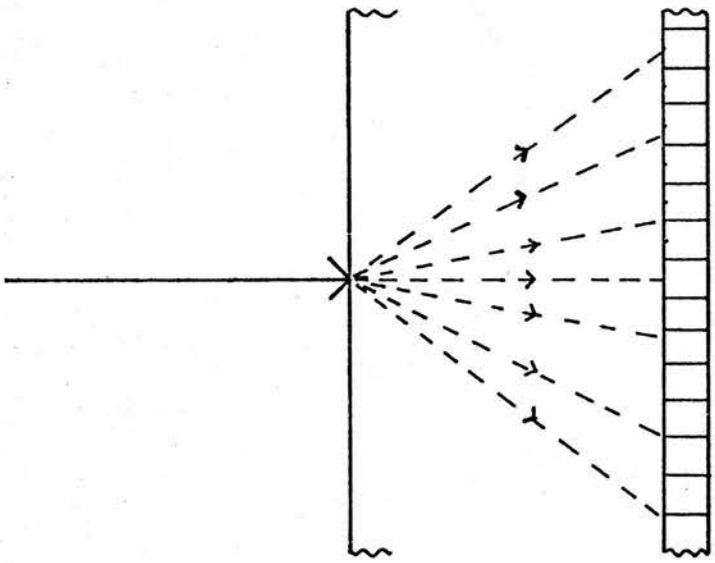

b. Broad, parallel beam and small detector.

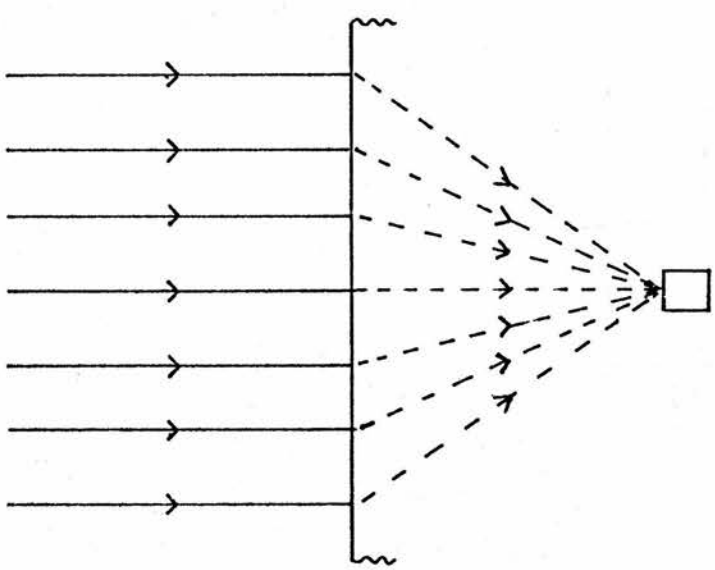

of a small detector in the plane. The configuration is depicted in figure 7.1a. This is also the geometry that Berger and Seltzer employed.

Alternatively, the geometry can be interpreted as that of an infinitely broad, parallel beam incident on the medium, with a very small detector, as shown in figure 7.1b. It is readily seen that the two situations are equivalent. The latter corresponds approximately to the practical situation. Normally the beam is slightly diverging, but has a considerably larger cross section than the detector, which is placed on the central axis. Ideally, one would require the radius of the beam area to be greater than the maximum range of the electrons. Note that there is no difficulty in principle in simulating any type of beam geometry with the Monte Carlo program. However, a great deal of extra complexity would have been involved for a very small difference to the results for the main quantities of interest.

7.1.3 Spectrum Geometry

Ideally, the thickness of the layers in which the spectrum is calculated should be as small as possible. However, two factors limit the size of the layers in a Monte Carlo calculation. Firstly, the thinner the layer the less is the total flux in that layer and consequently the poorer is the statistical accuracy for a given number of histories. Secondly, the cutoff T_c is determined by the layer size. A thin layer requires a low value for T_c which increases appreciably the execution time per history.

Given these factors and the relatively slow variation of the flux spectrum with depth except at the high-energy end, and in particular, the almost linear change of the stopping-power ratio with depth (Berger et al., 1975; Kessaris, 1970a), subdivisions of 0.1 r_o were chosen except at the greatest depth.

The spectrum geometries for each T_o were as follows: 0.0 - 0.1 r_o; 0.2 - 0.3 r_o; 0.4 - 0.5 r_o; 0.6 - 0.7 r_o; 0.8 - 0.9 r_o; 0.9 - 1.0 r_o; 1.0 - 1.1 r_o; and 1.2 - 1.4 r_o. The final geometry is the bremsstrahlung tail region where the flux is very low and the radiation quality is expected to change very slowly with depth. Thus a 0.2 r_o layer was employed to improve the statistical accuracy of the results.

The 0.1 r_o subdivisions fix the size of T_c, as mentioned above. T_c was chosen such that the c-s-d-a range of an electron of energy T_c was approximately one half of 0.1 r_o. The exact value of T_c is determined by the energies of the 1 bands as explained in section 5.5.2. The following table (table 7.1) gives r_o, T_c and the total execution time for each T_o run of 2000 histories:

T_o(MeV)	r_o(cm)	T_c(MeV)	Execution Time(sec)
5	2.51	0.438	634
10	4.90	0.664	873
20	9.20	1.008	1270
30	13.0	1.425	1501

Berger and Seltzer (1969) derived their results from 10,000 Monte Carlo histories and used subdivisions of 0.05 r_o. This results in only marginally better statistical accuracy than in the present case.

Figure 7.2 ELECTRON FLUX SPECTRA AT DIFFERENT DEPTHS FOR 20 MeV ELECTRON BEAM.
(T_c = 1.008 MeV, 2000 histories)

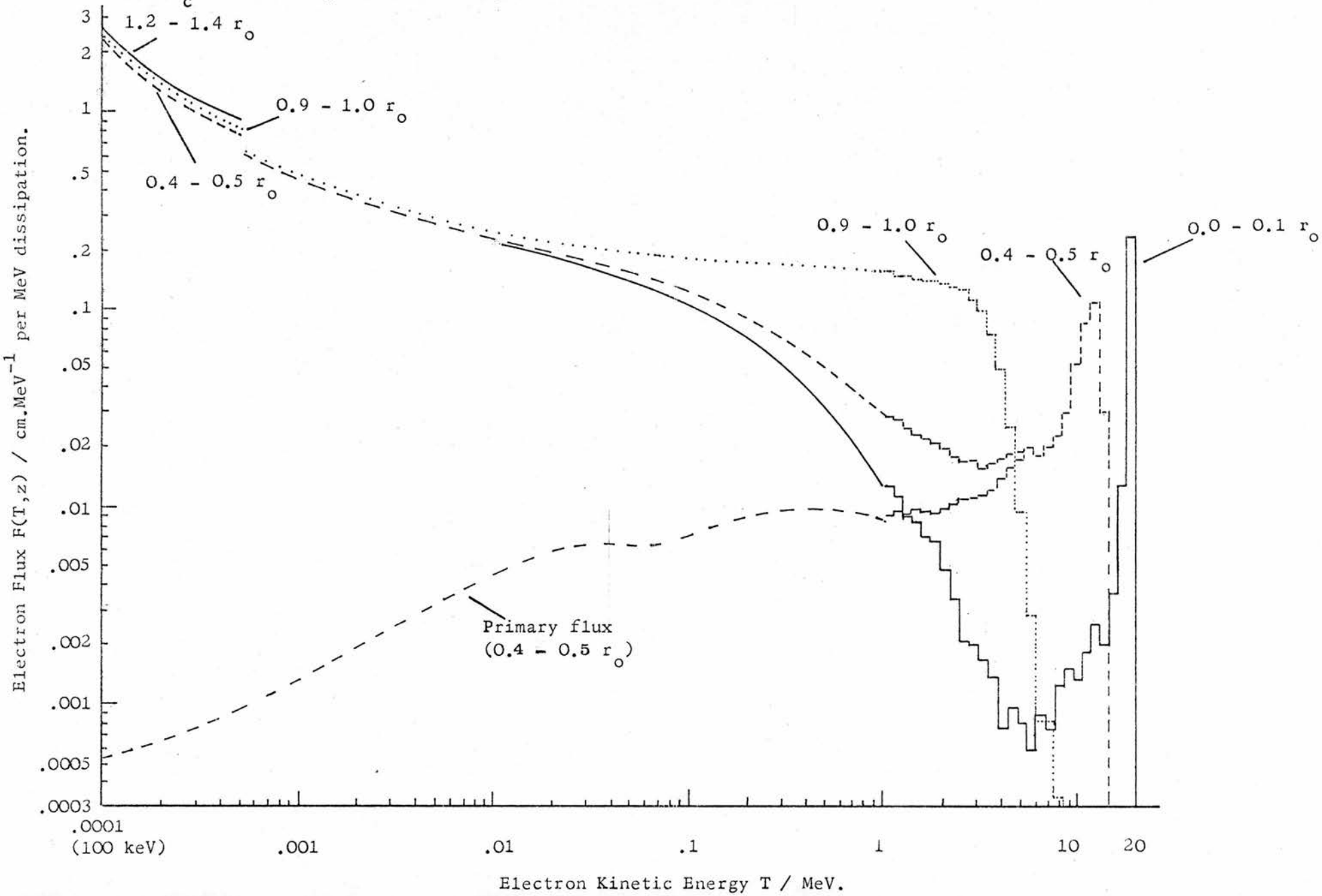

Figure 7.3 ELECTRON FLUX SPECTRA FOR 5, 10, 20, 30 MeV ELECTRON BEAMS AT Z = 0.4 - 0.5 r_o

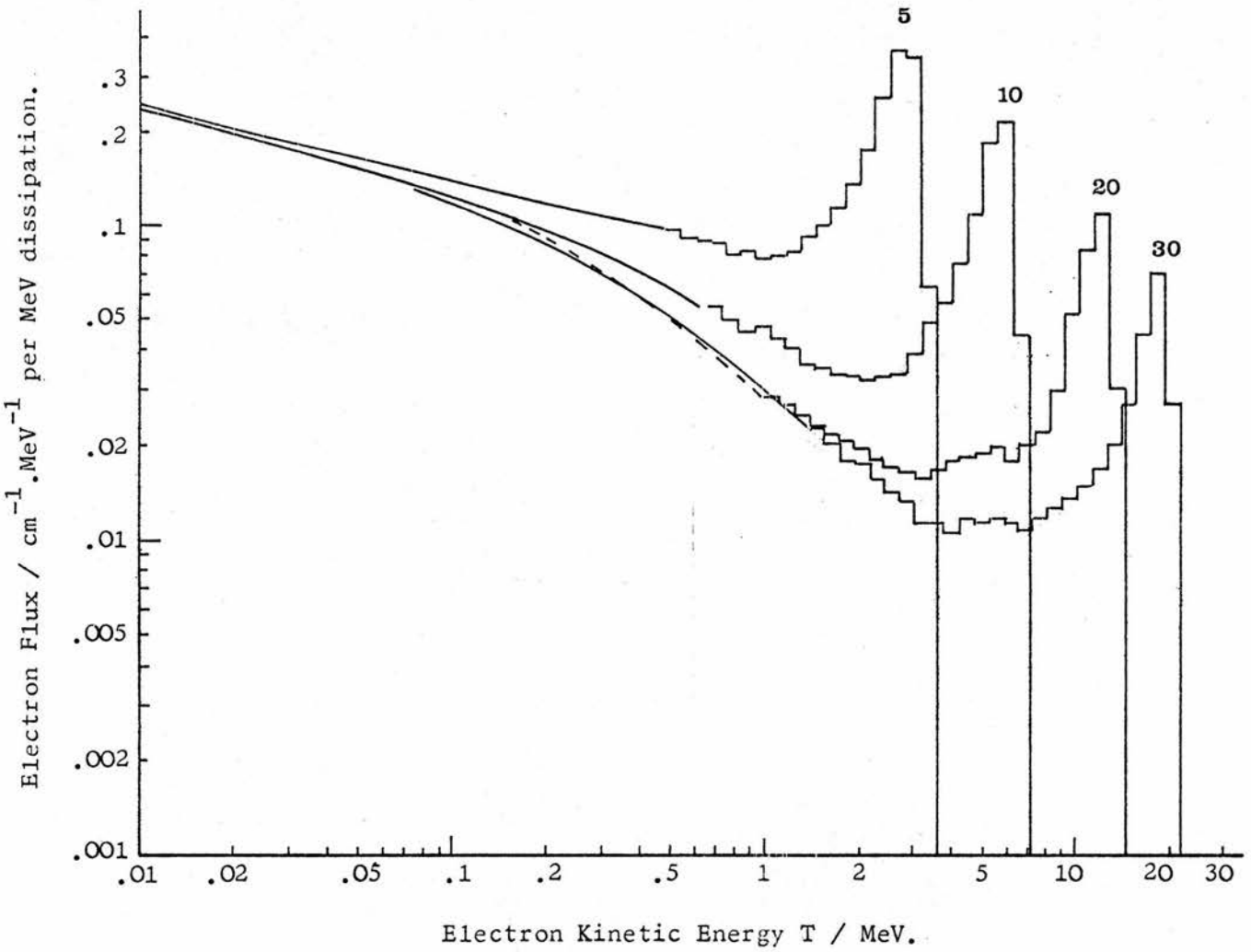

Figure 7.4 ELECTRON FLUX SPECTRUM AT LARGE z / r_o
(T_o = 30 MeV)

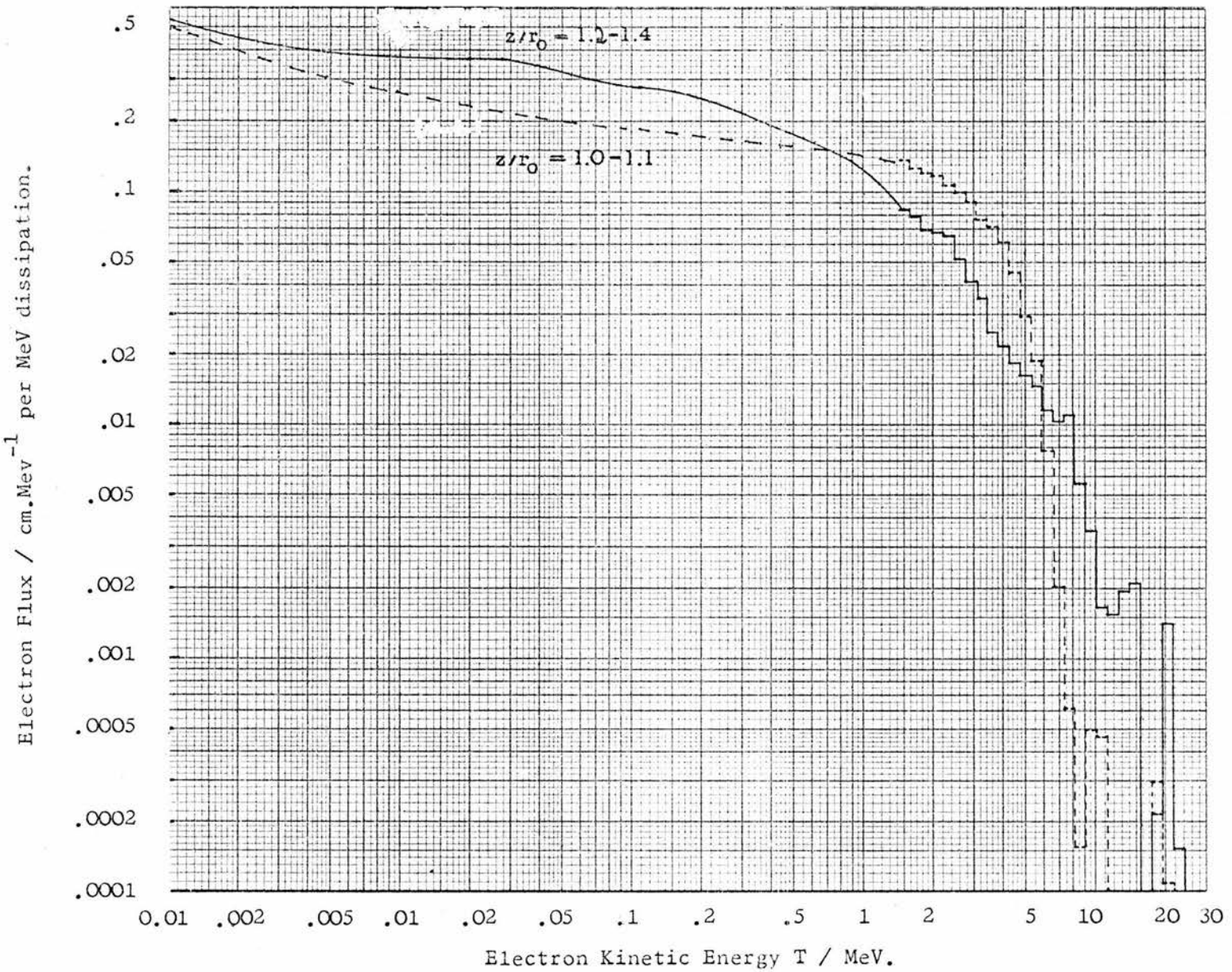

7.2 ELECTRON FLUX SPECTRA

7.2.1 Results

The principal features of the flux spectra $F(T,z)/D(z)$, normalized to unit dose, can be seen in figure 7.2 and 7.3. The Monte Carlo spectrum down to T_c has been plotted as a histogram and the spectrum from the depth-independent computation as a continuous curve. The energy of the primary electrons decreases gradually with increasing depth, with the maximum broadening out in the process. The low-energy flux, due to secondary electron build-up, is almost independent of the primary electron energy and depth as noted by Berger and Seltzer. The tail at the high-energy and of the 0.9 - 1.0 r_o spectrum in fig. 7.2 is due primarily to the electrons resulting from bremsstrahlung absorption and not to energy-loss straggling. The discontinuity at around 500 eV caused by the Auger electrons is seen to have a comparatively minor effect on the low-energy spectrum and furthermore, is of the same magnitude at all energies and depths, following the general trend at low energies.

It was of interest to look at the changes in the flux spectrum at very large depths. It was expected that the number of high-energy electrons would increase as the bremsstrahlung tail region was entered. This feature is shown in figure 7.4. The comparatively poor statistical accuracy of the two spectra was to be expected as the energy dissipation per incident electron between the depths 1.0 - 1.1 r_o and 1.2 - 1.4 r_o was about 0.2 and 0.02 respectively of the dissipation at 0.4 - 0.5 r_o, for instance.

Table 7.2 LOW-ENERGY FLUX SPECTRUM VALUES

Geometry	F(T,z)/D(z) ($cm.MeV^{-1}$ per MeV dissipation)			
z/r_o	T_o = 5 MeV	T_o = 10 MeV	T_o = 20 MeV	T_o = 30 MeV
0.0 - 0.1	0.102 2.40	0.104 2.38	0.109 2.37	0.110 2.37
0.2 - 0.3	0.118 2.44	0.117 2.41	0.115 2.39	0.112 2.38
0.4 - 0.5	0.137 2.49	0.122 2.44	0.122 2.41	0.117 2.40
0. 6 - 0.7	0.180 2.55	0.140 2.48	0.128 2.44	0.124 2.42
0.8 - 0.9	0.286 2.62	0.190 2.55	0.146 2.49	0.138 2.46
0.9 - 1.0	0.339 2.66	0.230 2.60	0.178 2.53	0.155 2.49
1.0 - 1.1	0.405 2.72	0.323 2.67	0.226 2.59	0.186 2.53
1.2 - 1.4	0.39 2.81	0.39 2.87	0.329 2.70	0.285 2.65

The upper F/D figure is for T = 0.1 MeV and the lower figure is for 100 eV.

It was obviously not practicable to plot all the 32 spectra calculated, but a tabulation of the results for six of the eight depths at each T_o is to be found in Appendix 7. The values of $F(T,z)/D(z)$ are given at a sufficient number of energies to enable $F(T,z)/D(z)$ at any T to be interpolated graphically. Some of the values from Appendix 7 are reproduced in table 7.2. At each depth and energy, the flux at 0.1 MeV and 100 eV is given. These figures demonstrate the extent to which the low-energy spectrum does change. The 'universal shape' below 0.1 MeV at depths up to near the end of the electron range that Berger and Seltzer (1969, 1969a) and ICRU (1972) discuss is clearly a better approximation the higher the initial energy. The flux at 0.1 MeV changes by a relatively small amount down to $z/r_o = 0.9 - 1.0$ for $T_o = 30$ MeV, but only down to $z/r_o = 0.4 - 0.5$ for $T_o = 5$ MeV. This is to be expected since 0.1 MeV is a smaller fraction of 30 MeV than of 5 MeV.

7.2.2 Comparison with other flux spectra

The most direct comparison can be made with the flux spectra calculated by Berger and Seltzer (1969, 1969a). Their flux normalized to unit dose is given in the units of electrons $cm^{-2}.MeV^{-1}$ per 10^{-7} rad dissipation. This can be written as $g.cm^{-2}.MeV^{-1}$ per 10^{-5} ergs which is equivalent to 6.243 $g.cm^{-2}.MeV^{-1}$ per MeV dissipation. Thus division by the factor 6.243 converts the Berger and Seltzer flux into the units used in this work. The flux spectra below 0.2 MeV for $T_o = 20$ MeV are compared in

Table 7.3 COMPARISON OF LOW-ENERGY FLUX WITH BERGER AND SELTZER (1969).

T_o = 20 MeV	F(T,z)/D(z) ($cm.MeV^{-1}$ per MeV dissipation)	
T (keV)	This work z/r_o = 0.4 - 0.5	Berger and Seltzer* z/r_o = 0.5
200	0.0932	0.0883
100	0.122	0.119
70	0.137	0.135
40	0.161	0.160
20	0.193	0.195
10	0.230	0.237
7	0.254	0.263
4	0.295	0.311
2	0.366	0.394
1	0.464	0.522
0.7	0.545	0.618
0.4	0.879	0.846
0.2	1.31	1.36

*Figures (in B+S units) taken from Table 3 (Berger and Seltzer, 1969) down to 0.4 keV and the 0.2 keV figure from Berger (1973).

Figure 7.5 COMPARISON OF THE LOW-ENERGY END OF THE ELECTRON FLUX SPECTRUM WITH BERGER AND SELTZER (1969).
(T_o = 20 MeV)

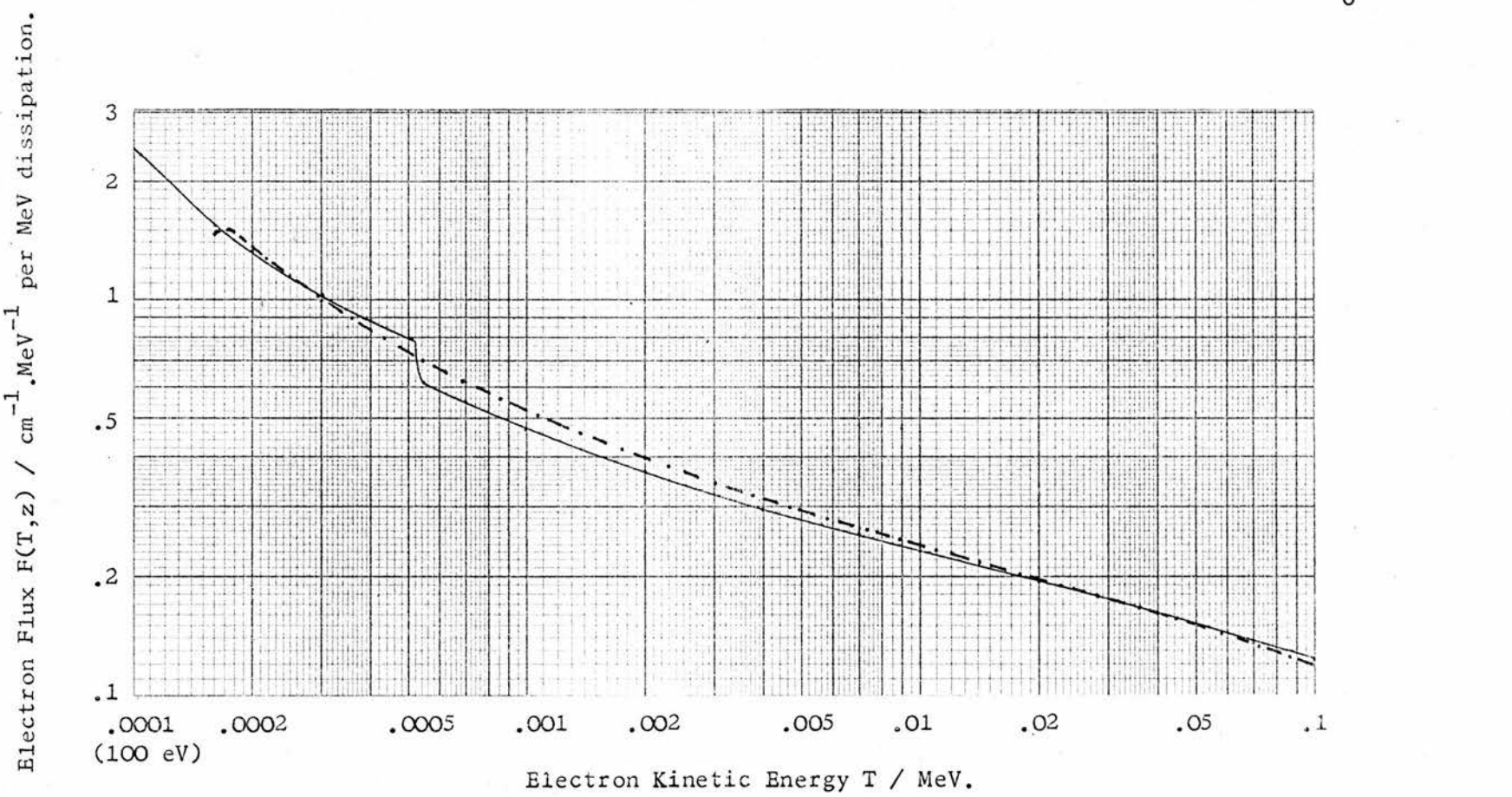

Figure 7.6 COMPARISON WITH BERGER AND SELTZER AT THE HIGH-ENERGY END OF THE SPECTRUM.
(T_o = 10 MeV)

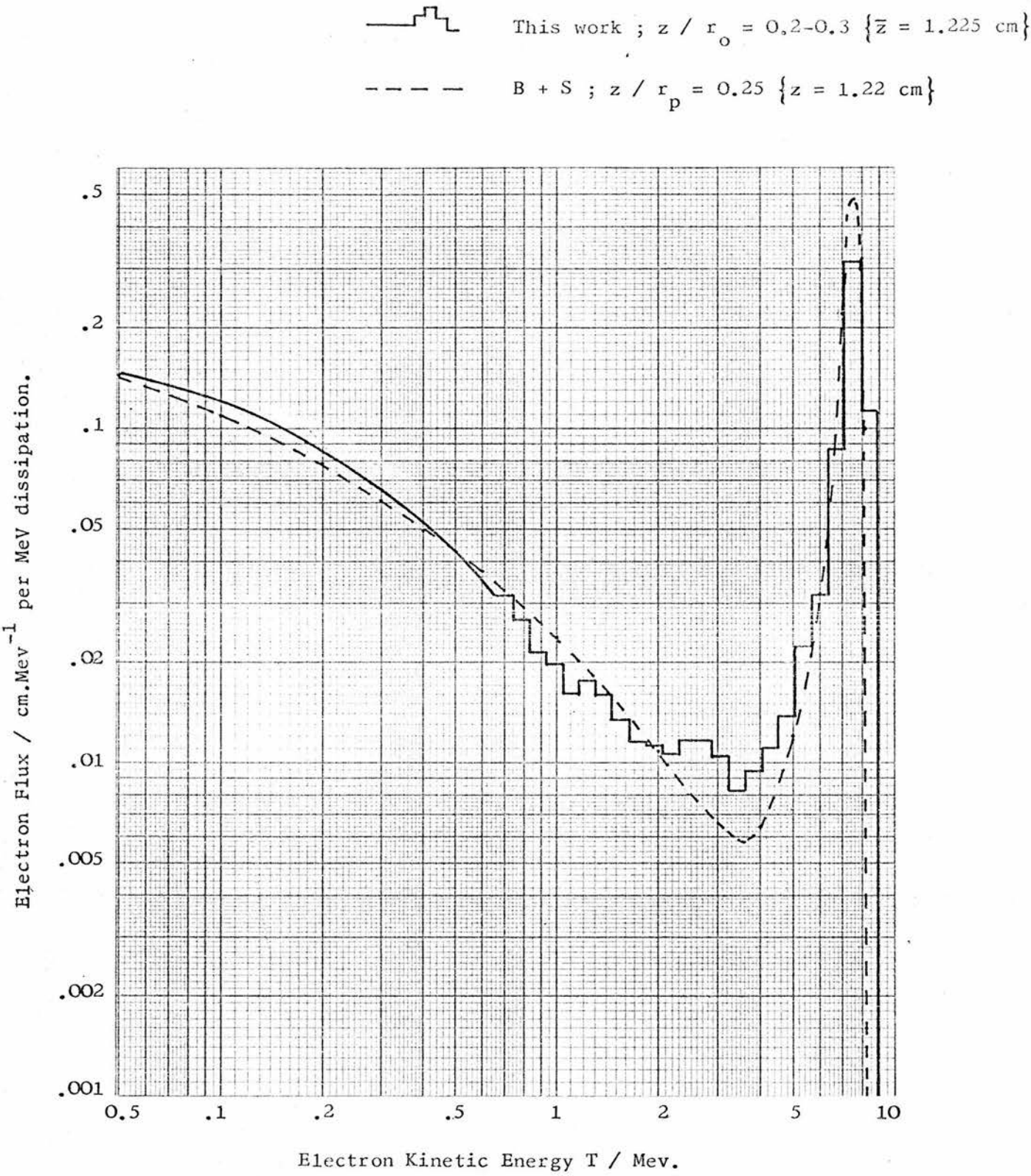

table 7.3 and plotted in figure 7.5. The agreement is very close, allowing for the fact that Berger and Seltzer did not include Auger electron production. Had the B+S computation been extended down to 100 eV, some divergence between the two curves would have been expected due to the modified stopping power evaluation below 500 eV in the present work (see sections 5.3.3 and 5.4.4).

In order to compare the spectra at the high-energy end, a close match is necessary between one of the z/r_o layers and one of the depths at which Berger and Seltzer give their results. Fortunately, their T_o = 10 MeV, z/r_p = 0.25 spectrum (Berger and Seltzer, 1969a) corresponds very closely to the z/r_o = 0.2 - 0.3 geometry in this work as Berger and Seltzer's r_p is equal to 1.002 r_o at 10 MeV (r_p is discussed below). The two flux spectra are given in figure 7.6. Again, the B+S units were converted as described above. The agreement is remarkably good.* In particular, the maximum and minimum values are at the same energy. The slightly broader energy distribution of the primary flux on either side of the maximum in this work may simply be due to the fact that the spectrum is an average over a 0.1 r_o layer, whereas Berger and Seltzers' layer is probably 0.05 r_o, though they do not specify what the size is in their 1969a paper.

---

*From the comparisons with the Berger and Seltzer results it was concluded that they <u>did</u> calculate correctly the energy dissipated by the flux spectra (see section 6.5).

Figure 7.7 COMPARISON OF PRESENT RESULTS WITH MEASUREMENTS BY EPP ET AL. (1972) AND CALCULATIONS BY KESSARIS (1970). (linear flux - linear energy scales)

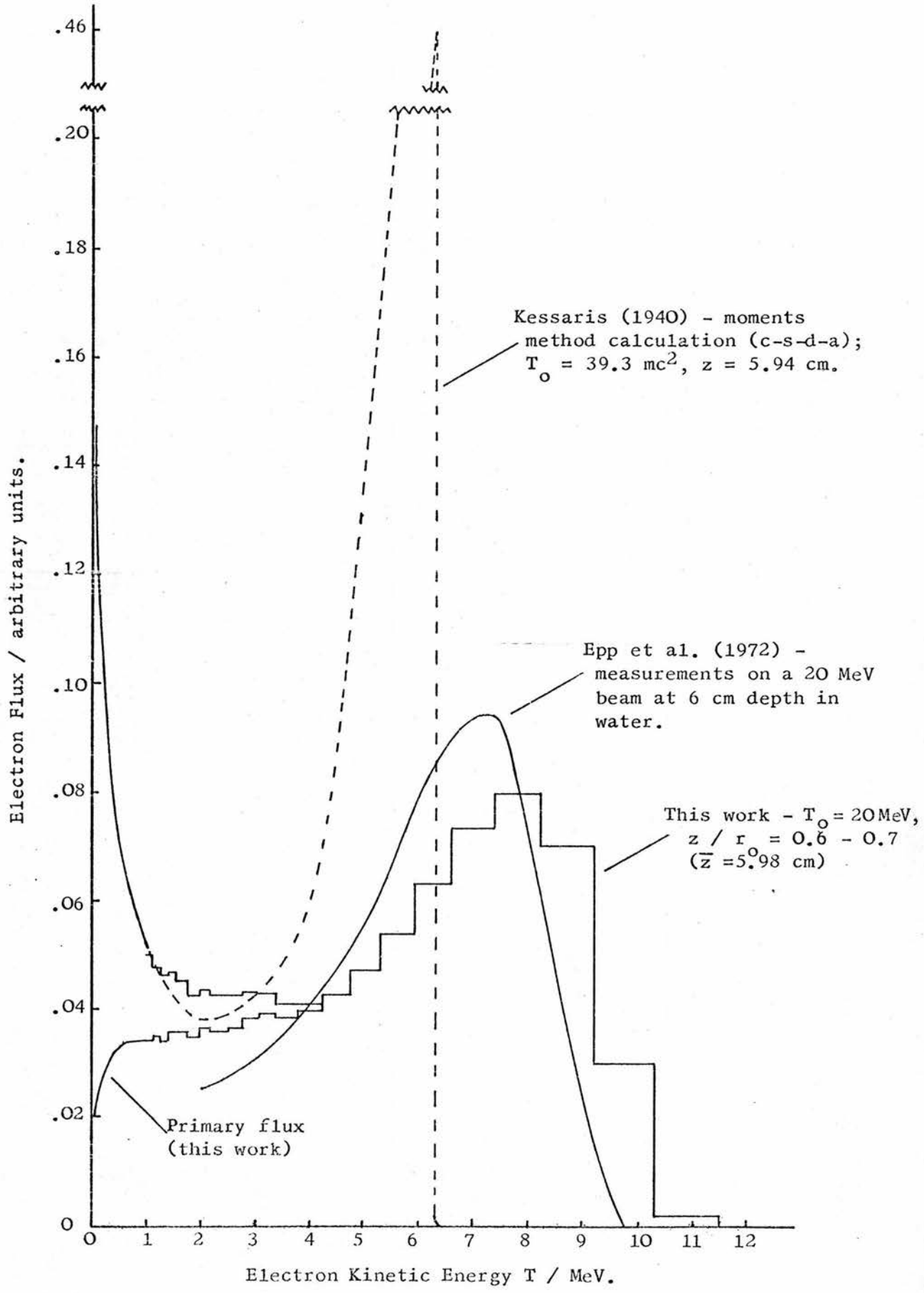

Epp et al. (1965, 1972) have measured the electron flux spectrum down to 2 MeV arising from broad, monoenergetic electron beams of energies 10, 15 and 20 MeV incident on a water phantom. Figure 7.7 shows how their measured spectrum for a 20 MeV beam at a depth of 6 cm (also given in fig. 1.10) compares with the calculated histogram for the $z/r_o = 0.6 - 0.7\ r_o$ geometry ($\bar{z} = 5.98$ cm). The absolute values of the flux cannot be compared but the shapes are very similar. The maximum flux from the Epp et al. measurements is at 7.2 MeV, which is about 0.5 MeV lower than the theoretical calculations. This could be accounted for in part by the slight divergence of the beam on which the measurements were carried out. The spectrum derived by Kessaris (1966, 1970) is also shown. Kessaris used the moments method under the continuous-slowing-down approximation. His values have been normalized such that the flux below 1 MeV is the same as that calculated in the present work. The lack of a tail on Kessaris' spectrum at the high-energy end is due to the fact that his theoretical treatment did not take account of ionization or bremsstrahlung energy-loss straggling. In addition, the very sharp peak is at about 6.3 MeV, nearly 1 MeV below the experimental value. It can be concluded from this comparison that the Kessaris spectra are somewhat unrealistic at such depths. However, the position of the maxima in Kessaris' results and in the present work were found to be in closer agreement at smaller depths.

It must be borne in mind when comparing the shape of the Monte Carlo spectrum with other work that

the histogram is an average over a 0.1 r_o layer (i.e. Δz = 0.92 cm for T_o = 20 MeV). Thus a certain amount of the broadening at the high-energy end is 'artificial'. As emphasised earlier, reducing the layer thickness necessitates increasing the number of histories, if the statistical accuracy is not to be decreased.

Figure 7.8 LOCAL ENERGY DISSIPATION SPECTRUM 20 MeV ELECTRONS.
(Δ = 100 eV)

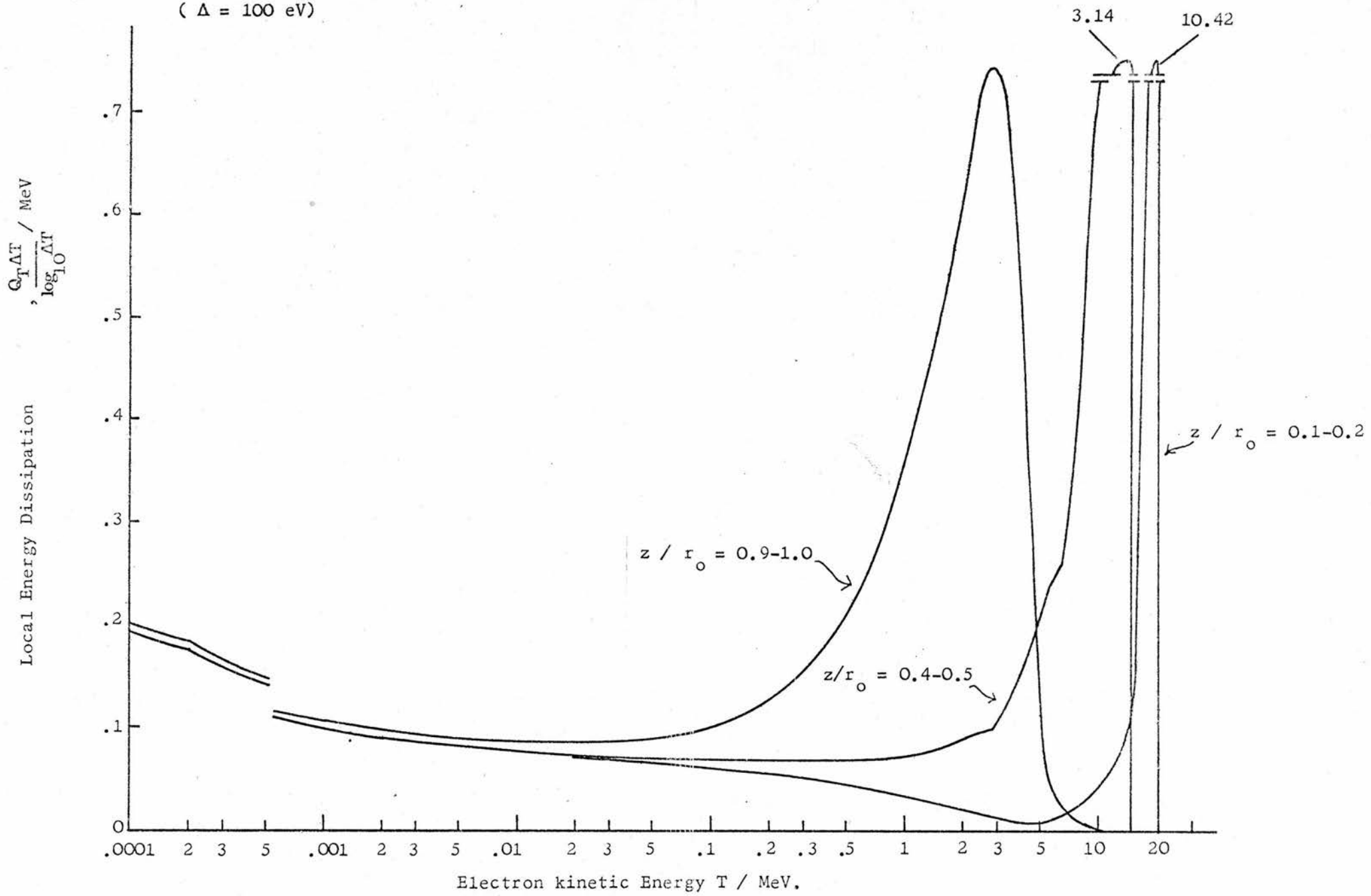

7.3 LOCAL ENERGY DISSIPATION DISTRIBUTIONS

7.3.1 The Q_T Spectrum

The local energy dissipation spectrum, Q_T, where 'local' refers to energy transfers less than a cutoff Δ, is derived from the flux spectrum, F(T) using the restricted collision stopping power, $L(T,\Delta)$. Thus

$$Q_T \Delta T = F(T).L(T,\Delta)\ \Delta T \qquad .....(7.1)$$

where $Q_T \Delta T$ is the local dissipation by the electron flux in the interval ΔT (see equ. 6.1 for example).

Burch (1959) made use of this spectrum, with a 100 eV cutoff, in his theoretical evaluation of $G(Fe^{3+})$ as is also the case in the present work in chapter 11. As indicated by the above expression, the Q_T spectrum is simply related to the more fundamental quantity, the electron flux spectrum. It will suffice to give the Q_T spectra at three depths for a 20 MeV electron beam (figure 7.8), normalized to 1 MeV total dissipation. The area under the curves represent the amount of energy locally dissipated by different sections of the flux spectrum. The 'kink' at 200 eV is due to the fact that the values of L_{100} and L_{total} are equal between 100 and 200 eV. (Recalling from section 5.4.3 that the flux in band 1, F_1, is given by N_1/L_{total}, then it can be seen that below T_c, $F(T).L(T,\Delta)$ in equ. 7.1 is equal to $N_1.L_{100}/L_{total}$.) Note that the total area under the curve between zero and 100 eV (not shown) would be equal to the track-end term. No comparisons can be made for high-energy electron beams with the Burch calculations of the Q_T spectrum as he only considered 1 and 2 MeV electrons slowing down in an infinite medium.

Figure 7.9 CUMULATIVE LOCAL ENERGY DISSIPATION - T_o = 20 MeV.
(or fraction of local absorbed dose contributed by electrons with K.E. greater than T)
Δ = 100 eV.

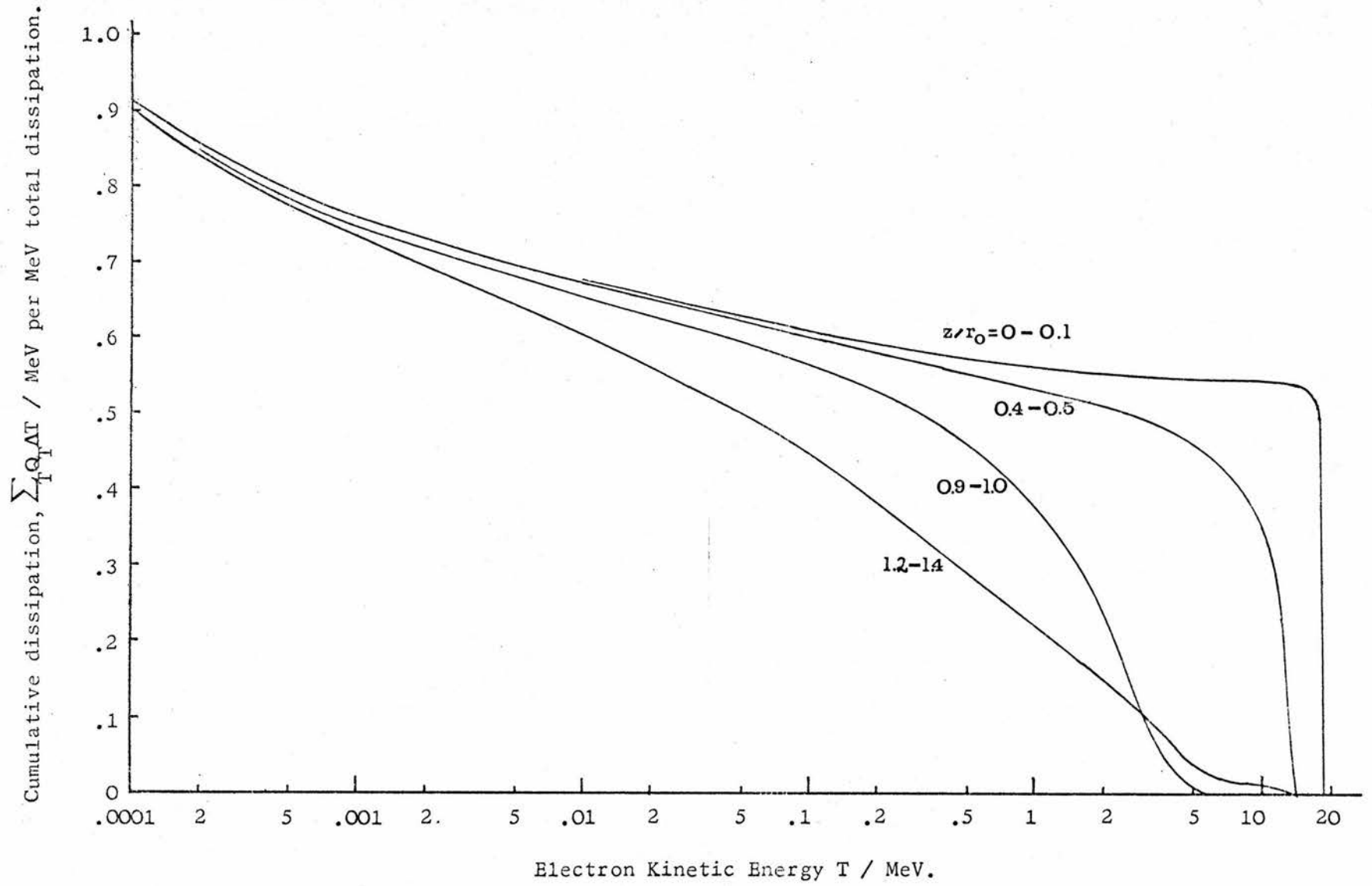

Table 7.4 100 eV TRACK ENDS - ENERGY DISSIPATION

Geometry z/r_o	Energy Dissipation (MeV)			
	T_o = 5 MeV	T_o = 10 MeV	T_o = 20 MeV	T_o = 30 MeV
0.0 - 0.1	0.0869	0.0860	0.0856	0.0857
0.2 - 0.3	0.0881	0.0868	0.0864	0.0861
0.4 - 0.5	0.0898	0.0879	0.0869	0.0866
0.6 - 0.7	0.0919	0.0896	0.0879	0.0874
0.8 - 0.9	0.0947	0.0922	0.0897	0.0886
0.9 - 1.0	0.0962	0.0938	0.0913	0.0897
1.0 - 1.1	0.0983	0.0964	0.0933	0.0914
1.2 - 1.4	0.102	0.104	0.0974	0.0957

7.3.2 The Cumulative Distribution

The local energy dissipation spectrum can also be displayed as a cumulative distribution $\sum_{T} Q_T . \Delta T$[+] as in figure 7.9. Here, the ordinate is the fraction of the local energy dissipation, or absorbed dose, contributed by electrons with K.E. greater than T. The value at 100 eV is not unity due to the contribution from the 100 eV track ends (the final term in equation 6.1). This energy is about 0.09 MeV per MeV dissipation and varies only slowly with T_o and depth. This is to be expected since the number of track ends, N_{100}, is proportional to the flux at 100 eV ($F_{100} = N_{100}/L_{total}$). The energy dissipation by the track ends at different depths and energies is given in table 7.4, where the local dissipation by the complete spectrum is 1 MeV. It is interesting to note that Burch's track-end contribution ($Q_T \Delta T$ for the 0 - 100 eV interval) from his 2 MeV electron spectrum, normalized to the same units as in table 7.4, is 0.0902. This is close to the value for T_o = 5 MeV at z/r_o = 0.4 - 0.5, i.e. at a depth where the effective primary energy is about 2.5 MeV.

Berger and Seltzer (1969a) also calculated a cumulative local dose distribution from their electron flux results for electron beams. They used a cutoff of 0.5 keV, so their curves begin at this energy. There is some doubt as to whether the 0.5 keV track ends are included in the total local dose as their distribution does go to unity at T = 0.5 keV (see also section 6.5).

[+] Note that $\sum_{0} Q_T . \Delta T$ calculated from the flux spectrum before normalization is the quantity D_{100} (see section 6.4.4).

Berger and Seltzer drew some general conclusions from their cumulative dose distributions for high-energy electron beams which are also given in ICRU (1972). In the ICRU report it is stated that, except at conditions of great depth, about 25% of the total absorbed dose is produced by electrons with energies less than 0.1 MeV and also that about 70% of the total dose is produced by electrons above 1 MeV. From figure 7.9, these figures would be 40% and 55% respectively. Setting aside the question raised above about the inclusion of the dose from the track ends, which anyway could not influence the 70% ICRU figure, it must be said that such conclusions are only meaningful <u>if</u> the value of the cutoff is specified. The 'total absorbed dose' that ICRU mention is actually the dose delivered in transfers less than 0.5 keV. In the present case the transfers are less than 0.1 keV and so, not unnaturally, the figures for fractions of the local dose delivered by different parts of the spectrum are not the same.

Figure 7.10 ELECTRON BEAMS : DEPTH-DOSE CURVES IN WATER.
(Smoothed values from MC histograms)

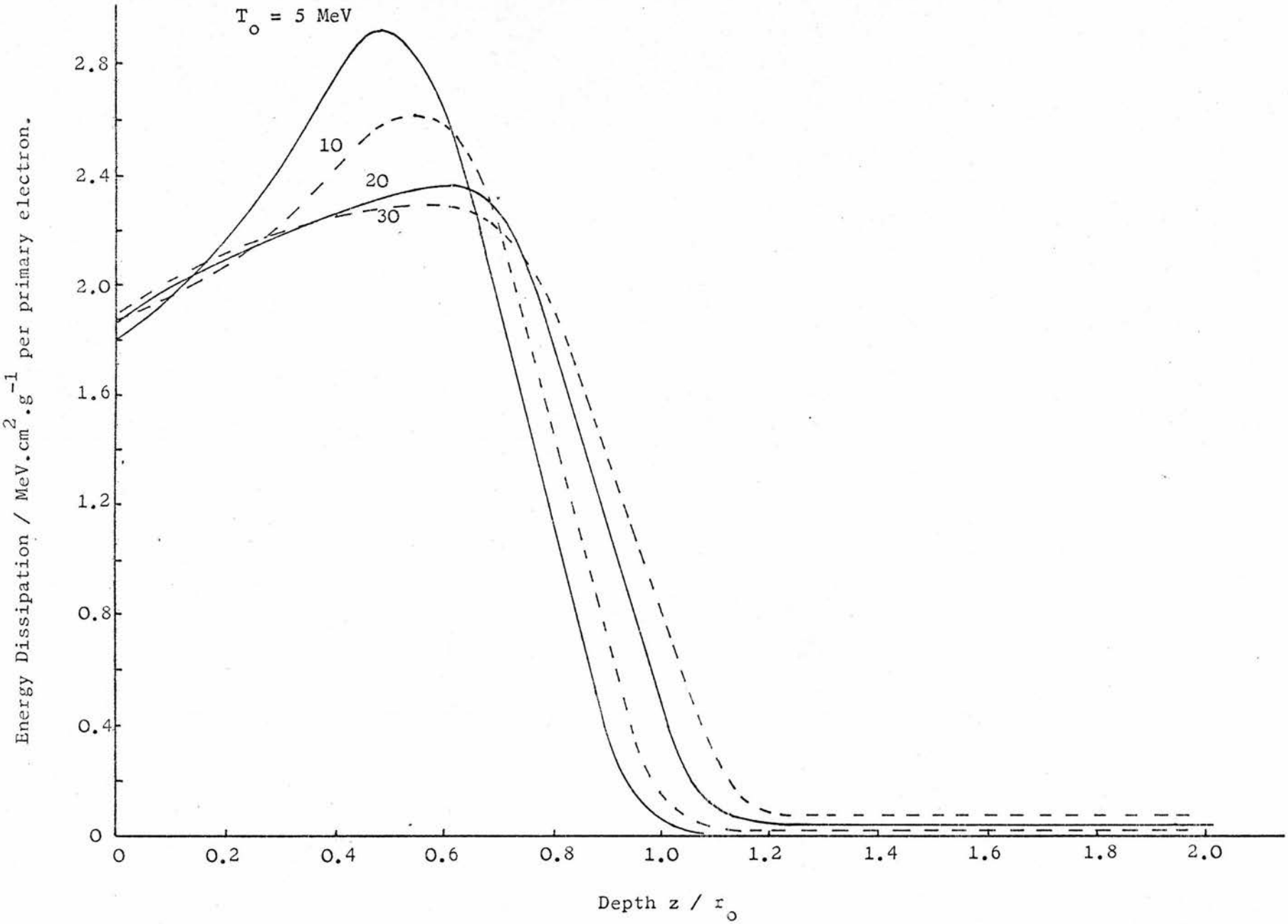

Figure 7.11 COMPARISON OF ELECTRON DEPTH-DOSE CALCULATIONS
(20 MeV electron beam in water)

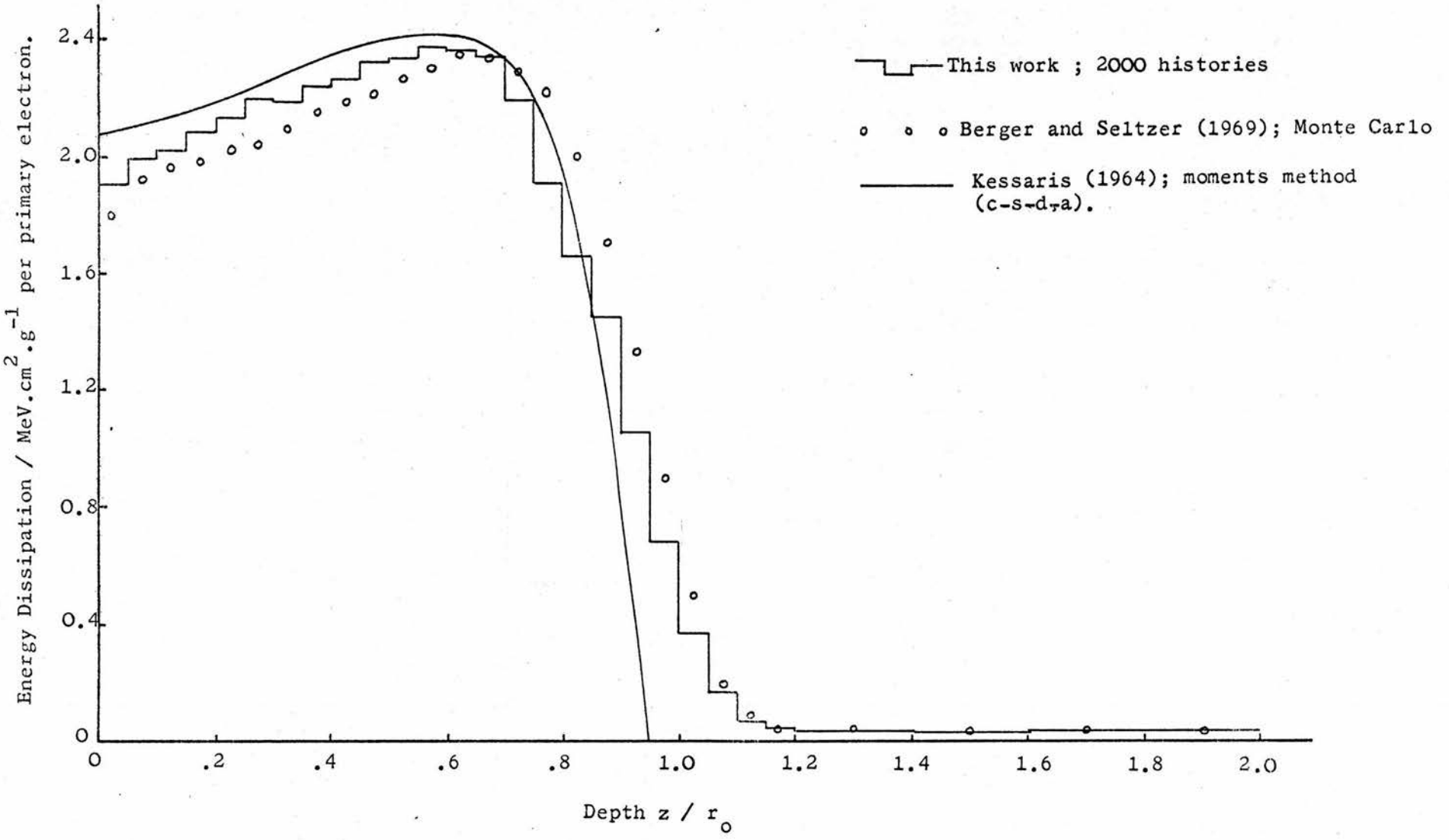

7.4 DEPTH-DOSE CURVES

Depth-dose curves drawn from the histogram computer output are given for the four incident electron energies in figure 7.10. The dose beyond the electron range due to bremsstrahlung is only significant at the two higher energies. The general trend towards a flatter maximum with increasing energy is also exhibited in the depth-dose curves calculated by Berger and Seltzer (1969a). The so-called practical range, r_p, defined as the point where the extrapolation of the linear portion of the depth-dose curve meets the z/r_o axis, is given in table 7.5 below, alongside the Berger and Seltzer values. The agreement is within 1% at all four energies.

T_o(MeV)	$\frac{r_p}{r_o}$(B+S)	$\frac{r_p}{r_o}$(fig.7.10)	$\rightarrow r_p$(cm)
5	0.952	0.955	2.40
10	1.002	1.008	4.94
20	1.075	1.085	9.98
30	1.144	1.155	15.0

Berger and Seltzer state that r_p values are insensitive to the beam geometry and that their figures are in good agreement with the experimental values obtained by Svensson and Pettersson up to 30 MeV.

The depth-dose results at T_o = 20 MeV from the present work, drawn as a histogram, and the Berger and Seltzer (1969) calculation are compared in figure 7.11. The differences are fairly small except in the 0.75 - 0.95 r_o region where the Berger and Seltzer values are as much as 15% higher. The Kessaris (1964) curve has been included

to demonstrate the effect of neglecting energy-loss straggling on the results.

Comparisons of calculated depth-dose curves with measured distributions are complicated by the difficulty in realizing experimentally radiation geometries and electron beams that correspond to the theoretical conditions. This has been discussed in some detail by Kessaris (1964). Up to recently, no measured depth-dose distributions produced by high-energy clinical electron beams were in particularly good agreement with theoretical values. Due to the many 'non-ideal features' of the practical irradiation situation it was difficult to say whether theory was inadequate or not (Lillicrap and Rosenbloom, 1972).

A recent paper by Brahme et al. (1975) has clarified the situation considerably. They measured the central axis depth-dose distributions of the 10 MeV electron beam from a medical microtron accelerator. The microtron accelerator differs from other accelerators in that the beam is more nearly monoenergetic, the geometry is 'cleaner', and there is a much smaller amount of scattering material in the beam path. Brahme et al. found that the shape of the depth-dose distribution from the microtron differed appreciably from those of existing betatrons and linear accelerators and was in much closer agreement with the Monte Carlo calculations of Berger and Seltzer, and hence with the results of this work.

7.5 CONCLUSIONS

The results of the calculation of the depth-dependent electron flux spectra are in excellent agreement with those obtained by Berger and Seltzer. In particular, the practically universal shape of the electron flux below about 50 keV is confirmed by the present work. The change in shape of the high-energy end of the spectrum with increasing depth and the depth-dose curves indicate that the penetration and scattering of the primary electron beam is very similar in the two calculations. This agreement with Berger and Seltzer, while not unexpected in view of the general similarity of the theoretical methods, is nevertheless encouraging given that there are substantial differences in the details of the computations. Where Berger and Seltzer used the more sophisticated Goudsmit-Saunderson multiple-scattering distribution and the Spencer-Fano theory for the slowing-down spectrum below T_c, the Gaussian distribution and a modification of Burch's energy-band scheme based on the c-s-d-a have been used in the present calculations. The inclusion of Auger electrons, a feature not included in the Berger and Seltzer work, seems to have made relatively little difference to the electron flux at low energies.

Some comments must be made on the accuracy of the results presented. It will be appreciated that it is difficult to estimate quantitatively the effect of the approximations employed in the simulation of the transport, energy loss and scattering of the electrons. It has been seen, for instance, that the precise nature of the

multiple-scattering distribution seems to have at most a very small influence on the results of, say, the flux spectrum at a particular depth. However, the effect of the differences in such distributions cannot be separated from the effect of differences in the treatment of energy-loss straggling and so on. Another factor is the particular value chosen for the mean ionization potential, I, which affects the penetration of the primary electrons through the stopping power.

Having made the above points, it does seem reasonable to expect that the flux spectrum in the energy range between 1 MeV and 1 keV, due almost entirely to secondaries, should be accurate. Below about 1 keV, the stopping power is in some doubt, as discussed in sections 5.3 and 5.4.4. However, this will not affect the conclusions about the similarity of the low-energy end of the spectrum at different energies and depths. Above 1 MeV, the flux is determined by the treatment of the transport of the primary electrons which brings in the difficulties discussed. Comparison with the scanty experimental data available is encouraging, bearing in mind the idealized geometry of the calculations.

There is also the question of the statistical accuracy of the results to consider. It is possible to compute the standard deviation on the values of the electron flux, but in general this is not a simple calculation and has not been attemptedin this work. The statistical uncertainty can more simply be estimated from the 'bumpiness' of the histograms produced. Naturally, the number of histories has been chosen to be sufficient

to reduce the uncertainty of the results to a small percentage in most cases. It cannot be claimed, however, that 2000 histories was a large enough number to determine accurately the high-energy end of the flux spectrum at great depths as shown in fig. 7.4. On the other hand, it is not important to know the spectrum at such depths, where the absorbed dose is a very small fraction of its maximum value.

For present purposes, the absolute accuracy of the flux spectrum at different energies and depths is much less important than the accuracy of certain quantities averaged over the spectrum, such as stopping-power ratios. Small statistical fluctuations in the flux spectrum can be expected to have a negligible effect on the values calculated for these average quantities. This is discussed further in the appropriate chapters.

CHAPTER 8

PHOTON BEAM RESULTS - ELECTRON FLUX SPECTRA AND RELATED QUANTITIES

8.1 INTRODUCTION

Electron flux spectra at different depths in water irradiated by high-energy photon beams have not so far been obtained by other workers, with the exception of Brysk (1954) for a 40 MV bremsstrahlung beam. It was emphasised in the first chapter that calculations of the important stopping-power ratios for ionization dosimetry had, up to the present time, been made in a very approximate fashion for high-energy photon radiation, in contrast to the attention given to electron beams. The electron flux spectra presented in this chapter allow this state of affairs to be remedied. In addition, the local energy dissipation spectra derived from the flux spectra, together with these distributions for electron beams, are required to investigate the experimentally suspected $G(Fe^{3+})$ difference.

The depth variation of the flux spectra, though always expected to be small compared to that for electron beams, is of interest in illustrating differences in the nature of the energy dissipation by photon beams of maximum energies ranging from 2 MV up to 31 MV. The results presented enable the assumptions usually made about the build-up to electronic equilibrium and the slow change of the equilibrium spectrum with depth to be examined in some detail.

Figure 8.1 DIFFERENCES IN PHOTON SPECTRA FROM X-RAY BEAMS OF THE SAME MAXIMUM ENERGY.
(Johns and Rawlinson, 1972)

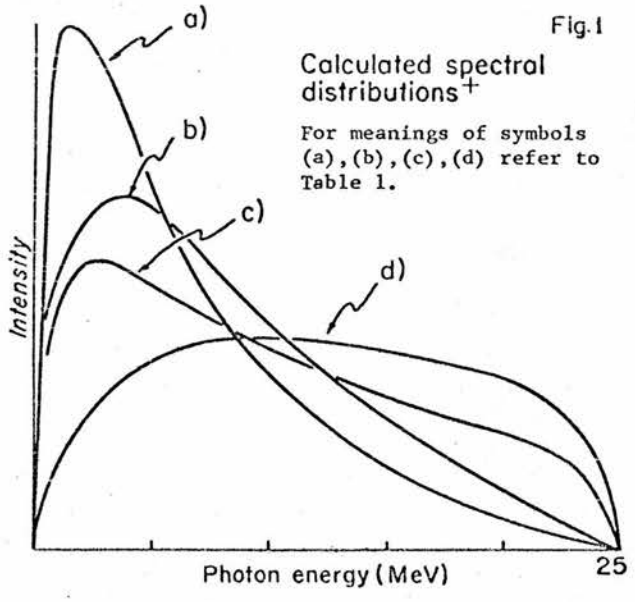

Table 1

Calculations for 25 Mev Bremmstrahlung for four spectra referred to as (a),(b),(c), and (d).

	Absorption in water		
	Average Energy Mev	Peak Depth cm	Effective Attenuation Coeff.
a. Thick target: Pb filter of thickness 17 gm/cm^2 (Linac	6.6	3.1	0.034 cm^{-1}
b. Thick target: Al filter of thickness 26 gm/cm^2	7.8	3.7	0.030 cm^{-1}
c. Thin target: Pb filter of thickness 18 gm/cm^2	9.9	4.4	0.028 cm^{-1}
d. Thin target: Al filter of thickness 32gm/cm^2 (Betatron)	11.6	4.8	0.025 cm^{-1}

+Thin- and thick-target spectra before filtration taken from the literature and adjusted for the filtration given in the above table (J. A. Rawlinson, private communication).

8.2 ENERGY SPECTRA OF PHOTON BEAMS

8.2.1 General

The high-energy photon beams used in radiotherapy, with the exception of ^{60}Co gamma rays, are produced by bombarding a target, usually of tungsten (Z=74) or gold (Z=79), with a beam of monoenergetic electrons. The resulting bremsstrahlung spectrum is not simply a function of the maximum energy of the photons, but is very much influenced by the thickness of the target and the presence of any flattening filter in the beam.

It has been pointed out recently by Rawlinson and Johns (1972) that the x-ray spectrum from a 25 MV linear accelerator (linac) with a thick target and a lead flattening filter is appreciably different to the spectrum from a 25 MV betatron with a thin target and an aluminium flattening filter (see figure 8.1 taken from their 1972 paper). In fact, they found that the 25 MV linac beam was similar to that from a 16 MV betatron.

As some considerable effort had gone into the construction of the cascade simulation to compute electron flux spectra, stopping-power ratios etc., it was clearly important to use 'realistic' photon spectra as input for the calculations. Where possible, it was desirable that that the spectra used should correspond to those produced by the type of high-energy machines on which the measurements in ionization and chemical dosimetry are usually carried out.

8.2.2 Theoretical Calculations

The theoretical formula given by Schiff (1946,1951), for the energy distribution of bremsstrahlung photons produced in the forward direction by electrons of a given energy,predicts photon spectra that are in fair agreement with experiment for thin targets above 10 MV (ICRU, 1962). At low energies, and for thick targets, the theoretical situation is less satisfactory.

For thick targets (i.e. where the electrons are completely stopped, as is the case with x-rays produced by linear accelerators) the energy loss and scattering of the electrons within the target must be taken into account. Hansen and Fultz (1960) developed an approximate method of dealing with this, but the only rigorous treatment in the energy range between 1 and 100 MeV has been the extensive Monte Carlo cascade computations by Berger and Seltzer (1970). These workers obtained good agreement with experimental results of O'Dell et al. (1968) for the photon spectra produced by 10 and 20 MeV electrons bombarding a thick tungsten target.

While the Monte Carlo photon-electron cascade simulation developed in this work could have been modified to deal with a high Z medium, much as tungsten, and so produce thick-target x-ray spectra, the extra complications and cost of the computer time would not have been justified. In particular, a more exact treatment of the energy and angular distributions of bremsstrahlung photons would have been necessary. A further point worth making is that the details of the maximum photon energy as well as the

Figure 8.2 MEASUREMENTS BY BENTLEY ET AL. (1967).
(2 MV X-ray beam)

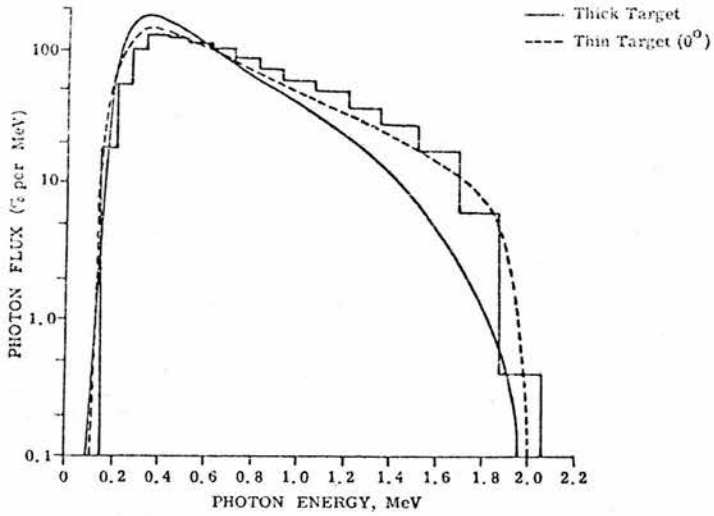

Fig. 6. Van de Graaff Generator; the histogram shows the photon flux spectrum. The smooth lines are the theoretical thick target and thin target spectra for an electron beam of energy 2·0 Mev. Target 3·04 gm cm^{-2} tungsten, external filtration: 0·89 gm cm^{-2} brass.

Figure 8.3 MEASUREMENTS BY LEVY ET AL. (1974).
('25 MV' linac)

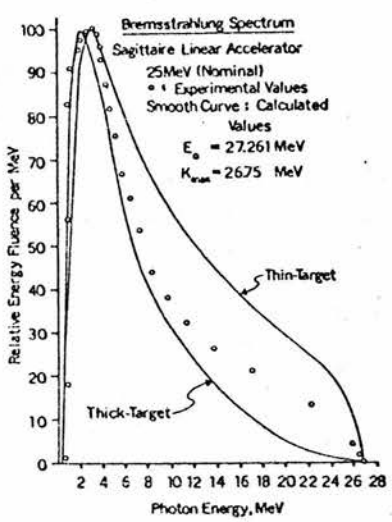

FIG. 6. A comparison of relative energy fluence per MeV interval vs photon energy, MeV, for thin- and thick-target calculated values and the experimental values. E_0 and K_{max} are the total electron energy and maximum photon energy, respectively.

composition and dimensions of the targets and flattening filters for many of the high-energy machines in clinical use are not readily available, in general, and can vary from one machine to another of the same manufacture. Thus, however accurate the calculation of the emerging photon spectrum might be, the parameters used in the computation may not correspond exactly to any of the photon beams in actual use.

8.2.3 Experimental Determinations

There are now several reports in the literature of measured photon energy distributions for x-ray beams from clinical machines. Bentley et al. (1967) determined the spectra produced by a 2 MV Van de Graaf generator and two 6 MV linacs. They used a NaI crystal spectrometer to measure the spectrum scattered at a particular angle from an aluminium sheet placed in the x-ray beam. The energy distribution of the primary radiation was deduced from the Klein-Nishina formula.

Their results for the 2 MV radiation are reproduced in figure 8.2, together with theoretical curves corresponding to thin and thick target spectra. The latter was evaluated using the approximate treatment of Hansen and Fultz. Surprisingly, the measured histogram is in close agreement with the thin-target calculation, emphasising the inadequacies in the theory at relatively low energies. For the measurements of the spectra from two different 6 MV linacs, they obtained closer agreement with the thick-target calculations. One of the machines, however, the Vickers, was found to have a maximum photon energy of

Figure 8.4 VARIATION OF MASS ATTENUATION COEFFICIENT WITH PHOTON ENERGY FOR MATERIALS USED IN FLATTENING FILTERS.
(Values from Hubbell, 1969)

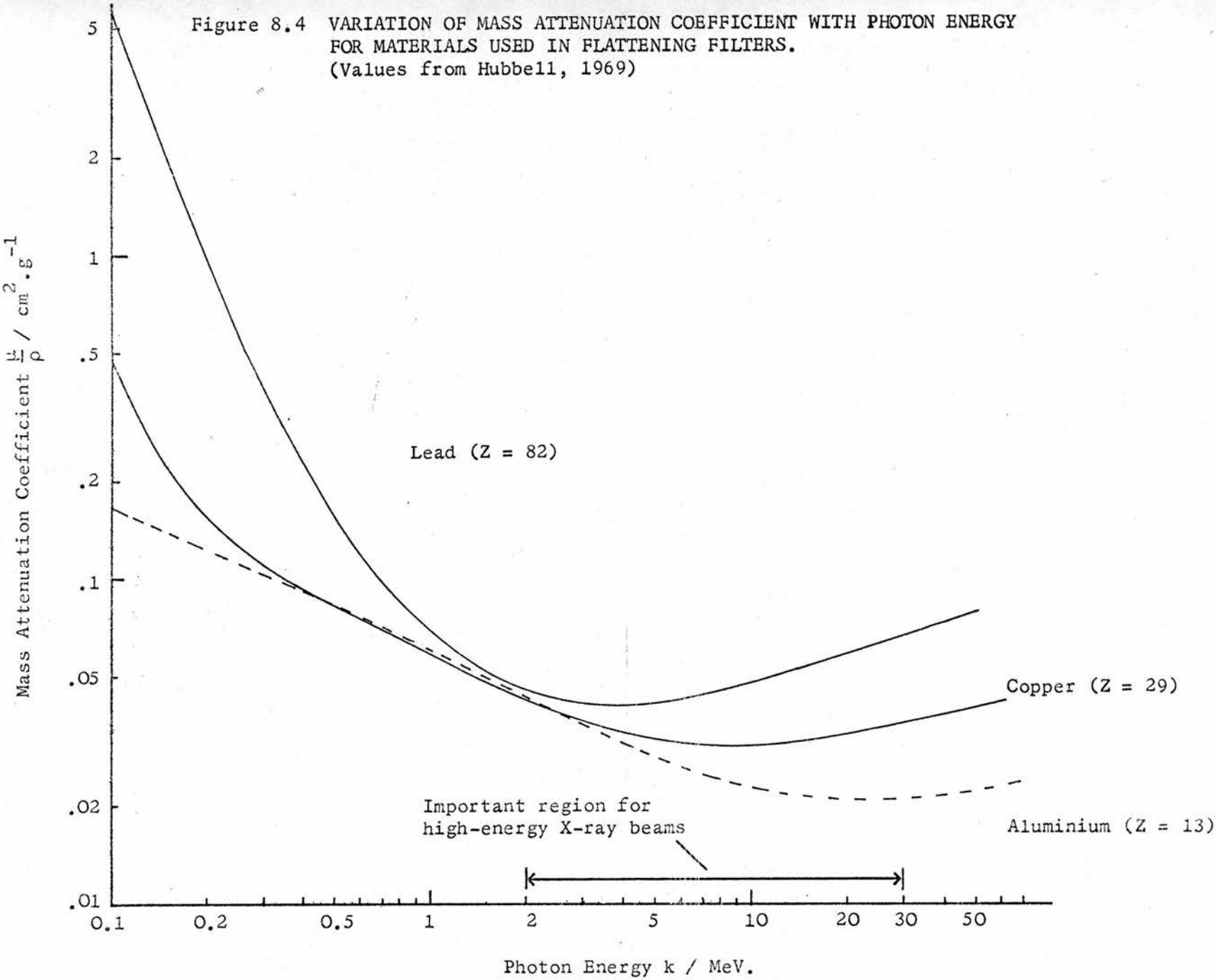

only 4.5 MeV despite its nominal 6 MV rating.

Levy et al. (1974) have recently measured the photon spectrum from a 19 MV betatron and a 25 MV linac using a similar technique to Bentley et al. In common with Bentley et al., they found only moderate agreement with theoretical predictions at the high-energy end. Figure 8.3 for the Sagittaire linac is taken from their paper. Note that the measured maximum photon energy, 26.75 MeV, is appreciably different from the nominal machine rating of 25 MV. The maximum energy fluence occurred at 3.4 MeV for both the linac and the betatron which Levy et al. attribute to the presence of the lead flattening filter in both machines.

8.2.4 Flattening filters

The effect of different flattening* filters on high-energy photon beams can be understood from figure 8.4 which shows the variation of the narrow-beam mass attenuation coefficient, μ/ρ, with photon energy. For lead, μ/ρ has a minimum at 3-4 MeV, and then steadily increases. It is clear that this has the effect of softening a high-energy beam. In aluminium, by contrast, the attenuation decreases with increasing energy up to about 30 MeV, and hence will tend to harden a photon spectrum. Copper, which is sometimes used instead of lead in high-energy machines, varies relatively little between 2 and 40 MeV and will have only a small effect on the spectrum. All three materials, however, will reduce the number of very low-energy photons.

*Also known as compensating filters.

Figure 8.5 31 MV BETATRON X-RAY SPECTRUM : EFFECT OF LEAD AND ALUMINIUM FILTRATION.

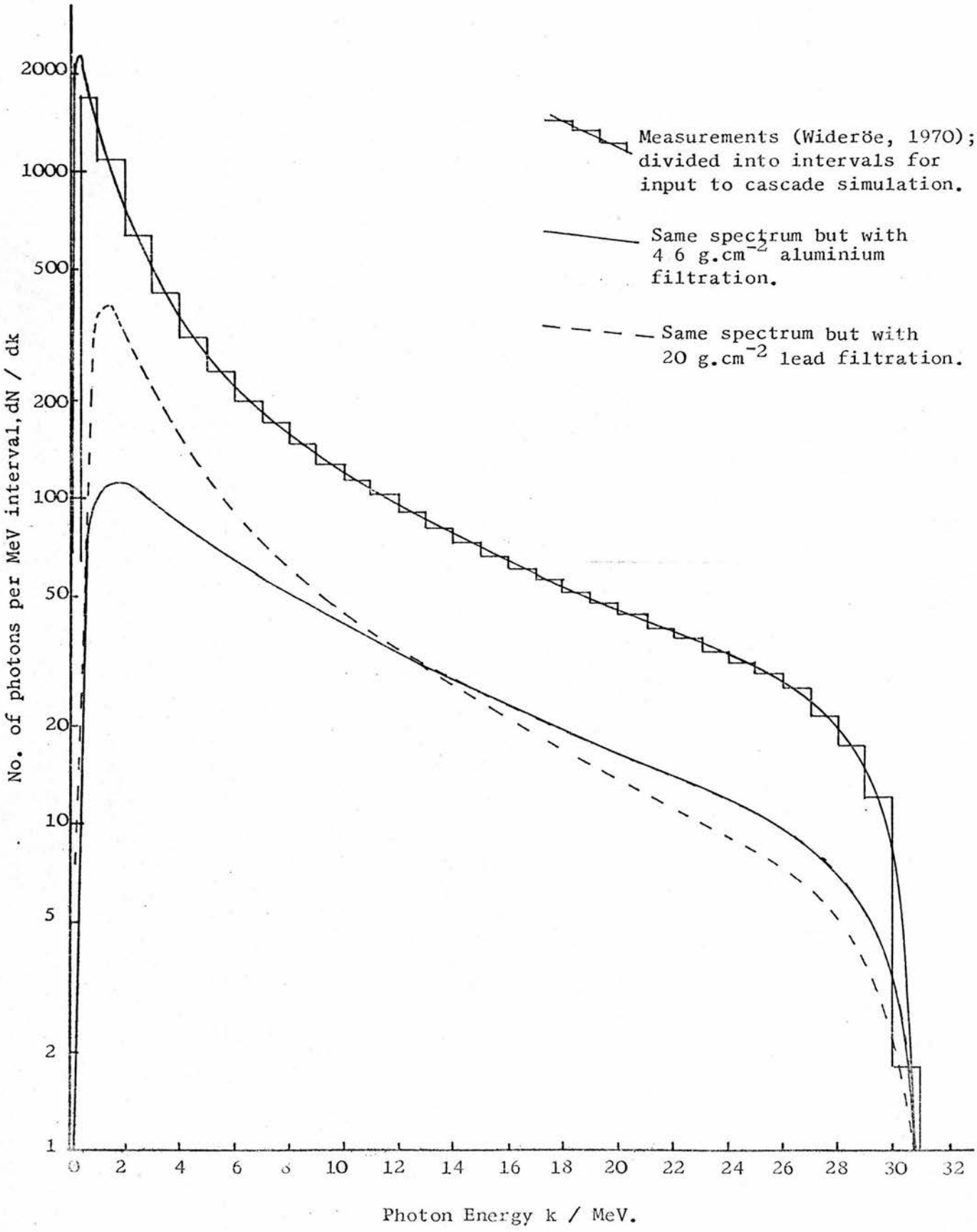

Figure 8.6 SPECTRUM OF SCATTERED PHOTONS FROM A COBALT-60 TELETHERAPY UNIT.

(adapted from fig. 6(c) in ICRU, 1970a)

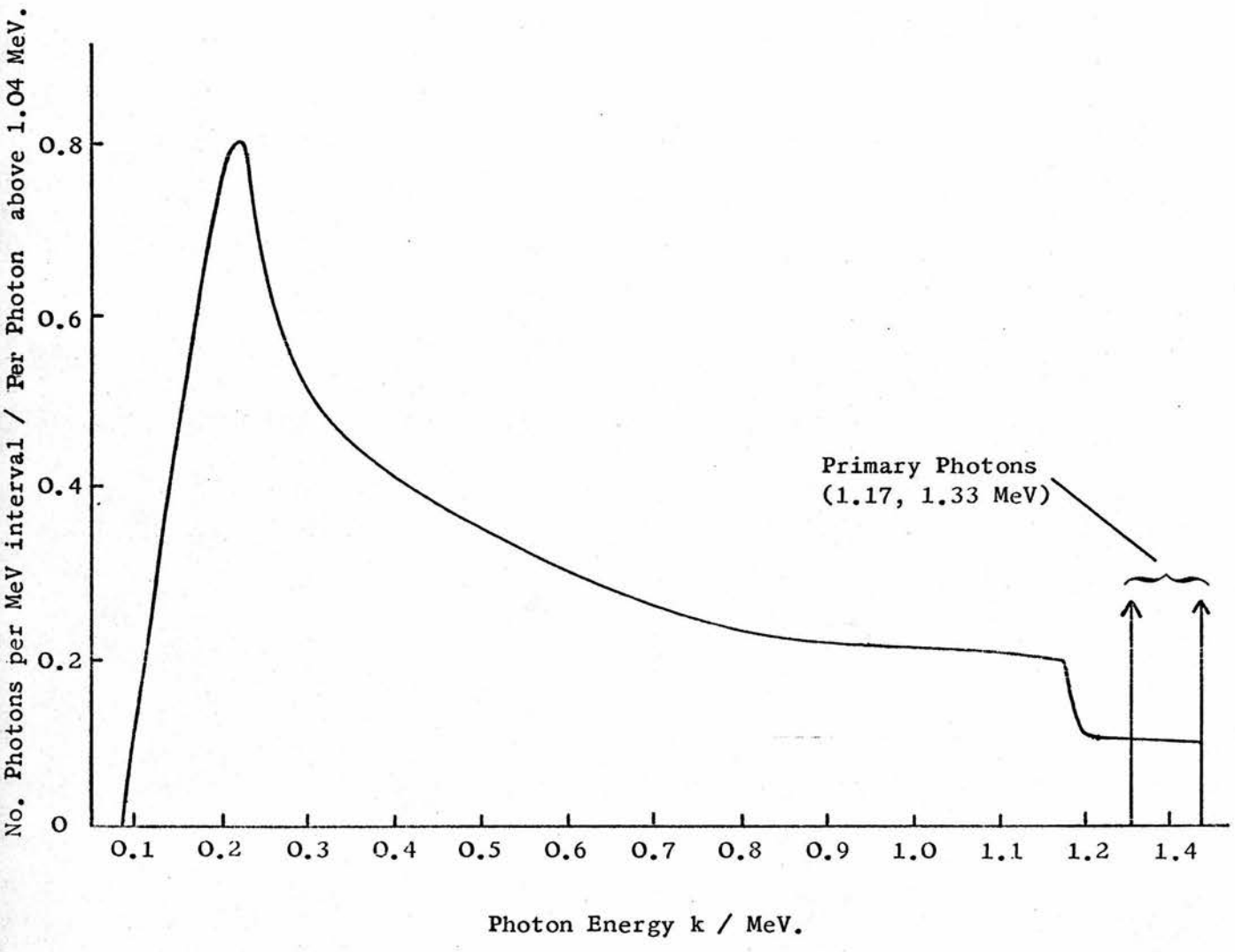

The effect of lead and aluminium filtration on a 31 MV betatron spectrum is shown in figure 8.5. The 'unfiltered' distribution is taken from Wideröe (1970) and is a Schiff spectrum modified for x-ray absorption in the glass wall of the betatron doughnut. Wideröe showed that this spectrum was in good agreement with measurements down to 6 MeV by Wäffler et al. on a Brown-Boveri betatron. The thicknesses of the filters, 20 $g.cm^{-2}$ Pb and 46 $g.cm^{-2}$ Al, were chosen such that the energy influence was reduced by about 60%. The figure for the lead filter is typical for high-energy machines. It should be mentioned that as the flattening filters are cone-shaped, the filtered spectrum will vary across the beam. Thus the spectra in fig. 8.5 correspond to the centre of the beam cross-section, where the thickness of the filter is a maximum.

8.2.5 ^{60}Co radiation

The photon beams for which calculations have been made include ^{60}Co gamma radiation. Although the cobalt source emits equal numbers of gamma rays of energy 1.17 and 1.33 MeV, the actual beam from a teletherapy unit contains an appreciable amount of lower energy scattered photon radiation. Measurements by several workers and recently a series of comprehensive Monte Carlo calculations by Berger have been carried for typical Cobalt therapy units (ICRU, 1970a). One of the scattered photon spectra given in the ICRU report is illustrated in figure 8.6. The units are photons per MeV per photon above 1.04 MeV, which is the normalization that Aitken and Henry (1964) employed

in making the measurements. The ratio of the exposure due to scattered radiation to that due to primary radiation for such a spectrum has been calculated as about 0.14 by Berger (ICRU, 1970a).

Table 8.1 PHOTON BEAM COMPUTATIONS

Radiation	Energy Spectrum	$\bar{k}_{int}$ (MeV)	Number of Histories	T_o (MeV)	ZEND[1] (cm)	CPU[2] time (sec)	Designation
2 MV (V.de.Gr.)	Van de Graaf Generator Thick tungsten target, brass filtration Measured by Bentley et al. (1967) - see fig. 8.1	0.94	16x500	1.008	30	133	A
^{60}Co (P+S)	Primary + scattered radiation. Taken from fig. 6c in ICRU (1970a) - see fig. 8.5	1.18	2x500 (primary) + 12x250 (scat.)	1.008	30	212 (4/75)	B
^{60}Co (P)	Primary radiation only - 1.17, 1.33 MeV	1.26	2x5000	1.008	30	135	C
4.5 MV (linac)	6-MV Vickers linac Thick tungsten target, brass + Al filtration. Measured by Bentley et al.	1.63	17x500	1.008	30	241	D
6 MV (linac)	6-MV Mullard linac Thick gold target, brass + Al filtration meas. by Bentley et al.	2.11	17x500	1.008	30	261	E
13 MV	Schiff distribution; thin gold target, 22 $g.cm^{-2}$ copper filt. (agrees well with meas. 15 MV linac spectrum above 7 MeV - Ward and Dolphin, 1960)	5.91	15x200	2.0168	25	249 (4/75)	F
19 MV (betatron)	Siemens Betatron Thin platinum target 20.4 $g.cm^{-2}$ Pb filtr.[3] Meas. by Levy et al. (1974)	6.912	15x500	1.425	35	750	G
26.8 MV (linac)	Sagittaire Linac Thick tungsten target 33.1 $g.cm^{-2}$ Pb filtr.[3] Meas. by Levy et al. - see fig. 8.2	8.27	16x500	1.425	35	1081	H

Table 8.1 cont'd.

Radiation	Energy Spectrum	$\bar{k}_{int}$ (MeV)	Number of Histories	T_o (MeV)	ZEND[1] (cm)	CPU[2] time (sec)	Designation
26.8 MV	Thin tungsten target 33.1 g.cm^{-2}Pb filtr.[3] Calculated by Levy et al. - see fig. 8.2	10.05	16x500	1.425	35	1485	I
31 MV (Betatron)	Schiff spectrum, with absorption in glass wall, given by Wideröe (1966) - (compares well with meas. on Brown-Boveri betatron). - see fig. 8.4	12.77	16x400 (30.5 - 15.5 MeV) + 16 x 200 (14.5 - 0.2 MeV)	2.0168	35	1314	J
31 MV	Spectrum as for J but extra 20 g.cm^{-2} lead filtration	11.78	16x80 + 15x40.	2.0168	30	456 (4/75)	K
31 MV	Spectrum as for J but extra 46 g.cm^{-2} Al filtration - see fig. 8.4	14.51	16x80 + 16x40.	2.0168	30	482 (4/75)	L

[1]ZEND is the depth at which the photon histories are terminated.

[2]This execution time does not include the extra 7 sec or so per spectrum geometry for the normalization of the flux spectrum and printout of the results (see section 6.4.3).

[3]Details of filtration from R.G. Waggener (private communication).

8.3 DESCRIPTION OF THE CALCULATIONS

8.3.1 Details of the Photon Beams

Computations have been carried out for a total of twelve different photon beams. The characteristics of these beams and other important details about the calculations are given in table 8.1. Where possible, the energy distributions were taken from experimental measurements, some of which have been mentioned in the previous section.

For ^{60}Co, the effect of including scattered radiation on the results can be looked at directly as separate computations for the primary and for the primary + scattered beams were included (C and B in table 8.1). Comparisons between the results for spectra A and B are of particular interest as 2 MV and ^{60}Co are the radiations used for the exposure calibration of ionization chambers (see chapter 10). The 13 MV beam was added in order to fill the gap between 6 MV and 19 MV, but only limited confidence can be placed in the accuracy of the calculated spectrum as Ward and Dolphin (1960) used a method of measuring the spectrum from the 15 MV linac* capable of yielding only approximate results. Also, they made no mention of any flattening filter (a Copper filter has been assumed). The calculated thin-target 26.8 MV spectrum (I) was included in order to look at suspected differences in the stopping-power ratios for beams of the same nominal energy i.e. H and I. Similarly, the effect of a different

---

*This 15 MV linac was one of the machines on which Law and Naylor (1971) carried out the determinations of $G(Fe^{3+})$ that showed up the puzzling G-value difference between electron and photon beams.

composition for the flattening filter for the 31 MV betatron beam can be investigated from the results of spectra K and L.

The photon energy distributions were represented by a manageable number of energy intervals, generally of equal width, with the same number of histories per interval weighted so as to produce the required energy distribution (see section 6.4.1.2). The number of intervals and histories per interval is given in the 4th column of table 8.1 The third column, $\bar{k}_{int}$, is the average photon energy calculated from the intensity spectrum i.e. weighted by the photon energy. It provides an indication of the quality of the beam. Note that there is a difference of 2.7 MeV in the $\bar{k}_{int}$ values for the two filtered 31 MV spectra (K and L), and an appreciable difference for the thin and thick target 26.8 MV beams (H and I).

8.3.2 Geometry

The irradiation geometry for the calculations is the same as that for the electron beams (see section 7.1.2). Again, when interpreted as a broad parallel beam incident on a large water phantom, with the results corresponding to those that would be measured by a small detector on the central beam axis, this is a fairly close approach to the usual experimental situation. It must be remembered, however, that scatter from the edges of the beam is more significant for primary photons than for primary electrons as the photon mean free path is very much greater than the electron range, even at high energies (mfp in water for 20 MeV photons is 55 cm compared to a c-s-d-a range of 9.2 cm for 20 MeV electrons).

With regard to the electron flux spectrum geometry, there is no convenient scaling factor for photon beams, unlike r_o for electrons. For therapy and dosimetry purposes, information is required about the dissipation energy down to a depth of 20 cm or more for all energies from 2 MV upwards. Thus the range of depths of interest is similar for all the photon beams. For absorbed dose calibrations, ICRU (1969) recommended that the point of measurement should be at a sufficient depth below the irradiated surface so that possible electron contamination of the beam could produce no appreciable change in the calibration factor and so that the electron flux spectrum could be approximately calculated by a depth-independent method i.e. the depth must be beyond the build-up region. Table 8.2, which follows, gives these depths:

Radiation	Depth of Water
^{137}Cs, ^{60}Co	5 cm
2 MV-10 MV	5 cm
11 MV-25 MV	7 cm
26 MV-50 MV	10 cm

For all the beams described in table 8.1, it was ensured that one of the geometries for which the spectrum was calculated should have a mean depth given by the above table, referred to as the calibration geometry.

For most of the computations, the geometries covered the region from z = 0 to z = ZEND in 1 or 2 cm 'slices'. For the 2 MV beam, for example, the subdivisions (in cm) were: 0-1, 1-2, 2.5-3.5, 4.5-5.5.(cal.), 8-10, 14-16

and 18-20. No attempt was made to look in detail at the build-up region at this x-ray quality, as the maximum of the depth-dose curve occurs within the first centimetre of the water medium, and would consequently be very difficult to measure anyway. The electron Monte Carlo cutoff, T_c, was set at 1.008 MeV. Thus very little of the total CPU time was required for the electron MC histories. The transport of electrons could only be a minor influence on the results for the 2 MV beam.

For the 31 MV betatron beam (J), the flux spectrum was computed for the subdivisions (cm): 0-2, 4-6, 9-11 (cal.), 18-20 and 26-28. T_c was set at 2.0168 MeV for these 2 cm 'slices'. At this quality there is an appreciable build-up region, over the first 5 cm or so. In fact, in order to look in somewhat finer detail at this region, a second computation was carried out with 1 cm intervals over the first 7 cm, with T_c being decreased to 1.158 and ZEND to 20 cm. Similar re-runs were made for the 26.8 MV thin and thick target beams (H and I).

It will be noticed in table 8.1 that only relatively few histories were executed for the 13 MV spectrum (F) and the two filtered 31 MV spectra (K and L). These runs, carried out some time after the others on the slower and more costly 4/75 computer, were added primarily in order to look at the stopping-power ratios at the calibration depth. For this purpose, it was sufficient to compute the electron flux spectrum over a 'thick' slice*(2-12 cm for

---

*This was deduced on the basis of the results already calculated, and <u>not</u> assumed in advance.

F, 4-24 cm for K and L), thus requiring a smaller number of histories. A further reduction in run time would have been achieved by increasing T_c, but this could not be done as the calculation of the depth-independent electron flux spectrum (see chapter 5) below T_c did not take into account bremsstrahlung production, which cannot be assumed to be negligible above 2 MeV.

Figure 8.7 ELECTRON FLUX SPECTRA FOR X-RAY BEAMS
(calibration depths)

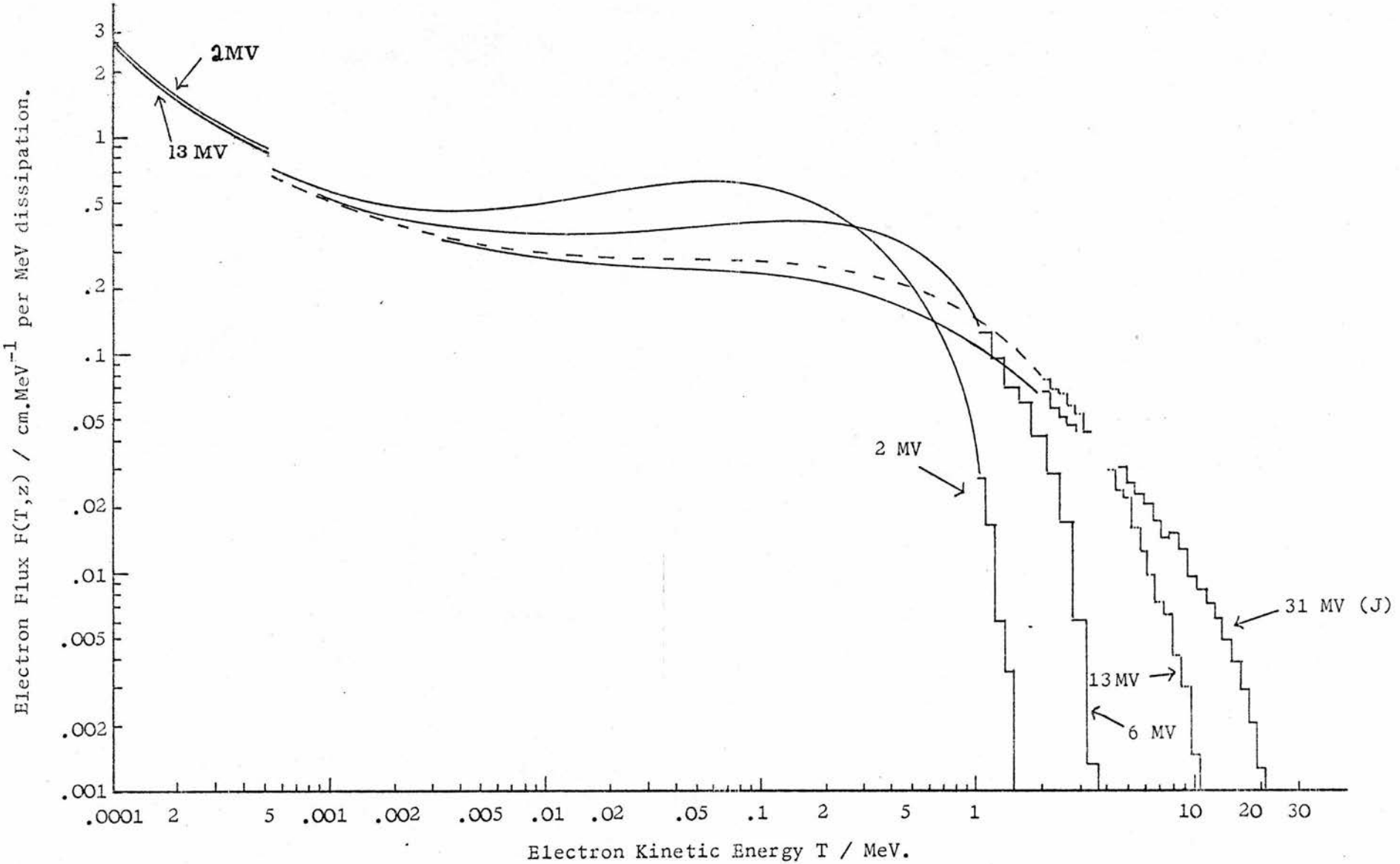

Figure 8.8 COMPARISON OF ELECTRON FLUX SPECTRA FROM 2 MV X-RAY AND COBALT-60 GAMMA RAYS. (Calibration depth)

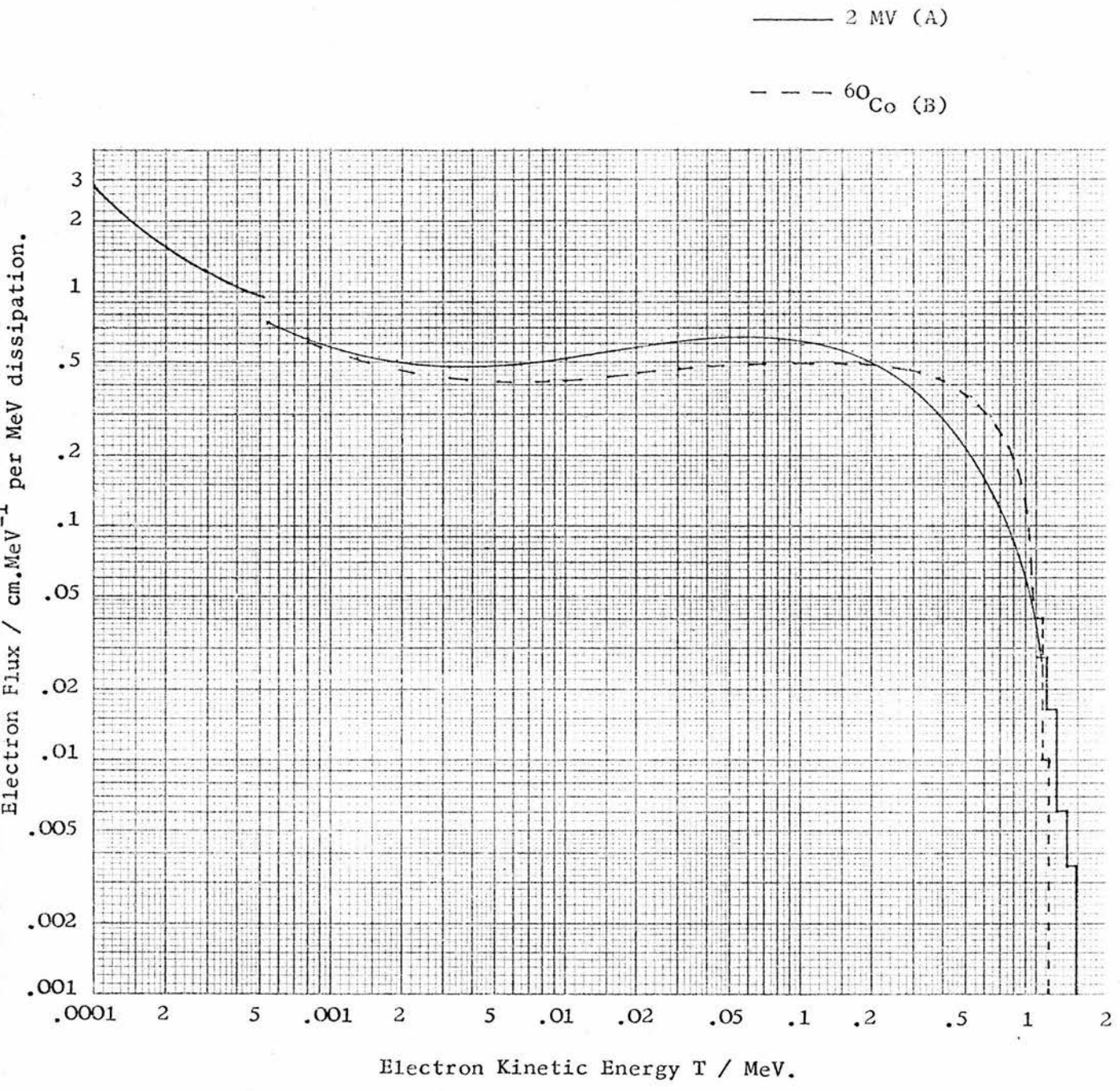

8.4 ELECTRON FLUX SPECTRA

8.4.1 Different Photon Beam Qualities

The electron flux spectra, normalized to unit absorbed dose, produced in water by a range of photon beams are illustrated in figure 8.7. The 2 MV x-ray spectrum is the 'softest' of the qualities considered in this work, and the 31 MV spectrum is the 'hardest'. The spectra all correspond to the calibration depth. The flux at 100 eV hardly varies at all, the value for 2 MV radiation being only 12% greater than that for the 31 MV radiation. The discontinuity due to the Auger electrons is about the same size for all the spectra. It is apparent that the flux spectrum is practically constant below 20 keV or so for the 13MV and 31 MV spectra, but the same cannot be said of the 6 MV and 2 MV beams, which only converge below about 1 keV. Thus generalizations about the independence of the electron flux for different incident beam energies, as for the electron beams, would appear to apply only to x-ray beams with maximum energies above 13 MV or so.

From the results illustrated above, it is clear that more pronounced differences in the shape of the flux spectra are to be expected at the softer beam qualities. The differences between the ^{60}Co and 2 MV flux spectra, both for a geometry with an average depth of 5 cm (calibration depth), are shown in figure 8.8. The ^{60}Co incident beam includes the scattered photon radiation (spectrum B). It can be seen that the Cobalt radiation is the slightly harder of the two, with more electrons above 0.2 MeV and

Figure 8.9 VARIATION OF ELECTRON FLUX SPECTRUM WITH DEPTH : 2 MV X-RAYS.

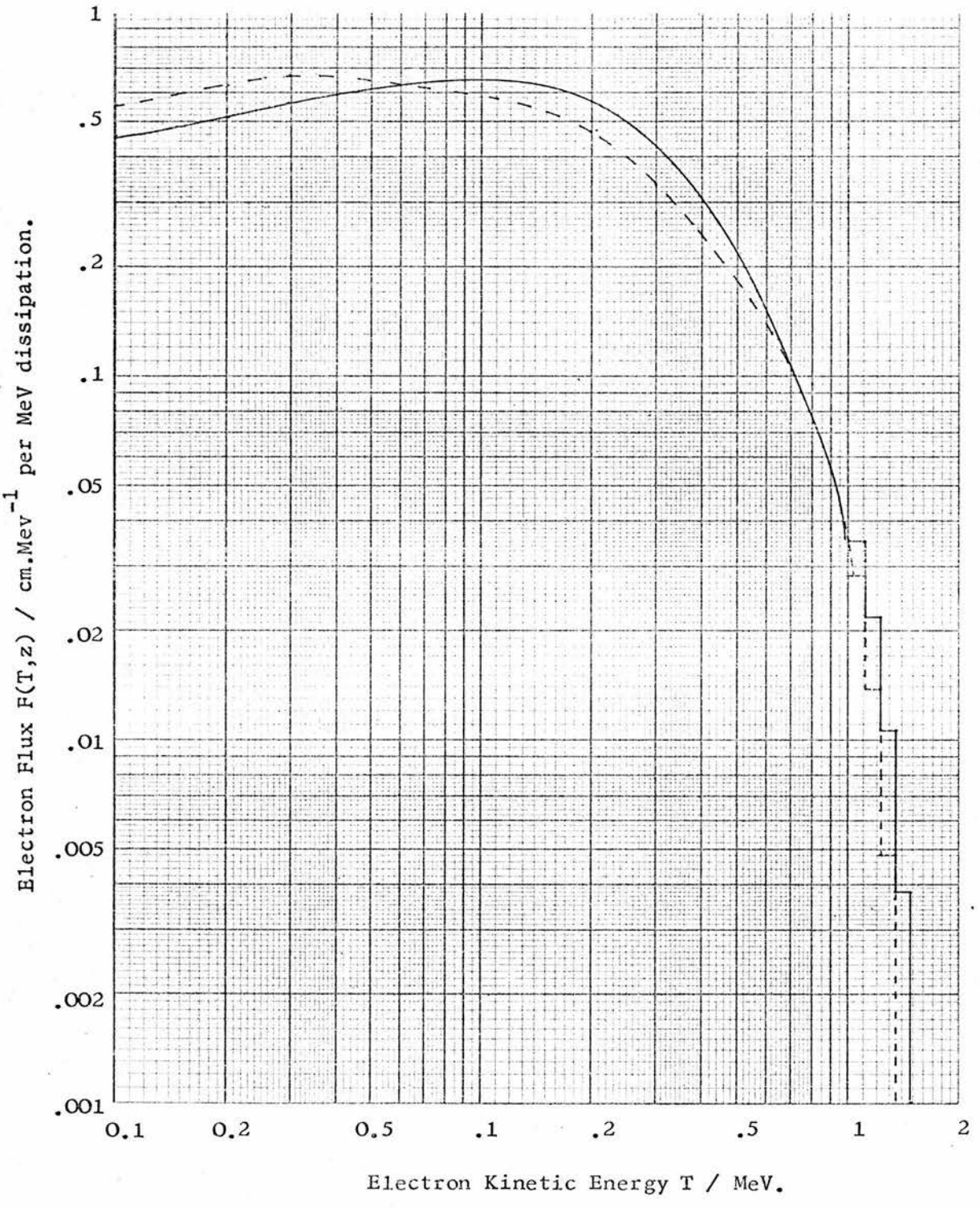

fewer between 0.2 MeV and 1 keV. The very close agreement below 500 eV was to be expected, especially as the average photon energies for the gamma- and x-radiation are similar (1.18 MeV and 0.94 MeV respectively). Comparisons at the calibration depth between closely-matched qualities at higher energies, for example the 26.8 MV thin- and thick-target x-ray beams (H and I), revealed only very small differences in the electron flux spectra, especially below about 5 MeV, but even slight differences at the high-energy end are significant in terms of the calculation of the stopping-power ratios, as will be evident in chapter 9.

8.4.2 Variation with Depth

8.4.2.1 2 MV X-Rays (low photon energies)

For relatively low photon beam energies, such as 2 MV, ^{60}Co and 4 MV, the ranges of the photon-ejected electrons are sufficiently small (about 0.4 cm on average for 2 MV x rays) that the electron flux at a given depth is essentially determined by the photon flux spectrum at that depth.

The nature and order of magnitude of the change in the electron flux spectrum with depth for the 2 MV beam is illustrated in figure 8.9. The dose at the 18-20 cm geometry is about 50% of that at the surface. The spectra at depths intermediate between those in the figure lie between the two curves shown. There is, then, a slight but steady shift towards lower electron energies with increasing depth. This must be due to an increase in the amount of scattered photon radiation, leading to the production of more low-energy electrons at greater depths.

As expected, the very low-energy end of the flux spectrum, below 1 keV, showed a negligible change, being within 2% at 100 eV for the two depths in fig. 8.9. A similar trend in the results for ^{60}Co and 6 MV beams was found.

At even lower photon energies, such as in the kilovoltage x-ray quality region, the change in the electron flux with depth is complicated by the filtering out of the low-energy photons in the primary x-ray spectrum by the absorbing medium. This effectively hardens the primary beam, which tends to offset the effect of the increase in scattered radiation. This effect can be observed in the LET distributions that Bruce et al. (1963) calculated from their measurements of the photon spectra at the surface and at 10 cm depth in water for 250 kV x rays and ^{60}Co and ^{137}Cs gamma rays. The LET distributions at the two depths for the 250 kV radiation (HLV 1.25 mm Cu) show practically no differences, whereas for ^{60}Co and ^{137}Cs, there is a small but definite shift towards lower electron energies at the greater depth, in agreement with the present findings (the Bruce et al. LET distribution for ^{137}Cs is reproduced in figure 1.6). The fact that the change in the electron flux spectrum with depth has been found to be very similar for 2 MV x-rays and ^{60}Co gamma rays (i.e. very few low-energy primary photons) indicates that any hardening of the 2 MV primary photon spectrum with depth is negligible compared to the effect of the increase in scattered radiation.

Figure 8.10 VARIATION WITH DEPTH OF ELECTRON FLUX SPECTRUM FROM A 31 MV X-RAY BEAM (J)

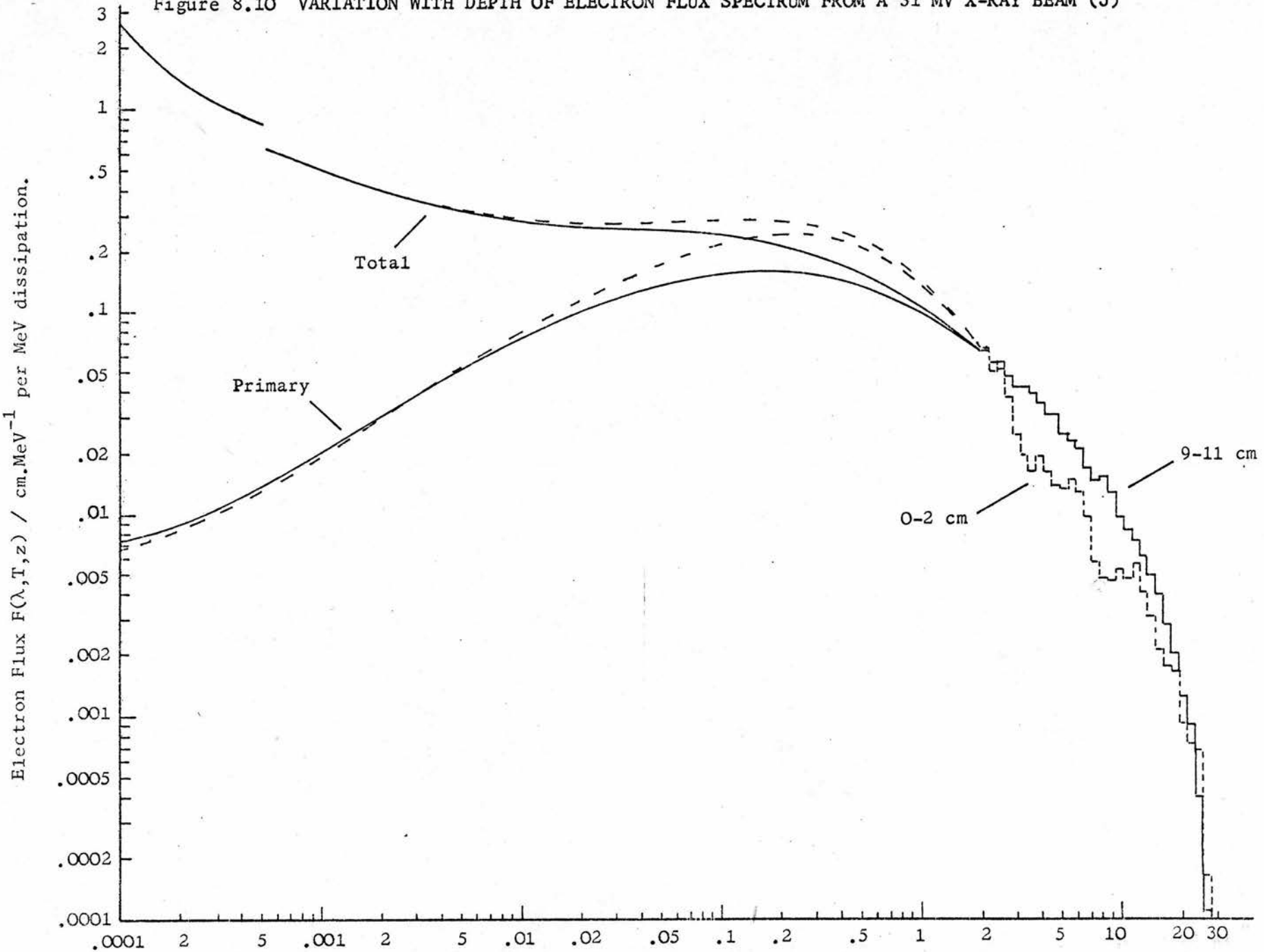

Figure 8.11 DETAILED VARIATION OF $F(\lambda,T,z)$ WITH DEPTH FOR 31 MV X-RAY BEAM.

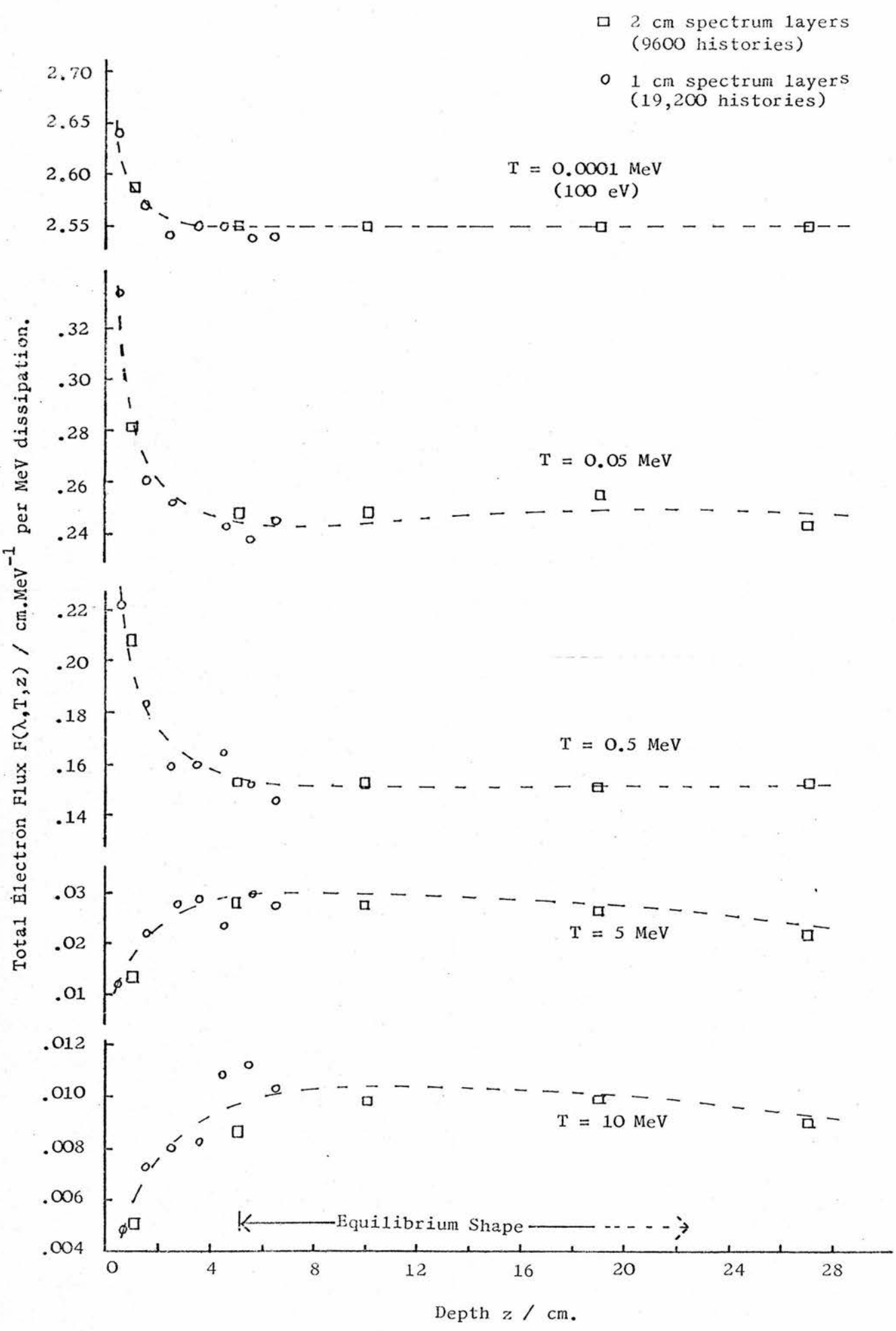

8.4.2.2 31 MV x-rays (high photon energies)

The situation for high-energy photon beams, where the effect of the electron ranges cannot be discounted, is somewhat different. The electron flux spectrum over a 2-cm surface layer and at the calibration depth is shown in figure 8.10 for the 31 MV x-ray beam (spectrum J). It can be seen that the electron flux in the surface layer is shifted by an appreciable amount towards the lower energies.

The way in which the electron flux at different energies varies over a wide range of depths is depicted in figure 8.11. The build-up to the equilibrium shape takes place within the first 4 cm or so. The fact that even the flux at 100 eV is appreciably different is a definite indication that the spectrum is 'softer' close to the surface ; all the results given so far show that the flux per unit dose at very low energies is insensitive to quite large differences at higher energies. Between 5 cm and 20 cm, there is very little change, but a slight softening at the electron spectrum can be detected for the 26-28 cm results at 5 and 10 MeV. The figures plotted were taken from two separate computations for the 31 MV x-ray spectrum (J) and give an indication of the size of the statistical fluctuations of the flux values.

The main features of the variation of the electron flux spectrum with depth illustrated in the above two figures can be understood as follows. The high-energy pair and Compton electrons resulting from the photon interactions are ejected predominantly in the forward direction. As the photon spectrum changes only slowly

Figure 8.12 DEPTH-DOSE CURVE FOR 31 MV X-RAY BEAM (J) IN WATER.
(Plane parallel beam, infinite field)

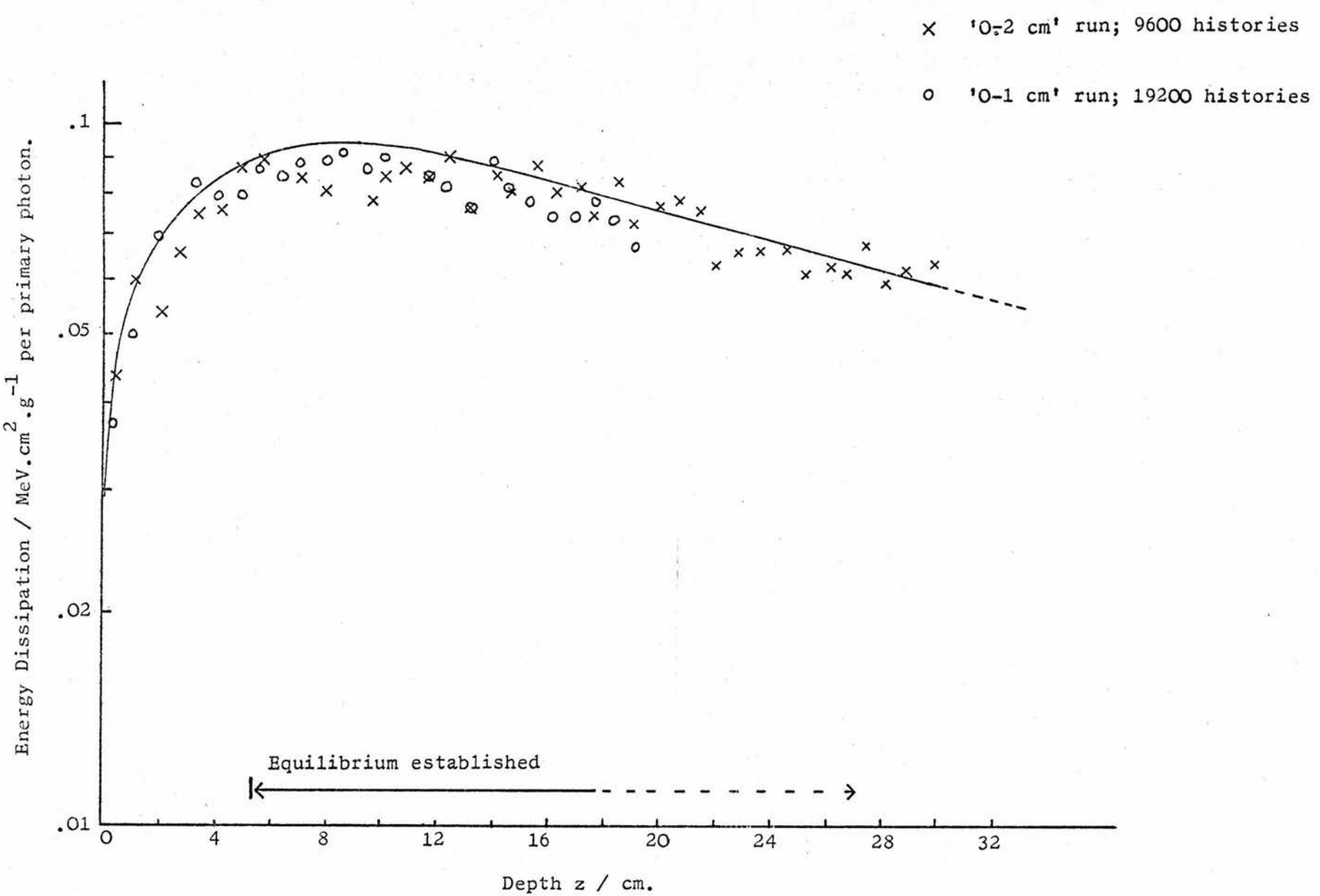

with depth, then at a given depth z, there will be equilibrium* for electrons up to an energy such that the ranges of these electrons are less than z (i.e. the numbers of such electrons starting and ending their tracks at that depth are equal).

For the 31 MV x-ray spectrum, the average photon energy, $\bar{k}_{int}$, is 12.8 MeV. The mean initial energy of the electrons produced is therefore about 8 MeV at which energy the c-s-d-a range, r_o, is 4 cm in water. Consequently, electronic equilibrium is expected to be largely established by this depth. Indeed, a glance at the depth-dose curve computed for the 31 MV beam drawn in figure 8.12 shows that the dose at 4 cm is almost 90% of its maximum value. The position of the maximum, at about 9 cm, which corresponds to the range of a 19 MeV electron, results from a balance between the range of the highest energy electrons and the gradual attenuation of the primary photon beam.

The greater number of electrons with energies above about 3 MeV in the equilibrium spectrum compared to the spectrum in the build-up region (see fig. 8.10) is due to the fact that in the former case the flux is due to electrons both starting at that depth and slowing down from higher initial energies at smaller depths, whereas in the latter case there can only be very few electrons from

---

*It should be remembered when looking at fig. 8.10 that the quantity plotted is the flux normalized to unit dose. Moving the 0-2 cm curve down by 0.8 cm removes this normalization, bringing the primary flux values between 0.2 and 1 MeV into coincidence and increasing the differences above 1 MeV.

Figure 8.13 THE CALCULATIONS OF BRYSK (1954) FOR A 40 MV SCHIFF X-RAY SPECTRUM.

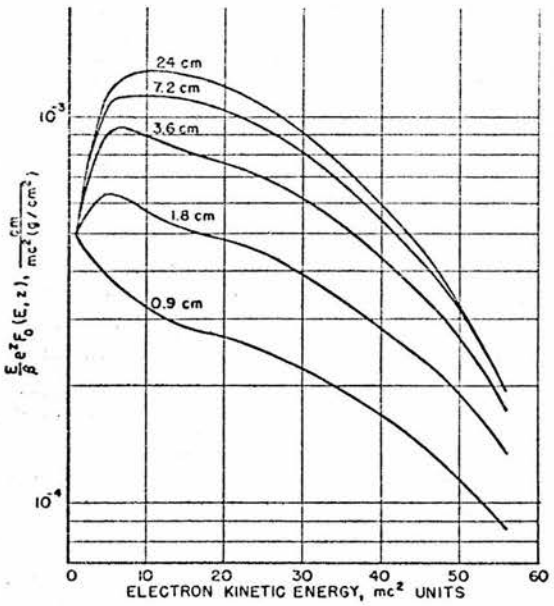

FIG. 5. Electron spectra at various depths z.

Figure 8.14 THE CALCULATION BY CORMACK AND JOHNS (1952) OF PRIMARY ELECTRON FLUX FOR A 25 MV BETATRON X-RAY BEAM.

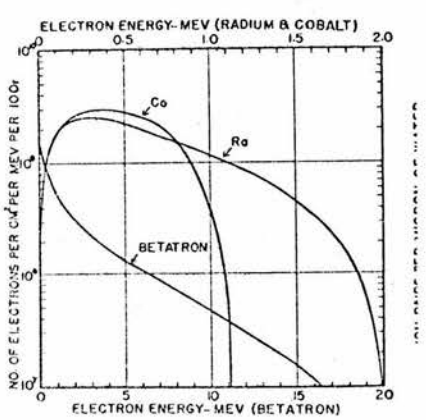

FIG. 7.

Distribution of electron energies at a point in a water phantom irradiated by betatron, radium and cobalt radiations. The number of electrons per MeV interval passing through 1 cm^2 at the point per 100 r of radiation is shown on a logarithmic scale.

Note that the upper scale of abscissae applies to the radium and the cobalt and the lower to the betatron radiation.

depths closer to the surface. The gradual softening of the electron flux spectrum at depths greater than the maximum region of the depth-dose curve, i.e. z 20 cm, (see fig. 8.11) can be due only to changes in the photon spectrum, which result from the increasing proportion of Compton-scattered radiation. This variation of the electron flux beyond the equilibrium depth will be similar in nature to the results for 2 MV x rays described above.

The changes in the electron flux spectrum with depth for the 19 MV and 26.8 MV x-ray beams (not shown) follow the same pattern as for the 31 MV beam, but the build-up region is somewhat smaller as the mean range of the photon-ejected electrons is less. For the 26.8 MV linac beam (spectrum H), for example, this range is about 2.5 cm and in fact the results indicate that the equilibrium-shape electron flux spectrum is virtually attained at a depth of 3 cm.

Brysk (1954) also calculated the electron flux spectrum at different depths in water resulting from an incident high-energy bremsstrahlung beam. He used the moments method and treated the diffusion of the electrons in the continuous-slowing-down approximation. His calculations were for a 40 MV Schiff x-ray spectrum and included only the primary electron flux down to 0.5 MeV, so no direct comparisons can be made with the results of the present work. Brysk found the same trend towards an equilibrium shape, this being attained by a depth of 7 cm or so according to the graph given in his paper and reproduced in figure 8.13.

Figure 8.15 PRIMARY ELECTRON FLUX FROM 26.8 MV THIN TARGET X-RAY SPECTRUM (I).
(Equilibrium depth region)

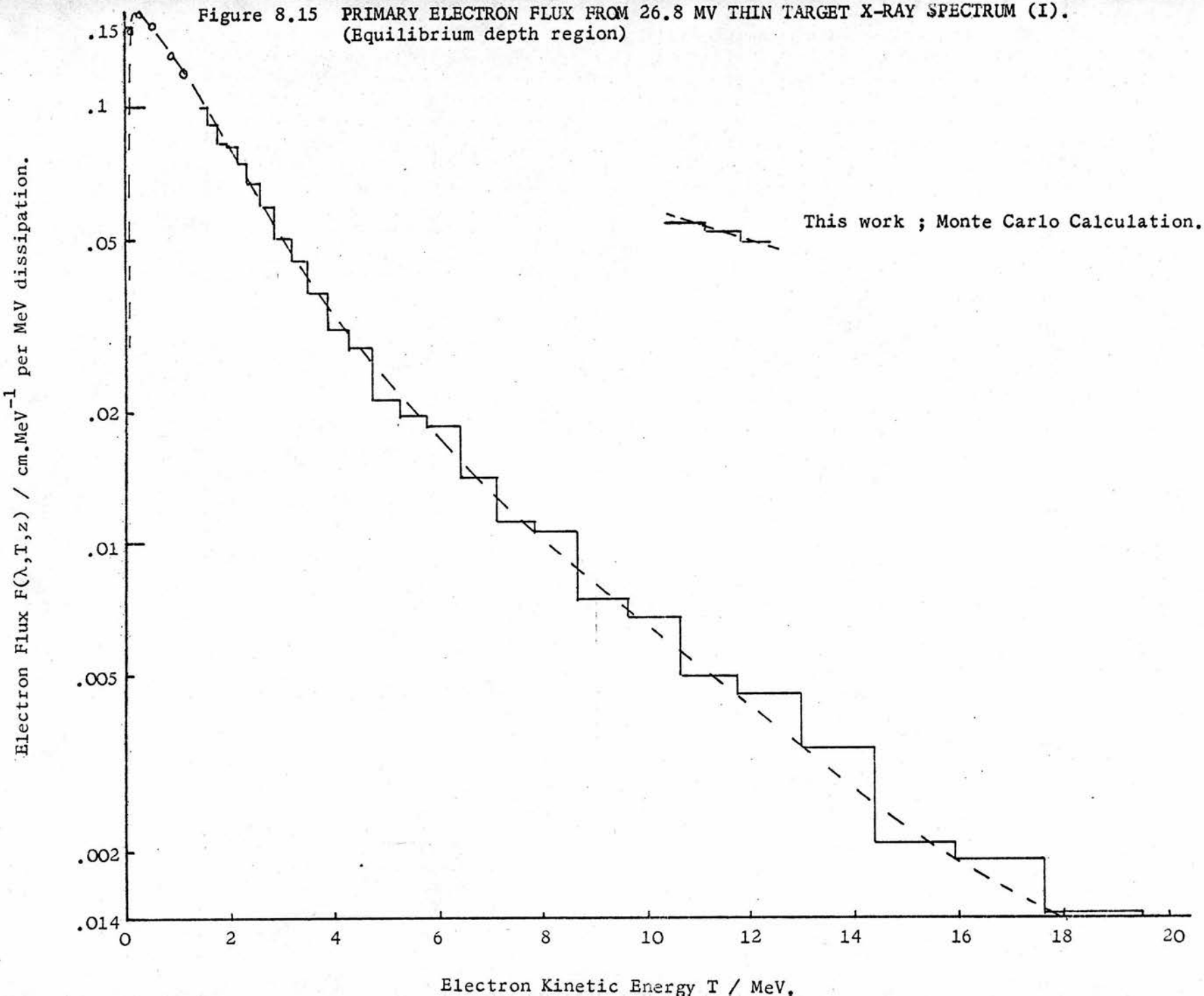

Brysk commented on the fact that his 0.9 cm curve resembled the elementary calculation of electron spectra by Cormack and Johns (1952) for a 25 MV betatron x-ray beam, given in figure 8.14 (see also the discussion in section 1.3.1). However, the quantity that Brysk plotted was the flux, F(E,z), multiplied by E, the electron kinetic energy. Thus it is not clear that he was comparing 'like with like'.

In fact, the calculations of the primary electron flux* that Cormack and Johns carried out were based on the assumption that electronic equilibrium extended to all electron energies. One would expect, therefore, that the curve labelled 'betatron' in fig. 8.14 should be a better approximation to the electron flux spectrum at the depth of equilibrium rather than at the surface. It must be noted, however, that the method that Cormack and Johns used did not take into account any modification of the photon spectrum at a depth due to scattered radiation. Nevertheless, a comparison of the Cormack and Johns betatron electron flux spectrum with the result from the present work for the 26.8 MV thin-target x ray beam, plotted with a linear energy scale in figure 8.15, indicates that the shapes are very similar.

---

*It is precisely this simple derivation of the flux that the ICRU (1969) recommendations for the calibration depth refer to (see section 8.3.2).

8.4.3 Comparison with Electron Beam Results

The question of the validity of assigning an 'equivalent' electron energy to a high-energy photon beam was discussed in the introduction (section 1.1). It is central to the main purpose of the present work - the theoretical examination of the 'G-value difference' between electron and photon beams and a more accurate evaluation of water/air stopping-power ratios for the ^{60}Co and high-energy x-ray beams in clinical use. Naturally, considerable differences in the electron flux spectra arising from photon and electron beams were to be expected but it is interesting to make comparisons from the results of the present computations.

Consider the 31 MV x-ray spectrum (J). The mean photon energy, $\bar{k}_{int}$, is 12.8 MeV. A photon of this energy gives rise to pair and Compton electrons of mean initial kinetic energy 7.8 MeV. Assuming that the depth is sufficient for electronic equilibrium to be established, then the mean instantaneous energy of these primary electrons can be estimated as half their initial energy. In this way the figure of 3.6 MeV is arrived at for the 'equivalent' energy of the 31 MV x-ray beam.

Turning now to the electron beams, for a 10 MeV beam at a depth of 0.6-0.7 $r_o(\bar{z} = 3.19$ cm), assuming a mean loss of 2 MeV.cm^{-1}, the average primary energy comes out to be 3.6 MeV. This is the same as for the 31 MV beam.

Figure 8.16 COMPARISON OF ELECTRON FLUX, SPECTRA FROM ELECTRON AND PHOTON BEAMS.
('smoothed' results)

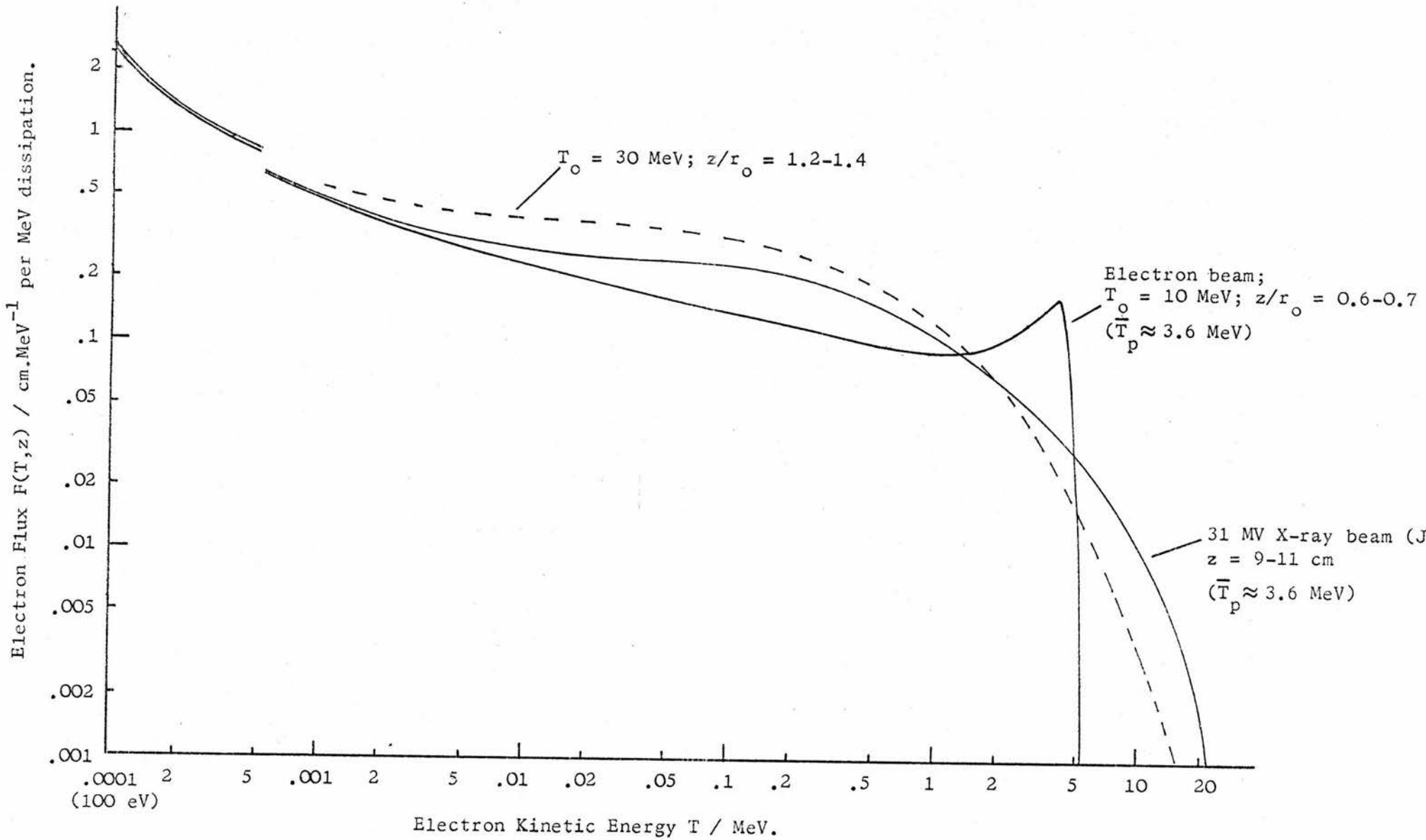

The electron flux spectra at the calibration depth for the 31 MV x ray beam and at 0.6-0.7 r_o for the 10 MeV electron beam are shown in figure 8.16. The differences are small below 10 keV and in particular, the number of Auger electrons is similar in the two cases. It might have been expected that the primary photon beam would have given rise to a greater number of Augers due to their production in Compton scattering and photoelectric absorption. It can be concluded, therefore, that for high-energy photon beams at least, the production of δ-rays from the oxygen K shell by photon-ejected electrons and their secondaries accounts for most of the Auger electrons.

There is a greater number of electrons in the middle energy range between 0.01 and 1 MeV arising from the photon radiation, due to the Compton electrons of relatively low initial energies. The flux in this region from the electron beam is made up almost entirely of secondary electrons, as very few primaries have an energy below about 0.25 MeV.

The absence of a maximum and the very gradual build up from the maximum electron energy characteristic of the electron flux produced by x-ray beams is never well approximated by the flux from monoenergetic electron beams, even for $z \simeq r_o$ as the number of electrons at the high-energy tends to fall off much more abruptly (see fig. 7.2). However, in the bremsstrahlung tail, the primary radiation is effectively a photon beam. Included in fig. 8.16 is the flux in the 1.2-1.4 r_o layer resulting from a 30 MeV electron beam, drawn here as a smooth curve (dotted) from the statistically rather poor results shown in fig. 7.4.

This curve is quite similar in shape to the flux from the 31 MV x-rays, though recognisably softer as would be expected as the bremsstrahlung is effectively thick-target.

More significant comparisons between 'equivalent' electron and photon beams are made in the next three chapters, where the equivalence is with respect to stopping-power ratios and ferrous sulphate G-values.

8.4.4 Tabulations of the Electron Flux Spectra

Tabulations of some of the results computed for incident photon beams are to be found in Appendix 8. The particular spectra given have been selected on the basis of having resulted from 'realistic' incident photon spectra i.e. including flattening filters, scattered radiation in the case of ^{60}Co etc. The only exceptions to this are the results for the 31 MV x-ray spectrum (J) which does not take into account the modification due to a flattening filter.* The tabulations comprise of the electron flux spectra for the following photon beams: 2 MV (A), ^{60}Co (B), 6 MV linac (E), 19 MV betatron (G), 26.8 MV linac (H), 26.8 MV thin-target (I), and 31 MV betatron (J). Table 8.1 should be consulted for details.

---

*The flux resulting from the 31 MV spectrum K_{-2}, which includes the effect of filtration by 20g.cm^{-2} lead, was derived from a much smaller number of histories (see section 8.3.2) and therefore is not included.

The results for the above qualities all correspond to the ICRU calibration geometry i.e. the constant equilibrium shape for the higher-energy beams, but in addition, the flux in the 0-1 cm layer for the 31 MV radiation (J) has been included as an example of the marked depth-dependence in the build-up region (see fig. 8.11). As with the tabulations for electron beams (Appendix 7), values are given at a sufficient number of energies to define the spectra. Three significant figures are retained, except at the high-energy end, to facilitate relative comparisons, though this does not necessarily indicate the absolute accuracy of the values.

Figure 8.17 LOCAL ENERGY DISSIPATION SPECTRUM : ^{60}Co RADIATION.

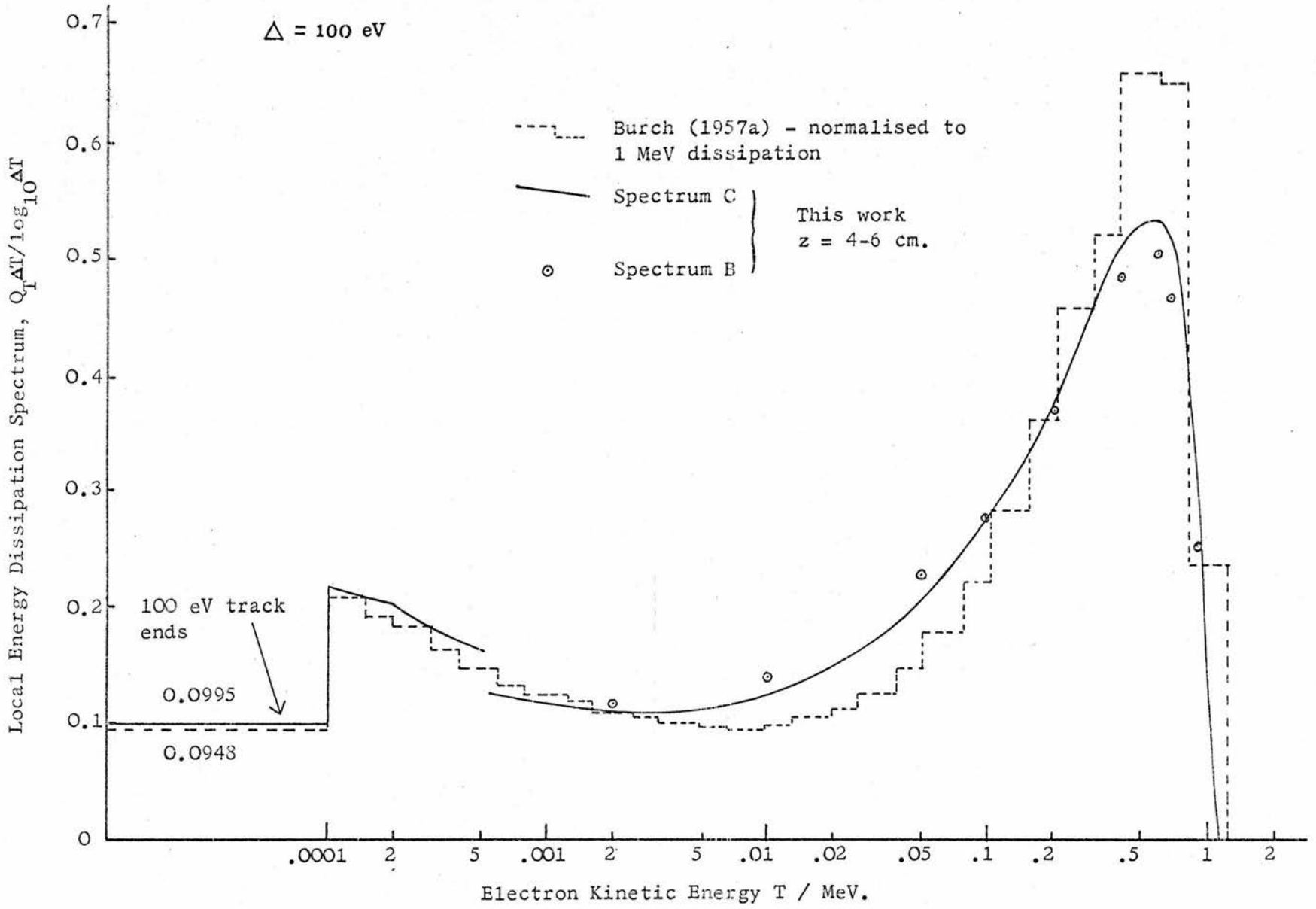

8.5 LOCAL ENERGY DISSIPATION DISTRIBUTIONS

8.5.1 The Q_T Spectrum

Similar remarks apply here to the local energy dissipation spectra derived from the electron flux spectra arising from photon beams as were made in section 7.3.1 concerning the electron beam results. However, direct comparisons can be made with the $Q_T \Delta T$ distributions that Burch (1957a) calculated. Burch's ^{60}Co results, re-normalized to 1 MeV total dissipation, have been plotted as the dashed histogram in figure 8.17. The histogram intervals correspond to the electron energy intervals that Burch used in his energy-band calculational scheme, which has been extensively discussed in chapters 1 and 5.

The full line was drawn from the present computation for the primary ^{60}Co photon spectrum (C) at the calibration geometry. (The small change resulting from including the incident scattered radiation is indicated by the circles on the graph.) Burch's initial photon spectrum also did not include any scattered radiation and furthermore, his initial electron distribution did not take into account the effect of the scattered photon flux produced in the absorbing water medium. The difference between the histogram and the curve in fig. 8.17 is due to a combination of the neglect of this scattered photon flux at a depth and the relatively large energy intervals that Burch employed. Also Burch did not consider Auger electron production.

Figure 8.18 LOCAL ENERGY DISSIPATION SPECTRUM : COMPARISON OF CALCULATION FOR 26.8 MV X-RAYS WITH THAT OF BURCH (1957a) FOR 25 MV X-RAYS.

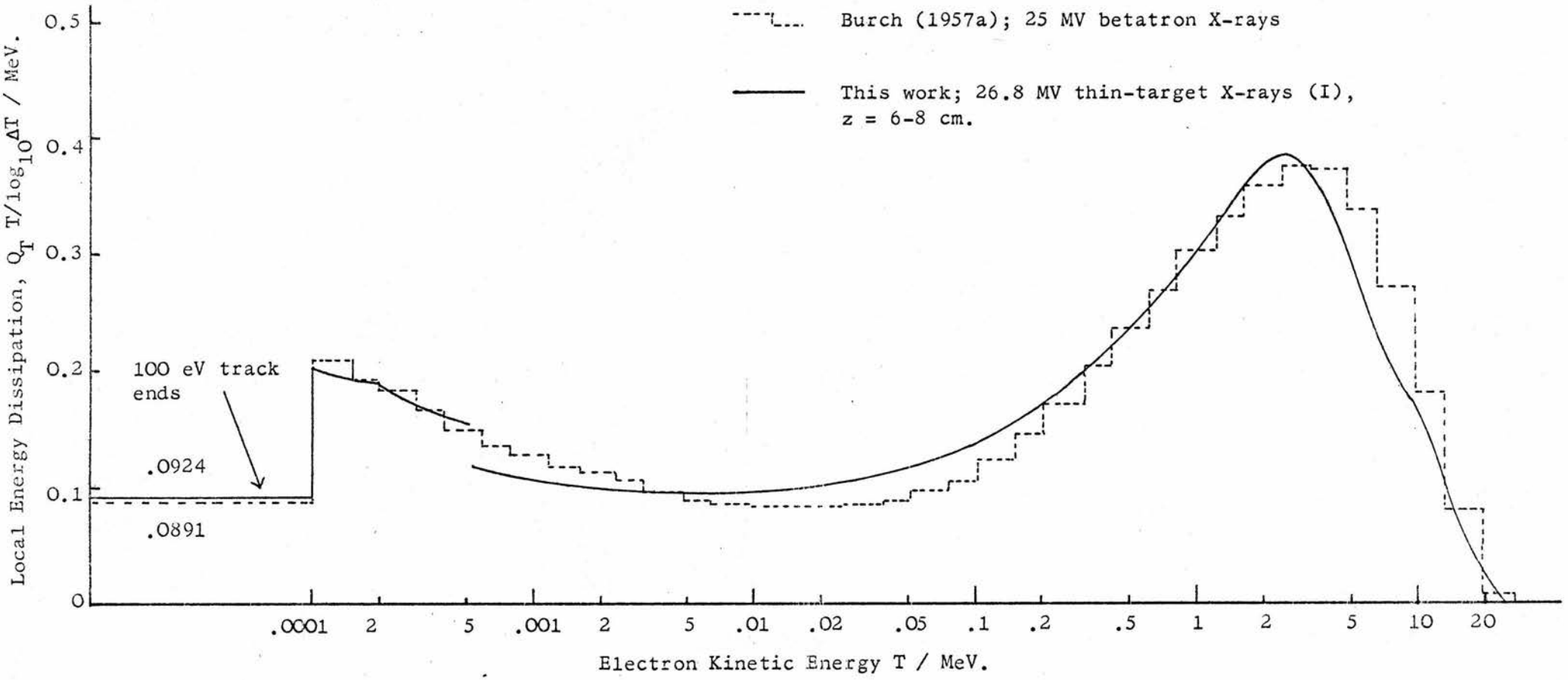

It is worth noting that a comparison between Q_T distributions rather than between electron flux spectra effectively removes the complication at low energies caused by the use of different values for the stopping power. It was pointed out in section 7.3.1 that the local energy dissipation at a given energy (for a cutoff of 100 eV as here) is proportional to the ratio L_{100}/L_{total}, whereas the flux is proportional to $1/L_{total}$. Thus the rather odd values that Burch used for L_{total} in his 1957a paper do not affect the comparison.

Burch also calculated a $Q_T\Delta T$ distribution for a 25 MV betatron spectrum. This spectrum was the one that Johns et al. (1950) had derived from the Schiff formula, with a correction for absorption in the betatron doughnut, the monitor chamber and 4 cm of Lucite. Note that the effect of any flattening filter was not included. Cormack and Johns (1954) calculated the initial distribution of electron energies produced in water by this photon spectrum and it was their initial electron distribution that Burch used in his derivation of the $Q_T\Delta T$ spectrum.*

In figure 8.18 a comparison has been made between Burch's results for the 25 MV betatron radiation and the present computation for the 26.8 MV thin-target x-ray beam (I), also a theoretically-derived photon spectrum including modification for a lead flattening filter

---

*This electron distribution was also used by Danzker et al. (1959) in their derivation of the total and primary electron flux in water (see section 1.3.1).

(see table 8.1), but a reasonably close 'match'. In effect, a comparison has already been made between results derived from these two x-ray spectra; the primary electron flux as calculated by Cormack and Johns (1954) and computed in this work were shown in figs. 8.14 and 8.15 above. The assumption of electronic equilibrium and the neglect of the effect of scattered photon radiation in the Cormack and Johns work also apply to Burch's calculation.

The differences above 2 MeV between the dotted histogram and the curve in fig. 8.18 cannot be considered to be significant in view of the differences in the initial photon spectra. At lower energies the agreement is, if anything, slightly better than in the comparison for Cobalt gamma radiation given above. This is most likely to be due to the smaller effect of the scattered photons at a depth for the betatron beams than for ^{60}Co. A 1 MeV photon gives up on average 44% of its energy in the first interaction in water, compared with 76% at 10 MeV and 85% at 20 MeV.

Comparisons between local energy dissipation spectra resulting from electron and photon beams could have been included in this section but have been left until chapter 11 where the possible significance of the differences between them for the calculation $G(Fe^{3+})$ is discussed.

Figure 8.19 CUMULATIVE LOCAL ENERGY DISSIPATION DISTRIBUTIONS : PHOTON BEAMS.
(calibration depths)

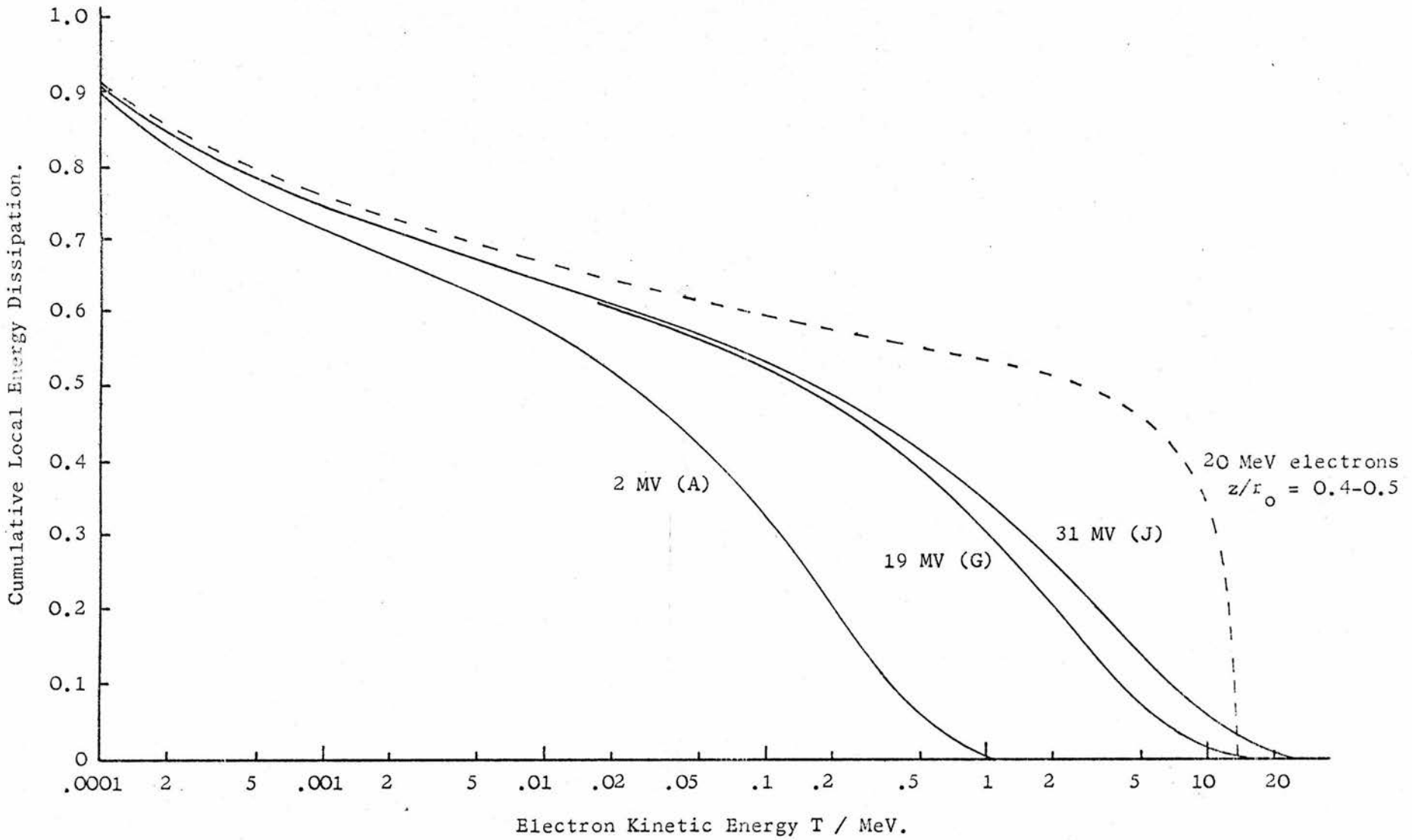

8.5.2 The Cumulative Distribution

The cumulative local energy dissipation distribution for three photon beams well separated in energy has been plotted in figure 8.19. There is a clear difference between the 2 MV curve and the 19 MV and 31 MV curves. The latter distributions are very similar, as is to be expected from the relatively small differences in the electron flux spectra below a few MeV from the higher energy photon beams (see fig. 8.7).

It would appear from the comparison with the electron beam distribution included on the figure that the high-energy photon beam distributions tend to a rather different constant curve below 1 MeV or so. Thus about 32% of the local dose is delivered by electrons with energies above 1 MeV, compared to 55% for the electron beams, and about 47% by electrons with energies less than 0.1 MeV, compared to 40% for the electron beams (see the corresponding section (7.3.2) in the previous chapter). The convergence of the 31 MV betatron and 20 MeV electron distributions at very low energies shows that the dissipation by the 100 eV track ends is the same to within a few per cent.

8.6 CONCLUSIONS

The results presented in this chapter with regard to the variation of the electron flux spectrum with depth confirm in detail the assumptions that have been made implicitly by other workers. Thus the spectrum has been shown to change shape only very slowly at depths beyond the build-up region. Comparisons of the equilibrium spectrum with the much less sophisticated calculations of Cormack and Johns (1954) and Burch (1957a) indicate that the neglect of scattered photon radiation in the latter treatments results in only small differences.

The results of a detailed examination of the way the electron flux spectrum produced by a 31 MV x-ray beam changes from the surface to a depth where electronic equilibrium is established indicate that the number of high-energy electrons is considerably less at the surface in agreement with the trend in the results of Brysk (1954). This is in contrast to the gradual 'softening' of the electron spectrum with depth for both the 2 MV and 31 MV beams as the depth-dose curve falls off.

An analysis of the expected accuracy of the computations, setting aside statistical considerations, is somewhat more straightforward than for the electron beam results. It is not difficult to deduce that the electron flux spectra will not be particularly sensitive to the model used to simulate the transport of the photon-ejected electrons. Indeed, it is only in the build-up region that the forward transport of these electrons significantly affects the results. As the

electrons have a very broad distribution of initial energies, the effect of energy-loss straggling is not going to be apparent. As far as the transport, scattering and absorption of the photons are concerned, the simulation is a direct analogue of the physical processes and makes use of cross-sections that do not involve any approximations that are likely to have any more than a very marginal effect on the results (see chapter 3). Thus, apart from the uncertainties at low energies due to the approximate treatment of Auger electron production and inadequacies in the knowledge of low-energy stopping powers, the calculation of the electron flux spectra from the various photon beams at different depths is expected to be accurate. In this respect, more confidence can be placed in the computations for photon beams than for electron beams.

The above remarks imply that the main uncertainties in the results are due to statistical fluctuations. The spectrum for the 0-2 cm geometry plotted in figure 8.10 suggests that a greater number of histories might have been desirable, but the values given in figure 8.11, taken from two separate sets of histories, do not leave any doubt as to the trend of the results. The stopping-power ratios derived from the flux spectra, which are quite critically dependent on the number of electrons at the high-energy end, will be shown to have a statistical accuracy of 0.2% or better at all depths, which is more than adequate.

The number of histories used was not sufficient to indicate in more than a general way the shape of the depth-dose curves for the different photon beams. This is clearly demonstrated by the spread of the values shown in figure 8.12 for the 31 MV radiation. Thus such questions as the difference in the depth-dose between the 26.8 MV thin- and thick-target beams could not be dealt with. However, investigations of this type are more profitably carried out experimentally (Rawlinson and Johns, 1973), especially as the theoretical results would need adjusting to correspond to the finite area and slight divergence of the beams used in practice.

It can be noted that Brysk (1954) calculated the depth-dose curve in water for a 40 MV betatron x-ray spectrum and his results were in excellent agreement with the measurements of Zendle et al. (1956) for a broad beam. This demonstrates that such photon-electron transport calculations are not sensitive to the treatment of electron diffusion, in line with what was said above, as Brysk used a simple c-s-d-a model. In fact, had the aim of the present work been the calculation of depth-dose curves for high-energy photon beams, a very much simpler simulation of electron transport could have been employed resulting in a much faster execution time and hence more information about the depth-dose for the same amount of computer time.

Though calculations of depth-dose curves are sensitive to beam geometry, theresults for the electron flux spectra should not be. Clearly, the effect of a finite rather

than infinite area beam will be to reduce somewhat the number of photons 'seen' on the central axis that have been scattered through large angles . However, the effect of scattered photons on the electron spectrum has already been shown to be small by the very gradual change of the spectrum with increasing depth. More importantly, the small increase in the number of electrons in the middle energy range that will result from a decrease in the beam width is very unlikely to alter the value of the stopping-power ratio.

The difficulties of performing calculations on photon beams that match closely the ones in clinical use have been emphasised in section 8.2. Experimentally determined photon spectra have been used where possible as the agreement between theoretical and measured distributions has often been unsatisfactory. In particular, many machines appear to produce a maximum photon energy somewhat different from that specified. The observable effect of different target thicknesses and flattening filters on the flux spectrum is fairly small, but the main significance of these differences lies in the values derived for the stopping-power ratios.

Conclusions about the validity of assigning an effective average electron energy to a photon beam cannot be drawn at this stage. The most relevant question in this respect is the degree to which theoretically-derived values for $G(Fe^{3+})$ and the water/air stopping-power ratios agree for 'equivalent' electron and photon beams. This is dealt with in the next three chapters.

CHAPTER 9

EVALUATION OF WATER/AIR MASS STOPPING-POWER RATIOS FOR ELECTRON AND PHOTON BEAMS

9.1 INTRODUCTION

All theories that seek to relate the ionization measured in a cavity, in this case filled with air, to the absorbed dose, in this case in water, require for their proper evaluation the electron flux spectrum produced in the cavity by the incident radiation.* The computed flux spectra are applied here to a modified version of the Spencer-Attix cavity ionization theory. In particular, it has been possible to remove the restriction concerning photon interactions in the cavity.

The emphasis in this work on performing computations on 'realistic' incident photon beams meant that questions about the effect of different target thicknesses and filtrations on the mass stopping-power (and hence on the more directly useful C_λ factors) could now be resolved. More fundamentally, the 'exact' calculations of the stopping-power ratios for bremsstrahlung beams could be compared to the values based on 'equivalent electron energy' assumptions.

It has already been stated that considerable attention has been given to the calculation of stopping-power ratios for high-energy electron beams, in contrast to the almost total absence of parallel work for photon beams. The electron beam results presented in this chapter are directly compared to the values of Harder (1965a),

---

*Except for very large cavities irradiated by photon beams.

Kessaris (1970a) and Berger et al. (1975). Some interesting conclusions are to be drawn from these comparisons.

9.2 CAVITY IONIZATION THEORY

9.2.1 General

The basic aim of cavity ionization theory can be expressed in the following equations

$$D_m = D_g . F_{mg} \qquad .....(9.1)$$

$$= J_g . (\bar{W}/e) . F_{mg} \qquad .....(9.2)$$

where

D_m is the energy deposited in unit mass of the medium;

D_g is the energy deposited in unit mass of the cavity;

F_{mg}, defined as the ratio D_m/D_g, is the quantity cavity theory seeks to evaluate;

J_g is the ionization measured per unit mass of cavity material; and $\bar{W}$ is the average energy expended by electrons in the gas per ion pair formed.

In the present calculations, the cavity material 'g' is air and the medium 'm' in which the absorbed dose is required is water. The values of $\bar{W}$ is assumed to be constant at 33.73 eV per ion pair (ICRU; 1969, 1972), giving the value 0.869 rad/R for $\bar{W}/e$. The quantity F_{mg}, the ratio of the energy deposited in unit mass of the medium to the energy deposited in unit mass of the gas, is generally known as the stopping-power ratio, although strictly it may not only consist of a ratio of stopping powers. It can be written as $\bar{s}_{mg}$ and then equ. 9.2 is the well-known Bragg-Gray relation.

The application of cavity ionization theory to the situation usually encountered in dosimetric ionization measurements, i.e. a small ion chamber in a medium irradiated by high-energy photons or electrons, is generally simplified by the fact that the ranges of the primary electrons in the cavity are much larger than the dimensions of the cavity and also that the contribution of photon interactions in the cavity to the electron flux is negligible. The cavity then effectively acts as an electron detector, with the flux in the cavity primarily determined by the electron and photon interactions in the surrounding medium. The opposite extreme to this is for incident photon radiation and a large cavity, such that the ranges of the primary electrons are much less than the dimensions of the cavity. In this case the cavity acts as a photon detector, and F_{mg} then becomes the ratio of the mass energy absorption coefficients averaged over the photon flux spectrum in the cavity:

$$F_{mg} = (\bar{\mu}_{en}/\rho)^{m} \; / \; (\bar{\mu}_{en}/\rho)^{g} \qquad .....(9.3)$$

These very general remarks will be seen to have some significance in what is to follow.

9.2.2 Spencer-Attix Theory

The Bragg-Gray theory did not take into account the effect of δ-rays. The assumption implicit in the Bragg-Gray theory was that the primary electrons deposited their energy on the spot i.e. that all δ-rays had effectively zero range. The specific achievement of the Spencer-Attix theory was to evaluate numerically the

effect of the finite ranges of δ-rays on the stopping-power ratio. In particular, the theory (Spencer and Attix, 1955), predicted a variation of the stopping-power ratio with cavity size, which the Bragg-Gray theory had no explanation for, and which was in reasonable agreement with experimental findings (ICRU, 1969; Burlin, 1962). As both Kessaris and Berger et al. used the Spencer-Attix theory in their evaluation of the stopping-power ratios for electron beams and as a modified version is employed in this work, it is important to look at the assumptions involved in the theory as well as the relevant details of the evaluation.

Spencer and Attix employed a two-group model for the energy dissipation. It was assumed that only energy transfers smaller than a cutoff Δ resulted in dissipation in the cavity, with Δ being of the order of the kinetic energy which an electron must have to just be able to cross the cavity. In order to evaluate the 'local' dose deposited in the cavity, the <u>total</u> electron flux spectrum down to the energy Δ was required. A modification of the Spencer-Fano theory was used to derive this spectrum (see discussion in section 1.3). Note that in the Bragg-Gray theory only the <u>primary</u> electron flux spectrum was involved.

The following expression for the energy deposited in unit mass of gas divided by the energy deposited in unit mass of wall material (i.e. $1/F_{mg}$ or $1/\bar{s}_{mg}$) was given by Spencer and Attix:

$$f_Z(T_o,\Delta) = T_o^{-1} \int_{\Delta}^{T_o} dT\ I_Z(T_o,T)\ S_{air}(T,\Delta) \qquad .....(9.4)$$

where $I_Z(T_o,T)$ is the equilibrium flux spectrum in the wall material (of atomic number Z) for an electron of initial energy T_o, and $S_{air}(T,\Delta)$ is the collision stopping power restricted to losses less than Δ. Note that the term T_o^{-1} is the energy deposited in unit mass of the wall material, as the spectrum $I_Z(T_o,T)$ is assumed to be normalized to one electron of initial energy T_o per unit mass of the wall material.

Spencer and Attix were careful to emphasize that their theory still retained the assumption in the Bragg-Gray theory that the electron flux was not modified by the presence of the cavity. More specifically, the total flux down to the energy Δ was assumed to be unmodified. Clearly, the electron flux at energies below Δ would become characteristic of the cavity material. As far as the 'slow electrons' (i.e. with energy less than Δ) crossing the wall were concerned, Spencer and Attix pointed out that their schematization was equivalent to assuming a balance between incoming and outgoing 'slow' electrons with no net energy transfer. This is more usually expressed by saying that there is secondary electron equilibrium across the cavity walls and has been shown to be a good approximation for cases where the cavity and wall material are of similar atomic number (ICRU, 1972).

The restricted collision stopping power, $S(T,\Delta)$, that Spencer and Attix employed is <u>not</u> identical to the quantity $L(T,\Delta)$, or L_Δ, given by equation 4.18, and used throughout this work. In order to include 'automatically'

the energy deposited by the track ends of energy Δ in the integral in equ. 9.4, $S(T,\Delta)$ is evaluated in a different manner to $L(T,\Delta)$ between $T = \Delta$ and $T = 2\Delta$.

In the usual definition of the restricted stopping power, all losses are included that are less than Δ or $T/2$, whichever is the smaller (Berger and Seltzer, 1964; ICRU, 1970; Rohrlich and Carlson, 1954). Spencer and Attix extended the range of integration over the Møller cross-section up to Δ no matter whether Δ exceeded $T/2$ or not. Thus if an electron with energy between Δ and 2Δ itself dropped below Δ as the result of a collision, its own energy was included in the stopping power. It will have already been noted that in this work the local absorbed dose, D_Δ, is evaluated using the conventional $L(T,\Delta)$ and the deposition by the track ends is included explicitly as a separate term, $N_\Delta.\Delta$ (see section 6.5). Furthermore, this term is <u>not</u> negligible ($\sim$10% of D_Δ for $\Delta = 100$ eV).

Burlin (1962, 1966) has looked in some detail at the predictions of the Spencer-Attix theory for a wide range of wall materials and effective cavity sizes. For ^{60}Co gamma rays he found that the theory predicted the ionization in an air cavity to within 5% of the measured value for cavity sizes corresponding to Δ between 1 keV and at least 0.1 MeV for a carbon-walled chamber. Over most of this range the prediction was actually within a few tenths of a per cent. For a copper-walled chamber, the corresponding figures were 1 keV to only 25 keV. Burlin demonstrated that the theory broke down for

relatively large cavity sizes when there was a large difference between the atomic number of the wall material and the cavity gas (air). He attributed this to the modification of the electron energy spectrum by the cavity and the effect of photon interactions in the cavity, neither of these phenomena being accounted for in the theory. The breakdown for small cavity sizes was shown to be due to the slow electron transfer phenomenom (Greening, 1954).

In this work the wall material is water which is fairly close to air in atomic composition, but not quite as close as carbon. Looking at the mean ionization potentials from Berger and Seltzer, (1964); I(air) = 86.8 eV, I(carbon) = 78.0 eV, I(water) = 65.1 eV and I(copper) = 314 eV. This indicates that carbon, water and air are all relatively closely-matched compared to copper. It is assumed that the modification of the electron spectrum established in the water wall will have a negligible effect on the stopping-power ratios. It must be added, however, that the range of electron energies under consideration extends well into the density effect region, unlike in Burlin's investigation. No experimental work has been done to verify that the Spencer-Attix theory correctly predicts the variation of ionization with cavity size at these high energies where the change of the stopping power ratio with energy is due primarily to the density effect and not to any difference in atomic number between wall material and cavity gas as at lower energies.

9.2.3 Present Evaluation of the Mass Stopping-Power Ratio

The expression for the mass stopping-power ratio given by Spencer and Attix (equ. 9.4) can be re-cast for present purposes as follows

$$S_a^W(T_o,z,\Delta) = \frac{\int_\Delta^{T_o} F(T_o,T,z).L^W(T,\Delta)/\rho_w \, dT + \Sigma N_\Delta^W.}{\int_\Delta^{T_o} F(T_o,T,z).L^a(T,\Delta)/\rho_a \, dT + \Sigma N_\Delta^a.} \quad .....(9.5)$$

where

T_o is the maximum electron energy,

$S_a^W(T_o,z,\Delta)$ is the water/air mass stopping-power ratio at depth z;

$F(T_o,T,z)$ is the electron flux spectrum in water;

$L^W(T,\Delta)$ and $L^a(T,\Delta)$ are the restricted collision stopping powers, evaluated from equation 4.18, for water and air respectively; and $\Sigma N_\Delta^W.\Delta$, $\Sigma N_\Delta^a.\Delta$ are the total track-end terms per unit mass of water and air respectively (see section 9.2.3.3).

It is this expression for $S_a^W(\Delta)$ that has been evaluated in this work for various values of the cutoff Δ, corresponding to different cavity sizes. The electron flux spectrum $F(T,z)$, computed for different depths in water, is used in the above expression to give the local energy dissipation both in water and in the air cavity. It can be repeated again here that any modification of the electron spectrum above $T = \Delta$ by the air cavity has been assumed to be negligible as far as calculating the stopping-power ratio is concerned, and that this would have been less

Figure 9.1 WATER/AIR MASS STOPPING POWER RATIOS: VARIATION WITH ELECTRON K.E.

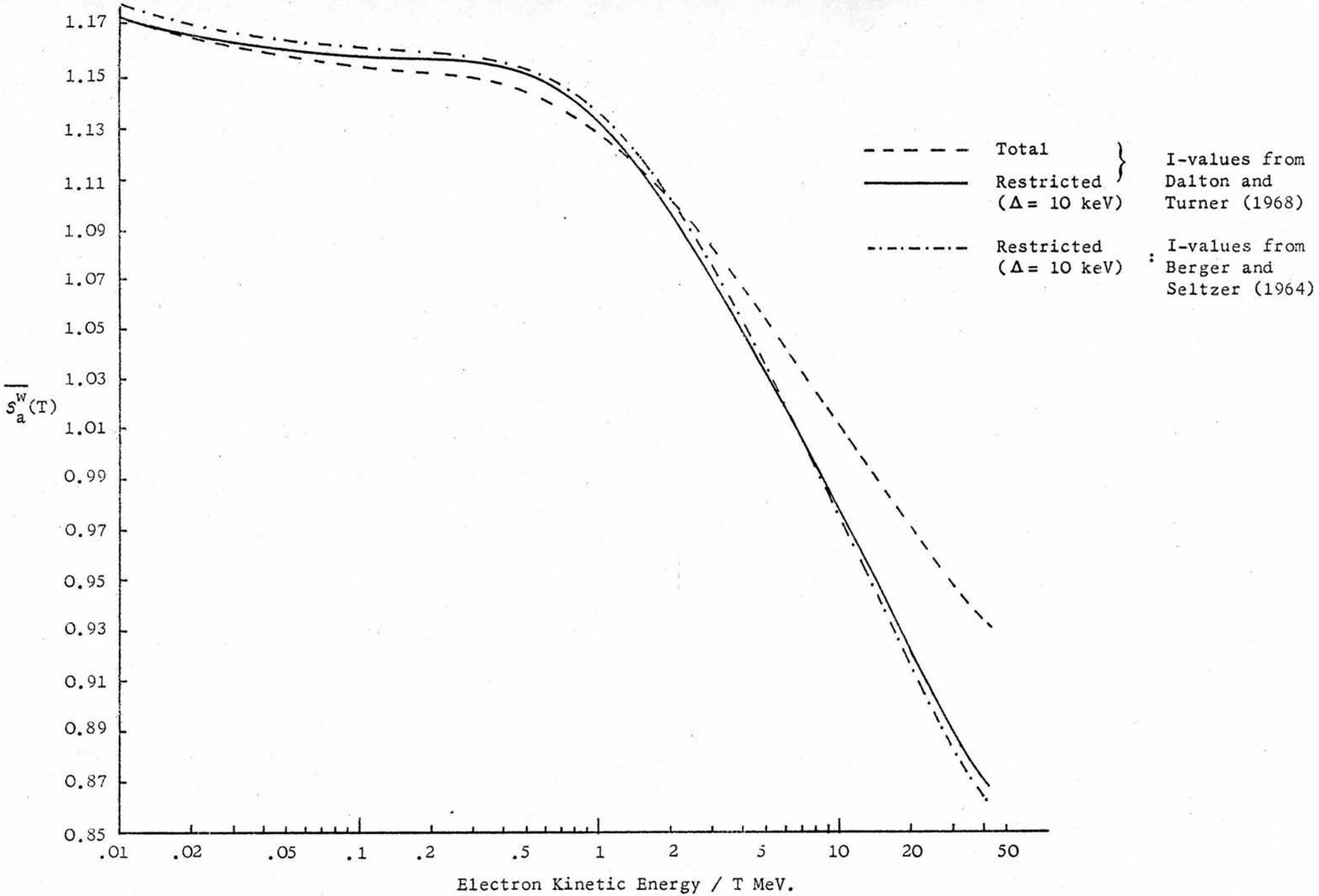

justifiable had the wall material, water, been less closely matched to the cavity gas, air. Note that even for the case of a perfect match between cavity and wall material, scattering effects due to the much greater density of the wall may need to be taken into consideration. This is specifically considered in the next chapter (section 10.2.4).

9.2.3.1 I-values

It has been stated in section 4.4.4 that the mean ionization potential used to evaluate the stopping power for water was taken from the recent compilation of I-values by Dalton and Turner (1968). Consequently, the I-value for air was taken from the same compilation in order to be consistent. Thus the values used in calculating the water/air stopping-power ratio are I(water) = 71.3 eV and I(air) = 92.9 eV.

The evaluation of $L^w(T,\Delta)$ includes the reduction due to the density effect given by Sternheimer, as detailed in section 4.4.4. It is this density effect reduction, present in water but not in air (at least not below 40 MeV), that is of crucial importance in stopping-power ratio calculations for electron energies above 1 MeV or so. The influence of the density effect is shown clearly in figure 9.1 which illustrates the variation of the quantity

$$\bar{s}^w_a(T) = (L^w(T,\Delta)/\rho_w)/(L^a(T,\Delta)/\rho_a) \qquad .....(9.6)$$

with electron energy T for Δ = 10 keV and for Δ = T/2 (i.e. the total collision stopping power ! broken line).

Also shown on the figure is the small difference in the value of $\bar{s}_a^w(T)$ that results from using the I-values given by Berger and Seltzer (1964), namely I(water) = 65.1 eV and I(air) = 86.8 eV.

9.2.3.2 The Cutoff, Δ

Values of $S_a^w(\Delta)$ have been calculated for the electron and photon beams at three cutoffs, Δ: 0.1, 0.01 and 0.001 MeV. The 10 keV cutoff corresponds to a practical electron range in air at STP of 2.1 mm and hence to a cavity size of that order.* Berger et al. (1975) used a cutoff of 15 keV, which corresponds to a cavity size of 4.2 mm. However, the value of Δ is not critical. Berger et al. showed that the water/air stopping-power ratio changed by 0.5% or less over a wide range of Δ-values, and in fact the difference between $S_a^w(\Delta)$ with Δ = 10 and Δ = 15 keV is only 0.10-0.15%.

As Δ is decreased, the stopping-power ratio is effectively calculated at a lower average electron energy. Thus $S_a^w(\Delta)$ will increase slowly as Δ decreases. In fact, the 1 keV** and 0.1 MeV cutoffs were included mainly to illustrate this variation. It can be noted that the variation of $\bar{s}_g^m(T)$ with T at low energies is much more pronounced for larger differences between the atomic number of the wall material and cavity gas.

---

*It is impossible to be precise about relating Δ to the cavity size. For a cylindrical cavity with its axis perpendicular to the radiation direction, for example, the difficulty is obvious.

**Burlin's measurements suggest that the results at this cutoff may not be strictly valid. See also section 9.2.3.3 on Auger electrons.

The application of the calculated water/air stopping-power ratios to a particular type of ionization chamber in common use, the Baldwin-Farmer thimble chamber, is considered in chapter 10 on the evaluation of C_E and C_λ factors from the appropriate stopping-power ratios.

9.2.3.3 Evaluation of the Track-End Term, $\Sigma N_\Delta . \Delta$

The expression for $S_a^w(\Delta)$ given in equ. 9.5 is effectively the local dose (i.e. energy dissipation per unit mass) in water, D_Δ^w, divided by the local dose in air, D_Δ^a. In order to evaluate these quantities correctly, the track-end terms $\Sigma N_\Delta . \Delta$ in both water and air must be included. Some consideration has already been given to the calculation of the track-end contribution for Δ's other than 100 eV in section 6.5 when the normalization of the electron flux spectra was discussed, but the evaluation of the different contributions to $\Sigma N_\Delta . \Delta$ for both water and air must be dealt with in more detail at this stage:

i) Electrons with energy Δ.

The most obvious contribution to the track-end energy dissipation is from the electrons that fall below Δ in energy. It has been shown that Spencer-Attix calculation of D_Δ^a takes care of these electrons through a modification of the restricted collision stopping power between $T = \Delta$ and $T = 2\Delta$. In the present scheme, the conventional stopping power, $L(T, \Delta)$, is used down to $T = \Delta$ and the energy dissipation by the track ends of energy is simply given by the number of electrons in the slowing-down spectrum at energy Δ, N_Δ, multiplied by their residual energy Δ.

In order to simplify the calculation of N_Δ, the values of Δ were actually chosen to correspond exactly to some T_l, the energy at the top of an l-band (see chapter 5). Thus the 0.001, 0.01, and 0.1 cutoffs were more precisely 0.00106, 0.01040 and 0.10239 MeV. Then the number of electrons with energy Δ is simply equal to N_l^*, the number of electrons starting at the top of band l in the low-energy electron flux computation. This value of N_l corresponds to water. The value corresponding to air is also required in order to evaluate $N_\Delta^a \cdot \Delta$.

Now the electron flux in water at energy T_l, or Δ, is given by

$$F_l = F(\Delta) = N_\Delta^w / L_{tot}^w \qquad .....(9.7)$$

where L_{tot}^w is the total collision stopping power at energy Δ. The evaluation of $S_a^w(\Delta)$ from equ. 9.5 is based on the assumption that the flux F(T) in the air cavity is the same down to energy Δ as that computed in water. Therefore, N_Δ^a must be given by

$$F(\Delta) = N_\Delta^a / L_{tot}^a$$

and hence for equal masses of water and air,

$$N_\Delta^a = N_\Delta^w \cdot \frac{L_{tot}^a / \rho_a}{L_{tot}^w / \rho_w} \qquad .....(9.8)$$

where the stopping powers, $L_{tot}^{w,a}$, are to be evaluated at the cutoff energy. Thus this contribution to the track-end term is weighted by the stopping power ratio at the cutoff energy. It should be noted that this is equivalent

---

*Using the notation of chapter 5, N_l should strictly be written as $N_{l-1}^{tot} + \Sigma N_l^\delta$, as in equ. 5.16 for Δ = 100 eV. For simplicity, it has been shortened to N_l in this chapter.

Figure 9.2 AUGER ELECTRON TRACK ENDS.

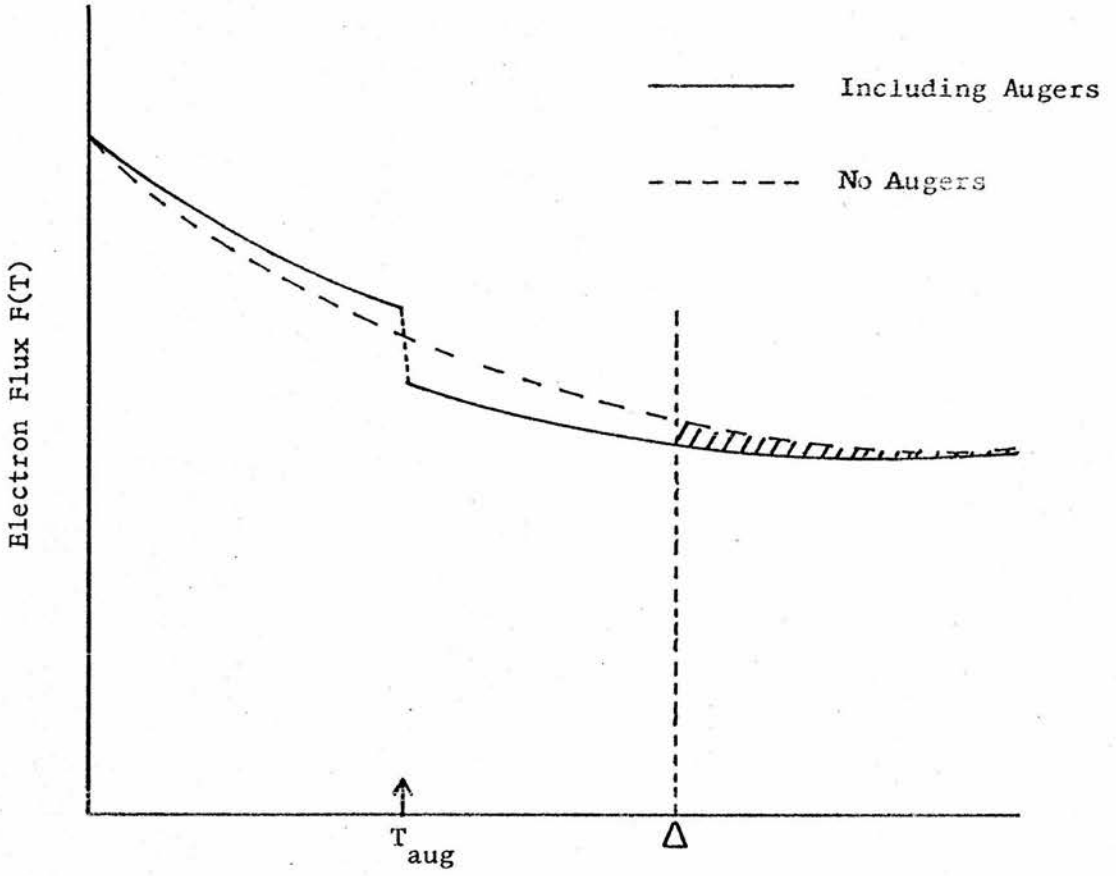

The shaded area represents the reduction in the flux due to Auger electron production. Hence there will be a reduction in the energy dissipation calculated from $\int_{\Delta}^{T_o} F(T).L(T,\Delta)dT$ which is counterbalanced by the inclusion of the Auger electrons in the track-end term.

to the way in which the track ends are dealt with in the Spencer-Attix evaluation. For the same electron flux spectrum, the same value of $S_a^w(\Delta)$ would be calculated.

ii) Auger Electrons.

Unless Δ is less than T_{aug}, some of the Auger electrons will not be accounted for in the integral over the electron flux in equ. 9.5. Specifically, for a cutoff Δ, these Auger electrons will be the ones that result from collisions in which the energy transfer is greater than $(\Delta + T_{aug})$ i.e. the δ-ray is included in the flux above Δ but with its energy reduced by T_{aug}. Figure 9.2 will help to clarify the argument. In addition, all the Auger electrons that result from photon interactions must be included. If the total number of such Auger electrons is written as $N_{aug}^w(\Delta)$, then the required energy dissipation in water is given by $N_{aug}^w(\Delta).T_{aug}$.

The question then arises as to how to calculate this contribution to the local energy dissipation in the air cavity. Ideally, one would need to take account of the production of Auger electrons from the oxygen and nitrogen atoms of which air is composed. However, such extra complications have not been incorporated into the calculation as $N_{aug}^w(\Delta).T_{aug}$ is very small compared to $N_\Delta^a.\Delta$ considered in i) above, at least for the 0.01 and 0.1 MeV cutoffs which are of most practical importance. Instead, $N_{aug}^w(\Delta).T_{aug}$ was simply weighted by the ratio of the mass stopping powers at $T = \Delta$ to give the value of $N_{aug}^a(\Delta).T_{aug}$, the contribution to the dose in the air cavity. Thus the Auger electron track ends are

effectively treated in the same way as the track ends of energy Δ in i). This is more or less equivalent to calculating the stopping-power ratio as if Auger electron production had not been taken into account in computing the electron flux spectrum.

It can be noted that for very small values of the cutoff, e.g. 1 keV, the term $N^{w}_{aug}(\Delta).T_{aug}$ becomes a few per cent of the total dissipation. Thus the Δ = 0.001 MeV stopping-power ratios might have been slightly influenced by a detailed treatment of Auger electron production in the air cavity.

iii) Photon-Ejected Electrons.

The Spencer-Attix theory did not consider the effect of photon interactions in the air cavity. However, in the present evaluation of $S^{w}_{a}(\Delta)$, such a consideration is inevitable. The local dose D_{Δ} must include the energy of the electrons with initial energies less than Δ which are produced directly by photon interactions, though for small Δ or for electron beams, the energy involved is only a small fraction of the total track-end dissipation. Note that this did not need to be considered in the computation of D_{100} (see sections 6.4.4 and 6.5) as there are virtually no electrons below 100 eV produced in photon interactions. In fact, this also applies to the 1 keV cutoff and to a lesser extent to the 10 keV cutoff.

Denoting the aggregate energy of all the photon-ejected electrons with initial energy less than Δ by $D^{w}_{ph}(\Delta)$, (per unit mass of water), then the energy deposited by the photons per unit mass of air will be given by

Figure 9.3 VARIATION OF WATER/AIR MASS ENERGY-ABSORPTION COEFFICIENT WITH PHOTON ENERGY.
(figures from Hubbell, 1969)

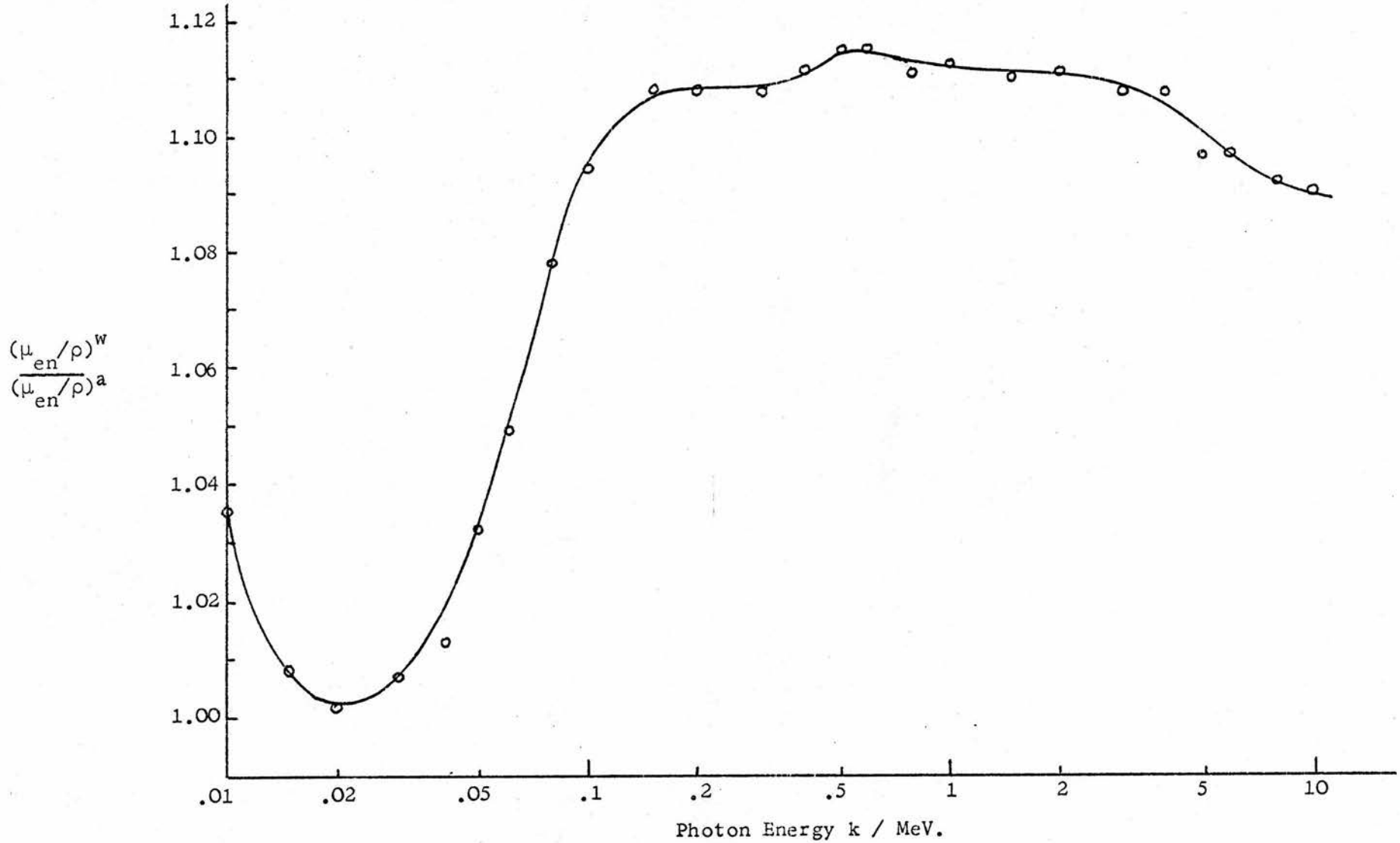

$$D^{a}_{ph}(\Delta) = D^{w}_{ph}(\Delta).\frac{(\bar{\mu}_{en}/\rho)^{a}}{(\bar{\mu}_{en}/\rho)^{w}} \qquad .....(9.9)$$

which will be written as $D^{w}_{ph}(\Delta).\bar{\mu}^{w}_{a}(\Delta)$.
The energy-absorption coefficients are averages over the energies of the photons that give rise to the electrons of energy less than Δ.

The calculation of $D^{a}_{ph}(\Delta)$ as above is equivalent to assuming that all photon-ejected electrons in the cavity with initial energy less than Δ arise as a result of photon interactions in the cavity, and equally well, that all photon-ejected electrons with initial energy greater than Δ arise from photon interactions with the wall material. This is clearly an oversimplication, as indeed is the two-group model for the stopping-power energy loss i.e. the Spencer-Attix theory, but it does incorporate in the evaluation of $S^{w}_{a}(\Delta)$ a term which takes account of the extent to which the cavity acts as a photon detector, albeit in an approximate manner.*

The variation of the water/air mass energy-absorption coefficient ratio with photon energy is shown in figure 9.3. This graph was used to estimate the value of the ratio to be used in equ. 9.9 for the different cutoffs. For Δ = 0.1 MeV, the water/air ratio was taken

---

*Burlin (1966) formulated a 'general theory of cavity ionization' which also included the ratio of mass energy-absorption coefficients and in addition took into account the modification of the electron spectrum by the cavity gas. His theory was a more comprehensive extension of the Spencer-Attix scheme than the present one, and was particularly designed to be applied to very dissimilar cavity and wall materials.

to be 1.105,* i.e. a factor 0.905 in equ. 9.9. For the 0.01 and 0.001 MeV cutoffs, this factor was 0.962 and 0.980 respectively, though the particular value at these cutoffs was immaterial as far as the numerical result for $S_a^w(\Delta)$ was concerned. It might be wondered why the value of the ratio $\bar{\mu}_a^w(\Delta)$ (see equ. 9.9) does not depend on the energy spectrum of the photon flux at the depth concerned. To a certain extent, this will be the case, but from a preliminary investigation of the values of $D_{ph}^w(\Delta)$ for the three cutoffs it could be deduced that the major contribution to $D_{ph}^w(\Delta)$ came from photons in the energy region just above Δ.

It is instructive to look at the magnitude of $D_{ph}^w(\Delta)$ for a few of the computations for electron and photon beams in order to see the effect of this modification of the stopping-power ratio calculation ; from equations 9.5 and 9.11, it will be seen that $S_a^w(\Delta)$ now includes $\bar{\mu}_a^w(\Delta)$. For the 20 MeV electron beam at a depth of 0.4-0.5 r_o, $D_{ph}^w(\Delta)$ is only 0.25% and 0.03% of the total dissipation for Δ = 0.1 and Δ = 0.01 MeV respectively. The corresponding figures for ^{60}Co photon radiation (B) at 4-6 cm depth are 13.5% and 1.1%. The figure at the 0.1 MeV cutoff for ^{60}Co is thus not so negligible and results in an effective mass stopping-power ratio significantly weighted towards the mass energy-absorption coefficient ratio, $\bar{\mu}_a^w(\Delta)$.

---

*This estimate would have been much more uncertain had the variation of $\bar{\mu}_a^w$ not been fortunately so slow in the 0.1 - 1 MeV region (see fig. 9.3).

The total track-end terms, ΣN^{w}_{Δ} and ΣN^{a}_{Δ}, for water and air respectively, are expressed in full as:

$$\Sigma N^{w}_{\Delta} = N^{w}_{\Delta}. + N^{w}_{aug}(\Delta).T_{aug} + D^{w}_{ph}(\Delta). \quad .....(9.10)$$

$$\Sigma N^{a}_{\Delta} = \left[N^{w}_{\Delta}. + N^{w}_{aug}(\Delta).T_{aug}\right].\frac{L^{a}_{tot}/\rho_{a}}{L^{w}_{tot}/\rho_{w}} + D^{w}_{ph}(\Delta).\frac{(\bar{\mu}_{en}/\rho)^{a}}{(\bar{\mu}_{en}/\rho)^{w}} \quad .....(9.11)$$

$$= N^{a}_{\Delta}.\Delta + N^{a}_{aug}(\Delta).T_{aug} + D^{a}_{ph}(\Delta)$$

The computation of N^{w} has already been dealt with (i.e. N_1). The calculation of $N^{w}_{aug}(\Delta)$ and $D^{w}_{ph}(\Delta)$ presented no problems in the photon-electron cascade program. A few extra lines of code had to be added to the routines COMPTON, PAIR and PHOTO to give $D^{w}_{ph}(\Delta)$ and similarly at all the places in the program where Auger electrons could be produced, to give $N^{w}_{aug}(\Delta)$.

It will be recalled that the electron flux, $F(T,z)$, was normalized to 1 MeV total dissipation by dividing by $D_{100}(z)$ (see section 6.5). Clearly, the dissipation $D(z)$ computed from the flux spectrum $F(T,z)/D_{100}(z)$ should come to 1 MeV whatever the value of Δ.* For the three values of Δ, this was found to be the case to within 2% and usually much less than this. This effectively demonstrated that the total track-end term, $\Sigma N^{w}_{\Delta}.\Delta$, had been evaluated correctly.

---

*Actually, this would not necessarily be true for a geometry such that electronic equilibrium did not extend up to Δ.

9.2.3.4 The Bragg-Gray Stopping-Power Ratio, $S_a^w(B\text{-}G)$

In addition to the evaluation of $S_a^w(\Delta)$ for the electron and photon beams at various depths, a calculation of the Bragg-Gray stopping-power ratio was also included for comparison purposes. This was evaluated using the primary electron flux spectrum and the total collision stopping powers for water and air:

$$S_a^w(B\text{-}G) = \frac{\int_o^T F_p(T,z).L^w_{tot}(T)/\rho_w dT}{\int_o^T F_p(T,z).L^a_{tot}(T)/\rho_a dT} \qquad .....(9.12)$$

The primary electron flux is comprised of all electrons that are not δ-rays. Thus all the photon-ejected electrons are considered to be primary electrons, and this includes the electrons produced by bremsstrahlung photons in the case of electron beams.* The lower limit of the integral, written as zero in the above expression, was in fact set equal to 1 keV in the calculation of $S_a^w(B\text{-}G)$. This avoided the problem of evaluating $L^a_{tot}(T)$ in the energy region where the stopping power formula is not valid. As the contribution of different portions of the low-energy part of the primary flux to the total dissipation is roughly proportional to dT, the 'last keV' is immaterial.

---

*This is consistent with the use of stopping-powers in equ. 9.12 which include all collision but no radiation losses.

Table 9.1 CALCULATED MASS STOPPING-POWER RATIOS FOR ELECTRON BEAMS (Water/Air)

a. T_o = 5 MeV

z/r_o	$\bar{z}$ (cm)	$s_a^w(T_o, z, \Delta)$ Δ (MeV)			s_a^w(B-G)
		0.001	0.01	0.1	
0.0 - 0.1	0.126	1.077	1.065	1.059	1.058
0.2 - 0.3	0.628	1.098	1.085	1.079	1.076
0.4 - 0.5	1.13	1.123	1.109	1.102	1.100
0.6 - 0.7	1.63	1.146	1.131	1.124	1.121
0.8 - 0.9	2.13	1.164	1.148	1.141	1.139
0.9 - 1.0	2.39	1.169	1.153	1.145	1.145
1.0 - 1.1	2.64	1.172	1.155	1.144	1.148
1.2 - 1.4	3.26	1.17	1.15	1.14	1.15

b. T_o = 10 MeV

0.0 - 0.1	0.245	1.033	1.022	1.016	1.018
0.2 - 0.3	1.23	1.055	1.044	1.038	1.034
0.4 - 0.5	2.21	1.084	1.072	1.065	1.060
0.6 - 0.7	3.19	1.116	1.102	1.096	1.091
0.8 - 0.9	4.17	1.145	1.131	1.123	1.121
0.9 - 1.0	4.66	1.157	1.142	1.134	1.133
1.0 - 1.1	5.15	1.166	1.149	1.140	1.141
1.2 - 1.4	6.37	1.18	1.15	1.14	1.15

Table 9.1 cont'd...

c. T_o = 20 MeV

z/r_o	$\bar{z}$ (cm)	$S_a^W(T_o, z, \Delta)$ Δ (MeV)			S_a^W(B-G)
		0.001	0.01	0.1	
0.0 - 0.1	0.460	0.987	0.977	0.972	0.976
0.2 - 0.3	2.30	1.014	1.004	0.998	0.995
0.4 - 0.5	4.14	1.041	1.030	1.024	1.019
0.6 - 0.7	5.98	1.076	1.064	1.058	1.053
0.8 - 0.9	7.82	1.113	1.100	1.093	1.089
0.9 - 1.0	8.74	1.132	1.118	1.111	1.108
1.0 - 1.1	9.66	1.148	1.133	1.125	1.124
1.2 - 1.4	12.0	1.146	1.128	1.116	1.123
d. T_o = 30 MeV					
0.0 - 0.1	0.630	0.960	0.951	0.946	0.953
0.2 - 0.3	3.25	0.988	0.979	0.973	0.971
0.4 - 0.5	5.85	1.016	1.006	1.000	0.996
0.6 - 0.7	8.45	1.051	1.039	1.033	1.028
0.8 - 0.9	11.1	1.087	1.074	1.068	1.064
0.9 - 1.0	12.4	1.108	1.094	1.087	1.084
1.0 - 1.1	13.7	1.129	1.114	1.107	1.104
1.2 - 1.4	16.9	1.139	1.122	1.111	1.116

9.3 MASS STOPPING-POWER RATIOS - RESULTS

9.3.1 Electron Beams

9.3.1.1 Tables of $S_a^w(T_o,z,\Delta)$ and $S_a^w(B\text{-}G)$

All the results for the four electron beam energies have been collected together in table 9.1a-d. They were derived from the 2000 electron-history computations that were described in chapter 7. The statistical uncertainty on each result is of the order of 0.1% except for the 1.2-1.4 r_o geometry where it is somewhat greater, especially at T_o = 5 and 10 MeV, due to the large statistical fluctuations in the electron flux in this bremsstrahlung tail region.*

The results clearly illustrate the marked increase in the stopping-power ratio with depth, due to the influence of the density effect on the stopping power in water. At a given depth, $S_a^w(\Delta)$ is generally between 1.5 and 2% higher for Δ = 0.001 than for Δ = 0.1 MeV, with the difference increasing slightly as the depth increases. Of course, this range of Δ-values corresponds to an enormous range of cavity sizes (or air pressures) and the results show in effect that the variation of the water/air stopping-power ratio with cavity size is very small.

---

*Berger et al. (1975) also estimated a very small statistical uncertainty in the mass stopping-power ratios derived from their Monte Carlo calculations, attributing this to the fact that any fluctuations in the electron flux spectrum tended to cancel out (i.e. in the numerator and denominator of equ. 9.5).

Figure 9.4 ELECTRON BEAMS : CALCULATED STOPPING-POWER RATIOS.

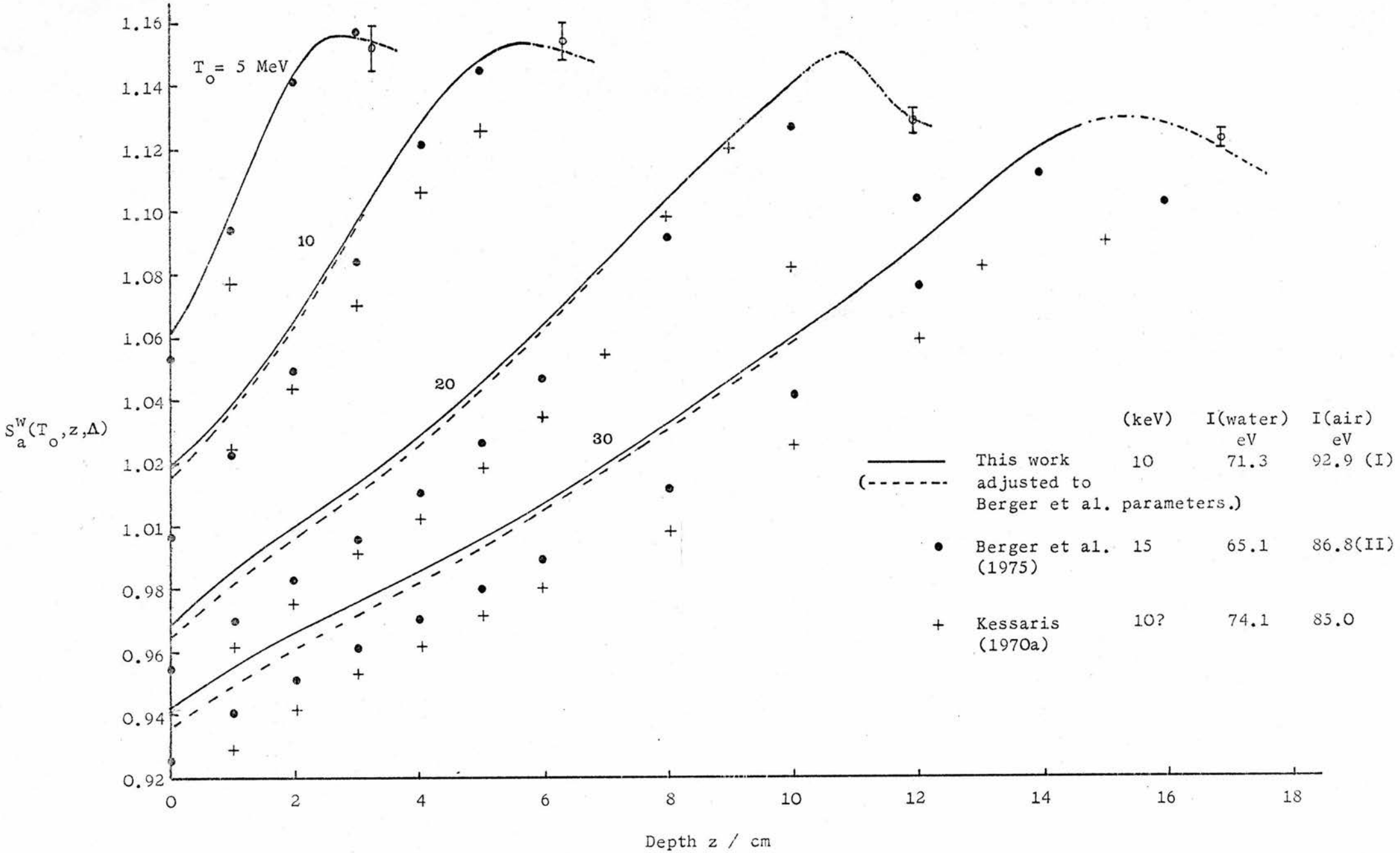

The Bragg-Gray stopping-power ratios are generally very close to, but slightly less than the Δ = 0.1 MeV $S_a^W(\Delta)$ values. Thus the Bragg-Gray evaluation corresponds to a rather large cavity. Note that for the 1.2-1.4 r_o geometry, $S_a^W(0.1)$ is lower than $S_a^W(B\text{-}G)$ at all four T_o. This is due to the influence of the dissipation by the photon-ejected electrons in the track-end term which, at this depth, weights $S_a^W(\Delta)$ significantly towards $\bar{\mu}_a^W(\Delta)$, which has the value 1.105 for the 0.1 MeV cutoff (see section 9.2.3.3).

9.3.1.2 Comparison with the Calculations of Berger et al. (1975) and Kessaris (1970a)

The values of $S_a^W(\Delta)$ for Δ = 10 keV, given in table 9.1, have been plotted as the continuous curves in figure 9.4. Also shown are the results of Berger et al. (1975) and Kessaris (1970a).* The maximum in $S_a^W(\Delta)$, exhibited by all three sets of results, is due to the transition at the end of the electron range from the degraded primary electron beam to a bremsstrahlung beam of somewhat higher average electron energy. Both the Kessaris and Berger et al. calculations were based on evaluating an expression for $S_a^W(\Delta)$ similar to equ. 9.5 using the total electron flux at different depths. The fairly large discrepancies evident in the figure call for some comment.

---

*The Kessaris figures were actually derived from the tabulation of C_E given in ICRU (1972) by dividing by the factor $\bar{I}(W/e).A$.

The Berger et al. values correspond to a 15 keV cutoff, and I-values slightly different from the ones used in this work. The effect of the differences in I-values can be gauged by referring back to fig. 9.1. The alternative set of I-values for which the restricted stopping-power ratio was also plotted in that figure corresponds to the Berger et al. $S_a^w(\Delta)$ results shown in fig. 9.4. It can be seen from fig. 9.1 that the present results for $S_a^w(\Delta)$ would have been decreased by about 0.3-0.5% for electrons of mean primary energy, $\bar{T}$, above 10 MeV or so had the Berger et al. I-values been used. The difference is much smaller at lower electron energies.* The effect of the cutoff being 10 keV rather than 15 keV is very small, 0.15% at most, as already mentioned in section 9.2.3.2.

When both these small differences have been allowed for (see dotted curve), reducing the discrepancy between the curve and the Berger et al. points by at most about 0.6%, the Berger et al. values still lie consistently between 1 and 1.5% below the present results for $\bar{T}$ above 10 MeV or so. Now Berger et al. calculated $S_a^w(T_o, z, \Delta)$ using the electron flux spectra computed by the Monte Carlo program developed by Berger and Seltzer (1969, 1969a). As it has already been shown in chapter 7 that their electron flux spectra and the ones computed in this work

---

*Berger et al. looked in some detail at the difference between $S_a^w(T_o, \Delta, z)$ evaluated with the I-values of set I and II (see fig. 9.4) but the exact values of the differences they obtained seem slightly too large below $\bar{T}$ = 10 MeV according to fig. 9.1 (by 0.3% at most). This is probably due to the marginally different way in which Berger et al. evaluated the density effect i.e. from the Sternheimer and Peierls (1971) formulation.

are in excellent agreement, then any significant differences in the stopping-power ratios must be due to differences in the way they have been derived from the flux spectra.

An expression for $S_a^w(T_o, z, \Delta)$ similar to equ. 9.5 was written down in the Berger et al. paper, the only difference being that the track-end terms were not included. However, it was also stated that the restricted collision stopping power, $L(T,\Delta)$, was evaluated from the expression for $L(T,\Delta)$ given in Berger and Seltzer (1964). This expression is identical to equ. 4.18 used in this work. It is quite clear that Berger et al. did not use the modified formulation for $L(T,\Delta)$ that Spencer and Attix (1955) employed* which 'automatically' included the track ends of energy Δ. Thus the contribution by the track ends to the local dose in water and air has been ignored in the Berger et al. evaluation of $S_a^w(\Delta)$ with no justification given for this.

Let us look at the effect of this on the value of $S_a^w(\Delta)$. Taking the calculation for T_o = 30 MeV at $z = 0.2 - 0.3\ r_o$ ($\bar{z}$ = 3.25 cm), the total track-end term $\Sigma N_\Delta^w \cdot \Delta$ for Δ = 10 keV was calculated as 0.057 MeV per MeV total dissipation. Now for Δ = 10 keV, $(L_{tot}^w/\rho_w)/(L_{tot}^a/\rho_a)$ is equal to 1.173 (see equ. 9.11). As $D_{ph}^w(\Delta)$ is negligible for this cutoff, the track-end term in air is given by 0.057/1.173 = 0.049. This has the effect of increasing this particular value of $S_a^w(\Delta)$ by 1.0% over

---

*Written by Spencer and Attix as $S(T,\Delta)$.

the value that is obtained if the track-end term is ignored in both D^{w}_{Δ} and D^{a}_{Δ}. To be precise, the 'correct' value of $S^{w}(\Delta)$ is 0.979, and without the track-end dissipation it is 0.969.*

Referring again to figure 9.4, it will be seen that if the Berger et al. value for T_o = 30 MeV at z = 3 cm is increased by 1%, it comes into exact agreement with the dotted curve. Thus the reason for the discrepancy is resolved. In fact, a similar exercise was carried out for all four T_o at different depths, and the discrepancy between the Berger et al. $S^{w}_{a}(T_o,z,\Delta)$ and the present 'adjusted' values was found to be 0.6% at the most, and generally much less, except for $z \gtrsim 1.1\ r_o$. Such differences close to and beyond the electron range cannot be regarded as significant. It is in this depth region that $S^{w}_{a}(\Delta)$ can be expected to be very sensitive to differences in the model adopted to simulate the spatial diffusion and energy loss of the primary electron beam, particularly with respect to the energy distribution of the bremsstrahlung photons. In addition, the statistical accuracy is not so high due to the small depth-dose level, which also means that the region is of minimal clinical and dosimetric importance.

---

*This difference becomes progressively smaller as $S^{w}_{a}(\Delta)$ approaches the value 1.173, when it is zero.

The Kessaris results are likewise somewhat below the curves in fig. 9.4. A glance at the key to the figure shows that the I-values Kessaris used were appreciably different from sets I and II. The difference between the Kessaris I(air) and I(water) is 10.9 eV compared to 21.6 and 21.7 eV for sets I and II respectively. A further complication in the comparison is that the electron flux spectra that Kessaris used, calculated by the Moments method employing the c-s-d-a (Kessaris, 1970), have been shown to be in only fair agreement with the Monte Carlo-derived flux spectra (see section 7.2.2). It does appear, however, that in evaluating $S_a^w(\Delta)$ from an expression similar to equ. 9.5, Kessaris did use the Spencer-Attix $S(T,\Delta)$ though he did not state this explicitly.* Kessaris also did not say exactly what value of Δ be used, but implied that it was in the region of 10 keV.

The neglect of energy-loss straggling in the Kessaris calculations resulted in 'unrealistic' values of the electron depth-dose curve at $z \sim r_o$. It is not surprising, therefore, to find that the Kessaris $S_a^w(\Delta)$ values at T_o = 20 and 30 MeV begin to decrease at somewhat smaller depths than the Berger et al. and the present results (look in particular at the Kessaris $S_a^w(\Delta)$ for T_o = 20 MeV at z = 10 cm in fig. 9.4).

---

*More specifically, this has been inferred from the fact that Kessaris makes several references to the Spencer-Attix $S(T,\Delta)$ in his 1970a paper.

Figure 9.5 DIFFERENCE BETWEEN 'HARDER FORMULA' AND 'EXACT' EVALUATION OF THE BRAGG-GRAY STOPPING-POWER RATIO.

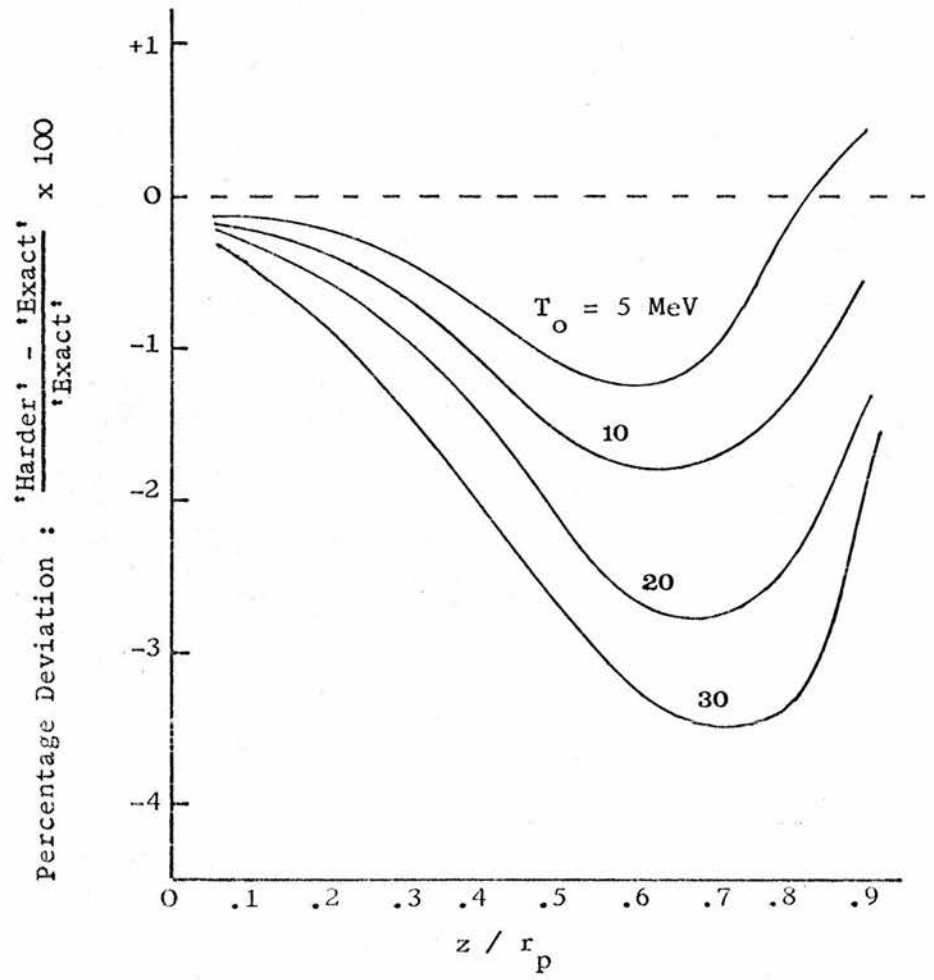

Finally, it can be noted that the ICRU (1972) report on electron-beam dosimetry recommended a series of C_E values based on these water/air stopping-power ratios calculations by Kessaris. The implications for C_E of the difference between the present $S_a^w(T_o,z,\Delta)$ results and those of Kessaris is dealt with in section 10.4.2 in the next chapter.

9.3.1.3 The 'Harder' approximation to $S_a^w(T_o,z)$

Harder (1965a) proposed a very simple method for estimating the mass stopping-power ratio for an electron beam of initial energy T_o at depth z. This can be written as:

$$S_g^m(T_o,z) = \frac{L_{tot}^m(T_m)/\rho_m}{L_{tot}^g(T_m)/\rho_g} \qquad .....(9.13)$$

where T_m is the mean primary electron energy at depth z, calculated from $T_m = T_o(1 - z/r_p)$. Using the values of the practical range r_p (derived from the electron beam depth-dose curves, given in section 7.4), this approximate stopping-power ratio has been evaluated for the four T_o up to $z \sim 0.9\ r_p$. Effectively, Harder's prescription is an approximation to the exact evaluation of the Bragg-Gray stopping-power ratio, as given by equ. 9.12. The validity of the approximation is illustrated in figure 9.5, using the 'exact' Bragg-Gray values, S_a^w(B-G), taken from table 9.1.

As one would expect, close to the surface the agreement is very close at all energies, but at greater depths differences begin to show up due to the combined effect

of multiple scattering and energy-loss straggling on the primary electron beam. Nevertheless, at T_o = 5 MeV the discrepancy hardly exceeds one per cent and even at T_o = 30 MeV it is less than 2% down to a depth of $z = 0.4\ r_o$. As z approaches r_p, the stopping-power ratios come into close agreement again. This is probably due to the fact that T_m is then in the energy region where the stopping power in water varies more slowly; hence the actual distribution of primary electron energy in the beam has only a minor influence on the value of the water/air stopping power ratio.

9.3.2 Photon Beams

Water/air mass stopping-power ratios have been calculated for all the photon beams (A - L in table 8.1) for which the electron flux spectra were computed. The evaluation of $S_a^w(\lambda,z,\Delta)^*$ for Δ = 0.001, 0.01 and 0.1 MeV from equ. 9.5 and $S_a^{w(B-G)}$ from equ. 9.12 was carried out in exactly the same way as for the electron beams. More general details of the photon beam computations and the results for the electron flux spectra, $F(\lambda,T,z)$, have been given in chapter 8.

9.3.2.1 Variation of the Stopping-Power Ratio with Depth

As the mean energy of the primary electron flux spectrum changes very little with depth for a photon beam, the stopping-power ratio is not markedly depth-dependent. Indeed, it is generally assumed that the

---

*The stopping-power ratio for photon beams will be written thus to distinguish it, where necessary, from $S_a^w(T_o,z,\Delta)$ for electron beams.

Figure 9.6 PHOTON BEAMS : VARIATION OF STOPPING-POWER RATIO WITH DEPTH.
(Δ = 10 keV)

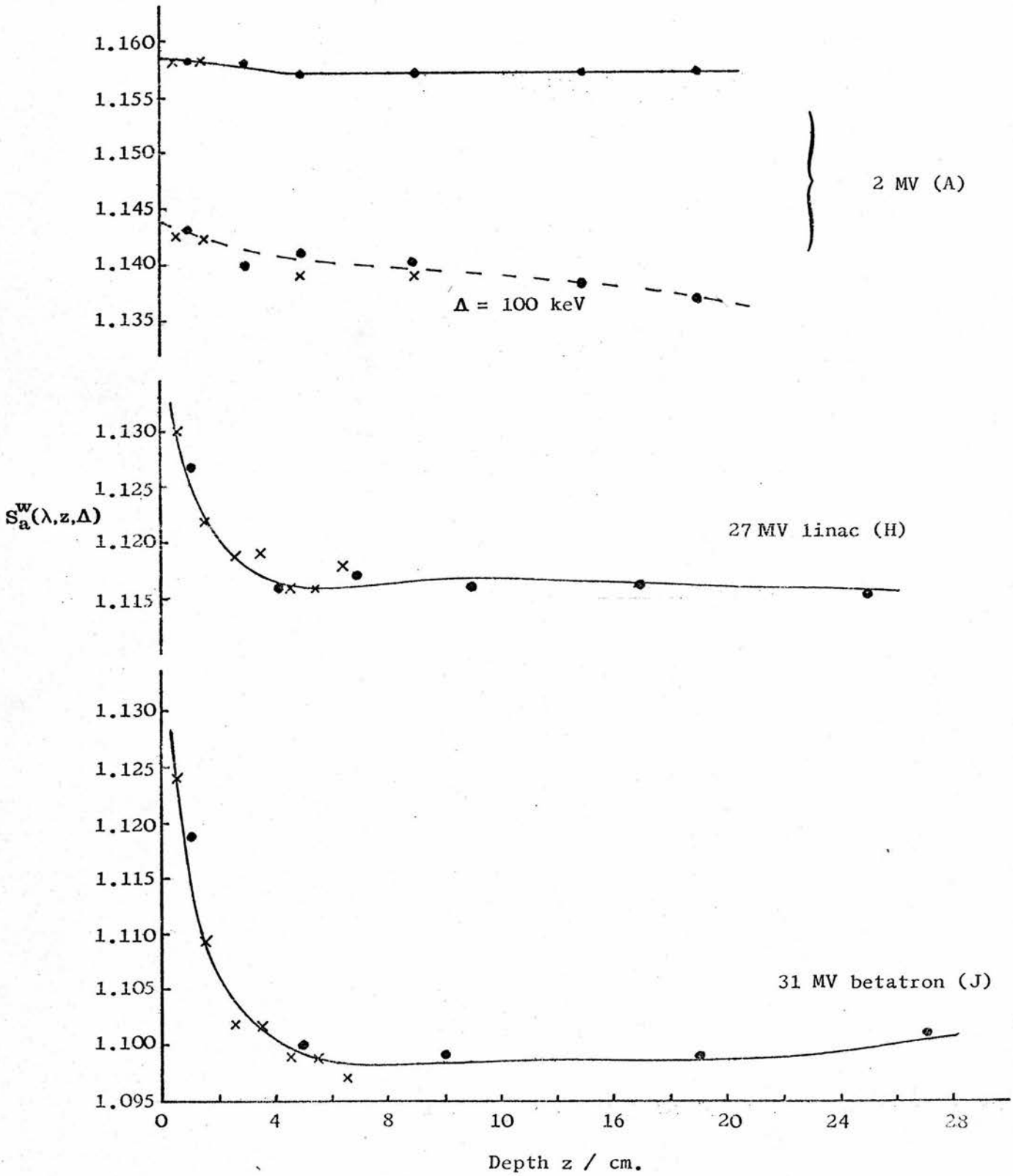

depth-dependence is negligible in deriving the absorbed dose in water from measurements with an air ionization chamber.

The continuous lines in figure 9.6 illustrate this very small depth-dependence, for Δ = 10 keV, at three qualities of x-ray beam. There are two sets of values plotted in the figure (• and ×) derived from different runs of the photon-electron cascade program. From the spread of the values, it can be deduced that the statistical uncertainty in the results is of the order of 0.2% or less.

The variation of $S_a^w(\lambda, z, \Delta)$ close to the surface at the 26 MV and 31 MV x-ray qualities was to be expected from the behaviour of the electron flux spectrum in this build-up region. It was shown in chapter 8 that the high-energy electron flux was considerably reduced in the surface layers below its value in the broad equilibrium-depth region. Thus the stopping-power ratio is greater corresponding to a lower mean primary electron energy.

For the 31 MV betatron spectrum (J) the change in $S_a^w(\lambda, z, \Delta)$ appears to be as much as 2.5% or so, whereas for the slightly 'softer' 26 MV linac beam the change is at most 1.5%. This rather large difference (i.e. between 1.5% and 2.5%) may be attributable in part to the fact that the 31 MV spectrum in question, J, contains a much larger number of low-energy photons due to the absence of a flattening filter. These low-energy photons will tend to be filtered out to a certain extent in the first few cm of water. Thus it is estimated that a 2% variation in

$S_a^w(\lambda, z, \Delta)$ over the build-up region is reasonable for a 31 MV betatron x-ray beam with a flattening filter (i.e. as the beam would be used in clinical practice). The variation of $S_a^w(\lambda, z, \Delta)$ beyond the initial decrease at the surface is extremely small, being within 0.2% up to the maximum depth shown. It should be noted that for the high-energy x-ray beams, the depth variation of the three other stopping-power ratios calculated is very similar to that illustrated for the Δ = 10 keV $S_a^w(\lambda, z, \Delta)$ results.

For the 2 MV x-ray beam, there is quite clearly no change at all in the Δ = 10 keV values. Two factors lead us to expect this. Firstly, the build-up region occurs extremely close to the surface as discussed in chapter 8. Secondly, the gradual softening of the electron flux spectrum with depth, demonstrated in that chapter, will not result in anything but a negligible increase in the stopping-power ratio as $\bar{s}_a^w(T)$ increases only very slowly with decreasing T below about 0.5 MeV : the density effect reduction in water is zero below this energy (see figure 9.1).

The results at the 2 MV quality for Δ = 0.1 MeV (100 keV) are a little more interesting (the broken line in fig. 9.6). A small, but quite definite decrease in $S_a^w(\lambda, z, \Delta)$ with increasing depth is evident. This is the result of the photon-ejected electron contribution to the total track-end dissipation. The value of $D_{ph}^w(0.1)$ was found to increase steadily from 16% of the total dissipation close to the surface to 26% at a depth of 15 cm or so. Thus the stopping-power ratio is

Table 9.2 CALCULATED MASS STOPPING-POWER RATIOS FOR PHOTON BEAMS (Water/Air)

Designation	Radiation Type*	$\bar{k}_{int}$ (MeV)	$S_a^W(\lambda, z, \Delta)$			S_a^W(B-G)
			Δ(MeV)			
			0.001	0.01	0.1	
A	2 MV	0.94	1.177	1.157	1.140	1.155
B	^{60}Co (P+S)	1.18	1.175	1.156	1.142	1.151
C	^{60}Co (P)	1.26	1.173	1.156	1.144	1.150
D	4.5 MV (linac)	1.63	1.171	1.153	1.140	1.148
E	6 MV (linac)	2.11	1.167	1.150	1.138	1.142
F	13 MV	5.91	1.139	1.124	1.115	1.115
G	19 MV (bet'n)	6.91	1.132	1.117	1.108	1.108
H	26.8 MV (linac)	8.27	1.131	1.116	1.108	1.108
I	26.8 MV (bet'n)	10.1	1.123	1.108	1.100	1.099
J	31 MV (bet'n)	12.8	1.114	1.099	1.091	1.090
K	31 MV (Pb f.f.)	11.8	1.114	1.100	1.092	1.091
L	31 MV (Al f.f.)	14.5	1.102	1.089	1.081	1.079

*For more details about the photon spectra, the reader is referred to table 8.1.

increasingly weighted towards $\bar{\mu}_a^w(0.1)$, i.e. 1.105, as the amount of scattered photon radiation increases with depth. In fact, the appreciable size of $D_{ph}^w(0.1)$ accounts for the fact that there is a difference of nearly 2% between the two $S_a^w(\lambda, z, \Delta)$ values at 5 cm depth (calibration). This difference can be compared to the smaller difference (1% or less) in the corresponding quantities for the electron beams and also for the high-energy photon beams.

9.3.2.2 Variation with Photon Beam Quality

The results for the twelve different photon energy spectra, all at the ICRU (1969) calibration depths* (given in section 8.3.2), are listed in table 9.2. The variation of $S_a^w(\Delta)$ with Δ at a given quality is similar to that for electron beams at 13 MV and above, the 1 keV cutoff value being about 2% greater than the 0.1 MeV cutoff value. Also at these qualities, the Bragg-Gray ratio is within 0.2% of $S_a^w(0.1)$.

For the qualities A-E, $S_a^w(0.1)$ is influenced appreciably by the term $D_{ph}^w(\Delta)$ i.e. by the dissipation by photon-ejected electrons. This has already been shown to result in a decrease of $S_a^w(0.1)$ with depth for the 2 MV beam. Note in particular that $S_a^w(0.1)$ increases between spectra A and C, whereas the other three stopping-power ratios steadily decrease, in line with the increase in $\bar{k}_{int}$. This rather odd behaviour of $S_a^w(\Delta)$ at relatively large values of Δ, where the

---

*In practice, this means that this was the average depth in the layer in which the flux spectrum was computed. Anyway, the depth-dependence has been shown to be extremely slow in this depth region so the precise value of $\bar{z}$ is immaterial.

Figure 9.7 PHOTON BEAMS : VARIATION OF STOPPING-POWER RATIO WITH AVERAGE PHOTON ENERGY.
(Δ = 10 keV, calibration depths)

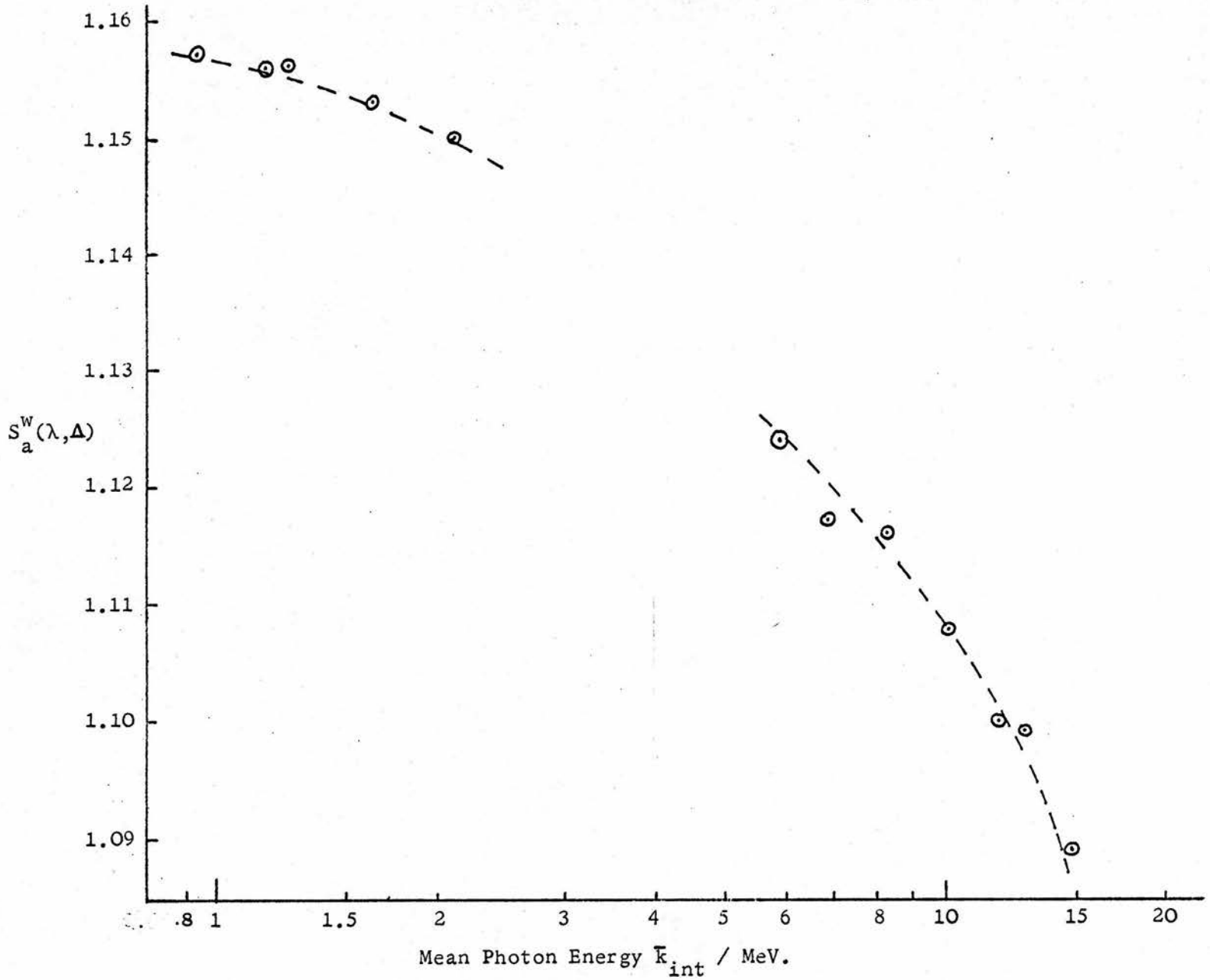

air cavity begins to act more like a photon detector than an electron detector, will be seen to be of some significance in the calculation of C_λ and C_E values in the next chapter.

The values in table 9.2 for the two 26.8 MV x-ray beams indicate quite clearly that the difference in the photon spectra (thin- and thick-target) leads to a difference in the stopping-power ratio, though only of 0.7-0.8% which is, if anything, a little smaller than had been expected. It can be seen also that the results for the 26.8 MV linac are almost identical to those for the 19 MV betatron.

The lead flattening filter does not appear to have appreciably softened the 31 MV x-ray beam as far as the stopping-power ratios are concerned. Clearly the filtering out of the low-energy photons has counterbalanced the effect of the reduction in the number of the photons at the high-energy end (see fig. 8.5). However, the stopping-power ratios for the aluminium-filtered 31 MV beam are a definite 1% lower than for the lead-filtered beam.

It was of interest to see to what extent the calculated stopping-power ratios correlated with the average photon energy in the spectrum, $\bar{k}_{int}$ (an energy fluence average). The variation of $S_a^w(0.01)^*$ with $\bar{k}_{int}$ is plotted in figure 9.7. It is evident that it is not possible to fit all the points on a smooth curve, especially at the high-energy end. This is most clearly demonstrated by the

---

*The 1 keV cutoff or Bragg-Gray values could equally well have been chosen.

Table 9.3 APPROXIMATE CALCULATIONS OF THE BRAGG-GRAY MASS STOPPING-POWER RATIO

Radiation	$\bar{T}_o$* (MeV)	$\bar{s}_a^w(\lambda)$	s_a^w(B-G)**
2 MV	0.34	1.152	1.155
^{60}Co	0.45	1.150	1.150 (Prim'y)
4 MV	0.7	1.147	1.148 (4.5 MV)
6 MV	1.5	1.138	1.142
12 MV	2.9	1.116	1.115 (13 MV)
14 MV	3.5	1.109	
18 MV	4.5	1.099	1.108 (19 MV)
20 MV	5.0	1.094	
25 MV	6.7	1.080	1.099 (27 MV,I)
30 MV	7.5	1.075	1.090 (31 MV,J)
35 MV	10.0	1.061	

*From table 1 in Greene and Massey (1966).

**From table 9.2.

values at $\bar{k}_{int}$ = 6.9 and 8.3 MeV (19 MV betatron and 26.8 MV linac resp.) and underlines the difficulty in comparing thin- and thick-target photon spectra.

9.3.2.3 Comparison of S_a^w(B-G) with 'Equivalent Electron Energy' Values

The most revealing way of looking at the photon beam results, and the most useful for practical purposes, is to compare them with the approximate values calculated on the 'equivalent electron energy' basis. As mentioned before in this work, it is these approximate stopping-power ratios that were used by Greene and Massey (1966, 1968) to derive the C_λ factors recommended by the ICRU (1969) report on photon beam dosimetry.

Greene and Masseys' water/air stopping-power ratios were calculated as follows. The mean photon energy was taken as 0.425 of the maximum energy of the spectrum. From this mean photon energy, an average initial electron energy, $\bar{T}_o$, was calculated using the Compton, pair and photoelectric cross-sections (column 2 in table 9.3). Assuming electronic equilibrium, the effective mass stopping-power ratio, $\bar{s}_a^w(\lambda)$, was evaluated from:

$$\frac{1}{\bar{s}_a^w(\lambda)} = \frac{1}{\bar{T}_o} \int_0^{T_o} \frac{L^a_{tot}(T)/\rho_a}{L^w_{tot}(T)/\rho_w} dT \qquad .....(9.14)$$

This is an approximation to the Bragg-Gray ratio. Note that $L_{tot}(T)$ is the total collision stopping-power.

Values of $\bar{s}_a^w(\lambda)$ are given in column 3 of table 9.3. These have been adjusted to correspond to the I-values used in this work. They were taken from a graph drawn using table A.1 in ICRU (1969) which lists values of $\bar{s}_a^w(\lambda)$

Figure 9.8 PHOTON BEAMS : COMPARISON OF APPROXIMATE AND RIGOROUS EVALUATIONS OF THE BRAGG-GRAY RATIO.

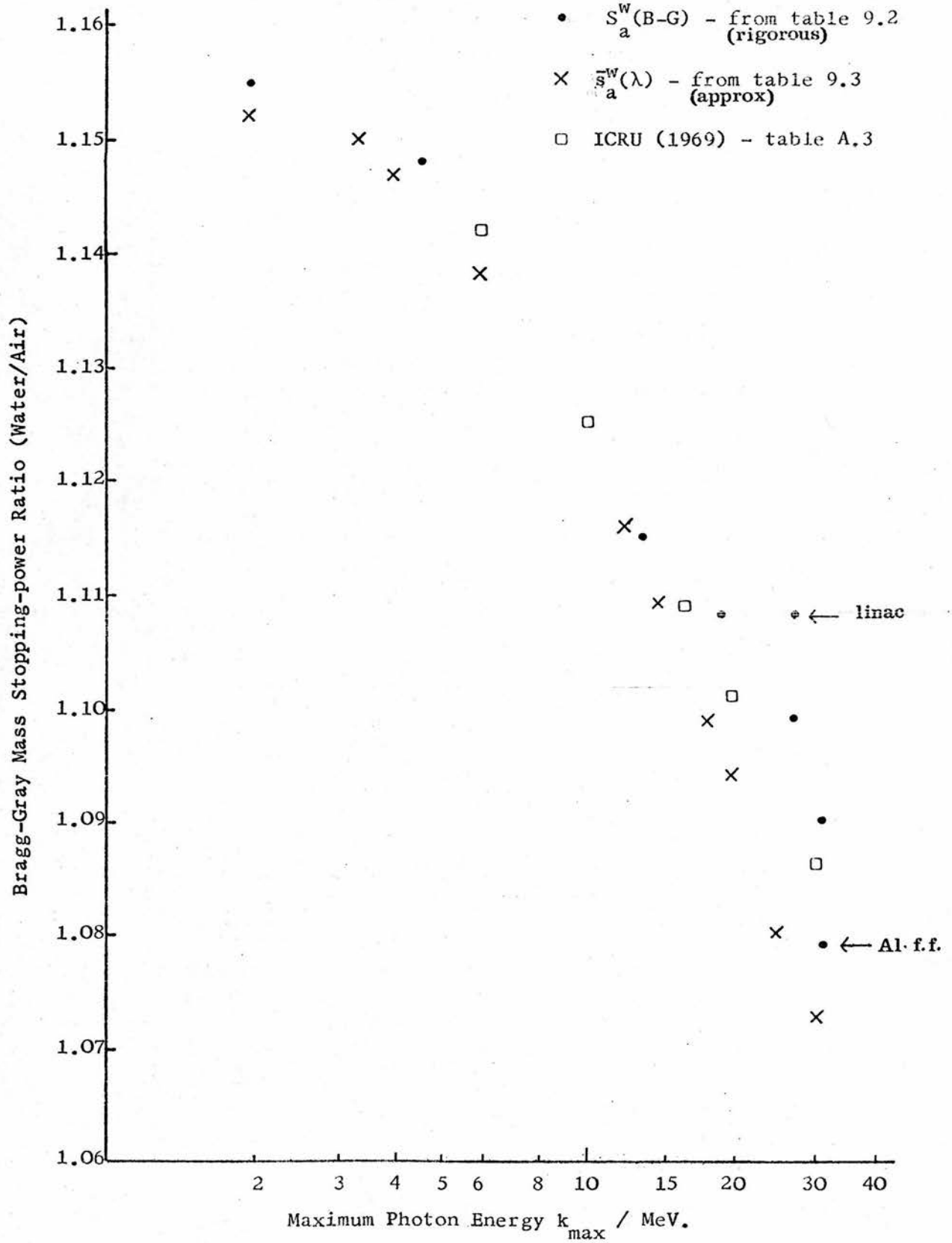

at certain $\bar{T}_o$ evaluated as in equ. 9.14 using the Berger and Seltzer (1964) I-values.*

The 'effective electron energy' values are seen to be always lower than S_a^w(B-G), the difference being small for low $\bar{T}_o$ as one would expect, but increasing to as much as 2% for the 31 MV x-ray beam. Only the high-energy thin-target spectrum results have been included in column 4 of the table, as it is only for these spectra that the '0.425 approximation' (see above) is reasonable. In fact, only one of them, the unfiltered 31 MV beam (J), is a more or less unadulterated Schiff spectrum. For this spectrum, $\bar{k}_{int}/31 = 0.412$, which is close enough to 0.425.

The stopping-power ratios in table 9.3 have been plotted against maximum photon energy, k_{max}, in figure 9.8. The ^{60}Co value appears to be equivalent to about 3.3 MV where it has been positioned. The 13 MV result does not quite follow the general trend, being only 0.25% or so above the value that would be calculated by the approximate procedure at that energy. However, it was emphasised in chapter 8 that only limited confidence could be placed in the 13 MV photon spectrum. In fact the ratio $\bar{k}_{int}/13$ comes out to be 0.45, which is rather a high value. The 26.8 MV linac (H) and the 31 MV aluminium filter (L) results have been put on the graph to emphasise the inadequacy of specifying an x-ray beam quality only by its maximum photon energy, k_{max}.

---

*The adjustment was a small increase of between 0.15 and 0.3% estimated from a graph similar to figure 9.1, but for the total collision stopping powers.

The third set of values on the figure has been taken from a less approximate calculation of the stopping-power ratio given in the ICRU (1969) report. Again they have been adjusted for the change in I-values. These ratios were calculated using a Schiff photon spectrum, filtered by 5 cm water. A distribution of initial electron energies was derived from the photon spectrum with the effect of radiation losses also taken into account. This derivation is in effect a much closer approximation to the present calculations which are, of course, based on the actual primary electron flux produced at a depth in water due to absorption and scattering of the incident photon beam. From fig. 9.8 it can be seen that this more rigorous ICRU calculation method does indeed produce values that are in closer agreement with the results of the present work. It would appear that the difference at 31 MV is only 0.5% compared to nearly 2% using the method which represents the electrons produced in the absorbing medium by only one average energy $\bar{T}_o$ (i.e. equ. 9.14). The discrepancy would probably have been considerably smaller than 0.5% if the 31 MV spectrum had not been modified at the very low-energy end by filtration by the glass wall of the betatron doughnut (see table 8.1 and fig. 8.5) and the ICRU method had included the effect of the scattered photons.

9.4 SUMMARY AND CONCLUSIONS

9.4.1 Details of the Calculations

Water/air mass stopping-power ratios have been evaluated for the high-energy electron and photon beams using a modified form of the Spencer-Attix cavity ionization theory. It is assumed as in the Spencer-Attix theory that the electron flux down to the cutoff energy Δ is not modified by the presence of the cavity. Deviations from this are expected to be negligible for the fairly close match between the water walls and air cavity to which the present calculations apply.

The difference from the Spencer-Attix evaluation lies in the way in which the contribution of the electron track ends to the local dose in the cavity, D_Δ, has been handled. Spencer and Attix automatically accounted for the track ends of energy Δ through the use of a restricted collision stopping power, $S(T,\Delta)$, that differs between $T = \Delta$ and $T = 2\Delta$ from the conventionally-defined $L(T,\Delta)$ employed in the present calculations. Careful consideration has been given to the way in which the dissipation by the track ends in the air cavity should be calculated when using $L(T,\Delta)$. For electron beams, and photon beams with the cutoff sufficiently small that photon interactions in the air cavity can be neglected, the present evaluation of the stopping-power ratio, incorporating the track-end dissipation, is equivalent to the Spencer-Attix formulation. However, the depth-dependent electron flux spectra computed in this work have been employed in the calculation whereas Spencer and Attix used an electron spectrum based on an approximate form of the depth-independent Spencer-Fano theory.

The track-end term must also include the dissipation by photon-ejected electrons with initial energy less than Δ, $D_{ph}(\Delta)$. For any Δ, $D^{w}_{ph}(\Delta)$, corresponding to water, is readily evaluated from the photon-electron cascade computation. The corresponding dissipation in the air cavity (of equal mass), $D^{a}_{ph}(\Delta)$, is assumed to be given by $D^{w}_{ph}(\Delta).(\bar{\mu}_{en}/\rho)^{a}/(\bar{\mu}_{en}/\rho)^{w}$ where the energy-absorption coefficients are averages over the energy region of the photons that give rise to electrons of energy less than Δ. In this approximate manner, the restriction on the size of Δ due to the neglect of photon interactions in the cavity in the Spencer-Attix theory has been removed.

Stopping-power ratios from this modified Spencer-Attix theory have been calculated for cutoffs of 0.001, 0.01 and 0.1 MeV. In addition, the Bragg-Gray ratio has been evaluated from the primary electron flux spectrum using the unrestricted collision stopping-powers. The I-values were taken from Dalton and Turner (1968): 71.3 eV and 92.9 eV for water and air respectively.

9.4.2 Electron Beam Results

For the 5, 10, 20 and 30 MeV electron beams, the 10 keV cutoff results were compared to similar calculations by Berger et al. (1975). The agreement was nowhere near as good as had been expected, especially in view of the fact that the depth-dependent electron flux spectra used in the Berger et al. work had already been shown to be in excellent agreement with the spectra computed in this work. However, a careful examination of the way in which Berger et al. actually evaluated the stopping-power ratio

revealed quite clearly that the track-end dissipation had been left out of their calculations. It is shown that this omission accounted for the difference between the two sets of results. There were also considerable discrepancies between the present results and those of Kessaris (1970a), though possibly for different reasons such as the difference in I-values and electron flux spectra. The Bragg-Gray ratios, which were closest to the Δ = 0.1 MeV values and about 1% less than the 10 keV ones, were compared to stopping-power ratios calculated using the simple 'Harder' formula. Agreement was very good at small depths but the Harder values were as much as 3.5% below the more exact figures at $z \sim 0.7\ r_p$ for T_o = 30 MeV, though within about 1% at all depths for the 5 MeV beam.

9.4.3 Photon Beam Results

For the photon beams, the variation of the stopping-power ratio with depth was shown to be negligible beyond the build-up region, as has usually been assumed to be the case in dosimetric ionization measurements. The exceptions to this were the 0.1 MeV cutoff results for 2 MV x-rays which displayed a small but non-neglibible decrease with increasing depth. This was due to the increasing dissipation by the photon interactions in the cavity, itself caused by the increase of low-energy scattered photon radiation with depth, which resulted in the effective stopping-power ratio being gradually reduced

towards the significantly lower energy-absorption coefficient ratio. Naturally, the unmodified Spencer-Attix values could not have shown this effect.

The Bragg-Gray ratios for the photon beams were compared with values based on the 'equivalent average electron energy' method, such as was used by Greene and Massey (1966) in calculating C_λ. Significant differences were apparent, especially for the higher-energy photon beams (i.e. above 19 MV or so). It was concluded that such approximate calculations do not provide sufficiently accurate values for the stopping-power ratios, resulting in values that are consistently too low. It was noted that stopping-power ratios given by ICRU (1969), calculated using a distribution of electron energies produced by a Schiff photon energy spectrum, were in much closer agreement with the present calculations for betatron beams.

It was found that the 27 MV linac x-ray beam stopping-power ratios were nearly 1% higher than those for the 27 MV betatron, being very close to those for the 19 MV betatron. In addition, for the 31 MV betatron, the aluminium-filtered spectrum results were definitely 1% lower than those for lead-filtered spectrum. An attempt to draw a smooth curve through the stopping-power ratios for a given cutoff plotted against the mean energy of the photon intensity spectrum, $\bar{k}_{int}$, was not particularly successful. Naturally, the differences in the stopping-power ratios due to thin- vs thick-target photon spectra or differences in the flattening filter material that

have been indicated for the higher-energy x-ray beams can reasonably be expected to be negligible for 6 MV x-rays for example.

9.4.4 Comparison with Experiment

There are no experimental results that can be directly compared with the calculated water/air stopping-power ratios. For practical reasons, most of the calorimetric determinations have been carried out with carbon-walled ionization chambers and hence carbon/air stopping-power ratios* have been determined (e.g. Pinkerton, 1969; Berger et al., 1975; Tedman, 1975; Bewley, 1963). The main practical value of the water/air ratios lies in their application in calculating C_E and C_λ factors which is fully dealt with in the next chapter. There have been several experimental determinations of these factors and these are discussed in sections 10.3.3 and 10.4.3. A consideration of the expected accuracy of determinations of the absorbed dose derived from cavity ionization measurements, in which the stopping-power ratio is only one of the factors, has been left until the final section of that chapter.

---

*Actually it is $\bar{W}.\bar{s}_{mg}$ that is measured.

CHAPTER 10

C_E AND C_λ FACTORS

10.1 INTRODUCTION

Routine dosimetric measurements at radiotherapy centres are usually carried out using a secondary standard thimble ionization chamber that has been calibrated against an absolute exposure standard at ^{60}Co gamma-ray or 2 MV x-ray quality. The exposure calibration is carried out at a national standards laboratory (NPL in the U.K.). The C_E and C_λ factors, for electron and photon radiation respectively, are then required to relate the reading of the instrument connected to the calibrated thimble chamber to the absorbed dose in water at the point of measurement for the particular electron or photon beam under measurement.

Expressions for deriving C_λ and C_E from the appropriate water/air stopping-power ratios are to be found in the ICRU reports on photon and electron dosimetry (ICRU, 1969, 1972 resp.). It would have been relatively straightforward to have presented tables of C_E and C_λ calculated using these expressions and the stopping-power ratios presented in the previous chapter. However, a careful examination of the assumptions involved in the derivations for C_E and C_λ given in the ICRU reports revealed some inconsistencies, particularly when consideration was given to the construction and dimensions of the Baldwin-Farmer* ionization chamber to which the factors apply. The walls of the chamber had been assumed to be water-equivalent for the calibration radiation in

---

*This is the instrument widely used in the U.K. In other countries very similar types are used which go under different names according to the manufacturer.

deriving C_λ (ICRU, 1969; Greene and Massey, 1966), but air-equivalent in deriving C_E (ICRU, 1972; Svensson and Patterson, 1967).

As considerable effort had gone into reducing approximations in the computation of the water/air stopping-power ratios, it was only reasonable to want to make use of them in a valid manner. In addition, much of the experimental evidence for the 'G-value difference' is based on measurements that involved C_E and C_λ, which underlines the importance of these factors in this investigation.

10.2 THEORETICAL EVALUATION

10.2.1 The Basic Relations

The basic expressions involved are:

$$D = R.N_c.C_\lambda \qquad .....(10.1)$$

for photon beams, and

$$D = R.N_c.C_E \qquad .....(10.2)$$

for electron beams; where

D is the absorbed dose at the point of interest in a water phantom for a given exposure* of electron or photon radiation;

R is the exposure-meter reading, corrected for temperature and pressure, obtained for that 'exposure' when the ionization chamber was placed in the phantom at the position of interest;

N_c is the calibration factor provided by a standardizing laboratory for determining exposure for 2 MV x-rays or ^{60}Co.

---

*The term exposure is retained for convenience, though it is only defined for photon beams. It does not affect the argument and could have been replaced by 'reading of the monitor chamber'.

The C_λ factor corresponding to the same radiation quality as at the calibration is written as $(C_\lambda)_c$ and is given by

$$(C_\lambda)_c = d_c.(\bar{W}/e).\left[\frac{(\mu_{en}/\rho)^w}{(\mu_{en}/\rho)^a}\right]_c \qquad .....(10.3)$$

$$= d_c.(\bar{W}/e).\bar{\mu}_a^w(\lambda_c)$$

where d_c is known as the displacement factor. The derivation of this relation can be found in Greene et al. (1971), for instance. It is not being disputed in the present work. It is required to relate $(C_\lambda)_c$ to C_λ and C_E for other electron and photon beams.

The absorbed dose at the point of interest in the water phantom can also be written down as:

$$D = J_a.(\bar{W}/e).(\bar{s}_{mg})_\lambda.p_\lambda \qquad .....(10.4a)$$

$$D = J_a.(\bar{W}/e).(\bar{s}_{mg})_E.p_E \qquad .....(10.4b)$$

where $\bar{s}_{mg}$ is a mass stopping-power ratio appropriate to the ionization chamber concerned and p is a perturbation correction for scattering effects (to be discussed in section 10.2.4). Note that the above relation makes no assumptions as to whether the instrument behaves as a Bragg-Gray cavity or what sort of walls it has etc. Nor is it any different in form for electron or photon radiation. For the calibration radiation equ. 10.4 is written as:

$$D = J_a.(\bar{W}/e).(\bar{s}_{mg})_c.p_c \qquad .....(10.5)$$

Now the exposure meter reading R must be proportional to the ionization in the cavity. Thus simply

$$R = K.J_a \qquad .....(10.6)$$

Figure 10.1 THE BALDWIN-FARMER ION CHAMBER.
(adapted from Barnard et al.,(1959)

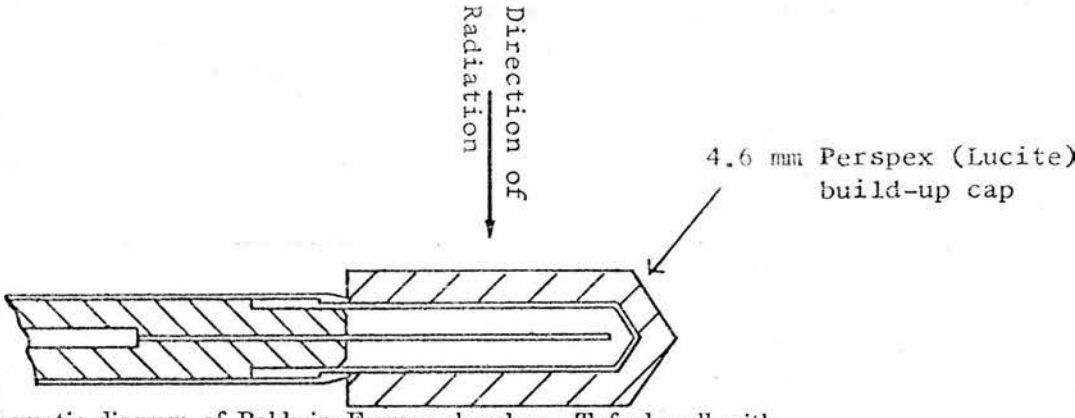

Fig. 5. Schematic diagram of Baldwin–Farmer chamber. Tufnol wall with inner coating of graphite (0·001 in. thick); total wall thickness, 74 mg/cm²; central electrode, elektron metal.

Table 10.1 WATER/LUCITE RATIOS

T (MeV)	$\bar{s}_1^w(T)$*	$k_{max.}$ (MV)	$\frac{(\mu_{en}/\rho)^w}{(\mu_{en}/\rho)_1}$ +
0.5	1.037	2	1.03
1	1.043	6	1.03
2	1.044	10	1.04
5	1.042	14	1.04
10	1.038	20	1.05
20	1.035	25	1.05
30	1.034	30	1.05

* $\bar{s}_1^w(T)$ is defined by equation 9.6 and has been evaluated from the Berger and Seltzer (1964) tabulation. Values would have been very similar had the Dalton and Turner (1968) I-values been used.

+ From Schulz (1970)

Eliminating R between (10.1), (10.5) and (10.6):

$$K = \frac{(\bar{W}/e).(\bar{s}_{mg})_c . p_c}{N_c.(C_\lambda)_c}$$

at the calibration quality.

At any other quality, say λ, also

$$K = \frac{(\bar{W}/e).(\bar{s}_{mg})_\lambda . p_\lambda}{N_c.C_\lambda}$$

Thus equating these two relations,

$$C_\lambda = (C_\lambda)_c . \frac{(\bar{s}_{mg})_\lambda . p_\lambda}{(\bar{s}_{mg})_c . p_c} \qquad .....(10.7a)$$

or equally well,

$$C_E = (C_\lambda)_c . \frac{(\bar{s}_{mg})_E . p_E}{(\bar{s}_{mg})_c . p_c} \qquad .....(10.7b)$$

Relation (10.7a) is the same as that obtained by Greene and Massey (1966) except that here no assumptions have been made yet as to exactly how the stopping-power ratio should be evaluated. In order to answer this question, it is necessary to look at the characteristics of the Baldwin-Farmer ionization chamber to which C_λ and C_E apply.

10.2.2 The Baldwin-Farmer Ionization Chamber

The construction of the cavity is illustrated in figure 10.1. The perspex build-up cap has been added to the diagram. The inner diameter of the cylindrical cavity is 0.6 cm. The legend under the drawing states that the thickness of the Tufnol wall is 74 $mg.cm^{-2}$. Now the chamber wall is specifically designed to be as closely air-equivalent as possible (Greening, 1974)*. It will therefore be assumed to be air-equivalent in what follows.

*Tufnol is a very empirical material and is fortuitiously approximately air-equivalent; its composition is close to that of Bakelite (priv. comm. from Prof. Farmer).

The important point is that it is quite clearly not water-equivalent.

Immediately on the outside of the air-equivalent cavity wall is the Perspex build-up cap. This is designed to be of a sufficient thickness to ensure electronic equilibrium when the chamber is calibrated in air for 2 MV or ^{60}Co radiation. It is also placed round the chamber when it is irradiated in the water phantom at any radiation quality (i.e. when it is used to determine the dose with the appropriate C_λ or C_E factor). Now Perspex (also known as Lucite) is very much closer to being water-equivalent than air-equivalent. Its density is about 1.2 times that of water and the I-value is within about 1% of that for water (Berger and Seltzer (1964) give I(lucite) as 65.6 eV; Dalton and Turner (1968) give 69.2 eV). Table 10.1 lists $\bar{s}_l^w(T)$ and $\bar{\mu}_l^w(k)$, the water/lucite ratios, for energies of interest. Both ratios are reasonably close to unity and remain practically constant with increasing energy, in contrast to the water/air stopping-power ratio, for example. These values are given to demonstrate that no serious error is involved in assuming that the lucite build-up cap is water-equivalent. Anyway, any factor representing the difference between lucite and water would only enter the expression for C_E or C_λ as a ratio for two different qualities.

10.2.3 Appropriate Stopping-Power Ratios

On the basis of the information given in the previous section, it seems justified to regard the B-F chamber as having a water wall and an air cavity of effective dimensions of the order of the Tufnol wall thickness i.e. 74 $mg.cm^{-2}$, although the actual cavity volume in which the ionization is measured has a diameter of only 0.6 cm. The effective cutoff, Δ, at which the water/air stopping-power ratio is to be evaluated is then about 0.3 MeV, corresponding to an electron range in air of 95 mm. One cannot be precise about the value of the cutoff, but it is clear that it should be of this order of magnitude.*

For electron and high-energy photon beams it was shown earlier in chapter 9 that the stopping power ratio varied very slowly with Δ, and furthermore that the 0.1 MeV cutoff value was close to the Bragg-Gray ratio. For qualities such as 2 MV x-rays and ^{60}Co, the situation is somewhat different. At large cutoff values, the cavity begins to behave less like an electron detector and more like a photon detector. A significant proportion of the dissipation in the cavity results from photon interactions in the cavity.

---

*More explicitly, the assumption is that the cavity size parameter is determined by the thickness of the air-equivalent walls, but the actual stopping-power in the cavity (which determines the dissipation) is calculated for gaseous air i.e. with no density effect reduction. Note that similar arguments were put forward to deal with the case of probes whose walls had a thin gas-equivalent lining in ICRU (1972). A cutoff of 0.1 MeV was considered to be a good approximation for evaluating the Spencer-Attix stopping-power ratio for such probes.

At the calibration quality, it is clear then that the B-F chamber is behaving to a significant extent as a photon detector as the Tufnol 'walls' are air-equivalent. In fact, Greening (1974) stated that it was readily determined experimentally that a typical commercial chamber (the Baldwin-Farmer) exposed to ^{60}Co radiation without a build-up cap gave two-thirds of the reading obtained with the build-up cap. Thus it can be assumed that a B-F chamber used for ^{60}Co radiation is approximately 2/3 rds 'photon detector' and only 1/3 rd'electron detector'. The effective stopping-power ratio will be given approximately by

$$\bar{s}_{wa} = \frac{1}{3}.S_a^w(B-G) + \frac{2}{3}.\bar{\mu}_a^w \qquad .....(10.8)$$

$$\simeq 1.123$$

This is appreciably different from the Bragg-Gray ratio of 1.150.

Turning now to the present evaluation of the water/air stopping-power ratio, $s_a^w(\Delta)$, the effective cutoff Δ for ^{60}Co radiation should be such that $D_{ph}^w(\Delta)^*$ is about 2/3 rds of D_Δ^w (see section 9.2.3.2) i.e. photon interactions in the cavity account for 2/3 rds of the total dissipation. In fact, for Δ = 0.3 MeV, the figure is only 28% with $S_a^w(\Delta) = 1.135$. For Δ = 0.5 MeV, $D_{ph}^w(\Delta)$ is 40% of the total dissipation and $S_a^w(\Delta)$ comes to 1.129.** This is reasonably close to the estimate of 1.123 given above. The corresponding figures for 2 MV x-rays are 66% and 1.121 for Δ = 0.5 MeV.

---

*The ratio of photon-ejected electron to total dissipation in the air cavity, $D_{ph}^a(\Delta)/D_\Delta^a$, will be of the same order. The 'w' figures have been used for convenience.

**These figures refer to the 'primary + scattered' ^{60}Co beam (B) at the calibration depth, 5 cm.

Figure 10.2 TRANSITION OF CAVITY FROM A PHOTON TO AN ELECTRON DETECTOR : PHOTON BEAMS.
(calibration depths)

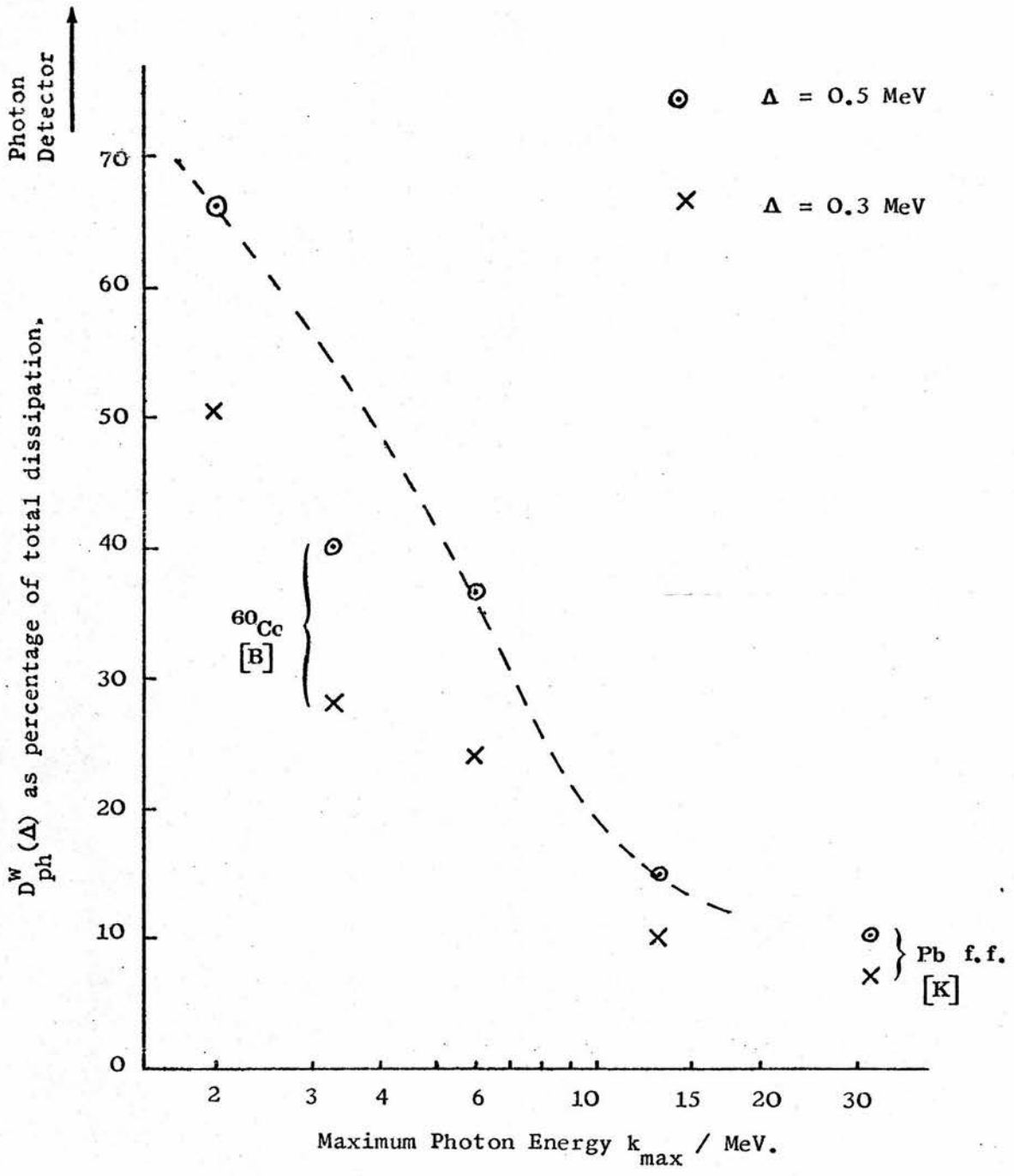

The inability of the procedure for calculating $S_a^w(\lambda, z, \Delta)$ to 'get the 2/3 rds figure right' is merely a demonstration of the approximate nature of the sharp cutoff model. Indeed, it was expected that $D_{ph}^w(\Delta)$ would be considerably too low for Δ = 0.3 MeV. It would be interesting to see what value for $S_a^w(0.3)$ for ^{60}Co would be calculated by the 'general theory' of Burlin (1966) which, as already mentioned, also incorporates the photon mass energy-absorption coefficient ratio and in addition allows for the modification of the electron spectrum above T = Δ by the cavity. Clearly the result could not be very different from the figure of 1.123 estimated above.

A decision had to be reached about which stopping-power ratios to use to evaluate equations 10.7a,b for C_λ and C_E. The following empirical procedure was employed. For all the four initial electron beam energies, the 0.3 MeV cutoff would be used (actually 0.310 MeV; a T_1 value). For electron beams the 'photon detector problem' does not arise.* Thus $(\bar{s}_{mg})_E$ was evaluated as $S_a^w(T_o, z, \Delta)$ for Δ = 0.3 MeV. For photon beams, the cutoff was taken as equal to 0.5 MeV for ^{60}Co and 2 MV radiation. Clearly for the 31 MV x-ray beam, 'the photon detector problem' was going to be much reduced.

The value of $D_{ph}^w(\Delta)$ for the 0.3 MeV and 0.5 MeV cutoffs at the different photon qualities is shown in figure 10.2. The rapid decrease with increasing k_{max} corresponds to the effective transition from a predominantly photon detector at 2 MV to an electron detector above 10 MV or so,

---

*Except for $z \gtrsim 1.2\ r_o$ where the primary radiation is bremsstrahlung. However, C_E is of no consequence at such depths.

for the cavity sizes represented by the two cutoffs. A parameter $\Delta_{eff}(\lambda)$ was defined for the photon beams, to be given by

$$\Delta_{eff}(\lambda) = 0.310 + 0.19\ \{D^{w}_{ph}(0.3)/0.504\} \quad .....(10.9)$$

Thus at 2 MV, Δ_{eff} is 0.50 MeV as $D^{w}_{ph}(0.3) = 0.504$ at this quality. At 31 MV, $D^{w}_{ph}(0.3) = 0.07$ giving Δ_{eff} as 0.34 MeV. At 6 MV, Δ_{eff} is 0.40 MeV and so on.*

It will be realized that the values of $S^{w}_{a}(\Delta)$ already presented in chapter 9 did not extend to extra cutoffs between 0.3 and 0.5 MeV. However, very little extra computing was necessary. Complete re-runs were only needed for the ^{60}Co, 2 MV and 6 MV photon beams, which were inexpensive anyway. The computations for the 13 MV, and 31 MV Pb- and Al-filtered x-ray beams were actually carried out after the evaluation of C_{λ} and C_{E} had been thought out, and so included the 0.3 and 0.5 MeV cutoffs. For the electron beams, a series of 200-history runs were made with $\Delta = 0.3$ MeV added. From these results, a sufficiently accurate estimate of $S^{w}_{a}(T_{o},z,0.3)$ could be made, with the help of the 0.1 MeV cutoff results from the 2000-history runs. The difference was only about 0.2% in any case.

---

*With hindsight, this rather involved empirical procedure for deriving the effective cutoff value was unnecessary. It would have been simpler to have set Δ at 0.5 MeV for all the photon and electron beams as it was only at ^{60}Co and 2 MV that there was any appreciable difference between $S^{w}_{a}(\Delta)$ for $\Delta = 0.5$ MeV and $\Delta = \Delta_{eff}$. Further, the 0.3 MeV cutoff was only an estimate for the B-F effective cavity size anyway.

10.2.4 Perturbation Factors p_λ and p_E

The ratio p_λ/p_c appears in the expression for C_λ and p_E/p_c is involved in C_E. The factors are intended to refer to the scattering effects that could arise due to the difference in density between the cavity gas and the walls. Harder (1968) dealt with this problem in some detail for the case of high-energy, monoenergetic electron beams and deduced expressions for p_E for different shapes of gas cavity. Briefly, Harder calculated the relative increase in the flux in the cavity caused by the much stronger multiple scattering of the electron tracks from the high-density walls into the cavity than the scattering out from the low-density cavity into the walls.* The theoretical values of p_E for a water-walled, cylindrical cavity of radius 0.25 cm irradiated perpendicular to its axis were given in the ICRU electron report (1972). The Baldwin-Farmer gas cavity has a radius of 0.3 cm, though its effective high-density wall is actually an air-equivalent/lucite/water sandwich. Nevertheless, it seems reasonable to assume that these values should apply as the stopping-power ratios have been calculated assuming that the electron flux in the cavity (down to $T = \Delta$) is the same as that in the surrounding water. These ICRU (1972) figures are listed in table 10.2:

---

*The multiple scattering in the cavity is assumed to be zero. Thus there is no need to specify the gas in the cavity.

$\bar{T}_p$/MeV	p_E
1	0.947
2	0.970
3	0.978
4	0.984
5	0.986
10	0.992
20	0.997

$\bar{T}_p$ is the mean primary electron energy at the depth of interest.

Harder used his theory to explain the measurements of Dutreix and Dutreix (1966), who had found differences in the electron beam depth-dose curves determined with ionization chambers of different sizes and shapes. Thus the theory on which the above values are based can be regarded as having been experimentally verified.

For photon beams, Harder was not sure how to apply his theory. As the average primary electron energy is of the order of 2-3 MeV for high-energy x-ray beams, the figure for p_λ from the above table would be about 0.97 - a perturbation of some 3%. This seemed to contradict the theorem of Fano (1954) which implied that there could be no such scattering effects due to differences in density for photon beams, provided there was elcctronic equilibrium in the irradiated medium. The existence of another scattering effect, resulting in a decrease in the flux in the cavity (i.e. in the opposite direction to the 'in-scattering'effect), seems to have come to Harder's rescue.*

---

*This effect was presumably assumed to be negligible in calculating p_E.

This effect is simply that the 'straighter' electron tracks in the gas cavity must have pathlengths in the cavity less than the pathlengths of the more 'tortuous' tracks in the solid walls i.e. the flux in the cavity is reduced below that in the walls (Harder, 1974). It is to be assumed, therefore, that the two scattering effects exactly balance out for photon beams at depths where electronic equilibrium is established. In the build-up region and again in the fall-off region of the depth-dose curve, though, this assumption cannot be made.*

For the purposes of this work, the perturbation factor p_λ (and p_c for the calibration radiation) has been assumed to be unity. As indicated above, no method has yet been worked out whereby a quantitative estimate of any deviation from unity could be obtained. Thus the matter cannot be regarded as entirely satisfactory.

---

*Much of this section is the result of an exchange of letters between Dr. Harder and myself.

10.3 C_λ FACTORS: RESULTS

10.3.1 Differences from the Greene and Massey Assumptions

Greene and Massey (1966) also arrived at the following expression (equ. 10.7a) for C_λ:

$$C_\lambda = (C_\lambda)_c \frac{(\bar{s}_{mg})_\lambda \; p_\lambda}{(\bar{s}_{mg})_c \; p_c}$$

However, they assumed that the B-F chamber behaved as a Bragg-Gray cavity with water walls. Consequently, they evaluated C_λ from the ratio of the water/air Bragg-Gray ratio at the calibration radiation to that at the quality λ. As we have seen in the discussion above, this assumption cannot be correct. At the calibration radiation, be it 2 MV x-rays or ^{60}Co gamma rays, the cavity behaves more like a photon detector than an electron detector. For 31 MV x-rays, however, most of the ionization in the cavity arises from photon interactions in water;* the cavity is quite definitely predominantly an electron detector just as it is for electron beams. Thus while the Bragg-Gray assumption may be reasonable for x-ray beams above about 10 MV, it becomes increasingly unreasonable as the photon energy decreases. This transition from an electron to a photon detector is effectively incorporated, of course, in the calculation of the stopping-power ratio, $s_a^w(\lambda, \Delta_{eff})$, that is used in evaluating C_λ in this work.

---

*At this quality, the 4.6 cm perspex build-up cap as well as the Tufnol cavity 'walls' can have very little influence on the ionization in the cavity; the range of the photon-ejected electrons is, on average, considerably greater than the thickness of the perspex sheath.

Table 10.3 CALCULATED C_λ VALUES (cal: 2 MV)

Designation	Radiation type	Δ_{eff} (MeV)	$S_a^w(\lambda, z, \Delta_{eff})$	C_λ*
A	2 MV	0.50	1.121	0.950
B	^{60}Co (P+S)	0.50	1.129	0.957
D	4.5 MV (linac)	0.42	1.130	0.958
E	6 MV (linac)	0.40	1.127	0.956
F	13 MV	0.35	1.110	0.941
G	19 MV (bet'n)	0.34	1.106	0.937
H	26.8 MV (linac)	0.34	1.106	0.937
I	26.8 MV (bet'n)	0.34	1.097	0.930
J	31 MV (bet'n)	0.34	1.087	0.922
K	31 MV (Pb f.f.)	0.34	1.088	0.922
L	31 MV (Al f.f.)	0.33	1.078	0.914

*For ^{60}Co calibration; 0.7% reduction.

Table 10.4** C_λ VALUES ON BRAGG-GRAY CAVITY ASSUMPTION (cal: 2 MV)

Radiation	ICRU (1969)	This work***
2 MV	0.95	0.950
^{60}Co	0.95	0.946 (Prim'y)
4 MV	0.94	0.944 (4.5 MV)
6 MV	0.94	0.939
12 MV	0.92	
14 MV	0.92	0.917 (13 MV)
18 MV	0.91	
20 MV	0.90	0.911 (19 MV)
25 MV	0.90	0.904 (27 MV,I)
30 MV	0.89	0.897 (31 MV,J)
35 MV	0.88	

**c.f. table 9.3.

***For ^{60}Co calibration; 0.4% increase.

Figure 10.3 CALCULATED C_λ VALUES.
(calibration = 2 MV X-rays)

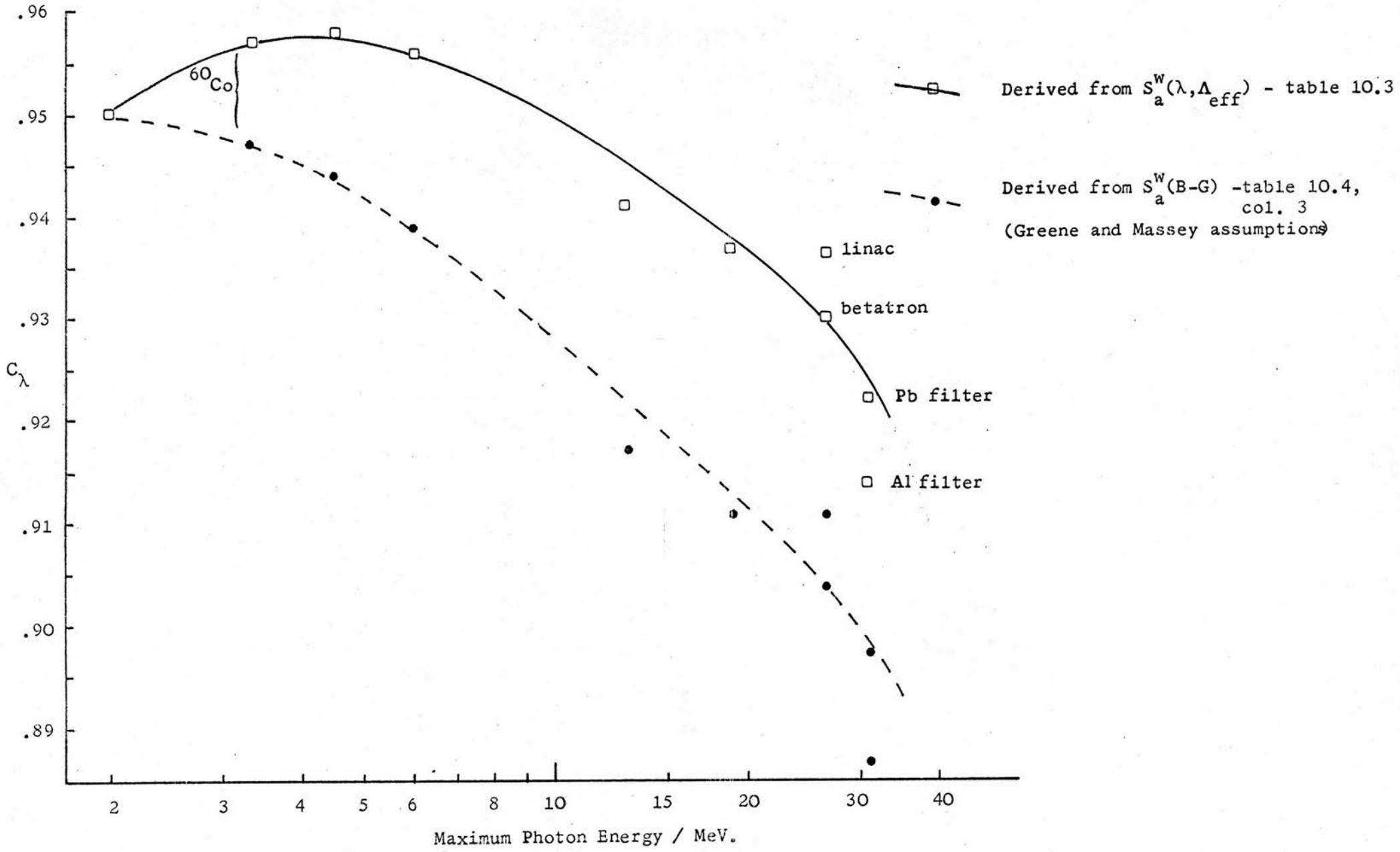

10.3.2 Calculated Values

The values of C_λ given in table 10.6 and plotted against k_{max} in figure 10.3 (solid line) have been evaluated from:

$$C_\lambda = 0.950 \frac{S_a^w(\lambda, z, \Delta_{eff})}{S_a^w(\lambda_c, z, 0.5)} \quad \text{.....(10.10)}$$

cf. (10.7a)

with the ratio p_λ / p_c set equal to unity (see section 10.2.4). The figure 0.950 for $(C_\lambda)_c$ resulted from substituting $d_c = 0.985$ (Greene and Massey, 1966), $(\bar{W}/e) = 0.869$ and $\bar{\mu}_a^w(\lambda_c) = 1.110$ (from figure 9.2) into equ. 9.17. Both d_c and $\bar{\mu}_a^w(\lambda_c)$ have been set at the same values for either 2 MV x-rays or ^{60}Co as the calibration radiation. However, for 2 MV x-rays, $S_a^w(0.5)$ is 1.121, but for ^{60}Co radiation it is 1.129. This results in a 0.7% difference between C_λ's for the different calibration qualities, the ^{60}Co values being the lower ones. Physically, this corresponds to the fact that the B-F air cavity (solid 'wall' and gas) is closer to a photon detector for the 2 MV x-rays than for the slightly harder ^{60}Co gamma rays.* All the values correspond to the ICRU (1969) calibration depths.

In order to make comparisons with the Greene and Massey C_λ values more meaningful, equation 10.7a was also evaluated using the Bragg-Gray ratios, S_a^w(B-G), given in table 9.2. This set of C_λ's has also been plotted in figure 10.3 (broken line) and is listed in table 10.4 alongside the ICRU (1969) values calculated by Greene and Massey (1968). The differences between these sets of C_λ's

*Only limited confidence can be placed in the size of this difference, i.e. 0.7%, but it is expected to be 'this way round'. Using the Bragg-Gray stopping-power ratios results in a small, but definite difference the other way round. It is likely that the difference should be somewhat smaller than 0.7%, in fact.

are due to the differences in the Bragg-Gray stopping-power ratios exhibited in figure 9.8 and have already been discussed in section 9.3.2.2. Greene and Massey purposely gave their C_λ values to only two figures due to the approximations in their calculation of the stopping-power ratios.

It can be noted that Levy et al. (1975) derived C_λ values of 0.919 and 0.916 for their measured x-ray spectra (G and H resp. in this work) using the less approximate ICRU (1969) method discussed in section 9.3.2.2. These compare favourably with the present result of 0.915 for both the 19 MV betatron and 26.8 MV linac x-ray beams calculated on the same assumptions: Bragg-Gray cavity, water walls.

It is evident from figure 10.3 that the use of more realistic assumptions about the B-F chamber in deriving the stopping-power ratios to evaluate C_λ results in a considerably different set of values. For a given photon beam, the difference amounts to as much as 2% above 10 MV. In addition, the prediction that C_λ should go through a maximum is a radical departure from the gradual decrease with increasing average photon energy that has been hitherto assumed. The maximum is due to the transition that the 'air' cavity goes through from being predominantly a photon detector to predominantly an electron detector.*

---

*It is to be emphasised that it is in this transition region that the present evaluation of $S_w^{air}(\Delta_{eff})_{^{60}Co}$ can only be regarded as approximate. Thus the C_λ^a at ^{60}Co, 4.5 and 6 MV in table 10.3 should be treated more as estimates than as accurate calculations.

If one compares the results given in table 10.3 with the currently accepted ICRU C_λ values, then at 30 MV the difference is between 0.89 (ICRU) and about 0.925 (from fig. 10.3, full line) i.e. the ICRU figure is 4% too low. This does not allow for possible differences due to the linac vs betatron problem. Thus for a 27 MV linac, the ICRU C_λ could be as much as 5% below the figure calculated in this work.

10.3.3 Comparison with Experimental C_λ Determinations

The situation with respect to experimental measurements of C_λ is not at all satisfactory. The only calorimetric determination reported in the literature is the work of Bewley (1963) using a carbon calorimeter. In order to determine C_λ factors using a calibrated Baldwin-Farmer chamber, he had to place the ionization chamber in a perspex block whereas the calorimeter was part of a carbon block. The dose to the perspex at the depth of the chamber was calculated from the measured dose in carbon. Thus the method cannot be regarded as particularly direct. Nevertheless, it must be stated that Bewley's results for C_λ are on balance closer to the ICRU (1969) C_λ values. They are listed in the following table (10.5):

Radiation	C_λ		
	Bewley	ICRU (1969)	This work
^{60}Co	0.966	0.95	0.957
4 MV	0.961	0.94	0.957
7.5 MV	0.928	0.93	-
14 MV	0.912	0.92	0.941 (13 MV)
20 MV	0.888	0.90	0.937 (19 MV)

The Bewley figures have been increased by 1% in line with the change in the NPL 2 MV calibration factor in Jan. 1969. Bewley did not give a specific error estimate on his C_λ results. All the x-ray machines were linacs except at 20 MV (betatron).

The other investigations of C_λ factors in the literature have all been carried using the Ferrous sulphate dosimeter to determine the absorbed dose. Thus values for $G(Fe^{3+})$ have had to be assumed. To illustrate the difficulty of interpreting such results, consider the following example. Hettinger et al. (1967) gave $C_\lambda = 0.915$ from $FeSO_4$ dosimeter measurements on a 34 MV betatron. They assumed $G(Fe^{3+})$ to be 15.5. Now this figure of 0.915 is very close to $C_\lambda = 0.913$ estimated from the full line in figure 9.10 at 34 MV (with the 0.7% reduction for ^{60}Co which was the calibration radiation for the Baldwin-Farmer chamber that Hettinger et al. used). On the other hand, Almond (1968) considered that the G-value for 34 MV x-rays should be 15.9 and therefore recalculated the Hettinger et al. C_λ as 0.894, which was then in closer agreement with the ICRU (1969) C_λ values. The point of view taken in this work is that $G(Fe^{3+})$ for high-energy photon beams is still very much an open question. Consequently, C_λ values determined by calibration against the $FeSO_4$ dosimeter cannot be regarded as providing confirmation or otherwise of the ICRU C_λ values. This expected variation of $G(Fe^{3+})$ with photon beam quality will be explored in some detail in the chapter that follows.

Table 10.6 VARIATION OF C_λ WITH DEPTH* - EXPERIMENT vs THEORY (cal: ^{60}Co)

Depth (cm)	^{60}Co This** work	^{60}Co Svensson*** (1971)	31 MV This work	32 MV Svensson*** (1971)
1	0.951	-	0.935	-
3	0.950	0.95	0.920	0.92
5	0.950	0.95	0.916	0.94
7	0.949	0.95	0.915	0.93
9	0.949	0.95	0.915	0.92
11	0.948	0.95	0.915	0.92
13	0.947	0.94	0.915	0.92
15	0.946	0.94	0.915	0.91

*ICRU (1969) only defines C_λ at the calibration depth.

**Note that the variation of $S_a^w(\lambda, z, \Delta)$ with depth for Δ = 0.5 MeV used to calculate these figures is less than that for Δ = 0.1 MeV shown in figure 9.6 for 2 MV x-rays.

***The Svensson figures have been normalized to agree (to the 2 sig. figs. he quotes) with the present results at the ICRU calibration depth.

Svensson (1971) presented an interesting set of C_λ measurements which indicated a small, but definite variation with depth for high-energy x-ray beams. His measurements were also based on the $FeSO_4$ dosimeter but his assumption that the G-value did not vary with depth for a given photon beam is reasonable. He found that for 27 to 43 MV x-radiation C_λ was about 1% higher at 5 to 6 cm than at other depths. This is not what is predicted by the results for the variation of the stopping-power ratio with depth given in section 9.3.2.1. There it was shown that the stopping-power ratio, and hence C_λ, could be expected to be 1-2% greater close to the surface (in the 3-4 cm build-up region) but would then be constant to within 0.2% up to depths of at least 30 cm or so (see table 10.6). The findings of Svensson would, however, be explainable if the value of p_λ deviated from unity both close to the surface and at much greater depths as Harder has suggested (see section 10.2.4).

Finally, some comments must be made about the experimental evidence that Greene et al. (1971) cited to support the assumptions involved in the Greene and Massey (1966) derivation of the C_λ factors.
Day, Greene and Massey (1965) carried out a series of measurements using ^{137}Cs and ^{60}Co gamma-rays, as well as 4 MV and 6 MV x-rays. They irradiated a Baldwin-Farmer chamber, fitted with Perspex caps of thicknesses varying from 0 to 15.5 mm, in a water phantem. The results showed that the error arising from the equilibrium cap being of Perspex rather than of water was less than 1% .This is in

line with the assumption also made in the present derivation of C_λ that the Perspex build-up cap can be treated as water-equivalent. However, the measurements of Greene (1962) seem difficult to understand. He compared the readings obtained with a Baldwin-Farmer chamber with those given by an identically irradiated all Perspex chamber. The ratio was constant to better than 0.5% for ^{60}Co gamma-rays and 2,4 and 20 MV x-rays. Greene et al. (1971) considered that the above measurements justified their assumption that the chamber material could be regarded as water-equivalent.

The stopping-power calculations for the Baldwin-Farmer chamber described in this chapter are based on the assumption that the chamber material is air-equivalent. Greene's findings, especially the change between 2 MV and 20 MV x-rays, cannot be reconciled with this and thus a question mark must hang over this aspect of the work.

10.4 C_E FACTORS: RESULTS

10.4.1 Differences from the ICRU (1972) Expression

Before evaluating C_E from equ. 10.7, it is instructive to look at the expression that is given for C_E in ICRU (1972). This is (in the notation of this chapter):

$$C_E = d_c.(\bar{W}/e).(\bar{s}_{mg})_E.p_E \qquad .....(10.11)$$

At first sight this does not bear much resemblance to equ. 10.7b. However, writing $(C_\lambda)_c$ in full using equ. 10.3,

$$C_E = d_c.(\bar{W}/e).\left[\frac{(\mu_{en}/\rho)^w}{(\mu_{en}/\rho)^a}\right]_c . \frac{(\bar{s}_{mg})_E.p_E}{(\bar{s}_{mg})_c.p_c} \qquad .....(10.12)$$

we see that the ICRU expression results if

$$(\bar{s}_{mg})_c.p_c = \left[\frac{(\mu_{en}/\rho)^w}{(\mu_{en}/\rho)^a}\right]_c \qquad .....(10.13)$$

But this *is* the case if the walls of the B-F chamber are assumed to be *air-equivalent at the calibration radiation*. As we have seen, this is not such a bad approximation.* Considering 2 MV x-rays, $(\bar{s}_{mg})_c$ is to be evaluated as $s_a^w(\Delta)$ for Δ = 0.5 MeV, and comes to 1.121. The expression in the square brackets, which can be written as $\bar{\mu}_a^w(\lambda_c)$, has been taken to be equal to 1.110 from figure 9.3. Thus for 2 MV x-rays as the calibration radiation, C_E is effectively calculated from

$$C_E = 0.990\ d_c.\ (\bar{W}/e).(\bar{s}_{mg})_E.p_E \qquad .....(10.14)$$

---

*It is, of course, inconsistent with the assumption of Greene and Massey (1966) and ICRU (1969) in deriving C_λ, i.e. *water*-equivalent walls at the calibration radiation.

Table 10.7 CALCULATED C_E VALUES (cal: ^{60}Co)*

Depth Water (cm)	Initial Electron Energy $_o$/MeV			
	5	10	20	30
1	0.920 (0.900)**	0.867 (0.858)	0.822 (0.819)	0.798 (0.797)
2	0.952 (0.902)	0.890 (0.879)	0.834 (0.831)	0.806 (0.805)
3		0.915 (0.900)	0.845 (0.841)	0.815 (0.813)
4		0.940 (0.912)	0.858 (0.853)	0.823 (0.821)
5		0.956	0.872 (0.865)	0.832 (0.830)
6			0.889 (0.881)	0.842 (0.839)
7			0.904 (0.893)	0.852 (0.848)
8			0.920 (0.905)	0.863 (0.859)
9			0.936 (0.908)	0.874 (0.869)
10			0.947	0.885 (0.878)
11				0.895 (0.886)
12				0.907 (0.896)
13				0.921 (0.906)
14				0.933

*For 2 MV x-ray calibration all values are increased by 0.7%.

**Figures in brackets correspond to p_E estimated from table 10.2 assuming mean loss of 2 MeV.cm^{-1}.

Figure 10.4 CALCULATED C_E VALUES.
(calibration : ^{60}Co; p_E = 1.000)

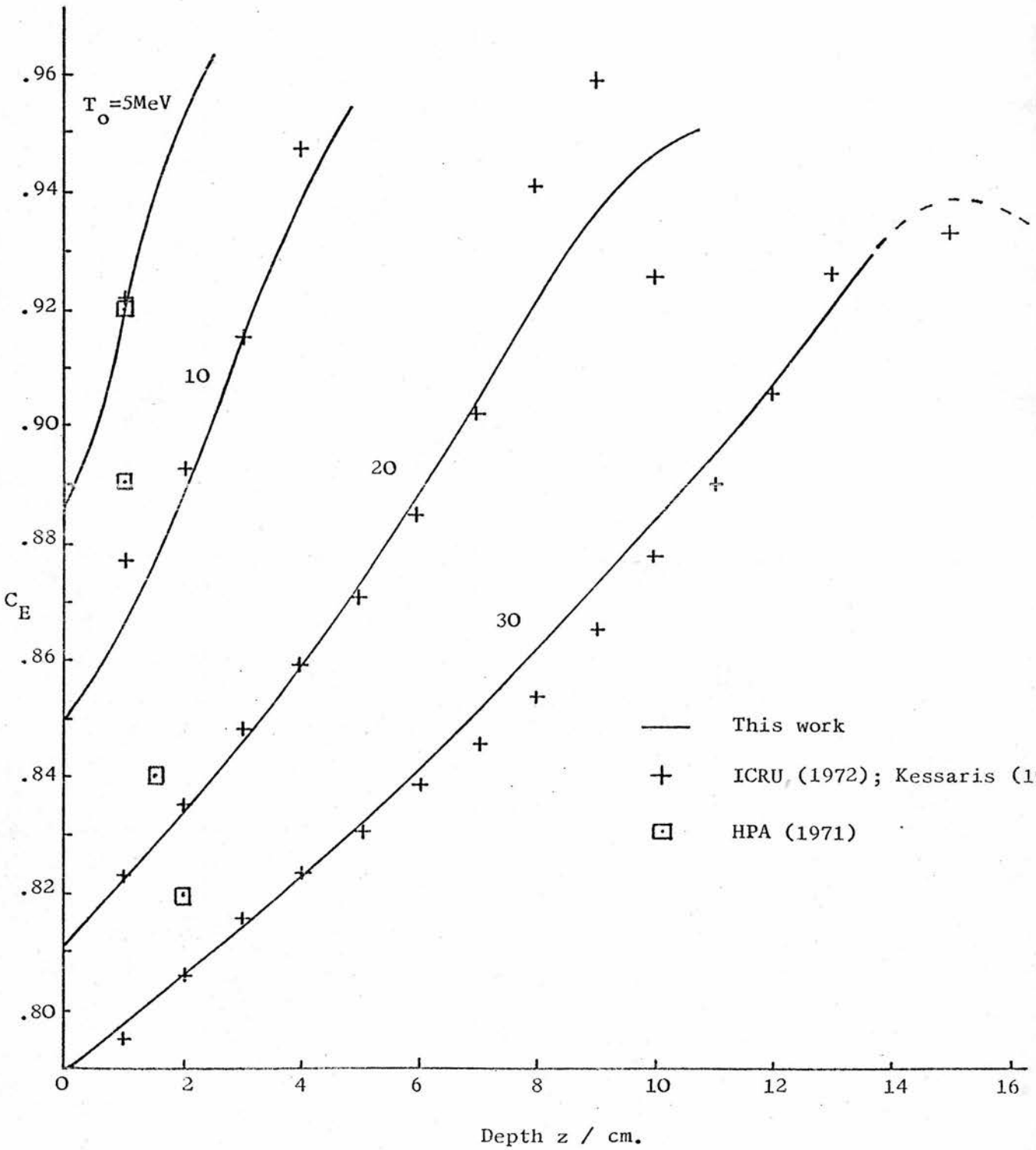

where the factor 0.990 is a quantitative measure of the extent to which the ICRU assumption about air-equivalent walls deviates from the actual situation. Note that if $(\bar{s}_{mg})_c$ in equ. 10.12 had been evaluated as the Bragg-Gray ratio, i.e. 1.155 for 2 MV x-rays, then the factor in equ. 10.14 would have been 0.961 and the ICRU C_E factors would have appeared to have been in serious error. In fact, Matsuzawa et al. (1974) derived an expression for C_E equivalent to equ. 10.12 and calculated a factor of 0.972 by assuming that the B-F chamber behaved as a Bragg-Gray cavity with lucite walls at the calibration quality (^{60}Co in their derivation). Their assumption about the Bragg-Gray cavity was then rightly criticized by Greening (1974), who brought forward the argument about 2/3 rds of the ionization being due to the air-equivalent walls.

10.4.2 Calculated Values

C_E has been calculated for the 5, 10, 20 and 30 MeV electron beams at depths down to $z \sim r_o$. The values given in table 10.7 and plotted in figure 10.4 (as continuous curves) were evaluated from:

$$C_E = \frac{S_a^w(T_o, z, 0.31).p_E}{S_a^w(\lambda_c, 0.50).p_c} \cdot (C_\lambda)_c \qquad \text{cf (10.7b)}$$

Putting $(C_\lambda)_c = 0.950$; $p_c = 1$; and $S_a^w(\lambda_c, 0.50) = 1.129$ for ^{60}Co,* then

---

*^{60}Co rather than 2 MV was chosen as that is calibration radiation that Kessaris (ICRU, 1972) stated his C_E values corresponded to. In fact, the only difference between ^{60}Co and 2 MV that the ICRU expression (equ. 10.11) could allow for is in d_c. This is taken to be the same for either calibration radiation (i.e. 0.985) in the ICRU reports and in this work.

$$C_E = 0.841\ S_a^w(T_o, z, 0.31).p_E \qquad .....(10.15)$$

This is, of course, the same expression as could have been derived from equ. 10.14, but with the factor 1.110/1.129 = 0.983 for ^{60}Co instead of 2 MV as the calibration radiation.

The perturbation factor, p_E, has been taken as unity in plotting the curves in figure 10.4 but the values in the table include an estimate of C_E using the p_E values from table 10.2. The C_E given in table 10.7 were actually taken from fig. 10.4 as equ. 10.15 was not evaluated at such convenient depths i.e. z/r_o = 0.-0.1 etc. (see table 9.1).

The C_E values given in ICRU (1972), calculated by Kessaris (1970a), and those recommended by the HPA (1971), calculated using the Harder formula for the stopping-power ratio, are also shown in figure 10.4. It can be seen that the ICRU values are in moderately close agreement with the present calculations, except at large depths. This agreement must be regarded as somewhat fortutituous, however. It was shown in figure 9.4 that the Kessaris stopping-power ratios were 2-3% lower than the results for $S_a^w(T_o, z, \Delta)$ for the 10 keV cutoff. The $S_a^w(T_o, z, \Delta)$ values used to evaluate C_E from equ. 9.27 correspond to a 0.3 MeV cutoff. These values are, on average, about 1% lower than the Δ = 10 keV figures, or 1-2% higher than the Kessaris figures. Then there is the factor 0.983 (for ^{60}Co calibration) that should be included in the calculation of C_E, but is not present in the ICRU (or HPA) expression. The result of all this is that the present results for C_E end up being close to the ICRU figures due to the cancelling of errors in the Kessaris evaluation.

10.4.3 Comparison with Experimental Determinations

Although there are several reports in the literature of calorimetric work with high-energy electron beams, most of the measurements have been for carbon-walled ionization chambers in carbon. There have not been any direct calorimetric determinations of water/air C_E values. Tedman (1975) measured C_E for carbon/air with his carbon calorimeter. He then had to multiply this by the appropriate mass stopping-power ratio for water to carbon in order to arrive at water/air C_E values, which come out to be somewhat higher than the Kessaris values. His measurement of C_E must be regarded as rather indirect, in common with Bewley's C_λ determinations with a carbon calorimeter. Short of using a water or water-equivalent calorimeter, which is beset with practical difficulties (Tedman, 1975), it is difficult to see how C_E could be more directly measured for a calibrated secondary standard ionization chamber (such as the Baldwin-Farmer) used in water.

Naturally, most of the C_E determinations have been carried out using the Ferrous-sulphate dosimeter to measure the absorbed dose in water (e.g. Svensson, 1971; Almond, 1970). As discussed in section 10.3.3 on C_λ measurements, such C_E measurements can only be considered in conjunction with the values assumed for $G(Fe^{3+})$. Svensson (1971) assumed that $G(Fe^{3+})$ did not change with initial electron energy or the depth of measurement. He used the value $G(Fe^{3+}) = 15.56$ that had been determined for 20 MeV electrons by Pettersson (1967) with a water calorimeter. Svensson plotted his measurements in terms

Figure 10.5 COMPARISON OF k/A MEASUREMENTS BY SVENSSON (1971) WITH CALCULATED C_E VALUES.
(calibration : ^{60}Co)

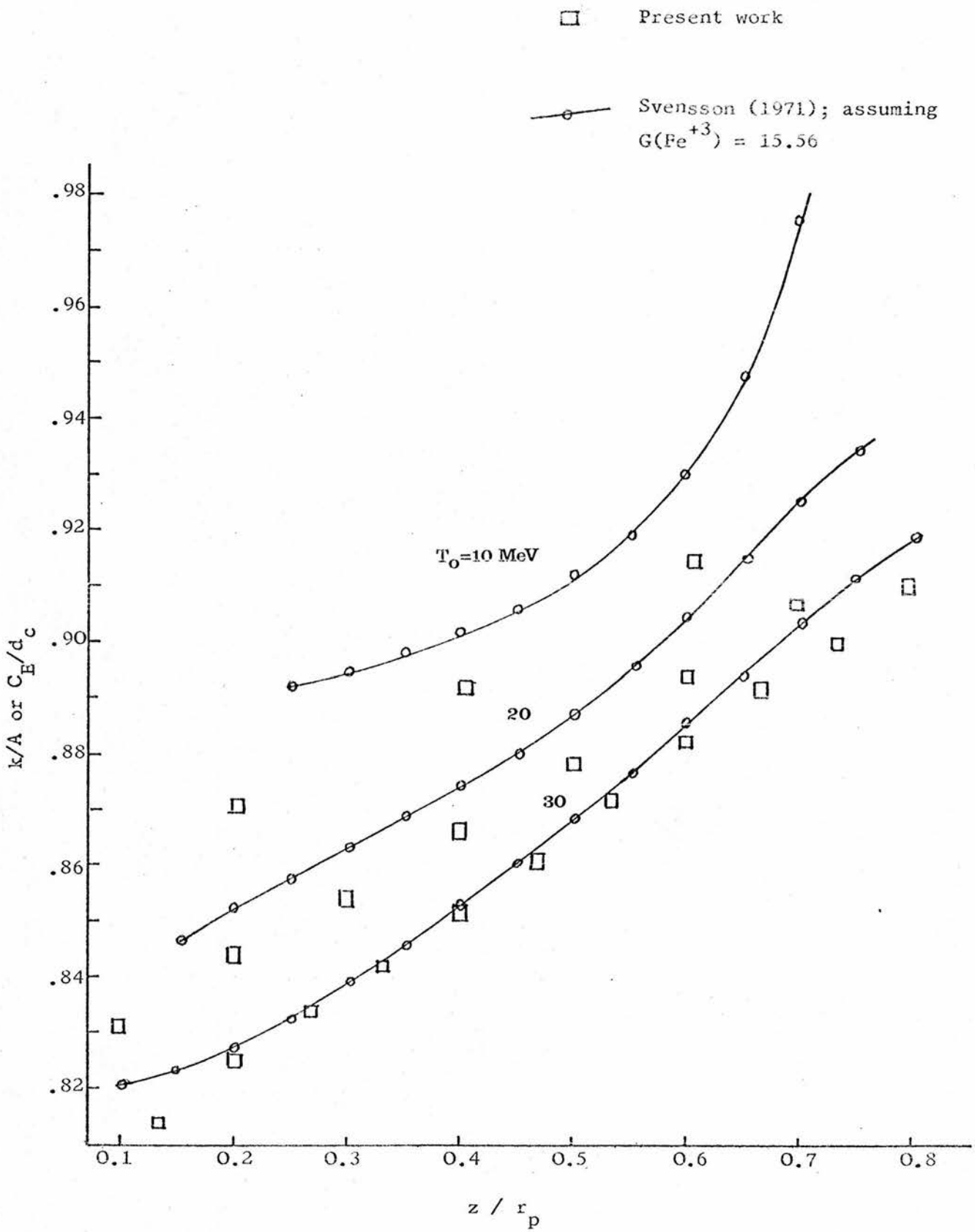

of k/A (the same as C_E/d_c in this work) against depth z/r_p for 10, 20 and 30 MeV electron beams. These k/A values are given in figure 10.5 where they are compared to the calculated values given in table 10.7. These figures are the set that includes p_E from table 10.2, divided by $d_c = 0.985$, with r_p taken from table 7.5. The measurements by Svensson were actually carried out using a Siemens Sondenfingerhutkammer which is similar to a Baldwin-Farmer chamber. The agreement is excellent for $T_o = 30$ MeV, except for $z \gtrsim 0.65\ r_p$, but at 10 and 20 MeV the calculated values are about 1% below the measured ones. This could be taken to indicate that the G-value is about 1% higher at $T_o = 10$ and 20 MeV than it is at 30 MeV.

As well as the uncertainty in the G-value, such comparisons are also complicated by the fact that the exposure calibration may not be equivalent between the different national standardizing laboratories. Svensson pointed out that his measured values would all have been decreased by 1.5% if the NPL 2 MV x-ray calibration had been used instead of the ^{60}Co Stockholm one.

The stopping-power ratios calculated in this work strictly correspond to large field sizes as that is the irradiation geometry employed in the electron flux spectra computations. Thus the results for C_E also apply to large field sizes. Svensson and Petterson (1967) systematically investigated the effect of various beam parameters on the absorbed dose calibration factors and concluded that the field size (larger than 5x5 cm), SSD (between 110 and 130 cm), and the construction of the collimating system had no

significant influence on C_E. Thus it can confidently be assumed that the C_E values presented in this chapter apply to the electron beams used in clinical practice.

10.5 SUMMARY AND CONCLUSIONS

Some of the fundamental assumptions involved in calculating C_E and C_λ have been examined in relation to the characteristics of a Baldwin-Farmer chamber. It has been shown that the effective size of the air cavity in the B-F chamber corresponds to a stopping-power ratio cutoff of 0.3-0.5 MeV. This is the result of assuming that the Tufnol lining of the gas cavity is air-equivalent as it is intended to be.

Equivalent expressions have been derived for C_λ and C_E and have been evaluated using water/air mass stopping-power ratios appropriate to the above assumptions. In particular, the values of these ratios reflect the fact that the B-F chamber behaves predominantly as a photon detector at the calibration quality (2 MV x-rays or ^{60}Co gamma-rays). It is mainly for this reason that the results for C_λ are markedly different from the ICRU (1969) values which were calculated by Greene and Massey on the basis of assuming that the B-F chamber behaved as a Bragg-Gray cavity at all photon beam qualities. The present C_λ are higher than the ICRU figures by as much as 3-4% for high-energy betatron and 4-5% for high-energy linac x-ray beams, part of the discrepancy arising from the more accurate evaluation of the stopping-power ratio and part from the difference in assumptions.

The results for C_E do not differ significantly from the calculations by Kessaris given in ICRU (1972). The ICRU values were calculated on the implicit assumption that the walls of the B-F cavity could be regarded as

entirely air-equivalent for the calibration radiation which is a more justifiable approximation than that employed in the ICRU (1969) C_λ calculations. The extent to which the B-F chamber deviates from the ICRU (1972) 'air-equivalent wall' assumption is automatically incorporated in the calculation of the stopping-power ratios used in evaluating C_E (and C_λ). The ICRU expression for C_E should be multiplied by a factor of approximately 0.990 and 2 MV x-rays or 0.983 for ^{60}Co gamma-rays as the calibration radiation.

The calculation of C_E and C_λ has now been placed on a consistent basis. Consider the following example. For a 10 MeV electron beam and for a 31 MV betatron x-ray beam, the B-F chamber acts quite definitely as an electron detector. It is therefore reasonable to use the Bragg-Gray stopping-power ratios at the qualities 'E' and 'λ' in evaluating C_E and C_λ for these two beams. For the 10 MeV electron beam at a depth of 0.65 r_o and for the 31 MV x-ray beam at the calibration depth, the Bragg-Gray ratios are both equal to 1.091. For 2 MV x-rays as the calibration radiation, C_E and C_λ are then both equal to 0.925 according to the present calculations (taking p_E = 1.00). Using the ICRU expressions for C_E and C_λ respectively, C_E comes to 0.934 and C_λ comes to 0.897 - a difference of 4%. This difference cannot possibly be justified.

There is not sufficient direct experimental evidence to lend definite support to either the ICRU C_E and C_λ values or to the present calculations. Much of the experimental work has been carried out using the ferrous-sulphate dosimeter to determine the absorbed dose in water.

As the G-values are themselves uncertain, especially for high-energy photon beams, these measurements do not particularly help to clarify the situation. It can be stated, however, that a comparison with the C_E measurements by Svensson (1971) indicated that the calculated C_E values are consistent with a G-value for high-energy electron beams of around 15.6. This is in agreement with the calorimetric determination of $G(Fe^{3+})$ by Petterson (1967). The implications of the C_E and C_λ results for ferrous-sulphate G-values will be examined in detail in the next chapter.

Finally, a word should be said about the expected accuracy of C_E and C_λ. Leaving aside the question of the effect of the assumptions involved in deciding on what the appropriate stopping-power ratios should be (i.e. size of cutoff etc.), the full expressions for C_E and C_λ involve a sizeable number of quantities. There is the average energy involved in forming an ion pair in air $\bar{W}$; the displacement factor d_c; the water/air ratio of the photon mass-energy absorption coefficients for the calibration radiation (these 3 factors are all involved in $(C_\lambda)_c$); I(water) and I(air) in the stopping-power ratio; and finally the ratio of the perturbation factors, p_λ/p_c or p_E/p_c.

The effect of an incorrectly assumed value for one or more of these quantities would be very difficult to disentangle from the combined effect of all of them. For example, $\bar{W}$ has been assumed to be constant for all incident photon and electron energies in line with the

ICRU (1969, 1972) recommendations. If $\bar{W}$ in fact increased slightly with increasing electron energy (as the measurements of Kretschko (1960) suggest), this could easily be compensated for by a slight increase in the density effect reduction. No calorimetric or ferrous-sulphate measurements would be able to detect this.

Again, apart from the uncertainty in the I(values) themselves, one of the central assumptions in charged particle stopping-power theory is that I is the same whether a substance is in a condensed or gaseous state. If this were to turn out not to be the case then the electron mass stopping power for the air-equivalent wall of the B-F cavity could not be assumed to be equal to that for gaseous air at energies below that where the reduction due to the density effect is important.

The uncertainty in the determination of the absorbed dose in water irradiated with 30 MV x-rays, on the basis of an exposure calibration at 2 MV, has been estimated as 3.3% in ICRU (1969). This overall uncertainty is not significantly reduced by the results of the present work. In particular, the stopping-power ratio cannot be considered to be known to better than $\pm$2% due to the uncertainty in I-values and the assumptions concerning the walls of the Baldwin-Farmer chamber at the calibration radiation. However, the uncertainty in <u>relative</u> dose determinations between high-energy photon and electron beams can be considered to have been reduced, depending only on the stopping-power ratios and perturbation factors at the qualities E and λ, all the other quantities being common to both C_E and C_λ.

CHAPTER II

FERROUS SULPHATE G-VALUES

11.1 INTRODUCTION

Of the chemical systems available for dosimetry, the ferrous sulphate system (Fricke dosimeter) is recognized to be the most suitable with respect to accuracy, reproducibility and linearity of response (ICRU, 1969). In particular, the dosimeter solution has a composition that is very close to water, so the conversion factors required to determine the absorbed dose in water from the absorbed dose in the dosimeter solution are close to unity* and have very little dependence on radiation quality provided the irradiation vessel is reasonably close to water-equivalent, which can easily be arranged (e.g. Perspex).

Much work has gone into improving the accuracy of the Fricke dosimeter with respect to eliminating the influence of impurities in the solution (Davies and Law, 1963), the effect of the size of the cells in which the solution is contained and storage effects in certain plastics (Svensson et al., 1967), and numerous experimental determinations in order to define $G(Fe^{3+})$ for a wide range of photon and electron energies (ICRU; 1969, 1970b, 1972). Though the relatively high absorbed dose required for an accurate result (a few thousand rads for 1% precision) and the care necessary in preparing the $FeSO_4$ solution rule out the

---

*For all energies of interest, μ_{en}/ρ is the same for both water and the $FeSO_4$ dosimeter solution and the mass collision stopping powers are within 2% of each other (Shalek and Smith, 1969).

Fricke dosimeter as a routine method of dosimetry, there is much to be said for its use as a standard against which other, more convenient instruments such as ionization chambers and solid-state detectors can be calibrated.

As has been indicated in the previous chapter, the Fricke dosimeter has been used to determine the C_E and C_λ factors for exposure-calibrated Baldwin-Farmer type instruments. However, the implicit assumption that $G(Fe^{3+})$ is better known than the factors involved in C_E and C_λ for the radiations concerned is not accepted in this work. The 'raison d'etre' for beginning this work, in fact, was the apparently inexplicable conclusion that Law and Naylor (1972) were forced to draw from their ionization-based measurements of $G(Fe^{3+})$: that there was a definite difference in the chemical yield between high-energy photon and electron beams of the same average electron energy (see the Introduction to this thesis). However, although the 'G-value difference' could have been explained away by uncertainties in C_E and C_λ, it seemed more likely at the time that it might be accounted for by a detailed theoretical investigation of any differences in the detailed way in which energy was dissipated in the dosimeter solution by electron and photon radiation. Such a theoretical investigation is reported in what follows. The chapter ends with a re-examination of the experimental evidence for the 'G-value difference' in the light of the theoretical findings and the revised C_E and C_λ factors presented in the previous chapter.

Figure 11.1 EXPERIMENTAL $G(Fe^{3+})$ DETERMINATIONS.

a. Photons

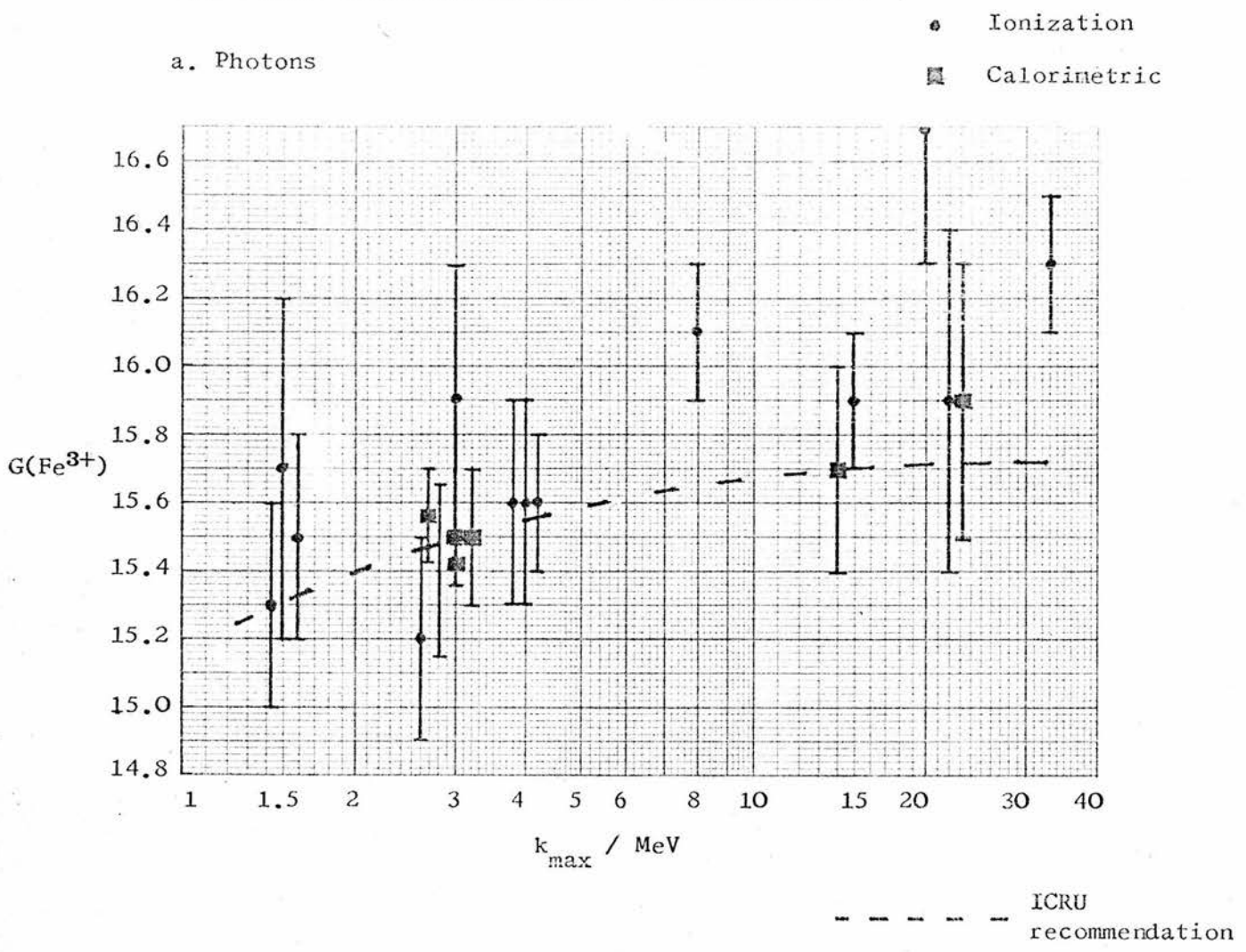

b. Electrons

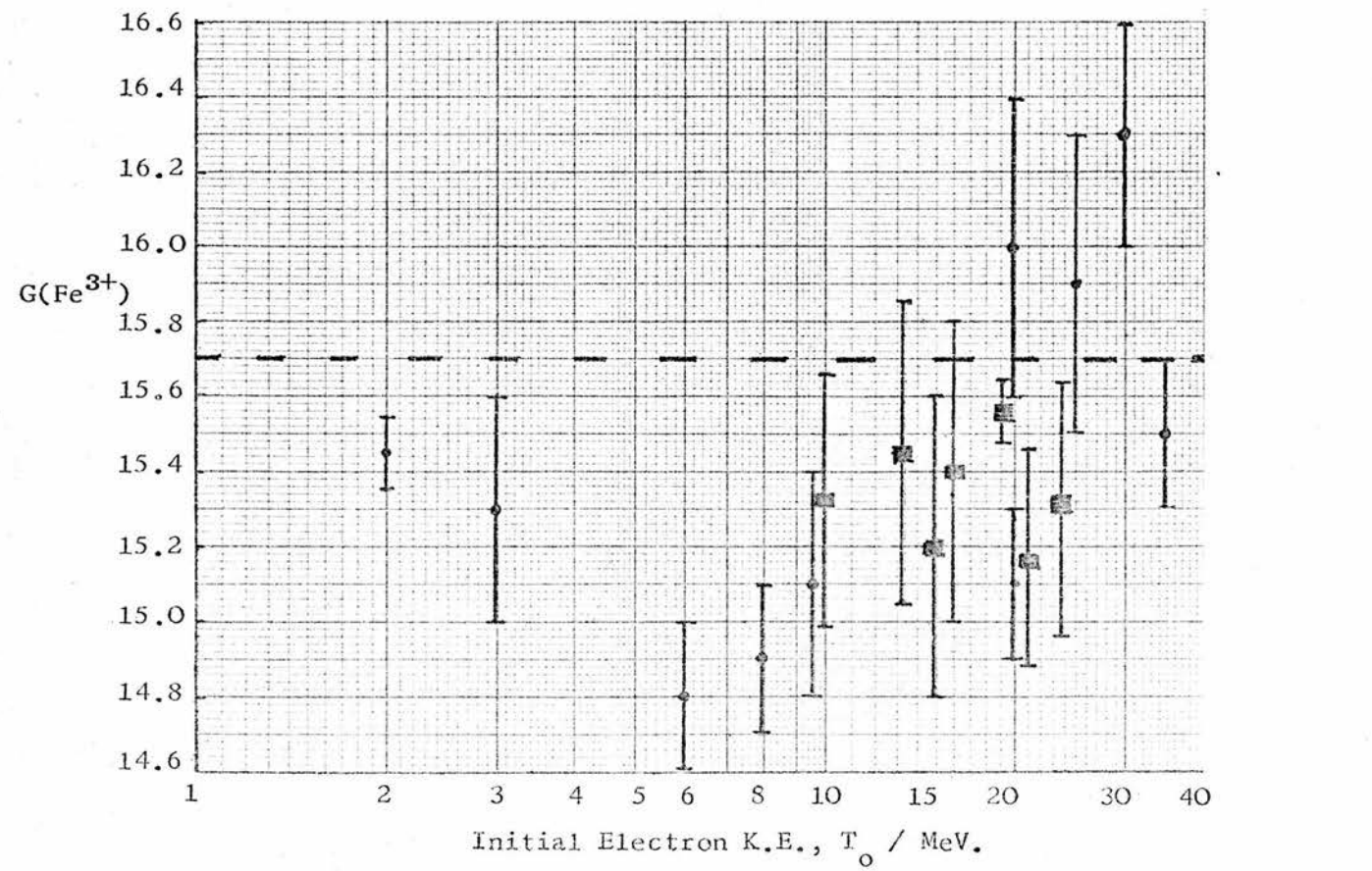

Figure 11.2 CALORIMETRIC $G(Fe^{3+})$ DETERMINATIONS.

a. Photons - from ICRU (1969) except for Almond (1968, 1974) at 22 MV

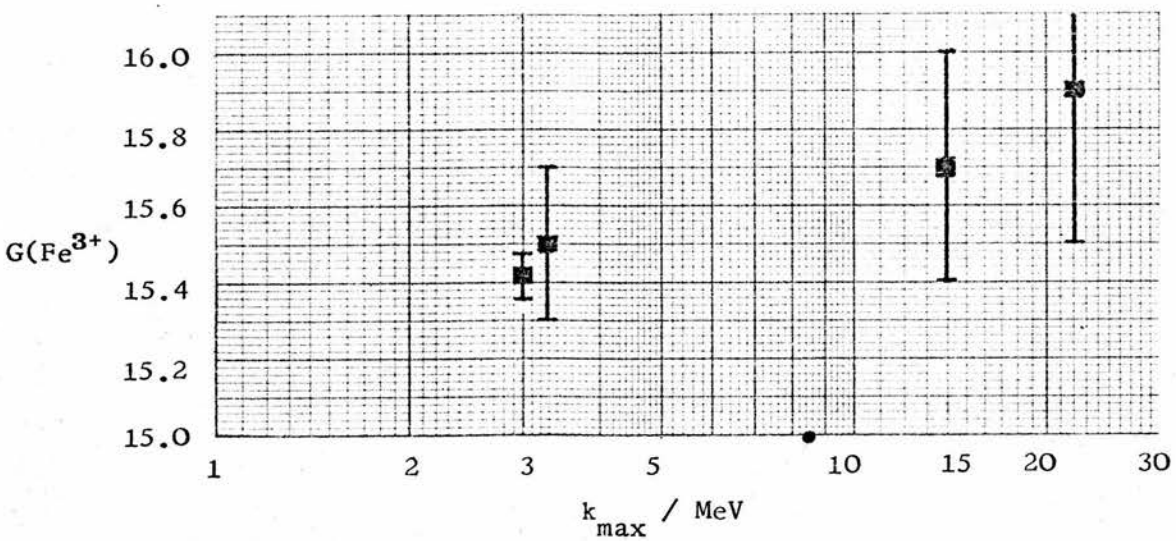

b. Electrons - from ICRU (1972) except for Tedman (1975) at 10.7 MeV

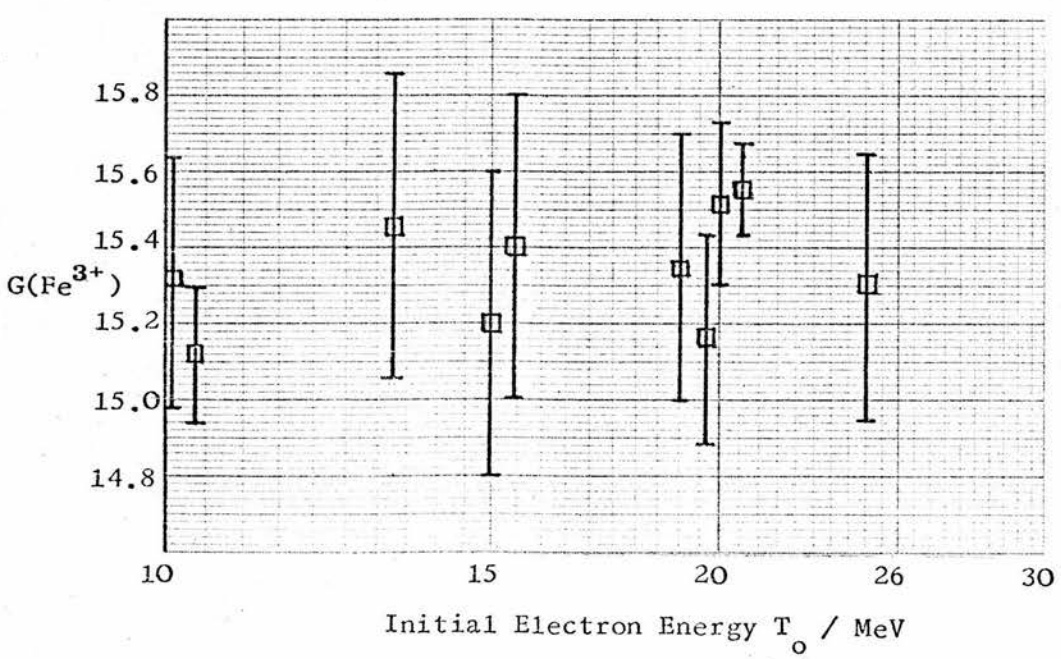

11.2 EXPERIMENTAL $G(Fe^{3+})$ FOR HIGH-ENERGY ELECTRON AND PHOTON BEAMS

In order to put the present experimental situation into some sort of perspective, the results of recent determinations* of $G(Fe^{3+})$ are shown in figure 11.1. The values for photon radiation have been taken from table 3.1 in ICRU (1969), with the addition of the ionization-based results from Law and Naylor (1971) for 8, 15 and 33 MV x-rays and the calorimetric result reported by Almond (1968, 1974) for 22 MV x-rays. The electron values were similarly taken from table 3.6 in ICRU (1972), with the addition of the Law and Naylor (1972) results at 5, 6, 8, 10, 20 and 35 MeV. ICRU (1972) states that the variation in the values can be put down to dosimetric uncertainties, the effect of the irradiation vessel upon chemical yield, variations in the extinction coefficient** and impurities in the chemicals of the solution.

The two graphs (11.1a and 11.1b) are intended to illustrate the considerable uncertainty in $G(Fe^{3+})$ for high-energy electron and photon radiation, despite the large number of experimental determinations. The broken lines are the values that are recommended in the respective ICRU photon and electron reports. It is clear that the experimental values by various workers are not in sufficiently good agreement to lend much confidence to these recommendations and indeed, $G(Fe^{3+})$ for 11 to 30 MV x-rays is given in ICRU (1969) as 15.7 ± 0.6 - i.e. allowing for a wide margin of error. For ^{60}Co radiation,

---

*For 0.8N H_2SO_4 dosimeter solution.

**This is involved in the reading of the spectrophotometer which measures the ferric ion concentration.

however, the situation is more satisfactory. From the mean of the seven determinations listed, ICRU (1969) recommend 15.5 $\pm$ 0.2. This value of 15.5 for ^{60}Co is considered to be sufficiently firmly based to act as a parameter in the theoretical work.

Enough has been said about ionization dosimetry in the last two chapters to fully emphasise the uncertainty connected with G-values derived from the currently accepted ionization dose conversion factors. In figure 11.2, only the calorimetric* determinations of $G(Fe^{3+})$ have been plotted in an attempt to clarify the situation.
The photon values speak for themselves. The measurements shown are simply not sufficient to define the behaviour of $G(Fe^{3+})$ with increasing photon energy. The same cannot be said for electron beams. The fairly numerous results all cluster around the 15.4-15.5 region.
Any theory that predicts a G-value for electrons any higher than 15.7 at the most will be flying in the face of a considerable body of experimental evidence.
The ICRU (1972) recommendation of 15.7 $\pm$ 0.6 seems quite definitely on the high side, but it must be remembered that this choice was influenced by the ICRU (1969) photon $G(Fe^{3+})$ recommendations, rather than the other way around (see the discussion in section 1.1).

---

*Note that the determination of $G(Fe^{3+})$ from measurements of the absorbed dose in carbon is considered to be a sufficiently direct method. The difficulties connected with deriving water/air stopping-power ratios from a carbon-walled ionization chamber (see section 9.4.4) do not arise where $FeSO_4$ dosimeter is concerned.

The results presented in figures 11.1 and 11.2 serve to emphasise the importance of examining the results by a single worker or group of workers over a wide range of radiation qualities in looking for experimental evidence on the way in which $G(Fe^{3+})$ varies. As regards the 'G-value difference', the work of Law and Naylor (1971, 1972) fits into this category, though the measurements were based on the ICRU C_E and C_λ factors. Thus their work cannot be considered to be 'hard' evidence.* If all ionization-based measurements are excluded, that leaves only Almond's results obtained with an aluminium calorimeter (Almond, 1967, 1968, 1974). These include only one measurement for a photon beam: $G(Fe^{3+}) = 15.9 \pm 0.4$ for 22 MV x-rays (see fig. 11.2a). It is to be emphasised that this measurement by Almond, which was only briefly mentioned in a letter to 'Physics in Medicine and Biology' (Almond, 1968) without any details, is the only direct calorimetric evidence for the 'G-value difference'. The calorimetric work of Fregene (1967) indicated that the G-value for 14 MV x-rays might be 1-2% higher than for ^{60}Co δ-rays (15.7 compared with 15.5) but no measurements were made for high-energy electron beams in that investigation.

---

*Their results are re-examined, using the C_E and C_λ calculated in chapter 10, in section 11.7.

Figure 11.3 VARIATION OF $G(Fe^{3+})$ WITH LINEAR ENERGY TRANSFER.
(adapted from ICRU, 1962)

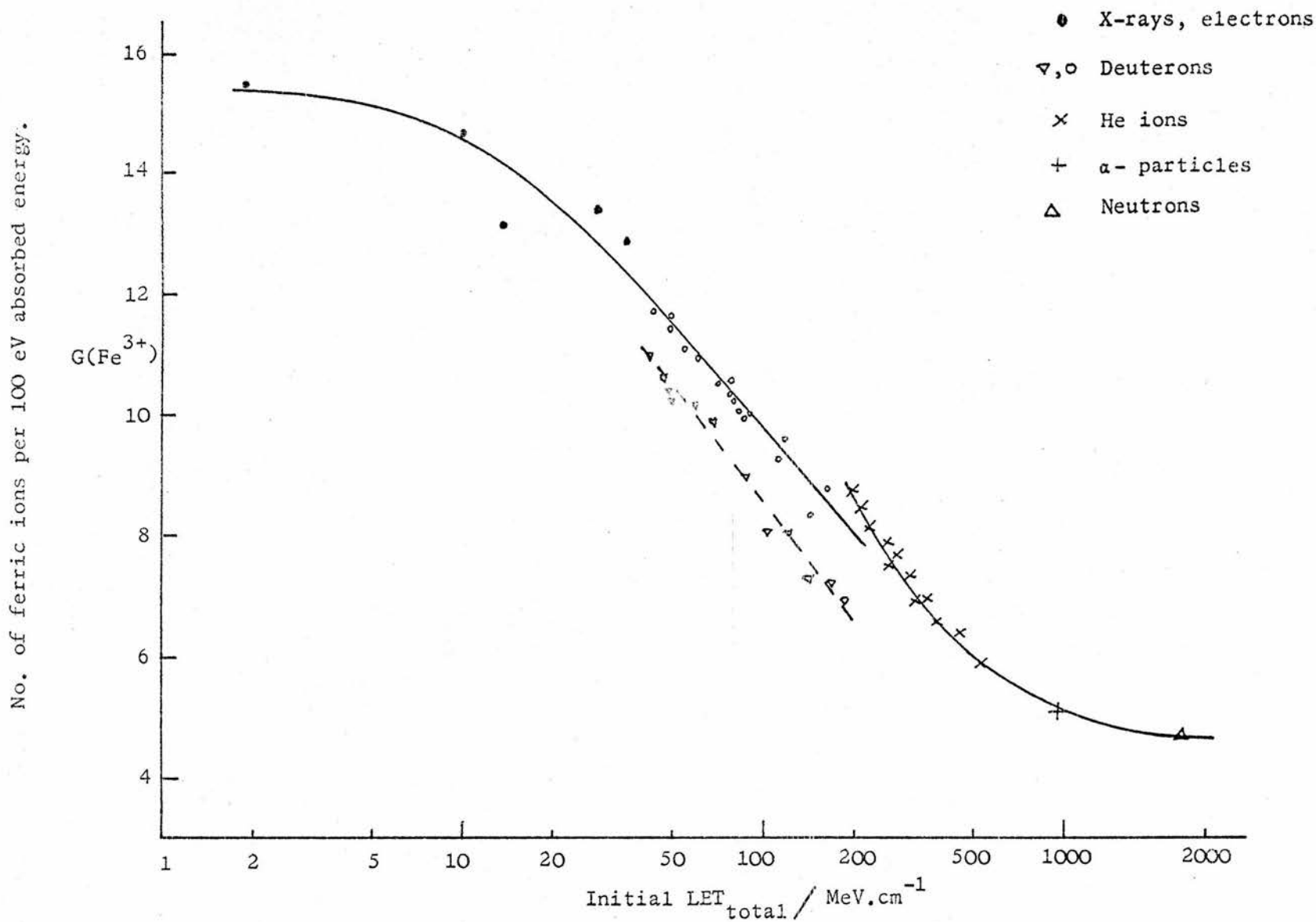

11.3 SOME THEORETICAL ASPECTS OF THE VARIATION OF CHEMICAL YIELD WITH RADIATION QUALITY*

11.3.1 LET Dependence

The chain of physical and chemical processes initiated by ionizing radiation that eventually results in the oxidation of a number of ferrous ions to ferric (Fe^{3+}) in the Fricke dosimeter is a very complex one. Nevertheless, it has been found that the chemical yield is basically a function of the Linear Energy Transfer (LET) of the charged-particle radiation i.e. the number of ionizations and excitations per unit track length. This LET dependence is illustrated in figure 11.3, taken from ICRU (1962). The quantity along the abcissa is the total stopping power at the initial energies of the radiations and is therefore a very crude description of the LET, effectively ignoring the effect of any secondary particles such as δ-rays. On the basis of a more detailed LET model (i.e. some sort of LET distribution), it is possible to account for the deviations of the values for the different radiations from a smooth curve. Note that the radiations of interest in the present work, high-energy electrons and photons, have an initial total LET varying only between 1.8 and 2.2 $MeV.cm^{-1}$ and therefore would all be plotted at virtually the same position on figure 11.3.

---

*The heading was chosen to indicate that this is by no means a comprehensive treatment of the subject.

The LET dependence can be explained in simple terms as follows.* The passage of high-energy charged-particle radiation through matter results in ionizations and excitations. The number and kinds of energetic states formed per unit energy absorbed are largely independent of the type of radiation. These energetic states degenerate rapidly and after 10^{-10} - 10^{-11} sec in water, thermalized chemically active species are formed. The time required to reach this stage is assumed to be so short that the spatial positions of the radicals are practically those of the initial states, uninfluenced by the chemical parameters such as solute concentration, pH, and temperature.

In condensed systems, therefore, the active species (or radicals) are initially distributed nonhomogenously in the irradiated medium in or near the paths of the ionizing particles. In many of the primary ionizations, the electrons are ejected with sufficient energy to produce additional energetic states and hence active species. Any such group of species produced as a result of an individual excitation or ionization is called a 'spur', and an ensemble of spurs is called a 'track'.

This heterogeneity in the initial spatial distribution of the radicals affects the subsequent course of the chemical reactions and is responsible for the influence of LET on radiation yields. For low-LET radiations, such as high-energy x-rays and electrons, adjacent spurs are widely separated and thus the reactions forming molecular products take place at the relatively low

---

*Much of the following was taken from Fricke and Hart (1966).

radical concentrations of the individual spurs. Hence the radical yield is high and the molecular product yield is low. For high-LET radiations, such as α-particles, or low energy electrons, adjacent spurs partly overlap and the reactions take place at the relatively high concentration of these overlapping spurs. Consequently, the molecular product yield increases and the free radical yield decreases.

Considering now the Fricke dosimeter, which has been standardised as 0.001 M $FeSO_4$ in 0.8 N H_2SO_4 (air-saturated), the ferric ion yield can be written:

$$G(Fe^{3+}) = 2\,G_{H_2O_2} + 3\,G_H + G_{OH} \qquad .....(11.1)$$

The yield of molecular H_2O_2 decreases with decreasing LET but the yields of the radicals H and OH increase, resulting in an overall increase of $G(Fe^{3+})$ with decreasing LET. This is what is observed.

11.3.2 The Burch (1959) Theory*

11.3.2.1 General Outline

A commendable attempt was made by Burch (1959) to predict theoretically the variation of the chemical yield with radiation quality in the ferrous and ceric sulphate dosimeters. Burch made it quite clear that his analysis made use of some unavoidably crude assumptions but nevertheless the theoretical model he adopted was a remarkably detailed one compared to the earlier work by physicists such as Gray (1951, 1955) in this field. It still remains the only theory which enables a numerical value for $G(Fe^{3+})$ to be calculated for a particular

---

*Burch's theory and some of his results have already been briefly discussed in section 1.3.1.1.

radiation quality from the charged-particle energy flux spectrum produced in water by the radiation. Burch's theory actually requires the local energy dissipation spectrum in water, $Q_T\Delta T$, where 'local' refers to energy losses less than 100 eV. It will be recalled that the present computations were specifically designed to calculate the total electron flux spectrum down to 100 eV, from which the $Q_T\Delta T$ distribution is easily derived (see section 7.3).

Burch wrote down a simplified scheme for the reactions occurring based on the theory of Allen (1954) on the yield of free H and OH in the irradiation of water. The basic reaction is the decomposition of water by the ionizing radiation:

$$H_2O \longrightarrow H + OH \qquad .....(11.2)$$

The immediate yield in this reaction was assumed to be the same for all radiations, on the basis that the average energy required to form an ion pair ($\bar{W}$) is practically independent of radiation quality. The other reactions, such as $H + H \rightarrow H_2$ and $OH + OH \rightarrow H_2O_2$, were assumed to depend on the local LET, by which Burch meant $(dT/dx)_{100}$. The yields of ferric ions, $G(Fe^{3+})$ and ceric ions, $G(Ce^{3+})$, per 100 eV absorbed energy were then related to the basic radical and molecular yields by relations such as equ. 11.1.

Burch's assumption that the yield of the reactions depended on the local LET is central to his theoretical approach and requires some eleaboration. Burch considered

that losses were 'local' if the energy transfer was less than 100 eV. All transfers greater than 100 eV resulted in δ-rays which were effectively treated as separate tracks with their own rate of local energy loss.* Referring back to what was said in section 11.2.1, these local losses are then the 'spurs' and the local LET is a measure of the extent to which the spurs overlap, which in turn is related to the balance between free radical and molecular yields. Note that this model involves much more detail about the structure of the charged-particle tracks than is implied in the use of some sort of average LET to characterize radiation quality as in figure 11.3. Thus the overall yield for a given radiation, $G(H_2)$ or $G(Fe^{3+})$ say, is actually a weighted average over the different parts of the electron spectrum e.g. a certain G-value for the local energy dissipation by the high-energy primary electron tracks (low LET) and possibly a very different G-value for the dissipation by the low-energy δ-ray tracks (high LET). Burch set out to derive this relationship between chemical yields and local LET.

Burch treated the intra-track combination according to the Jaffé columnar recombination formula. This formula relates the initial number of radical pairs per unit track length, P_o, to the number of unrecombined pairs per unit track length after time t, P, and involves the recombination constant α, diffusion constant D and the initial radius of the column, b. P_o was taken to be

---

*Naturally such an energy loss model could only be considered if the electron flux spectrum, including all the δ-rays, could be calculated down to the cutoff i.e. 100 eV. Burch (1957a) had already performed such calculations.

Figure 11.4 BURCH'S $G_{Fe}^{*}{}^{3+}$ VS. LOCAL LET RELATION.
(from Burch, 1959)

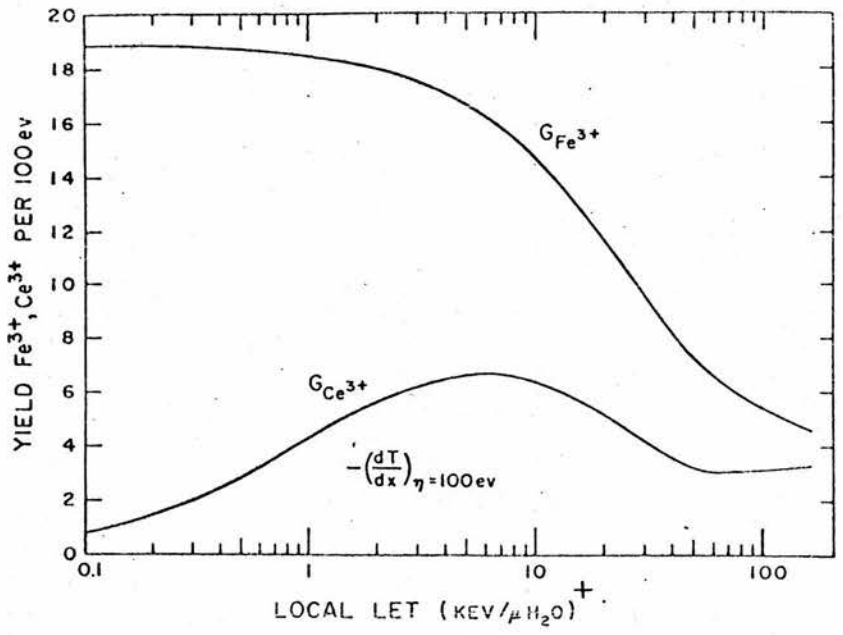

FIG. 2. Yield of Fe^{3+} and Ce^{3+} (ions per 100 ev) on linear ordinate scale against local LET (kev per micron H_2O) on logarithmic abscissa scale. (Local LET should not be confused with average, total, or instantaneous LET's frequently used in graphs of experimental results. Figure 2 has no direct experimental analog. It should be used in conjunction with equation 10 to calculate the over-all yield for a radiation whose local energy spectrum in the solution, $Q_T \Delta T$ versus T, is known.)

*$G_{Fe}3+$ denotes the 'instantaneous' local-LET yield ; G Fe^{3+} the overall yield.

+ ×10 = MeV.cm^{-1} .

proportional to $(dT/dx)_{100}$. It should be noted that Burch considered this formula to be valid for high local LET, as with α-particles or low energy electrons, but unreliable at low LET where radical pairs and clusters are randomly and, on the average, widely spaced.

The amount of local energy dissipated by particles with kinetic energies in the range T to T + ΔT was written as $Q_T \Delta T$. Thus for an average energy ω required to form a radical pair, the number of radical pairs formed by particles in this energy range was $Q_T \Delta T/\omega$. After further simplifying approximations, Burch derived the following expression for N_T, the number of unrecombined pairs after time t_o :

$$N_T = \frac{Q_T \Delta T}{\omega[1 + a(dT/dx)_{100}]}$$

where a was a constant combining together α; D; b; t_o and ω, and referred to as the combination formula constant. Burch associated different a's (i.e. a_1, a_2 etc.) with the different reactions.

By making use of experimental data for $G(Fe^{3+})$, $G(Ce^{3+})$ and $G(H_2)$ for ^{60}Co gamma rays and ^{210}Po α-particles, and the $Q_T \Delta T$ distributions for these radiations that he had previously calculated (Burch, 1957a), Burch was able to deduce the value of the a's for the reactions as well as R, the initial number of water molecules per 100 eV of local energy dissipation. The analysis was somewhat involved and it would not be appropriate to reproduce it here. Finally, the G vs local LET relations shown in figure 11.4 were arrived at. From these curves it was possible to

Table 11.1 ASSUMED AND CALCULATED YIELD VALUES FOR THE FERROUS-SULPHATE DOSIMETER (Burch, 1959).

Radiation	$G(Fe^{3+})$	
$^{60}Co\ \gamma$	15.47	assumed
$^{210}Po\ \alpha$	6.13	assumed
25 MV x-rays	15.7	
2 MeV electrons	15.7	
1 MeV electrons	15.55	
220 kV x-rays*	14.4	
100 kV x-rays	14.0	
Tritium	12.9	

*HVL approx. 2.5 mm Cu.

calculate the value of $G(Fe^{3+})$ or $G(Ce^{3+})$ for any radiation whose $Q_T \Delta T$ spectrum was known. Thus

$$G(Fe^{3+}) = \frac{\sum_{0}^{T_{max}} G_T \cdot Q_T \Delta T}{\sum_{0}^{T_{max}} Q_T \Delta T} \qquad .....(11.3)$$

where G_T is the value of $G_{Fe^{3+}}$ in figure 11.4 corresponding to electron energies between T and T + ΔT, i.e. the value of $(dT/dx)_{100}$ as a function of T is also required.* Note that the above relation can be written in terms of the dose distribution in local LET, $D_{100}(L_{100})dL_{100}$:

$$G(Fe^{3+}) = \frac{\int_{L_{min}}^{L_{max}} G(L_{100}), D_{100}(L_{100})\, dL_{100}}{\int_{L_{min}}^{L_{max}} D_{100}(L_{100})\, dL_{100}} \qquad .....(11.4)$$

From this expression it can be seen that $G(Fe^{3+})$ is effectively an average over the dose distribution in LET for Δ = 100 eV. Such a distribution has been shown in figure 1.3 for ^{60}Co radiation.

11.3.2.2 Results

The results that Burch obtained for $G(Fe^{3+})$** from evaluating equ. 11.3 with the $Q_T \Delta T$ distributions for a number of different photon and electron qualities are listed in table 11.1 together with the values he assumed for ^{60}Co gamma rays and ^{210}Po alpha particles.

---

*It is realized that the above description of Burch's theory is rather sketchy, but it will be seen that the important details for the purposes of this investigation are essentially contained in equ. 11.3 and figure 11.4.

**see note under fig. 11.4.

Note that the $Q_1\Delta T$ distributions for ^{60}Co and 25 MV photon radiation have been shown to be in fair agreement with the present more accurate computations of these distributions in chapter 8.

Burch was particularly pleased with his result of 12.9 for tritium β-particles as this was in excellent agreement with experimental determinations for this radiation. He felt it provided a good test of the theory as tritium β-radiation was intermediate in quality between ^{210}Po α-particles and ^{60}Co γ-rays. However, Burch did point out the definite discrepancy between his result of 15.7 for 2 MeV electrons and the experimental determination of 15.45 ± 0.11 by Schuler and Allen (1956). This lack of agreement with experiment for 2 MeV electrons suggested that the Burch theory as it stood could not be applied with very much confidence to the problem of the suspected 'G-value difference' for high-energy electron and photon radiation. In particular, though ICRU (1969) had taken Burch's result of $G(Fe^{3+}) = 15.7$ for 25 MV x-rays as the basis for their recommendation at this quality, it was not difficult to see that G was likely to come out considerably higher still (15.9 - 16.0) for high-energy electrons in view of the continuous increase of $G_{Fe^{3+}}$ with decreasing L_{100} in figure 11.4. This would not have been in line with experimental results which suggested that $G(Fe^{3+})$ levelled out at about 15.5 - 15.6 for electron beams (see fig. 11.2b). It looked, therefore, as if the form of the $G_{Fe^{3+}}$ vs local LET relation might well be

incorrect at the low-LET end and this was not inconsistent with Burch's remarks concerning the doubtful validity of applying the Jaffé formula at low LET.

11.4 ALTERNATIVE APPROACHES TO THE 'G-VALUE DIFFERENCE' PROBLEM

11.4.1 General

At the time that this work started, the writer did not fully appreciate to what extent dosimetric uncertainties, especially in ionization measurements, cast doubts on the experimentally determined $G(Fe^{3+})$ values. It seemed then that the 'G-value difference' definitely existed, even allowing for experimental errors. It also seemed far from certain that the comprehensive electron and photon beam calculations of local energy dissipation spectra, to be used eventually in conjunction with a Burch-type $G_{Fe}{}^{3+}$ vs local LET relation, were going to explain such a 'G-value difference'. Consequently, much effort was expended over a fairly long period of time in trying to see what other factors besides LET distributions and the like could possibly account for the fact that the $FeSO_4$ dosimeter appeared to be able to discriminate between electron and photon beams. Some of the more fruitful of these deliberations are discussed in this section.

11.4.2 Photonuclear Reactions

It was made clear in chapter 3 that the photon Monte Carlo simulation did not include photonuclear reactions, though at certain photon energies the cross-section for these interactions was of the order of 5% of the total interaction cross-section. If they had not been neglected, a small number of neutrons and possibly also some photons would have had to have been taken into account along with

the much larger numbers of Compton, pair and photo-electrons. For primary electron radiation, however, the number of such nuclear interactions is entirely negligible at the energies of interest (down by 1/137). Thus here was a difference between photon and electron beams.

What effect would these neutrons and protons have had on the calculated chemical yield? The answer was not difficult to deduce. These are high-LET radiations, which have a low $G(Fe^{3+})$. For neutrons, experimental $G(Fe^{3+})$ determinations have resulted in values between 4 and 10 depending on the neutron energy spectrum (Law et al., 1974). Thus the effect of the photonuclear reactions is clearly to lower the overall G-value for photon beams, though the size of the effect is negligible on the basis of the currently accepted cross-section data (see section 3.2.2). Even if such data were to turn out to have been substantially in error, no explanation could result for the 'G-value difference' which is due to the fact that $G(Fe^{3+})$ for photon beams has been found to be higher than for electron beams.

Similar considerations with respect to positrons, which are also produced in much larger numbers by primary photon than by primary electron radiation, have already been discussed in section 6.2. Any difference between the chemical yield from positrons and electrons of the same local LET is extremely improbable. It would be directly against all the present, well-established theoretical knowledge on ionization and excitation by charged particles.

Figure 11.5 VARIATION OF LOCAL LET WITH ELECTRON K.E. (Water)

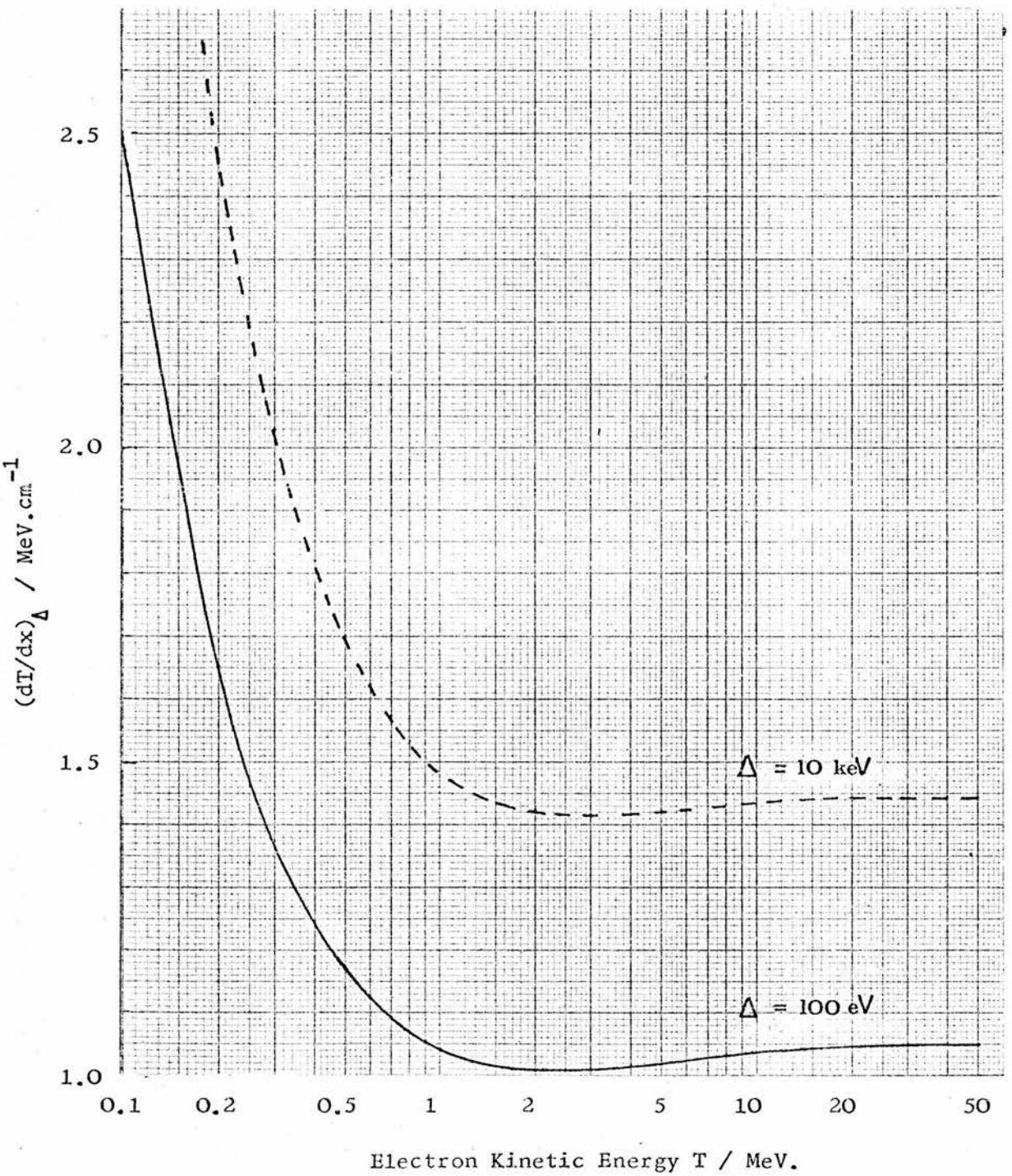

Figure 11.6 LOCAL ENERGY DISSIPATION SPECTRA:
PHOTON AND ELECTRON BEAMS.

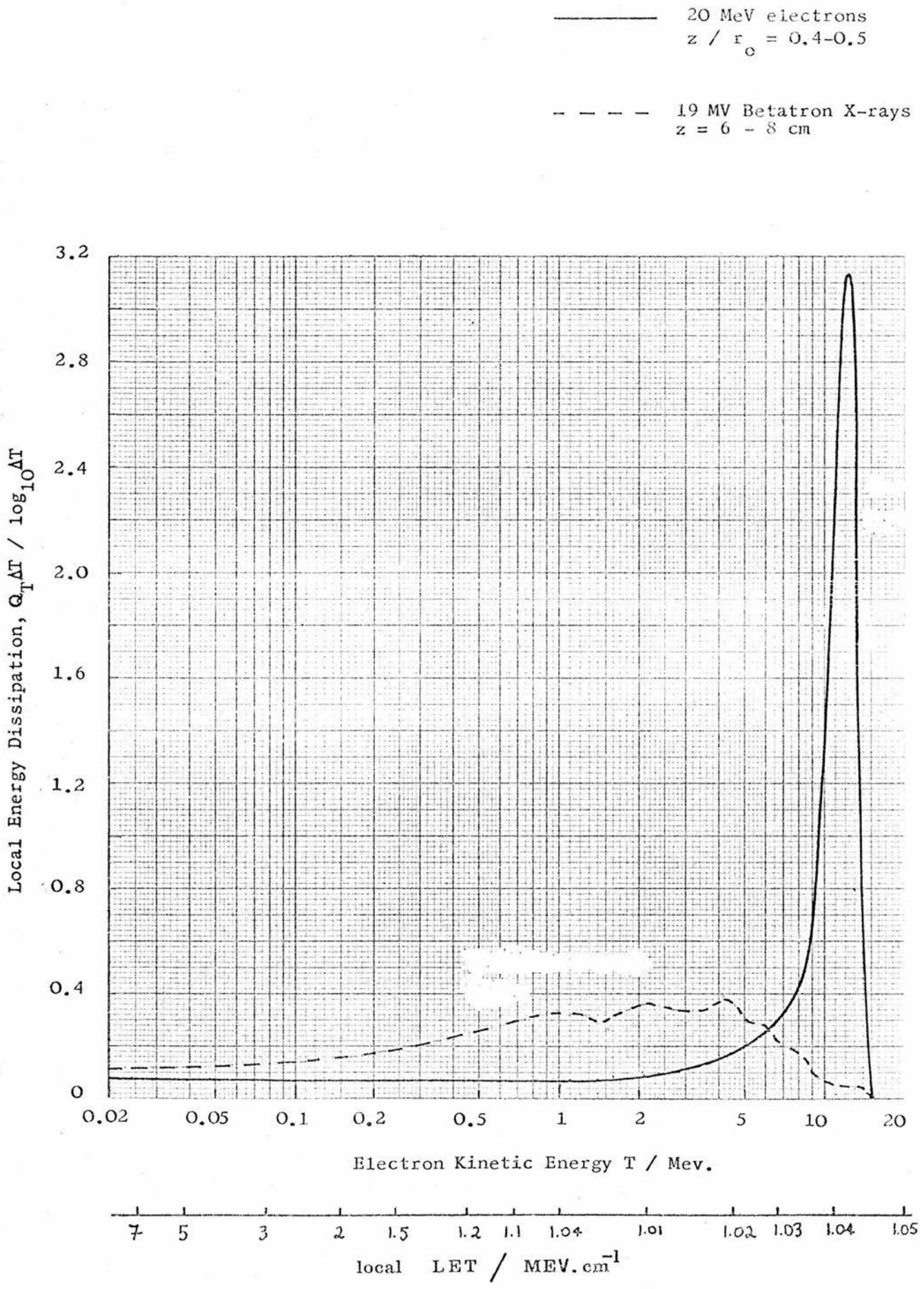

11.4.3 The Density Effect

The variation of the restricted collision stopping power with electron energy above 1 MeV in water is extremely slow. This can be seen in figure 11.5. On the assumption that the chemical yield is only a function of the local LET, then the value of $G_{Fe}{}^{3+}$ corresponding to the local energy dissipation by electrons of any energy above 1 MeV or so can only vary with electron energy by a negligible amount at the most. This will be true even if there is a rapid variation of $G_{Fe}{}^{3+}$ with local LET at the low LET end. In fact, Burch's theory suggests that the opposite is the case i.e. no variation at all (see figure 11.4).

The implication that the overall yield, $G(Fe^{3+})$, is totally insensitive to the shape of the local energy dissipation spectrum at the high-energy end is of particular significance for the 'G-value difference' question. It is precisely at the high-energy end that there are large differences between the electron spectrum produced by electron and photon beams. This is clearly illustrated by the present calculations of the Q_T spectra for a 20 MeV electron and a 19 MV betatron x-ray beam shown in figure 11.6. Preliminary calculations had indicated that if the G-value difference were to be accounted for, then the explanation would have to be connected in some way with these differences at the high-energy end.

The basic question that had to be answered was the following. Was there any conceivable reason why $G_{Fe}{}^{3+}$

Figure 11.7 COLLISION ENERGY LOSS BY A FAST CHARGED PARTICLE. (Schematic)

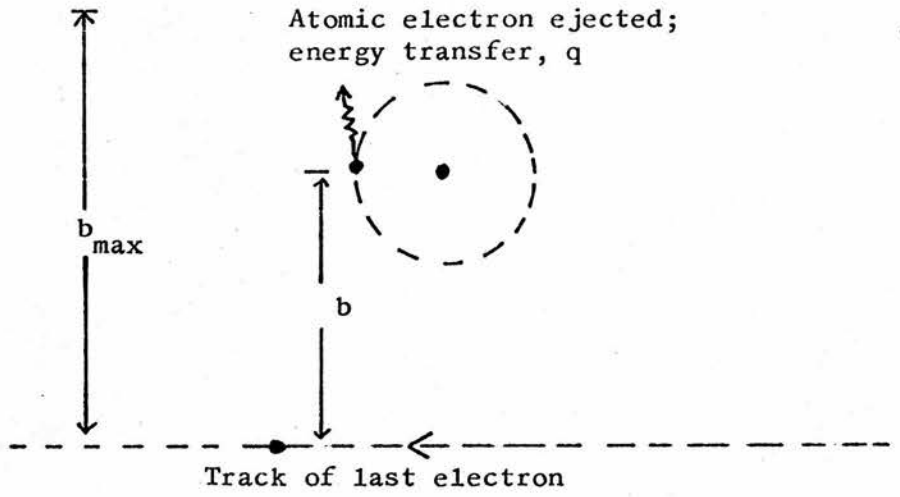

for the track* of a 1 MeV electron should be different to $G_{Fe^{3+}}$ for the track of, say, a 10 MeV electron or for that matter a 40 MeV electron? For all these energies the values of $(dT/d\rangle_{100}$, the local LET, are within 1% of each other. The immediate answer was yes, there was a possible reason - the density effect. At 1 MeV the density effect reduction is only a few per cent; at 10 MeV, it is 20% and at 40 MeV, it is over 30%. If this marked increase in the density effect could be shown to influence the detailed way in which the 'local' energy was transferred to the medium hence resulting in differences in the ratio of ionizations to excitations with electron energy, for example, then perhaps an explanation for the 'G-value difference ' had been found.

In order to put this speculation on some sort of quantitative basis, the 'physics' of the density effect was thoroughly investigated. The following details of charged-particle stopping-power theory seem relevant to the present discussion.** Firstly, from classical electromagnetic theory it is easily shown that the energy transfer q is proportional to $1/b^2$, where b is the impact parameter (see figure 11.7). Thus one can associate distant collisions with small energy losses. Secondly, at relativistic velocities the maximum impact parameter, b_{max}, increases due to the Lorentz contraction of the electric

---

*By 'track' is meant the energy losses less than 100 eV; all losses greater than this are assumed to result in separate tracks with their own local LET as explained earlier.

**This theory is dealt with in any atomic physics textbook but two of the better treatments are by Sternheimer (1961) and Bichsel (1968).

field of the fast charged particle (a full explanation for the increase of b_{max} would introduce details which are not relevant to what follows). In gases, where the maximum impact parameter is very much less than the inter-atomic distances, this increase in b_{max} results in what is known as the relativistic rise in the collision stopping power.

In condensed media at relativistic energies b_{max} is of the same order as the inter-atomic distances and screening effects begin to be important. The polarization of the atoms close to the track of the charged particle effectively reduces the electric field 'seen' by more distant atomic electrons. Thus these distant collisions, which result in the relativistic rise in the stopping power in gases, do not now take place. This is the origin of the so-called density effect. In fact, the levelling-off in the restricted collision stopping power with increasing energy evident in figure 11.5 is due precisely to the fact that the effective value of b_{max} is held constant as a result of the screening of distant collisions.

If it is assumed that there is some correlation between the impact parameter b and the distribution of energy losses even for small values of q close to the binding energies of the atomic electrons of the medium (where the classical relation given above cannot hold), then it appears that rather than resulting in a change in the energy transfer spectrum with increasing electron energy, the density effect acts to keep the spectrum

Figure 11.8 MEASUREMENT OF THE ENERGY-TRANSFER SPECTRUM AT LOW ENERGIES.
(from Rauth and Simpson, 1964)

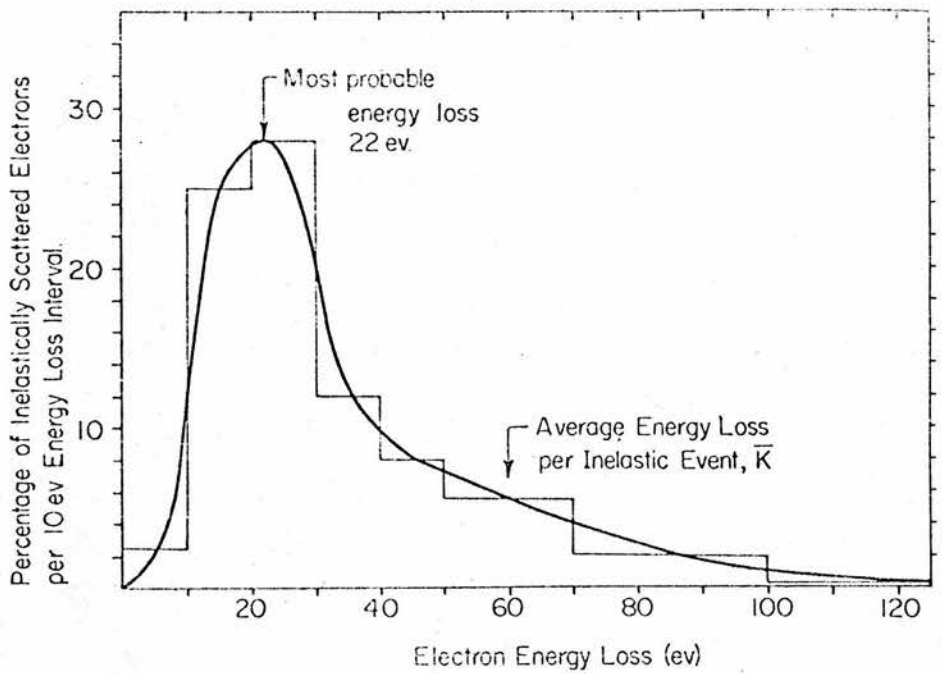

FIG. 5. The "first-collision" energy loss distribution for 20-kev electrons passing through a layer of Formvar. The percentage of the inelastically scattered electrons per 10-ev energy loss interval is plotted versus the energy loss. The experimental data for the 130 A Formvar film from Table IA was used to calculate the histograms through which the smooth curve is drawn. The points on this curve corresponding to the most probable energy loss and the average energy loss per inelastic event are indicated.

constant as it keeps the effective maximum impact parameter constant.* An example of a measured energy transfer spectrum is shown in figure 11.8. Had the density effect resulted in a shift of the spectrum towards lower energies as the electron energy increased, then it would have been reasonable to have assumed that the ratio of excitations to ionizations produced by the transfers smaller than 100 eV would have increased. This could well have resulted in a decrease in the number of water molecules initially decomposed per unit locally absorbed energy and hence in a lowering of the yield $G_{Fe^{3+}}$. This in turn could have explained why the $G(Fe^{3+})$ value for high-energy electrons should be lower than $G(Fe^{3+})$ for high-energy photon beams (see fig. 11.6). Unfortunately, this potentially significant line of reasoning had to be abandoned though not without some reluctance.

It is worth mentioning that the corollary to the deduction that the energy transfer spectrum is not altered by the density effect is that it is altered in gases, where the density effect is negligible. Thus it seems reasonable that the increase in the collision stopping power (the relativistic rise) due to the increase in the number of distant collisions should result in an increase in the relative numbers of very small energy transfers. Assuming that a large number of very small energy transfers are less effective than a smaller number of large energy

*The whole subject is complicated by the 'mixture' of classical and quantum ideas that is used to derive expressions for the stopping power and for the density effect correction. Quantum theory deals in terms of momentum transfers, not impact parameters, and b_{max} does not come into the calculation of the lower limit for the energy transfer which is expressed in terms of the mean ionization potential I.

transfers in producing ion pairs (by no means a confident assumption) then the result would be an increase in $\bar{W}$ with increasing electron energy at relativistic energies. Such an increase is in fact suspected (see section 10.5) but a much more quantitative approach is necessary before any definite conclusions can be drawn on this topic.

Finally, it is appropriate in this section to take up a point that was made in discussing the calculation of the restricted collision stopping power in section 4.2.1. There it was pointed out that the density effect reduction, δ, is always subtracted from the stopping power (evaluated from an expression such as 4.18) whatever value of the cutoff, Δ, is chosen. The implicit assumption in this procedure is that it is only losses less than Δ that are affected by the density effect. This did not seem to be a necessarily justifiable assumption at first sight, especially for cutoffs as low as 100 eV. However, when it came to putting some numbers into the expressions involved in stopping-power theory in connection with the G-value/density effect speculation discussed above, it became clear that the impact parameter associated with an energy transfer of 100 eV was many orders of magnitude less than the inter-atomic distances in condensed media. Thus it could be deduced that the density effect did only affect the energy transfers at the very low-energy end of the spectrum and therefore that the conventional way of calculating $(dT/dx)_{100}$ was reasonable.

11.4.4 The Validity of the Local LET Model

The use of LET to characterize radiation quality has come under a lot of criticism in recent years and has indirectly led to the development of the field known as Microdosimetry (see Rossi (1968) for example) which involves the consideration of fluctuations in the magnitude of individual energy transfers or groups of transfers; LET is a non-statistical quantity. It represents the average energy loss per unit tracklength and does not take into account statistical fluctuations in that energy loss, which may be appreciable at low LET. However, it must be made clear that the limitations of LET as a useful parameter to describe radiation action are much more apparent in the interpretation of radiobiological data than is the case for chemical yields. In fact, many studies have demonstrated that the variation of chemical yield can be accounted for in terms of the variation of LET, even though all the details of the physical and chemical mechanisms may not yet be understood. To give an example, the link between LET and molecular yield is simply explained in terms of the overlapping of spurs, whereas no such direct link exists between LET and cell-killing.*

---

*It can be noted that there is no experimental evidence for a difference in RBE between high-energy photons and electrons (see, for example, Sinclair and Kohn, 1964).

The value of the cutoff Burch chose, i.e. 100 eV, must be commented on. He did not put forward any particular reason for this choice in his 1959 paper, though in his earlier work on calculating the $Q_T \Delta T$ distributions (Burch, 1957) he had mentioned that 100 eV was also the cutoff that Lea (1946) had used in calculating LET values. In fact, Lea had estimated that 100 eV electrons produced clusters of ionizations sufficiently compact to behave as units. This more or less corresponds to the definition of a spur in radiation chemistry (see section 11.3.1). It can be noted that Mozumder and Magee (1966) envisaged spurs as containing radicals that originated in primary events with energy up to about 100 eV in their 'spurs, blobs and tracks' model of electron energy dissipation. It thus appears that 100 eV has 'remained in the literature' so to speak, even when radiation chemists themselves have looked at the problem of accounting for the variation of chemical yield with radiation quality. If a different cutoff were to be chosen, say 200 eV, it is difficult to see how this would alter the 'G-value difference' problem. Figure 11.5 included the variation of $(dT/dx)_\Delta$ for Δ = 10 keV as well as 100 eV. The same lack of variation with electron energy above 1 MeV is indicated for both cutoffs. Thus increasing the cutoff and hence the assumed spur size would not result in being able to assign different $G_{Fe}3+$ values to different electron energies above 1 MeV and hence exploit the differences in the electron spectra between high energy electron and photon beams.

Perhaps the most important point to bear in mind is that as far as the chemical yield from photon and electron radiation is concerned, the only ionizing particles involved are electrons. If for example the problem had been to account in detail for unexpected differences in the chemical yield produced by say low-energy electron radiation and α-particles, then it would have been necessary to relate the effect of the α-particle tracks to that of the electron tracks. In such a case, a different model for the very densely ionizing α-particle track to that for the electrons might have been appropriate and correspondence between the two models might have caused complications.* However, the only concern here is comparing 'electrons with electrons' or more explicitly, comparing the electron flux spectrum produced by a beam of electron radiation to that produced by a beam of photon radiation. Unless one brings in metaphysical ideas along the lines of the $FeSO_4$ solution being able to tell the difference between electrons of a given energy produced by photon interactions and electrons of the same energy resulting from the slowing down of the primary electron beam, then it is certain that the 'G-value difference', if it exists, must be explainable in terms of difference in the electron flux spectra produced in water by the electron and photon beams. Furthermore, the assumption that $G_{Fe^{3+}}$ is a function of local LET is equivalent to saying that G is a function of electron energy, as local

---

*It is realized that Burch (1959) included α-particle radiation, but see section 11.5.2.3.

LET is a function of electron energy (the very shallow minimum at about 2 MeV does not significantly alter the picture). Thus whether or not the link between a particular LET value and a particular $G_{Fe}3+$ value can be understood from a fundamental point of view, nevertheless the local LET description represents a comprehensive characterization of radiation quality for electron radiation. It can be confidently assumed that any differences in the overall chemical yield, $G(Fe^{3+})$ that cannot be accounted for, even by drastically adjusting the precise form of the $G_{Fe}3+$ vs L_{100} relation, do not exist.

Figure 11.9 LOW ENERGY ELECTRON $(dT/dx)_{100}$ IN WATER: COMPARISON WITH BURCH (1957, 1959) VALUES.

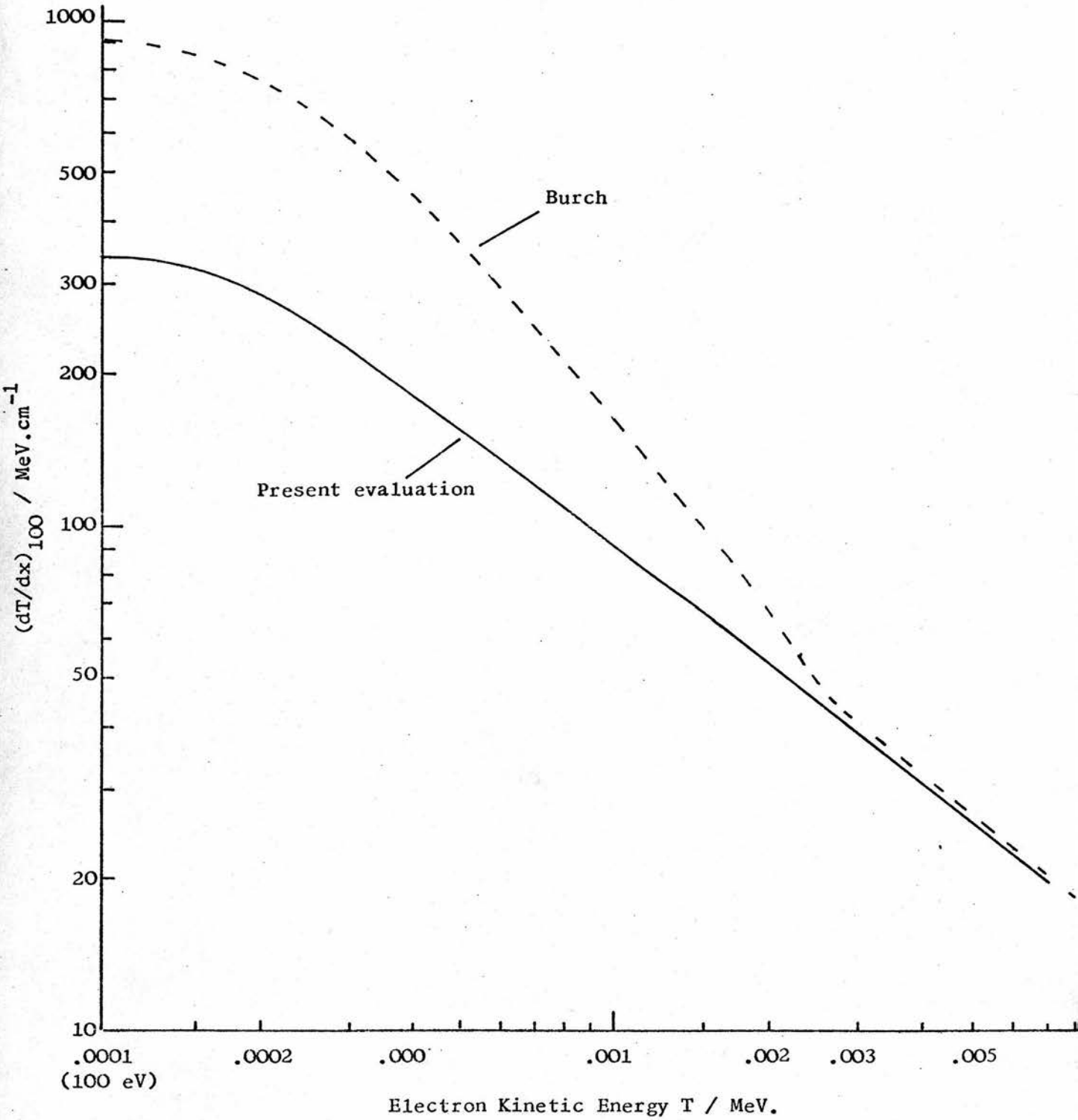

11.5 THE MODIFICATION OF THE $G_{Fe}3+$ vs LOCAL LET RELATION

11.5.1 Problems with the Burch Relation

While Burch's approach to the problem of calculating the chemical yield from the $Q_1 \Delta T$ distribution via the local LET model seemed adequate for the present purposes, some of the details in his work gave cause for concern. The most obvious of these concerned the electron stopping powers at low energies that he used. Below 3 keV, Burch dispensed with the Bethe-Bloch formula and instead estimated the stopping powers from the experimental work of Davis (1955) on the ranges of low-energy electrons in enzymes. The values Burch used in his chemical yield theory for $(dT/dx)_{100}$ are compared with the present evaluation of this quantity in figure 11.9. The difference is almost a factor of three at 100 eV. Unfortunately for Burch, subsequent experimental work on low-energy electron stopping powers has tended to yield values of around 300-400 $MeV.cm^{-1}$ at 100 eV (Holt, 1970). The present modified evaluation of the Bethe-Bloch theory below 500 eV, described in section 5.3, was designed to be consistent with recent experimental determinations.

The simplest solution to the above problem seemed to be to adjust the local-LET scale of Burch's $G_{Fe}3+$ curve (see fig. 11.4) to bring the LET values into line with the values used in this work. This would not alter Burch's $G(Fe^{3+})$ results for the electron and photon

radiation* but it would make a difference to the α-particle G-value. The local LET values that Burch used for the α-particle track (as opposed to the δ-rays produced by the α-particles which are, of course, indistinguishable from δ-rays produced by photon or electron beams) were not so very different from the current 'best' values. However, Burch took $G(Fe^{3+})$ for ^{210}Po α-radiation as equal to 6.13. This has subsequently been revised downwards to 5.1 as a result of further experimental work (Trumbore, 1958). Thus it looked as though the $G_{Fe^{3+}}$ vs local LET relation could be altered slightly at the high-LET end to fit in with both the more 'realistic' LET values and the $G(Fe^{3+}) = 5.1$ for ^{210} α-radiation. Whether or not this 'adjustment' would correspond to the re-calculated relation that would have resulted from putting the revised parameters into Burch's theoretical analysis was, of course, another question altogether. But then Burch did not consider his derivation of the G vs local LET relations to be in any sense rigorous, as has already been emphasised earlier. Had it been decided to attempt to work through Burch's theory with more up to date physical parameters, no great confidence could have been attached to this revision anyway.

---

*Note that the $Q_T \Delta T$ distribution essentially depends only on the ratio $(dT/dx)_{100}/(dT/dx)_{total}$ and not on the actual values for the stopping powers (see section 8.5.1).

It has already been mentioned that Burch considered that his tritium α-particle result indicated that his theory could not be too far out. However, he did not comment on the result calculated for 220 kV x-rays, $G(Fe^{3+}) = 14.4$ (see table 11.1). A considerable amount of experimental work on the ferrous sulphate dosimeter has now been carried out in the kilovolt x-ray region (ICRU, 1970b) and it is evident that 14.4 is almost certainly too low at this quality. In a review of $G(Fe^{3+})$ determinations, Shalek and Smith (1969) recommended 15.2 for x-rays with an effective energy of 100 keV (HVL 1.69 mm Cu)* and ICRU (1970b) recommended 14.7 ± 0.2. Though Burch had effectively 'fixed' the $G_{Fe^{3+}}$ curve so that the ^{60}Co G-value came out right, it could be deduced that the shape of the relation in the 1 - 5 $MeV.cm^{-1}$/(local LET region 0.1 - 0.5 $keV.\mu^{-1}$ in fig. 11.4) was almost certainly incorrect.** However, it did not seem too unlikely that the shape could be adjusted to give agreement with experiment for x-rays produced at around 200 kV as well as for tritium β and ^{60}Co γ radiation. Then one could see what $G(Fe^{3+})$ would come out for the high-energy photon beams and in particular, whether the 'G-value difference' was plausible. Such an empirical procedure*** is described in the next section.

---

*The 220 kV x-ray spectrum that Burch used to calculate the $Q_T \Delta T$ distribution had an HVL of 2.5 mm Cu i.e. harder than the spectra to which the recommendations apply, corresponding to an even higher G-value.

**Burch's 2 MeV electron result of 15.7 (see section 11.3.2.2) had already cast doubts on the theory for low-LET radiations. In addition, Burch had pointed out that the Jaffé formula was not expected to be valid at low LET.

***This type of empirical approach has proved successful in accounting for variations in the chemical yields from heavy particles (Burns, priv. comm.)

Table 11.2 'STANDARD' $G(Fe^{3+})$ VALUES IN EMPIRICAL PROCEDURE

Radiation	$G(Fe^{3+})$
^{210}Po α-particles	5.1
Tritium β-particles	12.9
280 kV x-rays*	14.75
^{60}Co γ-rays	15.5
20 MeV electrons	15.4 - 15.6

*Photon energy spectrum taken from measurements by Cormack et al. (1958); photon energy, $\bar{k}_{int}$ = 120 keV; HVL = 1.8 mm. Cu.

11.5.2 Empirical Modification

11.5.2.1 'Standard' $G(Fe^{3+})$ Values

In order to 'synthesise' a $G_{Fe}{}^{3+}$ vs local LET relation, it was necessary to specify some standard radiation qualities whose $G(Fe^{3+})$ values could be regarded as fixed. Burch had used only ^{60}Co γ-rays and ^{210}Po α-particles but then he had adopted a more fundamental approach. A purely empirical derivation of the way $G_{Fe}{}^{3+}$ should vary with local LET required several known $G(Fe^{3+})$ values and $Q_T \Delta T$ distributions. The 'standard' radiations and G-values employed are listed in table 11.2. The G-value for the 280 kV x-ray spectrum was estimated from the graph of $G(Fe^{3+})$ vs mean photon energy given in ICRU (1970) which is based on experimental determinations. However, it is perhaps the least well-known of the values listed. It will be evident from the discussion in section 11.2 that a fair amount of confidence can be attached to the ^{60}Co and the high-energy electron values.

11.5.2.2 Q_T Spectra for the 'Standard' Radiations

Local energy dissipation spectra, Q_T, had to be calculated for the five radiation qualities listed in table 11.2. This did not present any great problems as the photon-electron cascade computation had been specifically set up in order to carry out such calculations, though it hadn't been originally envisaged that it would be used for kilovoltage x-ray spectra for example.

For the ^{210}Po α-particles, which have an initial of 5.3 MeV, the local LET values were deduced from the data on heavy-particle stopping powers given in ICRU (1970).* Values of $(dT/dx)_{100}$ varied from a maximum of 2400 MeV.cm^{-1} at an α-particle kinetic energy of 0.2 MeV to 490 MeV.cm^{-1} as 5.3 MeV. These can be compared with values of between 474 and 1540 MeV.cm^{-1} that Burch (1957) used. The $Q_T \Delta T$ distribution for the α-particle track (i.e. for losses less than 100 eV) was calculated by the same method as Burch(1957a) had employed with the same ΔT intervals, the only difference being that values of the ratio $(dT/dx)_{100}/(dT/dx)_{total}$ involved in the calculation were taken from ICRU (1970); these values did not differ greatly from the values Burch had used. From this calculation, the α-particle track accounted for 60.85% of the total local energy dissipation, $\Sigma Q_T \Delta T$, the latter naturally being equal to 5.3 MeV.

The remaining 39.1% of the dissipation is then due to the δ-rays that the α-particle produces. For a 5.3 MeV α-particle, the maximum possible δ-ray energy is 2.9 keV from energy and momentum considerations. The initial energy spectrum of these δ-rays was derived from the following expression for $(N_\delta)_{T_1,T_2}$,** the number of δ-rays with energies between T_1 and T_2 per unit energy dissipation:

---

*The proton values given in table A2 of the ICRU report were converted to α-particle values, with corrections for electron capture deduced from fig. A6.

**This procedure was again taken from Burch (1957a).

$$(N_\delta)_{T_1,T_2} \propto \frac{(T_1-T_2)/(T_1T_2)}{(dT/dx)_{total}}^{*}$$

The Q_T spectrum (or $Q_T\Delta T$ distribution) corresponding to this initial δ-ray spectrum was calculated using the depth-independent electron slowing-down spectrum program described in chapter 5. Thus essentially all that was done was to re-calculate the $Q_T\Delta T$ distribution for the ^{210}Po α-radiation** using more up to date parameters than Burch had employed, while treating the δ-ray spectrum in exactly the same way as in the high-energy electron and photon beam computations in order to be consistent.

The Q_T spectrum for the tritium β-radiation was computed in a similar manner to that for the δ-rays produced by the ^{210}Po α-particles. The initial spectrum was taken from Burch (1957a); the maximum in the β-particle spectrum was 18 keV. For the 280 kV x-ray spectrum, the photon-electron cascade program was employed to calculate the Q_T spectrum for a depth of 1-3 cm which corresponds closely to dosimetric measurement depths. For ^{60}Co*** the depth was 4-6 cm and for the 20 MeV electron beam, 1-3 cm, both corresponding to the ICRU calibration depths. It should be noted that of these Q_T spectra computations, only the 20 MeV electron one was at

---

*The numerator simply results from assuming a $1/T^2$ distribution for the energy transfers.

**The range of α-particles in water is extremely short so that one is always dealing with the absorption of the complete α-particle tracks; no depth-dependence need be considered.

***Primary gamma-ray photons only i.e. spectrum C.

Figure 11.10 LOCAL ENERGY DISSIPATION SPECTRA FOR 3 OF THE 'STANDARD' RADIATIONS.

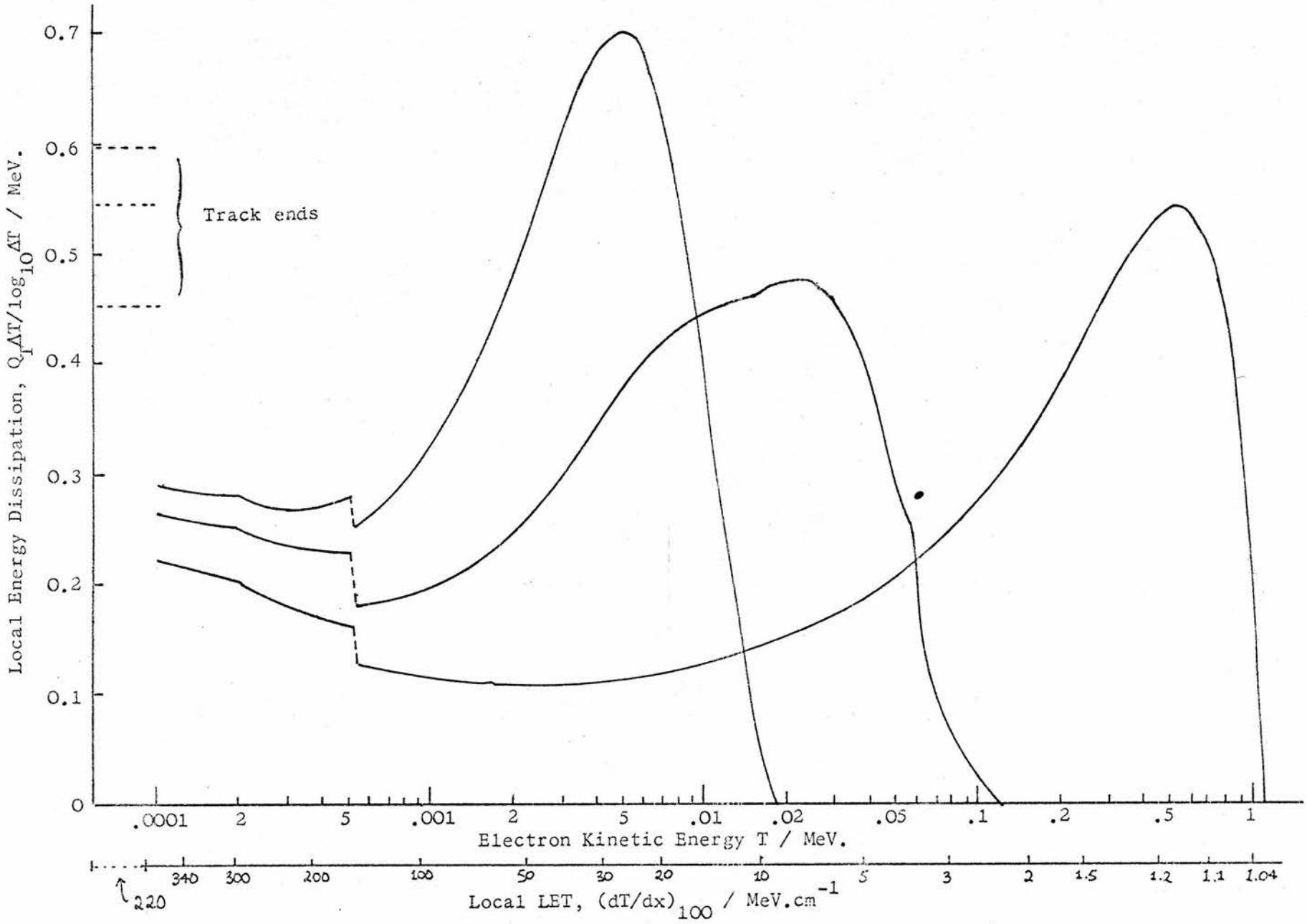

Figure 11.11 THE TWO $G_{Fe}3+$ vs. LOCAL LET RELATIONS.

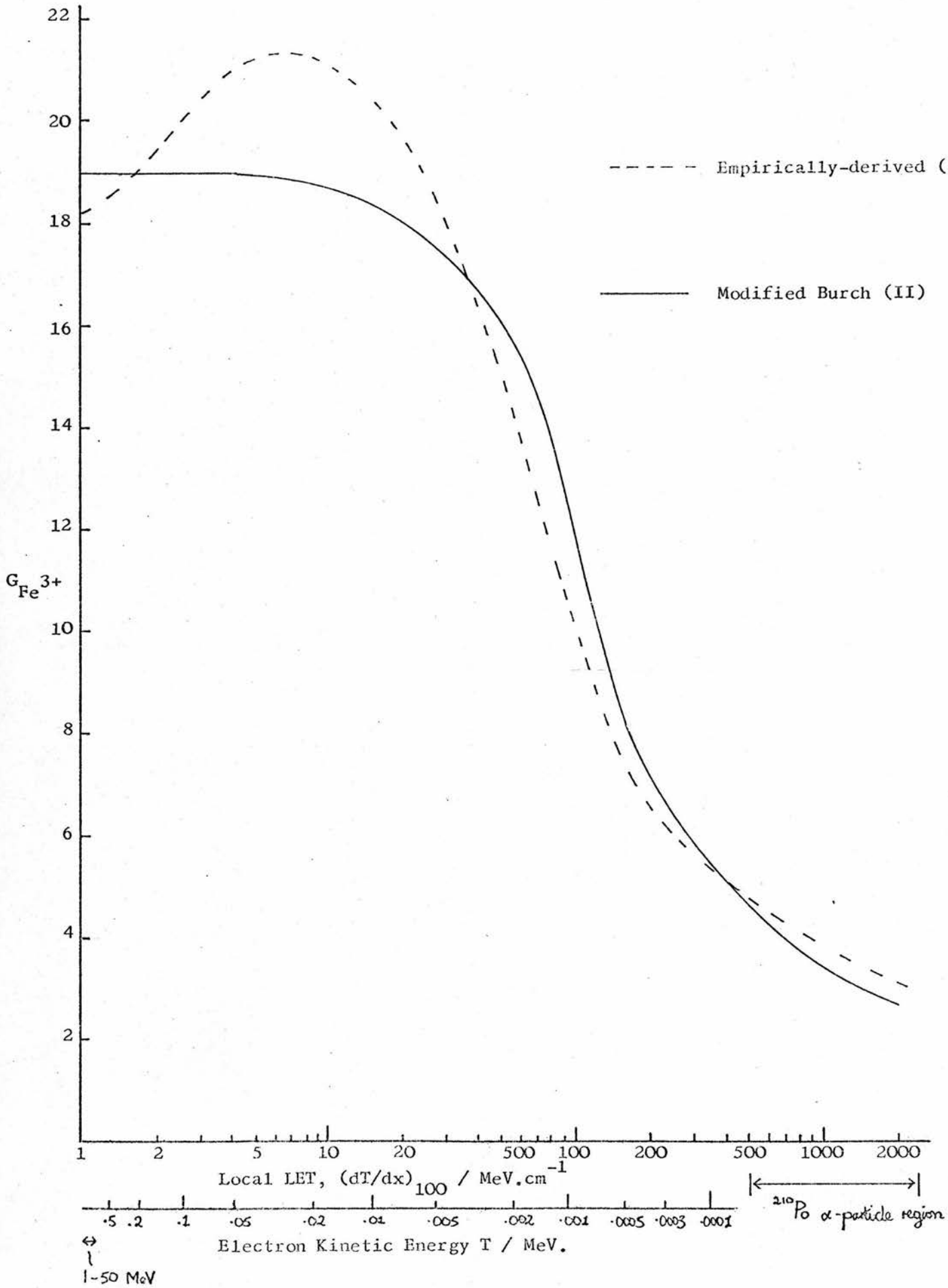

all expensive in terms of computer time, but a few hundred histories were quite sufficient to define the electron flux spectrum and hence the Q_T spectrum for this purpose (all these computations were, of course, carried out prior to the extensive 'final' series described in chapters 7 and 8).

The Q_T spectra calculated for the tritium β, 280 kV x-ray and ^{60}Co qualities are shown in figure 11.10. The scale along the abcissa has been marked both in electron kinetic energy and in local LET. Note how the 280 kV x-ray spectrum is roughly intermediate in quality between tritium and cobalt which is exactly what is required in order to try and 'fix' the value of $G_{Fe}3+$ over different regions of the local LET.

11.5.2.3 The Two $G_{Fe}3+$ vs local LET Relations

The empirical modification procedure was started by adjusting the Burch $G_{Fe}3+$ curve (fig. 11.4) so that it would correspond to the present $(dT/dx)_{100}$ values below 3 keV, as discussed in section 11.5.1. This 'modified Burch' relation is shown in figure 11.11 by the solid line. Note that there is no overlap between the α-particle primary track LET region, 500-2400 MeV.cm^{-1}, and the electron LET region which only extends up to 350 MeV.cm^{-1} (this was not the case for the electron $(dT/dx)_{100}$ values that Burch used, of course). It was, therefore, relatively easy to fix the part of the curve beyond 500 MeV.cm^{-1} so that $G(Fe^{3+})$ for ^{210}Po radiation came out correctly i.e. equal to 5.1. This also meant that assumptions about $G_{Fe}3+$ being the same for α-particles and electrons of the same LET were not put to the test.

Table 11.3 THEORETICAL $G(Fe^{3+})$ BASED ON DIFFERENT $G_{Fe^{3+}}$ LOCAL LET CURVES

Radiation	Geometry	$G(Fe^{3+})$		
		'Standard'	Empirical G-curve	Modified Burch G-curve
^{210}Po	∞ medium	5.1	5.1	5.1
Tritium	∞ medium	12.9	12.91	12.97
280 kV x-rays	1 - 3 cm	14.75	14.73	14.11
^{137}Cs	4 - 6 cm		15.63	15.22
*^{60}Co	4 - 6 cm	15.5	15.53	15.44
2 MeV electrons	∞ medium		15.41	15.71
*20 MeV electrons	1 - 3 cm	45.5	15.55	15.96

*To be regarded as preliminary values. Definitive results given in the next section.

Using the modified Burch relation, $G(Fe^{3+})$ for the 280 kV x-radiation was calculated to be 14.11 - much too low as expected.* If the tritium and cobalt G-values were not to be altered, and the 280 kV x-ray G-value was to be increased, then clearly the empirical $G_{Fe^{3+}}$ relation would have to go through a maximum in the 3-20 MeV.cm^{-1} region (see fig. 11.11). After a great deal of 'trial and error' adjustments and calculations, the relation shown by the broken line in fig. 11.11 was arrived at. The high-LET end was fixed by the ^{210}Po α-particle Q_T spectrum and the extreme low-LET end was fixed by the 20 MeV electron Q_T spectrum; the curve had to come down fairly rapidly on the low-LET side of the maximum in order that the high-energy electron G-value did not end up being too high.

The differences in the $G(Fe^{3+})$ values calculated from the two curves in figure 11.11 can be seen from table 11.3. In addition to the 'standard' radiations, some extra values were calculated at other qualities for comparison purposes. It can be noted that for 2 MeV electrons (complete track) the empirical $G_{Fe^{3+}}$ relation results in $G(Fe^{3+})$ = 15.41 which is in much better agreement with the experimental value of 15.45 by Schuler and Allen than the value derived from the modified Burch curve (see section 11.3.2.2). On the other hand, the value for ^{137}Cs γ-radiation (0.66 MeV photons) may be too high, though the

---

*This was lower than the value of 14.4 that Burch had calculated for his 220 kV x-ray spectrum, but it should be pointed out that the HVl for his spectrum was 2.5 mm Cu compared to 1.8 mm Cu for the 280 kV x-ray spectrum used here.

experimental values given in ICRU (1969) are too few to draw any definite conclusion about this.

Naturally, the question of most interest concerning the G-values calculated from the different $G_{Fe^{3+}}$ curves was whether either of them predicted the 'G-value difference'. Though the answer to this is given in detail in the next section, it can be said here that from preliminary calculations for the 31 MV betatron x-ray beam it almost certainly looked as if the answer was no. During the 'trial and error' derivation of the empirical $G_{Fe^{3+}}$ relation it was apparent that $G(Fe^{3+})$ would only come out higher for a high-energy photon beam than for high-energy electrons if the curve was made to have a completely implausible shape i.e. an extremely pronounced maximum and a very rapid fall-off at low-LET - much more so than that exhibited by the broken line in fig. 11.11. In addition, such an 'impossible' curve would also have resulted in a G-value of about 20 for the kilovoltage x-rays, which was simply not on.

Table 11.4 $G_{Fe^{3+}}(L_{100})$ vs $T(L_{100})$: VALUES USED IN CASCADE PROGRAMS

Electron Kinetic Energy (MeV)	$G(L_{100})$*	
	Modified Burch (II)	Empirical (I)
0.0001	5.55	5.40
0.0002	5.90	5.65
0.0003	6.75**	6.25**
0.0004	7.65	6.90
0.0005	8.50	7.50
0.0007	10.30	8.90
0.001	12.65	10.70
0.002	15.80	14.60
0.003	16.85	16.60
0.004	17.39	18.00
0.005	17.66	18.80
0.007	18.03	19.70
0.01	18.38	20.45
0.02	18.84	21.30
0.03	18.97	21.35
0.04	18.98	21.20
0.05	19.00	21.00
0.07	19	20.55
0.1	19	19.90
0.2	19	19.00
0.3	19	18.60
0.4	19	18.50
0.5	19	18.40
0.7	19	18.35
1	19	18.27
2	19	18.20
3	19	18.22
4	19	18.23
5	19	18.24
7	19	18.26
10	19	18.28
20	19	18.29
30	19	18.30
40	19	18.30

*or G(T).

**Corresponds also to the 100 eV track-end dissipation.

11.6 RESULTS OF $G(Fe^{3+})$ CALCULATIONS FOR HIGH-ENERGY ELECTRON AND PHOTON BEAMS

11.6.1 Some Computation Details

The two $G_{Fe}{}^{3+}$ curves shown in figure 11.11 were carefully tabulated as a function of the electron kinetic energy. These tabulated values are given in table 11.4. In this form, both sets of G(T) values were included in the permanent input data** for the photon-electron cascade programs (see section 6.4.1.1). For each spectrum geometry, the two values of $G(Fe^{3+})$ were evaluated as in equation 11.3 using the local energy dissipation spectrum derived from the total electron flux spectrum (sections 7.3.1 and 8.5.1).

It should be noted that a value of $G_{Fe}{}^{3+}$ must be assigned to the 100 eV track ends, which account for around 10% of the total local dissipation as was shown in chapters 7 and 8. In order to do this, an estimate has to be made of the effective LET for the last 100 eV of the electron 'track'. In the absence of a more valid procedure, this effective LET was taken to be equal to the range of a 100 eV electron (as given in ICRU, 1970) divided by its energy. This comes out to be about 220 $MeV.cm^{-1}$ which is the same as the local LLT at 300 eV (see table 11.4). Naturally, the track-end dissipation had been included in the approximate evaluation of $G(Fe^{3+})$ for the wide range of radiations described in the previous section, though it has not been explicitly mentioned until now.*

---

*Burch (1959) had used a 100 eV track-end $G_{Fe}{}^{3+}$ corresponding to an LET of 930 $MeV.cm^{-1}$ (see fig. 11.4).

**The electron energy values (.0001-40 MeV) shown in the table were also tabulated as input data.

Figure 11.12 THEORETICALLY-DERIVED $G(Fe^{3+})$ FOR ELECTRON BEAMS.

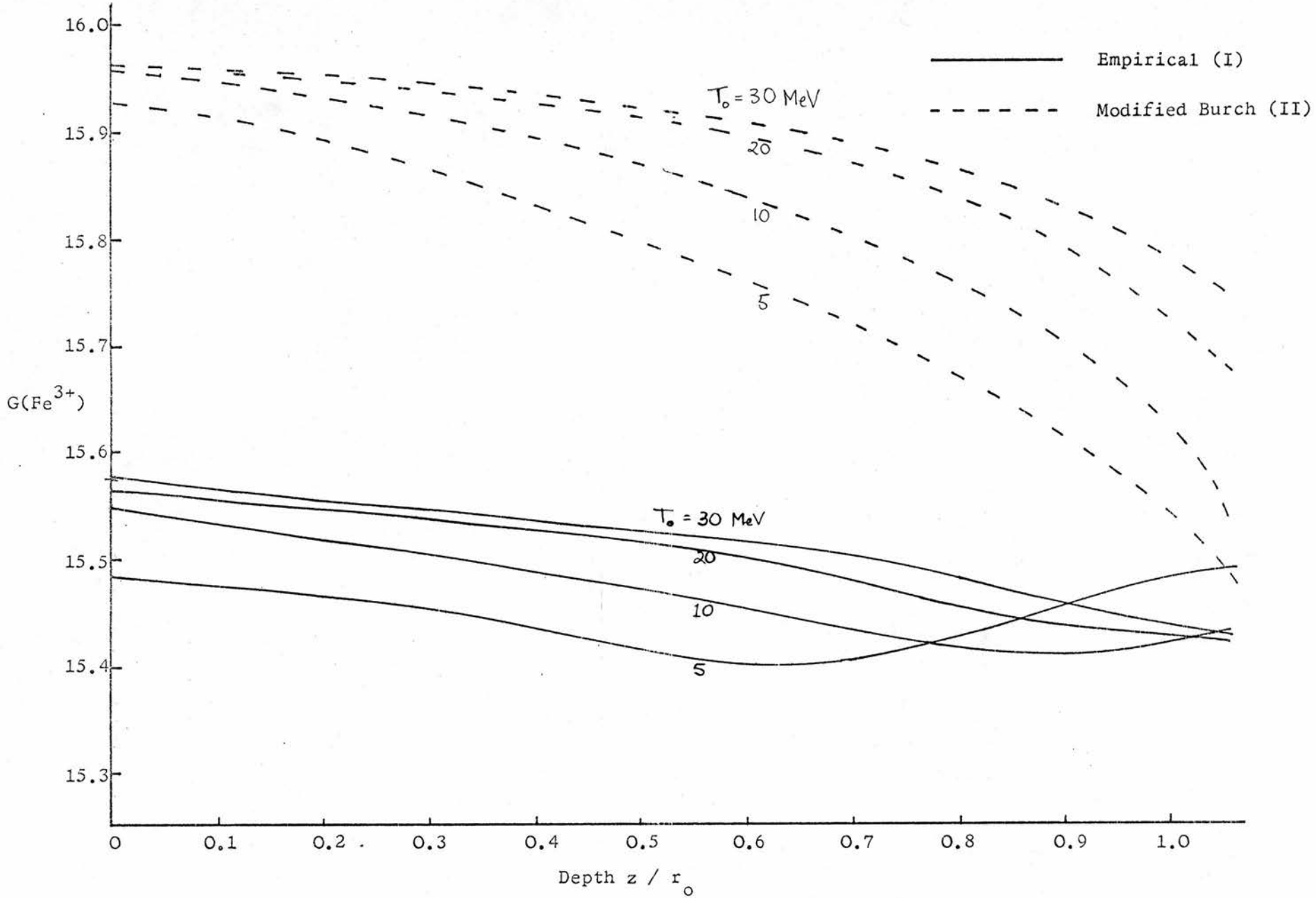

11.6.2 $G(Fe^{3+})$ for Electron Beams

All the electron beam $G(Fe^{3+})$ results are shown in figure 11.12. The considerable difference between the two G's was entirely to be expected from the differences between the curves in fig. 11.11 at the low-LET end. As had been 'guessed' from the start, the constant $G_{Fe^{3+}}$ value at low LET that was a feature of Burch's theory did result in appreciably higher $G(Fe^{3+})$ values for high-energy electrons than for ^{60}Co.* There is no doubt that of the two rather different sets of results plotted in figure 11.12, the ones derived from the empirical G(T) data (the solid lines) correspond more closely to experimental values (though it should be borne in mind that $G(Fe^{3+})$ for high-energy electron was 'fixed' for set I). This is easily seen by referring back to the calorimetric electron G-values shown in fig. 11.2b. In addition, the smaller depth-dependence in the lower set of results is more in line with experimental findings. Both sets of results predict an increase in $G(Fe^{3+})$ with increasing electron energy, T_o, with the increase becoming smaller as T_o increases. Even comparing the results for T_o = 5 MeV with those for T_o = 30 MeV, the difference is hardly ever more than 1% for either set except at large z/r_o for set I. Finally, it should be mentioned that the statistical fluctuations in the $G(Fe^{3+})$ results were certainly not larger than 0.01 for the 2000-history computations.

---

*In fact, the values calculated for $G(Fe^{3+})$ from the modified Burch relation (11) can more or less be correlated with the small changes in the numbers of very low energy electrons in the flux spectra for different radiations (see chapters 7 and 8).

Figure 11.13 THEORETICAL $G(Fe^{3+})$ FOR PHOTON BEAMS.
(calibration depths)

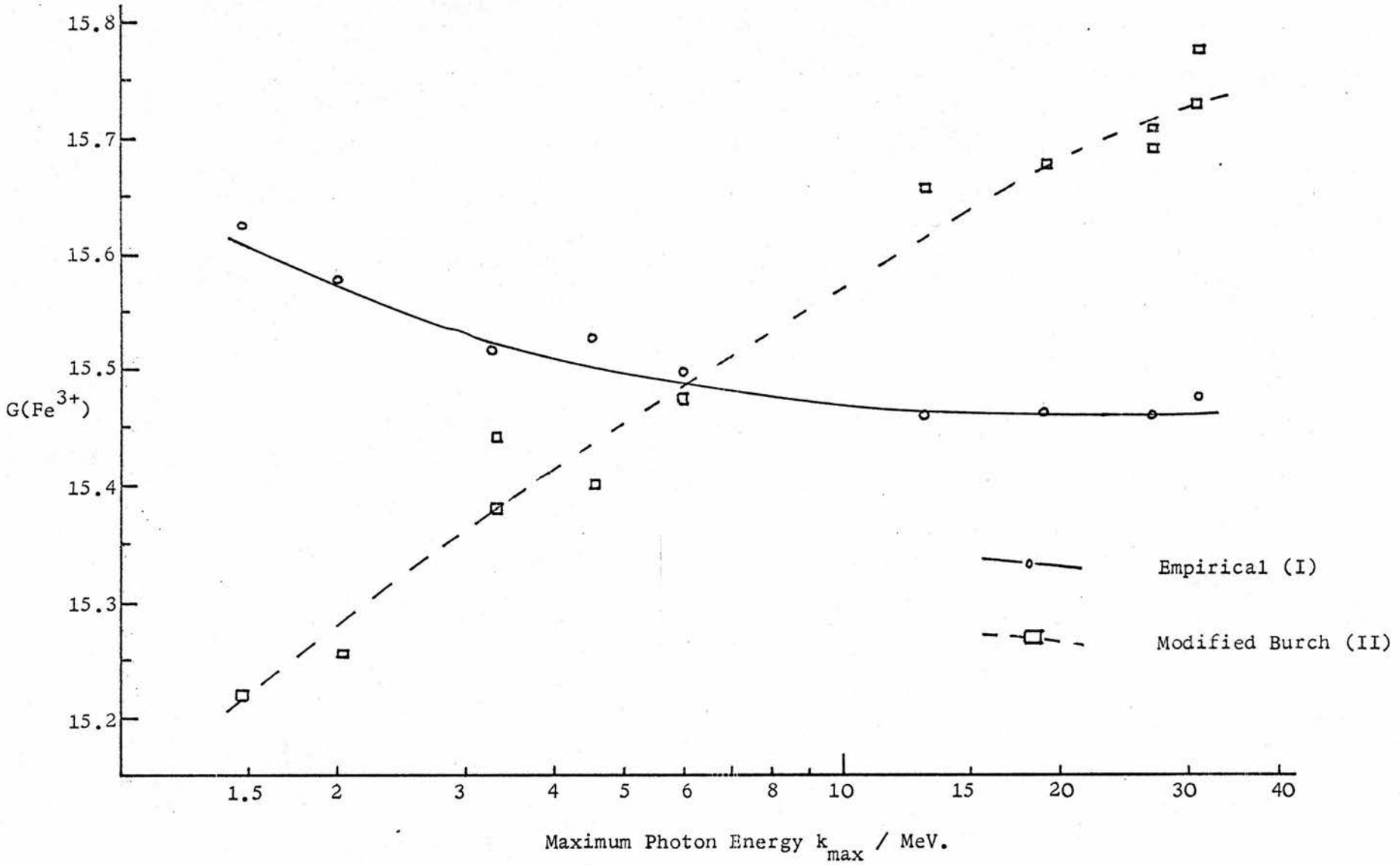

Figure 11.14 DEPTH-DEPENDENCE OF $G(Fe^{3+})$ FOR PHOTON BEAMS.

a. ^{60}Co radiation (B)

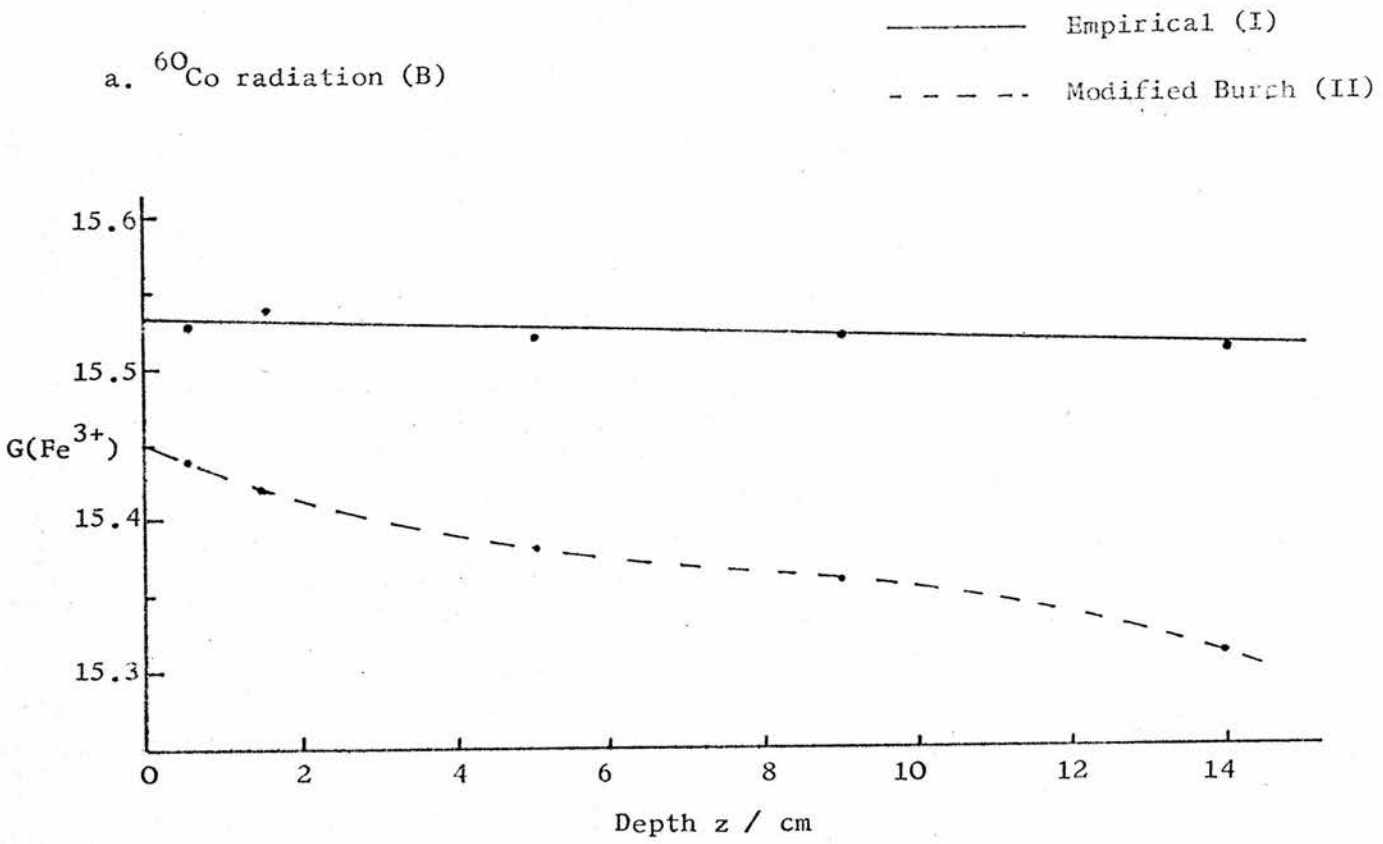

b. 31 MV X-rays (J)

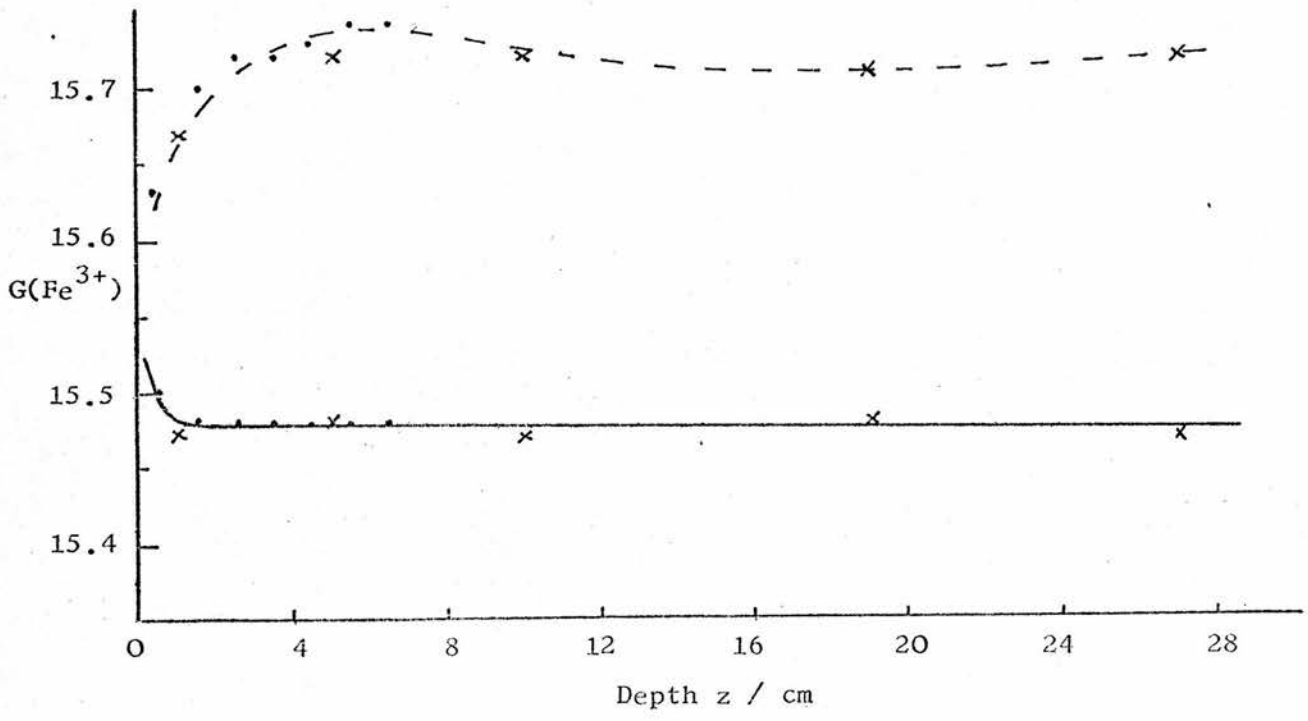

11.6.3 $G(Fe^{3+})$ for Photon Beams

The photon beam results are shown in figure 11.13. The values are plotted against the maximum photon energy, k_{max}, and correspond to the calibration depths. All the qualities listed in table 8.1 are included in the figure, with the addition of ^{137}Cs γ-radiation (from table 11.3; 0.66 MeV primary photons only, cf. spectrum C for ^{60}Co γ-rays). As for the electron beams discussed above, there is a marked difference between two sets of results. The $G(Fe^{3+})$ results based on the modified Burch $G_{Fe^{3+}}$ relation (II) show a gradual increase with increasing maximum photon energy. This is in line with the ICRU (1969) recommendations, based on very insubstantial experimental evidence (see fig. 11.2a). The results based on the empirical $G_{Fe^{3+}}$ relation (I), however, show $G(Fe^{3+})$ almost constant with increasing k_{max}, with the value for 31 MV x-rays slightly less than that for ^{60}Co radiation if anything.

The variation of $G(Fe^{3+})$ with depth for ^{60}Co and 31 MV radiation is illustrated in figure 11.14. These results do not call for much comment. For the 31 MV x-ray beam, both G's show a small variation in the build-up region, which is no more than 1% different from the virtually constant values at all other depths. The insignificant statistical variation of the results is indicated by the small difference in the plotted values calculated from two separate runs of the cascade program (cf. fig. 8.11 and 9.6). The modified Burch model predicts a small, but non-negligible decrease in $G(Fe^{3+})$ with increasing depth for the ^{60}Co γ-radiation. This is

Table 11.5 THEORETICAL $G(Fe^{3+})$ AT ICRU CALIBRATION DEPTHS

a. Electron Beams

$\bar{T}_o$ (MeV)	z (cm)	$\bar{T}_p$ (MeV)	$G(Fe^{3+})$	
			Empirical (I)	Mod. Burch (II)
5	1	3	15.43	15.83
10	2	6	15.49	15.89
20	3	14	15.53	15.93
30	3	24	15.55	15.95

b. Photon Beams

Radiation	$\bar{k}_{int}$ (MeV)	$\bar{T}_o$ (MeV)	$\bar{T}_p$ (MeV)	$G(Fe^{3+})$	
				Empirical (I)	Mod. Burch (II)
^{137}Cs (P)	0.66	0.26	0.13	15.63	15.22
2 MV	0.94	0.40	0.20	15.58	15.26
^{60}Co (P+S)	1.18	0.56	0.38	15.52	15.38
4.5 MV	1.63	0.82	0.41	15.53	15.40
6 MV	2.11	1.1	0.55	15.50	15.48
13 MV	5.91	3.6	1.8	15.46	15.66
19 MV	6.91	4.2	2.1	15.46	15.68
27 MV (linac)	8.27	5.1	2.6	15.46	15.69
27 MV (b'tron)	10.1	6.2	3.1	15.46	15.71
31 MV (Pb ff.)	11.8	7.1	3.6	15.47	15.73
31 MV (Al ff.)	14.5	8.6	4.3	15.47	15.78

Figure 11.15 THE 'VERDICT' OF THEORY ON THE 'G-VALUE DIFFERENCE'

a. Empirical (I)

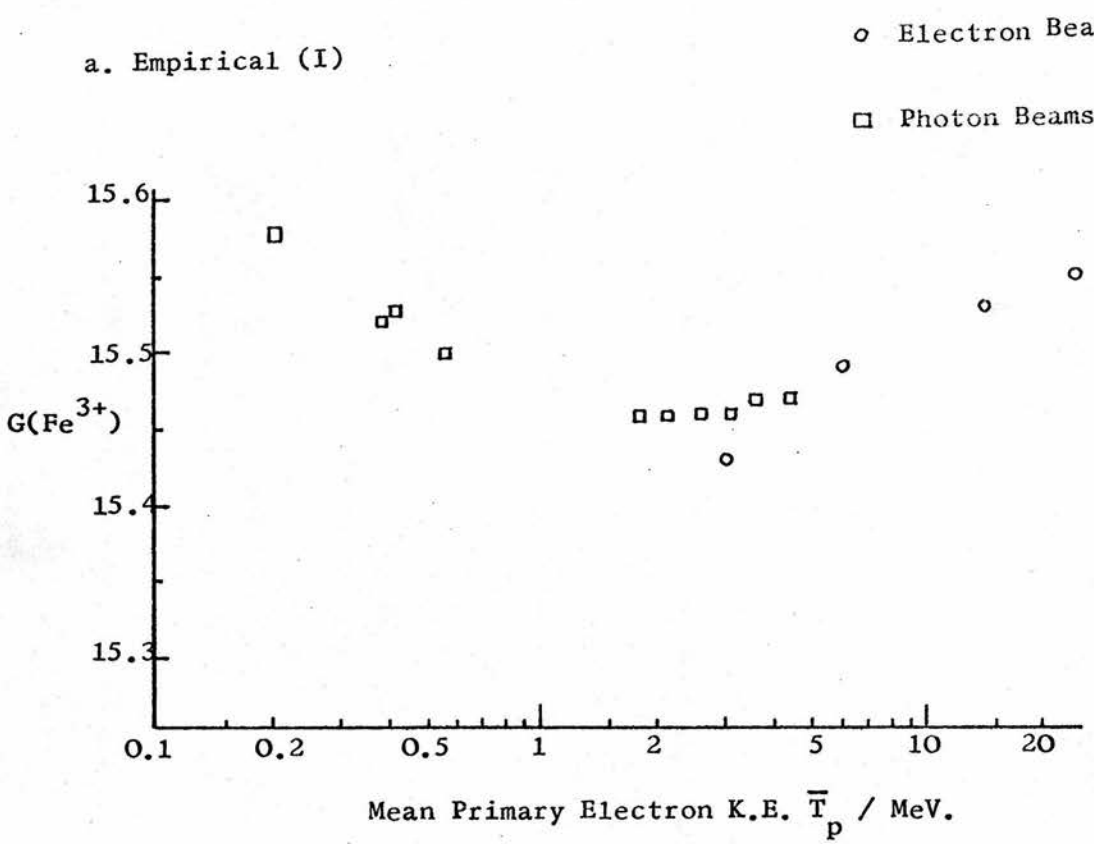

b. Modified Burch (II)

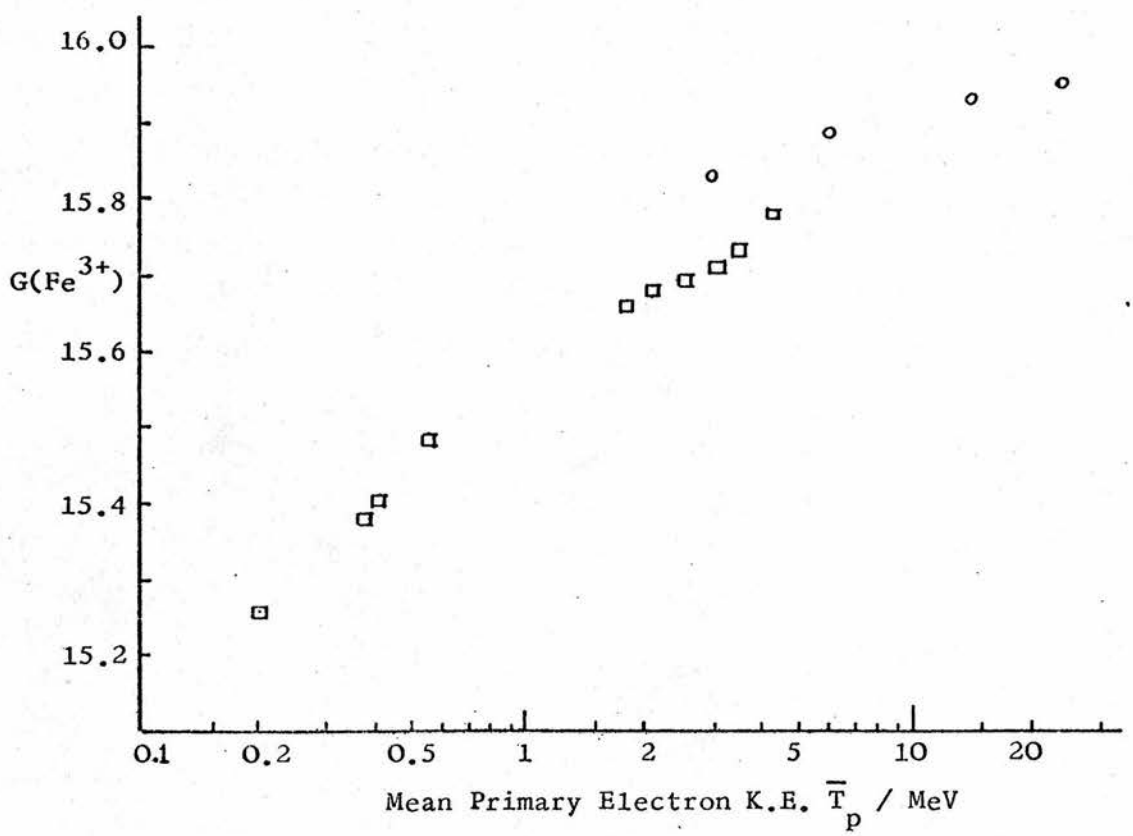

entirely absent on the empirical model. The writer is not aware of any experimental evidence for or against a small depth-dependence in $G(Fe^{3+})$ for ^{60}Co or similar quality photon radiation.

11.6.4 The 'G-Value Difference'

What do the above results have to say about the 'G-value difference'? This question is answered by the numerical values presented in table 11.5 and illustrated in figure 11.15. All the results given correspond to the recommended calibration depths (ICRU; 1969, 1972) for the electron and photon beams. For the electron beams, the mean primary energy, $\bar{T}_p$, has been calculated on the basis of an energy loss of 2 $MeV.cm^{-1}$ (the exact value of $\bar{T}_p$ is of no consequence anyway). A mean primary electron energy has been estimated for the photon beams also. The figures in column 3 of table 11.5b, designated by $\bar{T}_o$, are estimates of the mean initial energies of the electrons set in motion in water by the photons (cf. table 9.3). $\bar{T}_p$ has then been simply taken as half of $\bar{T}_o$.* As for the electron beams, the precise values are immaterial.

The photon and electron $G(Fe^{3+})$ results have been plotted together in figures 11.15a and 11.15b. Neither figure gives any hint of a 'G-value difference' such as is suggested by certain experimental measurements. The fact that the photon and electron values do not exactly coincide in the region of overlap is simply due to the questionable validity of the above procedure of assigning an effective electron energy to a photon beam.

---

*This will be about right for conditions of electronic equilibrium.

Nevertheless, the photon results shown in fig. 11.15b do appear to lie on a fairly smooth curve. This is in contrast to the findings for the stopping-power ratio results illustrated in figure 9.7, but was to be expected from the insensitivity of the G-value calculation to the shape of the high-energy end of the electron flux spectrum (see section 11.4.3).

As the two $G_{Fe}{}^{3+}$ vs local LET relations used to calculate the values of $G(Fe^{3+})$ from the local energy dissipation spectra had very different 'shapes' in the crucial* low-LET region, it must be concluded that the 'G-value difference' cannot possibly be accounted for on the basis of the present theoretical analysis. Furthermore, it has been shown that the analysis was particularly well-suited to the task of unearthing such a 'difference', if one existed. It must be emphasised, however, that too much confidence cannot be placed in the absolute values calculated for $G(Fe^{3+})$ from the empirically-derived relation (I) as firstly it was 'fixed' to give reasonable G-values for high-energy electrons and secondly, it is not based on any more fundamental theoretical approach. In particular, no reason is being put forward for why the curve should go through a maximum at low LET.

---

*'Crucial' because it is only in this region that there are appreciable differences between the electron flux spectra produced by photon and electron beams.

Table 11.6 RE-CALCULATION OF LAW AND NAYLOR $G(Fe^{3+})$ DETERMINATIONS

a. Law and Naylor (1971): Photon beams

Radiation	C_λ used → $G(Fe^{3+})$*		New C_λ → revised G	
8 MV linac	0.93	16.1 ± 0.2	0.953	15.7 ± 0.2
15 MV	0.915	15.9 ± 0.2	0.942	15.45 ± 0.2
33 MV - betatron	0.88	16.3 ± 0.2	0.920	15.6 ± 0.2

'New C_λ' estimated from Table 10.3/Fig. 10.3.

b. Law and Naylor (1972): Electron beams

T_o	T_p**	C_E used → $G(Fe^{3+})$*		New C_E → Revised G	
3	2.4	0.95***	15.3 ± 0.3	-	-
6	4.8	0.91	14.8 ± 0.2	0.878	15.35 ± 0.2
8	6.8	0.90	14.9 ± 0.2	0.876	15.3 ± 0.2
10	8.0	0.89	15.1 ± 0.3	0.858	15.55 ± 0.3
20	16.6	0.84	15.1 ± 0.2	0.834	15.2 ± 0.2
35	30.8	0.81	15.5 ± 0.2	0.800	15.65 ± 0.2

'New C_E' estimated from table 10.7/fig. 10.4 with 0.7% increase for 2 MV calibration and including p_E.

*Normalized to 15.5 at ^{60}Co.

**Assuming mean loss of 2 $MeV.cm^{-1}$.

***Baldwin-Farmer chamber not employed.

11.7 A RE-EXAMINATION OF THE EXPERIMENTAL EVIDENCE FOR THE 'G-VALUE DIFFERENCE'

11.7.1 The work of Law and Naylor (1971,1972)

It has been emphasised earlier in this chapter, and at other places in this work, that the bulk of the experimental evidence for the 'G-value difference' comes from determinations of $G(Fe^{3+})$ based on ionization measurements and in particular, the ionization measurements by Law and Naylor (1971, 1972). Having shown conclusively by detailed calculations that the 'difference' is not predicted theoretically*, it now seemed appropriate to re-calculate the Law and Naylor G-values using the C_E and C_λ that had also come out of the present theoretical work.

The first three columns in table 11.6a contain details of the Law and Naylor (1971) results for photon radiation with the C_λ values that they used for a Baldwin-Farmer chamber calibrated for 2 MV x-rays at the NPL. These C_λ were taken from the ICRU (1969) photon dosimetry report. The measurements were made at the ICRU calibration depths in Perspex phantoms. The use of Perspex instead of water makes no appreciable difference to the electron flux spectrum at the depth of the dosimeter and hence should have a negligible effect on the performance of either the Baldwin-Farmer chamber or the $FeSO_4$ dosimeter. The irradiation vessels were made of either Perspex or polyethylene, the latter also being

---

*In fact, the results in fig. 11.15 above suggest that the G-value for high-energy electrons should be slightly higher than for high-energy bremsstrahlung beams, whereas the 'difference' is the other way round.

reasonably close to water-equivalent. The authors pointed out that there was definite evidence that neither of these materials resulted in any chemical contamination. Law and Naylor normalized their results to 15.5 at ^{60}Co in order to minimize any errors due to the $FeSO_4$ technique or the NPL calibration factor.

Values of C_λ corresponding to the three x-ray beams have been estimated from figure 10.3* and are listed in column 4 of table 11.6a. These 'new C_λ' correspond to the assumptions made in chapter 10 about the air-equivalence of the B-F cavity walls at the calibration radiation. It can be seen that they are between two and four per cent higher than the ICRU values, as has been pointed out in that chapter. The final column gives the revised G-values obtained with these new C_λ factors. They have all been brought down by the change in C_λ and now the difference between the 15 MV and 33 MV values is well within experimental error. Note that the uncertainties given by Law and Naylor are estimates of standard error and include 1% for the uncertainty in the ratio between C_λ at ^{60}Co and at the energy concerned. These uncertainties have been included with the revised G-values.

Details of the Law and Naylor (1972) $G(Fe^{3+})$ results for electron beams are given in table 11.6b. The authors stated that the intention of the work with electrons was to make an analogous comparison with the photon results,

---

*The 33 MV Brown-Boveri betatron (St. Luke's, Guildford) has a lead flattening filter (C. Binks, private communication).

using as far as possible the same equipment and techniques as in the earlier paper. The measurements were carried out in Perspex and polystyrene phantoms at depths corresponding fairly closely to the HPA (1971) recommendations, and $G(Fe^{3+})$ was derived using the C_E values* given in that document. As in the photon work, the results were normalized to $G(Fe^{3+}) = 15.5$ at ^{60}Co.

The 'new C_E' values were estimated from the calculated results given in table 10.7 and figure 10.4. The p_E factor was included and account was taken of the fact that the C_E values given in chapter 10 correspond to ^{60}Co as the calibration radiation i.e. those values were increased by 0.7%. As computations were only performed for 5, 10, 20 and 30 MeV beams, the C_E given in table 11.6b for the 35, 8 and 6 MeV beams were interpolated on the basis of the values given for $\bar{T}_p$. The uncertainty in these C_E factors is thus slightly greater than for the 10 and 20 MeV beams, but is very much less than the statistical measurement uncertainties that Law and Naylor give. The C_E derived in this work are appreciably lower than the HPA values (see fig. 10.4) even allowing for the perturbation factor, p_E.** Thus the G-values are revised upwards and are now in reasonable agreement with experimental determinations based on calorimetry.

---

*except for $T_o = 3$ MeV.

**The HPA (1971) electron dosimetry guide states that their C_E values do include a small correction due to the perturbation caused by the B-F chamber, but does not give the magnitude of the correction at the different energies or any discussion of its origin.

Figure 11.16 RE-CALCULATED $G(Fe^{3+})$ RESULTS OF LAW AND NAYLOR FOR ELECTRON AND PHOTON BEAMS.

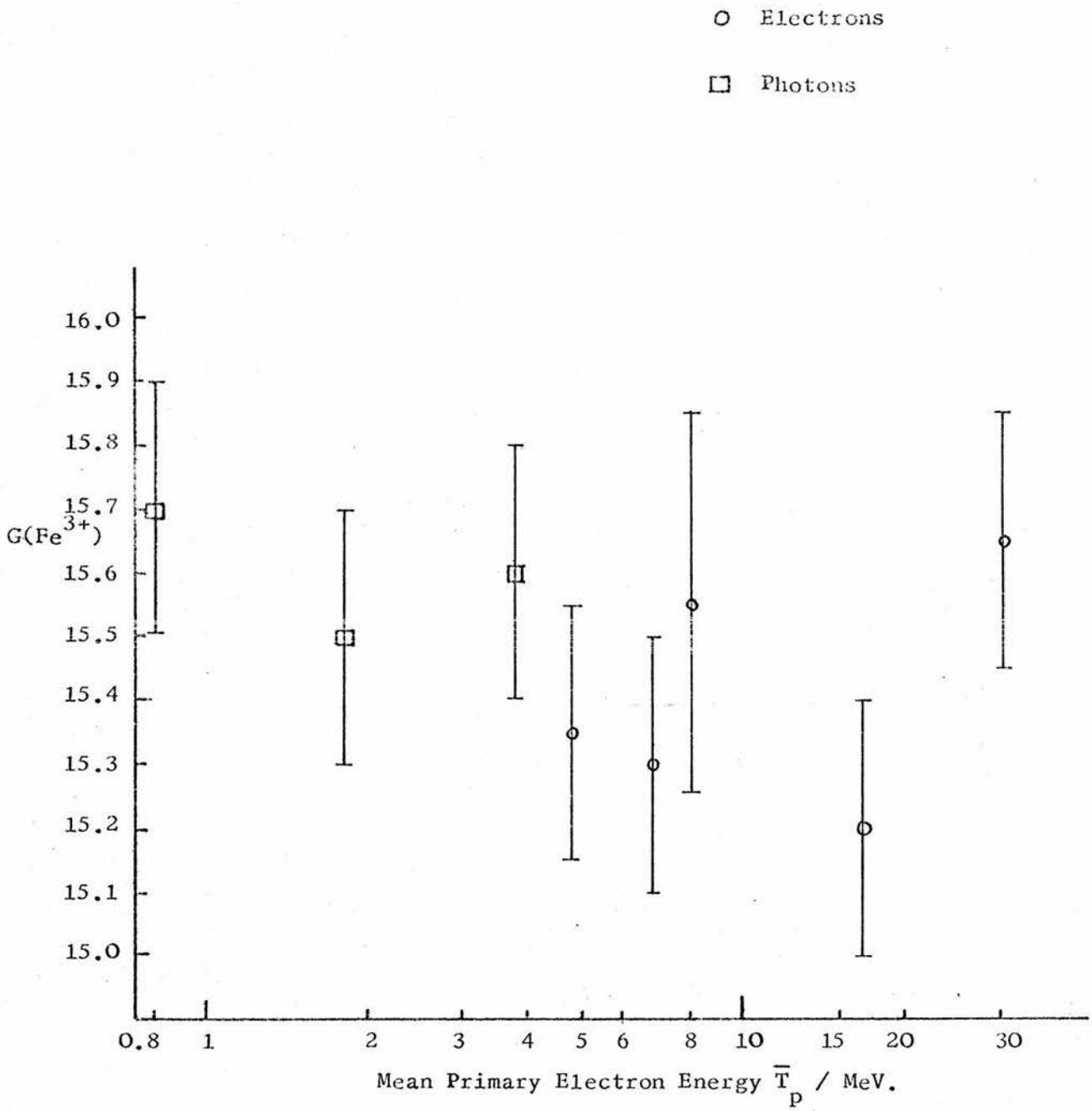

The 3-MeV result has not been re-calculated as a specially-constructed disc-shaped chamber was used for this measurement instead of the Baldwin-Farmer in order to minimize the perturbation effect. However, the 'C_E' estimated for this chamber by Law and Naylor seems almost certainly on the high side, implying that the result of 15.3 for G should actually be slightly higher, in line with the adjustments at the other electron energies.

Mean primary electron energies have been estimated for the 33 MV, 15 MV and 8 MV photon beams in the same way as in table 11.5. All the revised results of Law and Naylor given in tables 11.6, a and b, have been plotted in figure 11.16. This figure clearly demonstrates that any 'G-value difference' is now well within experimental error. It is important to note that this conclusion is not altered even if the Law and Naylor results are re-calculated using C_E and C_λ values both based on the assumption that the B-F chamber is a water-walled Bragg-Gray cavity at 2 MV x-rays (see chapter 10). In that case, C_E is drastically lowered at all energies (the 0.990 factor becomes 0.96 - section 10.4.1) although C_λ is not increased by as much as in table 11.6a. Then the photon and electron G-values both come out at around 16.0 which is not in line with the calorimetric evidence on $G(Fe^{3+})$ for electron beams, and is improbably high also for the photon beams even on the basis of the modified Burch theoretical results (II) presented in the previous section.

11.7.2 Other 'Parallel' Electron and Photon G(Fe^{3+}) Measurements

Similar investigations for both electron and photon beams using the $FeSO_4$ dosimeter and ionization chambers have also been carried out by Almond in the USA and by Svensson and colleagues in Sweden. The results of Hettinger, Petterson and Svensson (1967) for a 34 MV Brown-Boveri betatron x-ray beam have already been mentioned in section 10.3.3. There it was shown that their C_λ result of 0.916 for a B-F chamber calibrated at ^{60}Co and based on a G-value of 15.5 was in close agreement with the C_λ value of 0.913 from the present calculations for a 34 MV betatron beam with a lead flattening filter. Thus there is no need to revise their assumed G-value. Again, the agreement between the experimentally-determined C_E values of Svensson (1971) and the present calculations was consistent with a G-value of 15.6 (see section 10.4.3 and fig. 10.5). Thus there is no 'G-value difference' on the basis of the measurements by the Swedish group.

Almond (1968) reported measured C_λ of 0.910 for 18.5 MV x-rays and 0.894 for 22 MV x-rays. The 18.5 MV figure was based on a G-value of 15.8 recommended in a review by Shalek and Smith (1969). The 22 MV x-ray G-value was taken to be 15.9 on the basis of Almond's calorimetric measurement at this quality.* Using the C_λ factors derived in this work at 18.5 MV and 22 MV (taken from fig. 10.3), Almond's G-values come out as 15.4 and 15.3 respectively. Turning now to the measurements he carried

---

*These details have been confirmed by Almond - personal communication. The radiation was from a betatron.

out on electron beams (Almond, 1970) and performing a similar re-calculation procedure as for the Law and Naylor results, Almond's electron G-values end up around 15.6 - 15.8. So once again there is no suspicion that the photon G-value is at all higher than that for electron beams. In fact, it would appear as if Almond's results could be used to suggest that the opposite is the case.

.It should be remembered when intercomparing G-values based on C_E and C_λ determined by workers in different countries that there may be differences in the construction and dimensions of the exposure-calibrated ionization chambers used and also the exposure calibrations may not be completely equivalent.* Almond and Jahns (1971) made measurements of C_λ for a range of different ionization chambers, including the Victoreen Condenser chamber** commonly employed in the USA and also some Baldwin-Farmer chambers that had nylon instead of Turnol walls. In fact, their C_λ results were averages for all the chambers (i.e. the 22 MV and 18.5 MV values given above). The present calculations strictly apply to the 0.6 mm diameter Tufnol-walled Baldwin-Farmer chamber, though any differences in the theoretical values due to the use of nylon instead of Tufnol etc. might well turn out to be negligible, depending on how close to air-equivalent nylon is.

---

*In this respect, the ^{60}Co normalization by Law and Naylor (1971, 1972) was especially valuable.

**This chamber has a Bakelite wall and a diameter of 7.5 mm. Bakelite is close to Tufnol in composition.

Finally, the recent photon/electron intercomparison measurements by Svensson et al. (1974) can be mentioned. This work is of particular value as the $FeSO_4$ and ionization dosimetry systems were calibrated against a liquid ionization chamber. Svensson et al. assumed that the response of this dosimeter was independent of electron energy as the ratio between the collision mass stopping power for water to liquid was very nearly constant for electrons in the energy range 0.1 to 100 MeV. It was found that within experimental error there was no variation in the relative response of the $FeSO_4$ dosimeter and the liquid ionization chamber for 6 - 30 MeV electron radiation and for 27 - 34 MV x-rays. Thus Svensson et al. concluded that firstly $G(Fe^{3+})$ did not vary with electron energy in the range 6 - 30 MeV, and secondly that $G(Fe^{3+})$ was the same for both the electron and x-ray beams. Thus these measurements can be considered to be further experimental evidence for the non-existence of the 'G-value difference'. Furthermore, no assumptions about the response of an air ionization chamber were involved.

11.8 SUMMARY AND CONCLUSIONS

The importance of the ferrous sulphate dosimeter was emphasised but so was the inadequate knowledge of $G(Fe^{3+})$ for high-energy electron and photon beams, particularly the latter. The large variation in the results of determinations of $G(Fe^{3+})$ served to emphasise the importance of looking closely at the results of a single group of investigators as far as the 'G-value difference' was concerned. The evidence for this 'difference' from the ionization-based measurements by Law and Naylor was supported by the calorimetric work of Almond, though the latter included only one measurement for a high-energy photon beam.

As a prelude to the details of the theoretical investigation of the 'G-value difference', the reasons why the chemical yield should be a function of LET were discussed. The local-LET model employed by Burch (1959) was outlined and its shortcomings emphasised. In particular, it looked as though calculations of $G(Fe^{3+})$ based on Burch's theory could not be relied on for the low-LET radiations concerned in the 'G-value difference' and further, that such calculations were unlikely to predict such a difference. Consequently, some alternative approaches to the explanation of the 'difference' were discussed including the possible influence of the density effect. However, it had to be concluded that if the difference existed, then it would be revealed by a Burch-type approach utilizing the local energy dissipation spectrum with a cutoff of 100 eV.

Burch's use of improbably high values below 3 keV for the local LET, $(dT/dx)_{100}$, a G-value of 6.13 for ^{210}Po α-radiation when more recent values yield around 5.1, his $G(Fe^{3+})$ result for 220 kV x-rays that was almost certainly appreciably too low, as well as the very approximate nature of his derivation of the variation of $G_{Fe}{}^{3+}$ with local LET; all these factors suggested that a re-derivation of the $G_{Fe}{}^{3+}$ vs local LET relation based on an empirical rather than a fundamental approach was the way to proceed. Accordingly, the present 'best' experimental $G(Fe^{3+})$ values for several qualities ranging from ^{210}Po α-particles to 20 MeV electrons were taken as 'standard' and Q_T spectra computed for these 'standard' radiations. A $G_{Fe}{}^{3+}$ vs local LET relation was then arrived at by 'trial and error' which differed considerably from the modified Burch relation also derived; $G_{Fe}{}^{3+}$ had to go through a maximum at low LET in order that $G(Fe^{3+})$ should come out correctly at all the 'standard' qualities.

Values of $G(Fe^{3+})$ based on both the empirically-derived and the modified-Burch set of $G_{Fe}{}^{3+}$ values, tabulated as functions of electron energy in the photon-electron cascade programs, were calculated from the local energy dissipation spectra computed at various depths in water for the high-energy electron and photon beams. The results demonstrated conclusively that there was no '<u>G-value difference</u>' for either set of input data, though there were considerable differences in the two sets of $G(Fe^{3+})$ results. As had been expected from the start, though Burch's theory predicted that $G(Fe^{3+})$ was about

15.7 for a 25 MV x-ray beam (i.e. 0.2 higher than for ^{60}Co), it also resulted in a G-value of around 15.9 for high-energy electrons. The empirically-based results, on the other hand, predict that $G(Fe^{3+})$ remains virtually constant with increasingly photon energy at around 15.45 and is marginally lower than the value for high-energy electrons.

Finally, the experimental evidence for the 'G-value difference' was re-examined. The results of Law and Naylor (1971) for photon beams and Law and Naylor (1972) for electron beams were re-calculated using the C_λ and C_E values derived in chapter 10 whereas Law and Naylor had used the ICRU (1969) C_λ and the HPA (1971) C_E. The photon G-values were consequently revised downwards by 2-4% and the electron values revised upwards by 1-3%. The result was that the 'G-value difference' now came well within experimental error. It was similarly shown that the ionization-based G-values for photon and electron beams determined by Svensson and colleagues in Sweden and by Almond in the USA are also consistent with the no 'G-value difference' conclusion when the present C_λ and C_E factors are employed.

The overall conclusion to be drawn from these findings is that the 'G-value difference' had all along been the result of the use of incorrect C_E and C_λ factors and that when these quantities are derived in a consistent manner as in the present work, i.e. employing the same assumptions for both photon and electron beams, then the 'difference' disappears. Thus from being what seemed to be the only 'hard' experimental evidence for

the 'G-value difference', Almond's 22 MV x-ray calorimetric measurement is now the only evidence at all for the phenomenom. Both the theoretical and re-calculated experimental evidence given in this chapter make the case against the 'difference' overwhelming.

CHAPTER 12

COMMENTS AND CONCLUSIONS

12.1 THE RESULTS

The most important results to come out of this investigation can be summarized as follows:

1) The present computation of the depth-independent electron flux spectrum (i.e. below T_c), including all generations of δ-rays, based on Burch's approach (Burch, 1957a) but employing only the c-s-d-a and much finer energy intervals has been shown to give very similar numerical values as would have been obtained from the more sophisticated and mathematically more involved Spencer-Fano theory.

2) The Monte Carlo electron-photon program developed in this work produced depth-dependent electron flux spectra in water irradiated by high-energy electron beams which were in excellent agreement with the Monte Carlo calculations by Berger and Seltzer (1969, 1969a) down to the lowest energies (i.e. 200 eV in the latter work). The conclusions that Berger and Seltzer drew concerning the negligible variation of the flux spectra below about 50 keV with initial electron energy (at least at 5 MeV and above) and depth have been confirmed by the results presented here. The present, less rigorous treatment of electron multiple scattering and energy-loss straggling, compared with the Berger and Seltzer electron transport model, appears to have had very little effect on the electron flux spectra results.

3) For photon beams in the ^{60}Co/2 MV quality region there is a very gradual shift of the electron flux spectra towards lower electron energies with increasing depth in water.

4) For high-energy bremsstrahlung beams for (e.g. 31 MV x-rays) for which there is an appreciable build-up region in water, the electron flux spectrum is appreciably 'softer' at the surface than at a depth where electronic equilibrium has been approximately established. For such equilibrium depths there is a negligible change of the flux spectrum with depth at all electron energies, in line with what has generally been assumed.

5) A comparison of the electron flux spectra from a 31 MV x-ray beam (at a depth beyond the build-up region) and a 10 MeV electron beam (at a depth such that the mean primary electron energies produced by the two beams were similar) revealed considerable differences except below about 10 keV, where the two spectra became very close together.

6) The inclusion of the production of Auger electrons, due to interactions with the electrons from the oxygen K-shell, did not result in any appreciable increase in the number of electrons with energies below the 'discontinuity' just above 500 eV. This was equally the case for both the electron and the photon beams.

7) A detailed comparison of the present results with the Berger et al. (1975) computations of the water/air stopping-power ratios for electron beams showed that there

were considerable discrepancies, despite the apparent similarity and degree of rigour of the calculational methods. These differences are due to the fact that Berger et al.,in evaluating the Spencer-Attix theory, had neglected to include the dissipation by the electron track ends whereas considerable care had been taken to take this into account in the present evaluation. The stopping-power ratios derived by Kessaris (1970a) are between 2 and 3% lower than the present results (for a cutoff of 10 keV). The approximate evaluation of the Bragg-Gray stopping-power ratios from the simple Harder formula only gives good agreement (within 1%) with more exact calculations at low electron energies (below about 5 MeV) or at depths close to the surface.

8) The photon beam stopping-power ratio results are complicated by differences in the initial photon spectra from one x-ray machine to another. Nevertheless, several points clearly emerged. For photon beams in the ^{60}Co/2 MV quality region, Bragg-Gray stopping-power ratios derived by assigning a single effective electron energy to the photon beam are within about 0.5% of the present, more accurate, calculations. This does <u>not</u> apply to higher energy x-ray beams (above 15 MV or so) where the approximate values are always too low. For the 31 MV betatron x-ray beam, the difference is nearly 2%. All the stopping-power ratio results (i.e. Bragg-Gray and the three cuttoffs: 0.001, 0.01, 0.1 MeV) for the 27 MV linac beam (i.e. thick target) were very close to the corresponding values for the 19 MV betatron beam

(i.e. thin target), but nearly 1% higher than for the 27 MV betatron beam. There is negligible depth-dependence of the stopping-power ratios beyond the build-up region for all the photon beams, with the exception of ^{60}Co/2 MV qualities for the 0.1 MeV cutoff. The gradual decrease in the stopping power ratio with increasing depth in the latter case is a consequence of the effect of photon interactions in the air cavity which is taken into account in the present, modified evaluation of the Spencer-Attix theory.

9) The use of more realistic assumptions concerning the Baldwin-Farmer ionization chamber than were made by Greene and Massey in deriving the C_λ values given in ICRU (1969) has resulted in appreciably different results for C_λ. The present results are as much as 3-5% higher than the ICRU figures; the difference increases with increasing photon energy, and is greater for linacs than for betatrons. The assumptions implicitly involved in the ICRU (1972) C_E values were less unrealistic, but are inconsistent with the ICRU C_λ calculations. The C_E derived in this work are 1-2% lower than those given by HPA (1971) but are well within 1% of the ICRU values except at large depths. However, this close agreement is partly due to the cancelling out of errors in the derivation of the ICRU C_E by Kessaris (1970a).

10) As a result of detailed calculations of $G(Fe^{3+})$ for the electron and photon beams, based on two alternative $G_{Fe^{3+}}$ vs local LET relations, it was shown that it was

not possible to account for the 'G-value difference' on theoretical grounds. However, when the ionization-based $G(Fe^{3+})$ determinations by Law and Naylor (1971, 1972) are re-calculated using the C_E and C_λ values derived in this work, the 'difference' comes well within experimental error. Furthermore, the re-calculated results of Almond in the USA and Svensson and colleagues in Sweden no longer suggest any 'difference' either. Consequently, it is concluded that the 'G-value difference' has simply been the result of incorrect C_λ and C_E values (mainly the former). When C_E and C_λ are derived in a consistent manner as in this work, but unlike in the ICRU photon and electron dosimetry reports, then no 'difference' is observed.

12.2 SOME GENERAL COMMENTS

Though it is fair to say that the results concerning chemical and ionization dosimetry are the most important outcome of this work, it must be emphasised that the bulk of the time and effort went into the development of the computer programs to calculate the depth-dependent electron flux spectra. It must be asked whether the same results could have been derived from a much less involved computation.

As far as the $G(Fe^{3+})$ theory is concerned, the answer must be yes, though this was by no means obvious when the investigation began. Clearly a depth-independent calculation of the electron flux spectrum (and thus the local energy dissipation spectrum) for a photon beam would not have given very different results for $G(Fe^{3+})$ in view of the negligible change of $G(Fe^{3+})$ with depth

that was obtained. A simpler electron transport model, based entirely on the c-s-d-a, would have been adequate to have calculated $G(Fe^{3+})$ for electron beams at different depths, where again a small depth dependence was found, and the same conclusions about the 'G-value difference' would have been arrived at. However, the stopping-power ratios calculated from such a simplified calculation would only have been of limited value. The increase of the stopping-power ratio close to the surface for a high-energy photon beams could not have been demonstrated, nor could any confidence have been attached to the depth-dependence of C_E for electron beams.

As well as being able to handle calculations where depth-dependence is important, the Monte Carlo method is especially powerful in dealing with boundaries between different media. An example of a problem involving such a boundary is the calculation of the energy dissipation in the air cavity of an ionization chamber. Spencer and Attix (1955) extended the simple Bragg-Gray theory to tackle the problem of the dependence of the stopping-power ratio on cavity size. Since that development, cavity theory has been further extended by Harder (1968) who calculated perturbation factors for irradiation by electron beams to take into account scattering effects caused by the difference in density between the cavity gas and the walls. In the general theory of Burlin (1966) and in the present work, the effect of photon inter-interactions in the cavity has been explicitly considered, and Burlin also looked at the modification of the

electron spectrum in the cavity due to the difference in atomic number between wall and cavity material. However, while all these developments are undoubtedly great improvments over the elementary assumptions involved in the Bragg-Gray theory, the 'tacking on' of one correction factor after another to the basic stopping-power ratio seems inherently unsatisfactory. As both a rigorous test of the above theories and as a possible improvement on them, it would seem a good idea to actually calculate the energy dissipation in a cavity (i.e. as opposed to the electron flux spectrum) using a comprehensive Monte Carlo program that would automatically take into account the effect of the shape of the cavity and differences in density and atomic composition of all the materials involved in a particular ionization chamber. The validity of such an approach would only be limited by the accuracy of the basic physical data (i.e. I-values etc.) but that is the case for any cavity theory.

From the remarks made in the above paragraph it will be evident that the present derivation of stopping-power ratios appropriate to the Baldwin-Farmer chamber is not considered to be definitive, especially for photon radiation in the ^{60}Co/2 MV quality region for which photon interactions with the Tufnol wall adjacent to the air cavity are very important. Aside from the necessarily approximate manner in which the stopping-power ratios have been evaluated for such relatively low-energy photon beams, there is also the difficult question of just how close to air-equivalent Tufnol actually is. Furthermore,

the present approach had indicated that considerable care should be taken in choosing and specifying the materials used in the construction of exposure-calibrated secondary standard ionization chambers as the theory predicts appreciable differences in C_E and C_λ if the inner wall is water-equivalent rather than air-equivalent. Some experimental work with wall materials of varying thickness and composition would seem desirable in order to clarify the picture.

The original purpose of this investigation was to see if the 'G-value difference' could be accounted for theoretically. The approach was thus naturally orientated towards performing equivalent calculations for photon and electron beams in order to look for any possible differences in these radiations that might have a bearing on dosimetric measurements. Such an orientation inevitably led to a careful examination of the derivation of C_E and C_λ. The unearthing of inconsistencies in the expressions for these factors given in the recent ICRU reports on photon and electron dosimetry (ICRU; 1969, 1972) is, in fact, considered to be the most important 'discovery' in this work; the consistent derivation of C_E and C_λ presented here puts relative dosimetry between electron and photon radiation on a much firmer basis than has hitherto been the case. The not unexpected result that theory could definitely not accommodate the 'G-value difference' together with the almost total disappearance of the experimental evidence for the 'difference' upon the removal of the C_E/C_λ inconsistency has brought the whole investigation to a satisfying and self-consistent conclusion.

APPENDIX 1

ALGORITHM FOR THE GENERATION OF PSEUDO-RANDOM NUMBERS

The random numbers used in the Monte Carlo computations were generated from the following algorithm:

$$X_o = I$$

$$X_{n+1} = 65539\ X_n \bmod 2^{31}\ ^*$$

$$R_n = 2^{-31}\ X_{n+1}$$

where R_n is the required random number between 0 and 1.

This is an example of the power residue method, specially adapted for use on the IBM 360 computer; the algorithm was taken from the E.R.C.C.** documentation on IMP routines. The sequence is started by choosing a number, I, which can be any odd integer greater than 50,001. 2^{29} numbers are produced before the sequence repeats. The power residue method has been thoroughly investigated and has been shown to be an entirely satisfactory way of obtaining random numbers (IBM manual C20-8011, 1959).

---

*This is a shorthand way of writing 'the remainder when $65539\ X_n$ is divided by 2^{31}'. This step is actually evaluated by causing the IBM 370/155 or ICL 4/75 (in Edinburgh) to overflow.

**E.R.C.C. - Edinburgh Regional Computing Centre.

Figure A2.1 FLOW DIAGRAM FOR SELECTION OF PHOTON WAVELENGTH CHANGE IN COMPTON SCATTERING

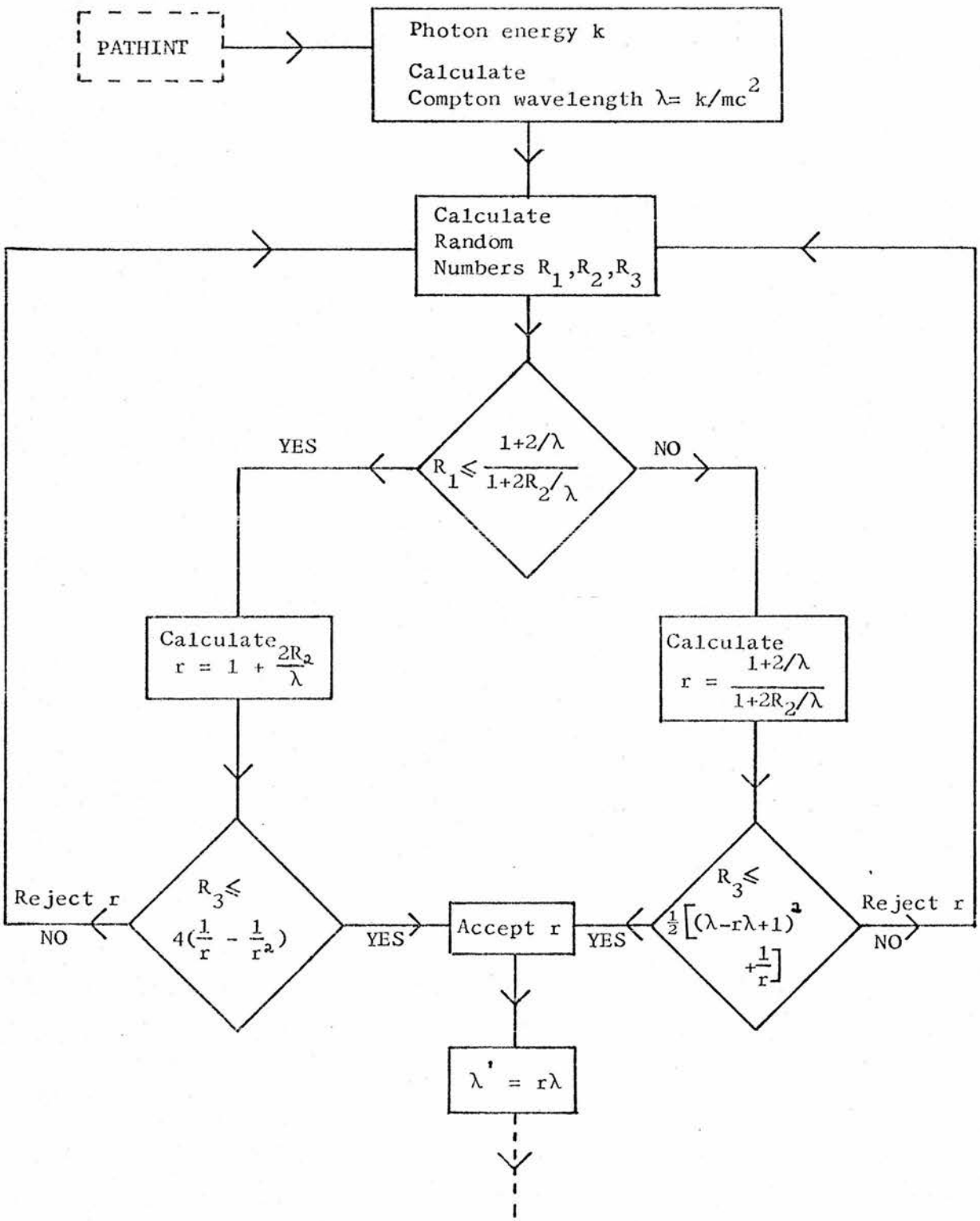

APPENDIX 2

THE SAMPLING OF PHOTON WAVELENGTH CHANGES FROM THE KLEIN-NISHINA DISTRIBUTION

This selection procedure is due to Kahn (1954) and the flow diagram used to program it, given in figure A2.1, is taken from Fano et al. (1959). It is actually a combination of the Rejection Technique and C.P.D. method. Fano et al. state that the average number of random number triplets required to select a random variate λ (the Compton wavelength) is equal to 3.0 for $\lambda = 0.05$ ($k \sim 10$ MeV), decreases to a minimum of 1.6 for $\lambda = 0.5$, and rises to a limiting value of 1.7 as $\lambda \to \infty$ ($k \to 0$). These figures for the efficiency of selection were borne out by tests carried out on the procedure to verify that the λ' was distributed according to the Klein-Nishina formula.

APPENDIX 3

DERIVATION OF THE C.P.D. EXPRESSION TO SAMPLE FROM A RESTRICTED EXPONENTIAL DISTRIBUTION

It is desired to select a random variable Ψ from an exponential distribution with mean angle Ψ_m, where Ψ is restricted to the range 0 to π. This easily accomplished as follows:

The cumulative probability distribution (C.P.D.) for angle Ψ, $Q(\Psi)$, is given by

$$Q(\Psi) = \frac{\int_0^{\Psi} \exp(-\Psi/\Psi_m)\, d\Psi}{\int_0^{\pi} \exp(-\Psi/\Psi_m)\, d\Psi} \qquad \ldots\ldots(A3.1)$$

On integrating

$$Q(\Psi) = \frac{\exp(-\Psi/\Psi_m) - 1}{\exp(-\pi/\Psi_m) - 1} \qquad \ldots\ldots(A3.2)$$

Putting $Q(\Psi)$ equal to random number R and solving for Ψ'

$$\Psi' = -\Psi_m \log_e 1 + R(\exp(-\pi/\Psi_m) - 1) \qquad \ldots\ldots(A3.3)$$

where Ψ' is the required random variable (cf. section 2.2.3).

Figure A4.1 FLOW DIAGRAM FOR PATAU REJECTION TECHNIQUE APPLIED TO THE MØLLER DISTRIBUTION.

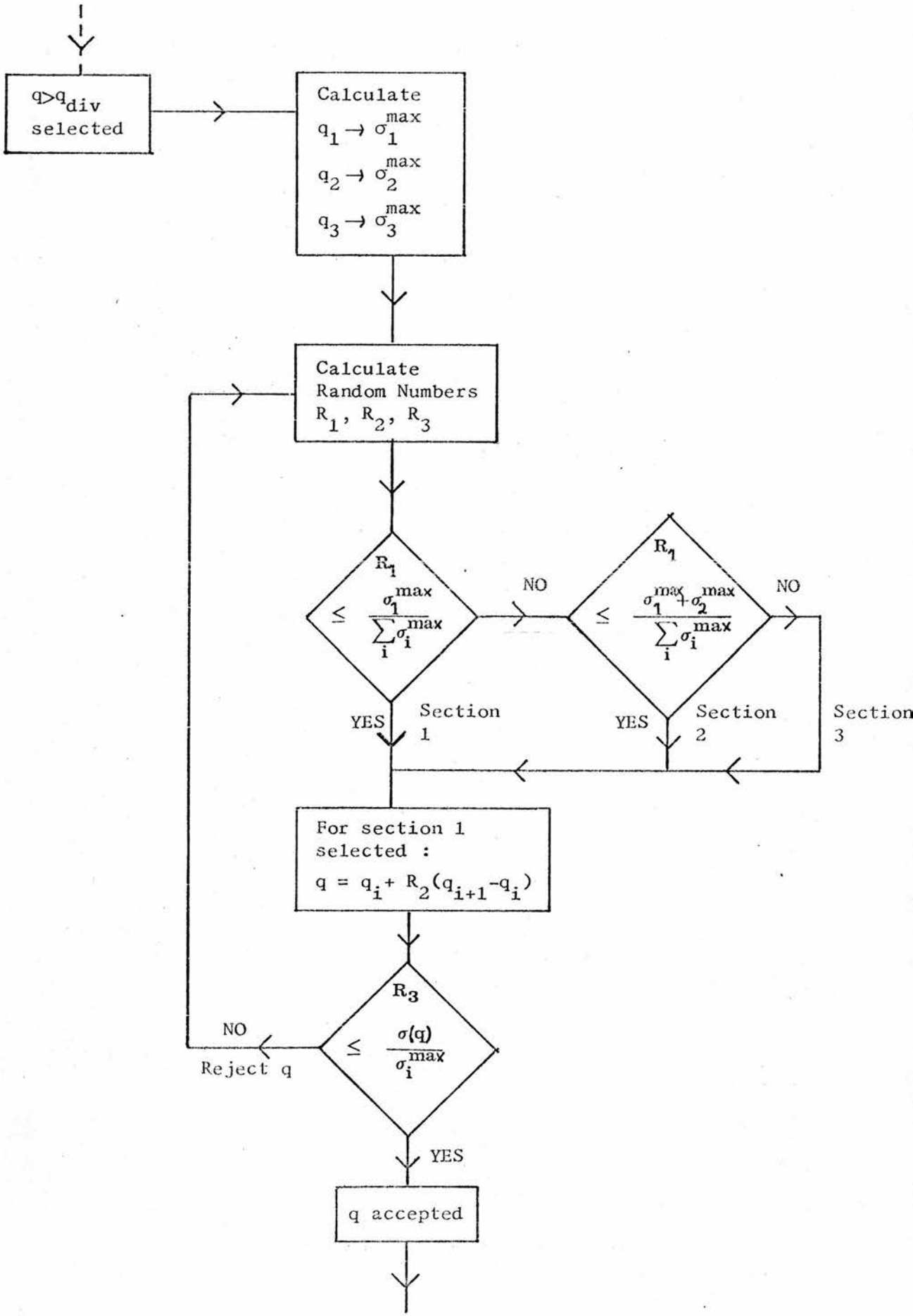

APPENDIX 4

THE USE OF PATAU'S IMPROVED-EFFICIENCY REJECTION TECHNIQUE TO SELECT THE ENERGY LOSS FROM THE MØLLER DISTRIBUTION

It was shown in section 4.4.1.2 that the exact Møller distribution had to be employed for energy transfers q such that $q_{div} < q \leq T/2$, and further that the selection of q by a straightforward rejection procedure (see fig. 4.1) would have been extremely inefficient. A modified rejection technique devised by Patau (1970, 1972) to deal with similar problems in his Monte Carlo work was found to be suitable here. The method results in a greatly improved efficiency of selection.

Briefly, the range of values the random variable can take is divided into a number of equal intervals (these cannot be equal log intervals, thus restricting the applicability of the method). The maximum of the probability distribution in each section is calculated.* Random number R_1 is then used to select the section from the relative sizes of these maxima. Random number R_2 selects a value of the random variable in that section. Random number R_3 determines whether or not that variable is accepted. If it is rejected, then the procedure starts all over again with new R_1, R_2 and R_3.

After some preliminary calculations, it was decided to divide the range of q values into 3 sections for any T. This kept the amount of computation down to a reasonable amount and yielded an acceptable efficiency (see table 4.2). The flow diagram for the procedure is given in figure A4.1.

---

*This is easy as the Møller distribution continually decreases with increasing q. Thus the maximum is at the lowest q in a section - the q_i in fig. A4.1.

APPENDIX 5

TO SHOW THAT THE DISTRIBUTION OF THE DISTANCE BETWEEN CATASTROPHIC EVENTS IS NOT ALTERED BY THE INTRODUCTION OF A MAXIMUM STEP SIZE

For a mean free path $\bar{s}$ between catastrophic events, the probability of an event within a distance s, P(s), is given by

$$P(s) = 1 - \exp(-s/\bar{s}) \qquad .....(A5.1)$$

Let the maximum allowed step size be s_{max}. The probability of $s > s_{max}$ is $\exp(-s_{max}/\bar{s})$. However, should s be chosen such that $s > s_{max}$, then another selection of s is made. The variable now becomes $s - s_{max}$ and the total probability of an event within the distance $s - s_{max}$, $P(s-s_{max})$, is given by

$$P(s-s_{max}) = \exp(-s_{max}/\bar{s}) \quad 1 - \exp(-(s-s_{max})/\bar{s})$$
$$= \exp(-s_{max}/\bar{s}) - \exp(-s/\bar{s}) \qquad .....(A5.2)$$

The total probability of an event within a distance s must be the sum of the separate probabilities for $s < s_{max}$ and for $s > s_{max}$ i.e. the sum of $P(s_{max})$ from equ. (A5.1), and $P(s-s_{max})$ from equ. (A5.2):

$$P(s_{max}) + P(s-s_{max}) = 1-\exp(-s_{max}/\bar{s}) + \exp(-s_{max}/\bar{s})-\exp(-s/\bar{s})$$
$$= 1 - \exp(-s/\bar{s})$$

which is the same as equ. (A5.1) for P(s). Q.E.D.

APPENDIX 6

A BREAKDOWN OF THE FINAL VERSION OF THE PHOTON-ELECTRON CASCADE PROGRAM - CASCF06

Line Nos.*	Description	Reference in Thesis
1	Code starts - %BEGIN (in IMP)	
2-100	Declaration of variables, arrays	
101-120	Description of function of program for operators benefit	
121-163	Permanent data read in (stream 1)	3.4.3;4.5.3 6.4.1;11.6.1
164-251	Variable data read in	6.4.1;fig.6.3
252-327	Calculation of various parameters e.g. r_1, $\Delta(T_c)$, $(dT/dx)_{100}$	
328	CPUTIME recorded - before MC histories begin	
334**	Cycle JJ=1,1,NEPH - Outer cycle for NEPH different photon energies, k_j	6.4.1;8.3.1
336	Cycle J=1,1,HISTNO(JJ) - Inner cycle for HISTNO(JJ) histores, H_j	ditto
338-452	Logical sequence for the simulation of photon and electron histories Calls on routines PHOSIM;CSDALOS; BREMLOS;NOKLOS	4.5;6.3.1; figs.4.12,6.2
453	CPUTIME recorded - after execution of all MC histories	6.4.3;7.1.3; table 8.1
454-495	Print-out of results starts with basic parameters e.g. no. of steps	3.4.6;4.5.3
496-511	Depth-Dose histogram printed out	4.6.3;7.4; fig.8.12
512-537	Routines MCSPECAL, LOWENCAL, SPECOUT executed for each spectrum geometry in turn	5.5.2;fig.5.6; 6.5
538	CPUTIME recorded - final instruction to be executed	

---

*Note that there are often two or more 'statements' of code per line.

**Naturally, there is no parallel statement to this in CASCEL6.

539-605	Routine CSDALOS - c-s-d-a electron pathlength steps; calls on NEWDIR, SPECTOT	4.4.4
606-717	Routine NOKLOS - catastrophic electron collision losses; calls on NEWDIR; δ-ray coords stored*	4.4.1
718-814	Routine BREMLOS - catastrophic electron radiation losses; calls on NEWDIR; photon coords stored	4.4.2
815-848	Routine NEWDIR - calculates new θ, ϕ due to deflection Ψ, Φ	2.3
849-867	Routine PHOSIM - logical sequence for photon simulation; calls on PATHINT, COMPTON, PAIR, PHOTO, RAYLEIGH	3.4.1;6.3.1; fig.3.7
868-915	Routine PATHINT - distance to, and type of next photon interaction selected	3.3.1;3.3.2; fig.3.1
916-1010	Routine COMPTON - selects energy loss, calculates deflection due to Compton scattering; calls on NEWDIR; stores Compton electron coords.*	3.3.3
1011-1194	Routine PAIR - selects energy and direction of pair positron and electron; calls on NEWDIR; stores positron and electron coords.*	3.3.4
1195-1261	Routine PHOTO - calculates energy of photoelectron, stores coords.*	3.3.5
1262-1292	Routine RAYLEIGH - selects photon deflection; call on NEWDIR	3.3.6
1299-1427	Routine SPECTOT - adds up electron pathlength contributions in the flux in different energy intervals for each spectrum geometry; calls on DELSORT	4.6.4;5.5.2
1428-1484	Routine MCSPECAL - calculates flux spectrum per unit energy, local energy dissipation spectrum, part of stopping-power ratio and $G(Fe^{3+})$ computation down to $T = T_c$; calls on COLLOSS, COLLAIR.	5.5.2;6.4.4; 9.2.3;11.6.1

---

*More explicitly:- for T_δ (or T_+, T_- etc.) $> T_c$ – energy, position, direction stored as input to MC simulation. For $T_\delta \leq T_c$ – only energy and position required for depth-independent spectrum computation below T_c.

1485-1651	Routine LOWENCAL - electron flux computation between T_c and 100 eV; including local energy dissipation spectrum etc. (cf. MCSPECAL)	Chapter 5; 9.2.3;11.6.1
1652-1778	Routine SPECOUT - flux spectrum normalized to 1 MeV total diss.; stopping-power ratios, $G(Fe^{3+})$ calculated; all results for each spectrum geometry printed out.	6.5;9.2.3; 11.6.1
1779-1791	Routine DENSEFF - calculates density effect reduction for electron stopping power in water	4.2.1;4.4.4
1792-1798	Routine COLLOSS - calculates mass collision stopping power for electrons in water for any cutoff; i.e. evaluation of equ. 4.18	4.4.4.1
1799-1809	Routine COLLAIR - as for COLLOSS but for air i.e. zero density effect reduction	
1813-1848	Routine DELSORT - adds up the 'continuous' losses from the electron c-s-d-a steps in terms of ΣK (section 5.5.1.1).	5.5.1;5.5.2
1850	%ENDOFPROGRAM	

N.B. There have been one or two minor alterations to the program wrt. stopping-power ratio calculations so the line nos. no longer exactly correspond to the above.

Table A7.1 ELECTRON FLUX SPECTRUM: T_o = 5 MEV

Electron Kinetic Energy	Total Electron Flux, normalized to 1 MeV total dissipation $F(T,z)/cm^{-1}.MeV^{-1}$					
	z/r_o					
T/MeV	0.0-0.1	0.2-0.3	0.4-0.5	0.6-0.7	0.8-0.9	1.0-1.1
5.00 - 4.48	0.976	0.000				
4.01 - 3.59	0.0131	0.622	0.000			
3.21 - 2.88	0.0045	0.0787	0.342	0.000		
2.57 - 2.30	0.0044	0.0318	0.253	0.0576	0.000	
2.06 - 1.85	0.0023	0.0222	0.133	0.273	0.0021	0.000
1.65 - 1.48	0.0047	0.0277	0.100	0.273	0.0509	0.0061
1.32 - 1.19	0.0070	0.0336	0.0827	0.249	0.194	0.0640
1.06 - 0.951	0.0098	0.0374	0.0788	0.221	0.349	0.0462
0.851 - 0.768	0.0137	0.0348	0.0814	0.209	0.381	0.155
0.682 - 0.611	0.0191	0.0457	0.0897	0.205	0.403	0.309
0.547 - 0.489	0.0215	0.0531	0.0969	0.197	0.404	0.492
0.382	0.0348	0.0604	0.103	0.184	0.365	0.541
0.205	0.0697	0.0868	0.118	0.184	0.345	0.453
0.102	0.101	0.117	0.137	0.181	0.288	0.404
0.0512	0.133	0.148	0.160	0.182	0.245	0.414
0.0256	0.171	0.180	0.191	0.202	0.237	0.332
0.0128	0.210	02.19	0.227	0.232	0.252	0.334
0.00640	0.256	0.261	0.270	0.274	0.286	0.349
0.00320	0.313	0.318	0.326	0.332	0.344	0.383
0.00160	0.392	0.398	0.406	0.416	0.428	0.458
0.000800	0.513	0.520	0.533	0.542	0.558	0.587
0.000547	0.610	0.619	0.631	0.646	0.665	0.694
0.000510	0.786	0.797	0.813	0.831	0.855	0.899
0.000400	0.878	0.891	0.908	0.929	0.956	1.00
0.000200	1.31	1.30	1.36	1.39	1.43	1.49
0.000100	2.40	2.44	2.49	2.55	2.62	2.72

Table A7.2 ELECTRON FLUX SPECTRUM: T_o = 10 MEV

Electron Kinetic Energy T/MeV	Total Electron Flux, normalized to 1 MeV total dissipation $F(T,z)/cm^{-1}.MeV^{-1}$					
	z/r_o					
	0.0-0.1	0.2-0.3	0.4-0.5	0.6-0.7	0.8-0.9	1.0-1.1
10.00 - 8.93	0.466	0.000				
7.98 - 7.12	0.0067	0.312	0.000			
6.36 - 5.68	0.0014	0.0315	0.212	0.000		
5.08 - 4.53	0.0017	0.0138	0.105	0.0421		
4.05 - 3.62	0.0012	0.0095	0.0560	0.162	0.000	0.000
3.23 - 2.89	0.0017	0.0103	0.0387	0.137	0.0310	0.0082
2.58 - 2.30	0.0027	0.0116	0.0329	0.112	0.121	0.000
2.06 - 1.84	0.0041	0.0112	0.0326	0.101	0.188	0.0050
1.64 - 1.46	0.0057	0.0133	0.0349	0.0954	0.210	0.0434
1.31 - 1.17	0.0084	0.0173	0.0407	0.0859	0.209	0.142
1.04 - 0.932	0.0134	0.0195	0.0473	0.0896	0.211	0.290
0.832 - 0.743	0.0130	0.0264	0.0500	0.0952	0.211	0.308
0.579	0.0239	0.0372	0.0587	0.102	0.210	0.391
0.410	0.0379	0.0529	0.0693	0.112	0.214	0.389
0.205	0.0674	0.0866	0.0920	0.123	0.199	0.366
0.102	0.103	0.115	0.121	0.139	0.190	0.321
0.0512	0.141	0.145	0.150	0.163	0.192	0.295
0.0256	0.175	0.182	0.183	0.191	0.208	0.289
0.0128	0.213	0.216	0.220	0.224	0.237	0.303
0.00640	0.254	0.258	0.261	0.267	0.278	0.331
0.00320	0.310	0.313	0.318	0.324	0.335	0.378
0.00160	0.389	0.392	0.397	0.405	0.417	0.454
0.000800	0.508	0.512	0.519	0.528	0.545	0.578
0.000547	0.604	0.610	0.617	0.629	0.648	0.683
0.000510	0.779	0.786	0.795	0.811	0.834	0.881
0.000400	0.870	0.878	0.888	0.910	0.932	0.981
0.000200	1.30	1.31	1.33	1.35	1.39	1.46
0.000100	2.38	2.41	2.44	2.48	2.55	2.67

Table A7.3 ELECTRON FLUX SPECTRUM: T_o = 20 MEV

Electron Kinetic Energy T/MeV	Total Electron Flux, normalized to 1 MeV total dissipation $F(T,z)/cm.^{-1}.MeV^{-1}$					
	z/r_o					
	0.0-0.1	0.2-0.3	0.4-0.5	0.6-0.7	0.8-0.9	1.0-1.1
20.00 - 17.90	0.228	0.000				
16.03 - 14.35	0.00349	0.137	0.000			
12.85 - 11.50	0.00245	0.0167	0.108	0.000	0.000	
10.30 - 9.22	0.00130	0.0110	0.0513	0.0300	0.00012	0.000
8.25 - 7.39	0.00122	0.0076	0.0220	0.0796	0.00050	0.000
6.61 - 5.92	0.00087	0.0065	0.0178	0.0629	0.0215	0.00106
5.30 - 4.75	0.00079	0.0052	0.0184	0.0469	0.0706	0.00342
4.25 - 3.80	0.00074	0.0059	0.0176	0.0409	0.0938	0.00770
3.40 - 3.05	0.00164	0.0070	0.0156	0.0428	0.100	0.0262
2.73 - 2.44	0.00204	0.0098	0.0169	0.0426	0.0941	0.0641
2.19 - 1.96	0.00479	0.0123	0.0195	0.0437	0.0949	0.119
1.75 - 1.57	0.00693	0.0164	0.0217	0.0452	0.0931	0.164
1.40 - 1.26	0.00869	0.0197	0.0247	0.0462	0.0930	0.205
1.13 - 1.01	0.0129	0.0237	0.0281	0.0500	0.0980	0.207
0.819	0.0172	0.0306	0.0348	0.0564	0.104	0.219
0.410	0.0399	0.0538	0.0584	0.0765	0.117	0.231
0.205	0.0729	0.0834	0.0909	0.102	0.132	0.231
0.102	0.107	0.113	0.121	0.127	0.146	0.225
0.0512	0.141	0.145	0.149	0.157	0.168	0.227
0.0256	0.175	0.179	0.183	0.185	0.197	0.245
0.0128	0.212	0.215	0.217	0.221	0.230	0.266
0.00640	0.253	0.256	0.259	0.263	0.271	0.299
0.00320	0.309	0.312	0.315	0.319	0.327	0.351
0.00160	0.387	0.390	0.393	0.398	0.407	0.430
0.000800	0.505	0.510	0.513	0.519	0.530	0.550
0.000547	0.602	0.607	0.611	0.618	0.631	0.658
0.000510	0.775	0.782	0.787	0.796	0.813	0.848
0.000400	0.866	0.873	0.879	0.890	0.908	0.946
0.000200	1.29	1.30	1.31	1.33	1.35	1.41
0.000100	2.37	2.39	2.41	2.44	2.49	2.59

Table A7.4 ELECTRON FLUX SPECTRUM: T_o = 30 MEV

Electron Kinetic Energy T/MeV	Total Electron Flux, normalized to 1 MeV total dissipation $F(T,z)/cm^{-1}.MeV^{-1}$					
	z/r_o					
	0.0-0.1	0.2-0.3	0.4-0.5	0.6-0.7	0.8-0.9	1.0-1.1
30.00 - 26.91	0.152	0.000			0.000	
24.13 - 21.64	0.00248	0.0847	0.000		0.00009	0.000
19.41 - 17.41	0.00138	0.0137	0.0707	0.000	0.000	0.00030
15.62 - 14.01	0.00064	0.00649	0.0268	0.0315	0.000	0.00008
12.56 - 11.27	0.00069	0.00567	0.0168	0.0461	0.00094	0.00008
10.10 - 9.06	0.00064	0.00482	0.0135	0.0339	0.0264	0.00050
8.13 - 7.29	0.00056	0.00441	0.0117	0.0265	0.0527	0.00061
6.54 - 5.86	0.00065	0.00447	0.0113	0.0273	0.0569	0.00782
5.26 - 4.72	0.00114	0.00525	0.0113	0.0270	0.0533	0.0295
4.23 - 3.79	0.00154	0.00587	0.0105	0.0256	0.0546	0.0606
3.40 - 3.05	0.00203	0.00728	0.0112	0.0256	0.0526	0.0753
2.74 - 2.46	0.00277	0.00900	0.0141	0.0261	0.0515	0.100
2.20 - 1.98	0.00418	0.0110	0.0184	0.0306	0.0538	0.116
1.77 - 1.59	0.00624	0.0143	0.0202	0.0333	0.0562	0.125
1.24	0.0102	0.0185	0.0247	0.0375	0.0612	0.134
0.819	0.0217	0.0289	0.0348	0.0484	0.0735	0.146
0.410	0.0460	0.0520	0.0586	0.0700	0.0926	0.156
0.205	0.0748	0.0799	0.0853	0.0931	0.115	0.170
0.102	0.109	0.111	0.115	0.123	0.137	0.185
0.0512	0.142	0.146	0.148	0.155	0.163	0.201
0.0256	0.177	0.177	0.184	0.187	0.194	0.223
0.0128	0.212	0.212	0.219	0.221	0.229	0.251
0.00640	0.254	0.255	0.260	0.262	0.269	0.287
0.00320	0.309	0.311	0.314	0.317	0.323	0.340
0.00160	0.387	0.389	0.392	0.396	0.402	0.418
0.000800	0.506	0.508	0.512	0.516	0.524	0.542
0.000547	0.602	0.605	0.609	0.614	0.623	0.644
0.000510	0.775	0.779	0.784	0.792	0.803	0.829
0.000400	0.866	0.870	0.876	0.884	0.897	0.925
0.000200	1.29	1.30	1.31	1.32	1.34	1.38
0.000100	2.37	2.38	2.40	2.42	2.46	2.53

APPENDIX 7

TABLES OF COMPUTED ELECTRON FLUX SPECTRA IN WATER FOR ELECTRON BEAMS

The results computed by the electron-photon cascade program for T_o = 5, 10, 20 and 30 MeV, for 2000 primary electron histories at each T_o, are given in tables A7.1, A7.2, A7.3 and A7.4 for the four T_o respectively. The upper half of each table corresponds to the Monte Carlo calculation from T_o down to T_c. Beginning with T_o, every other energy spectrum interval is given - e.g. in table A7.2, the flux in the highest interval (10 - 8.93 MeV) is tabulated but the next interval (8.93 - 7.98) has been omitted. The Monte Carlo values have <u>not</u> been 'smoothed'; they were taken straight from the computer printouts.

The lower half of the tables correspond to the depth-independent flux computation (see chapter 5, for instance). The actual number of energy bands for which the flux was computed (and which appear on the printout) was such that 10 bands covered a factor of two in energy (B_w = 10). Only every tenth flux value is given in the tables, but is sufficient to define the flux spectrum. Note that the energies 0.000547 and 0.000510 (MeV) have been specifically included to show the effect of the Auger electrons on the spectrum.

Table A8.1 ELECTRON FLUX SPECTRUM: 2 MV, ^{60}Co, 6 MV photon radiation

$F(T,z)$ is in units of $cm^{-1}.MeV^{-1}$, normalized to 1 MeV total dissipation				6 MV x-rays (E)	
2 MV x-rays (A)		^{60}Co γ (B)			
T/MeV	F(T,z) z = 4.5-5.5 cm	T/MeV	F(T,z) z = 4-6 cm	T/MeV	F(T,z) z = 4.5-5.5 cm
1.97 - 1.79	0.00000	1.33 - 1.26	0.00000	4.96 - 4.29	0.00014
1.79 - 1.63	0.00003	1.26 - 1.19	0.00000	4.29 - 3.71	0.00052
1.63 - 1.48	0.00077	1.19 - 1.13	0.00000	3.71 - 3.21	0.00130
1.48 - 1.34	0.00354	1.13 - 1.07	0.0102	3.21 - 2.78	0.00611
1.34 - 1.22	0.00603	1.07 - 1.01	0.0406	2.78 - 2.40	0.0171
1.22 - 1.11	0.0163			2.40 - 2.08	0.0286
1.11 - 1.01	0.0274	0.975	0.058	2.08 - 1.80	0.0429
		0.909	0.115	1.80 - 1.56	0.0602
0.941	0.0466	0.819	0.180	1.56 - 1.35	0.0709
0.819	0.0803	0.713	0.253	1.35 - 1.17	0.0980
0.579	0.164	0.579	0.333	1.17 - 1.01	0.129
0.410	0.286	0.410	0.418		
0.290	0.386		0.462	0.941	0.149
0.205	0.492	see	0.490	0.764	0.209
0.102	0.599	column 1	0.491	0.579	0.275
0.0542	0.637		0.483	0.410	0.342
0.0256	0.615		0.468		0.385
0.0128	0.526		0.422	see	0.408
0.00640	0.481		0.410	column 1	0.410
0.00320	0.475		0.428		0.395
0.00160	0.521		0.488		0.388
0.000800	0.636		0.609		0.366
0.000547	0.742		0.716		0.367
0.000510	0.954		0.922		0.398
0.000400	1.06		1.02		0.466
0.000200	1.56		1.52		0.589
0.000100	2.86		2.79		0.695
					0.895
					0.996
					1.48
					2.72

Table A8.2 ELECTRON FLUX SPECTRUM: 19 MV, 27 MV x-rays

$F(T,z)$ in $cm^{-1}.MeV^{-1}$, norm. to 1 MeV total dissipation

19 MV (betatron - G)		26.8 MV (linac - H)		26.8 MV (thin-target - I)	
T/MeV	F(T,z) z = 6-8 cm	T/MeV	F(T,z) z = 10-12 cm	T/MeV	F(T,z) z = 10-12 cm
18.25 - 16.48	0.00002	26.50 - 23.96	0.00001	26.25 - 23.74	0.00003
14.88 - 13.44	0.00071	21.66 - 19.59	0.00016	21.47 - 19.42	0.00067
12.14 - 10.96	0.00180	17.71 - 16.01	0.00095	17.56 - 15.88	0.00190
9.90 - 8.94	0.00381	14.47 - 13.09	0.00177	14.37 - 12.99	0.00341
8.07 - 7.29	0.0101	11.83 - 10.70	0.00355	11.75 - 10.63	0.00505
6.58 - 5.94	0.0179	9.67 - 8.74	0.00723	9.61 - 8.69	0.00748
5.37 - 4.85	0.0240	7.91 - 7.15	0.0116	7.86 - 7.11	0.0113
4.38 - 3.95	0.0396	6.46 - 5.84	0.0124	6.43 - 5.82	0.0187
3.57 - 3.22	0.0448	5.28 - 4.78	0.0189	5.26 - 4.76	0.0212
2.91 - 2.63	0.0538	4.32 - 3.90	0.0262	4.30 - 3.89	0.0309
2.37 - 2.14	0.0675	3.53 - 3.19	0.0393	3.52 - 3.18	0.0452
1.94 - 1.75	0.0797	2.89 - 2.61	0.0547	2.88 - 2.60	0.0591
1.58 - 1.43	0.0834	2.36 - 2.13	0.0590	2.35 - 2.13	0.0751
		1.93 - 1.74	0.0813	1.93 - 1.74	0.0829
		1.58 - 1.43	0.0975	1.58 - 1.43	0.0996
1.24	0.109	see	0.109	see	0.108
0.819	0.157	column 1	0.158	column 1	0.143
0.410	0.204		0.214		0.182
0.205	0.234		0.243		0.213
0.102	0.245		0.262		0.231
0.0512	0.261		0.264		0.243
0.0256	0.275		0.276		0.257
0.0128	0.285		0.286		0.270
0.00640	0.312		0.311		0.301
0.00320	0.357		0.357		0.350
0.00160	0.432		0.432		0.426
0.000800	0.555		0.555		0.548
0.000547	0.657		0.658		0.651
0.000510	0.847		0.848		0.838
0.000400	0.944		0.945		0.935
0.000200	1.41		1.41		1.39
0.000100	2.58		2.58		2.56

Table A8.3 ELECTRON FLUX SPECTRUM : 31 MV betatron x-rays (J)

F(T,z) in $cm^{-1}.MeV^{-1}$, norm. to 1 MeV total diss.

T / MeV	F(T,z)	
	z = 0-1 cm	z = 6-7 cm
30.50 - 27.85	0.00002	0.00001
25.43 - 23.22	0.00028	0.00042
21.20 - 19.36	0.00092	0.00109
17.68 - 16.15	0.00100	0.00270
14.74 - 13.46	0.00123	0.00459
12.29 - 11.23	0.00273	0.00840
10.25 - 9.36	0.00487	0.0103
8.55 - 7.81	0.00953	0.0161
7.13 - 6.51	0.00949	0.0218
5.94 - 5.43	0.0121	0.0257
4.96 - 4.53	0.0126	0.0296
4.13 - 3.77	0.0297	0.0339
3.45 - 3.15	0.0260	0.0408
2.87 - 2.62	0.0263	0.0547
2.40 - 2.19	0.0370	0.0597
2.00 - 1.82	0.0559	0.0733
1.67 - 1.52	0.0596	0.0761
1.39 - 1.27	0.0554	0.0929
1.08	0.101	0.101
0.819	0.179	0.119
0.410	0.271	0.162
0.205	0.327	0.198
0.102	0.325	0.220
0.0512	0.335	0.243
0.0256	0.314	0.253
0.0128	0.305	0.271
0.00640	0.324	0.298
0.00320	0.366	0.346
0.00160	0.440	0.422
0.000800	0.565	0.544
0.000547	0.669	0.646
0.000510	0.862	0.832
0.000400	0.961	0.929
0.000200	1.43	1.38
0.000100	2.63	2.54

APPENDIX 8

TABLES OF COMPUTED ELECTRON FLUX SPECTRA IN WATER FOR PHOTON BEAMS

The results computed by the photon-electron cascade program for 2 MV x-rays (A), ^{60}Co γ-rays (B), 6 MV x-rays (E), 19 MV betatron x-rays (G), 26.8 MV linac x-rays (H), 26.8 MV thin-target x-rays (I) and 31 MV betatron x-rays (J) are given in tables A8.1, A8.2 and A8.3. More details about these photon beams are to be found in table 8.1 (see also section 8.4.4).

Similar remarks apply here as for the electron beam tables in Appendix 7. Note that there are considerable statistical fluctuations in the Monte Carlo F(T,z) values in the 0-1 cm layer for the 31 MV beam. The flux in the 6-7 cm layer at this quality is negligibly different from that at the calibration depth i.e. 10 cm.

GLOSSARY

(by the chapters in which the quantities first appear)

Chapter 1

T	:	Electron kinetic energy.
$G(Fe^{3+})$	:	Number of ferric ions produced per 100 eV absorbed energy.
$F(T)$	:	Electron flux - pathlength of electrons with K.E. between T and T + dT.
D	:	Absorbed dose - energy dissipated per unit mass.
$L_{\Delta}(T)$	:	Collision stopping power restricted to losses less than Δ. (Linear Energy Transfer).
Δ	:	Energy transfer cutoff value.
Q_T	:	Local (<100 eV) energy dissipation spectrum.
$Q_T \Delta T$	:	Local energy dissipation between electron kinetic energies T and T + ΔT.
J_g	:	Ionization charge per unit mass of gas.
$\bar{W}$	:	Average energy absorbed per ion pair.
$\bar{s}_{mg}$	:	Mass stopping-power ratio.
C_E	:	Conversion factor for electron beams for use with exposure-calibrated secondary standard ionization chamber.
C_λ	:	Equivalent factor for photon beams.
$N(T)$	:	Electron source spectrum - no. per unit volume.
q	:	Energy transfer.
I	:	Mean ionization potential.
MV, kV	:	Used to denote maximum photon energy in an x-ray spectrum.
dT/dx	:	Stopping power.

Chapter 2

R	:	Random number between 0 and 1.
θ	:	Polar direction in X,Y,Z system.
ϕ	:	Azimuthal direction in X,Y,Z system.

Ψ : Polar deflection, relative to particle direction.

Φ : Azimuthal deflection, realtive to particle direction.

Chapter 3

k : Photon energy.

$\mu(k)$: Photon attenuation coefficient.

T_{aug} : Kinetic energy of Auger electron.

λ : Compton wavelength of a photon.

T_e : Kinetic energy of Compton electron.

E_- : Total energy of pair electron.

E_+ : Total energy of pair positron.

ZEND : Penetration-depth cutoff in photon transport simulation.

Chapter 4

T_o : Initial electron K.E.

T_c : Monte Carlo electron K.E. cutoff.

r_o : C-s-d-a electron range.

$\Delta(T)$: Cutoff for catastrophic energy losses in electron transport simulation.

μ_δ : Attenuation coefficient for catastrophic δ-ray events.

ε : Energy transfer in units of kinetic energy, T.

q_{div} : Energy transfer below which the Møller cross-section can be approximated by a $1/q^2$ distribution.

P_q : Probability that catastrophic collision loss is less than q_{div}.

E_o : Total electron energy.

μ_b : Attenuation coefficient for catastrophic bremsstrahlung events.

μ_{cat} : Total attenuation coefficient for catastrophic events.

s_{cat} : Mean free path between catastrophic events.

δ : Density effect stopping-power reduction.

T_a : Electron K.E. at beginning of a pathlength step.

T_b : Electron K.E. at end of a pathlength step.

$\overline{\psi^2}$: Mean square deflection in Gaussian multiple-scattering distribution.

s_{max} : Maximum allowed pathlength step.

δ_T : Maximum percentage change in electron K.E. corresponding to s_{max}.

T_δ : Kinetic energy of δ-ray.

H : Number of Monte Carlo histories.

Z_l, Z_h : Boundaries of a spectrum 'slice' or layer.

s_f : Part of electron pathlength step within spectrum layer.

Ip(...) : The integral part of (...).

N_i : Number of Monte Carlo spectrum intervals.

Chapter 5

I_{eff} : Effective I-value for the 8 'free' electrons below 500 eV in water.

B_w : Energy band width parameter; B_w bands cover a factor 2 in energy.

l_{100} : Number of energy band which has maximum energy of 100 eV.

T_l : Electron K.E. at top of band l.

$\bar{T}_l$: Geometric mean electron K.E. in band l.

N_l : Number of electrons slowing down in band l.

D_{100} : Energy dissipated by electron flux in transfers less than 100 eV.

ΣN_l^δ : Number of δ-rays starting at the top of band l produced by electrons in higher energy bands.

Chapter 6

H_j : Number of photon histories of energy k_j.

W_j : Weight attached to the H_j histories.

k_o : Initial photon energy.

$\bar{T}_i$: Geometric mean electron K.E. in MC spectrum interval.

D_Δ : Local energy dissipation per unit mass (local dose) for a cutoff Δ.

N_Δ : Number of electron track ends of energy Δ.

Chapter 7

r_p : Practical electron range.

Chapter 8

$\bar{k}_{int}$: Energy fluence (intensity) average over photon spectrum.

Chapter 9

$\bar{\mu}_{en}/\rho$: Photon mass energy absorption coefficient.

$S(T,\Delta)$: Restricted collision stopping power in Spencer-Attix theory.

$L(T,\Delta)$: Restricted collision stopping power as evaluated from equ. 4.18.

$S_a^w(T_o,z,\Delta)$: Water/air mass stopping power ratio for an electron beam, as evaluated from equ. 9.5.

$S_a^w(\lambda,z,\Delta)$: As above, but for a photon beam.

$\Sigma N_\Delta.\Delta$: Total dissipation per unit mass by the track ends.

$\bar{s}_a^w(T)$: Water/air mass stopping power ratio for electrons of kinetic energy T.

$D_{ph}(\Delta)$: Energy dissipation per unit mass from photon-ejected electrons with initial energies less than Δ.

$\bar{\mu}_a^w(\Delta)$: Water/air mass energy absorption coefficient ratio corresponding to the photon-ejected track ends.

$S_a^w(B\text{-}G)$: Water/air Bragg-Gray stopping-power ratio as evaluated from equ. 9.12.

$\bar{s}_a^w(\lambda)$: Approximate evaluation of the Bragg-Gray ratio for photon beams at equilibrium depths.

k_{max} : Maximum energy in photon beam (MV, kV).

Chapter 10

d_c : Displacement factor for Baldwin-Farmer type chamber at the calibration radiation.

$(C_\lambda)_c$: C_λ factor for the calibration radiation.

p_E, p_λ : Perturbation factors for ionization chambers for electron, photon beams respectively.

$\Delta_{eff}(\lambda)$: Effective cavity-size parameter for the B-F chamber for photon radiation λ.

$\bar{T}_p$: Mean primary electron energy for electron or photon beam.

$(\bar{s}_{mg})_E$: Stopping-power ratio appropriate to B-F chamber for electron beam E.

$(\bar{s}_{mg})_\lambda$: As above, but for photon beam λ.

Chapter 11

$G_{Fe^{3+}}$: Ferric ion G-value corresponding to energy dissipated at a particular local LET.

G_T or G(T) : As above, but expressed as a function of electron K.E.

REFERENCES

ABILLON E. (1972). p.529 of 'Third Symposium on Microdosimetry' (Stresa, 1971), Ebert, ed. (Euratom, Brussels).

AITKEN J.H. AND HENRY W.M. (1964). Int. J. Appl. Rad. 15, 713.

ALLEN A.O. (1954). Radiation Research 1,85.

ALMOND P.R. (1967). Phys. Med. Biol. 12, 13.

ALMOND P.R. (1968). Phys. Med. Biol. 13, 285.

ALMOND P.R. (1970). Int. J. Appl. Rad. 21, 1.

ALMOND P.R. (1974). Personal Communication.

ALMOND P.R. AND JAHNS M.F. (1971). Phys. Med. Biol. 16, 497.

BARNARD G.P., AXTON E.J. AND MARSH A.R.S. (1959). Phys. Med. Biol. 3, 366.

BENTLEY R.E., JONES J.C. AND LILLICRAP S.C. (1967). Phys. Med. Biol. 12, 312.

BERGER M.J. (1963). p. 135 in 'Methods in Computational Physics', vol. 1, Alder, Fernbach and Totenberg, Eds. (Academic Press, Inc. New York).

BERGER M.J. (1965). NBS report 8678. (U.S. Dept. of Commerce).

BERGER M.J. AND SELTZER S.M. (1964). NASA SP-3012 (National Aeronautics and Space Administration, Washington, D.C.).

BERGER M.J. AND SELTZER S.M. (1969). Ann. New York Acad. Sci. 161, 8.

BERGER M.J. AND SELTZER S.M. (1969a). 12th Int. Congr. Radiol., Tokyo (reprint courtesy of authors).

BERGER M.J. AND SELTZER S.M. (1970). Phys. Rev. C 2, 621.

BERGER M.J., SELTZER S.M., DOMEN S.R. AND LAMPERTI P.J. (1975). IAEA Symp. on Adv. Biom. Dosimetry. Vienna, March 1975 (pre-print courtesy of authors).

BETHE H.A. AND ASHKIN J. (1953). p. 304 in vol. I, Exp. Nucl. Phys., Ed. E. Segrè (John Wiley and sons inc.).

BEWLEY D.K. (1963). Br. J. Radiol. 36, 865.

BICHSEL H. (1968). p. 157 in vol. 1, 'Radiation Dosimetry', Eds. Attix and Roesch (Academic Press Inc., New York).

BINKHOFF R.D., HUBBELL H. H., CHEKA J.S. AND RITCHIE R.H. (1958). Health Physics, 1, 27.

BRAHME A., HULTÉN G. AND SVENSSON H. (1975). Phys. Med. Biol. 20, 39.

BRUCE W.R., PEARSON M.L. AND FREEDHOFF H.S. (1963). Radiation Research 19, 606.

BRYSK H. (1954). Phys. Rev. 96, 419.

BRUCE W.R. AND JOHNS H.E. (1960). Br. J. Radiol. Suppl. no. 9.

BURCH P.R.J. (1955). Radiation Research 3, 361.

BURCH P.R.J. (1957). Br. J. Radiol. 30, 524.

BURCH P.R.J. (1957a). Radiation Research 6, 289.

BURCH P.R.J. (1959). Radiation Research 11, 481.

BURCH P.R.J. AND BIRD P.M. (1956). p. 16 in 'Progress in Radiobiology', Eds. Mitchell, Holmes and Smith (The Kynoch Press, Birmingham).

BURLIN T.E. (1962). Br. J. Radiol. 35, 343.

BURLIN T.E. (1966). Br. J. Radiol. 39, 727.

COHEN A.J. AND KORAL K.F. (1965). NASA-TND-2782. (cited by Patau, 1972).

CORMACK D.V. AND JOHNS H.E. (1952). Br. J. Radiol. 25, 369.

CORMACK D.V., DAVITT W.E., BURKE B.E. AND RAWSON B.A. (1958). Br. J. Radiol. 31, 565.

DALTON P. AND TURNER J.E. (1968). Health Physics, 15, 257.

DANZKER M., KESSARIS N.D. AND LAUGHLIN J.S. (1959). Radiology 72, 51.

DAVIES J.V. AND LAW J. (1963). Phys. Med. Biol. 8, 91.

DAVIES M. (1955). Nature 175, 427.

DAY M.J., GREENE D. AND MASSEY J.B. (1965). Phys. Med. Biol. 10, 111.

ELLETT W.H., BROWNELL G.L. AND REDDY A.R. (1968). Phys. Med. Biol. 13, 219.

EPP E.R., WEISS H. AND HESLIN J. (1965). p. 324 of Proc. 11th Int. Congr. Radiology, Rome 1965. (Excerpta Medica Foundation, Amsterdam).

EPP E.R., WEISS H. AND HESLIN J. (1972). Radiation Research 51, 211.

EVANS R.D. (1968). p. 94 in vol. 1 of 'Radiation Dosimetry', Ed. Attix and Roesch (Academic Press Inc., New York).

FANO U. (1954). Radiation Research 1, 1954.

FANO U., SPENCER L.V. AND BERGER M.J. (1959). In 'Handbuch der Physik' (S. Flugge, ed.), vol. 38, part II, p. 660. Springer. Berlin.

FREGENE A.O. (1967). Radiation Research 31, 256.

FRICKE H. AND HART E.J. (1966). p. 167 in 'Radiation Dosimetry', vol. II, Eds. Attix and Roesch (Academic Press Inc., New York).

GOLDSTEIN H. AND WILKINS J.E., NYO-3079, Nuclear Development Associates Memo, NDA ^{13}C-41 (Dept. of Commerce, Washington, D.C.) - cited by Bruce and Johns, 1960.

GRAY L.H. (1951). J. Chim. Phys. 48, 1951.

GRAY L.H. (1955). J. Chim. Phys. 52, 519.

GREENE D. (1962). Phys. Med. Biol. 7, 213.

GREENE D. AND MASSEY J.B. (1966). Phys. Med. Biol. 11, 569.

GREENE D. AND MASSEY J.B. (1968). Phys. Med. Biol. 13, 287.

GREENE D., MASSEY J.B. AND MEREDITH W.J. (1971). Phys. Med. Biol. 16, 319.

GREENING J.R.G. (1954). Br. J. Radiol. 27, 163.

GREENING J.R.G. (1971). Personal Communication.

GREENING J.R.G. (1974). Phys. Med. Biol. 19, 746.

HANSEN W.E. AND FULTZ S.C. (1960). Univ. of California Rep., U.C.R.L. 6099. (cited by Bentley et al., 1967).

HARDER D. (1965). Thesis. University of Würzburg.

HARDER D. (1965a). p. 40 of 'Symposium on High-Energy Electrons-Montreux, 1964. Zuppinger and Poretti, eds., (Springer Verlag, Berlin).

HARDER D. (1966).p. 140 of 'Biophysical Aspects of Radiation Quality', IAEA Techn. Rep. Ser. No. 58 (IAEA, Vienna).

HARDER D. (1968). Biophysik, 5, 157.

HARDER D. (1974). p. 677 of 'Fourth Symposium on Microdosimetry' (Pallanza, 1973), Eds. Booz, Ebert, Eickel and Waker. (Euratom, Brussels).

HARDER D. AND POSCHET G. (1967). Phys. Letters 24B, 519.

HAYNES H. AND DOLPHIN G.W. (1959). Phys. Med. Biol. 4, 148.

HEITLER W. (1954). 'The Quantum Theory of Radiation'. (Oxford Univ. Press).

HETTINGER G., PETTERSSON C. AND SVENSSON H. (1967). Acta Radiol. (Ther.) 6, 214.

HOLT P.D. (1970). p. 42 in 'Charged Particle Tracks in Solids and Liquids' (Publ. by The Institute of Physics and the Physical Society).

HOLT P.D. (1974). Private Communication.

HPA (1971). 'A Practical Guide to Electron Dosimetry (5-35 MeV)', (The Hospital Physicists'Association, London).

HUBBELL J.H. (1969). National Bureau of Standards Report No. NSRDS-NBS29. (U.S. Dept. of Commerce).

ICRU* (1962). Report 10b 'Physical Aspects of Irradiation' (publ. by U.S. Dept. of Commerce).

ICRU (1969). Report 14. 'Radiation Dosimetry: X-Rays and Gamma Rays with Maximum Photon Energies Between 0.6 and 50 MeV' (publ. by ICRU, Washington, D.C.).

ICRU (1970). Report 16 'Linear Energy Transfer' (publ. by ICRU, Washington, D.C.).

ICRU (1970a). Report 18. 'Specification of High Activity Gamma Ray Sources' (publ. by ICRU, Washington, D.C.).

ICRU (1970b). Report 17. 'Radiation Dosimetry: X-Rays Generated at Potentials of 5 to 150 kV' (publ. by ICRU, Washington, D.C.).

ICRU (1971). Report 19. 'Radiation Quantities and Units' (publ. by ICRU, Washington, D.C.).

ICRU (1972). Report 21. 'Radiation Dosimetry: Electrons with Initial Energies Between 1 and 50 MeV' (publ. by ICRU, Washington, D.C.).

INADA T., HOSHINO K., AND MATSUZAWA H. (1969). p. 461 in 'Book of Abstracts, 12th Int. Congr. Radiol., Tokyo, 1969.

JOHNS H.E. AND RAWLINSON J.A. (1972). p. 232 in 'Digest of the 3rd Int. Conf. on Med. Phys. incl. Med. Eng.' Göteborg. (publ. by 3rd ICMP Executive Committee).

JOHNS H.E., KATZ L. AND HASLAM R.N.H. (1950). Phys. Rev. 80, 1062.

JOHNS H.E., TILL J.E. AND CORMACK D.J. (1954). Nucleonics. Vol. 12, No. 10, 40.

KAHN H. (1954). 'Applications of Monte Carlo'. United States Atomic Energy Commission Report AECU-3259 (cited by Zerby, 1963).

KESSARIS N.D. (1964). Radiation Research, 23, 630.

KESSARIS N.D. (1966). Phys. Rev. 145, 164.

KESSARIS N.D. (1970). Radiation Research 43, 281.

KESSARIS N.D. (1970a). Radiation Research, 43, 288.

KRETSCHKO J. (1960). Thesis. University of Frankfurt (cited by ICRU, 1972).

LAW J., LAWSON R.C. AND PORTER D. (1974). Phys. Med. Biol. 19, 643.

LAW J. AND NAYLOR G.P. (1971). Phys. Med. Biol. 16, 67.

LAW J. AND NAYLOR G.P. (1972). Phys. Med. Biol. 17, 400.

LEA D.E. (1946). 'Actions of Radiations on Living Cells' (Cambridge Univ. Press).

LEISS J.E., PENNER S. AND ROBINSON C.S. (1957). Phys. Rev. 107, 1544.

LEVY L.B., WAGGENER R.G., McDAVID W.D. AND PAYNE W.H. (1974). Medical Physics, 1, 62.

LEVY L.B., WAGGENER R.G. AND SPALLK R.J. (1975). Phys. Med. Biol. 20, 324.

LILLICRAP S.C. AND ROSENBLOOM M. (1972). Br. J. Radiol. 45, 229.

McCONNELL W.J., BIRKHOFF R.D., HAMM R.N. AND RITCHIE R.H. (1968). Radiation Research 33, 216.

McGINNIES R.T. (1959). NBS circular 597 (U.S. Dept. of Commerce).

MARSHALL M., GIBSON J.A.B. AND HOLT P.D. (1970). p. 529 in '2nd Symposium on Microdosimetry' Stresa, 1969 (Euratom, Brussels).

MATSUZAWA F. AND KAWASHIMA F. AND HIRAOKA T. (1974). Phys. Med. Biol. 19, 744.

MOZUMDER A. AND MAGEE J.L. (1966). Radiation Research, 28, 203.

NACP (1972). Acta Radiol. Ther. Phys. Biol. 11, 603.

NAS-NRC 1133 (1964). National Academy of Sciences - National Research Council, publication 1133. (U.S. Dept. of Commerce).

O'DELL A.A., SANDIFER C.W. KNOWLEN R.B. AND GEORGE W.D. (1968). Nucl. Instrum. Methods 61, 340.

PATAU J-P. (1972). Thesis.Paul-Sabatier University, Toulouse.

PATAU J-P., BLANC D., MATHIEU J. AND MASON G. (1970). p. 401 in ' Second Symposium on Microdosimetry', Stresa, 1969 (Euratom, Brussels).

PATAU, J-P., SAINT-PAUL A. AND BLANC D. (1972). p. 549 in 'Third Symposium on Microdosimetry,' Stresa, 1971 (Euratom, Brussels).

PERKINS J.F. (1962). Phys. Rev. 126, 1781.

PETTERSSON C. (1967). Arkiv f. Fysik 34, 385.

PINKERTON A.P. (1969). Ann. New York Acad. Sci. 161, 63.

RAUTH A.M. AND SIMPSON J.A. (1964). Radiation Research, 22, 643.

ROHRLICH F. AND CARLSON B.C. (1954). Phys. Rev. 93, 38.

ROSSI H.H. (1968). in 'Radiation Dosimetry' Vol. 1, Eds. Attix and Roesch (Academic Press Inc., New York).

SCHIFF I. (1946). Phys. Rev. 70, 87.

SCHIFF I. (1951). Phys. Rev. 83, 252.

SCHNEIDER D.O. AND CORMACK D.V. (1969). Radiation Research 11, 418.

SCHULER R.H. AND ALLEN A.O. (1956). J. Chem. Phys. 24, 56.

SCHULZ R.J. (1970). Phys. Med. Biol. 15, 563.

SCRAD (1971). Phys. Med. Biol. 16, 379.

SHALEK R.J. AND SMITH C.E. (1969). Ann. New York Acad. Sci. 161, 44.

SINCLAIR W.K. AND KOHN H.I. (1964). Radiology 82, 800.

SPENCER L.V. (1955). Phys. Rev. 98, 1057.

SPENCER L.V. (1959). 'Energy Dissipation by Fast Electrons.' NBS Monograph 1. (U.S. Dept. of Commerce).

SPENCER L.V. AND ATTIX F.H. (1955). Radiation Research 3, 239.

SPENCER L.V. AND FANO U. (1951). J. Res. of NBS 46, 446. (cited by Brysk, 1954).

SPENCER L.V. AND FANO U. (1954). Phys. Rev. 93, 1172.

STERNHEIMER R.M. (1952). Phys. Rev. 88, 851.

STERNHEIMER R.M. (1956). Phys. Rev. 103, 511.

STERNHEIMER R.M. (1961). In 'Methods of Experimental Physics' Vol. 5 - Part A. Ed. Yuan and Wu .

STERNHEIMER R.M. AND PEIERLS R.F. (1971). Phys. Rev. 3, 3681.

STORM E. AND ISRAEL H.I. (1967). University of California, Los Alamos Report LA-3753.

STORM E. AND ISRAEL H.I. (1970). Nuclear Data Tables A7, 565.

SVENSSON H. (1971). Acta Radiol. Ther. Phys. Biol. 10, 631.

SVENSSON H. AND PETTERSSON S. (1967). Arkiv f. Fysik 34, 377.

SVENSSON H., HETTINGER G. AND PETTERSSON C. (1967). p.251 'Symposium on solid state and chemical reaction dosimetry in medicine and biology (IAEA, Vienna).

SVENSSON H., HULTÉN G., HETTINGER G. AND WICKMAN G. (1974). 12th Int. Congr. Radiol. Madrid 1973 (courtesy of H. Svensson).

TEDMAN B.M. (1975). Thesis. University of Edinburgh.

TILL J.E. (1954). Thesis. University of Saskatchewan (cited by Schneider and Cormack, 1959).

TRUMBORE C.N. (1958). J. Am. Chem. Soc. 80, 1772.

TURNER J.E., ROECKLEIN P.D. AND VORA R.B. (1970). Health Physics 18, 159.

WARD G. AND DOLPHIN G.W. (1960). Phys. Med. Biol. 4,391.

WIDERÖE R. (1970). p. 42 in 'Symposium on High-Energy Electrons' Madrid, 1966, Eds. Gil y Gil and Gil Gayarre (General Directorate of Health, Madrid).

WILKIE R.H. AND BIRKHOFF R.D. (1963). ORNL 3469 (Oak Ridge National Laboratory).

WRIGHT K.A. AND TRUMP J.G. (1962). J. Appl. Phys. 33, 687.

YANG C.N. (1951). Phys. Rev. 84, 599.

ZENDLE B., KOCH H.W., McELHINNEY J., AND BOAG J.W. (1956). Radiation Research 5, 107.

ZERBY C.D. (1963). p. 90 in 'Methods in Computational Physics', Vol. 1, Alder, Fernbach and Rotenberg, Eds. (Academic Press, Inc., New York).

---

*ICRU is the 'International Commission on Radiation Units and Measurements'.

ACKNOWLEDGEMENTS

My thanks are due to:

The Faculty of Medicine of the University of Edinburgh for providing me with a Graduate Research Scholarship for the duration of this work.

Professor J.R. Greening, my supervisor, for the countless valuable discussions and for his encouragement throughout the project.

Dr. J. Law for many helpful discussions, particularly in the early stages of the work concerning the Ferrous-Sulphate dosimeter.

Keith Boardman, in the Department, and the advisory staff at the Edinburgh Regional Computing Centre, for their much appreciated help with programming problems.

All the members of the Department of Medical Physics and especially my fellow research students for their company, interest and assistance.

The workers in the field whom I have either met or corresponded with, for their interest and for their valuable help; of whom Hans Svensson, Dietrich Harder, Martin Berger, Peter Holt and W.G. Burns deserve a special mention.

Helen Scott and Dorothy McKinna for typing this manuscript.

Elisabet, for keeping me sane during this seemingly never-ending task.